

Springer Series in Materials Science 161

Jyotsna Dutta Majumdar
Indranil Manna *Editors*

Laser-Assisted Fabrication of Materials

 Springer

Springer Series in Materials Science

Volume 161

Series Editors

Robert Hull, Charlottesville, VA, USA
Chennupati Jagadish, Canberra, ACT, Australia
Richard M. Osgood, New York, NY, USA
Jürgen Parisi, Oldenburg, Germany
Zhiming M. Wang, Fayetteville, AR, USA

For further volumes:
<http://www.springer.com/series/856>

The Springer Series in Materials Science covers the complete spectrum of materials physics, including fundamental principles, physical properties, materials theory and design. Recognizing the increasing importance of materials science in future device technologies, the book titles in this series reflect the state-of-the-art in understanding and controlling the structure and properties of all important classes of materials.

Jyotsna Dutta Majumdar · Indranil Manna
Editors

Laser-Assisted Fabrication of Materials

 Springer

Editors

Jyotsna Dutta Majumdar
Department of Metallurgical and
Materials Engineering
Indian Institute of Technology
Kharagpur, West Bengal
India

Indranil Manna
Department of Metallurgical and
Materials Engineering
Indian Institute of Technology
Kharagpur, West Bengal
India

ISSN 0933-033X

ISBN 978-3-642-28358-1

ISBN 978-3-642-28359-8 (eBook)

DOI 10.1007/978-3-642-28359-8

Springer Heidelberg New York Dordrecht London

Library of Congress Control Number: 2012942705

© Springer-Verlag Berlin Heidelberg 2013

This work is subject to copyright. All rights are reserved by the Publisher, whether the whole or part of the material is concerned, specifically the rights of translation, reprinting, reuse of illustrations, recitation, broadcasting, reproduction on microfilms or in any other physical way, and transmission or information storage and retrieval, electronic adaptation, computer software, or by similar or dissimilar methodology now known or hereafter developed. Exempted from this legal reservation are brief excerpts in connection with reviews or scholarly analysis or material supplied specifically for the purpose of being entered and executed on a computer system, for exclusive use by the purchaser of the work. Duplication of this publication or parts thereof is permitted only under the provisions of the Copyright Law of the Publisher's location, in its current version, and permission for use must always be obtained from Springer. Permissions for use may be obtained through RightsLink at the Copyright Clearance Center. Violations are liable to prosecution under the respective Copyright Law.

The use of general descriptive names, registered names, trademarks, service marks, etc. in this publication does not imply, even in the absence of a specific statement, that such names are exempt from the relevant protective laws and regulations and therefore free for general use.

While the advice and information in this book are believed to be true and accurate at the date of publication, neither the authors nor the editors nor the publisher can accept any legal responsibility for any errors or omissions that may be made. The publisher makes no warranty, express or implied, with respect to the material contained herein.

Printed on acid-free paper

Springer is part of Springer Science+Business Media (www.springer.com)

*Dedicated to:
Professor B. L. Mordike—
A pioneer in Laser Materials Processing
and an academic par excellence*

Foreword

This book opens the window on a new mode of manufacturing. Lasers are penetrating manufacturing technologies to an extent so pervasive that it could be compared to the effect of electrical-driven motor technology on manufacturing at the end of the nineteenth century, or of battery-charged handtools a decade or two ago. We are entering the age of photon-driven materials manufacturing, of light-beam manufacturing technologies. The higher the laser powers available, the more diverse the laser characteristics (wavelength, pulse duration, beam format), the more these new technologies will multiply. Ultimately, they will impact or intercede with another social change fast sweeping our earth, the trends toward eco-friendly manufacturing, energy efficiency, and the avoidance of toxic chemical processing. The future of laser-based technologies toward all these goals is very promising. High power diode-pumped lasers have wall-plug efficiency of 30% or more—70% is ultimately not unrealistic. Commercial lasers are starting to fill new temporal and spectral domains. High picosecond and nanosecond systems are now powerful enough for insertion into industrial processing manufacturing production lines. The ubiquitous femtosecond laser is now a fiber laser, simple, rugged, and compact in design, suitable for industrial deployment. New laser sources, with new laser media or non-linear optical conversion schemes provide laser beams with a range of photon energies, with wavelengths ranging from the UV to the mid-IR. These developments have spurred the scientific understanding of the light–materials interaction regimes that underpin these technologies. Many university centers, funded in part by forward-looking corporate sponsors explore the many new processing modalities offered by current high power laser technologies. The study of the interaction science has now opened a bridge to another important partner in this industrial revolution, namely materials science and engineering, even the new materials science called nanoscience. Nanoparticles and nanomaterial components like carbon nanotubes, metallic nanowires, and complex nanoparticles, are now beginning to enter the manufacturing business. They are becoming cheap, can be manufactured en masse, and specified to specific needs—commercial businesses are beginning to drive their development. The introduction of laser sources of

pin-point variable, motional transportable high energy sources to these materials opens the whole new field of laser-synthesized materials, new alloys, metallo-ceramics, and nanoparticle doped dielectrics, to name a few. These I predict will open vast new levels to manufactured components.

This book sets the stage for some of these exciting developments. Drs. Dutta Majumdar, Manna, and Nath from IIT Kharagpur in West Bengal, India, open the book with introductions to laser-assisted fabrication and laser materials processing. These are then followed by chapters addressing laser machining by Drs. Brandt and Sun from IRI in Swinborne, UK, laser-assisted welding by Dr. Padmanabhan from ARCI, Hyderabad and direct laser cladding by Drs. Weishiet and Gasser from RWTH in Aachen, Germany. Andreas Oestendorf from the University of Bochum summarizes laser-assisted microfabrication and Jonathan Wolfson from Loughborough University reviews laser processing of polymers for biomedical applications. Drs. Pflöging and Rohde from Karlsruhe Institute of Technology in Germany describe laser micro and nanoprocessing of ceramics, polymers, and thin films, and Dr. Smurov Igor from the Ecole Nationale d'Ingenieurs, St. Etienne, France discusses all the important issue of temperature monitoring by optical methods in laser processing. Finally, Dr. Kukreja from RRCAT, Indore, India gives an overview of the future scope of Industrial Acceptability of Laser Assisted Fabrication. Overall this book, with contributions from well-known experts and practitioners in this new technology from European and Indian institutions provides perspectives of some of the many new manufacturing technologies that will evolve from this new field of laser-assisted manufacturing.

Orlando, FL, USA

Prof. Martin Richardson

Prof. Martin Richardson
Trustee Chair Director
Townes Laser Institute
Northrop Grumman Professor of X-Ray Photonics
Professor of Optics, Physics & Electrical Engineering
University of Central Florida
College of Optics & Photonics
4000 Central Florida Blvd
Orlando, FL 32816-2700
USA
Tel.: +1-407-8236819
e-mail: mcr@creol.ucf.edu
<http://lpl.creol.ucf.edu>
<http://www.townes.ucf.edu>



Foreword

Materials processing and manufacturing is central to the economic and technology development of any nation. During the past decade new technological needs in the area of microelectronics, nanoscience, aerospace, and biology had motivated for the development of more precision, higher resolution, and better surface and volume localization processing techniques. This development would not have been possible without the rapid development of new laser sources. The highly coherent, convergent, and monochromatic electromagnetic radiation of the laser beam can result in power densities of the order of 10^{15} W/cm² and hence can be useful for applications such as but not limited to surface melting, surface cladding, cutting, ablation, and texturing. The capabilities and limitations of any laser system for a particular application depend on the fundamental interaction mechanism of the electromagnetic radiation with materials. The various phenomena that take place during the interaction of an electromagnetic radiation with the surface of a material is absorption, reflection, refraction, scattering and transmission. The extent of the above effects further depends both on the characteristics of electromagnetic radiation and thermo-physical properties of the material. Hence, laser materials processing is a complex interdisciplinary subject demanding understanding of various branches of sciences and engineering to gather a thorough knowledge and understanding.

A 5-kW CO₂ laser was first developed in 1977 for materials processing. Although it was developed in the United States, it gained popularity in Europe and more specifically in Germany due to the high demand in automotive manufacturing. Later, in 1990 a 10-kW and in 1995 a 30-kW CO₂ laser was also introduced in the world market. Most of these developments were not just focused on high power but also on beam quality, thus enabling high processing speeds and higher accuracy. As a result of these activities, the market for laser systems for materials processing kept continuously growing. Apart from the automotive technology,

a wider distribution of laser technology was also stimulated with new fields of applications such as shipyard, aircraft, and steel making industries during those days. In the advent of the development of the state of art solid state and high power diode lasers, expensive, bulky, and least efficient CO₂ lasers are slowly fading away from the manufacturing arena and are being replaced by high power solid-state lasers.

The first lamp pumped Nd:YAG lasers in kilowatt range came to the market in the early 1990s. Due to the high monochromaticity and capabilities of beam guidance by fibers, Nd:YAG lasers gained popularity for three-dimensional processing in car body fabrication and other applications. A couple of years back another advancement in solid-state lasers came in the form of diode pumped Nd:YAG laser systems for materials processing. Due to the efficient pumping and cooling of the active medium the diode pumped Nd:YAG lasers are associated with better beam quality, higher power stabilities, longer maintenance intervals, and higher beam efficiency.

The above advancements not only led to rapid and economical shop floor production, but also improved the quality in terms of applications such as surface alloying, surface cladding, glazing, annealing, cutting, etc. Other developments that were associated with the laser system were its operation mode. Here, the output power of the laser beam was modulated to be either continuous with constant amplitude known as continuous wave (CW) mode, or periodic known as pulsed beam mode. Due to the constant output power of the laser, CW mode was mostly used for applications such as surface cladding, glazing, and annealing. For pulsed mode operation, pulsing was carried out by various ways such as normal pulsing, *Q*-switching, and mode-locking to achieve pulses in the range of milliseconds to femtoseconds. These short range pulses resulted in instantaneous high peak power for sudden temperature rise and cooling and thereby found new inroads into processes such as microdrilling, nanoscale laser processing, and micromachining of biomaterials and biological components, direct transfer, and microprinting of functional materials by laser-induced forward transfer (LIFT), self-organized surface nano structuring, thin film deposition, etc.

Some of the major advantages associated with laser-based microdrilling is its ability to cut holes without any direct contact, fast processing, flexibility for hole size and shape, compactness, and cost effectiveness. The high intensity of the laser beam associated with pulsed lasers also enables micromachining of any material. Further, the short range pulses enables controlled material removal and small heat affected zone (HAZ) owing to its short interaction time with material. Owing to the above interesting features, ultra-short range laser pulses (milliseconds to femtosecond) have already found engineering applications for microdrilling in inkjet printer nozzles, gas flow chemical sensors, biomedical sensors, fuel injection nozzles, aerosol atomisers, food packaging, solar cell technology, and turbine blade cooling. Hence, these lasers are nowadays a common microdrilling tool in

industry sectors such as semiconductor, aerospace, automotive, electro-optics, photonics, optical, food, etc.

Apart from drilling, lasers in both pulsed and CW mode are also effectively established for two-dimensional machining process such as cutting and shaping. Here, a highly intense laser beam is focused on the workpiece to melt or vaporize the workpiece throughout its thickness or depth and simultaneously expelling the molten metal using an assist gas to create a cutting front. One of the first industrial applications of laser cutting is cutting of slots in die boards using a 200-W laser. Currently, lasers are capable of cutting a wide range of metallic materials such as steels, superalloys, copper, aluminum, and brass, and nonmetallic materials such as ceramic, quartz, plastic, rubber, wood, and cloth. Because of their numerous interesting features as discussed earlier they are also used for precision cutting of biodegradable and metallic stents and hence play a big role in medical device industries. Apart from manufacturing, lasers are also used in medicine and surgery for applications such as noncontact osteotomy of hard tissue, corneal surgery, skin resurfacing, etc.

For almost a decade now lasers had proved their usefulness in terms of bulk processing of materials and can be conveniently used for many other diverse applications such as hardening of automotive engine cylinder bore by laser cladding and laser surface treatment, joining of metals by laser welding. But with advancement in science and technology and the growing demand for miniaturization, lasers are not far away in terms of nanoscale processing of materials. A highly intense laser beam from a pulsed laser can be effectively used to transfer a nanoscale pattern from one surface to the other by LIFT, create self-organized nanostructures, and nano thin films on substrate materials by laser ablation.

The above advancement in terms of new avenues of processing and product development using lasers has quite surprisingly not yet been touched upon in a single volume book. This book edited by Dr. Jyotsna Dutta Majumdar and Professor Indranil Manna is definitely going to fulfill those shortcomings and provide the readers a compact and yet broad knowledge gathering in advance processing and developments in the area of laser materials processing. The book includes the chapters on various aspects of laser-based processing ranging from surface modification, nano/micro machining, joining to laser-based diagnostics in materials ranging from metallic, ceramic, polymers to biomaterials. These chapters provide an overview of processing technology as well as research summary and all the chapters are prepared by experts in the field from industry, academia, and research laboratories in various parts of the globe thereby providing the perspectives of laser materials processing in these parts of the world. We are pleased to receive this book prepared under the guidance and leadership of Dr. Dutta Mazumdar and Professor Manna and I undoubtedly say that the book chapters collected in this volume are going to foster the needs of researchers and engineers with a valuable and deeper understanding of this exciting field.

Prof. Narendra B. Dahotre
Department of Materials Science and Engineering
Laboratory of Laser Materials
Synthesis and Fabrication
University of North Texas
Denton TX
USA



Preface

Due to its ability to deliver coherent beam with negligible divergence, laser as a source of heat enjoys immense importance in the field of macro and micro-processing of materials. Fabrication may be achieved by removal of materials (laser assisted cutting, drilling, etc.), deformation (bending, extrusion), joining (welding, soldering), and addition of materials (surface cladding or direct laser cladding). A faster processing speed, conservation of strategic alloying elements, a large heating/cooling rate associated with the processing and retention of metastability in the microstructure are the notable advantages associated with laser assisted fabrication of materials. However, in spite of the unique advantages associated with the technique, large-scale application of the technology needs to be ensured. Acceptance of the technology in industry scale is yet to be popular, predominantly due to lack of widespread knowledge on the different materials phenomena and the influence of laser parameters on it. However, extensive research efforts are undertaken and the significant contribution in this direction encompasses various fields like interaction of laser with materials, role of process parameters on the different materials processing and process optimization, solidification behavior of materials under non-equilibrium processing conditions, development of metastable microstructures/novel materials, and modeling/process control. A complete knowledge in this direction demands blending of the existing theory with the advanced research in this direction. The compilation on 'Laser assisted fabrication' is aimed at (a) Developing in-depth engineering concepts on various laser assisted macro and micro-fabrication techniques; (b) Engineering background-a review of engineering background of different micro/macro-fabrication techniques; thermal history of the treated zone; microstructural development and evolution of properties of the treated zone; (c) Application of laser assisted fabrication including laser cutting and drilling, welding, surface modification, laser forming, and rapid prototyping; (d) An in-depth understanding of laser assisted microfabrication of metallic, polymeric materials, and thin film and (e) finally introducing an industrially acceptable optical monitoring tool for control of laser

processing. It consists of 11 chapters. The contributions from the authors who have expertise in different areas of laser materials processing are gratefully acknowledged. Needless to mention, without the time and efforts spent by the reviewers this special issue would not have been presented in this form. The invitation, cooperation, and encouragement from Dr. Claus Ascheron and necessary help from Dr. Elke Sauer from Springer Verlag were of immense help to nucleate and expand the contribution in the present form.

Laser parameters play an important role in determining the properties of the processed zone. [Chapter 1](#) presents a brief introduction to different types of lasers and their general application, fundamentals of laser–matter interaction, and classification of laser material processing. The materials processing techniques covered have been broadly divided into four major categories; namely, laser assisted forming, joining, machining, and surface engineering. Besides discussing the scope and principle of these processes, each section enumerates a detailed update of the literature, scientific issues, and technological innovations. The entire discussion primarily focuses on correlating the properties with processing parameters and microstructure and composition.

Recently, a large numbers of lasers have been developed aimed at application for different purposes, especially, fabrication of miniature components. [Chapter 2](#) presents a brief overview of recent developments of lasers and its application in materials processing. The applications of excimer lasers (operating in short wavelengths in ultraviolet spectrum) and Ti-sapphire on micro-machining like MEMS, microelectronics, telecommunication, optoelectronics, and biomedical devices have been discussed in detail.

Laser cutting is a popular manufacturing technique which has a potential scope of applications in cutting of different materials, especially, difficult to cut materials. [Chapter 3](#) summarizes the up-to-date progress of laser assisted machining of metals, ceramics, and metal matrix composites. It also discusses the analysis of temperature distribution around the cutting region, material removal mechanisms, tool wear mechanisms, and the improvement in machined surface integrity of various engineering materials by the assistance of laser beam.

Laser as a source of heat can be effectively used for joining of materials by fusion welding and brazing in autogenous (without filler material) or with a filler or in hybrid modes. However, to overcome certain limitations associated with laser welding, modifications in process designing have been undertaken like laser-arc hybrid welding, remote welding, induction assisted welding, laser weld brazing, and SHADOW welding. The process may be extended to join plastics and ceramics. [Chapter 4](#) describes the basic principles of various laser-based joining processes, laser system technology, process parameters, metallurgical effects on different base materials, joint performance, and applications.

Direct laser cladding (DLD) is the emerging manufacturing technique for development of near net shape components. A rapid processing speed, one-step processing, possibility in retention of metastability in the microstructure and

development of components with improved properties are the advantages associated with the technique. [Chapter 5](#) describes the additive manufacturing techniques by direct laser cladding along with its practical applications examples.

Processing of materials on the micro scale requires pulsed and/or short wavelength laser systems with moderate average powers in the range of a few watts or below along with good beam qualities. [Chapter 6](#) provides an overview of pulsed laser assisted micromachining with a focus on structuring by laser ablation, laser generative processes, and finally nanomachining.

Polymers have numerous engineering applications where they need to be shaped. One of the important applications of polymeric materials is bio-implant materials, however, it is known that they offer excellent bulk properties for biological applications; however, their surface properties need to be tailored to improve their performance. [Chapter 7](#) presents the detailed investigations on CO₂ laser surface processing of nylon 6,6 and its effect on surface characteristics and properties of modified surface.

Laser assisted fabrication of materials on micro and nanoscale offers a cost-effective solution for advanced material research and application. Laser ablation and surface modification are suitable for direct patterning of materials and their surface properties. [Chapter 8](#) presents the application of lasers in patterning, rapid prototyping, and small-batch manufacturing. Especially, the applications of ultraviolet, NIR and IR laser radiation for precise and debris-free pattern generation, machining, and rapid manufacturing are discussed.

The thermal history of the processed zone plays an important role to determine the microstructure, thermal stress distribution, and properties of the fabricated components. However, due to very short laser-material interaction time during processing, measurement of temperatures by conventional techniques is difficult leading to the development of heat and mass-transfer model for prediction of performance of fabricated components. Recent developments in optical sensors led to invention of tools for precise measurement of temperature during laser processing. [Chapter 9](#) discusses different optical-based techniques for monitoring of temperatures during laser materials processing.

The stumbling block for industrialization of laser is due to the following facts: high installation cost, lack of understanding on the microstructures and properties in the fabricated component due to non-equilibrium processing by laser, optimum fabrication quality under narrow process parameters, and unavailability of data points on optimum process parameters. However, laser assisted cutting, surface hardening and similar material welding are the three important fabrications where laser as a source of heat are gradually getting popular. [Chapter 10](#) critically reviews the scope for the industrial acceptability and adaptability of high power lasers to assess the real potential of these research areas.

In conclusion, it may be stated that all the articles in the present issue present the details of laser assisted macro and micro-processing of materials, principle of individual technique and original research efforts on advanced field of laser materials processing. We sincerely acknowledge the secretarial help by Mr. Prashant Sharma and Subhasisa Nath, research scholars working with us for

helping us during the preparation of the volume. The cooperation and help from our family members are gratefully acknowledged. Finally, we wish the issue to be a successful, popular, and useful one to engineers, scientists, and researchers in the field of materials science and manufacturing technology.

Kharagpur, India

Jyotsna Dutta Majumdar
Indranil Manna

Contents

1	Introduction to Laser-Assisted Fabrication of Materials.	1
	Jyotsna Dutta Majumdar and Indranil Manna	
1.1	Introduction	1
1.2	Principle, Type, and Application of Laser	2
1.2.1	Solid-State Laser	3
1.2.2	Semiconductor or Diode Lasers	4
1.2.3	Gas-Based Lasers	5
1.2.4	Free-Electron Lasers	5
1.2.5	Ultra High Field Lasers.	5
1.2.6	Excimer Lasers	6
1.3	Laser–Matter Interaction for Material Processing	6
1.3.1	Lattice Heating.	6
1.3.2	Spatial Distribution of Deposited Energy.	7
1.3.3	Heat Transfer by Laser Irradiation	8
1.3.4	Plasma Formation During Laser Irradiation	9
1.3.5	Effect of Ultra High Power Laser Irradiation.	10
1.4	Application of Laser	10
1.5	Laser Assisted Fabrication of Engineering Materials.	11
1.6	Laser Assisted Shaping	14
1.6.1	Laser Assisted Bending.	14
1.6.2	Laser Rapid Prototyping	22
1.7	Laser Joining	28
1.8	Laser Machining.	35
1.8.1	Laser Cutting	35
1.8.2	Laser Drilling.	40
1.8.3	Laser Cleaning.	42
1.9	Laser Surface Engineering	43
1.9.1	Laser Transformation Hardening	44
1.9.2	Laser Surface Melting.	45
1.9.3	Laser Surface Alloying	47

1.9.4	Laser Composite Surfacing	53
1.9.5	Laser Shock Processing.	54
1.9.6	Laser Surface Engineering of Ceramics.	54
1.9.7	Laser Surface Engineering of Polymers.	55
1.10	Summary and Future Scope	57
1.11	Future Challenges.	58
	References	59
2	High Power Lasers in Material Processing Applications: An Overview of Recent Developments	69
	A. K. Nath	
2.1	Introduction	69
2.2	Recent Developments in High Power Lasers	74
2.2.1	High Power CO ₂ Laser	74
2.2.2	High Power Diode Laser	75
2.2.3	Nd:YAG Lasers	77
2.2.4	Diode Pumped Solid-State Rod Type and Slab Lasers	79
2.2.5	High Power Thin Disc Laser	81
2.2.6	Fiber Laser	82
2.2.7	Ceramic YAG Lasers	84
2.2.8	Excimer Lasers	85
2.2.9	High Average Power Pulsed Lasers	85
2.2.10	Ultrafast Lasers	86
2.3	Laser–Material Interaction	88
2.3.1	Basic Absorption Mechanism of Laser Radiation in Materials.	88
2.3.2	Effect of Spatial Characteristic of Laser Beam.	94
2.3.3	Effect of Laser Pulse Duration.	94
2.3.4	Material Removal Mechanisms	95
2.3.5	Recent Developments in Laser Material Processing Applications.	98
2.4	Conclusions	106
	References	106
3	Laser-Assisted Machining: Current Status and Future Scope.	113
	M. Brandt and S. Sun	
3.1	Introduction	113
3.2	Engineering Materials and Their Machinability	114
3.2.1	Ceramics	114
3.2.2	Nickel-Based Superalloy: Inconel 718.	114
3.2.3	Titanium and its Alloys.	114
3.2.4	Hardened Steels	115
3.2.5	Metal Matrix Composites	115

3.3	Laser-Assisted Machining and its Principles	116
3.3.1	Traditional Laser-Assisted Machining	116
3.3.2	Non-Traditional Laser-Assisted Machining	117
3.4	Temperature Rise on the Workpiece Surface Due to Laser Radiation	118
3.5	Improvement of Machinability by Laser Beam Assistance.	127
3.5.1	Cutting Force and Specific Cutting Energy	127
3.5.2	Material Removal Mechanisms and Chip Formation	132
3.5.3	Proposition of a Physical Model for Chip Segmentation	136
3.5.4	Tool Materials and Wear.	141
3.5.5	Surface Integrity.	147
3.6	Optimization and Energy Efficiency of LAM.	150
3.7	Numerical Simulation of LAM.	151
3.8	Future Scope of LAM.	153
	References	154
4	Laser-Based Joining of Metallic and Non-Metallic Materials	159
	G. Padmanabham and B. Shanmugarajan	
4.1	Introduction	160
4.2	Classification of Laser-Based Joining Processes.	161
4.3	Principle of Keyhole and Factors Affecting Keyhole Stability	162
4.4	Lasers and System Technology for Welding	163
4.5	Laser Welding Parameters	167
4.6	Pulsed Laser Welding	170
4.7	Laser Welding of Different Materials	174
4.7.1	Laser Welding of Steels	174
4.7.2	Aluminum Alloys.	182
4.7.3	Titanium Alloys	187
4.7.4	Nickel-Based Alloys	188
4.7.5	Magnesium Alloys	190
4.7.6	Conducting Materials	191
4.7.7	Dissimilar Materials	192
4.8	Limitations of Laser Welding.	193
4.9	Laser Welding Process Control Tools	193
4.9.1	Seam Tracking.	193
4.9.2	Weld Monitors.	196
4.9.3	Gap Bridging by Wire Feed.	197
4.10	Innovations in Laser Welding	197
4.10.1	Laser Hybrid Welding.	197
4.10.2	Induction-Assisted Laser Welding	200
4.10.3	Remote Welding	200
4.10.4	Dual Beam Welding	201

- 4.11 Laser Brazing. 202
 - 4.11.1 Zn-Coated Steels 203
 - 4.11.2 Aluminum–Steel Brazing. 205
- 4.12 Laser Selective Soldering 205
- 4.13 Laser Welding of Non-Metallic Materials 206
 - 4.13.1 Plastic Welding 206
 - 4.13.2 Laser Joining of Metal and Plastic 207
- 4.14 Applications of Laser Welding and Brazing. 209
 - 4.14.1 Tailor Welded Blanks 209
 - 4.14.2 Medical Devices. 212
 - 4.14.3 Automotive Body 213
 - 4.14.4 Li-Ion Battery 213
 - 4.14.5 Joining of Stiffeners to the Skin in the Fuselage
Belly Area 214
 - 4.14.6 Solar Absorber Plates Cu/Al Plate-Cu
Tube Welding 215
 - 4.14.7 Laser Hybrid Pipeline Welding 216
- References 217

5 Direct Laser Cladding, Current Status and Future Scope of Application. 221

A. Weisheit, A. Gasser, G. Backes, T. Jambor, N. Pirch
and K. Wissenbach

- 5.1 Introduction 221
- 5.2 Fundamentals of Direct Laser Cladding. 222
 - 5.2.1 Laser Beam Sources and Specific Advantages
of Laser Cladding. 222
- 5.3 Fundamentals of the Laser Cladding Process 223
 - 5.3.1 Fundamentals of Laser Remelting. 223
 - 5.3.2 Principle and Material Requirements
for the Laser Cladding Process. 225
 - 5.3.3 Powder Injection 226
- 5.4 Material Aspects of Laser Cladding 231
 - 5.4.1 Materials 231
 - 5.4.2 Microstructure 231
- 5.5 Applications. 231
- 5.6 Future Trends for Laser Cladding. 236
 - 5.6.1 Micro Laser Cladding 236
 - 5.6.2 Novel Materials 237
- 5.7 Additive Manufacturing. 239
- References 239

6	An Introduction to Laser-Assisted Microfabrication, Current Status and Future Scope of Application.	241
	A. Ostendorf	
6.1	Introduction	241
6.2	Laser Pulse Generation and Interaction with Matter	243
6.2.1	Gain Switching	243
6.2.2	Q-Switching.	244
6.2.3	Cavity Dumping	246
6.2.4	Mode-Locking	247
6.2.5	Active Mode-Locking	249
6.2.6	Passive Mode-Locking	250
6.2.7	Interaction of Short Pulses with Matter	251
6.3	Basic Processes	253
6.3.1	Structuring by Material Removal	254
6.3.2	Generative Processes.	261
6.3.3	Nanostructuring	264
6.4	Applications.	267
6.4.1	Cardiovascular Implants	267
6.4.2	Solar Cell Processing	269
6.4.3	Machining of Nozzles	271
6.5	Summary and Conclusions.	273
	References	273
7	Laser Surface Processing of Polymers for Biomedical Applications.	275
	David Waugh and Jonathan Lawrence	
7.1	Polymers as Biomaterials and In Vitro Experimentation	275
7.1.1	Polymeric Biomaterials	275
7.1.2	In Vitro Experimentation of Materials.	277
7.2	Wettability in Biomaterials Surface Science.	280
7.2.1	Contact Angle and Wettability	281
7.3	Surface Modification Techniques	283
7.3.1	Radiation and Photografting.	283
7.3.2	Plasma Surface Modification	285
7.3.3	Ion and Electron Beam Processing	286
7.3.4	Laser Surface Modification	287
7.4	Experimental Technique	290
7.4.1	Laser Irradiation Procedure	290
7.4.2	Topography, Wettability Characteristics, and Surface Chemistry Analysis.	291
7.4.3	In Vitro Experimentation.	292
7.4.4	SEM and Optical Microscopy Analysis of In Vitro Samples	294
7.4.5	Statistical Analysis	294

- 7.5 Effect of Laser Patterning on Topography 295
- 7.6 Effect of Laser Irradiation on the Wettability Characteristics 295
- 7.7 Effect of Laser Patterning on Osteoblast Cell Bioactivity and SBF Response 303
 - 7.7.1 SBF Response to Laser Patterning 303
 - 7.7.2 Osteoblast Cell Bioactivity: 24 h After Seeding 304
 - 7.7.3 Osteoblast Cell Bioactivity: 4 Days After Seeding 309
- 7.8 Summary 312
- References 314

- 8 Laser Micro and Nano Processing of Metals, Ceramics, and Polymers 319**
 - Wilhelm Pfleging, Robert Kohler, Isabelle Südmeyer and Magnus Rohde
 - 8.1 Introduction 319
 - 8.2 Fundamental Aspects of Laser Material Processing. 322
 - 8.3 Modeling and Simulation. 324
 - 8.4 Polymer Materials 329
 - 8.4.1 Thermally Driven Ablation 329
 - 8.4.2 Cold Laser Ablation 331
 - 8.4.3 Modification 334
 - 8.5 Ceramics, Glass–Ceramics, and Glasses 335
 - 8.5.1 Laser Patterning 335
 - 8.5.2 Modification of Surfaces by Dispersing and Cladding 338
 - 8.5.3 Structuring and Annealing of Battery Materials 346
 - 8.6 Joining with Laser Beams 354
 - 8.6.1 Welding of Thin Metal Sheets 354
 - 8.6.2 Metal–Ceramics Joining 358
 - 8.6.3 Laser Transmission Welding of Polymers 364
 - 8.7 Conclusion. 367
 - References 367

- 9 Temperature Monitoring by Optical Methods in Laser Processing 375**
 - I. Smurov and M. Doubenskaia
 - 9.1 Introduction 375
 - 9.2 Theoretical Background of Pyrometry. 377
 - 9.3 Diagnostics Facilities 379
 - 9.3.1 Pyrometers Performance Data 379
 - 9.4 Results and Discussion 383
 - 9.4.1 Surface Temperature Evolution in Pulsed and Pulsed Periodic Laser Action of Millisecond Range 383

9.4.2	Laser Welding	389
9.4.3	Laser Cladding.	399
9.4.4	Selective Laser Melting.	414
9.5	Conclusions	418
	References	420

10 Emerging Laser Materials Processing Techniques for Future

	Industrial Applications	423
	L. M. Kukreja, R. Kaul, C. P. Paul, P. Ganesh and B. T. Rao	
10.1	Introduction	423
10.2	Laser Rapid Manufacturing	424
10.2.1	Laser Rapid Manufacturing of Colmonoy-6 Bushes	427
10.2.2	Laser Rapid Manufacturing of Low-Cost Tools	429
10.2.3	Laser Rapid Manufacturing of Porous Materials.	432
10.2.4	Laser Rapid Manufacturing of Bimetallic Components.	436
10.2.5	Mechanical Properties of Laser Rapid Manufactured Structures of Inconel 625 and Type 316L SS	444
10.2.6	Prognostication.	447
10.3	Laser Surface Melting Treatment for Enhanced Resistance of Austenitic Stainless Steel Against Inter-Granular Corrosion	449
10.3.1	Laser Surface Treatment of Type 304 SS	449
10.3.2	Post-Weld Laser Surface Treatment of Type 316(N) SS Weld Metal	451
10.3.3	Pre-Weld Laser Surface Treatment of Type 304 SS	453
10.3.4	Prognostication.	456
10.4	Laser Shock Peening Surface Treatment for Enhanced Fatigue Performance of Automobile Components.	457
10.4.1	Laser Shock Peening Treatment with Pulsed Nd:YAG Laser.	457
10.4.2	Prognostication.	458
10.5	CO ₂ Laser-GTAW Hybrid Welding	459
10.5.1	Interaction of Gas Tungsten Arc (GTA) and Laser-Generated Plasma During Hybrid Welding	459
10.5.2	Prognostication.	461
10.6	Laser Profile Cutting of Metal Sheets	461
10.6.1	Laser Piercing with Power Modulation for Improved Profile Cutting	461

10.6.2	Laser Power Modulation Controls Adverse Effects of Periodic Power Fluctuations.	465
10.6.3	Laser Cutting with Power Modulation Improves Cut Edge Quality	467
10.6.4	Laser-Assisted Oxygen (LASOX) Cutting of Thick Steel Plates.	469
10.6.5	Prognostication.	471
10.7	Summary and Conclusions.	471
	References	475
Index	479
Curriculum Vitae	483

Contributors

Gerhard Backes RWTH Aachen University, Aachen, Germany, e-mail: gerhard.backes@ilt.fraunhofer.de

Prof. M. Brandt Industrial Research Institute Swinburne, 264 Plenty Road Bundoora, Bundoora, VIC 3083, Australia, e-mail: milan.brandt@rmit.edu.au

P. Ganesh Laser Welding and Surface Engineering P.O.CAT, Raja Ramanna Centre for Advanced Technology, Indore 452 013, India, e-mail: ganesh@rrcat.gov.in

Dr. Andres Gasser Fraunhofer-Institut fuer Lasertechnik, ILT, Steinbachstr. 15, 52074 RWTH, Aachen, Germany, e-mail: andres.gasser@ilt.fraunhofer.de

Prof. Smurov Igor Ecole Nationale d'Ingénieurs de Saint-Etienne (ENISE), DIPI Laboratory, 58 rue Jean Parot, 42023 Saint-Etienne Cedex 2, France, e-mail: smurov@enise.fr

Torsten Jambor RWTH Aachen University, Aachen, Germany, e-mail: torsten.jambor@ilt.fraunhofer.de

Rakesh Kaul Laser Welding and Surface Engineering P.O.CAT, Raja Ramanna Centre for Advanced Technology, Indore 452 013, India, e-mail: rkaul@rrcat.gov.in

Robert Kohler Institute for Materials Research, Karlsruhe Institute of Technology, Karlsruhe, Germany

Prof. L. M. Kukreja Laser Welding and Surface Engineering P.O.CAT, Raja Ramanna Centre for Advanced Technology, Indore 452 013, India, e-mail: kukreja@rrcat.gov.in

Prof. J. Lawrence Loughborough University, Leicestershire LE11 3TU, Great Britain, UK, e-mail: J.Lawrence@lboro.ac.uk

Dr. J. Dutta Majumdar Indian Institute of Technology, Kharagpur, West Bengal 721302, India, e-mail: jyotsna@metal.iitkgp.ernet.in

Prof. I. Manna Central Glass and Ceramic Research Institute, Kolkata 700032, India, e-mail: imanna@metal.iitkgp.ernet.in

Dr. Doubenskaia Maria DIPI Laboratory, Ecole Nationale d'Ingénieurs de Saint-Etienne (ENISE), 58 rue Jean Parot, 42023 Saint-Etienne Cedex 2, France

Prof. A. K. Nath Department of Metallurgical and Materials Engineering, Indian Institute of Technology, Kharagpur 721302, West Bengal, India, e-mail: aknath@mech.iitkgp.ernet.in

Prof. Andreas Ostendorf Ruhr-University Bochum, 44780 Bochum, Germany, e-mail: andreas.ostendorf@ruhr-uni-bochum.de

Dr. G. Padmanabhan Centre for Laser Processing of Materials (CLPM), ARCI, Hyderabad 500005, India, e-mail: gp@arci.res.in

Dr. C. P. Paul Laser Materials Processing Division, Raja Ramanna Centre for Advanced Technology P.O. CAT, Indore 452 013, India, e-mail: paulcp@rrcat.gov.in

Dr. Wilhelm Pflöging Institute for Materials Research, Karlsruhe Institute of Technology, Karlsruhe, Germany, e-mail: Wilhelm.Pflöging@kit.edu

Dr. Norbert Pirch Fraunhofer-Institut fuer Lasertechnik, ILT, Steinbachstr. 15, 52074 RWTH, Aachen, Germany

B. Tirumala Rao Raja Ramanna Centre for Advanced Technology P.O. CAT, Indore 452 013, India, e-mail: trao@rrcat.gov.in

Dr. Magnus Rohde Institute for Materials Research, Karlsruhe Institute of Technology, Karlsruhe, Germany, e-mail: Magnus.Rohde@kit.edu

Dr. B. Shanmugarajan Centre for Laser Processing of Materials (CLPM), ARCI, Hyderabad 500005, India, e-mail: bshanmu@arci.res.in

Isabelle Südmeyer Institute for Materials Research, Karlsruhe Institute of Technology, Karlsruhe, Germany

Dr. S. Sun Industrial Research Institute Swinburne, 264 Plenty Road Bundoora, Bundoora, VIC 3083, Australia, e-mail: shoujin.sun@rmit.edu.au

Dr. David Waugh University of Lincoln, Brayford Pool, Lincoln LN6 7TS, UK, e-mail: DWaugh@lincoln.ac.uk

Dr. Andreas Weisheit Fraunhofer-Institut fuer Lasertechnik, ILT, Steinbachstr. 15, 52074 RWTH, Aachen, Germany, e-mail: andreas.weisheit@ilt.fraunhofer.de

Dr. Konrad Wissenbach Fraunhofer-Institut fuer Lasertechnik, ILT, Steinbachstr. 15, 52074 RWTH, Aachen, Germany, e-mail: konrad.wissenbach@ilt.fraunhofer.de

Symbols

E_2	Excited or higher energy state
E_1	Ground state
ν	Photon of frequency
h	Planck's constant
I	Laser beam intensity
I_0	Incident beam of initial intensity
t	Time
R	Reflectivity coefficient
α	Absorption coefficient
R_E	Reflectivity for electron beam
x_p	Distance
$f_E(x/x_p)$	Spatial energy deposition profile
$C(z)$	Concentration of a given species at a vertical distance z
R_p	Projected range/distance
Q_T	Ion dose
ρ	Density
t_p	Pulse duration
α^{-1}	Laser absorption depth
κ	Thermal diffusivity
K	Thermal conductivity
c_p	Specific heat
T	Temperature
Q	Power density
T_m	Melting temperature
T_i	Interface temperature
η	Power (or energy) transfer coefficient
ε	Rate of melting
P	Incident laser power
v	Welding speed
d	Sheet thickness
W	Beam width
ΔH_m	Enthalpy

P_1	Laser power (Watt)
M^*	Mass flow rate of laser gas (g/s)
n	Real part of refractive index
k	Extinction coefficient
n^*	Complex form of refractive index
R	Reflectivity of a material
A	Absorptivity of a material
T	Transmitivity of a material
λ	Laser wavelength
σ_0	Electrical DC conductivity of the material
$I(z)$	Intensity at a depth z
I_0	Incident laser intensity
α	Absorption coefficient
$P(z)$	Laser power absorbed
l_a	Attenuation length (nm)
E_g	Energy band gap
H	Planck's constant
ν	Laser frequency
γ	Adiabaticity parameter
ε	Strength of the electric field
ω	Frequency of the electric field
m	Reduced mass of electron
e	Electric charge of electron
ρ	Density of the material
L_v	Latent heat of vaporization of the material
M^2	Beam product (beam diameter \times half-divergence angle)
$\theta_{1/2}$	Half-divergence angle of a real beam
d_b	Laser beam diameter
f	Focal length
d_f	Focal spot diameter
l_d	Thermal diffusion length
κ	Thermal diffusivity of the material
τ_1	Laser pulse duration
Z_a	Ablation depth
T	Temperature
Z	Axial coordinate
κ	Thermal conductivity
ρ	Density
C_p	Specific heat
ω	Workpiece rotation speed
V_Z	Feed speed
R_w	Workpiece radius
t	Time
tp	Preheat time
z	Axial coordinate

z_c	Axial location of the laser center
ϕ	Circumferential coordinate
ϕ_c	Circumferential location of the laser center
q''	Heat flux
q'''	Volumetric heat generation
F_c	Cutting force
$\overline{V_w}$	Average workpiece velocity
F_{ct}	Friction force
V_{chip}	Average chip velocity
d	Depth of cut
L_f	Tool feed
T_{mr}	Material removal temperature
P_{CO_2}	Laser power for the CO ₂ laser
P_{YAG}	Laser power for the Nd:YAG laser
D_w	Diameter of the workpiece
f	Feed
V_c	Cutting speed
u_c	Specific cutting energy
w	Width of the cut
L_1	Laser-tool lead distance
F_f	Feed force
D	Laser spot size
L_2	Tool-beam distance
$T_{s,ch}$	Near-chamfer surface temperature
$T_{mr,se}$	Average material removal temperature
σ_y	Yield strength of workpiece at a given strain rate
β	Angle of kinetic friction for sliding motion
μ	Coefficient of friction
θ	Shear plane angle
α	Rake angle
K_{IC}	Fracture toughness of workpiece
VB_{max}	Maximum flank wear
VB_{ave}	Average flank wear
T_{int}	Tool–chip interface temperature
η	Preheating efficiency
u_{total}	Total specific energy
r_{foc}	Beam spot radius at the focal plane
f	Focal length
λ	Wavelength of the laser
r	Radius of the raw beam
K	Beam quality
ρ	Density
C_p	Heat capacity
κ	Thermal diffusivity

P_M	Mean laser Power
E_P	Pulse energy
τ_P	Pulse duration
T_F	Pulse-to-pulse time (ms)
PRR	Pulse repetition rate (s^{-1})
D	Spot area (mm^2)
V	Welding speed (mm/s)
P_P	Peak power (kW)
P_D	Power density (kW/mm^2)
C_D	Duty cycle
I_m	Threshold irradiance
T_{melt}	Melting point
T_0	Ambient temperature
d	Beam diameter
J_{max}	Function of ratio of thermal diffusivity to the product of the traverse speed and diameter of the incident beam
Φ	Phase difference
ν_0	Central mode frequency
τ_P	Pulse width
n_e	Electron number density
k_B	Boltzmann constant
k_e	Electron thermal conductivity
v_F	Fermi-velocity
τ	Electron relaxation constant
D	Diffusion coefficient
T_e	Electron temperature
T_l	Lattice temperature
C_l	Lattice thermal capacity
τ_a	Ablation interval
δ	Optical penetration length
ρ	Density
Ω	Specific enthalpy of evaporation
P_L	Average output power
λ	Wavelength
q	Number of photons
NA	Numerical aperture
θ	Contact angle
γ_{sv}	Solid surface energy
γ_{lv}	Liquid surface energy
γ_{sl}	Solid-liquid interfacial energy
γ_s^d	Dispersive component surface free energy
γ_s^p	Polar component surface free energy
γ_s^h	Hydrogen component surface free energy
γ_s^i	Induction component surface free energy
γ_s^{ab}	Acid-base component surface free energy

γ^T	Total surface energy
ε	Laser fluence
E	Pulse energy
I	Maximum peak Intensity
P	Maximum peak power
A	Focal spot area
T	Pulse duration
ν_{rep}	Laser repetition rate
δ_w	Thermal diffusion length
R	Reflectance
T	Laser processing time
ρ	Density
C_p	Specific heat capacity
λ, K	Thermal conductivity
η	Absorption efficiency
P_{Las}	Power density of laser beam
ν_{Scan}	Scanning velocity
d	Ablation depth
P_L	Laser power
V	Feed rate
R	Ablation rate
ε_t	Ablation threshold
α_{eff}	Effective absorption coefficient
ε_o	Characteristic laser fluence
σ_1	Single-photon absorption cross-section
ρ_o	Density of absorbing constituents
α	Absorption coefficient
α_{eff}	Effective absorption coefficient
T_B	Temperature of non blackbody
T_o	Temperature of blackbody
$L(\lambda, T_o)$	Spectral radiant intensity
ε	Spectral emissivity
λ	Wavelength
N	Number of pyrometer wavelengths
E	Energy per pulse
T_{max}	Maximum peak temperature
τ_{lt}	Melt life-time
τ_s	Duration of solidification
$\Delta\tau$	Pulse duration
F	Powder feeding rate
P	Laser power
ν	Laser cladding speed
G_c	Carrier gas flow rate

Chapter 1

Introduction to Laser-Assisted Fabrication of Materials

Jyotsna Dutta Majumdar and Indranil Manna

Abstract Light amplification by stimulated emission of radiation (laser) is a coherent and monochromatic source of electromagnetic radiation that can propagate in a straight line and hence, finds diverse applications. High power lasers can perform various manufacturing operations or material processing. This contribution provides the principle of laser materials processing and an overview of the engineering application of laser material processing. The manufacturing processes covered have been broadly divided into four major categories; namely, laser assisted forming, joining, machining, and surface engineering. Followed by a brief introduction to different types of lasers and their general application, fundamentals of laser–matter interaction and classification of laser material processing have been provided. The scope and principle of an individual process is described followed by a detailed update of the literature, scientific issues, and technological innovations. The entire discussion primarily focuses on correlating the properties with processing parameters and microstructure and composition.

1.1 Introduction

Laser, the acronym of light amplification by stimulated emission of radiation is a coherent and monochromatic source of electromagnetic radiation with wavelength ranging from the ultraviolet to the infrared range [1–4]. Lasers can deliver very

J. D. Majumdar (✉) · I. Manna
Metallurgical and Materials Engineering Department,
Indian Institute of Technology, Kharagpur 721 302, West Bengal, India
e-mail: jyotsna@metal.iitkgp.ernet.in

I. Manna
Central Glass and Ceramic Research Institute,
Kolkata 700 032, West Bengal, India
e-mail: imanna@metal.iitkgp.ernet.in

low (\sim mW) to extremely high (1–100 kW) focused power with a precise spot size/dimension and spatial/temporal distribution on a given substrate through any intervening medium [1–4]. As a result, lasers have wide-ranging applications in different materials processing [5, 6].

The initial foundation of the laser theory was laid by Einstein [7]. Subsequently, Kopfermann and Ladenburg [8] presented the first experimental confirmation of Einstein's prediction. In 1960, Maiman [9] invented the first working ruby laser for which he was awarded the Nobel Prize. Subsequently, several new lasers including semiconductor lasers, Nd:YAG lasers, CO₂ gas lasers, dye lasers, and other types of gas lasers were designed and fabricated with better reliability and durability. By the mid 1970s, more reliable and powerful lasers were developed for industrial applications such as cutting, welding, drilling, and melting. During the 1980s and early 1990s, lasers were successfully applied for heating, cladding, alloying, glazing, and thin film deposition.

Depending on the type of laser and wavelength desired, the laser medium could be solid, liquid, or gaseous. Different laser types are commonly named according to the state or the physical properties of the active medium. Consequently, there are glass or semiconductor, solid state, liquid, and gas lasers. Gas-based lasers can be further subdivided into neutral atom lasers, ion lasers, molecular lasers, and excimer lasers. The typical commercially available lasers are (a) solid state or glass laser (Nd:YAG, Ruby), (b) semiconductor or diode laser (AlGaAs, GaAsSb and GaAlSb), (c) dye or liquid lasers (solutions of dyes in water/alcohol and other solvents), (d) neutral or atomic gas lasers (He–Ne, Cu or Au vapour), (e) ion lasers [argon (Ar⁺) and krypton (Kr⁺) ion], (f) molecular gas lasers (CO₂ or CO), and (g) excimer laser (XeCl, KrF). The wavelengths of the presently available lasers cover a wide spectral range from the far infrared to the soft X-ray.

1.2 Principle, Type, and Application of Laser

Laser comprises three principal components, namely, a gain medium, a device for exciting the gain medium, and an optical delivery/feedback system. Additional provisions of cooling the mirrors, guiding the beam, and manipulating the target are necessary to facilitate material processing. Figure 1.1 schematically shows the operating principle of a CO₂ laser. As illustrated in Fig. 1.1a, the laser device consists of three main parts: a gain or laser medium CO₂, an optical resonator or cavity with two mirrors (mirror 1 and 2, placed at opposite ends), and an energizing or pumping source that supplies energy to the gain medium to activate CO₂ into amplifying state [10]. The chemical species in the gain medium (composition, bond energy, band gap, etc.) determines the wavelength of the optical output. Between the two mirrors, one is a fully reflecting and the other a partially reflecting one. From the quantum mechanical principle, when an external energy is supplied to an atom/molecule, the irradiated species attains an excited or higher energy state (E_2) only to spontaneously and instantaneously return to the ground state (E_1) by emitting the energy difference

as a photon of frequency (ν):

$$\nu = (E_2 - E_1)/h, \quad (1.1)$$

Where, h is the Planck's constant. This phenomenon is known as spontaneous emission, which subsequently may excite another atom and stimulate it to emit a photon by de-exciting it to a lower energy level through a process called stimulated emission of radiation. This process in the initial stage occurs randomly and can multiply itself (Fig. 1.1b). However, the emitted radiation is coherent with the stimulating source so that the wavelength, phase, and polarization between the two are identical. A photon interacting with a ground state atom may get absorbed in order to excite it to a higher energy state. This situation, called 'population inversion' is created by the pumping source. The photons moving along the optical axis interact with a large number of excited atoms, stimulate them and in the process get amplified. They are reflected back and forth by the resonator mirrors and pass through the excited medium creating more photons. In each of these cycles, a percentage of these photons exit through the partially transmitting mirror as intense laser beam (Fig. 1.1c). Finally, the laser beam is guided on to the workpiece by using reflecting mirrors and prisms. Instead of CO₂, the active medium could be a solid (e.g. Nd:YAG or neodymium doped yttrium–aluminium–garnet), liquid (dye) or another gas (e.g. He, Ne, etc.). In addition, there is the free-electron laser, which exploits a beam of accelerated electron moving through a magnetic assembly (modulator) as an active medium to generate a periodic magnetic field. For a ready reference, the characteristic features of some commonly used lasers, other than CO₂ laser, will now be outlined in brief.

1.2.1 Solid-State Laser

One of the most commonly used solid-state lasers is based on neodymium doped yttrium aluminium garnet (Nd:YAG) [11]. Here, neodymium atom is utilized in its trivalent state in the yttrium aluminium garnet crystal (Y₃Al₅O₁₂ or YAG). The excitation is accomplished by irradiating the material by a flash and arc lamp. The output power of this laser for continuous wave operation is in the range of a few watts up to a few kW. The output energies for pulsed lasers range from a few mJ to a few tens of Joules. The total efficiency is around 2%. Nd:YAG laser is commonly used for materials processing (cutting, drilling, welding, marking, surface engineering), medical (endoscopic surgery), and military (long range finders) applications. The major advantages of Nd:YAG laser over CO₂ laser lie in its smaller wavelength (1.06 μ m) and ability to deliver laser radiation through optical fibers. To increase the overall efficiency, attempts are being made to introduce new active materials containing sensitizer atoms to increase the overall efficiency of laser by absorbing the larger fraction of pump radiation and transferring it to active atom.

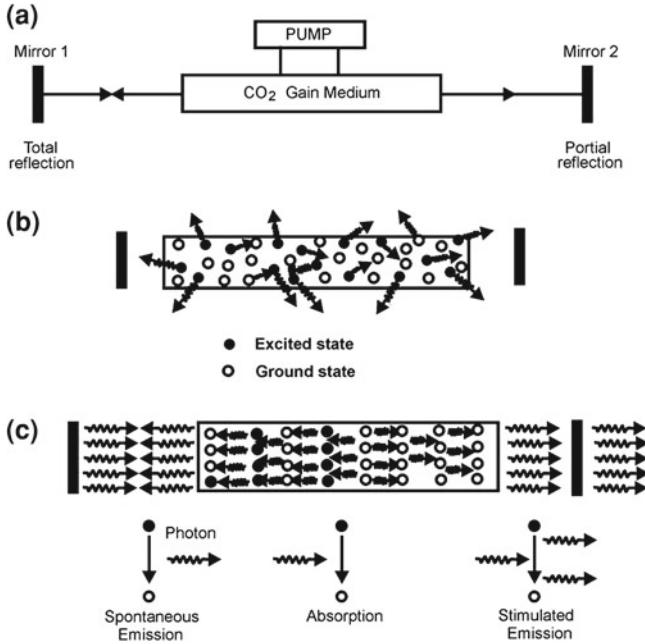


Fig. 1.1 Schematic setup showing generation of laser (a) the major constituents of the machine, (b) excitation and de-excitation of the atoms in the medium, and (c) stimulated emission and formation of laser beam [10]

1.2.2 Semiconductor or Diode Lasers

Laser action in GaAs and GaAsP laser diodes at cryogenic temperature was demonstrated as early as 1962 [11, 12]. The application of diode laser in that period was limited by the poor output power. However, these semiconductor lasers are now becoming increasingly popular both as a pump source for solid-state laser and in materials processing because of their unique features like small size, low weight, high efficiency, and reliability. More frequently used diodes are based on double hetero-junction using ternary compounds such as AlGaAs (p) and GaAs/GaAlAs (n). In this type of laser, the emitted radiation comes from the stimulated emission resulting from the recombination of electrons in the conduction band with holes in the valence band. However, several diode bars mounted into the multi-channel heat sinks are stacked on top of each other to further increase the power. Diode lasers have a potential scope of application in materials processing and gaining increasing popularity because of its lower installation/ maintenance cost and greater efficiency over CO₂ and Nd:YAG lasers [13].

1.2.3 Gas-Based Lasers

As already stated, CO₂ lasers seem to be one of the earliest developed and most popular lasers among the commercially available lasers for material processing because they are electrically more efficient (15–20%) and produce higher powers (0.1–50 kW) than other lasers in the continuous mode [14]. Despite being less efficient in energy coupling with metals due to longer wavelength (10.6 μm), the higher wall plug (~ 12%) and quantum (~ 45%) efficiency along with higher level of output power of CO₂ lasers more than compensate for the poor laser–matter energy coupling capability. On the other hand, Nd:YAG and Ruby lasers possess shorter wavelength and are more suited to pulsed mode of applications requiring deeper penetration, smaller area coverage, and precision treatment of materials for specific purposes. However, sheer size/volume of the CO₂ laser unit and operational/maintenance complexities are major disadvantages that have contributed in shifting attention toward solid-state lasers.

1.2.4 Free-Electron Lasers

Free-electron lasers are capable of operation over the entire electromagnetic spectrum from the microwave to the vacuum ultraviolet regions at average powers up to several kilowatts and peak powers up to a gigawatt [15]. At present, there are two principal areas for future free-electron laser development: higher average power and shorter wavelengths. Free-electron lasers consist of an electron beam propagating through a periodic magnetic field, called a wiggler or undulator [15]. Undulators are also used in incoherent synchrotron light sources. Lasing occurs because the wiggler and radiation combine to produce a heat wave that travels slower than the speed of light and can be synchronous with the electrons. The free-electron laser is continuously tunable, capable of high peak and average powers, and can produce a wide variety of pulse formats. The average power of this laser can be further raised. In continuous mode, a record average power of 1.7 kW has been produced at a wavelength of 3 μm. Similar power levels of about 2 kW in 1 ms pulse have also been produced in the infrared region. The high average power goal is several tens of kilowatts at infrared to ultraviolet wavelengths. The most likely configuration for generating a free-electron laser is an oscillator driven by a radiofrequency linear accelerator.

1.2.5 Ultra High Field Lasers

The development of lasers that are capable of producing short pulses of very high power has progressed enormously over the past 10 years [13]. There are two main types of ultra high field lasers in common use. On account of its broad gain bandwidth, Ti:sapphire (TiS) lasers enable pulses of very short durations (few tens of

femtoseconds) to be produced and energies of up to 1 J can be achieved at relatively high repetition rates (typically 10 Hz). Higher energy pulses (with a focused intensity of 10^{25} W/m²) can be obtained from Nd:glass lasers with a longer (several hundred femtoseconds) pulse durations and lower repetition rates [16, 17].

1.2.6 Excimer Lasers

Gas lasers make use of unstable molecules as the active material that is formed within the same electrical discharge used for the excitation. These molecules originate from the association of noble gas atoms such as Ar, Kr, Xe with halogen atoms such as F, Cl, Br. The available average power can reach the few hundred watts level in commercial units with an energy per pulse of the order of one joule and pulse repetition frequencies in the 100 Hz range. The achievable efficiencies can reach 4%, and the use of corrosion resistant materials has improved the discharge tube lifetime. These lasers are used for spectroscopy and photochemistry experiments in the ultraviolet range and for many applications related to surface treatment.

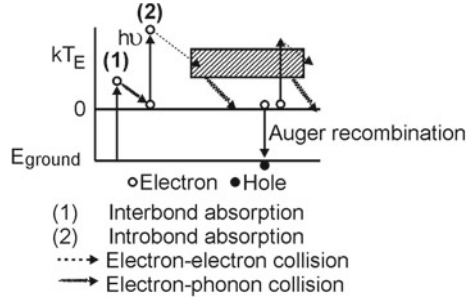
1.3 Laser–Matter Interaction for Material Processing

Laser–matter interaction within the near-surface region achieves extreme heating and cooling rates (10^3 – 10^{10} K/s), while the total deposited energy (typically, 0.1–10 J/cm²) is insufficient to affect, in a significant way, the temperature of the bulk material. This allows the near-surface region to be processed under extreme conditions with little effect on the bulk properties.

1.3.1 Lattice Heating

The initial stage in all laser assisted material processing applications involves the coupling of laser radiation to electrons within the metal. Initially, this occurs by the absorption of photons from the incident laser beam promoting the electrons from the valence/conduction bands to states of higher energy. Electrons that have been excited in this manner can divest themselves of their excess energy in a variety of ways. For example, if the photon energy is large enough (> several eV), the excited electrons can be removed entirely from the metal, causing the photoelectric effect. Most laser processing applications, however, utilize lasers emitting photons with relatively low energy. The energy of CO₂ laser photons is only 0.12 eV while the photons obtained from the Nd:YAG laser have about 1.2 eV of energy. Electrons excited by absorption of CO₂ or Nd:YAG laser radiation does not therefore have enough energy to be ejected from the metal surface. Such electrons must,

Fig. 1.2 Schematic diagram depicting electron excitation and carrier relaxation process in solids subjected to intense laser irradiation [18]



nevertheless, lose energy to return to an equilibrium state after photon excitation. This occurs when excited electrons are scattered by lattice defects like non-crystalline regions in a crystal such as dislocations and grain boundaries. In either case, the overall effect is to convert electronic energy derived from the beam of incident photons into heat. It is this heat that is useful (indeed necessary) in all material processing applications.

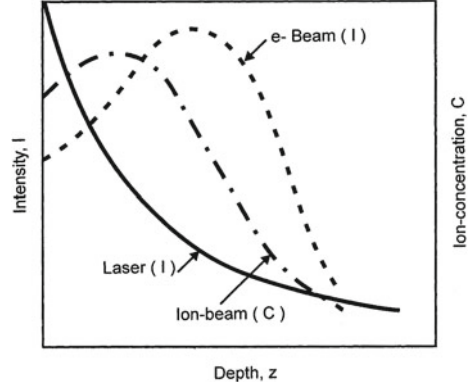
Figure 1.2 summarizes the process of electron excitation and excited carrier relaxation involved during laser–matter interaction schematically [18]. Photon interaction with matter occurs usually through the excitation of valence and conduction band electrons throughout the wavelength band from infrared (10 μm) to ultraviolet (0.2 μm) region. Absorption of wavelength between 0.2–10 μm leads to intraband transition (free electrons only) in metals and interband transition (valence to conduction) in semiconductors. Conversion of the absorbed energy to heat involves (a) excitation of valence and/or conduction band electrons, (b) excited electron–phonon interaction within a span of 10^{-11} – 10^{-12} s, (c) electron–electron or electron–plasma interaction, and (d) electron–hole recombination within 10^{-9} – 10^{-10} s (Auger-process). Since free carrier absorption (by conduction band electrons) is the primary route of energy absorption in metals, beam energy is almost instantaneously transferred to the lattice by electron–phonon interaction. Similarly, transition in semiconductor or polymers having ionic/covalent bonding with energy gap between conduction and valence bands is marginally slower.

1.3.2 Spatial Distribution of Deposited Energy

The spatial profile of deposited energy from laser beam is illustrated in Fig. 1.3. The laser beam intensity I at a depth z for the normally incident beam of initial intensity I_0 is given by [18]

$$I(z, t) = I_0(t)(1 - R)\exp(-\alpha z). \tag{1.2}$$

Fig. 1.3 Spatial profile of deposited energy intensity (I) or concentration (C) with depth (z) following irradiation/implantation of solid matter by laser, electron, and ion beams, respectively [18]



Here, I_0 is the incident intensity, t is time, R and α are the reflectivity and absorption coefficient, respectively. Since α is very high ($\sim 10^8 \text{ m}^{-1}$) for metals, light is totally absorbed within a depth of 10–20 nm. The efficiency of optical coupling is determined by the reflectivity (R). R for metals is relatively low at short wavelengths, rises abruptly at a critical wavelength, then remains very high at long wavelength [18].

For comparison, the deposited energy profile from the other two important directed-energy-sources, namely electron and ion beams, are also shown in Fig. 1.3. The energy deposition profile for electron beam irradiation of matter is given by a Gaussian function,

$$I(z, t) = I_0(t)(1 - R_E)f_E(x/x_P) \quad (1.3)$$

Here, R_E is the reflectivity for electron beam, x_P is the distance (x) that coincides with the peak intensity, and $f_E(x/x_P)$ is the spatial energy deposition profile. The deposition profile depends on the energy loss, hence on incident energy and atomic number. Thus, electron beam is more suited to deep penetration welding than to surface engineering applications. The concentration (C) of the implanted species in ion beam irradiation does not coincide with the top surface but lies underneath the surface as follows:

$$C(z) = \frac{Q_T}{\sqrt{2\pi} \Delta R_P} \exp \left[- \left(\frac{z - R_P}{\sqrt{2} \Delta R_P} \right)^2 \right] \quad (1.4)$$

Here, $C(z)$ is the concentration of a given species at a vertical distance z , R_P is the projected range/distance and Q_T is the ion dose.

1.3.3 Heat Transfer by Laser Irradiation

Usually, the deposited energy of laser irradiation is converted into heat on a timescale shorter than the pulse duration or laser interaction time [18]. The resulting

temperature profile depends on the deposited energy profile and thermal diffusion rate during laser irradiation. Thermal diffusivity (D) is related to thermal conductivity (k) and specific heat (c_p) as follows:

$$D = k/(\rho c_p) \quad (1.5)$$

where, ρ is the density. The vertical distance (z) over which heat diffuses during the pulse duration (t_p) is given by, $z = (2Dt_p)^{1/2}$. Here, z in comparison to laser absorption depth (α^{-1}) determines the temperature profile. For laser irradiation of metals, the typical value of α^{-1} is much less than z .

Under the one-dimensional heat flow condition, the heat balance can be expressed as [6]:

$$\rho c_p \frac{\partial T(z, t)}{\partial t} = Q(z, t) + \frac{\partial}{\partial z} k \frac{\partial T(z, t)}{\partial z} \quad (1.6)$$

where, T and Q are the temperature and power density at a given vertical distance of depth (z) and time (t), respectively. Q follows the functional relation with z as in Eq. (1.2). The heat balance Eq. (1.6) may be solved analytically if the coupling parameters (α and R) and materials parameters (ρ , k and c_p) are not temperature and phase dependent. However, phase changes are unavoidable except in solid-state processing. Thus, the heat balance equation is solved by numerical techniques like finite difference/element or controlled volume methods.

Depending on the temperature profile, the irradiated material may undergo only heating, melting, or vaporization. For surface melting and subsequent re-solidification, the solid–liquid interface initially moves away from and then travels back to the surface with a velocity as high as 1–30 m/s. The interface velocity is given by $v \propto (T_m - T_i)$, where T_m and T_i are the melting and interface temperatures, respectively [18]. Further details on mathematical modeling of heat transfer and phase evolution in laser material processing may be obtained in several textbooks dealing with laser material processing [4–6, 18].

1.3.4 Plasma Formation During Laser Irradiation

Laser-driven processes in which vaporization takes place are important for many applications like laser drilling and cutting, laser-induced surface chemical reactions in the reactive atmospheres, etc. [16, 19]. What is common to all these diverse applications of laser is the formation of a charged vapor stream. The ionized vapor contains not only the electrons and simple ions (as usually understood in a simple picture) but also the clusters of metals, reacted particles of oxides, nitrides, etc., which are charged and behave as Coulomb particles. They may form very complex structures of Coulomb liquids and solids, and show some new effects. Such plasma, called ‘dusty’ or ‘colloidal’ plasma has been considered in many studies [20]. Chu and Lin

[21], Melzer et al. [22], and Piel and Melzer [23] presented direct evidence of generation of plasma during laser-induced vaporization. Gnedovets et al. [24] synthesized ultrafine particles by laser vaporization of materials (metals, metal oxides, carbon) in a high-pressure atmosphere of chemically active (hydrogen, oxygen, air) and inert (helium, argon, xenon) gases as a result of vapor condensation. The dimensions of particles increased with increasing the ambient gas pressure. A particle nucleation and growth theory is used to describe the formation of the dispersed condensate in the erosive plasma. Cauble et al. [25] showed that the particle size, the particle–particle distance, and the particle density developed by laser assisted vaporization technique would depend on the laser power, gas pressure, and evaporation rate (i.e. on the boiling point of the material). Moreover, the vapor particle size should decrease with decreasing pressure and evaporation rate [26].

1.3.5 Effect of Ultra High Power Laser Irradiation

At very high intensities, the interaction between the radiation and matter gives rise to quite different phenomena from that observed at lower intensities [16]. For example, the energy acquired by an electron driven by the very high oscillating electric field of the intense radiation is approximately 10 MeV for laser intensity of 10^{24} W/m². Electrons with this energy can produce Bremsstrahlung or continuous radiation in the γ -ray range that is sufficiently energetic to induce (γ , n) nuclear reactions. Electrons can be accelerated to 100 MeV by plasma waves created by intense laser pulses and these interactions can also give rise to beams of energetic protons with applications in time-resolved imaging and tomography. Ultra high field lasers have been used to compress materials to ultra-high pressures and characterize their thermodynamic and transport properties [26]. When an ultra-high power laser pulse is focused into dense plasma, magnetic fields up to 10^9 G are generated and this has been predicted by both computer simulations and analytical calculations [16]. These fields are predicted to be localized near the critical density surface, i.e., the region where the laser frequency equals the plasma frequency and where most of the laser absorption takes place.

1.4 Application of Laser

Figure 1.4 presents a brief overview of the application of lasers in different fields with diverse objectives [2]. The list is neither complete nor exhaustive but is meant for providing an overview with representative examples. It serves only to show the diversity of the application of laser. In some applications, the power output is of main concern, e.g. atomic fusion and isotope separation. Sometimes, the main reason for using laser lies in spectral purity and coherence (pollution detection, length/velocity measurement, interferometry, etc.), low divergence (laser show, pointer/guide, audio-player), or a combination of all of them (communication, holography, metrology).

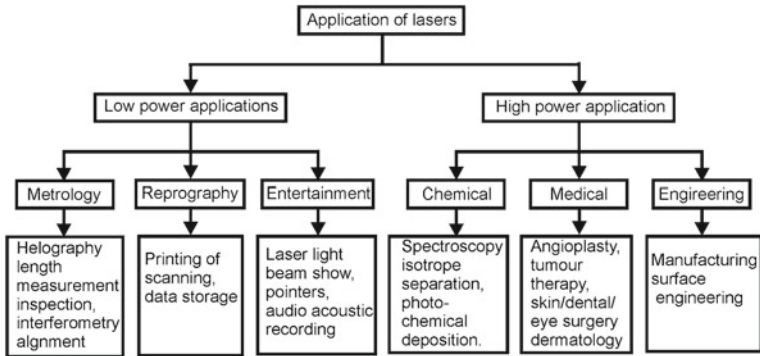


Fig. 1.4 Application spectrum of laser for the benefit of mankind [2]

Accordingly, a host of lasers capable of delivering a wide variety of wavelength, energy, temporal/spectral distribution, and efficiency have been developed over the past several decades [1–3].

1.5 Laser Assisted Fabrication of Engineering Materials

The increasing demand for laser in materials fabrication can be attributed to several unique advantages like fast processing speed, complete automation worthiness, non-contact processing, elimination of subsequent finishing operation, reduced processing or operational cost, improved product quality, greater material utilization, and minimum heat affected zone [1–3]. Figure 1.5 shows a general classification of the laser assisted fabrication techniques. In general, application of laser to materials fabrication can be grouped into two major classes (a) applications requiring limited energy/power and causing limited microstructural changes only within a small volume/area without change of state and (b) applications requiring substantial amount of energy to induce the change in state and phase transformation in large volume/area. The first category includes polymer curing, scribing/marking of integrated circuit substrates, etc. The second type of application encompasses cutting, welding, surface hardening, alloying, and cladding. The average power or energy input is relatively low in the first category, while that for the second category is higher as the processes involve single or multiple phase changes within a very short time. Almost all varieties of lasers can perform both types of operations in continuous wave and pulsed mode provided appropriate power/energy density and interaction time for the given wavelength are applied.

The classification based on state or phase change is too academic to be of practical use to end users. From the application point of view, laser material processing, as earlier stated, can be broadly divided into four major categories, namely, forming (changing shape or producing a component to manufacture a near net shape

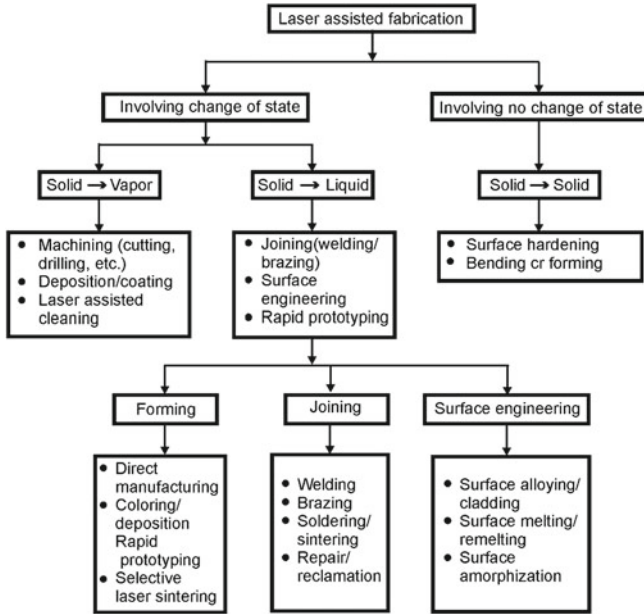


Fig. 1.5 General classification of laser assisted fabrication of materials for engineering applications

or finished product), joining (combining components by fusion welding, brazing, etc.), machining (removing material by cutting, drilling, etc.) and surface engineering (processing confined only to the near-surface region) [2–4]. Figure 1.5 presents this classification with a few representative examples from each category of application. However, this classification is based on the general definition and scope of the processes as understood in conventional practices.

The domain for different laser assisted fabrication techniques as a function of laser power and interaction time is illustrated in Fig. 1.6 [2]. The processes are divided into three major classes, namely involving only heating (without melting/vaporizing), melting (no vaporizing), and vaporizing. It is evident that transformation hardening, bending, and magnetic domain control which rely on surface heating without surface melting require low power density. On the other hand, surface melting, glazing, cladding, welding, and cutting that involve melting require high power density. Similarly, cutting, drilling, and similar machining operations remove material as vapor hence, need delivery of a substantially high power density within a very short interaction/pulse time. Since all laser material processing operations can be defined by an appropriate combination of power density and interaction time, one is tempted to combine these two into a single scalar parameter like energy density (power density multiplied by time, J/mm^2) for the sake of simplification and convenience. However, the exercise is bound to prove futile and not advisable as both the quantum of energy and its temporal and spatial interaction with matter (rather than their product) is crucial to achieve the desired microstructural/phase/state changes and properties for

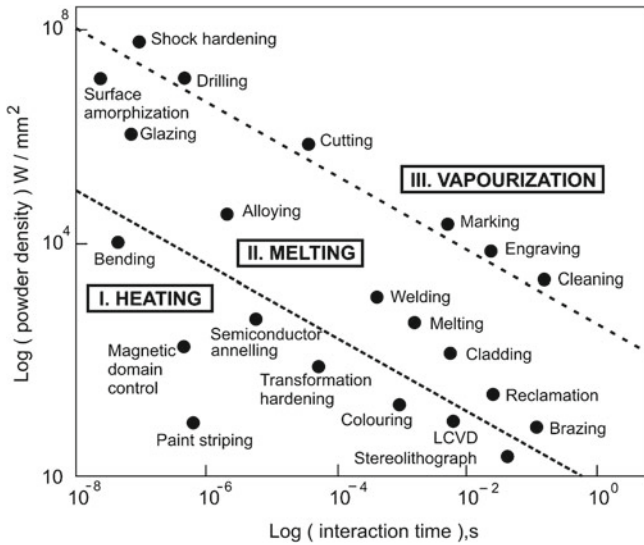


Fig. 1.6 Schematic process map in terms of combination of laser power density and interaction time for different types of laser material processing involving either no (only heating) or change of state (melting or vaporization) [2]

a given material. For instance, application of 10^{-2} J/mm² energy density may induce either surface hardening (say, for a given material combination of 10^2 W/mm² power density and 10^{-4} s interaction time) or surface melting (say, for a combination of 10^4 W/mm² power density and 10^{-6} s interaction time).

In laser assisted fabrication, a high-power laser beam interacts with the workpiece while a high relative speed is maintained between the two. The workpiece is usually mounted on a table capable of translation along two mutually perpendicular directions with a speed precisely controlled by a computer numerical controller. For convenience, the laser beam is kept stationary and the specimen is moved at a high speed. Several laser and material variables, either independent or dependent, play important roles in determining the final properties and characteristics of the processed zone. The independent variables are laser power, beam size, beam configuration, traverse speed of the workpiece, surface roughness, temperature, and surface condition of the substrate. The dependent variables are absorption coefficient, coverage rate, composition, and microstructure of the surface/near-surface region, hardness, residual stresses, heat-affected zone (HAZ) size, physical, mechanical, and electrochemical properties of the workpiece.

Laser power necessary for surface melting of metallic materials is generally high due to high reflectivity and thermal conductivity of metals. Reflectivity of the metal surface is actually related to electrical conductivity. The beam size determines the power density on the specimen surface (power density is defined as the power divided by the cross-sectional area of the laser beam). As already explained, the

combination of laser power density and interaction time should be carefully chosen during processing of materials by laser as this very combination primarily determines the scope and success of the process and properties for a given materials (Fig. 1.6).

Beam configuration or beam profile plays an important role in determining the energy distribution at the interaction zone during laser processing. Four types of beam profiles, namely Gaussian, multimode, square (or rectangular), and top hat are commonly used for material processing [2]. A Gaussian beam is most suitable for cutting and welding applications rather than for surface treatment because, being a 'sharp tool,' it tends to vaporize and melt the substrate deeply. In contrast, multimode, top hat, and square profiles ('blunt tools') are preferred for surface engineering. These beam profiles offer suitable surface casing with wider coverage rates and uniform case depths. Square and rectangular beam profiles are generated by using an optical integrator or scanner.

In the following sections, we will now review the individual classes of laser material processing and the current status of understanding.

1.6 Laser Assisted Shaping

The high power laser beam may be used as a source of heat to shape components in the desired dimension, shape, geometry, design, and properties. Laser material processing offers a unique possibility of manufacturing finished components directly from the raw materials without any elaborate intermediate operation [1–4, 27]. A one-step fabrication is most attractive, obviously for the tremendous economy in time, cost, material, and manpower associated with it than that necessary in the usual route of fabrication involving several intermediate stages/steps. Shaping of components by laser may be achieved by thermal stress assisted deformation (bending), direct forming of component from powder or wire by rapid prototyping/manufacturing, and reclamation/repairing [1–4]. These processes distinguish themselves from other laser material processing methods in their proclaimed objective of single-step manufacturing of a finished or semi-finished product than contributing toward any other intermediate processing steps like machining, joining, or surface engineering. For brevity, we will address all these laser assisted versions of otherwise conventional manufacturing processes as laser forming. In this section, laser assisted manufacturing techniques like laser bending and direct laser manufacturing techniques will be discussed in detail.

1.6.1 Laser Assisted Bending

Laser assisted bending involves modifying the curvature of sheet metal by thermal residual stresses induced by laser assisted heating without any externally applied mechanical forces [28–34]. Laser assisted bending also serves the purpose of straight-

ening thin sheets by a similar laser-based non-contact process. The process assumes significance due to the ease and flexibility of non-contact processing, amenability to various types of materials and direct manufacturing of components with diverse shape/geometry, properties and composition with high precision/ productivity. Laser assisted bending involves a complex interplay between the thermal profile and stresses generated by laser irradiation, which in turn depend on many parameters such as laser power density, interaction/pulse time, material properties (thermal, physical or chemical), and dimension/geometry of the work piece (thickness, curvature, etc.). Bending of strong and difficult-to-bend metals (body centred cubic, BCC or hexagonal close packed, HCP), intermetallics, composites, and ceramics have been an important motivation for the increasing interest in laser assisted bending. The success of laser bending of semiconductor and polymeric sheets are of great interest to the semiconductor and packaging industry.

There are three mechanisms of laser assisted bending, i.e., temperature gradient mechanism, buckling mechanism, and upsetting mechanism [30–35]. Many applications involve a complex combination of these mechanisms rather than only one of them.

1. Temperature Gradient Mechanism

Temperature gradient mechanism is operative when a steep temperature gradient across the thickness of sheet metal is encountered, particularly when the beam diameter is typically of the order of sheet metal thickness or width and the traverse rate is fast enough to maintain a steep temperature gradient. Figure 1.7a explains the thermal history and mechanism associated with temperature gradient assisted bending of sheet. At the initial stage of laser heating, the surface of the metal facing laser is heated up leading to counter-bending of the sheet away from the laser beam as a result of rapid thermal expansion of the top-surface than the bottom layer. Further heating leads to decreasing the flow stress in the heated area and increasing thermal expansion of the surface layer. At a certain temperature, the geometry and degree of counter-bending reach the maximum elastic strain that the metal can endure beyond which plastic compressive strain sets in with further increase in temperature and thermal expansion. These plastic compressive strains accumulate until laser irradiation shifts to allow cooling to begin mainly due to self-quenching with the heat flowing into the surrounding bulk to cool the irradiated zone within 10–20 s. During cooling, shrinkage of the heated material occurs both due to natural contraction on cooling and plastic compression induced by prior laser heating. Due to the differential lengths between the top and bottom surface layers of the sheet, a bending angle develops toward the laser beam.

2. Buckling mechanism

The buckling mechanism will occur if the beam diameter of laser is large compared to the sheet metal thickness, laser beam intensity profile is Gaussian or multiple Gaussian, and the processing time is low, resulting in a small temperature gradient across the sheet metal thickness. Figure 1.7b describes the principle of laser bending by buckling mechanism. Primarily, the material is heated, which in turn leads to the thermal expansion and generation of compressive stresses in the neighboring heated

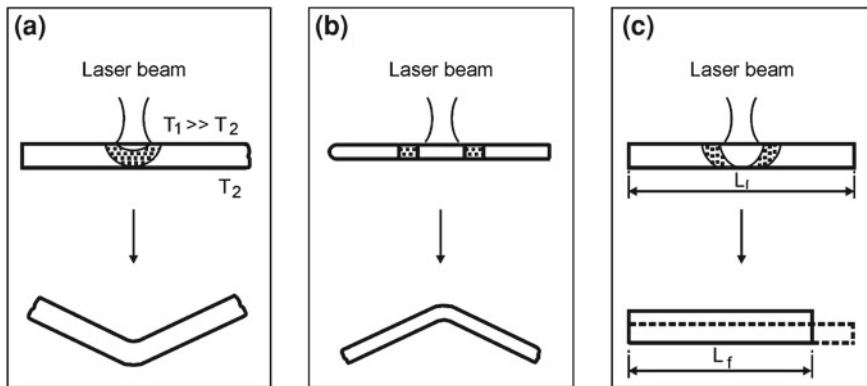


Fig. 1.7 Deformation modes of laser bending based on (a) temperature gradient mechanism, (b) buckling mechanism, and (c) upsetting mechanism, respectively. T_1 and T_2 are temperatures on opposite surfaces. L_i and L_f are the initial and final lengths of the sheet [30]

region. If the heated area is large enough with a small natural deviation from the perfect plane, an instability, or buckle, develops. At the center of the buckle, the temperature is extremely high, therefore the flow stress in this region is relatively low and the bending of the sheet in this region is totally plastic. In contrast, the root (or end) of the buckle, which is far away from the center of the laser beam, is heated to a much lesser extent with smaller temperature rise. If the flow stress is relatively high, this small temperature rise can only result in complete elastic bending. By controlling appropriate parameters, positive (concave bending toward the laser beam) or negative (convex bending away from the laser beam) bending can be achieved with the buckling mechanism [35]. As the beam moves along the surface, the buckle shifts along the bending edge. The relative motion between the beam and work piece along the surface can also alter the stiffness of the work piece. At the start of the buckling process, the bending legs are held in the original plane due to the stiff surrounding material. However, the force that holds the bending legs straight decreases with increase in amount of forming. Therefore, the elastic part of the buckle relaxes and only the plastic part remains in the sheet, resulting in an angular bend. Because the buckling mechanism results in more energy being coupled to the work piece, bending angle often up to 15° is achieved after a single pass.

3. Upsetting Mechanism

The upsetting mechanism occurs if the laser beam diameter is in the order of or less than the sheet metal thickness with a very low traverse speed. The low processing speed will result in almost homogeneous heating across the thickness of the sheet metal. Owing to the temperature increase, the flow stress decreases in the heated area and the thermal stress approaches the elastic limit. Additional heating leads to a plastic compression of the heated material as it is hindered in free expansion by the surrounding bulk material. Therefore, a large amount of thermal expansion is converted into plastic compression. During cooling the material contracts and the

plastic compressive strain remains in the sheet for exactly the same reason as in the temperature gradient mechanism. Owing to the constancy of volume, there is an increase in the sheet thickness in the compressed area. Figure 1.7c shows the process of laser assisted upsetting that leads to shrinkage of initial length, L_i to smaller final length, L_f with a concomitant increase in thickness from the initial dimension (shown by broken lines).

The concept of laser bending may be extended to straightening of a welded component in a car body to reduce distortion arising out of welding [35], and deep drawing [36]. Laser bending may be combined with conventional forming to blend the high speed of conventional forming with the accuracy of laser forming without any special setup [37]. In laser assisted deep drawing, a laser beam is used to heat the wire to a critical temperature in order to make the wire plastic and easily deformable. Wire feeding and pulling rates are maintained through a feeder and puller roller at a predetermined speed to achieve the desired drawing ratio. The process was applied to nickel wire and was reported to exhibit an increased drawability as compared to the conventional technique, though laser parameters were reported to play a role in determining the drawing limit [36]. Brittle materials can also be successfully drawn without any rupture or micro-crack using laser.

The prediction/optimization of laser parameters may be attained by a detailed theoretical model. Deformation behaviors of Ti-based alloys were extensively studied Chen et al. [38] using finite element method. Marya and Edwards [39] analyzed the laser bending of two titanium alloy sheets, Ti-6Al-2Sn-4Zr-2Mo (near-alpha alloy) and Ti-15V-3Al-3Cr-3Sn (beta alloy) using a conduction model with a traveling Gaussian heat source. Temperature and bending angle were predicted and correlated with process parameters. Bending was found to initiate at 0.48 of the melting temperature and attained a maximum value at approximately 0.65 of the melting temperature. The effect of process parameter on bending angle was explained by analytical model developed by Cheng and Lin [40] and also 3-D finite element simulation by Kovacevic et al. [41]. The experimental results were suitably compared with the theoretical prediction. Laser bending of cold rolled steel was studied by Peng and Lawrence [42] where, the effects of the plastic anisotropy on bending deformation during the laser forming process have been investigated both experimentally and numerically. Most of the research articles concern a detailed experimental observation of studying the effect of laser parameters on the bending characteristics of different materials. Studies on AISI 1008 steel and mild steel show that bending angle increases with increase in laser power and number of repetitions, on the other hand, it decreases with increase in can-speed and beam size/diameter for [43, 44]. The bending angle usually increases with increase in thermal-effect index (coefficient of thermal expansion divided by the product of density and specific heat). However, strength or modulus has no significant influence on it [43]. Among the geometric parameters, sheet thickness influences the bending angle the most, and the latter decreases sharply with increase in sheet thickness [43]. The bending behavior of AISI 304 austenitic stainless steel wire (0.1 mm diameter) to develop complex frame structures such as zigzag or crank wire frames was studied by Yoshika et al. [45] with a Nd:YAG laser offering 0.02 – 0.2 J energy. Besides fabricating to the desired complex shape, it

also improved the strength of the frame structure. The investigation on laser bending of AISI 304 stainless steel of different thicknesses using continuous wave CO₂ laser showed that the rate of bending increased with increase in applied power density and the effect was more significant at a higher number of passes. However, an optimum range of laser power should be selected so that the applied power density is capable of bending without excess melting, evaporation, or crater formation. The rate of bending increased with increase in the number of passes due to increase in cumulative thermal stress. The thermal stress generated in each pass was proportional to the thermal gradient. Furthermore, cross-sectional thickness at the bent region is progressively reduced during successive passes due to material flow away from the bent region after each pass. Microstructural analysis of different regions of the bent surface and its variation with laser parameters were undertaken to understand the mechanism of bending. Figure 1.8a–c show the microstructure of the (a) irradiated region, i.e. inner side of bending, (b) solid-liquid interface and (c) heat affected zone of the irradiated zone, of laser bent AISI 304 stainless steel lased with a power density of $19.6 \times 10^7 \text{ W/m}^2$, scan speed of 4 m/min and 10 passes. Figure 1.8a suggests that laser irradiation causes melting and high rate of quenching of the near-surface region to develop a very fine-grained and equiaxed microstructure at the near-surface region. Refinement of microstructure achieved in laser bending operation is beneficial in increasing the strength without sacrificing the ductility of the inner side of the laser bent zone. Although melting occurs at the irradiated region, subsequent rapid solidification leads to formation of a defect-free and continuous remelted region or interface (Fig. 1.8b). It is apparent that fine dendrites form and grow from the former solid-liquid interface. Microstructure in the narrow heat effected zone shows evidences of grain coarsening due to heat flow beyond the thin surface wetted region (Fig. 1.8c) [46]. A detailed XRD analysis of the bent zone revealed that, while phase aggregate remained the same, lattice strain due to thermal effect led to measurable broadening of peaks [46].

Besides microstructure, laser bending affects microhardness in different zones depending on the laser parameters adopted. Figure 1.9 shows the variation of microhardness with distance at different regions of laser bent steel (lased with a power of $54.3 \times 10^7 \text{ W/m}^2$, scan speed of 5,000 mm/min). Microhardness increases to 250 VHN as compared to 190 VHN of the substrate at the inner bent zone. The microhardness further increases after multiple passes (275 VHN after 40 passes) possibly due to recrystallization and grain refinement effect. The sudden rise in hardness immediately after the melt zone is attributed to the formation of Cr₂₃C₆ precipitates along the zone near to the solid-liquid interface [46].

Subsequent grain coarsening in the heat affected zone reduces the hardness considerably resulting in a sudden drop in microhardness (Fig. 1.9). On the other hand, microhardness of the outer bent zone (reverse side of the irradiated zone) is marginally increased due to working effect (as also evident from Fig. 1.9). The microhardness of melt zone and outer zone along the centerline of the bent sheet is, however, found to vary with laser parameters. Increase in the number of passes increases the microhardness of the irradiated zone due to microstructural refinement [46]. On the other hand, the hardness of the outer bent region increases with increased number of passes

Fig. 1.8 Scanning electron micrographs of the (a) irradiated region, i.e., inner side of bending, (b) solid–liquid interface, and (c) heat affected of laser bent AISI 304 stainless steel irradiated with a power density of $19.6 \times 10^7 \text{ W/m}^2$, scan speed of 4,000 mm/min and 10 number of passes [46]

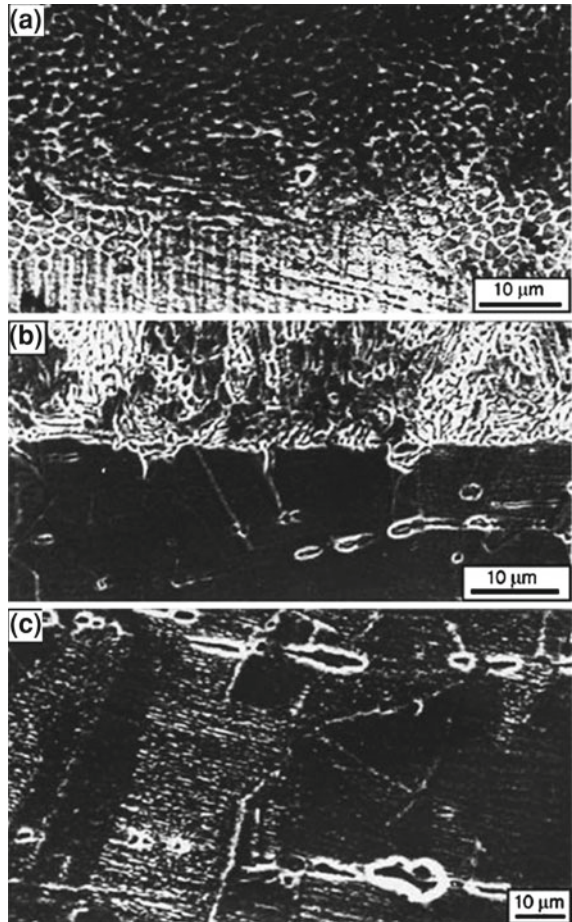
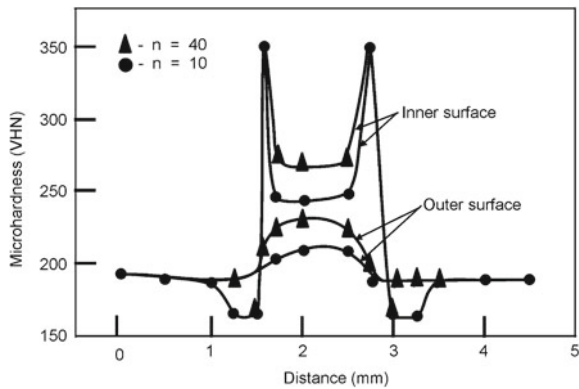


Fig. 1.9 Distribution of microhardness along the length of laser bent AISI 304 stainless steel (sheet thickness of 0.9 mm, lased with a power of $54.3 \times 10^7 \text{ W/cm}^2$, scan speed of 5,000 mm/min) [46]



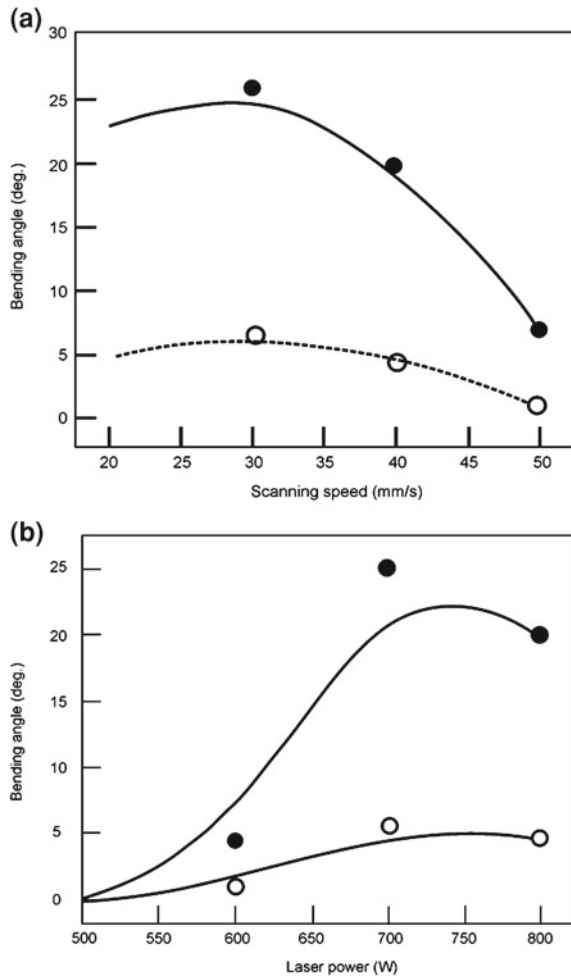
mainly because of a larger degree of deformation induced at greater thermal stress developed due to repeated irradiation. Hence, laser bending is a unique technique of bending of sheet metals with an improved mechanical property at the centerline of laser bending.

In case of materials which undergo phase transformation, the phase transformation stress should also be taken into account. Wang et al. [47] studied the bending of St C45 steel (C: 0.08, Si: 0.3–0.1, Mn: < 0.4, P : < 0.025, S : < 0.025) by a continuous wave CO₂ laser and observed that the final deformation angle was found to depend on a combined action of thermal strain and phase transformation strain. Bending of tube is primarily achieved through thickening of the scanned region instead of thinning of the un-scanned region, and the scanned region assumes a slightly protruded shape [48]. The importance of the process lies on bending of metal matrix composite and difficult to bend materials. Laser assisted bending has been studied in Ti and its alloys [49–56]. Magee et al. [50–52] studied the influence of process variables on laser bending of $\alpha + \beta$ Ti alloy (Ti–6Al–4V) using a continuous wave CO₂ laser. Blake et al. [53, 54] studied the effect of beam divergence, feed rate, laser power, and pulse width on the angle and range in laser assisted bending of Ti–6Al–4V and Ti–15V–3Cr–3Sn–3Al using a 400-W pulsed Nd-YAG and 50 W desktop CO₂ laser. Similarly, Maher et al. [55] and Hatayama and Osawa [56] investigated the effect of process variables on the bending behavior of pure Ti. Marya and Edwards [39] studied the interactions between process variables, materials properties, and residual angular distortions (bending angle) during laser assisted bending of Ti–6Al–2Sn–4Zr–2Mo and Ti–15V–3Al–3Cr–3Sn alloys.

Okuda et al. [57] studied the deformation mechanism of Mg alloy by finite element modeling. Chan et al. [58] compared the deformation behavior of chromium sheet having limited room temperature ductility subjected to roll compression and laser bending technique. In roll compression test, a bending angle of 90° was achieved without fracture at a temperature of 100°C. However, the maximum bending angle achieved by non-contact laser bending was 23.5° and the same was found to increase with increase in applied power density and number of irradiation.

The deformation behavior of SiCp reinforced 6,092 aluminum matrix composite using a 2 kW Nd:YAG laser was studied by Liu et al. [59]. Figure 1.10 shows the variation of bending angle as a function of (a) laser scanning velocity at laser powers of 500 W and (b) applied power at an average scan speed of 5 mm/s. It is evident that the bending angle decreases with increase in scan speed because of the decrease in interaction time between the laser beam and composite. On the other hand, the bending angle increases with increase in applied power. However, when the applied power is above 700 W, there is no more increase in the bending angle. Under a suitable condition for bending, a linear relationship between the bending angle and the number of irradiation passes was observed. Ramos et al. [60] investigated the microstructures of Alclad 2024–T3 Al–Cu alloy following bending by a CO₂ laser. It was observed that the irradiated zone experienced different stages of thermal annealing including recovery (sub-grain formation), recrystallization, and grain growth depending on the deposited thermal energy. Recrystallized zone suffered partial melting at the grain

Fig. 1.10 Variation of bending angle as a function of (a) scanning speed at an applied power of 800 W, and (b) applied power at a scan speed of 40 mm/min for laser bent SiC dispersed 6092Al matrix composite lased with a continuous wave Nd:YAG laser [59]



boundary corners or triple points leading to precipitation along grain boundaries on cooling.

In spite of its poor room temperature ductility, Ti_3 Al-based intermetallic alloy was reported to be laser bent by Yet Chan and Liang [49] primarily due to the differential degree of thermal expansion of the intermetallic across the thickness. A linear relationship between laser bending angle and line energy was observed when the line energy was between 1 and 5 J/mm². Significant changes in microstructures were observed in the alloy after bending without formation of cracks or voids. The hardness profile and microstructure of the deformed specimen revealed that there was a steep temperature gradient across the thickness and the laser bending mechanism was related to that gradient.

1.6.2 Laser Rapid Prototyping

One of the most recent applications of laser in material processing is the development of small, complex, and intricate components by coupling laser with computer controlled positioning stages and computer-aided engineering design [61–66]. This technology is based on repetitive deposition and processing of material layers known as additive freeform fabrication technique [67, 68]. The advantages offered by these techniques include the capabilities to produce components of intricate shape with a greater accuracy, faster processing speed, economy in energy and material consumption, etc. Over 40 different types of additive free-forming technologies have been identified for component development with size ranging from desktop unit to machine tools [69, 70]. In all cases, these technologies are capable of manufacturing parts/components in a single step without the use of specialized tooling, thereby reducing the time needed to manufacture components. Each of these technologies employs the use of computer-aided design and modeling to directly deliver energy or deposit materials in selective layers during fabrication. Depending on the process, a post processing activity may be needed ranging from powder sintering photopolymer curing or excess material removal to produce the final component. Powder-based additive free forming techniques use powders as raw material in shaping material. In ultraviolet selected laser sintering, a thin layer of photo-curable suspensions of ceramic powders is cured by an ultraviolet laser in selected areas [71, 72]. The extrusion free forming technique uses temperature sensitive monomers or reactive compounds in aqueous ceramic slurry to fabricate solid, “gelled” ceramic bodies [73].

On the other hand, the laminated tape method uses ceramic green tapes prepared from evaporation casting of non-aqueous slurries to fabricate parts with a laser-cut, stack, and laminate sequence similar to the laminated object manufacturing process [74, 75]. With this technique, complex high density silicon nitride components with internal passages have been developed for potential use in rocket engine injectors [76].

Ceramic three dimensional printing methods involve the use of an ink-jet mechanism to inject organic binder into a ceramic powder substrate. Freeform powder melding is a more recent development which uses deposition of sinterable part powders and unsinterable tool powder in selected areas of each layer to build a three-dimensional part. In stereolithography, the solid object is made by scanning an ultraviolet laser beam over the surface of a bath of epoxy resin that hardens on exposure to the ultraviolet light. Once a layer is complete, the base plate moves down a little in the bath and a new layer of liquid flows in over the top to enable the next layer to form on top. The layer building continues until the component is ready in the desired dimension [77]. In selective laser sintering, instead of liquid resin, a fluidized powder bed or sheet is used that is heated close to its melting point. The carbon dioxide laser beam scans over the powder and heats the grains so that they undergo incipient melting and sintering. Subsequently, the base plate moves down

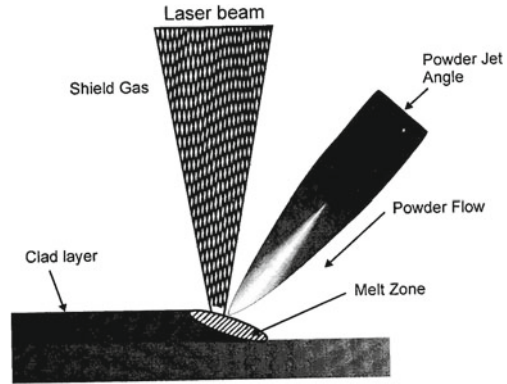
slightly, and the next layer of powder is spread across the surface by a rotating roller [77]. The process continues until the desired shape or object is ready.

In laminated object manufacturing, the pre-form is built from the layers by pulling long and thin sheets of pre-glued paper/plastic across the base plate and fixing it in place with a heated roller that activates the glue [74]. A computer controlled laser head scans the surface and cuts out the outline of the desired object. As the base plate moves down, the whole process starts again. At the end of the build process, the little cross-hatched columns are broken away to free the object. In the fused deposition process, the object is made by squeezing a continuous thread of the material through a narrow nozzle (heated by laser) that is moved over the base plate [74]. As the thread passes through the nozzle, it melts only to harden again immediately as it touches (and sticks to) the layer below. For certain shapes, a support structure is needed, and this is provided by a second nozzle squeezing out a similar thread, usually of a different color to make separating the two easier. At the end of the build process, the support structure is broken away and discarded freeing the object/model. The models made from wax or plastics in this method are physically robust. This new fabrication concept allows construction of complex parts, starting from a three-dimensional computer-aided design model without a mold.

Laser assisted direct metal deposition refers to the additive layered manufacturing technology for building components from a computer-aided design model [2]. Metal powders, injected into the laser focal zone, are melted and then re-solidified into fully dense metal in the wake of the moving molten pool created by the laser beam. Successive layers are then stacked to produce the entire component volume of fused metal representing the desired model. These processes have been proven suitable for fabricating components from nearly any metal system to near net shape accuracy with mechanical properties approaching and in some cases exceeding the properties found in conventionally processed wrought structures.

Figure 1.11 shows the schematic of direct laser fabrication process. Single-step processing by laser engineered net shaping and direct laser fabrication produce cost saving realized by elimination of conventional multi-step thermomechanical processing. Design features such as internal cavities or overhanging features can be made without joined assemblies. Hard to process materials such as intermetallics, refractory metals, and high temperature alloys can be processed in a single step. Functionally graded compositions can be created within three-dimensional components to vary the properties to match localized requirements due to service environment. The technology offers the designer a rapid prototyping capability at the push of a button, without the need to fabricate dies or use of forming equipment or extensive machining and joining processes to produce a part. Future development is still required for these processes to be commercially accepted and used in the industry. Parts are deposited with a surface roughness of 10 μm , arithmetic average, making a secondary finishing operation necessary for some applications to achieve high accuracy and polished surface texture. Residual stress measurement and control is also required to avoid distortion of the deposited components. Motion path and control code needs to be optimized to reduce the overall process time from the computer-aided model to the

Fig. 1.11 Schematic of laser deposition process. Powder is carried and delivered by argon gas through the nozzle into the laser beam and the molten metal deposits on the substrate underneath



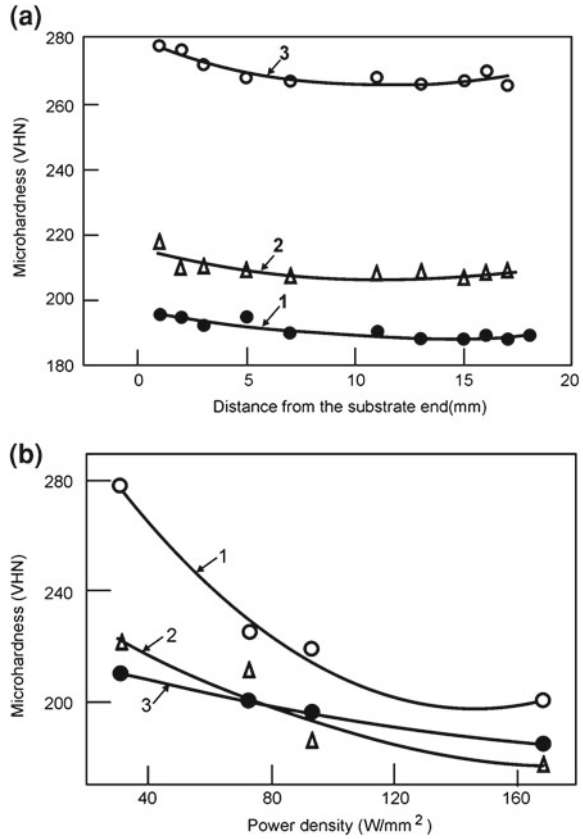
finished part. Lewis and Schlienger [78] have explained the process and its possibility of application in detail.

Laser engineered net shaping is a process in which near-net-shape metal structures are built from powdered metal layer by layer from computer-generated designs. Zhang et al. [79] discussed the characteristics of laser engineered net shaping, directed light fabrication, and shape deposition manufacturing. The fundamental of selective laser sintering has been studied by Goode [80]. Dai and Shaw [81] developed a 3-D thermomechanical finite element model to investigate the transient temperature and residual stress fields in laser assisted fabricated part. The model system chosen was 93Cu + 7Sn and NiMo mixed with 70% (MoW)2NiB2:30%NiMo. McAlea et al. [82] discussed the laser-based rapid prototyping technique and compared with the sand and investment casting technique. The possibility of application of laser assisted deposition in fabrication of part in the packaging industry and microelectronic component have been discussed by Bauer et al. [83] and Micheli and Boyd [84], respectively. Griffith et al. [85] described the use of contact and imaging techniques to monitor the thermal signature during laser engineered net shaping. The understanding of solidification behavior, residual stress, and microstructural evolution with respect to thermal behavior were discussed.

Metal rapid prototypes and fabrication of molds using hybrid processes of selective laser cladding and milling techniques have been studied by Jeng and Lin [86]. The injection molding machine used in this study was a metal powder injector with precise temperature control. The chemical composition of the metal powder used in the injection machine was W (93%), Ni (4.9%), and Fe (2.1%). The density of the alloy was 7.9 Mg/m³. The selective cladding process was employed to build up the material layer-by-layer, and the milling operation was employed to level the top surface of the clad to increase the accumulation of powder and accurately control the clad height. Similarly, fabrication of a 3-D structure using micro-electro-discharge machining and laser assembly and application of laser welding of wire, subsequent deposition, and milling for rapid prototyping were discussed by Kuo et al. [87] and Choi et al. [88], respectively. Direct laser sintering of iron, Cr-V tool steel,

7Fe–4.3C, 97Al–3Fe, 93.3Cu–2.8Sn–3.9C and 93.4Fe–1.6C–2.5Cu2.5MoS₂ alloys were undertaken and the effect of process parameters on sintering behavior was studied [89]. Tang et al. [90] and Wang et al. [91] carried out selected laser sintering of Cu-based alloys. Khaing et al. [92] developed a 3-D soft and porous structure from a mixture of Ni, bronze and Cu powders using EOS INT M250 laser sintering machine. Kathuria [93] investigated selected laser sintering of 3 dimensional components made of Co, Ni, and Cu alloys. Hayano [94] and Tolochko et al. [95] fabricated dental root implants made of Ti by selected laser sintering. Components of different shapes from AISI 304 stainless steel were fabricated by Jeng et al. [96] using selective laser cladding technique using a Rofin Sinar RS820 1500 W CO₂ laser. The effect of process parameters on the clad height and surface quality has been studied for direct laser deposited AISI 316L stainless steel using diode laser and continuous wave CO₂ lasers [97, 98]. Dutta Majumdar et al. [99, 100] observed that the morphology and degree of fineness of the microstructure of AISI 316L components fabricated using a 1.5 kW continuous wave diode laser were directly related to the laser parameters. The range of grain size (maximum to minimum) was taken as a measure of homogeneity. It was found that the range of grain size and micro-porosity reduced to a minimum with increase in scan speed. Figure 1.12a shows the variation of average microhardness of direct-laser clad AISI 316L stainless steel along the wall growth direction for laser assisted fabricated AISI 316L stainless steel processed with the respective power density and scan speed combinations of (1) 0.091 kW/mm², 2.5 mm/s; (2) 0.091 kW/mm², 5 mm/s; (3) 0.031 kW/mm², 5 mm/s (with a common powder feed rate of 136 mg/s). Figure 1.12b reveals a similar analysis of variation of microhardness with applied power density obtained by laser fabrication with identical conditions of laser cladding. From Fig. 1.12a, it is evident that the microhardness is uniform throughout the cross section along the wall height with a marginally higher value near the substrate and a lower value at the intermediate region. The marginally higher value of microhardness near the substrate region is mainly because of refinement of microstructure due to a high quenching rate from the underlying substrate. On the other hand, lower level of microhardness at the intermediate region is attributed to the grain coarsening effect. Application of a lower power density (plot 3 vis-à-vis plot 2) increases the average microhardness. Similarly, application of a lower scan speed (plot 1 vis-à-vis plot 2), increases the average microhardness of the fabricated layer. Hence, the microhardness of the fabricated layer marginally varies with the position and is highly dependent on the applied laser parameters. Figure 1.12b further suggests that average microhardness of the fabricated layers decreases with increase in applied power density. This effect is attributed to coarsening of grains revealed from a detailed microstructural investigation [99]. A close comparison of plot 1 with plot 2 shows that average microhardness value increases with increase in scan speed. With increasing the scan speed, due to a shorter time of interaction a low energy is supplied during melting resulting in refinement of grains, and hence, increase in average microhardness. The effect of powder flow rate on the microhardness does not however, show any specific trend (plot 2 vis-à-vis plot 3). From the variation of microhardness with laser parameters, it may be concluded that hardening of the formed parts is mainly because of grain refinement

Fig. 1.12 Variation of average microhardness with (a) distance or length and (b) applied power density for laser fabricated AISI 316L stainless steel using different combinations of power density, scan speed and feed rate (marked as 1, 2, 3) [100]



and for an improved microhardness, a combination of low power and high scan speed should be chosen. Furthermore, the critical potential for pit formation (E_{PP1}) (550 mV(SCE)) was superior to that of the conventionally processed AISI 316L stainless steel substrate (445 mV(SCE)) also due to pronounced uniformity and refinement of grain size.

Metallic foam is increasingly becoming popular due to its unique combinations of low density and high compressive strength [101]. Aluminum foam has evoked a special interest due to its lightweight structure and possibilities of various structural applications in automotive, aerospace and allied industries. However, manufacturing techniques associated with aluminum foam limits the application of it on a wider scale. Kathuria [102] attempted to fabricate Al-7% Si foam using Nd-YAG laser and obtained a localized and unidirectional expansion of the foam in the direction of laser irradiation with as high as 60% porosity and closed-cell structure. The synthesis involved mixing the alloy powder with a foaming agent, cold isostatic pressing of the mixture to form a foamable sandwich precursor, and heating it up to its melting point by a high power laser beam. Laser irradiation is useful in inducing rapid

decomposition of the foaming agent into hydrogen or some other gaseous product and allowing precipitation of intermetallic phases to strengthen the matrix phase. Zhang et al. [103], Mei et al. [104], Arcella and Froes [105] and Abbott and Arcella [106] attempted fabrication of fully dense and rapidly solidified components by direct laser deposition. Srivastava et al. [107, 108] developed TiAl alloy by direct laser fabrication using gas atomized Ti₄₈Al₂Mn₂Nb powder as feedstock and a VFA 600 W CO₂ laser unit. The microstructure was heterogeneous and extremely fine compared to the conventionally processed material. A post heat treatment was found to improve the microstructural and compositional homogeneity. Banerjee et al. [109–111] developed Ti–6Al–4V–TiB, Ti–25%V and Ti–TiB composites using laser engineered net-shaping process. Tomochika et al. [112] attempted to synthesize NiTi intermetallic compound by laser assisted melting of a combination of pure Ti (300 μm diameter) and pure Ni wire (250/350 μm diameters) followed by high pressure Ar gas assisted atomization and coating on aluminum substrate. The particle size of the atomized powder ranged from 10 to 125 μm and the thickness of the coating was 3 mm. The sintered compact of equi-atomic blend of Ti and Ni was single phase NiTi martensite with martensitic (M_f) and austenitic finish (A_f) temperatures of 320 K and 365 K, respectively. Zhang et al. [113] developed TiAl intermetallics by laser engineered net shaping using a continuous wave Nd:YAG laser. Wu and Mai [114] developed Ti and TiAl alloy parts with various geometries by direct laser fabrication. Tang et al. [115] prepared Ti/TiN in situ composites by laser induced reaction between Ti powder and N₂ gas and evaluated their mechanical properties. For complex alloy systems, the microstructure of the direct laser clad component was found to be different from the single clad layer and varied with the numbers of passes.

Karlsen et al. [116] developed the Co-Cr-Mo superalloy for bio-implants with improved biocompatibility. Ni- and Co-based superalloys were fabricated by the direct laser metal deposition technique [116–118]. The tensile strength of the laser consolidated Co-based superalloy was reported to be 50% higher than that of as-cast or powder fabricated components attributed to the exceptionally fine columnar dendrite microstructure produced by the rapid solidification [117].

A new rapid prototyping method has been developed by combining selective laser sintering and gel-casting technique for the fabrication of complex-shaped Al₂O₃ ceramic parts [119]. The process involves aqueous gelcasting to form high mechanical strength Al₂O₃-based green body by in situ polymerization of Al₂O₃ slurry containing monomer and cross-linker, and sintering of the green compact by selective laser sintering machine. The main advantages of the method lie in the absence of any container or die, minimum contamination, and possibility of having high liquid temperatures. Furthermore, the process allows solidification to proceed with a planar and stable liquid–solid interface accompanied by high thermal gradient and high crystal growth rates.

Larrea et al. [120] described the procedure for preparing large surfaces of eutectic composites of Al₂O₃ – ZrO₂, with thickness up to 250 mm, using a modified laser zone melting. The surface of a ceramic precursor is scanned with a rectangular CO₂ laser beam of 20 × 0.5 mm size which induces surface melting. The microstructure

consisted of fine, alternating, and interpenetrating Al_2O_3 and ZrO_2 single crystal lamellae.

Laser can be a useful tool for in situ rapid fabrication of composite components like cutting tools, shear blades, etc. Lu et al. [121] fabricated TiC dispersed Cu–Ti–C and Cu–Ni–Ti–C composites by laser scanning (using a CO_2 laser) of ball milled powder mixtures of Cu–Ti–C and Cu–Ni–Ti–C. Liu and Du Pont [122] developed crack-free functionally graded TiC/Ti composite materials by laser engineered net shaping with compositions changing from pure Ti to approximately 95 vol% TiC. Kathuria [123] fabricated porous components of 93 % Cu+7 % Sn and 70% (MoW) $_2$ NiB $_2$:30% NiMo alloy powders using Nd:YAG laser. Wang et al. [124] fabricated W/W $_2$ Ni $_3$ Si ternary in situ metal silicide matrix composites using direct laser deposition. Duan and Wang [125] developed rapidly solidified Cr $_3$ Si metal silicide ‘in situ’ composites by laser melting of Cr–Si–Ni alloy powders. Cheng et al. [126] studied the influence of process parameters on structure and integrity of Al/SiC composite by direct laser deposition.

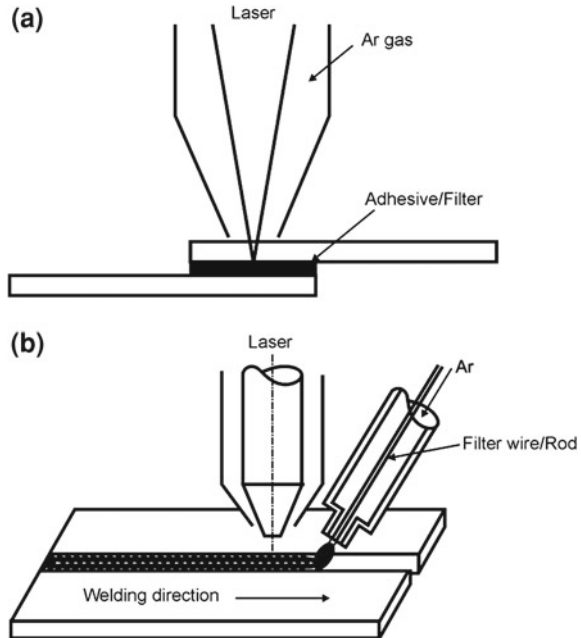
An intelligent laser processing based on size-dependent optical absorption coefficient of metal particles has enabled fabrication of almost mono-dispersed metallic nanoparticles on a chosen substrate [127]. Using this method, Ag clusters with mean diameters of 10 nm and size distributions of 0.13 have been prepared [127].

Irradiation with the second harmonic generation of 1.06 μm Q-switched Nd:YAG laser on powdered nonlinear crystals suspended in a photopolymeric solution enabled high resolution rapid prototyping [65]. One such structure developed by this method was a 3-D periodic photonic band-gap structure of aluminum oxide that consisted of layers of parallel rods forming a face-centered tetragonal lattice [128]. A similar laser-driven direct-write deposition technique (from trimethylaminealane and oxygen precursors) was successfully utilized to fabricate a 3-D microstructure consisting of aluminum oxide and aluminum [129]. These laser deposited rapid prototype ceramic components are useful as micromechanical actuators like microtweezers and micro-motors.

1.7 Laser Joining

Joining of similar or dissimilar materials may be achieved by using high power laser beam as a source of heat. Laser assisted joining offers the following advantages over conventional fusion or arc welding processes: high welding speed, narrow heat affected zone (HAZ), low distortion, ease of automation, ability for single-pass joining of thick sections, and better design flexibility with controlled bead size [2, 77]. Laser assisted joining may include welding, brazing, soldering, and micro welding. However, as joining of materials requires a laser source capable of delivering high power density, pulsed or continuous wave Nd:YAG, CO_2 laser and diode lasers are commonly used for joining. Laser assisted joining is applicable to both inorganic/organic and similar/dissimilar materials with an extremely high precision, versatility, and productivity that can only be matched by electron beam welding.

Fig. 1.13 Schematic views of laser assisted (a) lap welding, and (b) butt welding

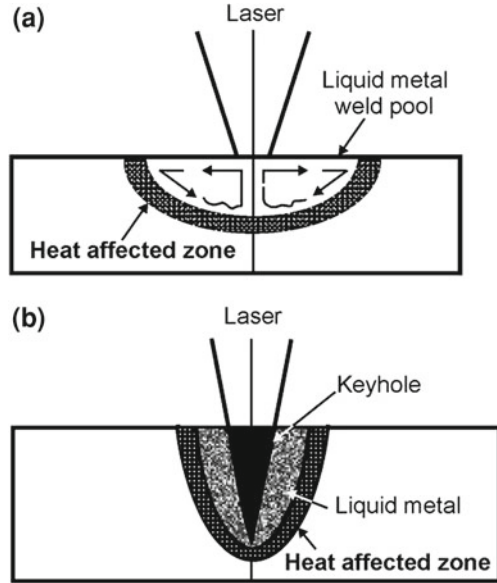


Moreover, laser assisted joining can be done in atmosphere (with proper shrouding), unlike the vacuum processing needed in electron beam welding.

Laser welding is the emerging and most important operation among the laser joining processes [2, 130–154]. Figure 1.13a, b show the schematic set up for laser welding with (a) lap welding and (b) butt welding configuration. The focused laser beam is made to irradiate the work piece or joint at the given location with a finite beam size, configuration and speed. A shroud gas at adequate flow rate protects the weld pool from undue oxidation. Laser heating partially melts and fuses the work pieces or plate edges and joins the adjoining surfaces once solidified after the beam is withdrawn. In case of welding with filler, melting is primarily confined to the feeding wire tip while a part of the substrate being irradiated melts to ensure a smooth joint. In either case, the work piece rather than the beam travels (say, along y in Fig. 1.13a and along x in Fig. 1.13b) at a rate conducive for welding with a minimum heat affected zone.

There are two fundamental modes of laser welding depending on the beam power/configuration and its focus with respect to the work piece: (a) conduction welding and (b) keyhole or penetration welding (Fig. 1.14a, b). Conduction welding occurs when the beam is out of focus (above the surface) and power density is low / insufficient to cause boiling at the given welding speed. In deep penetration or keyhole welding, the beam focus lies below the surface so that sufficient energy per unit area is available to cause evaporation and formation of a hole in the melt pool. The ‘keyhole’ behaves like an optical black body in that the radiation enters the hole and

Fig. 1.14 Schematic of **a** conduction melt pool (*semi-circular*), **b** deep penetration (*key hole*) fusion zone and weld [178]



is subjected to multiple reflections before being able to escape. The transition from conduction mode to deep penetration mode occurs with increase in laser intensity and duration of laser pulse applied to the work piece.

The welding efficiency can be expressed in terms of the power (or energy) transfer coefficient (η) where η is the ratio between laser power absorbed by the work piece and incident laser power. η is usually very small but can approach unity once a keyhole has been established. The melting efficiency or melting ratio (ε) is given by,

$$\varepsilon = \frac{v d W \Delta H_m}{P} \quad (1.7)$$

where, ε is the rate of melting, P the incident laser power, v the welding speed, d the sheet thickness, W the beam width, and ΔH_m the enthalpy or heat content of the metal at the melting temperature. The maximum value of ε is 0.48 for penetration welds and 0.37 for conduction welds [135].

Laser assisted welding has been successfully implemented in a large number of metallic materials [138, 155–178]. High speed laser welding of tin plate and tin free steel for container industries was reported by Majumdar and Steen [158]. Yang and Lee [159] measured the low cycle fatigue strength and residual stress of laser spot welded mild steel (using a continuous wave CO₂ laser) and compared the weld strength with that welded by resistance spot welding. Finite element modeling revealed that residual tensile stress was distributed over the inner and outer rims of the fusion zone. Banas [160] conducted high power laser welding experiments with austenitic stainless steel and showed an equivalent strength in the weld joint as

compared to that of the base metal. Shielding gas was also found to play a major role in determining the quality of the weld zone [161]. It was observed that shielding gas determines the period, size and shape of the plasma created by laser irradiation depending on the ionization potential, dissociation potential, thermal conductivity, and atomic weight of shielding gas. Ghaini et al. [162] studied the influence of laser pulse energy, duration, and travel speed on weld dimension, microstructure, and hardness during overlapping laser assisted bead-on-plate spot welding of low carbon steel using a pulsed Nd:YAG laser.

Kwok et al. [163] fabricated austenitic (S30400 and S31603), duplex (S31803) and super duplex (S32760) stainless steels by laser penetration welding with a continuous wave Nd:YAG laser in an argon atmosphere. The welds exhibited passivity but their pitting corrosion resistance deteriorated as compared with that of the unwelded specimens which is attributed to micro-segregation in the weld zone of S31603, and to the presence of δ -ferrite in S30400, and the change of the ferrite/austenite phase balance in duplex grades S31803 and S32760 in the weld zone.

Laser parameters also play a role in determining the optimum quality of the weld zone. Depending on the base metal thickness, parameters like laser power, welding speed, defocusing distance, and shielding gas should be carefully selected so that weld joints having complete penetration, minimum fusion zone size, and acceptable weld profile are produced [140]. Chan et al. [165] carried out welding of 0.5, 0.6, 0.8, and 1.0 mm thick steel sheets to form tailored weld blanks with different thickness ratios of 2 (0.5/1.0 mm), 1.67 (0.6/1.0 mm), and 1.25 (0.8/1.0 mm) using an Nd:YAG laser. The forming limit diagrams of the tailor-welded blanks indicated that the higher the thickness ratio, the lower the formability of the tailored weld blanks [165]. Costa et al. [167] studied the weldability of hard metal (K40, 88% WC, 12% Co, and K10, 94.4% WC, 5.6% Co) to steel with a high power continuous wave CO₂ laser or Nd:YAG laser and pulsed Nd:YAG laser. Weld bead size, microstructure, bending strength, and hardness were evaluated to correlate the mechanical properties with the concerned welding parameters to obtain full penetration and high strength joints. K40 (88% WC, 12% Co) quality tips have higher resistance after welding, compared to that in K10 samples, that contained cracks after welding. It was concluded that laser welding particularly with continuous wave Nd:YAG laser was an effective joining technique for hard metals, vis-à-vis brazing or mechanical clamping, for manufacturing cutting tools with small weld beads and heat affected zone and a minimum residual stress.

Electro-galvanized steel sheet with zinc coating (thickness of 7.5 μm) was laser welded using a continuous wave CO₂ laser with 23 mm beam diameter having near Gaussian beam configuration. Subsequent electrochemical tests in 1 N NaCl solution revealed the presence of Zn-Fe intermetallic phases in the heat affected zone that accounted for improved adhesion and better sacrificial protection against corrosion [168]. Iqbal et al. [169] developed a new method of using two tandem laser beams for lap welding of galvanized steel sheets. This involves a pre-cursor beam and a higher power actual beam, generated independently or otherwise split from the same source. The first beam cuts a slot, thus making an exit path for the zinc vapors, while the second beam performs the desired welding. The process is easier as it does not need any preprocessing, prearranging with additional components or contour limitations

and the welders may proceed with the jobs as per non-coated steel and applying the technique, the weld zone can get rid of all or a part of the zinc vapour porosity at lower or higher speed, respectively. The experimental results seem promising showing the total absence of zinc in the welds. However, selection of proper source, beam alignment (between weld and cut), and proper sheet clamping are important.

Laser welding of lightweight metals like Al, Mg, Ti, and their alloys for aerospace applications have been reviewed by Schubart et al. [179]. Both conduction-mode and keyhole-mode welding are possible in aluminum [138]. Weld pool shapes in aluminum depend on the mean power density of the laser beam and the laser pulse or interaction time. Transition from conduction- to keyhole-mode welding is known to occur in aluminum at a power density of about 10 GW/m^2 , compared to about 4 GW/m^2 for stainless steel. In both materials, large occluded vapor pores near the root of keyhole-mode welds are common at higher power density due to hydrogen. This porosity problem can be reasonably eliminated by surface milling and vacuum annealing [138].

In comparison with electron beam welding, laser welding yielded a higher fusion-zone depth to width ratio, cooling rate and porosity, and a lower solute loss and post-weld tensile strain [139]. A similar investigation on microstructural evaluation following autogenous bead-on-plate CO_2 laser welding of an Al-8.5Fe-1.2V-1.7Si alloy (in wt. %) on 2 mm thick sheet showed that the fusion zone microstructure consisted of faceted precipitates of around $10 \mu\text{m}$ embedded in cellular-dendritic α -Al matrix with submicrometer intercellular phases [180]. Continuous wave Nd:YAG laser welding of AA5083-O wrought aluminium alloy with a high Mg content (4.5%) and A356 cast aluminium alloy with 7% Si and a cast oxide layer was carried out by Haboudou et al. [181]. Braun [182] made a detailed study on butt welding of 6013 aluminium alloy sheet using a 3-kW Nd:YAG laser with two kinds of filler metals: gas atomized powders of aluminium alloys AlMg5, AlSi12, AlSi12Mg5, and AlSi10Mg, as well as powder mixtures of Al and Si and the binary alloys Al-5Mg, Al-5Zr, Al-5Cr, and Al-10Mn. The weld region exhibited a dendritic/cellular structure in the fusion zone and a partially melted zone adjacent to the fusion boundaries. The hardness of the fusion zone depended upon composition of the filler metals. Post-weld artificial aging improved the hardness due to the precipitation of strengthening phases. Optimum tensile properties were obtained with joints made with the filler powder AlSi12. The dispersoid forming elements Zr, Cr, and Mn added to a mixed Al-7Si powder did not prove beneficial in terms of weld quality. When exposed to an intermittent acidified salt spray fog, joints in the as-welded T4 and post-weld heat treated T6 conditions exhibited corrosion behavior similar to that of the base sheet in the tempers T4 and T6. As-welded 6013-T4 joints were susceptible to stress corrosion cracking when immersed in an aqueous solution of $0.6\text{M NaCl} + 0.06\text{M NaHCO}_3$. Sensitivity to environmentally aided cracking was associated with grain boundary precipitation in the heat affected zone.

Yue et al. [183] studied the influence of laser parameters on the welding behavior of a SiC particulate reinforced 2124 Al alloy composite using a pulsed Nd-YAG laser. Defects like solidification cracks and porosities were the common defects in laser welded Al-2124/SiC composite, formed mostly at high laser intensities and

short pulse durations. Wang et al. [184] have demonstrated the versatility of laser welding by carrying out in situ weld alloying and laser beam welding to join SiC reinforced 6061Al metal matrix composite using titanium as filler alloying element. Microstructural studies show that the detrimental needle-like aluminum carbides are completely eliminated and the central fusion joint consists of TiC, Ti₅Si₃, and Al₃Ti along with some large pores.

Microstructure and properties of 0.5-mm thick welded sheets of commercial purity titanium have been studied and compared following high vacuum electron beam welding, CO₂ laser beam welding and tungsten inert gas welding processes [185]. It was observed that electron beam welding is more suitable for defect-free welding of commercial purity titanium. Ti₃Al–Nb alloy is one of the strong candidates for structural applications at moderate temperature in aerospace field because of its relatively low density and high elastic modulus. Wu et al. [186] welded Ti–24Al–17Nb (at.%) alloy with a fast axial flow type CO₂ laser of 3.0 kW rated power. The weld microstructure consisted primarily of ordered β phase (namely β 2 phase) and was independent of the laser parameters. The size and orientation of the solidification structures in the weld and bend ductility of the joints were related to the welding condition. The microstructure became coarser and the tendency for defect formation decreased as the heat input increased. The tensile strength and ductility of the joints were equal to that of the base material.

Laser welding of Ti-based alloys were extensively studied by Uenishi et al. [187], Li et al. [188] and Hsu et al. [149]. The microstructure of the fusion zone was strongly influenced by laser parameters. Hsu et al. [149] studied the effect of CO₂ laser welding of binary Ti₅₀Ni₅₀ and Ti_{49.5}Ni_{50.5} on shape-memory and corrosion characteristics of these alloys. Although martensite start (M_s) temperature was slightly lowered, no deterioration in shape-memory character of either alloy was observed. The same alloy registered satisfactory performance in potentiodynamic corrosion tests in 1.5 M H₂SO₄ and 1.5 M HNO₃ solutions. However, a significantly higher corrosion rate and a less stable passivity was noted in artificial saliva. On the other hand, the pseudoelastic behavior of the laser weld of Ti_{49.5}Ni_{50.5} alloy (in cyclic deformation) indicated that the stress (σ_m) required to form stress-induced martensite and permanent residual strain (ϵ_p) were higher after welding due to the more inhomogeneous nature of the weld metal.

Spot welding of Ta plates was performed with a pulsed Nd:YAG laser (50 W) coupled with a step index fiber. A series of spot welds was achieved with a peak power of 3 kW (i.e. a power density of $42 \times 10^9 \text{ Wm}^{-2}$) and pulse duration between 1 and 16 ms [189]. The presence of small and large key holes suggested that the key-hole geometry and solidification time primarily determined whether volume defects (porosity) would form and optimization of process parameters could minimize the tendency of defect formation.

Bead-on-plate welds were produced on 4-mm thick V-4Cr-4Ti alloy sheets using a 1.6 kW pulsed YAG laser with fibre-optic beam delivery [190]. The effect of process parameters (laser power, interaction time, welding atmosphere) on weld depth, porosity, and oxygen uptake was studied to determine optimum pulse

parameters as follows: 4 J/ms pulse energy, 3 ms pulse length, and 132 Hz pulse repetition rate.

Laser beam welding of Hastelloy X was performed using a 1.2 and 6 kW CO₂ laser with lap and butt joints [191]. Cracks in the fusion zone were observed which could be eliminated by changing the beam diameter and alignment. Metallurgical analysis using electron microscopes revealed pronounced signature of redistribution of alloying elements in the weld zone.

Song et al. [192] studied the weldability of AZ31B magnesium alloy sheets by laser-arc hybrid welding process. A sound overlap-welded joints of magnesium alloy AZ31B sheets without defects was obtained. Among the welding parameters, defocusing distance and laser-to-arc distance were key factors to affect the penetration depth and bead shape. It was also found that the cross section of hybrid overlap-welded joint assumed a “thumb pin” shape due to the nature of energy deposition in laser-arc hybrid welding. Hybrid overlap-welded joints actually comprises two parts: one due to laser irradiation alone, while the other due to the action of both laser and arc. The study showed that tensile strength and corrosion resistance of laser-arc hybrid welded AZ31B alloy was 80% equivalent to that of the base metal, respectively. In another attempt, Liming et al. [193] compared the weldability of AZ31B magnesium alloy using hybrid laser-TIG (LATIG) welding, laser beam welding (LBW) and gas tungsten arc (TIG) welding and found that the welding speed of LATIG was higher than that of TIG but comparable to LBW, and penetration of LATIG was twice that of TIG and four times that of LBW. In addition, arc stability was better in hybrid laser-TIG welding than TIG welding, especially at high welding speed and low TIG current. It was found that the heat affected zone of joint was only observed in TIG welding, and the size of the grains was evidently coarse.

Kim et al. [194] studied the welding of Cu₅₄Ni₆Zr₂₂Ti₁₈ metallic glass using pulsed Nd:YAG laser. It was observed that crystallization could be suppressed both in weldment and heat affected zone at a welding speed of 60 mm/min. On the other hand, crystallization areas with a band shape were observed at a welding speed of 20 mm/min.

Wang et al. [195] studied the scope of welding between SiC dispersed 6061 Al matrix composite. Formation of needle-like detrimental phases of Al₄C₃ following the partial or complete dissolution of SiC reinforcement particles in the central weld was a serious problem. The harmful needle-like carbide formation was avoided by addition of Ti as an alloying element in the composites [184]. Central fusion zone consisted of TiC, Ti₅Si₃, and Al₃Ti.

Sierra et al. [196] studied the weldability of a low carbon steel to 6,000 series aluminium alloy in key-hole welding mode using a continuous wave Nd:YAG laser. Defect-free welding can be obtained on overlapping Al + steel joints with the weld zone composed of solid solution of aluminium in iron and FeAl phases when penetration of steel in aluminium was below 500 μm. Embrittlement at the joining zone was observed, mainly located on the weld-aluminium interfaces comprising Fe₂Al₅ and/or FeAl₃ phases with thicknesses between 5 μm and 20 μm.

Majumdar et al. [197] developed crack-free weld between a commercially available Ti alloy (Ti-6 wt% Al-4 wt% V) and a wrought Al alloy (Al-1 wt%

Mg-0.9wt% Si). Intermetallic compounds (mainly TiAl and Ti₃Al) were formed in the fusion zone depending on the amount of Al and Ti melted by the laser. These intermetallic phases are very brittle and the solid-state cracks are formed near the Al side of the interface because of the stress developed after the solidification. In order to minimize the dissolution of Al in the fusion zone and to increase the toughness of the intermetallic phases, Nb foil is added as a buffer between the Ti alloy and Al alloy work pieces. It is observed that the partially melted Nb acts as a barrier to dissolve Al in the fusion zone and facilitates a good joining condition for welding of Ti alloy with Al alloy.

Mai and Spowage [198] studied welding of steel to Kovar, copper to steel and copper to aluminium using a 350-W pulsed Nd:YAG laser. Laser welding of steel and Kovar resulted in significant intermixing of both materials within the fusion zone. Although the steel plate was completely melted, a complete metallurgical bond could not be obtained at the interface between the Cu-plate and the weld metal, mainly due to the high thermal conductivity of copper. The weldability of copper to aluminium is regarded as relatively good. The Cu–Al phase diagram shows a wide range of Cu–Al phases that may be formed. In addition, non-equilibrium cooling conditions are known to promote the formation of a series of metastable phases. Under optimum processing parameters, crack-free welds between copper and Al 4047 were obtained.

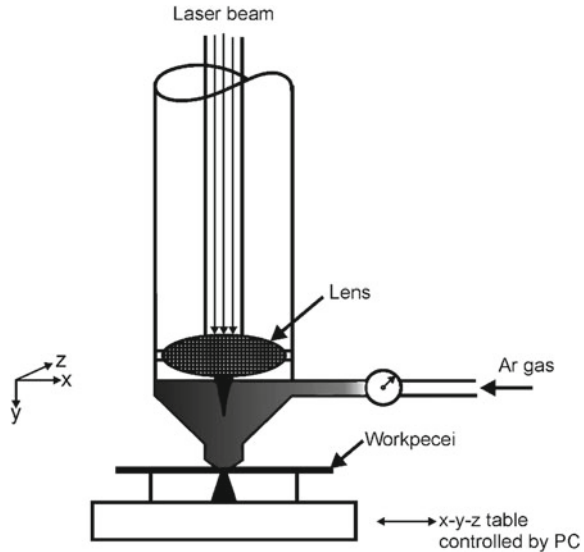
1.8 Laser Machining

Machining of materials can be achieved by laser-induced concomitant melting and evaporation from the surface or bulk of the work piece. A high power laser may be utilized to carry out drilling, cutting, cleaning, marking, and scribing up to a limited dimension or depth of all varieties of materials [2, 4]. In this section, the principle of different laser assisted machining processes would be discussed highlighting the scope/versatility of the processes emphasizing the recent advances and future scope of applications.

1.8.1 Laser Cutting

Cutting is the most widely practiced industrial application of laser among the machining operations. The advantages of laser cutting over other techniques are: flexibility, scope of automation, ease of control over depth of cut, cleanliness, non-contact processing, speed, amenability to a wide variety of materials (ductile/brittle, conductor/non-conductor, hard/soft), negligible heat affected zone, and narrow kerf [2]. Figure 1.15 shows the schematic of a laser assisted cutting setup. The specimen is fixed in X–Y sweeping stage. The laser beam is used to irradiate the material surface with a particular interaction time so as to cause controlled removal of solid from the surface. The main processing parameters for laser assisted cutting

Fig. 1.15 Schematic of laser assisted cutting setup [2]



are applied power density, interaction, time and shrouding environment. There are six different mechanisms for laser assisted cutting of materials, namely vaporization cutting, melting and blowing (or simply melting), burning and blowing, thermal stress cracking, scribing, and cold cutting [2].

1. Vaporization cutting

In vaporization cutting, the focused beam raises the surface temperature above the boiling point and generates a keyhole, which causes a sudden increase in absorptivity due to multiple reflections leading to quicker extension of the hole. As the hole or kerf deepens, vapor forms, ejects out of the hole or kerf, and stabilizes the molten walls of the hole. This method is more useful in cutting materials that do not melt such as wood, carbon, and plastic. The parameters controlling the laser cutting operation are beam diameter, laser power, traverse speed, gas composition, material thickness, reflectivity, and thermophysical properties of the work piece. Vaporization cutting of ceramics depends largely on the power density of the laser beam. Normally, the intensity should be near to or greater than 10^{12} W/m² for complete vaporization before cutting/evaporation.

2. Fusion cutting (melting and blowing)

In this process, a laser beam is used to melt the material and cutting is undertaken by blowing the molten material away with a sufficiently strong gas jet. This process requires only one tenth of the power for vaporization. If the gas (oxygen) reacts exothermically with the workpiece then another heat source is added to the process and is termed as reactive fusion cutting. Usually the reactive gas is oxygen or some other gas mixture containing oxygen. The burning reaction starts usually at the top when the temperature reaches the ignition temperature leading to the formation of

oxide that blows into the kerf and covers the melt. Formation of striation is a problem associated with reactive fusion cutting when the cutting speed is very slow. Chen and Siores [199] discussed the problem of striation formation in detail during the laser cutting process. Pietro and Yao [200] developed a transient 2-D model to investigate the effect of various CNC velocity profiles on the resulting cutting front temperature. It was shown that cutting efficiency increased with the cutting speed because of the greater energy coupling to the work piece. Steady-state cutting front temperature also increased with increasing cutting speed. Boundary encroachment and bulk heating effects (due to workpiece geometry) caused the front velocity to increase dramatically on approaching the edge of the workpiece so that the beam coupling was significantly reduced without changing the processing speed. A nonlinear velocity profile was evaluated via an optimization strategy that stabilized the cutting front temperature to its steady-state value. Duan et al. [201–203] developed a theoretical model for predicting the 3-D stationary geometry of the cutting front during laser assisted fusion cutting. The effect of various laser processing parameters, multiple reflections and inert gas pressure on the geometric shape of the cutting front and cut-edge quality were analyzed in detail.

3. Controlled Fracture

This approach is useful for cutting brittle material. During this process, laser beam heats a small volume of the surface causing it to expand and produce tensile stresses around the irradiated zone. If there is a crack in this space, it will act as a stress raiser, and cracking will continue in the direction of hot spot. The process requires very little power. The heat produced on the surface separates the substrate controllably along the moving path of the laser beam. Because the extension of the breaking frontier is larger than the movement of the laser spot, the actual fracture trajectory deviates from the desired trajectory while cutting a curve or an asymmetric straight line. To eliminate this deviation, the iterative learning control method is introduced to obtain the optimal laser beam movement path [204].

4. Scribing

During the process, a laser beam is used to weaken the structure by making a groove or line of holes following which it is mechanically broken. Absence of formation of debris and low heat affected zone are the advantages associated with this technique [2].

5. Cold Cutting

This is the process of breaking the bond of organic materials by irradiating it with excimer laser working in the ultraviolet region [2]. This process is useful in cutting plastic, machining of human hair, micro-surgery, and engineering with single cells, tumor surgery, etc. Correlation of cutting characteristics with laser parameters and analysis of process windows for laser cutting is essential to attain a defect-free cutting operation [205]. Experimental observations showed that the differences between upper and lower corner stresses are temporarily dependent on the passivation breakthrough caused by upper corner cracks. In a recent model on metal cutting with a gas assisted CO₂ laser, laser cutting is considered as a surface reaction and absorption

process that needs an adjusting parameter to represent the absorptivity for different materials at different incident angles [206]. Computation of the mass diffusion rate at the gas/solid boundary of the cutting front should include the exothermic heat released during cutting. It is shown that a very small level of impurity in oxygen exerts a significant influence on the cutting performance. Earlier, the combined effect of chemical reactions taking place between a gas jet and molten metal was considered adopting a laminar boundary layer approach [207]. Li et al. [208] presented an analytical model for laser cutting.

Laser parameters controlling the quality of cutting zone include laser power density, interaction time, position of the laser beam with respect to the surface, and the gas composition. The empirical relationship among laser power (P , W), sheet thickness (d , mm), cut width (s , mm), and cutting speed (V , mm/min) was established as: $P = 390d^{0.21} s^{0.01} V^{0.16}$ (ignoring variation of thermal properties of material with temperature) [209]. The composition of cutting gas also plays an important role in determining the quality of cut. It was found that high purity oxygen was conducive for better cutting performance as compared to inert gas. However, striation formation at the cut edge is often encountered during oxygen cutting of mild steel attributed to (1) cyclic variation in the driving force of the oxidation reaction owing to changes in the oxygen partial pressure in the melt zone melt (2) viscosity and surface-tension effects associated with melt removal [210].

Machinability of galvabond steel sheet with a good quality was achieved using continuous wave CO₂ laser by proper control of the cutting parameters [211]. Laser cutting was successfully applied for cutting of stainless steel, aluminium, and mild steel with a CO₂ laser and showed that laser cuts had narrower kerf width with better accuracy than that by mechanical cutting [212]. Metal matrix composites are difficult to machine. Pulsed laser cutting of Al–Li/SiC metal matrix composite was extensively studied by Yue and Lau [213] to optimize the process parameters to minimize the heat-affected zone, improve the quality of the machined surface, and predict the maximum depth-of-cut for the composite. The effects of femtosecond laser machining on surface characteristics and subsurface microstructure of a Nitinol alloy were studied by Huang et al. [214].

Superalloys have high strengths at elevated temperatures, which make them attractive for various structural applications at high temperature. The same property makes these materials difficult to machine at room temperature due to excessive tool wear and poor surface finish. Laser assisted machining offers the ability to machine superalloys more efficiently and economically by providing the local heating of the workpiece prior to material removal by a single point cutting tool. The machinability of Inconel 718 under varying conditions was evaluated by Anderson et al. [215]. With increasing material preheating temperature from room temperature to 620°C (by laser heating), the benefit of laser assisted machining was demonstrated by a 25% decrease in specific cutting energy, 2–3-fold improvement in surface roughness and 200–300% increase in ceramic tool life over that in conventional machining. Moreover, an economic analysis shows significant benefits of laser assisted machining of Inconel 718 over conventional machining with carbide and ceramic inserts.

One of the most useful and niche applications of laser is cutting of ceramics. Ceramics have excellent resistance to heating, wear, and corrosion, and are routinely used in many industrial applications. However, the high hardness and brittleness of ceramics makes them difficult and expensive to machines using conventional cutting methods or tools. Laser cutting provides a good means for cutting of ceramics in non-contact mode with excellent precision. In laser machining of ceramics, the removal process is a combination of several mechanisms, the extent and magnitude of each varying according to the nature and power of the laser beam and the type of ceramic substrate being machined. Basically, the machining process consists of three inherent stages, i.e., vaporization cutting, melting, and ejection and controlled fracture [216]. However, the success of laser cutting of ceramics crucially depends on resolving a few fundamental problems like formation of cracks during cutting due to thermal shock. Lu et al. [217] studied the problem of cracking of ceramic plates during laser assisted cutting and identified that the most relevant parameters for laser cutting were laser power (P) and scan speed (v), specific heat (c), conductivity, (k) and thermal expansion coefficient (α). Tsai and Chen [218] attempted synchronous application of Nd:YAG and CO₂ laser for laser cutting of thick ceramic substrates by controlled fracture. The focused Nd:YAG laser was used to scribe a groove crack on the surface of the substrate and defocused CO₂ laser was utilized to apply large thermal stress. During dual beam irradiation, thermal stress concentration along the tip of the groove-crack would make it extend through the substrate, followed by the substrate separating along the moving path of the laser beam in a controlled manner. Under an output power of 60 W for both CO₂ laser and Nd:YAG laser, the maximum cutting speed achieved was 1.5 mm/s for a thick alumina sample. The temperature and stress distributions were analyzed by using the finite element software ANSYS and microstructure (micro-mechanism of the fracture process) was studied by scanning electron microscopy. The relationships among laser power, cutting speed, and specimen geometry/thickness were determined from the experimental and stress analysis. In this regard, Tsai and Chen [219] proposed a new image processing system to determine the laser movement path by iterative path revision algorithm useful for monitoring laser assisted cutting.

The effect of laser power, scan speed, mode of cutting, and shield gas composition on cutting of thick ceramic tiles using continuous wave CO₂ laser was studied by Black and Chua [220] and Black et al. [221]. Crack formation was one of the major problems associated with the cutting process. Large thermal gradient between the cut zone and associated glazed zone was responsible for the crack formation. Proper choice of laser parameters was essential to allow sufficient time to cool and minimize the tendency for crack formation.

Rebro et al. [222] evaluated the processing conditions for a defect-free laser assisted machining of pressureless sintered mullite ceramics which otherwise is difficult due to its low thermal diffusivity and inferior tensile strength. To achieve the benefits of strength reduction due to softening of mullite, laser power of 170–190 W provided positive results. These settings allowed machining of semicontinuous chips, significant reduction in specific cutting forces, increase in tool life, and retention of surface characteristics of the workpiece. Numerical modeling of workpiece temper-

ature along with experimental measurement by a pyrometer was performed to determine the temperature at the material removal zone during laser assisted machining and to analyze the temperature gradient information for detecting the onset of cracking. With a designed gradual heating method, laser assisted machining of mullite has been successfully performed without inducing any surface or subsurface cracks and at the same time, extending the tool life of carbide tools and producing good surface integrity. Graff and Meijer [223] reported on CO₂ laser cutting of newly developed materials (synthetic aluminium laminates) for the aeronautic and automotive industry at the same speed as homogeneous aluminum alloys with the presence of some damage. A dedicated computer simulation model was also developed using appropriate mass, power, and force balance equations considering splitting of the laminate in several horizontal layers according to the concerned thermophysical and optical properties.

1.8.2 Laser Drilling

Drilling is a machining operation with a stationary workpiece to produce usually circular and vertical holes on the workpiece. High power CO₂ laser or Nd:YAG laser may be used to drill a hole. Laser drilling can be done both in pulsed and continuous wave modes with suitable laser parameters. The advantage of using laser is that it can drill holes not only vertically but also at an angle inclined to the surface (e.g. fine lock pinholes in Monel metal bolts). Mechanical drilling is slow and causes extrusions at both ends of the hole that have to be cleaned. Mechanical punching is fast but is limited to shallow with greater than 3 mm in diameter. Electrochemical machining is quite a slow process (180 s/hole) though produces a neat and precise hole. Electro discharge machining is expensive and slow with a typical rate like 58 s/hole. Electron beam drilling is fast at 0.125 s/hole but needs a vacuum chamber and is more expensive than a Nd:YAG laser processing. In comparison, a Nd:YAG laser can produce a hole in 4 s to outsmart all other methods [2].

The ability to machine very small features like holes into a metal, ceramic, semiconductor, or polymer sheet/film by laser ablation with an unmatched precision, accuracy, and speed has opened a very useful scope of application of laser material processing in the microelectronic industry. For instance, holes with a diameter of 300 nm and depth of 52 nm could be drilled in metal films with minimum distortion and heat affected zone using 200 fs and 800 nm pulses from a Ti:sapphire laser focused to a spot size of 3000 nm. Lehane and Kwok [224] have developed a novel method for improving the efficiency of laser drilling using two synchronized free-running laser pulses from a tandem-head Nd:YAG laser capable of drilling through 1/8-in-thick stainless steel targets at a standoff distance of 1 m without gas-assist. The combination of a high-energy laser pulse for melting coupled with a properly tailored high-intensity laser pulse for liquid expulsion results in efficient drilling of metal targets. The improvement in drilling is attributed to the recoil pressure generated by rapid evaporation of the molten material by the second laser pulse. Similarly,

Zhu et al. [225] have carried out a detailed experimental study of drilling submicron holes in thin aluminum foils with thicknesses ranging from 1.5 to 50 μm , and W, Mo, Ti, Cu, Fe, Ag, Au, and Pb foils of 25 μm thickness with femtosecond Ti:sapphire laser pulses of 800 nm width. The influence of laser parameters and material properties on hole drilling processes at submicron scale has been examined and a simple model to predict the ablation rate for a range of metals has been developed. Laser precision machining has been applied to fabricate metallic photonic band-gap crystals operating in the microwave frequency [226]. Transmission measurements showed that the periodic crystals exhibited a cutoff frequency in the 8–18 GHz range allowing no propagation below this level. Furthermore, the cutoff frequency could easily be tuned by varying the interlayer distance or the filling fraction of the metal. Combination of plates with different hole-diameters creates defect modes with relatively sharp and tunable peaks.

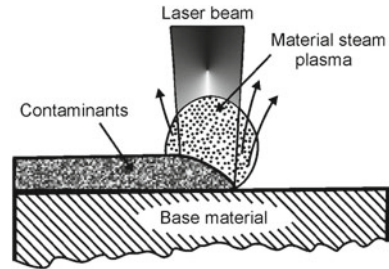
The microelectronics industry is moving toward smaller feature sizes so as to improve design and performance and lower cost. Small distances between chips together with the short interconnection routes are conducive for faster operation. Laser processing for via generation, direct pattern processing, image transfer, contour cutting, and trimming now find increasing application in the microelectronic packaging industry. On the other hand, smaller space between conductive patterns increases the risk of short circuits (caused by pattern faults, solder bridges, migration, etc.) that emphasizes the need to ensure reliability of laser processing [227].

The microelectronics industry is moving toward smaller feature sizes so as to improve the design and performance and lower cost. Small distances between chips together with the short interconnection routes are conducive for faster operation. Laser processing for via generation, direct pattern processing, image transfer, contour cutting, and trimming now find increasing applications in the microelectronic packaging industry. On the other hand, smaller space between conductive patterns increases the risk of short circuits (caused by pattern faults, solder bridges, migration, etc.) that emphasizes the need to ensure reliability of laser processing.

For micromachining, femtosecond pulses offer an advantage over current technology of employing nanosecond pulses because of the reduced effects of thermal diffusion [228]. Using the femtosecond pulses, holes with a diameter of 300 nm, roughly 10% of the spot size was produced, whereas the smallest diameter made using the nanosecond pulses was roughly 60% of the spot size. The depth of the femtosecond hole was 52 nm. Also the fact that the fluence threshold is lower for femtosecond pulses than for nanosecond pulses, which is useful for certain machining situations, such as medical surgery, where low fluences are desirable to reduce the effects of collateral damage, that is, damage to tissue located outside the desired region.

Demands for producing micro crack-free, high quality and high-aspect ratio microholes and microfeatures in glass substrates have been increasing for a number of applications such as in MEMS device packaging, optical fiber alignment, mini-vision systems, and microelectronic packaging. However, due to the poor thermal properties of most glasses the fabrication of finely machined features, e.g. grooves, microholes etc. has been a challenging task. Different types of glass materials were

Fig. 1.16 Schematic of laser assisted cleaning



machined by using short pulse solid-state lasers with pulse duration in the ns to fs range [229].

1.8.3 Laser Cleaning

Removal of small particles or continuous layers from a metal surface can be carried out by laser beam using a selected area irradiation at an optimum combination of incident power, interaction/pulse time, and gas flow rate (that sweeps the dislodged atoms from the surface). Figure 1.16 schematically shows the mechanism of laser cleaning. At the initial stage, a plasma plume is formed due to ionization of the atoms vaporized from the surface and blocks the beam-surface contact. As the irradiation stops, the temporary compression on the surface changes into tension and causes spallation of the oxidized layer. A dramatic improvement of cleaning efficiency in terms of area and energy is possible when laser beam irradiates the workpiece at an oblique or glancing angle of incidence rather than direct or perpendicular irradiation of the surface. The influence of pulsed laser irradiation on the oxide scale removal from the surface of stainless steels oxidized using a pulsed Nd:YAG laser was investigated by Psyllaki and Oltra [230]. At an appropriate angle of incidence, laser irradiation with energy density of $\sim 10^4 \text{ J/m}^2$ resulted in expulsion of the oxide layer without any material removal from the underlying metal. The side wall and bottom polymers resulting from reactive ion etching of via holes can be removed by a non-contact dry laser cleaning technique using pulsed excimer laser irradiation [231].

Similarly, laser cleaning is capable of removing the polymers by subthreshold ablation, even at fluences limited by the damage threshold ($= 2,500\text{--}2,800 \text{ J/m}^2$) of the underlying Al–Cu metal film with titanium nitride (TiN) anti-reflective coating. Comparing ablation results obtained using Nd-YAG laser and excimer laser shows that although the shorter 7 ns Nd-YAG laser pulse gives a greater etch thickness than the 23 ns excimer laser pulse, it also tends to damage the metal films and the silicon substrates of the via wafers more easily.

Single crystal SiC substrate was successfully photo-etched at a remarkably high etch rate of 35 nm/s by (133, 141, 150, 160, 171 and 184–266 nm) multi-

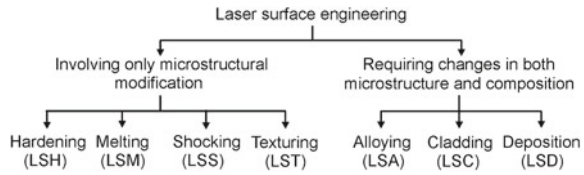
wavelength laser ablation, combined with a chemical posttreatment in a solution of $\text{HCl} + \text{H}_2\text{O}_2 + \text{H}_2\text{O}$ and $\text{HF} + \text{H}_2\text{O}$ [232]. The analysis of the etched samples by scanning electron microscopy and scanning probe microscopy indicated that an array of square holes having well-defined patterned structures and clean substrate surfaces were obtained. X-ray photoelectron spectroscopy analysis indicated that the SiC samples etched by multi-wavelength laser have a similar stoichiometry after chemical posttreatment as the virgin SiC. The mechanism of high-quality ablation using multi-wavelength laser was discussed and compared with that for ablation using 266 nm single wavelength. The chemical post-treatment contributed to removing the residues from the laser photolysis of SiC.

1.9 Laser Surface Engineering

Failure of engineering components or materials due to chemical (corrosion and oxidation) or mechanical (wear and erosion) interaction is most likely to initiate from the surface because both external and internal surfaces/interfaces are more prone to environmental degradation, and intensity of externally applied load is usually the highest at the surface [233]. The engineering solution to minimize or eliminate such surface initiated failure lies in tailoring the surface composition and/or microstructure of the near-surface region of a component without affecting the bulk [2, 3, 233–235]. In this regard, the more commonly practiced or conventional surface engineering techniques like galvanizing, diffusion coating, carburizing, and nitriding possess several limitations like high time/energy/material consumption, poor precision and flexibility, lack in scope of automation/improvisation, and requirement of complex heat treatment schedule. Furthermore, thermodynamic constraint of restricted solid solubility and kinetic limitation of thermally activated solute transport to solid-state diffusion impose further limits to the level of improvement possible through these conventional or near-equilibrium processes [234, 235].

In contrast, surface engineering methods based on application of electron, ion, and laser beams are free from many of the above restrictions of equilibrium surface engineering methods. A directed energy electron beam is capable of intense heating and melting the surface of all engineering solids [236]. However, electron beam delivers a Gaussian energy deposition profile, and hence, is more suitable for deep penetration welding or cladding of similar or dissimilar solids (Fig. 1.3). Moreover, the scope of generation of X-ray by rapid deceleration of high-energy electrons impinging on a solid substrate necessitates adequate safety provisions to prevent possible health hazards. On the other hand, ion beam processing offers practically an unlimited choice, flexibility, and precision of tailoring the surface composition and microstructure by implantation of a single or multiple elements that has otherwise no or restricted solid solubility in a given substrate [6, 3, 237]. However, the peak concentration of implanted species, like the energy deposition peak in electron beam irradiation, lies underneath and does not coincide with the surface (Fig. 1.3b, c). Furthermore, the requirements of an expensive ionization chamber,

Fig. 1.17 General classification of laser surface engineering [113]



long beam delivery system, and huge time needed to implant on a large surface area are serious impediments against large-scale commercial exploitation of ion beam assisted surface engineering. Laser circumvents the majority of the limitations cited above with regard to both conventional and electron/ion beam assisted surface engineering methods and offers a unique set of advantages in terms of economy, precision, flexibility, and novelty (thermodynamic and kinetic) of processing and improvement in the surface-dependent properties of interest [1–4]. One of the major advantages of laser in surface engineering is its exponential energy deposition profile vis-à-vis the Gaussian profile of that in electron or ion beam irradiation (Figure 1.3).

Laser surface engineering enables delivery of a controlled quantum of energy (10^4 to 3×10^5 J/m²) or power (10^8 – 10^{11} W/m²) with precise temporal and spatial distribution either in pulses (10^{-3} to 10^{-12} s) or continuous wave (CW). The advantages of laser surface engineering include an extremely fast heating/cooling rate (10^4 – 10^{11} K/s), very high thermal gradient (10^6 – 10^8 K/m), and ultra-rapid resolidification velocity (1 – 30 m/s), inducing possibility of development of novel microstructure and/or composition in the near-surface region with large extension of solid solubility and formation of metastable including nanocrystalline and amorphous phases [233–235].

Figure 1.17 presents a brief classification of different laser surface engineering methods that involve mainly two types of processes. The first type is meant only for microstructural modification of the surface without any change in composition (hardening, melting, remelting, shocking, texturing, and annealing), while the second involves both microstructural as well as compositional modification of the near-surface region (alloying, cladding, etc.).

1.9.1 Laser Transformation Hardening

Transformation hardening is a standard heat treatment for ferrous alloys (steel, cast iron, etc.) that involves heating to austenite (face centered cubic) phase and subsequent quenching to ambient or subambient temperature to enforce a shear-induced austenite to martensite (body centered tetragonal) transformation. In laser transformation hardening, only a thin surface layer of the substrate (instead of the entire bulk) is rapidly heated to the austenite phase field followed by rapid self-quenching to produce the desired martensitic microstructure [238]. Heating and cooling rates of 10^4 K/s or greater are typical of the laser surface hardening process and the entire

thermal cycle in the irradiated volume may be accomplished in less than 0.1 s. The application of high power lasers in surface engineering is a well-known process that has been in vogue over the past two decades and is now revolutionizing automobile and aerospace industries. Dutta Majumdar and Manna [239] have presented a detailed review on the fundamentals of laser hardening, associated benefits compared to the conventional hardening techniques.

1.9.2 Laser Surface Melting

Laser surface melting is another important and effective technique primarily to modify the microstructure of the near-surface region. The advantages of laser surface melting lie on microstructural refinement and homogenization of microstructure. Laser surface melting of 440C martensitic stainless steel was found to be more effective in improving the corrosion resistance (in NaCl solution) by carbide refinement, while laser transformation hardening was useful in enhancing the cavitation erosion resistance by formation of an appropriate amount of martensite and austenite [240, 241]. Laser surface melting has been proven to be an effective route in desintization of AISI 304 stainless steel by dissolving the carbides formed and suppression of its re-precipitation due to rapid quenching and homogenizing the microstructure leading to a significant improvement in corrosion resistance [242, 243]. Laser surface melting of DIN X42Cr13 samples showed a higher abrasive wear resistance than the same after tempering treatments due to strain-induced transformation of austenite into martensite and the work hardening of austenite during the wear tests [244]. Wilde et al. [245] showed that laser surface melting of AISI 4135 low alloy steel resulted in reduction in the hydrogen absorption kinetics as measured by the permeation test, and an improved resistance to hydrogen-induced fracture in the slow strain rate tensile test under galvanostatic charging conditions.

Laser surface melting was also proven to be an important technique for tailoring the surface properties of Al, Ti, Cu, Mg, and other important nonferrous metals and alloys to extend the service life of components. Laser surface melting of 7075-T651 Al alloy using an excimer laser was found to improve the resistance to stress corrosion cracking attributed to dissolution of grain boundary precipitates and supersaturation of solutes with the matrix making it more noble [246]. Laser surface melting of 2024-T351 aluminium alloy using a continuous wave CO₂ laser was found to improve its uniform corrosion resistance and pitting corrosion resistance attributed to homogenization of microstructure [247]. It is also an effective route in improving high temperature oxidation resistance [248]. Wong et al. [249] reported that the corrosion behavior of laser surface melted Al–Si alloy (using a continuous wave CO₂ laser) was significantly improved in 10% H₂SO₄ and 10% HNO₃ solutions, though similar level of improvement was not observed in 10% HCl+5% NaCl solution. It was also proven to be an effective route in improving wear resistance because of microstructural refinement and improved microhardness achieved by laser surface melting [250]. Watkins et al. [251] melted the surface of a series of Al-transition

metal alloys (Al–Cu, Al–Si, Al–Zn, Al–Fe) and obtained unique microstructural and compositional characteristics including improved hardness, wear and pitting corrosion resistance using a selected set of laser parameters. SiC dispersed Al alloy composite is the most promising class of metal-matrix composite for applications in automobile and aircraft industries. However, these composites undergo severe degradation in chloride containing environment.

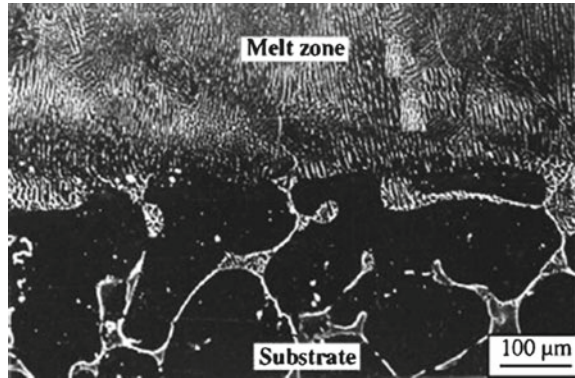
Vanderberg and Draper [252] laser surface melted commercial Al bronzes (containing 5 at% Fe, 13–28 at% Al) and found a variety of phases formed in the near-surface region. The microstructure consisted of α -phase (fcc solid solution), β_1 phase (product of ordering transformation of the high temperature disordered bcc phase β .) and even β phase (martensite formed by shear transformation on quenching). Rapid quenching in laser treatment also resulted in β_1 retention (by suppressing of martensite change) at Al concentration that was lower than what was usually observed with splat-quenching experiments.

Magnesium and its alloys are widely used in automotive and aerospace applications because of their light weight. However, poor wear and corrosion properties are of serious concern for its application as structural components. Laser surface melting of magnesium and its alloys were reported to be effective to refine the microstructure and improving corrosion resistance in AZ91D/AM60B [253], AZ91 [254], Mg-ZK60 [255] and other commercial Mg-based alloys [256]. Detailed studies on kinetics and mechanism of laser-surface-melted MEZ (a Mg–Zn alloy) were reported by Dutta Majumdar et al. [257]. Figure 1.18 shows the cross-section of the laser surface melted MEZ alloy, lased with a power of 2 kW and scan speed of 200 mm/min, consisting of fine columnar grains growing epitaxially from the liquid–solid interface [257]. The underlying substrate grains are significantly coarser with grain boundaries decorated with thick films of Mg/Zr/Ce-rich compound (confirmed by energy dispersive spectroscopy). Furthermore, the melted zone–substrate interface is crack/defect-free and well compatible with practically with no noticeable amount of heat-affected zone. A detailed evaluation of mechanical property shows that microhardness of the melted zone has significantly increased by 2–4 times (85–100 VHN) than that of the substrate (35 VHN) primarily due to grain refinement and solid solution hardening. While average microhardness varies with the concerned laser parameters, the maximum microhardness is achieved following laser surface melting with a power of 1.5 kW power and 200 mm/min scan speed. A detailed study of pitting corrosion shows that both the extent and rate of pitting are significantly reduced following laser surface melting.

Yu et al. [258] surface melted Mg–SiC (17 vol.%) composite using KrF excimer laser with Ar and N₂ as shrouding environment and achieved considerable improvement in corrosion resistance in 3.56 % NaCl solution primarily due to microstructural refinement. Similar surface melting in N₂ atmosphere improved the corrosion resistance further because of the formation of magnesium nitrides.

Laser surface melting of Ti–6Al–4V in nitrogen atmosphere leads to formation of a defect-free nitride zone consisting of TiN dendrites in α -Ti matrix. An increased surface roughness with a periodic texturing was noted on the nitrated surface [259, 260]. The residual stress on the surface nitrated zone was found to vary from

Fig. 1.18 Scanning electron micrograph of the cross-section of laser-surface-melted MEZ sample (lased with a power of 2 kW and a scan speed of 200 mm/min). The defect-free interface with significant grain refinement in the laser-melted zone may be noted [257]

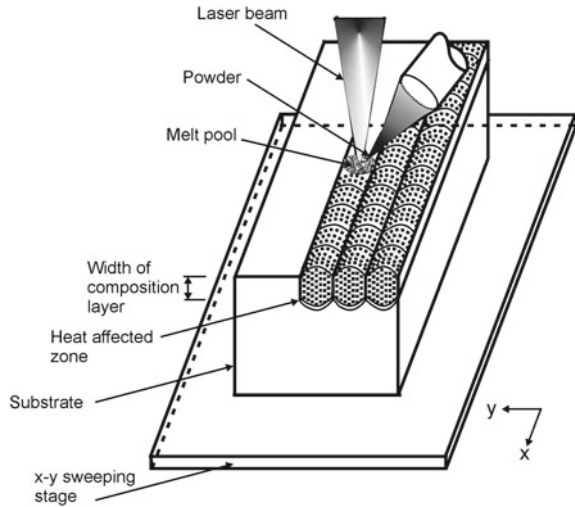


tensile to compressive. The residual compressive stress was developed when applying a high power and a very low gas flow rate. A significant improvement in microhardness of the nitrided zone is achieved (600–1,200 VHN) as compared to 280 VHN of as-received Ti–6Al–4V substrate. Pitting corrosion resistance in Hank’s solution was also found to be improved due to laser gas alloying of Ti–6Al–4V with nitrogen.

1.9.3 Laser Surface Alloying

Laser surface alloying involves melting of alloy ingredients (either pre-deposited or simultaneously added in the form of powder or wire) along with a part of the underlying substrate to form an alloyed zone for improving the surface dependent engineering properties of substrate [261–264]. Figure 1.19 illustrates the scheme of laser surface alloying with a continuous wave laser. It includes three major parts: a laser source with a beam focusing and delivery system, a microprocessor controlled sweeping stage where the specimen is mounted for lasing and the arrangement for delivering the alloy ingredients in the form of powder. The process includes melting of the alloy ingredient along with the part of substrate, subsequent inter-mixing, and rapid solidification to form the alloyed zone confined to a very shallow depth from the surface. A 20–30% overlap of the successive molten/alloyed track is intended to ensure microstructural/compositional homogeneity of the laser treated surface in laser alloyed zone that has a composition distinctly different from that of the underlying base substrate. The sweeping stage ($x - y$ or $x - y - z - \theta$) allows laser irradiation of the intended area of the sample surface at an appropriate rate and interaction time/frequency. The depth, chemistry, microstructure, and associated properties of the alloyed zone depend on the suitable choice of laser/process parameters, i.e., incident power/energy, beam diameter/profile, interaction time/pulse width, pre- or co-deposition thickness/ composition, and concerned physical properties

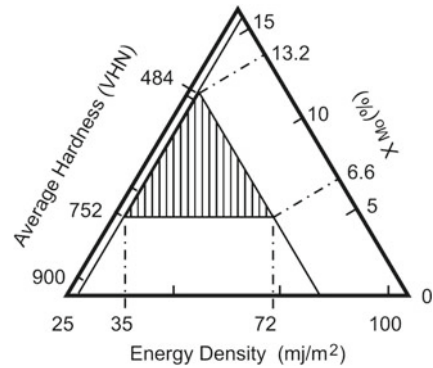
Fig. 1.19 Schematic of the experimental setup for laser surface alloying and the stages of irradiation, melting, intermixing, and solidification involved in laser surface alloying



like reflectivity, absorption coefficient, thermal conductivity, melting point, and density.

Dutta Majumdar and Manna [265] observed a significant improvement in pitting corrosion resistance of AISI 304 stainless steel by laser surface melting of plasma spray deposited Mo. Figure 1.20 shows the optimum conditions (shaded region) for the formation of a homogeneous microstructure and composition for improvement in pitting corrosion resistance and mechanical property [265]. Potentiodynamic anodic polarization tests of the substrate and laser surface alloyed samples in 3.56 wt. % NaCl solution (both in forward and reverse potential) showed that the critical potential for pit formation (E_{pp1}) and growth (E_{pp2}) were significantly (2–3 times) improved from 75 mV(SCE) in the substrate to 550 mV(SCE) after laser surface alloying. E_{pp2} has also been found to be nobler in as-lased specimens than that in the stainless steel substrate. The poor pitting corrosion resistance of the plasma sprayed stainless steel samples (without laser remelting) was due to the presence of surface defects present in the plasma deposited layer. Standard immersion test was conducted in a 3.56 wt. % NaCl solution to compare the effect of laser surface alloying on the pitting corrosion resistance. It was concluded that laser surface alloying imparted an excellent microhardness, pitting corrosion, and erosion–corrosion properties to austenitic stainless steel due to Mo both in solid solution and as precipitates. In the past, attempts were made to enhance oxidation resistance property by laser surface engineering techniques [77]. The effect of laser surface alloying of 2014–T6 (Al–4.65Cu–0.5Mg–0.8Si wt.%) Al-alloy with 25Cr–75Al, 75Cr–25Al, 25W–75Al, 75W–25Al, 8Al–72Zr–20Ni and 35Al–50Ti–15Ni powder mixtures using an ElectroX 2 kW continuous wave CO₂ laser on the microstructure and corrosion behavior were studied [251]. Jain et al. [266] vacuum deposited Cr film (thickness varying from 650 to 1350 nm) on Al substrate and irradiated with single pulses (with a full width at half-maximum of 7 ns) Nd-glass laser operating in

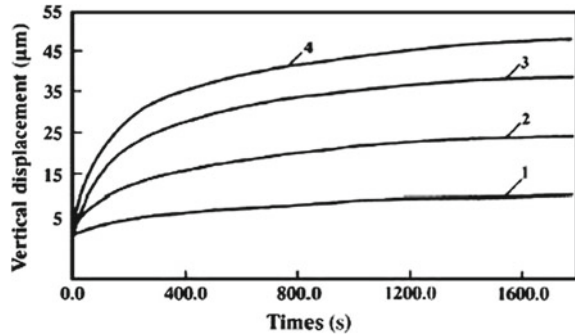
Fig. 1.20 Optimum conditions (*shaded region*) for the formation of a homogeneous microstructure and composition in laser-surface-alloyed AISI 304 stainless steel with Mo [265]



a TEM00 mode at peak power densities of 6,000 – 15,000 GW/m² in air. Almost complete removal of chromium at 8,000 J/m² is followed by the rapid diffusion of chromium. Similar attempt of laser surface alloying of Al with Mo was undertaken by laser surface alloying with a composition ranging from 14.8 to 19.1 wt.% Mo and resulted in VHN 85–100 in hardness and 84–92 GPa in Young's modulus (determined by nano indentation [267]). Tang et al. [268] observed that laser surface alloying of Mg–Ni–Al bronze with Al was more effective in enhancing corrosion and cavitation erosion resistance in a 3.56 wt.% NaCl solution than that after laser surface melting. Improvement in wear resistance of Al alloys seems to necessitate addition of ceramic or intermetallic particles by laser surface cladding or alloying. Dutta Majumdar et al. [269] developed a titanium boride-dispersed Al-based metal matrix composite on the surface of pure Al by melting the surface of as-received substrate using a continuous wave CO₂ laser and simultaneous deposition of a mixture of K₂TiF₆ and KBF₆ (in the weight ratio of 2:1) through an external feeder (at a feed rate of 4 g/min).

The microstructure of the surface layer consisted of uniformly dispersed titanium boride (TiB) and titanium diboride (TiB₂) particles in grain refined Al matrix [269]. Figure 1.21 shows the variation of wear loss (in terms of depth of wear) as a function of time for as-received and laser composite surfaced Al with TiB₂ (lased with a power of 1.2 kW and scan speed of 700 mm/min) using a friction and wear monitor unit with an applied load of 500 and 900 g, respectively. It is evident that the rate of wear increases both with time and applied load. In pure Al (curves 3 and 4), the wear rate is very high at the initial stage of wear (up to 5 min) following which the same decreases. On the other hand, the magnitude and rate of wear is significantly lower in laser composite surfaced Al than that of as-received Al, though the same increases with increase in load for both as-received and laser composite surfaced Al with TiB₂. The kinetics of wear was, however, found to vary with laser parameters. Maximum wear resistance was achieved in laser composite surfaced Al lased at a power of 1.2 kW and scan speed of 700 mm/min. It is relevant to mention that wear resistance of the composite layer was found to increase with increase in microhardness of the composite layer. Hence, the improved wear resistance of laser composite surfaced Al was attributed to improved microhardness of the composite layer because of both

Fig. 1.21 Cumulative wear loss (in terms of vertical displacement) as a function of time for as-received Al with an applied load of 500 g (plot 3), 900 g (plot 4) and laser composite surfaced Al with TiB₂ (with a power of 1.2 kW and scan speed of 700 mm/min) with an applied load of 500 g (plot 1), 900 g (plot 2) using a friction and wear monitor unit [269]



grain refinement and precipitation of fine and hard TiB₂ and TiB particles in the matrix.

Aihua et al. [270] developed a graded coating consisting of a Ni-clad Al bond layer, a 50 wt.% Ni-clad Al + 50 wt.% (Al₂O₃ – 13 wt.%TiO₂) intermediate layer and an Al₂O₃ – 13 wt.%TiO₂ overlayer (or ceramic layer) on an Al–Si alloy substrate by plasma spraying followed by laser surface remelting. While the plasma-sprayed coatings seem prone to spallation at the different depths originating from macrocracks in the ceramic layer during thermal cycling, the laser-remelted coatings, containing a network of microcracks in the ceramic layer reveal a significantly reduced tendency of spallation at the interface between the intermediate and bond layer. Thus, laser remelting improved the spalling resistance of plasma-sprayed coating to thermal shock, though cracking due to thermal shock remains a problem to be solved. Uenishi et al. [271] obtained Al₃Ti -dispersed intermetallic-matrix composite on Al by laser surface cladding.

Dutta Majumdar and Manna [272] attempted to enhance the wear and erosion resistance of Cu by laser surface alloying with Cr (electrodeposited with 10 and 20 μm thickness, t_z). Figure 1.22 shows the scanning electron micrograph of the top surface of laser surface alloyed copper with chromium showing the presence of fine chromium of dimensions ranging from 100 to 500 nm in grain refined copper matrix. Chromium was found to be present both in solid solution and in the form of precipitates [272]. Laser surface alloying extended the solid solubility of Cr in Cu to a maximum of 4.5 wt. %. The microhardness of the alloyed zone was found to improve significantly (as high as 225 VHN) following laser surface alloying as compared to 85 VHN of the base metal. Since hardness is related to Cr present in solid solution and dispersed as precipitates in the matrix, the variation of average microhardness of the alloyed zone as a function of the total Cr content, Cr dissolved in solid solution or volume fraction of Cr precipitated shows that hardness increases with all these microstructural factors, especially with the degree of solid solubility extension of Cr in Cu. Figure 1.23 shows the variation of scratch depth as a function of load for pure Cu as well as laser surface alloyed Cu with Cr subjected to scratching with an oscillating steel ball in a computer-controlled scratch tester. It is evident that the rate of increase of scratch depth with both load and number of scratches is much higher in

Fig. 1.22 Scanning electron micrograph of the top surface of laser surface alloyed Cu with Cr (lased with a power density of $1,270 \text{ MW/cm}^2$, interaction time of 0.08 s at a predeposition thickness of $20 \mu\text{m}$) [272]

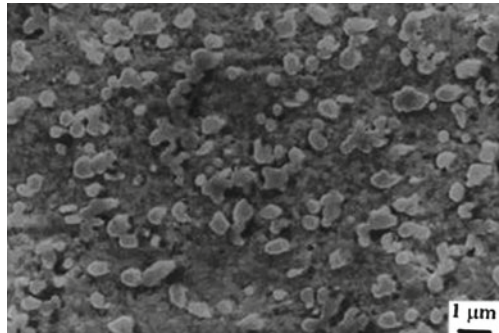
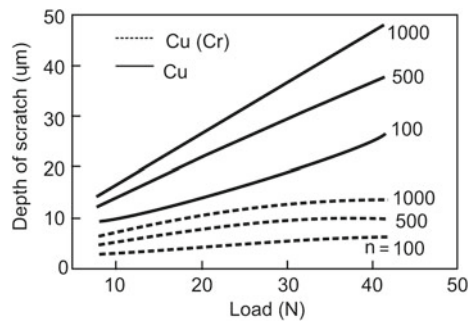


Fig. 1.23 Variation of scratch depth (z_{sc}) with (a) L and (b) n_{sc} for pure Cu (broken line) and laser alloyed Cu(Cr) (continuous line), respectively [272]



pure Cu than in laser alloyed sample. Figure 1.24 compares the kinetics of material loss (Δm) of laser surface alloyed Cu (lased with 1590 MW/m^2 power, 0.08 s interaction time, with a pre-deposit thickness of $20 \mu\text{m}$) with that of Cu as a function of time (t) under an accelerated erosive wear condition conducted both at room and high temperature in a slurry bath containing 20 wt. % sand. Laser surface alloying has significantly decreased the kinetics of erosion loss in laser surface alloyed Cu than in pure Cu under comparable conditions. Though the extent of material loss increases with an increase in temperature for both pure Cu and laser alloyed Cu, the rate of erosion loss in laser alloyed specimen is negligible as compared to the substantial change in erosion loss with temperature change for pure Cu, especially beyond 370 K.

Laser surface alloying of Ti with Si, Al, and Si + Al (with a ratio of 3:1 and 1:3, respectively) was conducted to improve the wear and high temperature oxidation resistance of Ti [273–275]. Figure 1.25 reveals a typical hypereutectic microstructure on the top surface of the alloyed zone consisting of uniformly distributed faceted Ti_5Si_3 phase in a two-phase eutectic aggregate of $\alpha\text{-Ti}$ and Ti_5Si_3 [276]. The high volume fraction of the primary phase and degree of fineness of the eutectic products signify complete dissolution and uniform intermixing of Si in the alloyed zone, and a rapid quenching experienced by the latter, respectively. Subsequent oxidation studies conducted at 873–1,023 K showed that laser surface alloyed Ti with Si and Si + Al significantly improved the isothermal oxidation resistance (Fig. 1.26). In addition to

Fig. 1.24 Comparison of material loss per unit area (Δm) of Cu(Cr) with that of Cu as a function of (a) time (t), and (b) temperature (T) due to erosion in flowing SiO_2 -dispersed water medium [272]

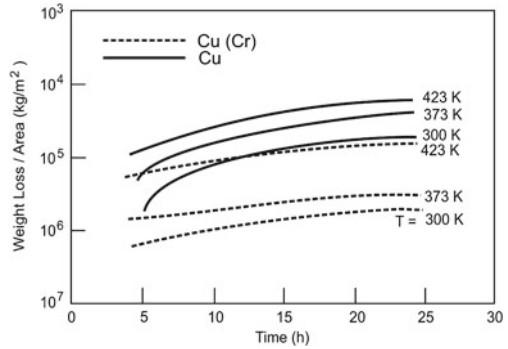
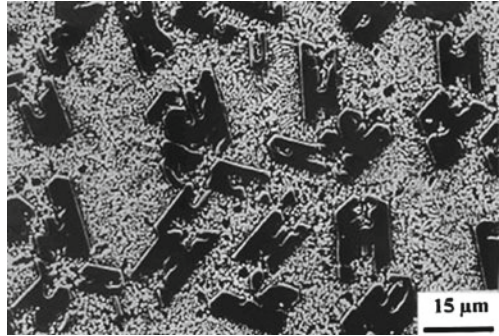


Fig. 1.25 Scanning electron micrograph (SEM) of the top or laser alloyed surface of Ti with Si (lased with a power of 4 kW, scan speed of 300 mm/min and powder feed rate of 17 mg/s) [275]

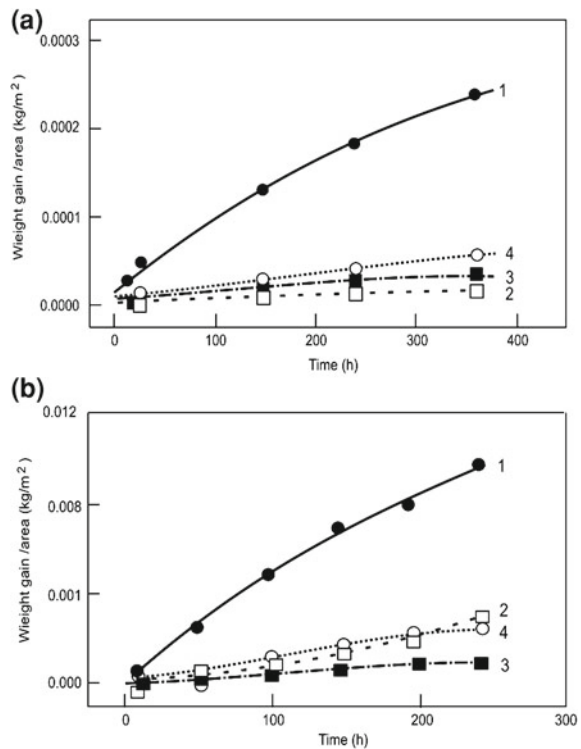


oxidation, the effect of laser surface alloying of Ti with Si or Si + Al on wear resistance was also studied. Under comparable conditions of scratching, Ti undergoes the most rapid wear loss followed by that in laser surface alloyed specimens. The laser alloyed sample with Si undergoes the minimum wear loss. The improved wear resistance of laser surface alloyed Ti with Si was attributed to the formation of a hard Ti_5Si_3 precipitates in the alloyed zone [273].

Manna et al. [276] made an attempt to develop an alternative electrode material for neural stimulation electrode by laser surface alloying of Ti with Ir that can mimic the normal spatiotemporal pattern of neuronal activation by reversible charge transfer. Laser surface alloying was also attempted on magnesium and its alloys to improve wear and corrosion resistance properties. Wang and Wue [277] have achieved significant improvement in corrosion resistance of SiC dispersed Mg by LSC with Al-12Si alloy layer. Ignat et al. [288] studied the effect of laser surface alloying on surface alloying of WE43 and ZE41 Mg alloy with Al using a 3 kW continuous wave Nd:YAG laser and found that the alloyed zone microstructure consisted of Al_3Mg_2 and $\text{Al}_{12}\text{Mg}_{17}$ intermetallics with an improved microhardness and corrosion property.

Similar investigations of laser surface alloying of MEZ with Al + Mn (in 3:1 and 1:1 by weight) using a continuous wave CO_2 laser significantly improved the wear and corrosion properties of the base alloy [279].

Fig. 1.26 Kinetics of isothermal oxidation in terms of weight gain per unit area for as-received Ti (plot 1) and laser surface alloyed Ti with Si (plot 2), 3Si + Al (plot 3), and Si + 3Al (plot 4) [274]



1.9.4 Laser Composite Surfacing

Metal matrix composites generally possess an enhanced wear resistance than the base substrate or the matrix. Although reinforcement of the dispersoid enhances mechanical properties, the degree of reinforcement cannot be unlimited as excessive amount of reinforcement reduces the toughness. Development of composite layer on the surface by conventional means is extremely difficult.

Laser melting of substrate and subsequent feeding of ceramic particles into the molten matrix is an effective means of developing composite layer on the surface through a process called laser composite surfacing. Several attempts have been made to develop a composite layer on metallic matrix by this technique. Cheng et al. [280] have added a mixture of WC–Cr₃C₂–SiC–TiC–CrB₂ and Cr₂O₃ to produce a metal matrix composite surface on stainless steel UNS-S31603. Following laser surface melting, cavitation erosion resistance improved in all cases except for Cr₂O₃. Wu and Hong [281] have attributed the improvement in hardness and corrosion/wear resistance of stainless steel to the presence of amorphous phase in the Zr-rich surface (with 7.8–14.5 wt. % Zr) following laser surface alloying of stainless steel with Zr nanoparticles. Agarwal and Dahotre [282] have reported a substantial improvement in resistance to adhesive/abrasive wear of steel following laser surface alloying with

TiB₂. The surface composite layer containing about 69 vol. % TiB₂ particles recorded an elastic modulus of 477.3 GPa. Similar improvement in wear resistance of mild steel was reported by Tondou et al. [283] due to formation of a FeCr + TiC composite coating formed by laser assisted self-propagating high temperature synthesis. Earlier, Zhukov et al. [284] achieved a similar carbide dispersed composite coating on steel by laser-assisted self-propagating high temperature synthesis. Improvement in hardness and wear resistance has been achieved by laser surface alloying of ferritic steel with Cr₃C₂ + SiC [285]. Development of in situ boride (TiB₂) dispersed composite layer on the surface of AISI 304 stainless steel substrate was achieved with an improved wear resistance [286].

1.9.5 Laser Shock Processing

Laser shock processing involves rapid irradiation of the component surface with a laser (at a power density of $\sim 10^{12}$ W/m²) resulting in generation of shock wave (due to a volume expansion of the plasma plume formed on the surface) and subsequent alteration of microstructure/state of stress. The effect of shock wave may be enhanced when it is propagated through water. This novel laser processing has the capability to improve material hardness and fatigue strength in a number of alloys [287]. The effects of laser shock processing (with a Nd:glass phosphate laser with a 600 ps pulse-width and up to 120 J pulse energy at power densities above 10^{16} W/m²) on the microstructure, microhardness, and residual stress of low carbon steel were studied by Chu et al. [287]. Surface hardness increased up to 80% after the laser shock processing up to 100 μ m in depth and introduced residual compressive stress on the surface. The strengthening effect was attributed to the presence of a high dislocation density.

Peyre et al. [288] showed that laser shock processing offered a better pitting corrosion behavior of AISI 316L stainless steel than that obtained by shot peening in saline environment. Low residual stress and work hardening levels were observed, when compared to that obtained by conventional shot-peening treatment, mainly because of the absence of martensitic transformation in the case of laser processing.

1.9.6 Laser Surface Engineering of Ceramics

Lawrence and Li [289] glazed the surface of Al₂O₃-based refractory by means of high power diode laser and augmented the wear rate and wear life characteristics within both normal and corrosive (NaOH and HNO₃) environmental conditions. Life assessment testing revealed that diode laser generated glaze increased the wear life of the Al₂O₃-based refractory by 1.2–13.4 times depending upon the environmental conditions. Such improvements are attributed to the fact that the microstructure of the Al₂O₃-based refractory was altered from a porous, randomly ordered structure

to a much more dense and consolidated structure after laser treatment that contained fewer cracks and porosities.

Sciti et al. [290] surface treated alumina and silicon carbide ceramics with a KrF excimer laser and studied the influence of laser fluence (1.8 and 7.5 J/cm^2), number of laser pulses (1 – 500), frequency (1 – 120 Hz), pulse duration (25 ns) and shrouding environment on the characteristics of the treated surface. Microstructural analyses of surface and cross-section of the laser processed samples at low fluence (1.8 J/cm^2) evidenced that the surface of both ceramics is covered by a scale due to melting/resolidification. At high fluence (7.5 J/cm^2), there are no continuous scales on the surfaces as material is removed by decomposition/vaporization. On alumina surface, a network of microcracks formed, while on silicon carbide, products of different morphologies (flat and rugged areas, deposits of debris and discontinuous thin remelted scales) were detected.

Schmidt and Li [291] studied the influence of laser glazing of sintered alumina as well as alumina–silica mixtures on surface characteristics and service life using a high power diode laser and high speed motion analysis system for use in a multitude of applications as insulators, crucibles, vacuum system windows, etc. The laser glazed material seems robust and exhibits good adherence to the bulk ceramic.

Stoltz and Poprawe [292] modified the surface conductivity of dielectric ceramics by continuous wave and pulsed laser irradiation. Conductive structures on Al_2O_3 was developed with CO_2 laser and on AlN with excimer laser irradiation (pulse width = 25 ns). Laser-treated specimens were subjected to a detailed characterization of electrical resistivity, chemical composition, structure and morphology.

Polycrystalline ceramics, notably alumina (polycrystalline aluminum oxide) are used widely in the electronics industry as substrates for metal-film deposition, as well as in other industrial applications. Multishot pulsed XeCl excimer laser irradiation of commercial fine-grained polycrystalline alumina substrates is found to significantly improve the bonding characteristics between the metal and film [293]. Laser irradiation produces a smoother surface finish increasing the adhesion strength of subsequently deposited copper films to the laser-treated alumina surface by a factor of 3 – 5 under optimum lasing conditions. X-ray photoelectron spectroscopy measurements suggest that electrical activation of the near-surface region may also contribute to the enhanced copper adhesion.

1.9.7 Laser Surface Engineering of Polymers

Laser-induced surface modification and laser-induced patterning of polymeric surfaces by deposition, etching and ablation has drawn considerable attention of late. Wong et al. [294] irradiated the surface of polyethylene terephthalate with KrF excimer laser (having a wavelength of 248 nm) and studied the surface image using atomic force microscopy. The surface roughness and ripple spacing increased with laser energy. Merging of the ripples (due to surface tension forces) is the driving force for the increased ripple spacing. With appropriate laser treatment, the hydrophobicity

of polyester can be greatly enhanced, making the treated polyester highly unwettable. This provides the textile industry a new method for making a high tech water repellent textile product. Adhi et al. [295] irradiated the surface of polytetrafluoroethylene films by femtosecond UV radiation from an excimer laser (KrF: λ : 248 nm, t_p : 380 fs) in air and investigated the surface using X-ray photoelectron spectroscopy, and bulk by fourier transform infrared spectroscopy. There was no signature of incorporation of hydrogen and/or oxygen, or the formation of a cross-linked network of carbon indicating chemically clean processing in contrast to nanosecond excimer laser processing which chemically degrades the surface. Huang et al. [296] discussed a method of improving adhesion to fluorocarbon resin by irradiation with an XeCl excimer laser. The respective adhesive force between the polymer and metal, and contact angles with water was measured by the shear test method and an Ne–He laser system. The adhesive force improved when the polymer surface was irradiated in the presence of water or solutions of boric acid, sodium hydroxide, copper sulfate, and sodium aluminate. These results were interpreted in terms of a simple laser heating model.

Drinek et al. [297] photolyzed hexamethylcyclotrisilazane (HMCTS) at 84 K using ArF excimer laser and film changed into a polymer having siloxane units in air at room temperature. However, fragments generated by laser irradiation of this polymer in the frozen film made a similar polymer film having a siloxane structure on a PVA film in air. The polymeric film with siloxane units prepared by the cryogenic laser ablation method displayed hydrophobic properties. Lu et al. [298] surface modified polyimide film by pulsed ultraviolet (UV) laser. Irradiation caused a photochemical reaction in the hydrophilic groups. In addition, a ripple microstructure was formed on the suz laser beam was 20 – 50°. Csete and Bor [299] generated laser-induced periodic surface structures on oriented and amorphous thick, as well as on spin-coated thin, polycarbonate films by polarized ArF excimer laser. Studies on the influence of the film structure and thickness on the development of periodic surface structure revealed that the line-shaped structure would transform into droplets below a critical thickness of the spin-coated films. This droplet formation was explained by the laser-induced melting across the film and subsequent dewetting on the substrate. The thickness of the layer melted by laser irradiation was computed by a heat conduction model, compared well with the critical thickness for spin-coated film. Hartwig [300] studied the influence of eximer laser radiation (248 nm) on the surface properties of an epoxy resin. At low laser energy density, the lap shear strength with the epoxy based adhesive was on an appropriate level with an improved reproducibility, but at higher energy densities the lap shear strength decreased due to the decomposition of the resin surface, as revealed by X-ray photoelectron spectroscopy results. Frerichs et al. [301] conducted a detailed investigation on laser ablation of different polymers like polyamide, polystyrene, polycarbonate, and polypropylene using a 248 nm excimer laser to study the effect of laser parameters on surface structuring. Arenholz et al. [302] showed that the adhesion of metal films on polymer foils could be improved by laser irradiation of the polymer surface prior to metal deposition. As a model system, metal films of different Co alloys, such as CoNi, CoCr, and CoNi-oxide, were chosen to form deposits on polytetraethylene foils. Laser irradiation was performed by means of a 248 nm KrF and 308 nm XeCl laser light in

1 – 20 pulses with fluences of typically 5 mJ/cm^2 and 40 mJ/cm^2 , respectively. Post irradiation metal deposition was carried out by electron-beam evaporation immediately after laser-beam irradiation. Laser irradiation of untreated poly-tetra-ethylene foils resulted in the formation of wall-type or map-type structures the mean distance of which was found to be related to laser parameters.

Different methods of laser treatment are suitable to generate grating-like periodic structures on polymer surfaces. One possibility is the projection of a mask and realization of periodic ablation [303]. The resulting periodicity is limited by the resolution of the applied optical system and by the complex response of the material to the laser illumination [304]. This method is suitable for generating structures in the micrometer-size region without difficulty. Smaller structures can be induced in the near field of the grating by the Talbot effect [305, 306].

1.10 Summary and Future Scope

Laser assisted fabrication offers a range of direct or single-step, contact-less and novel method of fabricating finished products/components of metallic, ceramic and polymeric origin. The possibilities offered by laser-assisted fabrication include bending, rapid prototyping, direct manufacturing, machining, welding, and surface engineering. Laser bending is attractive to the automobile and aircraft industry both for the precision and productivity involved in the process. Laser bending that primarily depends upon ‘temperature gradient’ and ‘buckling’ mechanisms is routinely applied in tailoring the curvature of aluminum, iron, and titanium-based metals and alloys. Laser assisted manufacturing is a major laser forming process that has found commercialization in many applications. The main reasons for interest in this process stems from the scope of direct (one-step) manufacturing of round or square sections, hollow tubes, and more complex geometry with the same machine and identical fixture. Solid parts are usually made in layers. Thus, the interfaces of the consecutive layers remain the weakest point. Investigations are warranted to predict the stresses generated at the edges and corners, surface roughness/contour, and compositional distribution in the solid object. Development or epitaxial repair of single crystal superalloy component will be a real breakthrough. In this regard, more comprehensive treatments of heat and mass transfer in specific applications are warranted to establish the reproducibility of the laser forming processes.

Laser machining requires controlled removal of material by vaporizing within a narrow dimension incurring least heating of the surrounding. The process can be extended to cutting, drilling, scribing, marking, or cleaning. In all these processes, material removal without damaging the surrounding and maintaining precision and accuracy is a challenge. The recent advances are now based on selecting appropriate wavelength, using multiple beams, allowing inclined/oblique incidence and removing material in stages. A large variety of materials starting from human/animal tissues to diamond can be laser machined. However, an appropriate choice of laser power and wavelength is crucial for the success of the operation. Future challenges

include increasing the capability to machine thicker sections, curved surfaces, and dissimilar/heterogeneous materials. Similarly, assessment of material damage needs more close control and monitoring of the microstructural change/damage across the cut. Development of intelligent machines for machining diverse materials would require interfacing a vast database with the hardware. Thus, continued efforts are needed to model laser machining processes with suitable experimental validation of the predicted results.

1.11 Future Challenges

This article has presented an overview of the fundamentals of laser, laser–matter interaction, and application of laser with regard to material processing divided into four major categories, namely forming, joining, machining, and surface engineering. Although lasers were invented in the early twentieth century, commercial high power lasers capable of delivering adequate power density for material processing involving heating, melting, and vaporising from all engineering solids (metallic, ceramic, semi-conducting, polymeric, and composites) were developed nearly 40 years ago and the application of laser in materials fabrication became popular only in the 1980s and onwards. The challenges in this regard lie in the development of novel and nonequilibrium microstructure including amorphous and extended solid solutions by ultrarapid cooling developed by laser melting and associated rapid solidification. Although attempts were made in developing amorphous/bulk metallic glass structure by laser surface cladding, complete amorphization could not be achieved due to the presence of heterogeneous nucleation sites at the solid–liquid interface and successive annealing of the zone during laser processing by successive laser passes. Hence, extensive efforts need to be undertaken in the development of a laser system for this purpose and designing of experiments in this regard.

The extensive amount of literature reviewed in this article clearly suggests that the field is far from being saturated and is rather rapidly growing into new and unexplored areas of application. The biggest advantage of laser is its ability to be a contact-less heating tool that can deliver the desired quantum of thermal energy in all solids at a precise location irrespective of their chemical bonding/nature, physical dimension (small or big), and state of aggregate (pure, mixed, composite) with minimum damages to the surrounding. Although the laser-induced heating or thermal profile decays exponentially with depth, the possibility of coupling laser with modern engineering practices like computer-aided design and manufacturing using robot-controlled stage and pneumatic/mechanically-driven delivery system (of wire, powder, sheet) has enabled creation of large components practically of any desired dimension and geometry. The versatility is further extended in the ability of laser to simultaneously heat, add, join, or remove materials of dissimilar nature like conducting and nonconducting, hard and soft, and dense and porous. Laser is now utilized to close surface porosities on coated and welded products and also for creating graded aggregate with controlled porosity, composition, and microstructure. This microstructural or

compositional gradation can be achieved within very narrow to wide length scales and along horizontal or vertical directions.

Acknowledgements The authors gratefully acknowledge the continuous supports from Prof. W. M. Steen, Prof. K. G. Watkins; Prof. A. K. Nath, Prof. B. L. Mordike, Dr. Andreas Weisheit, Dr. Rolf Galun, Prof. Lin Li for extending their laser facilities for research work and scientific collaboration. Experimental results presented in this chapter were mostly performed by their students: Dr. B. Ramesh Chandra, Dr. A. Basu, Dr. A. Biswas, Dr. S. Chatterjee, Mr. Subhasisa Nath and Mr. Prashant Sharma. Financial assistance from German Academic Exchange Service (DAAD), N. Delhi; Department of Science and Technology (DST), New Delhi; Council of Scientific and Industrial Research (CSIR); New Delhi; Board of Research on Nuclear Science (BRNS), and Bombay and Naval Research Board (NRB); New Delhi are gratefully acknowledged.

References

1. J.F. Ready, D.F. Farson, T. Feeley, *LIA Handbook of Laser Materials Processing* (Springer, Berlin, 2001) pp. 1.
2. W.M. Steen, K. Watkins, *Laser Material Processing* (Springer, New York, 2003) pp. 1.
3. B.L. Mordike, *Materials Science and Technology*, vol. 15, eds. by R.W. Cahn, P. Haasen, E.J. Kramer (VCH, Weinheim, 1993), p. 111
4. J. Mazumdar, *Lasers for Materials Processing*, ed. by M. Bass (North Holland Pub. Co., New York, 1993), p. 113
5. N.N. Rykalin, A. Uglov, A. Kokora, *Laser Machining and Welding* (MIR, Moscow, 1978), p. 1
6. S.T. Picraux, D.M. Follstaedt, *Laser-Solid Interactions and Transient Thermal Processing of Materials*, eds. by J. Narayan, W.L. Brown, R.A. Lemons (North-Holland Pub. Co., New York, 1983), p. 751
7. A. Einstein, *Z. Phys.* **18**, 121–128 (1917)
8. H. Kopfermann, R. Ladenburg, *H. Phys. Chemie. Abt.* **139**, 375–385 (1928)
9. T.H. Maiman, *Nature* **187**, 493–494 (1960)
10. O. Svelto, *Principles of Lasers* (Plenum Press, New York, 1986) pp. 1.
11. M.I. Nathan, W.P. Dumke, G. Burns, F.H. Dill Jr, *J. Appl. Phys. Lett* **1**, 62–64 (1962)
12. R.N. Hall, G.E. Fenner, J.D. Kingsley, T.J. Soltya, R.O. Carlson, *Phys. Rev. Lett* **9**, 366–368 (1962)
13. M.H.R. Hutchinson, *Spectrochim. Acta—Part B* **58**, 1155–1161 (2003)
14. G. Bekefi, *Principles of Lasers Plasmas* (New York, Wiley, 1976) pp. 1.
15. G. Patrick, O. ÓShea, P. Henry, *Science* **292**, 1853–1858 (2001)
16. M.D. Perry, D. Pennington, B.C. Stuart, G. Tietbohl, J.A. Britten, C. Brown, S. Herman, B. Golick, M. Kartz, J. Miller, H.T. Powell, M. Vergino, V. Yanovsky, *Opt. Lett.* **24**, 160–162 (1999)
17. Y. Kitagawa, Y. Sentoku, S. Akamatsu, M. Mori, Y. Tohyama, R. Kodama, K.A. Tanaka, H. Fujita, H. Yoshida, S. Matsuo, T. Jitsuno, T. Kawasaki, S. Sakabe, H. Nishimura, Y. Izawa, K. Mima, T. Yamanaka, *Plasmas* **9**, 2202–2207 (2002)
18. C.W. White, M.J. Aziz, *Surface Alloying by Ion, Electron and Laser Beams*, eds. by L.E. Rehn, S.T. Picraux, H. Wiedersich, (ASM, Metals Park, Ohio, 1987), p. 19
19. S. Lugomer, G. Bitelli, *Vacuum* **47**, 13–22 (1996)
20. J.H. Chu, J.-B. Du, I. Lin, *J. Appl. Phys. D* **27**, 296–300 (1994)
21. J.H. Chu, I. Lin, *Physica* **205**, 183–190 (1994)
22. A. Melzer, T. Trottenberg, A. Piel, *Phys. Lett. A.* **191**, 301–308 (1994)

23. A. Piel, A. Melzer, *Adv. Space. Res.* **29**, 1255–1264 (2002)
24. A.G. Gnedovets, E.B. Kul'batskii, I. Smurov, G. Flamant, *Appl. Surf. Sci.* **96**(98), 272–279 (1996)
25. R. Cauble, P.M. Celliers, G.W. Collins, L.B. da Silva, D.M. Gold, M.E. Foord, K.S. Budil, R.J. Wallace, A. Ng, *J. Suppl. Ser.* **127**, 267–273 (2000)
26. G.W. Collins, P.M. Celliers, L.B. DaSilva, R. Cauble, D.M. Gold, M.E. Foord, N.C. Holmes, B.A. Hammel, R.J. Wallace, A. Ng: *Phys. Rev. Lett.* **87**(16), art. no. 165504 (2001)
27. J. Laeng, J.G. Stewart, F.W. Liou, *Inter. J. Prod. Res.* **38**, 3973–3996 (2000)
28. Y. Namba, in *Proceedings International Conference of Lasers and Electro-Optics (ICALEO '85)*, Laser Institute of America, Orlando, Boston, MA, Sept 1985, pp. 403–407
29. Y. Namba, in *Proceedings Laser Advanced Materials Processing (LAMP '87)*, High Temperature Society of Japan, Osaka, Japan, June 1987, pp. 601–606
30. F. Vollersten, in *Laser Assisted Net Shape Engineering Meisenbach, Mechanisms and models for laser forming*, eds. by M. Geiger, F. Vollersten, (Bamberg, 1994), pp. 345–360
31. F. Vollersten, M. Rödle, in *Laser Assisted Net Shape Engineering Meisenbach, Model for the temperature gradient mechanism in laser bending*, eds. by M. Geiger, F. Vollersten, (Bamberg, 1994) pp. 371–378
32. F. Vollersten, S. Holzer, *VDI-Z.* **136**, 35–38 (1994)
33. M. Geiger, F. Vollersten, *Ann CIRP.* **42**, 301–304 (1993)
34. H. Arnet, F. Vollertsen, *J. Eng. Manuf.* **209**, 433–442 (1995)
35. F. Vollersten, I. Komel, R. Kals, *Mater. Sci. Eng.* **3**, 107–119 (1995)
36. Y. Li, N.R. Quick, A. Kar, *J. Maters. Proc. Technol.* **123**, 451–458 (2002)
37. M. Geiger, *Synergy Laser Mater. Process. Technol.* **120**, 322–326 (2002)
38. D. Chen, S. Wu, M. Li, *J. Maters. Proc. Technol.* **148**, 30–34 (2004)
39. M. Marya, G.R. Edwards, *J. Mater. Process. Technol.* **108**, 376–383 (2001)
40. P.J. Cheng, S.C. Lin, *J. Maters. Proc. Technol.* **108**, 314–319 (2001)
41. R. Kovacevic, Z. Hu, M. Labudovic, H. Wang, *Int. J. Mach. Tools Manuf.* **41**, 589–607 (2001)
42. C. Peng, Y.Y. Lawrence, *J. Manuf. Sci. Eng. (Trans. ASME).* **127**, 572–582 (2005)
43. W. Shichun, Z. Jinsong, *J. Maters. Proc. Technol.* **110**, 160–163 (2001)
44. J. Lawrence, M.J.J. Schmidt, L. Li, *Int. J. Mach. Tools and Manu.* **41**, 967–977 (2001)
45. S. Yoshioka, T. Miyazaki, M. Imai, Y. Shirai, T. Misu, in *Proceedings Conference on Laser Materials Processing, ICALEO '98*, Orlando, Florida, Nov 1998, Section E, pp. 161–169.
46. J. Dutta Majumdar, A.K. Nath, I. Manna, *Maters. Sci. Engg.* **385**, 113–122 (2004)
47. X.F. Wang, J. Takacs, G. Krallics, A. Szilagy, T. Markovits, *J. Mater. Process. Technol.* **127**, 388–391 (2002)
48. W. Li, Y.L. Yao, *Trans. ASME* **123**, 674–681 (2001)
49. K.C. Chan, J. Liang, *Mater. Lett.* **49**, 51–55 (2001)
50. J. Magee, K.G. Watkins, W.M. Steen, N.J. calder J. Sidhu, J. Kirby, in *Conference ICALEO '97, Laser Materials Processing*, Vol. 83. II, San Diego, California, USA, 17–20 Nov 1997, pp. E156–E165
51. J. Magee, K.G. Watkins, W.M. Steen, R.L. Cooke, J. Sidhu, *Conference, ICALEO '98, Laser Materials Processing*, Orlando, Florida, Section E, 16–19 Nov 1998, pp. 141–150
52. J. Magee, J. Sidhu, R.L. Cooke, *Opt. Lasers Eng.* **34**, 339–353 (2000)
53. R.J. Blake, in *Conference, ICALEO '96, Laser Materials Processing*, Detroit, Michigan, USA, 14–17 Oct 1996, pp. E105–E114
54. R.J. Blake, R.M. Pearson, A.B. Royell, W.E. Simon, *J. Laser Appl.* **10**, 199–204 (1998)
55. W. Maher, K.O. Tong, C. Bampton, M. Bright, J. Wooten, C. Rhodes, in *Conference, ICALEO '98, Laser Materials Processing*, Orlando, Florida, 16–19 Nov 1998, pp. 141–150.
56. T. Hatayama, M. Osawa, *Netsu Shori (J. Jpn. Soc. Heat Treat.)* **40**, 116–121 (2000)
57. K. Okuda, S. Shimoyama, M. Nunobiki, *Key Engg. Maters.* 257–258, 541–546 (2004)
58. K.C. Chan, Y. Harada, J. Liang, F. Yoshida, *J. Maters. Proc. Tech.* **122**, 272–277 (2002)
59. F.R. Liu, K.C. Chan, C.Y. Tang, *Mater. Sci. Eng. A.* **396**, 172–180 (2005)

60. J.A. Ramos, J. Magee, K.G. Watkins, W.M. Steen, F. Noble, in *Conference, ICALEO '98, Laser Materials Processing*, Orlando, Florida, 16–19 Nov 1998, Section E, pp. 178–185
61. M. Marya, G.R. Edwards, in *5th International Conference on Trends in Welding Research*, Pine Mountain, GA, USA, 1–5 June 1998, pp. 982–987. Florida, Section E, 16–19 Nov 1998 pp. 121–130
62. W. Wiehua-Wang, M.R. Holl, D.T. Schwartz, J. Electrochem. Soc. **148**, 363–368 (2001)
63. A. Greco, A. Licciulli, A. Maffezzoli, J. Mater. Sci. **36**, 99–105 (2001)
64. L. Lu, J.Y.H. Fuh, Z.D. Chen, C.C. Leong, Y.S. Wong, Mater. Res. Bull. **35**, 1555–1561 (2000)
65. K. Daneshvar, M. Raissi, S.M. Bobbio, J. Appl. Phys. **88**, 2205–2210 (2000)
66. M.C. Wanke, O. Lehmann, K. Muller, W. Qingzhe, M. Stuke, Science. **275**, 1284–1286 (1997)
67. O. Lehmann, M. Stuke, Science **270**, 1644–1646 (1995)
68. M. Burns, *Automotive Fabrication: Improving Productivity in Manufacturing*, (PTR Prentice-Hall Inc., Englewood Cliffs, 1993)
69. B.K. Paul, S. Baskaran, J. Mater. Process. Technol. **61**, 168–172 (1996)
70. D. Kochan, *Solid Freeform Manufacturing* (Elsevier, Amsterdam, 1993)
71. J. Pacheco, *Rapid Prototyping*, Contract no. DLA900-90-D-0134, (Department of Defense, Manufacturing Technology Information Analysis Center, Chicago, 1993)
72. M.L. Griffith, J.W. Halloran, in *Proceedings of the Solid Freeform Fabrication Symposium*, eds. by H.L. Marcus et al., (University of Texas, Austin 1994), p. 396
73. M.L. Griffith, T.M. Chu, W.C. Wagner, J.W. Halloran, in *Proceedings of the Solid Freeform Fabrication Symposium*, eds. by H.L. Marcus et al., (University of Texas, Austin, 1995), p. 31
74. R.S. Crockett, J. Okelly, P.D. Calvert, B.D. fabes, K. Stuffle, P. Greegan, R. Hoffman, in *Proceedings of the Solid Freeform fabrication Symposium*, eds. by H.L. Marcus et al., (University of Texas, Austin, 1995), p. 17
75. J.D. Cawley, P. Wei, Z.E. Liu, W.S. Newman, B.B. Mathewson, A. H. Heuer, in *Proceedings of the Solid Freeform fabrication Symposium*, eds. by H.L. Marcus et al., (University of Texas, Austin, 1995), p. 9
76. C. Groffin, J. Daufenbach, S. McMillin, Bull. Am. Ceram. Soc. **73**, 109 (1994)
77. J. Dutta Majumdar, I. Manna, Sadhana **28**, 495–562 (2003)
78. K. Lewis, E. Schlienger, Mater. Design **21**, 417–423 (2000)
79. Y.Z. Zhang, L.K. Shi, J. Cheng, M.Z. Xi, J. Xu, J Adv. Maters **35**, 36–40 (2003)
80. E. Goode, Adv. Mater. Process. **161**, 66–67 (2003)
81. K. Dai, L. Shaw, Acta Materialia. **52**, 69–80 (2004)
82. K. McAlea, C. Nelson, U. Heimadi, S. Seitz, in *Conference on Rapid Prototyping/ Laser Applications in the Automotive Industries*, Florence, Italy, 16–19 June 1997, pp. 159–167
83. A. Bauer, J. Ganz, K. Hesse, E. Kohler, Appl. Surf. Sci. **46**, 113–120 (1990)
84. F. Micheli, I.W. Boyd, Opt. Laser Technol. **18**, 75–82 (1987)
85. M.L. Griffith, M.E. Schlienger, L.D. Harwell, M.S. Oliver, M.D. Baldwin, M.T. Ensz, M. Essien, J. Brooks, C.V. Robino, J.E. Smugeresky, W.H. Hofmeister, M.J. Wert, D.V. Nelson, Mater. Design **20**, 107–113 (1999)
86. J.-Y. Jeng, M.-C. Lin, J. Mater. Process. Technol. **110**, 98–103 (2001)
87. C.L. Kuo, J.D. Huang, H.Y. Liang, Int. J. Adv. Manuf. Technol. **21**, 796–800 (2003)
88. D.S. Choi, S.H. Lee, B.S. Shin, K.H. Whang, Y.A. Song, S.H. Park, H.S. Jee, J. Maters. Proc. Technol. **113**, 273–279 (2001)
89. A.L. Kovalev, V.P. Mishina, D.L. Wainstein, V.I. Titov, V.F. Moiseev, N.K. Tolochko, J. Maters. Eng. Perform. **11**, 492–495 (2002)
90. Y. Tang, H.T. Loh, Y.S. Wong, J.Y.H. Fuh, L. Lu, X. Wang, J. Maters Proc. Tech. **140**, 368–372 (2003)
91. X.H. Wang, J.Y.H. Fun, Y.S. Wong, L. Lu, H.T. Loh, Y.X. Tang, H.H. Zhu, Mater. Sci. Forum, 437–438, 273–276 (2003)
92. M.W. Khaing, J.Y.H. Fuh, L. Lu, J. maters. Proc. Technol **113**, 269–272 (2001)

93. Y.P. Kathuria, in *Proceedings, 60 Years of Scientific Co-operation in Welding, Jubilee Conference*, Timisoara, 19–21 Nov 1997, pp. 199–205
94. S. Hayano, *Titanium Japan* **50**, 43–47 (2002)
95. N.K. Tolochko, V.V. Savich, T. Laoui, L. Froyen, G. Onofrio, E. Signorelli, V.I. Totov, J. Mater. Design Appl. **216**, 267–270 (2002)
96. J.-Y. Jeng, S.-C. Peng, C.-J. Chou, *Int. J. Adv. Manuf. Technol.* **16**, 681–687 (2000)
97. A.J. Pinkerton, L. Li, *Int. J. Mach. Tools Manuf.* **44**, 573–584 (2004)
98. A.J. Pinkerton, L. Li, *Appl. Surf. Sci.* **208–209**, 405–416 (2003)
99. J. Dutta Majumdar, A. Pinkerton, Z. Liu, I. Manna, L. Li, *Appl. Surf. Sci.* **247**, 320–327 (2005)
100. J. Dutta Majumdar, A. Pinkerton, Z. Liu, I. Manna, L. Li, *Appl. Surf. Sci.* **247**, 373–377 (2005)
101. G.J. Davies, S. Zhen, *J. Mater. Sci.* **18**, 1899–1902 (1983)
102. Y.P. Kathuria, *J. Mater. Proc. Technol.* **142**, 466–470 (2003)
103. Y. Zhang, M. Xi, S. Gao, L. Shi, *J. Mater. Proc. Technol.* **142**, 582–585 (2003)
104. J. Mei, J. Liang, R. Sharman, W. Voice, X. Xu, in *Conference on Rapid Prototyping of Materials*, Columbus, 7–10 Oct 2002, pp. 133–138
105. F.G. Arcella, F.H. Froes, *JOM*. **52**, 28–30 (2000)
106. D.H. Abbott, F.G. Arcella, *Adv. Mater. Proc.* **153**, 29–30 (1998)
107. D. Srivastava, I.T.H. Chang, M.H. Loretto, *Mater. Design* **21**, 425–433 (2000)
108. D. Srivastava, I.T.H. Chang, M.H. Loretto, *Intermetallics* **9**, 1003–1013 (2001)
109. R. Banerjee, P.C. Collins, A. Gene, H.L. Fraser, *Mater. Sci. Eng. A* **358**, 343–349 (2003)
110. R. Banerjee, P.C. Collins, D.C. Bhattacharyya, S. Banerjee, H.L. Fraser, *Acta Materialia* **51**, 3277–3292 (2003)
111. R. Banerjee, P.C. Collins, H.L. Fraser, *Adv. Engg. Mater. (Germany)* **4**, 847–851 (2002)
112. H. Tomochika, H. Kikuchi, T. Araki, M. Nishida, *Mater. Sci. Eng. A* **356**, 122–129 (2003)
113. X.D. Zhang, C. Brice, D.W. Mahaffey, H. Zhang, K. Schwendner, D.J. Evans, H.L. Fraser, *Scripta Materialia* **44**, 2419–2424 (2001)
114. X. Wu, J. Mei, *J. Mater. Process. Technol.* **135**, 266–270 (2003)
115. Y.X. Tang, L. Lu, Y.H.J. Euh, H.T. Loh, Y.S. Wong, C.H. Ng, *Mater. Sci. Forum* **437(438)**, 301–304 (2003)
116. W.L. Karlsen, J. Kotila, J.E. Lind, *Int. J. Powder Metall.* **40**, 29–41 (2004)
117. L. Xue, J.Y. Chen, M.U. Islam, in *Conference on Laser Materials Processing, ICALEO 1999*, San Diego, 15–18 Nov 1999
118. S. Das, T.P. Fuesting, G. Danyo, L.E. Brown, J.J. Beaman, D.L. Bourell, *Mater. Design* **21**, 63–73 (2000)
119. K. Cai, D. Guo, Y. Huang, J. Yang, *J. Eur. Ceram. Soc.* **23**, 921–925 (2003)
120. A. Larrea, de la G.F. Fuente, R.I. Merino, V.M. Orera, *J. Eur. Ceram. Soc.* **22**, 191–198 (2002)
121. L. Lu, J.Y.H. Fuh, Z.D. Chen, C.C. Leong, Y.S. Wong, *Mater. Res. Bull.* **35**, 1555–1561 (2000)
122. W. Liu, J.N. DuPont, *Scripta Materialia*. **48**, 1337–1342 (2003)
123. Y.P. Kathuria, *Surf. Coat. Technol.* **116–119**, 643–647 (1999)
124. H.M. Wang, D.Y. Luan, L.Y. Zhang, *Scripta Materialia* **48**, 1179–1184 (2003)
125. G. Duan, H.M. Wang, *J. Mater. Sci. (U.S.A.)* **37**, 1981–1985 (2002)
126. J. Cheng, Y.Z. Zhang, P.Z. Zhang, L.K. Shi, M.Z. Xi, *Heat Treat. Met. (China)* **3**, 32–35 (2002)
127. J. Bosbach, D. Martin, F. Stietz, T. Wenzel, F. Träger, *Appl. Phys. Lett.* **74**, 2605–2608 (1999)
128. M.C. Wanke, O. Lehmann, K. Muller, W. Qingzhe, M. Stuke, *Science. Assoc. Adv. Sci.* **275**, 1284–1286 (1997)
129. Y.F. Lu, H. Qiu, *J. Appl. Phys.* **88**, 1082–1087 (2000)
130. S. Fukumoto, A. Hirose, K.F. Kobayashi, *Mater. Sci. Technol.* **9**, 264–271 (1993)
131. C.A. Forbis-Parrott, *Weld. J.* **70**, 37–42 (1991)
132. S.T. Riches, *Weld. Met. Fabr.* **61**, 79–83 (1993)
133. R.S. Parmar, *Welding Engineering and Technology* (Khanna Publishers, New Delhi, 1999)
134. J. F. Lancaster, *Metallurgy of Welding* (George Allen and Unwin, 1980)

135. W.W. Duley (eds.), *Laser Welding* (Wiley, New York, 1999) pp. 1.
136. K.H. Leong, P.A. Kirkham, K.C. Meinert Jr., *J. Laser Appl.* **12**, 181–184 (2000)
137. A. Hirose, H. Todaka, K. Yamaoka, N. Kurosawa, K.F. Kobayashi, *Metall. Mater. Trans. A* **30**, 2115–2120 (1999)
138. D.C. Weckman, H.W. Kerr, J.T. Liu, *Metall. Mater. Trans. B* **28**, 687–700 (1997)
139. M.F. Lee, J.C. Huang, N.J. Ho, *J. Mater. Sci.* **31**, 1455–1468 (1996)
140. I.R. Whitaker, D.G. McCartney, *Mater. Sci. Eng. A* **196**, 155–163 (1995)
141. E. Biro, Y. Zhou, D.C. Weckman, K.J. Ely, *J. Laser Appl.* **13**, 96–104 (2001)
142. T. Fuhrich, P. Berger, H.J. Hugel, *J. Laser Appl.* **13**, 178–186 (2001)
143. M. Farid, P.A. Molian, *J. Mater. Sci.* **15**, 3817–3826 (2000)
144. E.S. Ng, I.A. Watson, *J. Laser Appl.* **11**, 273–278 (1999)
145. A.M. El-Batahgy, *Mater. Lett.* **32**, 155–163 (1997)
146. Z. Szymanski, J. Kurzyna, W. Kalita, *J. Phys. D (Appl. Phys.)* **30**, 3153–3162 (1997)
147. Wood-Hi-Cheng, Wei-Han-Wang, Jyh-Cheng-Chen: *IEEE Trans. Compon. Packag. Manuf. Technol.* **19**, 764–769 (1996)
148. G. Wang, K.N. Tandon, *Microgravity Sci. Technol.* **8**, 131–133 (1995)
149. T.T. Hsu, Y.R. Wang, S.K. Wu, C. Chen, *Metall. Mater. Trans. A* **32**, 569–576 (2001)
150. O. Perret, M. Bizouard, Ph. Naudy, G. Pascal, D. Nore, Y. Horde, Y. Delaisse, *J. Appl. Phys.* **90**, 27–30 (2001)
151. L.W. Tsay, C.Y. Tsay, *Inter. J. Fatigue.* **19**, 713–720 (1997)
152. A. Hirose, S. Fukumoto, K.F. Kobayashi, *Key Eng. Mater.* **104–107**, 853–872 (1995)
153. M. Marya, G.R. Edwards, *J. Mater. Eng. Perform.* **4**, 435–443 (2001)
154. T. Shida, M. Hirokawa, S. Sato, *Weld. Res. Abroad.* **43**, 36 (1997)
155. E.L. Baarden, D.J. Schmatz, R.E. Bisaro, *Weld. J.* **52**, 227 (1973)
156. R.A. Willgoss, J.H.P.C. Megaw, J.N. Clark, *Opt. Laser Technol.* **11**, 73 (1979)
157. R. C. Crafer, in *Proceedings of 4th International Conference on Advances in Welding Processes*, Harrogate, Yorks, 9–11 May 1978, pp. 267–278
158. J. Majumdar, W.M. Steen, *Met. Trans. A* **13**, 865 (1982)
159. Y.S. Yang, S.H. Lee, *J. Mater. Process. Technol.* **94**, 151–156 (1999)
160. C.M. Banas, *Laser Welding Developments*, in *Proceedings GECB International Conference on Welding Research Related to Power Plants*, 17–21 Sept 1972, Southampton, England
161. B.G. Chung, S. Rhee, C.H. Lee, *Mater. Sci. Eng. A* **272**, 357–362 (1999)
162. F. Malek Ghaini, M.J. Hamed, M.J. Torkamany, J. Sabbaghzadeh, *Scripta Materialia* **56**, 955–958 (2007)
163. C.T. Kwok, S.L. Fong, F.T. Cheng, H.C. Man, *J. Mater. Process. Technol.* **176**, 168–178 (2006)
164. N.A. McPherson, K. Chi, T.N. Baker, *J. Mater. Proc. Technol.* **134**, 174–179 (2003)
165. A.-M. El-Batahgy, *Mater. Lett.* **32** (1997) 155–163
166. S.M. Chan, L.C. Chan, T.C. Lee, *J. Mater. Process. Technol.* **132**, 95–101 (2003)
167. Z. Sun, M. Kuo, T. Moio, *J. Mater. Sci. Lett.* **17**, 355–357 (1998)
168. A.P. Costa, L. Quintino, M. Greitmann, *J. Mater. Process. Technol.* **141**, 163–173 (2003)
169. R. Akhter, K.G. Watkins, W.M. Steen, *Mater. Lett.* **9**, 550–556 (1990)
170. S. Iqbal, M.M.S. Gualini, F. Grassi, *J. Mater. Process. Technol.* **184**, 12–18 (2007)
171. L.W. Tsay, M.C. Young, C. Chen, *Corr. Sci.* **45**, 1985–1997 (2003)
172. E. Capello, P. Chiarello, B. Previtali, M. Vedani, *Mater. Sci. Engg. A* **351**, 334–343 (2003)
173. W.S. Chang, S.J. Na, *J. Mater. Proc. Technol.* **120**, 208–214 (2002)
174. Y.-F. Tzeng, *J. Mater. Process. Technol.* **102**, 40–47 (2000)
175. Z. Li, G. Fontana, *J. Mater. Proc. Technol.* **74**, 174–182 (1998)
176. T. Narikiyo, H. Miura, S. Fujinaga, A. Ohmori, K. Inoue, *J. Phys. D Appl. Phys.* **31**, 2331–2337 (1998)
177. J. Onoro, C. Ranninger, *J. Mater. Proc. Technol.* **68**, 68–70 (1997)
178. H. Kusuda, T. Takasago, F. Natsumi, *J. Mater. Proc. Tech.* **71**, 136–140 (1997)
179. A. Roustila, N. Kuromoto, A.M. Brass, J. Chene, *J. Nucl. Mater.* **211**, 156–167 (1994)

180. E. Schubert, M. Classen, I. Zerner, C. Walz, G. Sepold, *J. Maters. Proc. Technol.* **115**, 2–8 (2001)
181. A. Haboudoua, P. Peyrea, A.B. Vannes, G. Peix, *Mater. Sci. Eng. A* **363**, 40–52 (2003)
182. R. Braun, *Mater. Sci. Eng. A* **426**, 250–262 (2006)
183. T.M. Yue, J.H. Xu, H.C. Man, *Appl. Compos. Mater.* **4**, 53–64 (1997)
184. H.M. Wang, Y.L. Chen, L.G. Yu, *Mater. Sci. Eng. A* **293**, 1–6 (2000)
185. Q. Yunlian, D. Ju, H. Quan, Z. Liying, *Mater. Sci. Eng. A* **280**, 177–181 (2000)
186. A.P. Wu, G.S. Zou, J.L. Ren, H.J. Zhang, G.Q. Wang, X. Liu, M.R. Xie, *Intermetallics* **10**, 647–652 (2002)
187. K. Uenishi, K.F. Kobayashi, *Intermetallics* **4**, 95–101 (1996)
188. Z. Li, S.L. Gobbi, I. Norris, S. Zolotovskiy, K.H. Richter, *J. Maters. Proc. Technol.* **65**, 203–208 (1997)
189. K. Girard, J.M. Jouvard, Ph. Naudy, *J. Phys. D: Appl. Phys.* **33**, 2815–2824 (2000)
190. Z. Xu, K. Natesan, C.B. Reed, D.L. Smith, *Int J. Ref. Met. Hard Mater.* **18**, 231–236 (2000)
191. L.i. Zhang, S.L. Gobbi, K.H. Richter, *J. Maters. Proc. Tech.* **70**, 285–292 (1997)
192. G. Song, L. Liu, P. Wang, *Mater. Sci. Eng. A* **429**, 312–319 (2006)
193. L. Liming, W. Jifeng, S. Gang, *Mater. Sci. Eng. A* **381**, 129–133 (2004)
194. J.H. Kim, C. Lee, D.M. Lee, J.H. Sun, S.Y. Shin, J.C. Bae, *Maters. Sci. Engg. A* 449–451, 872–875 (2007).
195. Y.L. Chen, L.G. Yu, H.M. Wang, *Proc. SPIE* **3862**, 443–447 (1999)
196. G. Sierra, P. Peyre, F. Deschaux-Beaume, D. Stuart, G. Fras, *Mater. Sci. Eng. A* **447** 197–208, (2007)
197. B. Majumdar, R. Galun, A. Weisheit, B.L. Mordike, *J. Maters. Sci.* **32**, 6191–6200 (1997)
198. T.A. Mai, A.C. Spowage, *Mater. Sci. Eng. A* **374**, 224–233 (2004)
199. F.L. Chen, E. Siores, *J. Mater. Proc. Technol.* **141**, 213–218 (2003)
200. P. Di Pietro, Y.L. Yao, *Int. J. Mach. Tools Manuf.* **35**, 673–688 (1995)
201. J. Duan, H.C. Man, T.M. Yue, *J. Phys D: Appl. Phys.* **34**, 2127–2134 (2001)
202. J. Duan, H.C. Man, T.M. Yue, *J. Phys. D: Appl. Phys.* **34**, 2135–2142 (2001)
203. J. Duan, H.C. Man, T.M. Yue, *J. Phys. D: Appl. Phys.* **34**, 2143–2150 (2001)
204. C.-H. Tsai, C.-J. Chien, *Opt. Lasers Eng.* **41**, 189–204 (2004)
205. J.B. Bernstein, Joo-Han-Lee, Gang-Yang, T.A. Dahmas, *IEEE Trans. Semicond. Manuf.* **13**, 228–234 (2000)
206. S.L. Chen, *J. Eng. Manuf.* **212**, 113–128 (1998)
207. B.S. Yilbas, A.Z. Sahin, *Opt. Laser Tech.* **27**, 175–184 (1995)
208. Y. Li, W.P. Latham, A. Kar, *Opt. Lasers Eng.* **35**, 371–386 (2001)
209. I. Belic, J. Stanic, *Opt. Laser Technol.* **19**, 309–311 (1987)
210. A. Ivarson, J. Powel, J. Kamalu, C. Magnusson, *J. Mater. Process. Technol.* **40**, 359–374 (1994)
211. J. Wang, W.C.K. Wong, *J. Mater. Process. Technol.* **95**, 164–168 (1999)
212. H.Y. Zheng, Z.Z. Han, Z.D. Chen, W.L. Chena, S. Yeo, *J. Maters. Proc. Technol.* **62**, 294–298 (1996)
213. T.M. Yue, W.S. Lau, *Mater. Manuf. Process.* **11**, 17–29 (1996)
214. H. Huang, H.Y. Zheng, G.C. Lim, *Appl. Surf. Sci.* **228**, 201–206 (2004)
215. M. Anderson, R. Patwa, Y.C. Shin, *Int. J. Mach. Tools Manuf.* **46**, 1879–1891 (2006)
216. J.H. Zhang, T.C. Lee, X. Ai, W.S. Lau, *J. Mater. Process. Technol.* **57**, 304–310 (1996)
217. G. Lu, E. Siores, B. Wang, *J. Mater. Process. Technol.* **88**, 154–158 (1999)
218. C.-H. Tsai, H.-W. Chen, *J. Mater. Process. Technol.* **136**, 166–173 (2003)
219. L. Hong, L. Li, C. Ju, *Opt. Lasers Eng.* **38**, 279–289 (2002)
220. I. Black, K.L. Chua, *Opt. Laser Technol.* **29**, 193–205 (1997)
221. I. Black, S.A.J. Livingstone, K.L. Chua, *J. Maters. Proc. Tech.* **84**, 47–55 (1998)
222. P.A. Rebroy, Y.C. Shin, F.P. Incropera, *Int. J. Mach. Tools Manuf.* **44**, 677–694 (2004)
223. R.F. de Graaf, J. Meijer, *J. Mater. Process. Technol.* **103**, 23–28 (2000)
224. C. Lehane, H.S. Kwok, *Appl. Phys A* **73**, 45–48 (2001)

225. X. Zhu, D.M. Villeneuve, Y.A. Naumov, S. Nikumb, P.B. Corkum, Appl. Surf. Sci. **152**, 138–148 (1999)
226. N. Katsarakis, E. Chatzitheodoridis, G. Kiriakidis, M.M. Sigalas, C.M. Soukoulis, W.Y. Leung, G. Tuttle, Appl. Phys. Lett. **74**, 3263–3265 (1999)
227. Z. Illyefaalvi-Vitez, Microelectron. Reliab. **41**, 563–570 (2003)
228. P.P. Pronko, S.K. Dutta, J. Squier, J.V. Rudd, D. Du, G. Mourou, Opt. Commun. **114**, 106–110 (1995)
229. S. Nikumb, Q. Chen, C. Li, H. Reshef, H.Y. Zheng, H. Qiu, D. Low, Thin Solid Films **477**, 216–221 (2005)
230. P. Psyllaki, R. Oltra, Mater. Sci. Eng. A **282**, 145–152 (2000)
231. Y.F. Lu, Y.P. Lee, M.S. Zhou, J. Appl. Phys. **83**, 1677–1684 (1998)
232. J. Zhang, K. Sugioka, S. Wada, H. Tashiro, K. Toyoda, Appl. Phys. A **64**, 367–371 (1997)
233. P.A. Molian, *Surface Modification Technologies-An Engineers Guide*, ed. by T.S. Sudarshan, (Marcel Dekker Inc., New York, 1989) p. 421
234. C.W. Draper, J.M. Poate, Inter. Met. Rev. **30**, 85–108 (1985)
235. C.W. Draper, C.A. Ewing, J. Mater. Sci. **19**, 3815–3825 (1984)
236. C.W. Draper, in *Laser and Electron Beam Processing of Materials* eds. by C.W. White, P.S. Peercy, (Academic, New York, 1980), p. 721
237. C.W. White, M.J. Aziz, in *Surface Alloying by Ion, Electron and Laser Beams*, eds. by L.E. Rehn, S.T. Picraux, H. Wiedersich, (ASM, Metals Park, Ohio 1987), p. 19
238. J. Mazumder, J. Metals. **35**, 18–26 (1983)
239. E. Kennedy, G. Byrne, D.N. Collins, J. Mater. Process. Technol. **155–156**, 1855–1860 (2004)
240. K.H. Lo, F.T. Cheng, H.C. Man, Surf. Coat. Technol. **173**, 96–104 (2003)
241. K.H. Lo, F.T. Cheng, C.T. Kwok, H.C. Man, Mater. Lett. **58**, 88–93 (2003)
242. Q.Y. Pan, W.D. Huang, R.G. Song, Y.H. Zhou, G.H. Zhang, Surf. Coat. Technol. **102**, 245–255 (1998)
243. U.K. Mudali, M.G. Pujar, R.K. Dayal, J. Maters. Eng. Perform. **7**, 214–220 (1998)
244. R. Colação, C. Pina, R. Vilar, Scripta Materialia **41**, 715–721 (1999)
245. B.E. Wilde, M. Manohar, C.E. Albright, Mater. Sci. Engg. A **198**, 43–49 (1995)
246. T.M. Yue, Y.X. Wu, H.C. Man, Surf. Coat. Technol. **114**, 13–18 (1999)
247. R. Li, M.G.S. Ferreira, A. Almeida, R. Vilar, K.G. Watkins, M.A. McMahon, W.M. Steen, Surf. Coat. Technol. **81**, 290–296 (1996)
248. N. Hari Prasad, R. Balasubramaniam, J. Mater. Process. Technol. **68**, 117–120 (1997)
249. T.T. Wong, G.Y. Liang, C.Y. Tang, J. Mater. Process. Technol. **66**, 172–178 (1997)
250. Y.B. Liu, J.D. Hu, Z. Y. Cao, P.K. Rohatgi, Wear **206**, 83–86 (1997)
251. K.G. Watkins, Z. Liu, M. McMahon, R. Vilar, M.G.S. Ferreira, Mater.Sci. Eng. A **252**, 292–300 (1998)
252. A. Michaelides, C. Panagopoulos, Surf. Coat. Technol. **57**, 173–177 (1993)
253. D. Dube, M. Fiset, A. Couture, I. Nakatsugawa, Mater. Sci. Eng. A **299**, 38–45 (2001)
254. D. Schippman, A. Weisheit, B.L. Mordike, Surf. Eng. **15**, 23–26 (1999)
255. T.M. Yue, A.H. Wang, H.C. Man, Scripta Mater **38**, 191–198 (1997)
256. G. Abbas, Z. Liu, P. Skeldon, Appl. Surf. Sci. **247**, 347–353 (2005)
257. J. Dutta Majumdar, R. Galun, B.L. Mordike, I. Manna, Mater. Sci. Eng. A **361**, 119–129 (2003)
258. T.M. Yue, Q.W. Hu, Z. Mei, H.C. Man, Mater. Lett. **47**, 165–170 (2001)
259. A. Biswas, L. Li, U.K. Chatterjee, I. Manna, S.K. Pabi, J. Dutta Majumdar, Scripta Materialia **59**, 239–242 (2008)
260. A. Biswas, L. Li, U.K. Chatterjee, I. Manna, J. Dutta Majumdar, Metall. Mater. Trans. A, Phys. Metall. Mater. Sci. **40**, 3001–3008 (2009)
261. J.P. Chu, J.M. Rigsbee, G. Banas', F.V. Lawrence Jr, H.E. Elsayed-Ali, Metall. Mat. Trans. A **26**, 1507 (1995)
262. R. Fabbro, J. Fournier, P. Ballard, D. Devaux, J. Virmont, J. Appl. Phys. **68**, 775 (1990)

263. P. Ballard, J. Fournier, R. Fabbro, J. Frelat, L. Castex, *J. De Physique Colloque C 3*(Supplement. 49), C3-401 (1988)
264. A.H. Clauer, C.T. Walters, S.C. Ford, in *Laser in Materials Processing*, ed. by M. Bass, (American Society of Metals, Metals Parks, OH, 1983), p. 7
265. J. Dutta Majumdar, I. Manna, *Mater. Sci. Eng. A* **267**, 50–59 (1999)
266. A.K. Jain, V.N. Kulkarni, D.K. Sood, *Thin Solid Films* **70**, 86 1–9 (1981)
267. A. Almeida, M. Anjos, R. Vilar, R. Li, M.G.S. Ferreira, W.M. Steen, K.G. Watkins, *Surf. Coat. Technol.* **70**, 221–229 (1995)
268. C.H. Tang, F.T. Cheng, H.C. Man, *Surf. Coat. Technol.* **200**, 2606–2609 (2006)
269. J. Dutta Majumdar, B. Ramesh Chandra, A.K. Nath, I. Manna, *Surf. Coat. Technol.* **201**, 1236–1242 (2006)
270. W. Aihua, Z. Beidi, T. Zengyi, M. Xianyao, D. Shijun, C. Xudong, *Surf. Coat. Technol.* **57**, 169–172 (1993)
271. K. Uenishi, K.F. Kobayashi, *Intermetallics* **7**, 553–559 (1999)
272. J. Dutta Majumdar, I. Manna, *Mater. Sci. Eng. A* **268**, 216–226, 227–235 (1999)
273. J. Dutta Majumdar, B.L. Mordike, I. Manna, *Wear* **242**, 18–27 (2000)
274. J. Dutta Majumdar, B.L. Mordike, S.K. Roy, I. Manna, *Oxid. Met.* **57**, 473–498 (2002)
275. J. Dutta-Majumdar, A. Weisheit, B.L. Mordike, I. Manna, *Mater. Sci. Eng. A* **266**, 123–134 (1999)
276. I. Manna, W.M. Steen, K.G. Watkins, in *Surface Engineering in Materials Science I Conference Proceedings*, eds. by S. Seal, N.B. Dahotre, J.J. Moore, B. Mishra, (TMS, Warrendale, PA, 2000), PP. 377–384, 15086–7528
277. A.H. Wang, T.M. Yue, *Compos. Sci. Technol.* **61**, 1549–1554 (2001)
278. S. Ignat, P. Sallamand, D. Grevey, M. Lambertin, *Appl. Surf. Sci.* **225**, 124–134 (2004)
279. J. Dutta Majumdar, B.L. Mordike, R. Galun, I. Manna, *Lasers Eng.* **12**, 147–170 (2002)
280. F.T. Cheng, C.T. Kwok, H.C. Man, *Surf. Coat. Tech.* **139**, 14–24 (2001)
281. X.L. Wu, Y.S. Hong, *Metal. Mater. Trans. A.* **31**, 3123–3127 (2000)
282. A. Agarwal, N.B. Dahotre, *Wear.* **240** 144–151 (2000); A. Agarwal, N.B. Dahotre, *Metal. Mater. Trans. A.* **31** 401-408 (2000)
283. S. Tondou, T. Schnick, L. Pawlowski, B. Wielage, S. Steinhauser, L. Sabatier, *Surf. Coat. Tech.* **123**, 247–251 (2000)
284. W. Jiang, P.A. Molian, *Surf. Coat. Tech.* **135**, 139–149 (2001)
285. E. Gemelli, A. Galerie, M. Caillet, *J. Mater. Sci.* **31**, 6627–6630 (1996)
286. J. Dutta Majumdar, B. Ramesh Chandra, I. Manna, *Tribol. Int.* **40**, 146–152 (2007)
287. J.P. Chu, J.M. Rigsbee, G. Banas, H.E. Elsayed-Ali, *Mat. Sci. Eng. A* **260**, 260–268 (1999)
288. P. Peyre, X. Scherpereel, L. Berthe, C. Carboni, R. Fabbro, G. Be'ranger, C. Lemaitre, *Mat. Sci. Eng. A* **280**, 294–302 (2000)
289. J. Lawrence, L. Li, *J. Mat. Process. Technol.* **142**, 461–465 (2003)
290. D. Sciti, C. Melandri, A. Bellosi, *J. Mat. Sci.* **35**, 3799–3810 (2000)
291. M.J.J. Schmidt, L. Li, *Appl. Surf. Sci.* **168**, 9–12 (2000)
292. B. Stolz, R. Poprawe, *Surf. Coat. Technol.* **112**, 394–400 (1999)
293. D.H. Lowndes, M. DeSilva, M.J. Godbole, A.J. Pedraza, T. Thundat, R.J. Warmack, *Appl. Phys. Lett.* **64**, 1791–1793 (1994)
294. W. Wong, K. Chan, K.W. Yeung, K.S. Lau, *J. Mat. Process. Technol.* **132**, 114–118 (2003)
295. K.P. Adhi, R.L. Owings, T.A. Railkar, W.D. Brown, A.P. Malshe, *Appl. Surf. Sci.* **218**, 17–23 (2003)
296. F. Huang, Q. Lou, J. Dong, Y. Wei, *Appl. Surf. Sci.* **174**, 1–6 (2003)
297. V. Drinek, H. Niino, J. Pola, A. Yabe, *Appl. Phys. A* **73**, 527–530 (2001)
298. Q.H. Lu, M. Li, J. Yin, Z.K. Zhu, Z.G. Wang, *J. Appl. Poly. Sci.* **82**, 2739–2743 (2001)
299. M. Csete, Z. Bor, *Appl. Surf. Sci.* **133**, 5–16 (1998)
300. A. Hartwig, G. Vittr, V. Schlett, *Int. J. Adhes. Adhes.* **17**, 373–377 (1997)
301. H. Frerichs, J. Stricker, D.A. Wesner, E.W. Kreutz, *Appl. Surface Science.* **86**, 405–410 (1995)

302. E. Arenholz, J. Heitz, M. Wagner, D. Bzuerle, H. Hibst, A. Hagemeyer, *Appl. Surf. Sci.* **69**, 16–19 (1993)
303. H.J. Leamy, S.T.T. Rozgonyi, G.K. Celler, *Appl. Phys. Lett.* **32**, 535–537 (1978)
304. P.A. Temple, M.J. Soileau, *IEEE J. Quantum Electron.* **17**, 2067–2072 (1981)
305. van H.M. Driel, J.E. Sipe, J.F. Young, *J. Lumin.* **30**, 446–471 (1985)
306. C.T. Walters, *Appl. Phys. Lett.* **25**, 696–698 (1974)

Chapter 2

High Power Lasers in Material Processing Applications: An Overview of Recent Developments

A. K. Nath

Abstract High power lasers have witnessed many interesting developments in the recent past. CO₂ lasers have been ruling the roost in the industry for material processing applications for over a long time. Lamp pumped Nd:YAG laser, despite some limitations like poor beam quality and low efficiency, have been finding many applications in material processing. Diode pumped fiber lasers can be rated as one of the most important developments in recent times because of their high efficiency, excellent beam quality, reliable, and robust design. The demand for fabricating miniaturized components involved in various applications, such as of MEMS, microelectronics, telecommunication, optoelectronics, and biomedical devices has created much interest in micromachining with lasers. Excimer lasers operating in short wavelengths in ultraviolet spectrum have been traditionally very popular in these applications. An overview of some of these developments in the field of lasers and their applications in manufacturing is presented.

2.1 Introduction

High power lasers, as a tool of unprecedented precision and power are finding usage in a wide spectrum of material processing applications, e.g., laser cutting, welding, drilling, marking, scribing, surface hardening, surface alloying, surface cladding, surface texturing, shock peening, forming, micromachining, and rapid manufacturing. Lasers, which are widely used for these applications include high power CO₂ laser, lamp pumped Nd:YAG laser, diode laser pumped solid-state lasers, diode laser, fiber laser, and excimer lasers. High power CO₂ laser and the lamp pumped Nd:YAG laser have been the workhorse in the industry for material processing applications.

A. K. Nath (✉)
Mechanical Engineering Department, Indian Institute of Technology,
Kharagpur 721 302, West Bengal, India
e-mail: aknath@mech.iitkgp.ernet.in

However, recent developments in high power diode lasers followed by the diode pumped solid-state (DPSS) rod, thin disk, and fiber lasers have begun to change this scenario by making their own niche in many material processing modalities, as well as entering in the domain of the more established CO₂ and lamp pumped solid-state (LPSS) lasers. The worldwide market share of industrial lasers for material processing applications has been more than 50% of the total sale of all lasers excluding the low power diode lasers, whose market has been dominated by the optical communication and storage applications. The market trend for the last couple of years is shown in Fig. 2.1. Figure 2.2 shows the market trend of various industrial lasers for material processing applications during the period 2003–2009. This indicates a steady growth of the industrial laser market till 2007 and then a decline in 2009 due to the deep global recession. It can be seen that the demand of high power CO₂ lasers used in cutting and welding, as well as in marking and scribing has remain almost steady over the years up to 2007, and that of LPSS lasers has declined gradually. A part of the LPSS laser market is being taken over by the steady growth of the market share of “diode laser pumped solid state lasers” including fiber laser as they have better efficiency, beam quality, and longer life than LPSS lasers. The diode laser got introduced in the material processing arena as an efficient pump source of solid-state lasers in place of lamp pump source. Its high power versions, though at present handicapped by their beam quality, are also finding direct materials processing applications, e.g., surface treatment, plastics welding and soldering, etc. Excimer lasers, which are used for microlithography and various other micro-processing applications, have also maintained a steady growth over the years. The technological development of high average power ultra-short Ti-sapphire laser and more recently that of femtosecond fiber laser has brought out these lasers from the realm of the research laboratory to the industry for micro- and nanomachining applications, such as, MEMS and micro-fluidic device machining [1–6].

Lasers are usually characterized by four main parameters, namely the wavelength, beam quality, temporal profile, and power. The choice of a laser for a particular application is decided by these parameters along with the other practical considerations, such as the high laser efficiency, compact size, ease of beam maneuverability and delivery, low capital, and maintenance costs. Table 2.1 presents a comparison of the various characteristics of important industrial lasers. Diode lasers have good overall efficiency and need little maintenance; however, the laser beam quality is relatively poor compared to other lasers. The beam quality determines the focusing power of the laser beam and hence, the laser power density on the work-piece. The quality of a laser beam is expressed by the beam parameter product (beam diameter \times beam divergence) or M^2 parameter and this varies with laser power. Variation of laser beam quality with output power for different lasers is shown in Fig. 2.3 [7]. The typical regimes for various industrial applications are also indicated in the figure. Since the high power diode laser has all the characteristics, its beam quality is highly attractive for most material processing modalities, and thus research and development to improve its beam quality is being pursued vigorously. In the area of DPSS disk and fiber lasers also, R&D effort is continuing to increase output power with improved beam quality and to develop high average power

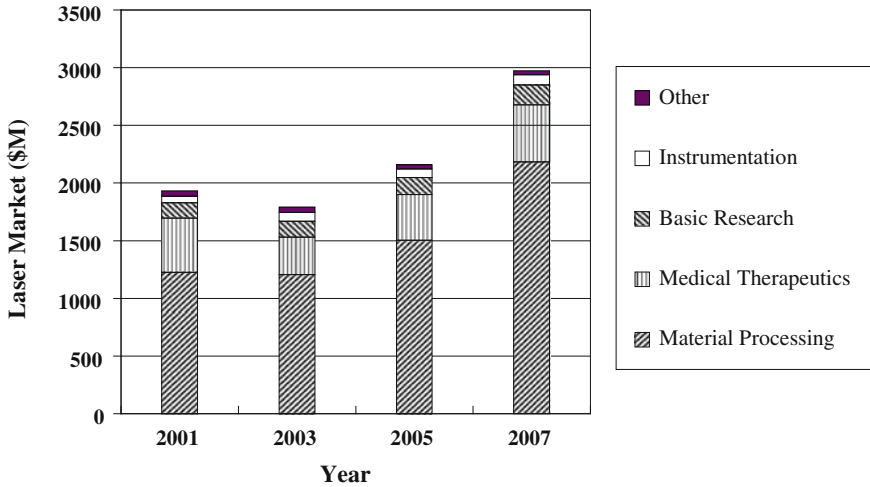


Fig. 2.1 Laser market for different applications (Source laser focus world)

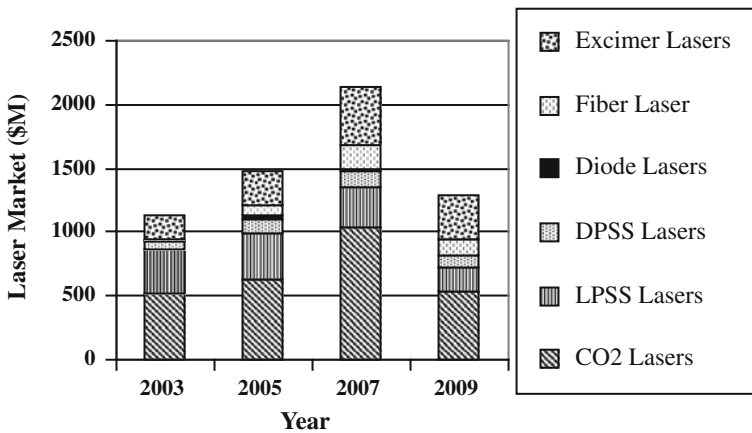


Fig. 2.2 Laser market for different industrial lasers (Source laser focus world)

ultrafast fiber lasers to replace the Ti-sapphire laser, which is a too complex system to operate in the industrial environment. As of today, fiber lasers have an edge over all other lasers in terms of attributes including efficiency, beam quality, maintenance, and beam delivery, and therefore are poised for a great leap in their popularity and reduction in their cost with mass production. Because of their high beam quality many material processing modalities with exceptional characteristics such as striation-free cutting, deep penetration welding with high depth to width ratio have been realized [8–10]. In several other applications such as laser surface hardening, remelting, surface alloying, and cladding, the resultant morphology and microstructure are

Table 2.1 Common industrial lasers for material processing applications

Parameters	CO ₂ laser	Nd:YAG laser	Diode laser	Fiber laser	Excimer lasers	Ultrafast lasers
Wavelength	10.06 μm	1.06 μm	0.8–0.98 μm	1.07 μm	125–351 nm	TSL* : 0.7 – 1 μm; FL* : 1.03 – 1.08 μm
Efficiency	5–20%	LP: 1–3%; DP: 10–20%	30–60%	10–30%	1–4%	TSL: < 1%FL; > 5%
Mode of operation	CW & pulse	CW & pulse	CW & pulse	CW & pulse	Pulse	TSL: 10kHz–80 MHz, FL: 30–100 MHz
Output power	Up to 20 kW	Up to 16 kW	Up to 4 kW CW	Up to 10 kW	Average power: 300 W	Average power TSL: 1–5 W (36–100 fs); FL: 1–830 W (100–640 fs)
Pulsed energy free running pulse duration	1–10 J / 100 ns–10 μs ~ J / ~ 100 ns	up to 120 J / 1–20 ms / 1.2 J / ~ 3 ns	Single diode ~ μJ / 100 ns QCW pulsed up to 50 kHz frequency	Up to 15 J / 0.2–20 ms ~ mJ / 40–500 ns	Up to 1 J 20–30 ns up to 1 kHz rep / rate	TSL : 15 nJ–290 μJ / 36–100 fs FL: 30 nJ / 100 fs ~ 10 μJ / ~ 700 fs
Peak power	10s MW	50 MW	40 W	10 MW	10–100 MW	100 kW–10 MW
Beam quality factor: mm. mrad (typical)	3–5	0.4–20	10–100	~ 0.3 – 4	160 × 20	
Fiber delivery	Not possible	Possible	Possible	Possible		Possible
Maintenance periods (hrs)	2,000	200 (lamp life)	Maintenance—free typical life 100,000 hrs	Maintenance—free pump diode life ~ 100,000 h	10 ^{8–9} pulses thyatron life	TSL: high maintenance; FL: low maintenance
Price (\$/W)	35–120	100–120	60–90	100	1,000	TSL: 100–150 K FL: 30–50 K

TSL- Ti sapphire laser, FL fiber laser, LP lamp pumped, DP diode laser pumped

Table 2.2 Advantages and disadvantages of different lasers and their applications

Laser type	Advantages	Disadvantages	Laser applications
CO ₂ lasers	Simple laser design, reliable and compact (slab geometry), good beam quality, low-cost, high efficiency	Low absorption in metals, sensitive to laser induced plasma, flexible fiber beam delivery not available	Laser cutting, welding, surface treatment: hardening, remelting, alloying, cladding, texturing; drilling, marking, scribing, rapid manufacturing
Nd:YAG laser (rod geometry)	Higher absorption than CO ₂ laser, diode pumped laser-high efficiency, flexible beam delivery, less sensitive to laser induced plasma	Lamp pumped laser-low efficiency, limited life of lamps, and poor beam quality at higher laser powers	Laser cutting, welding, marking, annealing, drilling, surface treatment, rapid manufacturing
Disc laser	All of Nd:YAG laser, scalable to higher powers	Limited beam quality at high powers	Same as of Nd:YAG lasers
Fiber laser	Compact and robust design; excellent beam quality, high efficiency, air-cooled and maintenance-free operation, long lifetimes, scalable to higher powers, flexible beam delivery	High cost of pump diode lasers and related reliability issues	Laser cutting, welding, surface treatment, surface structuring, drilling, marking, scribing, selective sintering, direct metal deposition- rapid manufacturing
Diode lasers	Most efficient, most compact, high reliability, low running cost, easy integration with CNC, flexible beam delivery	Poor beam quality	Brazing, soldering, plastic welding, surface hardening, cladding, rapid manufacturing, laser pump source
Excimer lasers	High absorption by most materials, high resolution due to short laser wavelengths; short duration pulses and shallow absorption depth- high precision micromachining	Issues related to high voltage, high gas pressure electrical discharge, Toxic and corrosive (halogen) laser gases, needs regular gas filling	Micromachining, wire stripping, drilling, Fiber Bragg gratings writing, photolithography; pulse laser physical and chemical vapour deposition, Corneal sculpting to correct myopia
Ultrafast Ti- sapphire and fiber lasers	Laser pulse shorter than thermal diffusion time- little heat affected zone (HAZ), no debris or recast materials, no damage to adjacent structure, no cracks, processing of all types of materials possible. Fiber laser: 'All-in-fiber' concept-compact and robust design	Ti-Sapphire laser- bulky and complex design, sensitive to environment, high price and servicing cost, less efficiency, shorter life. Fiber laser- undesired nonlinear effects at higher energy	Micro-drilling, fine cutting, scribing, micro- & nano-structuring, photomask ablation, thin film structuring, in-vivo imaging & clinical applications, subcellular ablation etc

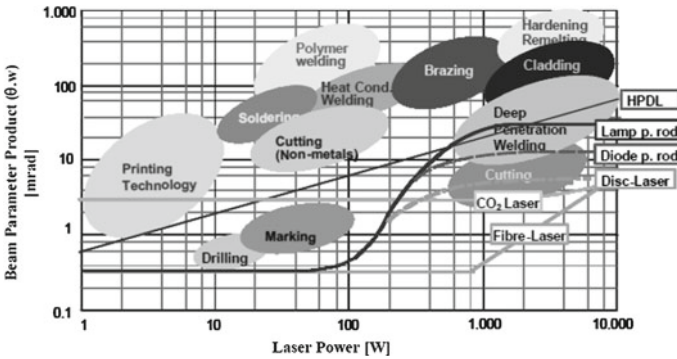


Fig. 2.3 Beam parameter product versus laser power for different laser types and typical regimes for industrial applications [7]

dependent on the rise in temperature, heating and cooling rates, temperature gradient and solidification velocity which depend on the laser parameters. Recently, several interesting effects in laser surface modifications have been realized exploiting the non-conventional laser beam shapes and temporal laser power modulation. Table 2.2 summarizes the advantages and limitations of various lasers and their material processing applications. In this presentation an overview of the recent developments in high power lasers, their interaction with materials, and some of the laser material processing applications is presented.

2.2 Recent Developments in High Power Lasers

2.2.1 High Power CO₂ Laser

High power CO₂ laser operating at 10.6 μm wavelength has been the workhorse in laser material processing for a long time. This is because of its high efficiency, high power capability, better beam quality, and versatility. High power continuous wave (CW) CO₂ lasers with powers up to 20kW are commercially available and powers even above 100kW have been achieved in the laboratory and for defense applications [11]. The lasing medium is a mixture of CO₂, N₂ and He gases and this is excited by passing electrical discharge. Several different electrical discharge schemes have been developed for creating uniform and stable discharge to excite large gas volumes. The electrical to laser conversion efficiency of CW-CO₂ lasers is typically in the range of 10–20%. For removing the remaining electrical power which is dissipated as heat in the laser medium, different techniques have been developed. The conventional CW-CO₂ laser is excited either by DC or RF discharge and heat is removed by diffusion cooling. The laser power in this type of CO₂ laser scales with

discharge length only, as 50–75 W/m [12]. In multi-kilowatt CO₂ lasers the waste heat is usually removed by convective cooling, i.e., by circulating the gas through heat exchangers. The laser power P_l in convective cooled CW CO₂ laser increases with the increase of gas flow velocity and scales as [12]:

$$P_l(\text{Watt}) = 120 M^*(\text{g/s}) \quad (2.1)$$

where M^* is the mass flow rate of laser gas.

Two gas flow configurations known as the fast axial flow and the transverse flow, in which gas is flown parallel and perpendicular to the optic axis, respectively have been used [13–18]. While the axial flow configuration supports better beam quality, this requires specially designed Roots blower or high speed turbo blower of high pressure heads for gas circulation. On the other hand, transverse flow configuration normally supports multimode laser beam, which however is easy to scale up to high powers using axial or centrifugal blowers. Because of better beam quality fast axial flow CO₂ lasers are more popular for metal sheet cutting and welding applications in the industry. Despite these benefits, however, the gas flow causes some inherent disadvantages, e.g., instabilities by turbulences, high cost, large size, and frequent service of blowers and considerable cost by gas consumption.

The latest development is high power CWCO₂ laser is the RF discharge excited diffusion cooled extended electrode CWCO₂ laser, also called CO₂ slab laser, which was coincidentally developed and patented by Opower in Germany and Tulip in Canada [7]. The basic principle of this laser is depicted in Fig. 2.4 [7]. The distance between the two electrodes is about a millimeter and the laser power scales up with the electrode area typically as 10 kW/m² [19, 20]. Because of the short gap, the waste heat can be removed directly through the water cooled electrodes by diffusion cooling without requiring any gas flow. Since the active medium is of the shape of a thin and wide slab, a special type of optical resonator, usually stable–unstable resonator, is used to extract laser power efficiently in a good quality beam. By special beam forming optics consisting of spherical and cylindrical mirrors, as well as a spatial filter, a high quality laser beam with $M^2 \leq 1.1$ has been generated [7]. The maximum power commercially available in slab technology today is 8 kW. They can provide laser beam of Gaussian power distribution for cutting applications and doughnut-shaped beam also for welding applications. Because of the excellent beam quality, CO₂ slab laser can cut and weld even high reflecting materials like aluminum at high speeds with low kerf width and large depth to width weld aspect ratio [7].

2.2.2 High Power Diode Laser

Although the first diode laser was demonstrated in 1962, the development of high power diode lasers is more recent. The most common type of semiconductor diode laser is formed from a direct band gap p–n junction and is pumped by injecting electric current. When forward biased by applying +ve voltage at p-type and –ve

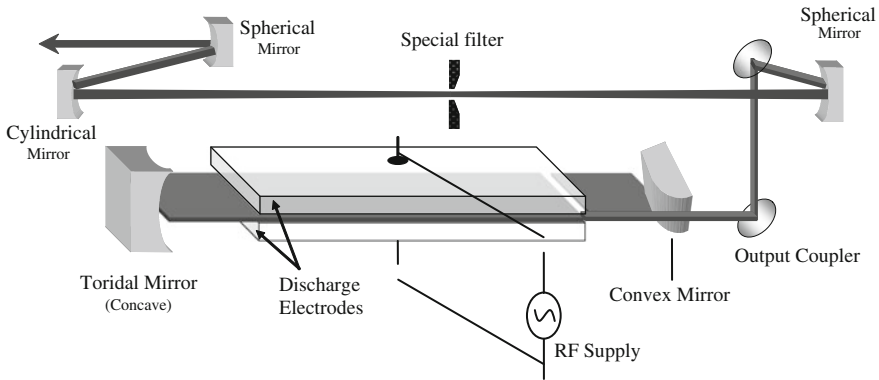


Fig. 2.4 Schematic diagram of a RF excited CO₂ slab laser [7]

voltage at n-type, holes and electrons recombine at the p–n interface and they emit light by spontaneous emission process such as in light emitting diode (LED), and under certain conditions, population inversion is achieved and spontaneous emission leads to laser light by stimulated process. A large number of diode lasers based on semiconductors of group III–V compounds have been operated, the most popular high power diode lasers for pumping solid-state lasers and material processing applications being based on GaAlAs/GaAs and InGaAs/GaAs diodes, which emit in 720–880 and 940–990 nm ranges, respectively [21]. Laser radiation is actually emitted from a thin layer of p–n junction, which is about 1 micron in thickness. The typical size of a single diode element is about $1-2 \times 50-200 \times 1,000-2,000 \mu\text{m}$. From a traditional diode laser element typically only a few milliwatts laser power could be obtained which was constrained by technological problems, such as, the waste heat removal from a tiny surface area (typically $1 \text{ kW}/\text{cm}^2$), catastrophic laser mirror damage, and stability of semiconductor materials. Today the single diode laser developed with the state-of-the-art technology can give maximum laser power in the range of a few watts ($< 10 \text{ W}$) with an electro-optic efficiency of 50–60%. This has become feasible due to careful investigation of the crystalline structures, detailed understanding of failure mechanisms, and considerable improvement of the manufacturing processes. Figure 2.5a shows schematically a single diode laser and the beam emerging out of the laser. Since the laser beam is emerging out from the narrow junction region (junction height \times width = $1-2 \times 100-200 \mu\text{m}$), the full divergence angle along the height of the junction is very large in $70-90^\circ$ range (fast axis) and $10-20^\circ$ (slow axis) along the width of the junction. Diode laser power is increased by arranging several individual lasers in a one-dimensional array on one monolithic element approximately 10 mm long, referred to as diode laser bar, Fig. 2.5b. Laser powers up to 120 W are typically obtained from a single bar although more than 500 W have been recently achieved in laboratory assembly [22]. The highly diverging laser beam along fast axis is collimated by aspheric cylindrical microlenses to produce parallel beams. Lasers of powers less than 120 W are usually air cooled and

the higher power bars are mounted on special water-cooled microchannel heat sinks for efficient removal of waste heat. Laser power has been further scaled up to kW level by staking a number of laser bars on top of one another forming a 2D array, Fig. 2.5c. With the cylindrical microlens mounted on each laser bar the output beam of the 2-D diode laser array is stacked up as shown in (Fig. 2.5c).

The number of diode bars in one stack can be as high as 30, giving out about 4kW or more output power. Since the number of stacks that can be used is almost unlimited, laser power is theoretically not limited. However, the laser beam quality reduces as the overall laser beam size increases with the increase in the number of stacking bars, while the beam divergence remains the same as that of a single diode laser emitter. This results in the reduction of the brightness of laser though the laser power is increased with the increase in the number of bars. Various schemes, such as, spatial multiplexing, polarization multiplexing, and wavelength multiplexing have been devised for increasing the number of stacks without increasing the beam size so that the beam quality is not adversely affected with the increase of laser power [23]. Further research is continued for combining outputs of a number of diode laser stacks, coherently to improve the beam quality and brightness of high power diode laser [24]. Currently, high power CW diode lasers of 4kW direct output and 2.5kW fiber-delivery beams are commercially available [21]. With appropriate lens combination the direct diode laser system produces a rectangular beam of mm range dimensions at the focus. High power diode lasers are finding direct applications in those modalities in which highly focused lased beam is not required such as the surface hardening [21, 23, 25, 26].

2.2.3 *Nd:YAG Lasers*

The lamp pumped CW and high repetition rate pulsed Nd:YAG lasers were the second most popular lasers after CO₂ laser in materials processing applications; their lasing wavelength of 1.06 μm being 10 times shorter than that of CO₂ laser facilitated higher absorptivity during processing, lower sensitivity against laser induced plasma, and the use of flexible optical fibers for beam delivery. The active medium of the lamp pumped Nd:YAG laser is traditionally of cylindrical rod shape and is pumped and cooled along the radial direction, while the laser beam propagates axially. High power CW Nd:YAG laser of 2kW CW and 4kW modulated powers and pulsed lasers of 20kW peak power and pulse energy up to 120J are commercially available. Electrical to laser energy conversion efficiency of lamp pumped Nd:YAG lasers is typically about 3%, efficiency more than 5% has been reported in experimental pulsed Nd:YAG laser [27]. The disadvantages of the lasers include short lifetime (several hundred hours only) of the xenon flash lamp and krypton arc lamp needing frequent replacement and a relatively low electro-optic efficiency of the laser. The major part of the pump energy is dissipated as heat in the rod, which is conducted out radially by surface cooling which induces a radial temperature gradient in the gain medium. Due to this the gain medium exhibits thermally induced lensing and birefringence

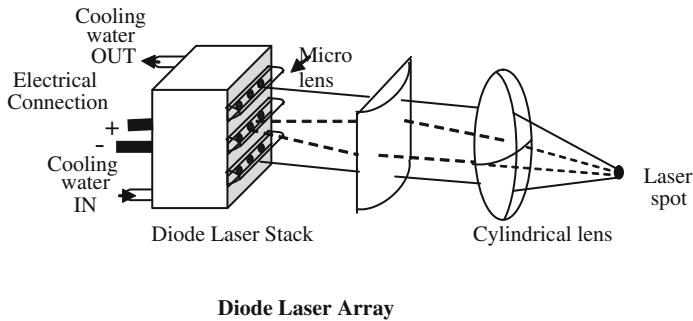
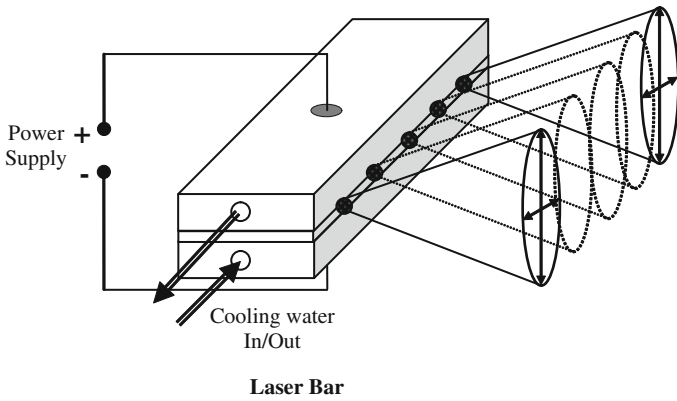
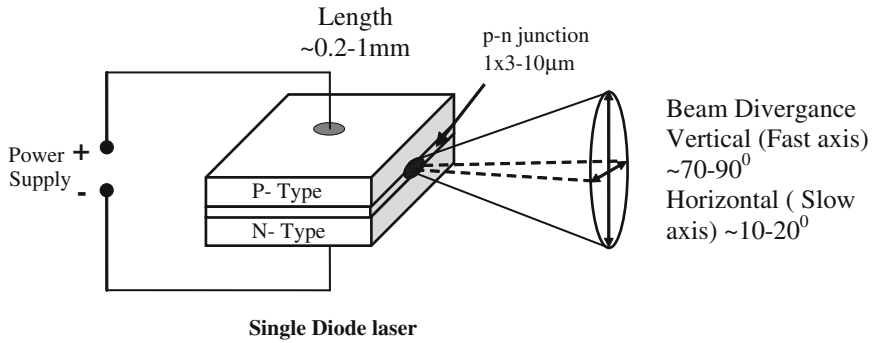


Fig. 2.5 Schematic diagrams of diode lasers. **a** Single element diode laser. **b** Diode laser bar. **c** 2D array high power diode laser

effects [28]. This results in relatively poor beam quality of Nd:YAG laser, especially at high powers compared to CO₂ laser. With the recently available high power diode lasers, diode pumped solid-state lasers (DPSSL) have been developed which have effectively overcome these disadvantages. Diode lasers have a long life of more than

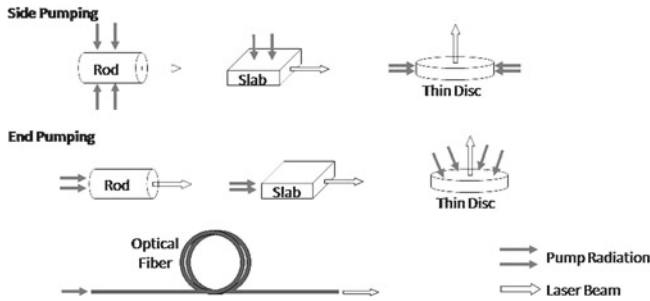


Fig. 2.6 Schematic of various basic pumping configurations with diode laser and laser crystal geometries, from [29]

100,000 h and their emission wavelength can be exactly matched to the absorption peak of the lasing medium. The high electrical to laser power conversion efficiency of pump diode lasers, the more selective excitation of the laser medium, and the small difference in the pump and laser photons energies enhanced the DPSSL efficiency by more than a factor of 5 compared to lamp pumped systems [29]. This has resulted in lower waste heat dissipation in the laser medium and a higher beam quality. Various geometries of the laser medium for DPSSL—rod, discs and fibers and the pump laser beam direction with respect to the optic axis have been investigated in view of attainable beam quality and means of power scaling. An overview of the various promising concepts can be found in the review paper by Hugel [29]. The basic pumping configurations and crystal geometries are summarized in Fig. 2.6. In the “first generation” of DPSSL the crystal geometries and the cooling techniques were basically the same as in lamp pumped lasers. In this configuration though the thermal gradient was reduced, and not eliminated. R&D continued to overcome these problems and this has resulted in the development of the next generation of high power DPSSLs: the thin disc and fiber lasers.

2.2.4 Diode Pumped Solid-State Rod Type and Slab Lasers

In DPSSL, two types of pump geometries namely the end and side pumping have been used (*cf.* Figs. 2.7 and 2.8) [30, 31]. Lasers based on several other solid-state laser media such as Yb:YAG, Nd:YVO₄, and Nd : GdVO₄ were also developed. Among them the Yb:YAG laser has proven to be a better candidate for high power output. In Yb:YAG the difference between the pump and laser photon energies is smaller compared to that in Nd:YAG system, and this reduces the thermal loading in the Yb:YAG laser and increases the optical efficiency. The end pumped schemes support better quality laser beam; however, they are not suitable in high power operations due to the possibility of thermal fracture [32]. Laser powers up to 407 W with optical efficiency of 54% were reported in end pumped multi-segmented

Fig. 2.7 a Schematic of a three-fold symmetric pump configuration of a side-pumped Nd:YAG laser. **b** Side view of laser pump head showing only one diode laser module for the sake of clarity [31]

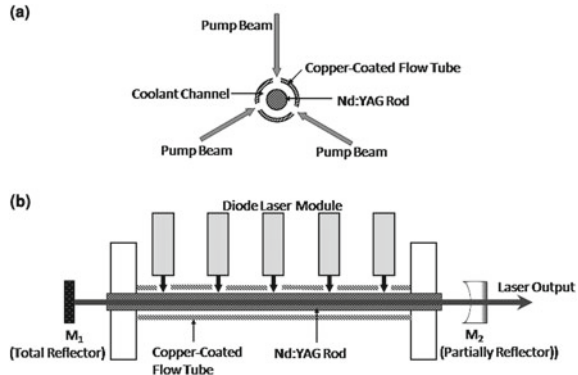
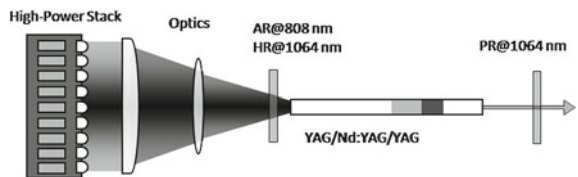


Fig. 2.8 Schematic of an end-pumped Nd:YAG laser [30]



composite crystal Nd:YAG laser [30]. End pumped lasers often use Nd:YVO₄ which has a wider absorption band and thus is less sensitive to the drift of the pump radiation wavelength due to the temperature shift or the aging of the diodes. The high beam quality and the short resonator length of the end pumped configuration, as well as the short fluorescence lifetime of Nd : YVO₄ make this setup a preferred combination for the generation of short Q-switched pulses and also for frequency conversion [7].

Alternatively, the side pumped schemes allow power scalability. Here, the well proven multi-rod technology of lamp pumped devices has been directly exploited. Extensive studies to optimize the pump house geometry for efficient and uniform coupling of pump radiation [31, 33–35], resonator design and doping concentration in lasing medium have been carried for improving the laser performance. Bruesselbach and Sumida [36] achieved maximum 2.65 kW from a single Yb:YAG rod pumped by diodes. Optical to optical conversion efficiency of up to 50% and electrical to optical efficiencies of up to 13% at high power levels have been reported [29, 31]. Laser systems with side pumped rod-shaped multiple crystals are commercially available in 1–4 kW power range. A laboratory prototype of maximum 8 kW laser power has been recently developed [7].

Although the side pumped rod lasers are scalable to high powers, the output beam is usually multimode, i.e., the beam product parameter is high. In order to get high power with high beam quality lamp pumped and more recently diode pumped slab laser have been developed [37, 38]. In this design the temperature gradient is maintained nearly one dimensional by arranging the pumping and cooling properly and the laser beam is extracted in such a way by proper resonator design so that the

Fig. 2.9 Schematic of a diode laser pumped zigzag slab laser [39]

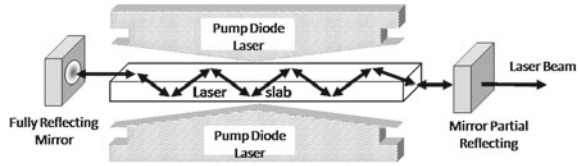


Fig. 2.10 Schematic of a diode laser pumped slab laser with hybrid resonator [40]

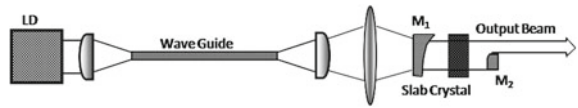
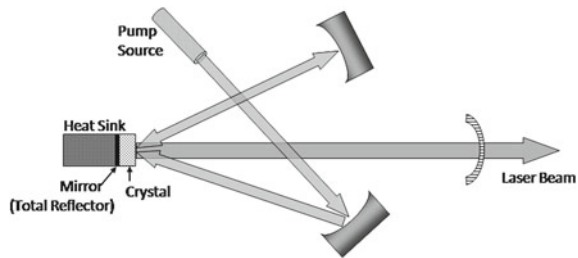


Fig. 2.11 Schematic of a diode pumped disc laser

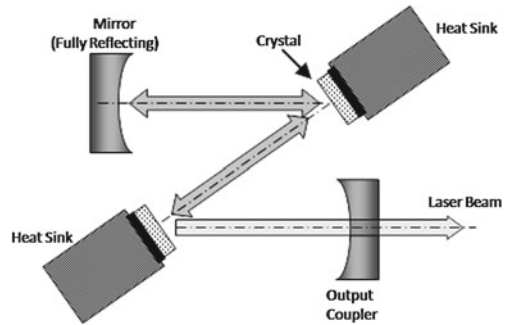


effect of temperature gradient is averaged out. Figures 2.9 and 2.10 show various schemes such as zigzag laser path, and hybrid resonator which are reported to produce high quality laser beam [39, 40].

2.2.5 High Power Thin Disc Laser

To circumvent the poor beam quality in rod-type laser due to thermal lens effect it was proposed to use a thin disc as a laser medium [41, 42]. In this the height of the cylindrical disc, l , is so small compared to its diameter, d , i.e., $l/d \ll 1$, the laser active medium cannot be cooled any longer on its circumference. The laser is cooled through one of the large faces as shown in Fig. 2.11. Thin disc is mounted onto a heat sink with its rear side. Unlike in side pumped rod laser, in thin disc the waste heat flows along the axis and for uniform face-pumping there is little temperature gradient along the radial direction. Thus, the problem of thermal lens effect is minimized and better quality laser beam is generated. Extensive research was carried out in developing high power, high efficiency disc laser with high beam quality using Yb: YAG laser medium [43]. As an active material, Yb:YAG allows much higher doping concentrations (up to 30%) than Nd:YAG (0.1–2%) doping. One of the typical pumping configurations of multiple discs laser is schematically shown in Fig. 2.12. CW lasers of power up to 16kW are now commercially available with 6 mm-mrad beam quality and 25% electro-optic efficiency [44].

Fig. 2.12 Schematic of a multiple discs laser for power scaling



2.2.6 Fiber Laser

One of the most important laser developments in recent time is the fiber laser. Although first made in 1961, it was a long way of many technology breakthroughs such as high power diode lasers, low loss doped glass fiber, diode-fiber coupling devices, and Bragg grating, etc. for the fiber laser to reach its present state of high power, high efficient, excellent beam quality, compact size, robust design, and long life. The active gain medium of a fiber laser is an optical glass fiber doped with rare-earth elements such as neodymium, ytterbium, and erbium, and is pumped by diode lasers operating in 950–980 nm wavelength range. Among the various dopings, ytterbium (Yb) is the most commonly used element in high power fiber laser for material processing applications because of its low quantum defects (small difference in pump and lasing photons energies) resulting in high ($\sim 94\%$) quantum efficiency. The wavelength of Yb doped fiber laser is $1.07 \mu\text{m}$. High power fiber lasers are based on double-clad fiber (cf. Fig. 2.13) [29]. The gain medium forms the core of the fiber, which is surrounded by two layers of cladding. The lasing mode propagates in the core, while the pump beam propagates by the outer cladding layer. The outer cladding keeps this pump light confined. This arrangement allows the core to be pumped with a much higher power beam than that could otherwise be made to propagate in it, and allows the conversion of pump light of relatively low brightness into a much higher brightness laser beam. The typical core diameter of a single mode fiber laser is about $10 \mu\text{m}$ and the inner clad diameter is about $400 \mu\text{m}$. They do not suffer from thermal problems unlike Nd:YAG rod laser, as fiber allows very easy heat dissipation due to high surface area to volume ratio. Fiber lasers are built with “all fiber” technology, which is immune to misalignment, and do not require any adjustment during operation. Instead of external resonator mirrors Bragg gratings written into the core of a fiber are used as reflectors of optical resonator. Fiber Bragg Gratings consist of periodic refractive index variations. The longitudinal period of grating determines the wavelength of the reflected light, and the magnitude of the refractive index variation controls the percentage of reflected radiation. The maximum laser power which can be extracted from a single fiber is limited by the threshold power density for optical damage and the onset of nonlinear phenomena in

Fig. 2.13 Schematic of a clad-pumped fiber laser [29]

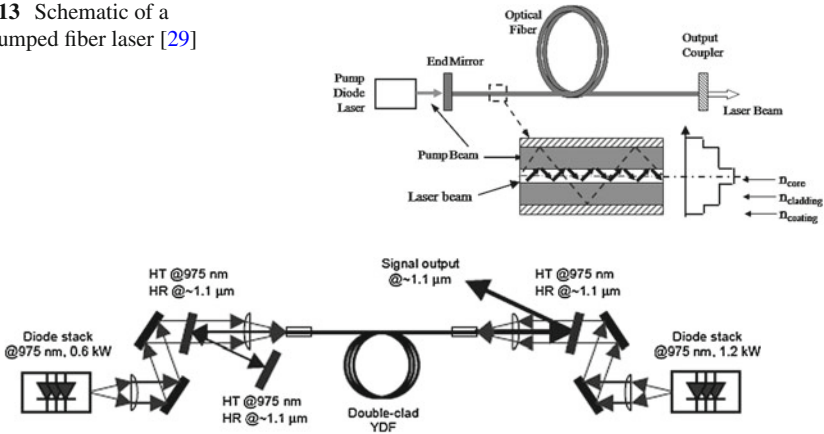
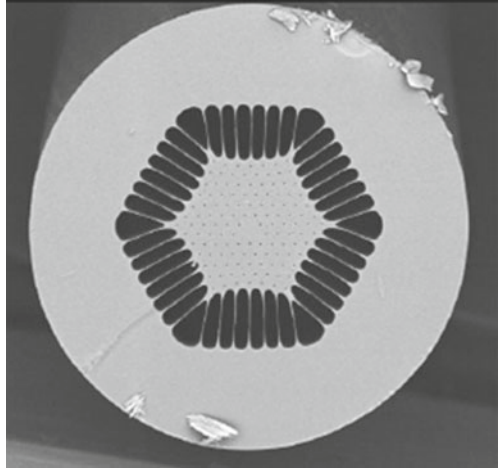


Fig. 2.14 Ytterbium doped fiber laser: experimental arrangement with two diode-stack pump sources. *HR* high reflectivity [48]

the active core, which tend to deteriorate the laser performance [45, 46]. In commercial systems the laser power from a single fiber laser is limited at about 800 W with about 1–2 times diffraction limited beam quality, whereas in laboratory 3 kW have been demonstrated [7, 47–49]. A typical fiber laser system is schematically shown in Fig. 2.14 in which high power diode lasers stacks of total power of 1.8 kW were used for pumping from both ends of the fiber [48]. The output power of 1.36 kW was generated with beam quality of $M^2 = 1.4$. Power scaling to high levels has been done by placing several fibers in parallel and combining their outputs into a single beam delivery optical fiber of about 100 μm diameter. High power fiber lasers up to 10 kW power are commercially available now [50]. The electrical to optical efficiency is more than 30% for Yb-doped fiber laser. Because of the very good beam quality, high efficiency, versatility, robust design, and compact size high power fiber laser is becoming the first choice for laser cutting, welding, rapid manufacturing, micromachining, and other manufacturing applications.

When the laser power is increased by combining the laser output of several fibers placed side by side the beam product parameter increases, i.e., the beam quality reduces. The laser power in the lowest order mode from a single fiber is limited mainly by nonlinear effects and optical damage due to the tight confinement of the laser radiation in the fiber core. These effects can be avoided by reducing the laser power density in the core by increasing its diameter. But the higher diameter core produces multi-mode laser beam defeating the purpose. A new technology, the air-silica microstructured fibers, also called photonic crystal or holy fiber has been recently developed which promises to take fiber laser another notch up in performance and compactness [51, 52]. Such fibers consist of a pure silica core surrounded by a regular array of air holes that leads to exceptional guiding properties which cannot be obtained in conventional step-index fibers, Fig. 2.15 [46, 53]. It has been shown

Fig. 2.15 Scanning electron microscope image of an air-clad ytterbium-doped large-mode-area fiber [46]



that photonic crystal fibers (PCF) can be strictly single mode in large core diameters over a large wavelength range [54]. Limpert et al demonstrated PCF lasers with large-mode-area Yb doped fibers and obtained 320 W output power in single-mode beam quality from a 60 cm-long fiber with a mode field area of $2,000 \mu\text{m}^2$ [55]. In a conventional step-index fiber such a large field area will generate a multimode output. Large core significantly suppresses the deleterious nonlinear effects, which therefore allows for scalability in the performance of a high-peak-power fiber laser and amplifier system. In CW operation laser power as high as 6 kW in a diffraction-limited beam quality has already been demonstrated from a fiber amplifier. R&D to further power scaling maintaining the diffraction limited beam quality exploiting various beam combination techniques is continuing [56]

2.2.7 Ceramic YAG Lasers

Traditionally, the hosts of the solid-state laser gain media are made of either single crystalline materials or glasses. Because of the difficulties in growing large size single crystals with spatially varying high doping concentration to make high efficiency and high brightness solid-state lasers, efforts were directed toward developing ceramic YAG lasers which have several advantages over single crystals such as ease of producing large size gain medium of multi-phase transition materials with arbitrary shapes, size, and spatially varying doping profiles at relatively low production cost [57–59]. Recently, diode pumped, hybrid composite Yb-YAG ceramic lasers of up to 340 W CW output power has been reported [60, 61]. Ceramic gain media could be attractive particularly in high-volume applications and those which need large gain media.

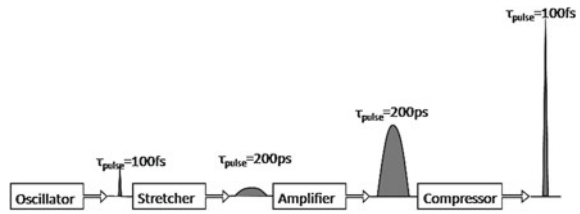
2.2.8 Excimer Lasers

These lasers represent an interesting and important class of molecular gas lasers providing ultraviolet output in 157–351 nm wavelength range. Excimers are molecules which are formed in electronically excited state and whose ground state is either repulsive or very weakly bound. Lasing has been obtained in a large number of homonuclear noble gases (Ar_2^* , Kr_2^* , Xe_2^*) and halogen (F_2^*) and heteronuclear noble gas—halogen (ArF^* , KrF^* , XeCl^* , XeF^* , XeB^* etc.) the most popular excimer lasers in scientific, medical, and manufacturing applications are the ArF^* , KrF^* , XeCl^* and F_2^* lasers operating at 193, 248, 308, and 157 nm respectively. These lasers are operated at multi-atmosphere gas pressures and are excited by pulsed electrical discharge or electron beam. The typical laser pulse duration is 10–50 ns. Excimer lasers with pulse energy up to 1 J, high repetition rate up to 1 kHz and average laser power up to 300 W are commercially available. Excimer lasers are playing an important role as unique tools for micro-structuring by direct photo ablation. They are being used to ablate various metals, ceramics, and organic and biological materials with great precision. Applications include drilling very precise holes in thin plastic films for uses such as in inkjet head, via drilling and microstructuring of microelectronics, solar cells and medical devices; microlithography for making semiconductor chips and thin film deposition by photoablation, etc. Details of the basics of excimer lasers, their state-of-art technology and various industrial and medical applications can be found in [62].

2.2.9 High Average Power Pulsed Lasers

In many material processing applications such as laser drilling, marking, spot welding, surface peening, micromachining and ablation ,etc. high repetition rate, high average power, short duration lasers are preferred. Several types of lasers such as TEA CO_2 laser, free running Nd:YAG pulsed laser, modulated power CW CO_2 and Nd:YAG lasers, Q-switched CO_2 and Nd:YAG lasers, and Excimer lasers producing laser pulses in the ms-ns pulse duration range and average laser powers up to kW level have been developed. Q-switched fiber lasers have also been developed which are becoming popular for applications like marking, drilling, trimming, micromachining, cutting, and scribing of silicon and solar cells, etc. due to their several attractive characteristics mentioned earlier. Several Q-switching schemes have been developed using semiconductor saturable-absorber mirrors, acousto-optic modulator (AOM), and hybrid Q-switching using an AOM and stimulated Brillouin scattering. A brief overview of these schemes can be found in [47]. Today, compact and efficient Q-switched fiber lasers of average power up to 200 W, 150 kW peak power, 40–500 ns pulse duration and 20–400 kHz repetition rate are commercially available. More recently, pulsed fiber lasers of 0.2–20 ms pulse duration, 15 J maximum pulse

Fig. 2.16 Principle of CPA for high-power ultrashort-pulse generation. The pulse-width's manipulation is to overcome damage of optical materials by high-power laser pulses in the amplifier [62]



energy and 150 W average power have also been developed, which are poised to replace the lamp pumped pulsed Nd:YAG lasers.

2.2.10 Ultrafast Lasers

Over the past decade, the high power ultrafast lasers have attracted much attention for scientific, medical and micro-machining applications. Intense development has been witnessed in two ultrafast laser systems namely the pulse Ti-sapphire and fiber lasers, aimed toward enhancing the laser pulse energy and pulse repetition frequency, and reducing the pulse duration for various applications [63–65]. These ultrafast lasers are based on master oscillator and power amplifier (MOPA) employing the chirped pulse amplification (CPA) process [64]. The basic CPA process is to generate an ultrafast laser pulse or a pulse train in a broad gain bandwidth laser oscillator usually by mode-locking, stretch the pulse in time domain by passing through a dispersive device, amplify the stretched pulse in a high gain amplifier, and then compress the amplified laser pulse to a very high peak power pulse. This has been shown schematically in Fig. 2.16. If the laser pulse is not stretched before this enters the high gain amplifier, the laser pulse can get deteriorated and the amplifier active medium can get damaged due to various nonlinear effects at very high optical power densities of the amplifying laser pulse. Stretching the pulse in time domain reduces the peak intensity.

Ti-sapphire laser operates in a very wide spectral (660–1,180 nm) range in both CW and ultrashort pulse modes. Pumping is done by either the green output of Ar^+ ion laser or the second harmonic of Nd:YAG or Nd:YLF laser. As per the present state of the art, Ti-sapphire laser can provide relatively higher pulse energy in shorter duration laser pulse compared to pulse fiber laser. High repetition rate (1–40 kHz), high average power (10–40 W) ultrafast Ti-sapphire lasers with ~ 36 –100 fs pulse duration have been developed for micromachining applications [66, 68]. Figure 2.17 shows schematically a typical Ti-sapphire laser system [63]. As is apparent from Fig. 2.17, Ti-sapphire laser system has a very large number of active and passive optical components, very precisely aligned in free-space. Due to this design complexity and high cost ultrafast Ti-sapphire laser could face steep competition from the fast developing femtosecond fiber lasers, which are robust and relatively less complex as they use optical fibers and fiber coupled devices and are also more

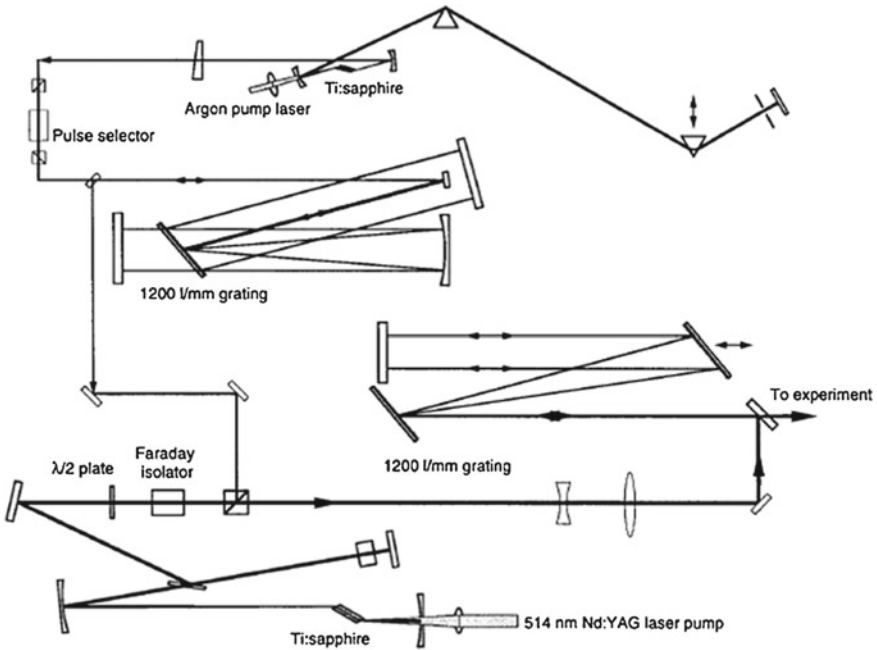


Fig. 2.17 Optical layout of a Ti:sapphire ultrafast CPA laser system consisting of oscillator, grating stretcher, regenerative amplifier, and grating compressor [62]

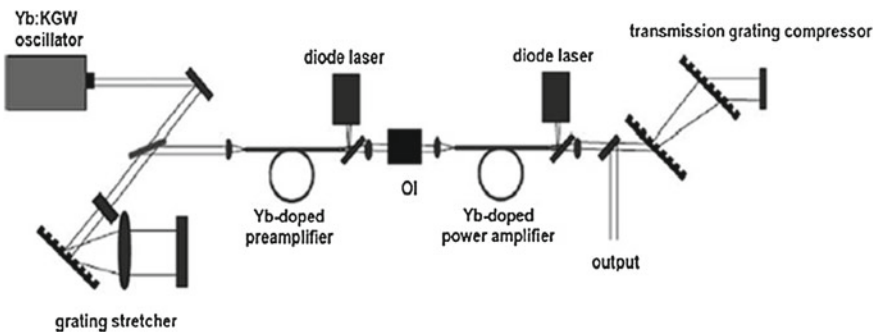
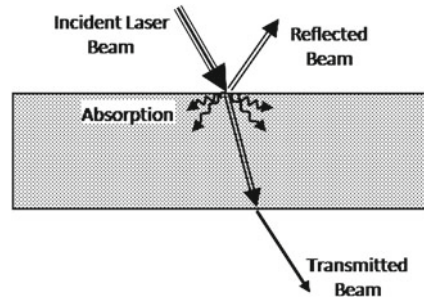


Fig. 2.18 Schematic setup of the high average power fiber CPA system, *OI* optical isolator [65]

economical to own and maintain (cf. Fig. 2.18) [65]. The state-of-the-art femtosecond fiber lasers can deliver as short as 100 fs laser pulses [69] and average power as high as 835 W in trains of 660 fs pulses of $\sim 10 \mu\text{J}$ per pulse energy at 78 MHz repetition rate [70].

It can be concluded that the most remarkable development in high power lasers in recent times has been of fiber lasers which have favorable characteristics such as good beam quality, fiber deliverable, high overall efficiency, high power, CW and a very

Fig. 2.19 Possible phenomena in laser material interaction



wide range of pulse duration, compact and user-friendly design, maintenance-free and economical, to become the first choice for many material processing applications.

2.3 Laser–Material Interaction

When a laser beam is incident on a material, a part of the laser beam is reflected and/or scattered at the surface, the remaining part penetrates in the material, of which a part is absorbed and the rest is transmitted out (cf. Fig. 2.19). The absorbed laser energy usually heats the material raising its temperature (pyrolytic process). Depending upon the absorbed laser power density and the interaction time the laser beam can heat, melt, vaporize, and ablate material, and can also form plasma. In case of laser photon energy, $h\nu$ more than the molecular bond energy, photons can get directly absorbed by molecular bonds and break the bond (photolytic process). These phenomena are schematically depicted in Fig. 2.20. Exploiting these effects by controlling the laser power density and laser interaction time, different laser material processing modalities have been realized, as demonstrated in Chap. 1. The reflection of laser beam at the surface, absorption in materials, and the material removal are greatly influenced by the four attributes of laser beam-wavelength, power, spatial, and temporal characteristics. Allmen and Blatter [71] have presented a detailed description of various laser interaction phenomena with matter. Effects of different laser parameters on laser beam absorption and material removal are briefly described in the following sections.

2.3.1 Basic Absorption Mechanism of Laser Radiation in Materials

Laser radiation of wavelengths ranging from infrared to ultraviolet interacts mainly with electrons (free or bound) in a material, since ions are too heavy to respond significantly to the high frequencies ($\nu > 10^{13}$ Hz) of laser radiation. Therefore, the absorption characteristics of materials are primarily determined by the energy states of electrons bound in semiconductors and insulators or free in metals. Generally,

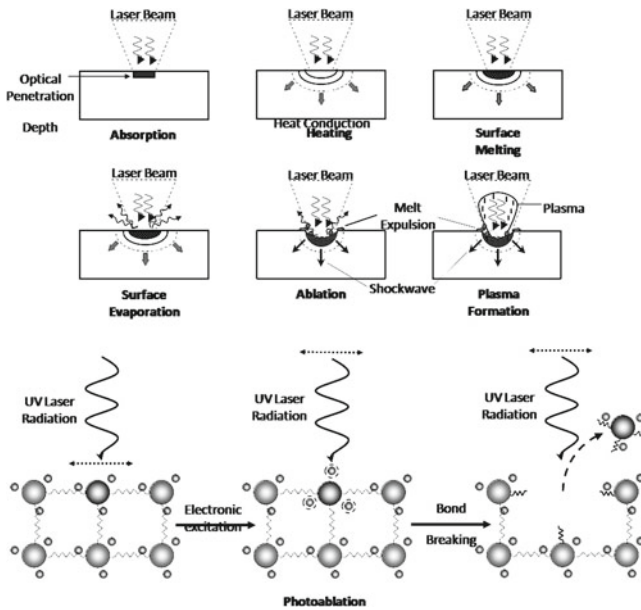


Fig. 2.20 Various effects of laser material interaction (a) absorption (b) heating (c) surface melting (d) surface vaporization (e) ablation (f) plasma formation, and (g) photo-ablation

bound electrons respond weakly to the laser radiation except for radiation having photon energy, $h\nu$ equal or more than the valence and conduction band gap energy. Here, h and ν are the Planks constant and the frequency of laser photon respectively. Free electrons are able to be accelerated and to couple laser energy with the material more efficiently. However, since the electric field of the laser radiation is periodically changing its direction at a high frequency ($> 10^{13}$ Hz), the oscillating electrons re-radiate their kinetic energy unless they undergo frequent collisions with other electrons and ions in the material. Since the free electron density and ion density in metals are very high ($\sim 10^{23}/\text{cm}^3$), oscillating electrons interact with others very frequently and absorb the laser energy in a timescale of 10^{-16} s [72]. This absorption process is known as the inverse Bremsstrahlung process. The energy is shared among the electron subsystem very quickly through electron–electron collisions in a timescale of $t_e \approx 10^{-15} - 10^{-14}$ s. This electron energy is transferred to the lattice through electron-phonon collision process in a timescale of $t_i \approx 1$ ps (10^{-12} s) [73, 74]. As the electron and lattice subsystems come in thermal equilibrium heating takes place in the target material.

In semiconductor materials in which conduction band is empty and there are few free electrons, the laser beam having photon energy, $h\nu$ less than the band gap energy, E_g is not absorbed at low intensities ($< \text{MW}/\text{cm}^2$), but only the beam having photon energy more than the band gap energy ($h\nu \geq E_g$) is absorbed by valence band electrons through interband transition. When the conduction band is partially filled

with electrons, further absorption takes place by intraband excitation of electrons, similar to metals. Dielectric materials such as glass, quartz, ceramics, and many organic polymeric materials, which also do not have free electrons are transparent to visible and near infrared ($\sim 1 \mu\text{m}$) laser wavelength; however, they readily absorb $10.6 \mu\text{m}$ wavelength radiation of CO_2 laser beam through vibrational energy excitation. Organic materials also do not have free electrons, however, when the laser photon energy exceeds the molecular bond excitation energy, such as of $\text{C}=\text{C}$, $\text{C}=\text{O}$, $\text{N}=\text{N}$, etc. they can strongly absorb laser photons. The absorption of photon can either directly break the bonds releasing gaseous products or the excitation energy may dissipate into heat. The photon energy of excimer lasers operating in UV region is comparable to the bond energy of many organic materials. Thus, in addition to the thermal effects, the laser–material interactions may be associated with photochemical processes such as photoablation of the material [75].

2.3.1.1 Absorption Characteristics of Materials: Linear Absorption

The reflectivity at the surface and the attenuation of laser radiation in a material can be determined by the refractive index of the material. The refractive index of an absorbing material is complex and is given by

$$n^* = n + ik \quad (2.2)$$

where n and k are the real part of refractive index and the extinction coefficient respectively. The transparent material has negligible k . The reflectivity at any angle is given by Fresnel law of reflection and at normal incidence this is given by [76]

$$R = \{(n - 1)^2 + k^2\} / \{(n + 1)^2 + k^2\} \quad (2.3)$$

The reflectivity R , absorptivity A and transmittivity T of a material are related as

$$R + A + T = 1 \quad (2.4)$$

For opaque materials such as metals, $T=0$ and the absorptivity, A is given by

$$A = 1 - R = 4n / \{(n + 1)^2 + k^2\} \quad (2.5)$$

The real and imaginary parts of the complex refractive index, n and k , respectively depend on the laser wavelength. The value of k is relatively large compared to that of n for most engineering metallic materials such as iron, aluminum, copper, titanium, and nickel, etc. in the visible and infrared ($0.4 - 10 \mu\text{m}$) wavelength range [76, 77]. Therefore, the reflectivity (Eq. 2.2) is very high for most metals in this wavelength range at room temperature. The variation of reflectivity with wavelength of some common metals is presented in Fig. 2.21. Wavelength of Nd:YAG and CO_2 lasers are also indicated in the figure. The general trend is that the reflectivity increases with increasing wavelength. With the increased temperature of the material as the

electron collision increases the absorptivity also increases. As the melting temperature approaches, absorptivity tends to saturate at a very high value, and becomes almost independent of wavelength, Fig. 2.22 [78]. In the long laser wavelength region ($\geq 10 \mu\text{m}$) the absorptivity can be given by the following relation:

$$A \approx 0.365(\lambda\sigma_0)^{-0.5} \quad (2.6)$$

where, σ_0 is the electrical DC conductivity of the material. Temperature dependence of A can be related to that of σ_0 which decreases with increase in temperature [79]. The part of the laser beam which penetrates into the material is attenuated along the depth due to absorption and the laser intensity follows the Beer–Lambert law [76]

$$I(z) = (1 - R)I_0\exp(-\alpha z) \quad (2.7)$$

where, I_0 is the incident laser intensity, $I(z)$ is the intensity at a depth z , and α is the absorption coefficient. And, the laser power absorbed, $P(z)$ in a unit volume at z is given by

$$P(z) = (1 - R)I_0\alpha\exp(-\alpha z) \quad (2.8)$$

Absorption coefficient, α is related to the extinction coefficient k as

$$\alpha = 4\pi k/\lambda \quad (2.9)$$

The length over which laser radiation is attenuated by an exponential factor is called the attenuation length, l_a and is given by

$$l_a = 1/\alpha = \lambda/4\pi k \quad (2.10)$$

For most metals the absorption coefficients are in the range of $10^5 - 10^7 \text{ cm}^{-1}$ in $0.5 - 10 \mu\text{m}$ wavelength and the attenuation lengths are in the range of a few 10 's nm.

In semiconductors and insulators in which there are few free electrons the extinction coefficient k is negligible for laser wavelength having photon energy less than the band gap energy. At shorter wavelengths ($h\nu \geq E_g$) when electron can undergo valence to conduction band transition, a large number of electron and hole pairs are formed and the extinction coefficient k and absorption coefficient α become significantly large resulting in strong absorption of laser beam.

It can be concluded from the above description that most metals have very high reflectivity and therefore, very little laser energy is absorbed at room temperature. The laser beam is attenuated within a very thin optical skin depth which is in the range of 10 's nm. Absorptivity is higher for shorter wavelengths and this increases with the increase in surface temperature. In addition to the thermal effects, the laser–material interactions may be associated with photochemical processes such as photoablation of the material.

Fig. 2.21 Variation of reflectivity with wavelength for polished surface of several metallic materials. The wavelengths of two important lasers (Nd:YAG and CO₂) are superimposed on the figure [77]

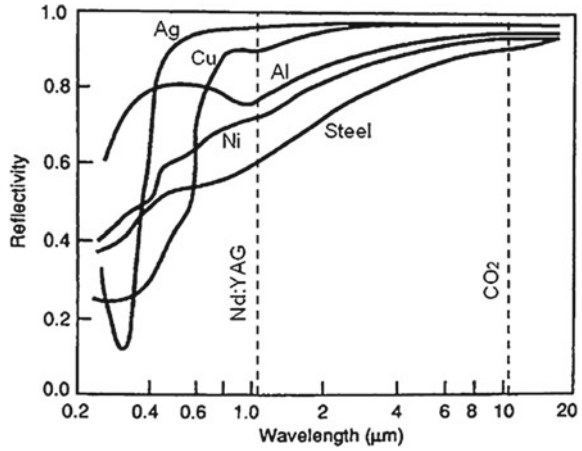
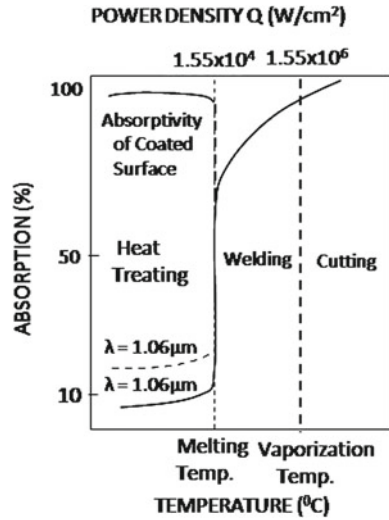


Fig. 2.22 Effect of temperature on laser-light absorptivity [78]



2.3.1.2 Nonlinear Absorption Processes

In the above description of the absorption process the absorptivity is independent of the laser intensity, i.e., the absorption coefficient is linear. In semiconductors, as the incident intensity of laser radiation of photon energy $h\nu \geq E_g$ increases, the electron density in conduction band also increases through interband excitation and with the increase of electron-hole pair density the absorption coefficient increases. In such a case the absorption coefficient becomes dependent on the laser intensity. Similarly, dielectric materials such as glass, quartz have a very wide energy band gap and are transparent to the visible and near infrared laser wavelengths. The linear absorption is negligible and they cannot absorb laser radiation when the laser power densities

are below 100 MW/cm^2 . However, at higher laser power densities ($> 10^{10} \text{ W/cm}^2$) produced by ns and shorter laser pulses, electrons from valence band are excited to conduction band through nonlinear photoionization processes such as multiphoton ionization (MPI) and tunneling photoionization (TPI) [80]. Laser power densities in the range of $10^{10} - 10^{14} \text{ W/cm}^2$ are readily realized when an ultrashort ($< \text{ps} - \text{fs}$) laser pulse is focused on a material.

In MPI, a single electron can absorb several photons simultaneously to gain enough energy to cross the band gap. The number of photons, n absorbed is such that

$$nh\nu > E_g. \quad (2.11)$$

where E_g is the band gap or ionization energy of the material.

On the other hand, at higher values of electric field associated with ultra-high power density produced by the focused ultrafast laser pulses, the valence electrons can be injected into the conduction band via TPI process also.

Whether MPI or TPI will dominate, can be determined by the so-called adiabaticity parameter, γ given by [81, 82]

$$\gamma = \omega(2mE_g)^{1/2}/e\varepsilon \quad (2.12)$$

where, ε and ω are the strength and frequency of the electric field, respectively produced by the focused laser beam, and m and e are the reduced mass and electric charge of electron respectively.

When $\gamma \ll 1$ electric field strength is high and TPI dominates over MPI and when $\gamma \gg 1$, MPI dominates.

Electrons excited into the conduction band by the nonlinear photoionization processes work as seed electrons and they continue to absorb laser energy through the inverse Bremsstrahlung process. If the kinetic energy of the free electrons exceeds a critical value, they can ionize other bound electrons inducing the avalanche ionization process (AIP). In the avalanche process the free-electron density increases exponentially and forms electron-ion plasma. MPI and TPI processes have been found playing a dominant role in producing plasma and material ablation for ultrashort laser pulses in 100fs range and AIP is found to play an important role for relatively longer laser pulses [79, 81]. The threshold intensity for AIP is generally found to scale like $1/\lambda^2$ and decreases with pulse duration [71]. When the electron density in plasma reaches a critical value ($10^{18} / \text{cm}^3$) for laser pulse duration, ($\tau_l > \text{ns}$ and $\sim 10^{21} / \text{cm}^3$ for $\tau_l < \text{ps}$) at which the plasma frequency is equal to the laser radiation frequency the plasma absorbs enough laser energy resonantly that irreversible optical damage and material ablation take place [62]. The threshold laser fluence, $F_{\text{th(fs-ps)}}$ for ablation by ultrashort laser pulses can be estimated using the relation [72, 74],

$$F_{\text{th(fs-ps)}} = \rho L_v / \alpha = \rho L_v \lambda / 4\pi k \quad (2.13)$$

where, ρ and L_v are the density and latent heat of vaporization of the material. Equation 2.12 shows that the threshold fluence for ablation of material with ultrafast laser pulse depends on laser wavelength and the material properties.

2.3.2 Effect of Spatial Characteristic of Laser Beam

The laser spot size, which determines the laser power density at the focal point, is a very important parameter in several laser processing applications such as laser cutting deep penetration welding, marking, drilling and micromachining, and this depends on the spatial characteristic of the laser beam. The spatial characteristic which determines the laser beam quality is expressed by either M^2 or beam product (beam diameter \times half-divergence angle) parameter. These are related as

$$M^2 = (\pi/2\lambda)(\text{beam product parameter})$$

The half-divergence angle of a real beam can be given by [76]

$$\theta_{1/2} = 2M^2\lambda/\pi d_b \quad (2.14)$$

where λ and d_b are the laser wavelength and beam diameter respectively.

When the laser beam is focused on the workpiece with a lens of focal length, f the focal spot diameter, d_f can be estimated by:

$$d_f = 2f\theta_{1/2} = 4M^2\lambda f/\pi d_b \quad (2.15)$$

For the lowest order TEM₀₀ mode laser beam, $M^2 = 1$ and this produces the minimum spot diameter, given by

$$d_{f\min} = 4\lambda f/\pi d_b \approx \lambda F \quad (2.16)$$

where f/d_b has been equated to the F number of lens assuming that the diameters of the lens and the beam are equal. The minimum value of F number of a lens can be nearly 1, which can produce the minimum focal spot diameter,

$$d_{f\min} \approx \lambda \quad (2.17)$$

Therefore, in laser applications such as micromachining where small laser beam size is desired, laser of shorter wavelength like copper vapor laser, higher harmonics of Nd:YAG laser, and excimer lasers with good beam quality are preferred.

2.3.3 Effect of Laser Pulse Duration

Laser material interactions exhibit significant differences when the interaction time changes to very small time durations in the range of electron-lattice thermalization

time (~ 1 ps) or smaller (100's fs). As mentioned in Sect. 3.1.1 when a laser pulse is incident on a material the laser pulse energy is deposited within the attenuation length, l_a near the surface. The conversion of laser energy into heat and its subsequent conduction into material establishes the temperature distribution in the material. The distance over which thermal energy is conducted during the laser pulse can be determined by the thermal diffusion length, given by $l_d = 2(\kappa\tau_l)^{1/2}$, where κ is the thermal diffusivity of the material and τ_l is the laser pulse duration. When the laser pulse duration τ_l is long enough so that $l_d > l_a$, the thermal diffusion is significant and the rise in temperature in the material is governed by this process. Thus, for laser pulse duration from CW to 10's ps, the laser interaction process is basically thermal and the threshold laser fluence for material vaporization/ablation varies as the square root of the laser pulse duration. Similar to the case of ultrafast laser pulse (Eq. 2.12), the threshold laser fluence for ns-ps order laser pulses can be estimated by

$$F_{\text{th(ns-ps)}} = \rho L_v l_d = 2\rho L_v (\kappa\tau_l)^{1/2} \quad (2.18)$$

In the long pulse duration regime collateral thermal effects occur around the processing zone due to the diffusion of heat. When the laser pulse is short ($\tau_l \leq 1$ ps), the electron subsystem is heated up to a very high temperature and electron-ion subsystems tend to thermalize; however, there is not enough time for energy to be transferred to the lattice, i.e., material does not get heated up. At high laser intensities ($10^{10} - 10^{14}$ W/cm²) generated by ultrafast laser pulses, ions get enough energy to break the bonding of the lattice structure and they break off instantly without having time to transfer their energy to their neighboring ions, thus direct solid-vapor transition occurs [73, 74]. For such short duration laser pulses the thermal diffusion depth is limited to a small skin depth ($l_d < l_a$) and therefore, the thermal effects are negligible. When the laser pulse duration is in the range of 10's fs, the electron subsystem gets heated up but heating of ions is negligible during the laser pulse. Depending on the laser intensity, various phenomena occur during and after the laser pulse in ps-ns timescale leading to vaporization and ablation of material. These mechanisms are described in brief in Sect. 3.4. In the ultrashort pulse regime the threshold laser fluence for material ablation is independent of laser pulse duration, Eq. 2.12. Since there is relatively less thermal effect the quality of machining with ultrafast laser pulses is much superior to that of longer duration laser pulses. For comparison the holes drilled in a thin steel foil by ns and fs laser pulses are shown in Fig. 2.23. While the hole drilled by ns laser pulses has significant collateral thermal damage, no such damage is seen in the hole produced by fs laser pulses.

2.3.4 Material Removal Mechanisms

The various effects caused by the laser beam incident on a material viz. heating, melting, vaporization, and plasma formation depend upon the laser power density and the interaction time. At laser power densities up to several MW/cm² the mechanism of material removal is vaporization and melt-expulsion by the recoil pressure

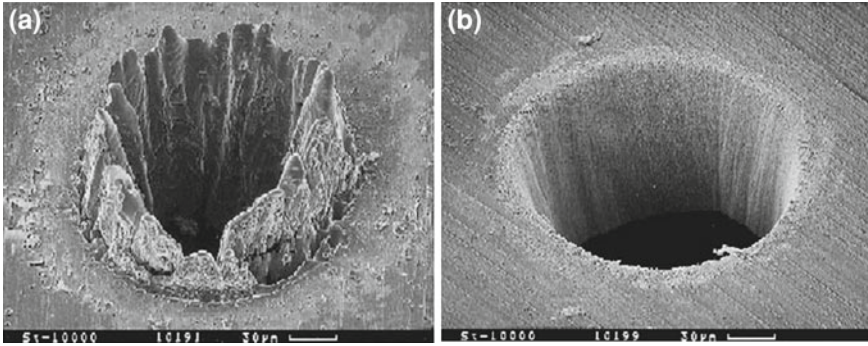


Fig. 2.23 SEM photographs of holes drilled through a 100 μm steel foil with (a) a pulse duration of $t = 3.3 \text{ ns}$ and a fluence of $F = 4.2 \text{ J/cm}^2$ and (b) $t = 200 \text{ fs}$ and $F = 0.5 \text{ J/cm}^2$ using Ti: sapphire laser pulses at 780 nm [67]

of vapor [74]. At relatively lower power densities material removal by the melt-expulsion could dominate over the vaporization process. At higher laser power densities, beyond 1 GW/cm^2 produced by ns and shorter laser pulses, explosive vaporization occurs which is called as laser ablation. The surface temperature is instantaneously heated past its vaporization temperature through linear absorption and/or nonlinear multi-photon absorption, tunneling ionization and AIP, the latter being responsible for absorption of laser radiation especially in transparent materials. The vaporization temperature at the surface is exceeded within a fraction of the laser pulse duration; energy dissipation through vaporization from the surface is slow relative to the laser pulse duration. Before the surface layer can vaporize, the underlying material reaches its vaporization temperature. Temperature and pressure of the underlying material are raised beyond their critical values, causing the surface to explode. The vaporization process is so fast that material may not have time to go through the liquid phase and often melting is not observed around the crater. At laser power densities in the MW/cm^2 – GW/cm^2 range, vaporization, ablation, or both these processes can simultaneously occur. At GW/cm^2 range laser power densities the vapor or the atmosphere near the surface gets ionized and plasma is formed. This makes the situation much more complex, since plasma could absorb the laser radiation. When the plasma expands, dissipates, and rarefies, then laser energy can reach the surface again and another cycle of plasma generation, decoupling, and dissipation happens. This type of phenomenon could make the laser processing like keyhole welding unstable and the process efficiency low [83–87]. The vapor plasma created by laser pulses of GW/cm^2 power density and ns duration range could exert recoil pressure as high as 10^5 MPa over the irradiated surface [88]. Such high recoil pressures can generate very strong shock waves in the material. This effect has been exploited in laser shock peening to induce compressive stress in materials for improving the surface properties [89, 90].

2.3.4.1 Material Removal Mechanism in fs Laser Processing

During laser irradiation by fs duration pulses the electron temperature rises to $10^4 - 10^5$ K while ions and lattice are not heated up much in this timescale. As a result a strong non-equilibrium between the electron and lattice subsystems is established. The chain of events that occurs during the laser pulse and thereafter as the electron-lattice energy transfer takes place, ultimately leads to ablation of material. A number of thermal and non-thermal processes occur on a wide range of spatial length and timescales [72, 91–93]. The physics of laser ablation by ultrafast laser pulses has been studied in detail both experimentally [94–97] and theoretically using numerical models [91, 92, 98, 99]. With the time-resolved experiments, Linde and Tinten [96] have demonstrated that the removal of material from the surface of metals and semiconductors following irradiation with ps and fs laser pulses occurred on a relatively long (ns) timescale. They interpreted the short pulse laser ablation in terms of transient thermal process involving states of matter with unusual thermodynamic, hydrodynamic, and optical properties. Theoretical models on the mechanisms that lead to ablation by intense laser pulses are generally based on heat conduction equations [100], hydrodynamics [101, 102], and molecular dynamics [92, 93, 103, 104]. According to these studies, depending upon materials' properties and laser fluence, the ablation could proceed through one or more of the following processes:

1. Coulomb explosion [98, 105–107]: A very strong electric field of the order of 10^{11} V/m exceeding the binding energy of atoms is generated due to nonlinear photoemission of electrons especially in dielectric materials and this could lead to ablation of several monolayers of material. This has been observed mainly in dielectric materials, and not much in metals.
2. In strongly absorbing solids, depending upon the amount of energy dissipated in different regions of the target and the internal and external conditions such as inertial confinement, ablation could proceed via following different routes as a function of increasing absorbed energy [91]:

Spallation—Near ablation threshold laser fluence, failure of the material following the creation of defects induced by tensile stresses of high temperature electrons caused by fast heating process, Phase explosion—Formation of homogeneous nucleation of gas bubble inside superheated liquid at higher laser intensities leading to decomposition of liquid into a mixture of liquid droplets and gas,

Fragmentation—At still higher energies disintegration of a homogeneous material (supercritical fluid) into clusters under the action of large strain rates

Vaporization—collective ejection of monomers

For a material with linear absorption, the energy density at a given depth varies logarithmically and, therefore, deep into the target where the energy density is just above threshold, ablation proceeds by spallation; and further above with increasing energy density the system undergoes phase explosion, fragmentation, and vaporization [91]. From the above description it is concluded that in case of ultrafast laser pulses material is removed by various non-thermal and thermal processes in an ns timescale after the end of the laser pulse. The resulted quality of laser processing

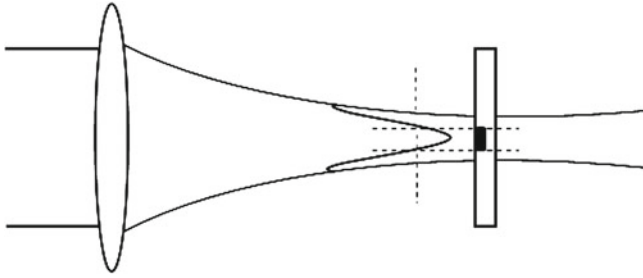


Fig. 2.24 Intensity profile of the laser focus spot can be controlled so that only a small portion near the center is above the breakdown threshold. Using this geometry, sub-focus-spot-size breakdown spots can be obtained [62]

depends on the laser fluence and laser pulse duration. In case of ultrafast laser pulses the depth of material removal increases with the increase of laser fluence at two different rates. At relatively low laser fluences, F_a at which heat conduction is not significant after the end of laser pulse, the ablation depth can be given by

$$Z_a = \alpha^{-1} \ln(F_a / F_{th(fs-ps)}) \tag{2.19}$$

At high laser fluencies, F_a at which heat conduction after the laser pulse is significant and contributes to material removal, the depth of ablation can be given, similar to ps-ns duration laser pulses as

$$Z_a = 2(\kappa \tau)^{1/2} \ln(F_a / F_{th(ps-ns)}) \tag{2.20}$$

Another important characteristic of fs laser processing is that this can not only produce high quality machining, but subwavelength range feature size also. In this time regime, the threshold laser power density for the nonlinear absorption process is more deterministic or precise. The laser ablation occurs only when the laser intensity exceeds a certain threshold value. When a Gaussian laser beam is focused on a material, nonlinear absorption and material ablation occur up to a certain radial distance from the center of focused laser spot where the laser intensity exceeds the threshold (cf. Fig. 2.24). Thus, fs lasers, in principle can produce feature size smaller than the laser wavelength. This along with very small thermal diffusion length, l_d makes the fs laser a tool of unprecedented precision for micromachining applications.

2.3.5 Recent Developments in Laser Material Processing Applications

The research and development in laser material processing applications (LMPA) viz. laser cutting, welding, drilling, marking, scribing, surface hardening, surface alloying

and cladding, surface texturing, shock peening, forming, micromachining, selective laser sintering and rapid manufacturing has been continued unabated since the invention of the first laser in 1960. Experimental and theoretical studies of various laser material processing applications are being widely pursued to establish new processing specialties and predictive theoretical models, develop a better understanding of various processes, and optimize the laser and process parameters to realize the best processing results [6, 7, 21, 29, 108–122]. The induction of recently developed high power lasers such as diode laser, fiber laser, and femtosecond laser has brought about many novel and interesting developments in materials processing applications [1, 3, 7, 21, 29].

2.3.5.1 LMPA with Fiber Lasers

Excellent beam quality of fiber laser has made it feasible to improve the quality of laser processing in general. One of the examples is the striation-free cutting with fiber laser, which became feasible because of the excellent beam quality of fiber laser. Despite various efforts over the last three decades to understand the mechanisms of striation formation and to optimize laser and process parameters for their elimination, neither the formation mechanisms could be fully understood, nor could they be eliminated [123–126], till the recent report of striation-free cutting by Lin et al. [8]. Striations affect the surface roughness, appearances, and geometry precision of laser cut products. Lin et al. [8] demonstrated striation-free laser cutting of mild steel by high power fiber laser using oxygen gas assist. This was achieved at certain critical cutting speed which was determined by the condition that the time of laser/material interaction within the beam spot is approximately equal to the advancement time of the vaporization front through the depth of the workpiece. Figure 2.25 shows the cross sections of laser cut edges with and without striations at two different cutting speeds. This study has established the existence of a steady-state, striation-free cutting parameter window for mild steel, similar windows for other materials of different thicknesses with oxygen and inert gas cutting is still open for realization. Meng et al. [127] have demonstrated the good quality cutting of AISI 316L stainless steel cardiovascular stents with very little dross and heat affected zone, using fiber laser, Fig. 2.26. Because of the very small focal spot size and high laser power density, fiber laser can cut materials with very high speed with minimum kerf width and heat affected zone. Therefore, fiber laser integrated with linear motor-based high speed CNC workstation is poised to compete with die and punch in cutting thin sheets [128].

Good quality welding with high depth to width aspect ratio has been demonstrated in various materials such as steels, Al-alloys, Ti alloys with fiber lasers [9, 10, 129, 130]. Kawahito et al. [9] and Quintino et al. [10] have demonstrated deep penetration welding with narrow weld-width and high melting efficiency in steels with high power fiber lasers at 6–8 kW power. Kawahito et al [9] have also demonstrated welding of 1mm thick metallic glass $Zr_{55}Al_{10}Ni_5Cu_{30}$ at 72 m/min speed at 2.5 kW power maintaining the amorphous nature of the material. Allen and

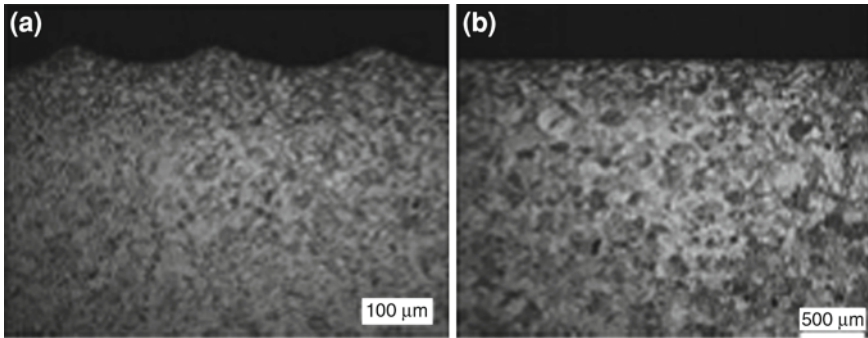


Fig. 2.25 Cross-section views of cuts of mild steel sheet with fiber laser (a) with striation at 30 mm/s cutting speed and (b) without striation at 70 mm/s [8]

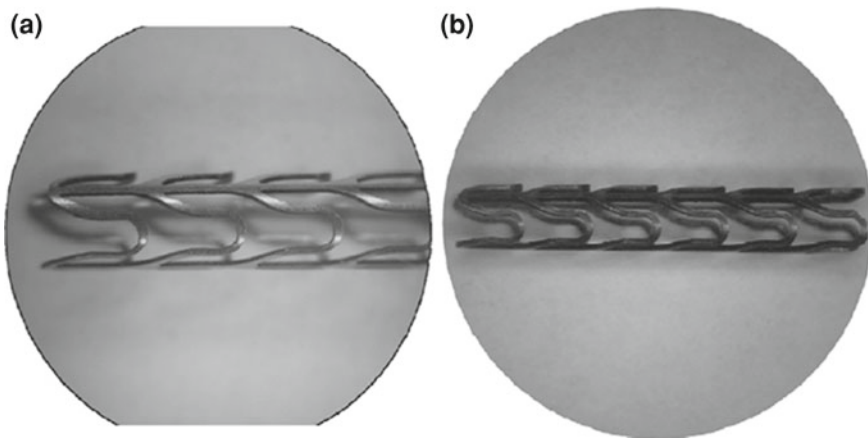


Fig. 2.26 316L stainless steel cardiovascular stent: (a) cut with fiber laser and (b) cut with YAG laser [127]

co-workers have investigated fusion welding of 12.7 mm thick Al-alloy plate by auto-genous fiber laser welding and hybrid laser-MIG welding processes [129]. Katayama and co-workers have reported good quality of 10mm thick Al plates with high power fiber laser at 640 kW/mm^2 laser power density and 10 m/min welding speed [130]. Fiber lasers also have potential applications in the photovoltaic cells processing, such as wafer cutting, marking, vias drilling, edge isolation, surface texturing, and buried contacts with significant cost reduction [131]. Figure 2.27 presents various laser applications for solar cell production. Another interesting development which has attracted attention for micromachining of Si-wafer, IC and photovoltaic devices is the water jet-guided laser processing [132–136]. The CW or pulsed laser beam of Nd:YAG or fiber laser is coupled in a few cm long water jet of about $50 - 100 \mu\text{m}$ diameter which works as a wave-guide. Water jet-guided laser processing has several

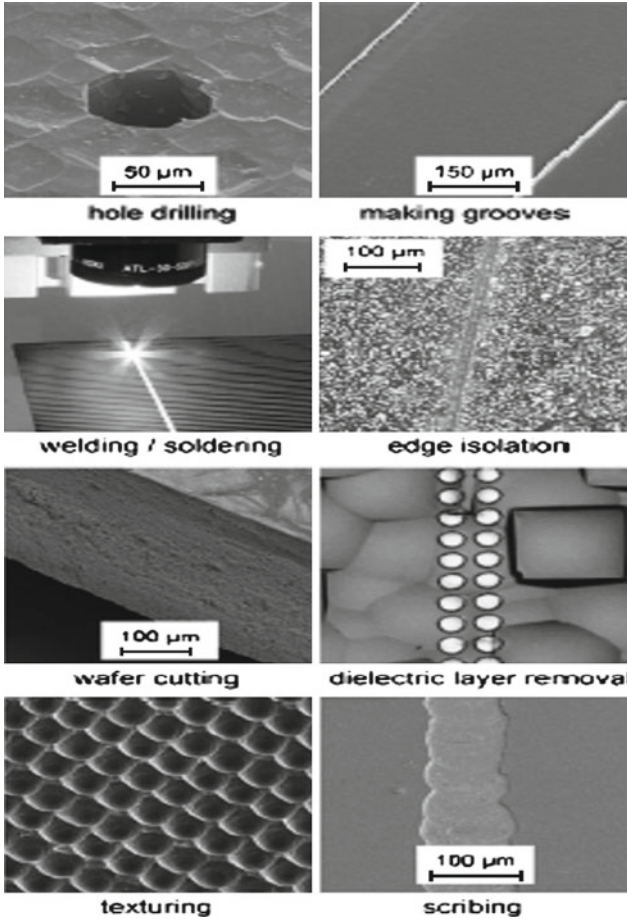


Fig. 2.27 Laser applications for solar-cell production: hole drilling of back-contact solar cells with pulsed fiber laser, SiO₂ removal for groove production, laser welding / soldering of contacts, edge isolation, wafer cutting, removal of dielectric layers for improved contact performance, texturing to increase the absorption of sunlight and therefore to enhance the efficiency of the cell, and scribing of thin-film cells [131]

advantages in comparison to conventional laser cutting, such as the large working distance because of no focal point of beam, narrow and parallel kerf width, clean processing, no contamination, and very small heat affected zone due to cooling by the water jet.

2.3.5.2 LMPA with Non-Conventional Laser Beam

Recently, several studies have been reported on the effect of non-conventional laser beam spatial shapes and temporal modulation of laser power on laser surface hardening, metal forming, re-melting, and laser cutting [137–142]. When the surface modification is carried out with a high power laser beam the resulting microstructure, phases, and mode of solidification depend strongly on the temperature history, i.e., the rise in surface temperature, soaking time, temperature gradient, and cooling rate, and these could be controlled by optimizing the laser and process parameters.

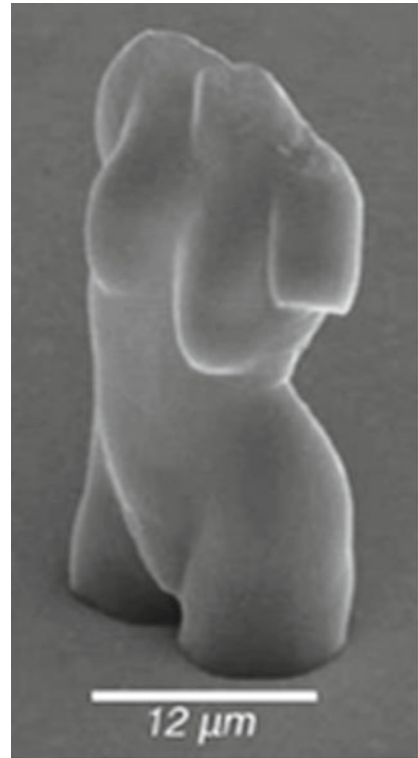
Miokovic et al. [137] presented a detailed characterization of the microstructures, microhardness and retained austenite created in quenched and tempered AISI 4140 steel following a temperature-dependent laser surface hardening treatment with varying number of heating and cooling cycles, heating and cooling rates, and minimum temperature. The depth of hardening zone was found to increase with the increase in the number of cycles and this was attributed to increase in carbon diffusion, carbide dissolution, and austenite and martensite homogenization.

Exploiting the temporal modulations of laser power Parvathavarthini et al. [138] and Kaul et al. [139, 140] developed a novel laser surface treatment process for generating a sensitization resistant microstructure in AISI 316(N) stainless steel weld metal and AISI 304 austenitic stainless steel. Improvement in intergranular corrosion and enhanced immunity against sensitization of laser re-melted surface in AISI 304 austenitic stainless steel was attributed to the formation of duplex microstructure (austenite + ferrite) and higher fraction of low angle grain boundaries [139, 140] and evolution of fine grains near fusion boundary region in modified type 316(L) stainless steel weld metal [138]. Laser irradiation with moving laser beam of different shapes such as circular, diamond, doughnut, rectangular, and triangular produced different isotherm on the laser irradiated surface, rise in temperature, heating and cooling rates, and an optimum laser beam shape can be employed for a particular laser material processing application [141, 142]. Laser surface melting of austenitic stainless steel at high speed carries the risk of centerline solidification cracking due to the formation of tear drop-shaped melt pool [141]. Khare et al. [141] demonstrated that by employing a square-shaped laser beam in place of the circular beam the surface microstructure of laser melted region could be engineered which is less prone to crack. Sheikh and Li [142] presented a review of non-conventional laser geometries that can be utilized to improve many laser material processes including laser transformation hardening, metal forming, surface remelting, and laser cutting.

2.3.5.3 Laser Micro- and NanoMachining

The ever-increasing thrust toward fabrication of ultrasmall features on integrated chips is driving the modern micro- and nanomachining technology. Over the past decade lasers have been exploited in micromachining for fabricating miniaturized components involved in various applications, such as MEMS, microelectronics, telecommunication, optoelectronics, and biomedical devices [3, 74, 143, 144].

Fig. 2.28 SEM image of the micro-model of Venus torso fabricated by TPP of ORMOCER resin by fs laser and UV radiation [163]



Advances in laser technology along with the better understanding of laser–materials interaction have made possible many interesting developments in micro- and nano-manufacturing. This has established the laser micromachining as a viable, attractive, cost-effective and enabling technology.

The minimum feature size that can be produced by laser micromachining depends on the laser parameters, the material properties, and machining technique employed. The ultrafast lasers have allowed the laser micro-machining process of different materials to advance a step further in terms of quality and reduced feature size [3, 6, 8, 67]. As the thermal diffusion length is less than even the optical skin depth for fs laser pulses, the machining is realized with high precision without any mechanical and thermal damages [67]. Three machining techniques namely direct writing, mask projection, and interference techniques are employed using ns- and fs- based lasers for micromachining applications [74]. Material is removed by either laser ablation or laser assisted chemical etching process. A few examples of micromachining with ns-lasers include rapid prototyping of micromechanical devices using Q-switched Nd:YAG laser and excimer lasers [3, 145, 146], dicing and cleaving of Si-wafers [147, 148], processing of polymers with excimer lasers [149], 3D microstructuring with excimer laser [150] processing hard materials, microlithography [3], drilling

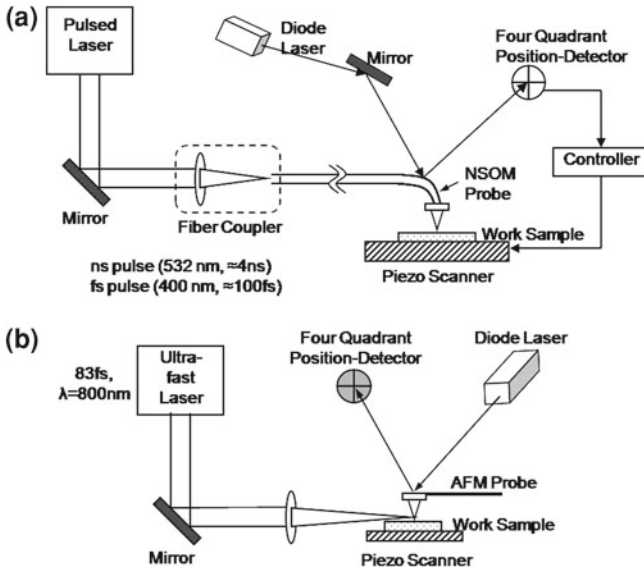


Fig. 2.29 Schematics of experimental setup for ns and fs laser micro- and nano-machining with (a) aperture-based and (b) aperture-less near-field optical scanning microscope (NSOM)

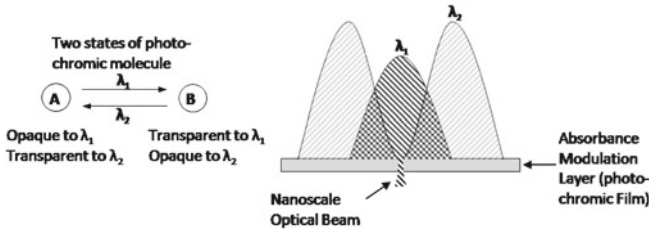


Fig. 2.30 Schematics of (a) two reversible states of photochromic material used for absorption modulation photolithography and (b) illumination configuration for creating sub-wavelength aperture at λ_1 by modulating absorption with λ_2 [166]

micro-holes for ink-jet printers and microfabrications [151, 152], writing fiber Bragg gratings [153, 154], microablation of glass materials [155] and micro-structuring [156, 157]. Exploiting various nonlinear effects induced by ultrafast lasers the scope of micro- and nanomachining has been further advanced in terms of quality improvement and size reduction [158–162]. Several new techniques have been developed to produce feature size smaller than half of the wavelength, limited by diffraction [62, 159, 160]. Hanada et al. [158] developed a new process of laser-induced plasma-assisted ablation (LIPAA) for micromachining of glass materials. Zimmer and Böhme [161] have reported high quality etching of grating of ~ 530 nm period in transparent material by laser-induced backside wet etching (LIBWE) with organic and metallic absorbers using ultrashort pulsed lasers. As the ablation via nonlinear absorption

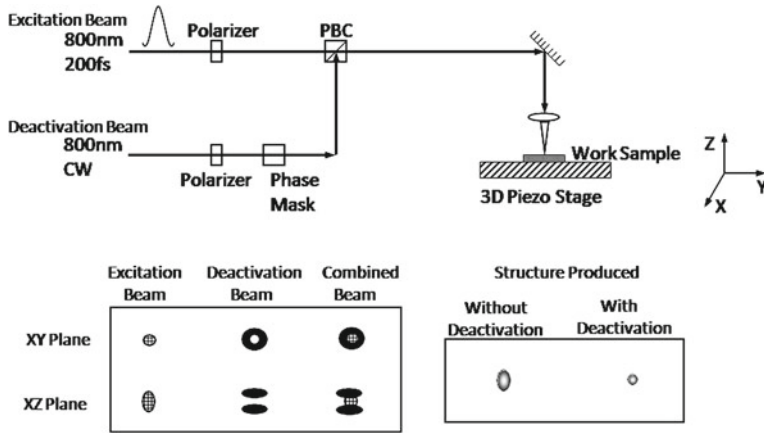


Fig. 2.31 Schematics of (a) experimental setup for RAPID lithography, *CW* continuous wave. *PBC* polarizing beam cube, (b) intensity distribution of the excitation beam and deactivation beam at the focal region [168]

processes, such as two-photon absorption and multiphoton absorption processes (MAP) occur above a certain threshold, the feature size produced by the ultrafast laser pulses can be smaller than the spot size in submicron range [62]. Chen and Nikumb [158] demonstrated laser fabrication at submicron scale on silicon wafer using nonlinear optical switching effect of a photochromic film. Wu et al. [160] have presented an overview of work related to the fabrication of three-dimensional microstructure and photonics devices by means of the two-photon polymerization (TPP) technology. Figure 2.28 shows a micro-Venus torso fabricated by TPP of Ormcer resin irradiated by fs laser pulses and UV-lamp with a resolution down to 100 nm [163]. Haske et al. [164] have demonstrated free-form fabrication by MAP with resolution as fine as 65 nm using 520 nm wavelength light. In a recent development a novel technique for imparting morphological and structural changes in materials at the nanometric level has been demonstrated by coupling ns and fs laser beam to aperture-based and apertureless near-field scanning optical microscopic (NSOM) probes, Fig. 2.29a, b [4, 165]. More recently, combining NSOM and polymer pen lithography a new technique, termed as beam pen lithography has been developed for generating a large number of subdiffraction limits (100 nm) or large features in parallel [162]. Menon and co-workers have recently introduced a method for large area, near-field patterning of photoresist with feature size in the range of 36 nm [166].

More recently, the feature size has been controlled by absorbance modulation of a photochromic film coated on the photoresist which act as a saturable absorber at one wavelength and the saturation intensity is controlled by the intensity at another wavelength (cf. Fig. 2.30). In MAP feature size is controlled in the transverse dimensions, i.e., perpendicular to the direction of the propagation of the laser beam and the axial extent of features, i.e., along the direction of laser beam, which is determined by the depth of focus of the laser beam, is larger by several orders of magnitude. Fourkas

and co-workers have developed a novel technique named as resolution augmentation through photo-induced deactivation (RAPID) photolithography to fabricate features with resolution down to a 40nm size along the laser beam axis [167, 168]. The RAPID set has been schematically shown in Fig. 2.31 [168].

These techniques have demonstrated that the visible light holds great potential for nanoscale lithography; however, several challenges have to be met before this can compete with the current approaches using electron- beam, ion-beam, and synchrotron radiation for manufacturing of integrated circuits. Development of better performing photochromic and photoresist materials, and enhancement of the feature density and throughput will be witnessed in the coming future.

2.4 Conclusions

Recent developments in high power diode laser, diode pumped disc and fiber lasers and ultrafast lasers have facilitated significant improvements in various laser material processing applications in terms of quality, speed, and process flexibility. High power diode lasers, owing to their high overall efficiencies, compact size, and long life are making niches in surface treatment and conduction welding. High power CW as well as pulsed (ms-fs range) fiber lasers hold great potential as a tool of unprecedented precision and power for materials processing applications. A better understanding of laser material interaction process, especially of the phenomena involved in high intensity ultrafast pulse laser processing has been established and this can help in optimizing the laser processing parameters for various applications including micromachining, thin film deposition and surface cleaning, and production of nanoparticles also. With the judicious selection of laser wavelength, laser pulse duration, beam shape, and laser power modulation, significant improvement in the quality of various material processing specialties has been realized. Research in novel laser design, material interaction with ultrashort laser pulses, new materials, and applications is continuing as intensely as ever, opening up previously inconceivable opportunities and applications.

References

1. C. Momma, U. Knoop, S. Nolte, *Prog. Biomed. Res.* **2**, 39–44 (1999)
2. F. Dausinger, in *RIKEN Review No. 50*, Focused on Laser Precision Microfabrication (LPM 2002), pp. 77–82 (Jan 2003)
3. J. Meijer, *J. Mater. Process. Technol.* **149**, 2–17 (2004)
4. D. Hwang, S.G. Ryu, N. Misra, H. Jeon, C.P. Grigoropoulos, *Appl. Phys. A* **96**, 289–306 (2009)
5. D. Ramanathan, P. Molian, *J. Med. Devices*, **4**, 014501-1–014501-3 (2010)
6. D. Bruneel, G. Matras, R. LeHarzic, N. Huot, K. Konig, E. Audouard, *Opt. Lasers Eng.* **48**, 268–271 (2010)

7. F. Bachmann, in *International Conference on Lasers: Applied Technology 2007*, ed. by V. Panchenko, V. S. Golubev, A. Ionin, A. Chumakov. High-Power Lasers and Applications, Proceedings of SPIE, vol. 6735, pp. 1–13 (2007)
8. L. Li, M. Sobih, P.L. Crouse, Ann. CIRP **56**, 193–196 (2007)
9. Y. Kawahito, T. Terajima, H. Kimura, T. Kuroda, K. Nakata, S. Katayama, A. Inoue, Mater. Sci. Eng. B **148**, 105–109 (2008)
10. L. Quintino, A. Costa, R. Miranda, D. Yapp, V. Kumar, C.J. Kong, Mater. Des. **28**, 1231–1237 (2007)
11. G.W. Sutton, Proc. SPIE **4632**, 21 (2002)
12. A.K. Nath, V.S. Golubev, Pramana J. Phys. **51**, 3 (1998)
13. H. Sugawara, K. Kuwabara, S. Takemori, A. Wada, K. Sasaki, in *Technical Digest Conference on Laser, Laser and Electro-Optics*, Anaheim, California, paper TUC 3, (1984), p. 54
14. K.H. Wu, IEEE J. Quantum Electron. **23**, 1981–1985 (1987)
15. K.M. Abramski, A.D. Colley, H.J. Baker, D.R. Hall, Appl. Phys. Lett. **54**, 1833–1837 (1989)
16. E. J. Lerner, Laser Focus World **35**, 506, Sept 1998
17. D. Schoucker, Lasers Eng. **4**, 179 (1995)
18. A.K. Nath, T. Reghu, C.P. Paul, M.O. Ittoop, P. Bhargava, Opt. Laser Technol. **37**, 329–335 (2005)
19. A.D. Colley, H.J. Baker, D.R. Hall, Appl. Phys. Lett. **61**, 136 (1992)
20. S. Yatsiv, A. Gabay, M.A. Brastel, in *Proceedings of CO₂ Lasers and Applications II*, ed. by H. Opower, SPIE, vol. 1276 (The Hague, Netherland, 1990), p. 142
21. L. Li, Opt. Lasers Eng. **34**, 231–253 (2000)
22. D. Lorenzen, M. Schroder, J. Meusel, P. Hennig, H. Konig, M. Philippens, J. Sebastian, R. Hulsewede, Proc. SPIE **6104**, 1–12 (2006)
23. F. Bachmann, Appl. Surf. Sci. **208–209**, 125–136 (2003)
24. B. Liu, Y. Liu, Y. Braiman, Opt. Express **18**, 7361–7368 (2010)
25. E. Kennedy, G. Byrne, D. N. Collins, J. Mater. Process. Technol. **30**, 1855–1860 (2004)
26. F. Lusquiños, J.C. Conde, S. Bonss, A. Riveiro, F. Quintero, R. Comesaña, J. Pou, Appl. Surf. Sci. **254**, 948–954 (2007)
27. B.N. Upadhyaya, S.C. Vishwakarma, A. Choubey, R.K. Jain, S. Ali, D.K. Agrawal, A.K. Nath, Opt. Laser Technol. **40**, 337–342 (2008)
28. R. Weber, B. Neuenschwander, H. P. Weber, Opt. Mater. **11**, 245–254 (1999)
29. H. Hugel, Opt. Lasers Eng. **34**, 213–229 (2000)
30. D. Kracht, R. Wilhelm, M. Frede, K. Dupre, L. Acerman, Opt. Express **13**, 10140–10144 (2005)
31. R. Sundar, K. Ranganathan, A.K. Nath, Opt. Laser Technol. **19**, 1426–1431 (2007)
32. Y.F. Chen, IEEE J. Quantum Electron. **35**, 234–239 (1999)
33. K. Ranganathan, P. Sundar, P. Misra, T. P. S. Nathan, Appl. Opt. **43**, 5855–5859 (2004)
34. S. Lee, S. K. Kim, M. Yun, H. S. Kim, B. H. Cha, H. J. Moon, Appl. Opt. **41**, 1089–1094 (2002)
35. N. Pavel, Y. Hirano, S. Yamamoto, Y. Koyata, T. Tajime, Appl. Opt. **39**, 986–992 (2000)
36. H. Bruesselbach, D.S. Sumida, IEEE J. Sel. Top. Quantum Electron. **11**, 600–603 (2005)
37. K. Ranganathan, P. Misra, A.K. Nath, Appl. Phys. B **86**, 215–217 (2007)
38. M. Sato, S. Naito, N. Iehisa, N. Karube, Proc. SPIE **3889**, 182 (2000)
39. T.S. Rutherford, W.M. Tulloch, E.K. Gustafson, R.L. Byer, in *OAS TOPS 34, Advanced Solid State Lasers*, ed. by H. Injeyan, U. Keller, C. Marshall (2000)
40. P. Shi, D. Li, H. Zhang, Y. Wang, K. Du, Opt. Commun. **229**, 349–354 (2004)
41. A. Giesen, H. Hügel, A. Voss, K. Wittig, U. Brauch, H. Opower, Appl. Phys. B **58**, 365 (1994)
42. C. Stewen, K. Contag, M. Larionov, A. Giesen, H. Hugel, IEEE J. Sel. Top. Quantum Electron. **6**, 650–657 (2000)
43. A. J. Kemp, G. J. Valentine, D. Burns, Prog. Quantum Electron. **28**, 305–344 (2004)
44. A.J. Kemp, G.J. Valentine, D. Burns, Prog. Quantum Electron. **28**, 305–344 (2004)
45. G.P. Agrawal, *Nonlinear Fiber Optics* (Academic, San Diego, 1995)

46. J. Limpert, A. Liem, M. Reich, T. Schreiber, S. Nolte, H. Zellmer, A. Tünnermann, J. Broeng, A. Petersson, C. Jakobsen, *Opt. Express* **12**, 1313–1319 (2004)
47. <http://www.optics.rochester.edu/geveihua/hflaser.pdf>
48. Y. Jeong, J. K. Sahu, D. N. Payne, J. Nilsson, *Opt. Express* **12**, 6088–6092 (2004)
49. V. P. Gapontsev, N. S. Platonov, O. Shkuribin, L. Zaitisev, in *Proceedings of CLEO 2003*, Baltimore, USA postdeadline paper CThPDB9 (2003)
50. <http://www.ipgphotonics.com>.
51. J. Limpert, T. Schreiber, S. Nolte, H. Zellmer, A. Tunnermann, *Opt. Express* **11**, 818–823 (2003)
52. J. Canning, *Opt. Lasers Eng.* **44**, 647–676 (2006)
53. J.C. Knight, T.A. Birks, P.St.J. Russell, D.M. Atkin, *Opt. Lett.* **21**, 1547–1549 (1996)
54. T.A. Birks, J.C. Knight, P.St.J. Russell, *Opt. Lett.* **22**, 961–963 (1997)
55. J. Limpert, O. Schmidt, J. Rothhardt, F. Röser, T. Schreiber, A. Tünnermann, S. Ermeneux, P. Yvernault, F. Salin, *Opt. Express* **14**, 2715–2720 (2006)
56. A. Tunnermann, T. Schreiber, J. Limpert, in *FThJ4, OSA 93rd Annual Meeting, Frontiers in Optics* (San Jose, CA, 2009), 11–15 Oct
57. A. Ikesue, T. Kinoshita, K. Kamata, K. Yoshida, *J. Am. Chem. Soc.* **78**, 1033–1040 (1995)
58. J. Lu, J. Song, M. Prabhu, J. Xu, K. Ueda, H. Yagi, T. Yanagitani, A. Kudryashov, *Jap. J Appl. Phys.* **39**, L1048–L1050 (2000)
59. T. Dascalu, N. Pavel, T. Taira, *Appl. Phys. Lett.* **83**, 4086–4088 (2003)
60. M. Tsumekane, T. Taira, *Opt. Lett.* **31**, 2003–2005 (2006)
61. T. Taira, *C.R. Physique* **8**, 138–152 (2007)
62. X. Liu, D. Du, G. Mourou, *IEEE J. Quantum Electron.* **33**, 1706–1716 (1997)
63. D. Basting, G. Marowsky (eds.), *Excimer Laser Technology* (Springer-Verlag, Berlin Heidelberg, 2005)
64. S. Backus, G. Durfee C., M.M. Murnane, H.C. Kapteyn, *Rev. Sci. Instrum.* **69**, 1207–1223 (1998)
65. J. Limpert, F. Röser, T. Schreiber, I. Manek-Hönninger, F. Salin, A. Tünnermann, *C.R. Physique* **7**, 187–197 (2006)
66. G. Matras, N. Huot, E. Baubeau, E. Audouard, *Opt. Express* **15**, 7527–7539 (2007)
67. C. Momma, S. Nolte, B. N. Chichkov, F.V. Alvensleben, A. Tünnermann, *Appl. Surf. Sci.* **109–110**, 15–19 (1997)
68. I. Matsushima, H. Yashiro, T. Tomie, *Opt. Lett.* **31**, 2066–2068 (2006)
69. K. Kieu, W. H. Renninger, A. Chong, F. W. Wise, *Opt. Lett.* **35**, 593–595 (2009)
70. T. Eidam, S. Hanf, E. Seise, T. V. Andersen, T. Gabler, C. Wirth, T. Schreiber, J. Limpert, A. Tünnermann, *Opt. Lett.* **35**, 94–96 (2010)
71. M. von Allmen and A. Blatter: *Laser-Beam Interactions with Materials: Physical principles and Applications*, 2nd edn Springer-Verlag, Germany, (1995)
72. Y. L. Yao, H. Chen, W. Zhang, *Int. J. Adv. Manuf. Technol.* **26**, 598–608 (2005)
73. M. Satta, D.R. Ermer, M.R. Papantonakis, C. Flamin, F. Richard, R.F. Haglund Jr., A. Mele, *Appl. Surf. Sci.* **154–155**, 172–178 (2000)
74. N.B. Dahotre and S. P. Harinkar, *Laser Fabrication and Machining of Materials*, (Springer + Business Media, LLC, NY, 2008)
75. L. Torrisi, A. Borrielli, D. Margarone, *Nucl. Instrum. Methods Phys. Res. B* **255**, 373–379 (2007)
76. W.M. Steen, J. Mazumder, *Laser Material Processing*, 4th edn. (Springer-Verlag, London 2010)
77. J.F. Ready, *Industrial Applications of Lasers* (Academic, San Diego, 1997)
78. J. Grum, *J. Achiev. Mater. Manuf. Eng.* **24**, 17–25 (2007)
79. H. Hugel, F. Dausinger, *Handbook of the Eurolaser Academy*, vol.2. ed. by D. Schoucker (Chapman & Hall, London, 1998)
80. A.Q. Wu, I.H. Chowdhury, X. Xu, *Phys. Rev. B* **72**, 085128(7) (2005)
81. L.V. Keldysh, *JETF (USSR)* **47**, 1945 (1964)

82. P.G Eliseev, O.N Krokhin, I.N Zavestovskaya, *Appl. Surf. Sci.* **248**, 313–315 (2005)
83. A. Matsunawa, D. Kim J., N. Seto, M. Mizutani, S. Katayama, *J. Laser Appl.* **10**, 247–254 (1998)
84. H. Zhao, R. White D., T. DebRoy, *Int. Mater. Rev.* **44**, 238–266 (1999)
85. G. Li, Y. Cai, Y. Wu, *Opt. Lasers Eng.* **47**, 990–994 (2009)
86. T. Sibillano, A. Ancona, V. Berardi, P.M. Lugara, *Opt. Commun.* **251**, 139–148 (2005)
87. A.K. Nath, D. Hansdah, S. Roy, A. Roy Choudhury, *J. Appl. Phys.* **107**, 123103–123109 (2010)
88. <http://tdhplc.lbl.gov/C-Research/Fundamental.htm>
89. P. Peyre, R. Fabbro, L. Berthe, C. Dubouchet, *J. Laser Appl.* **8**, 135–141 (1996)
90. C.S. Montross, T. Wei, L. Ye, G. Clark, Y.W. Mai, *Int. J. Fatigue* **24**, 1021–1036 (2002)
91. L. J. Lewis, D. Perez, *Appl. Surf. Sci.* **255**, 5101–5106 (2009)
92. N.M. Bulgakova, I.M. Burakov, Y. P. Meshcheryakov, A. Stoian, A. Rosenfeld, I.V. Hertel, *J. Laser Micro/ Nanoeng.* **2**, 76–86 (2007)
93. N. N. Nedialkov, S. E. Imamova, P. A. Atamasov, P. Berger, F. Dausinger, *Appl. Surf. Sci.* **247**, 243–248 (2005)
94. A. Cavalleri, K. Sokolowski-Tinten, J. Bialkowski, M. Schreiner, D. Vonder Linde, *J. Appl. Phys.* **85**, 3301 (1999)
95. S. Tinten K., J. Bialkowski, A. Cavalleri, V. Linde D., A. Oparin, J. Meyer-ter-Vehn, S.I. Ansimov, *Phys. Rev. Lett.* **81**, 224 (1998)
96. D.V. Linde, K.S. Tinten, *Appl. Surf. Sci.* **154–155**, 1–10 (2000)
97. A.V. Rode, E.G. Gamaly, B.L. Davies, B.T. Taylor, J. Dawes, A. Chan, R.M. Lowe, P. Hanford, *J. Appl. Phys.* **92**, 2153–2158 (2002)
98. R. Stoian, D. Ashkenasi, A. Rosenfeld, E.E.B. Campbell, *Phys. Rev. B* **62**, 13167 (2000)
99. A. Russe, C. Rischel, S. Fourmaux, I. Uschmann, S. Sebban, G. Grillon, Ph. Balcou, E. Forster, J.P. Geindre, P. Audebert, J.C. Gauthier, D. Hulin, *Nature* **410**, 65 (2001)
100. N. Chichkov B., C. Momma, S. Nolte, F. Von Alvensleben, A. Tunnermann, *Appl. Phys. A* **63**, 109 (1996)
101. D. Perez, L.J Lewis, *Phys. Rev. Lett.* **89**, 255504 (2002)
102. C. Mancini R., *Mater. Res. Soc. Symp. Proc.* **285**, 63 (1993)
103. L.V. Zhigilei, B.J. Garrison, *Appl. Phys. A* **69**, 575 (1999)
104. P. Lorazo, L.J. Lewis, M. Meunier, *Appl. Surf. Sci.* **168**, 276 (2000)
105. M. Henyk, F. Costache, J. Reif, *Appl. Surf. Sci.* **186**, 381 (2002)
106. R. Stoian, A. Rosenfeld, D. Ashkenasi, I.V. Hertel, N.V. Bulgakova, E.E.B. Campbell, *Phys. Rev. Lett.* **88**, 097603 (2002)
107. F. Costache, J. Reif, *Thin Solid Films* **453–454**, 334 (2004)
108. I. Yadroitsev, L. Thivillon, Ph. Bertrand, I. Smurov, *Appl. Surf. Sci.* **254**, 980–983 (2007)
109. P. Kruth J., G. Levy, F. Klocke, T.H.C. Childs, *Ann. CIRP* **56**, 730–759 (2007)
110. W.M. Steen, *J. Opt. A* **5**, S3–S7 (2003)
111. G.P. Dinda, A.K. Dasgupta, J. Mazumder, *Mater. Sci. Eng. A* **509**, 98–104 (2009)
112. J. Dutta Majumdar, I. Manna, A. Kumar, P. Bhargava, A.K. Nath, *J. Mater. Process. Technol.* **209**, 2237–2243 (2009)
113. M. Masanta, P. Ganesh, R. Kaul, A.K. Nath, A. Roy Choudhury, *Mater. Sci. Eng. A* **508**, 134–140 (2009)
114. C.P. Paul, P. Ganesh, S.K. Mishra, P. Bhargava, J. Negi, A.K. Nath, *Opt. Laser. Technol.* **39**, 800–805 (2007)
115. N. Samant, N.B. Dahotre, *J. Eur. Ceram. Soc.* **29**, 969–993 (2009)
116. B.S. Yilbas, A.F.M. Arif, B.J. Abdul Aleem, *Opt. Laser. Technol.* **42**, 760–768 (2010)
117. R. Komanduri, Z.B. Hou, *Int. J. Mach. Tool Manu.* **44**, 991–1008 (2004)
118. N.S. Bailey, W. Tan, Y.C. Shin, *Surf. Coat. Technol.* **203**, 2003–2012 (2009)
119. S. Nisar, M.A. Sheikh, L. Li, S. Safdar, *Opt. Laser. Technol.* **42**, 1022–1031 (2010)
120. B. Vamsi Krishna, S. Bose, A. Bandyopadhyay, *Acta Biomater.* **3**, 997–1006 (2007)
121. A. Crespo, R. Vilar, *Scr. Mater.* **63**, 140–143 (2010)

122. I. Yadroitsev, A. Gusarov, I. Yadroitsava, I. Smurov, *J. Mater. Process. Technol.* **210**, 1624–1631 (2010)
123. Y. Arata, H. Maruo, I. Miyamoto, S. Takeuchi, *Trans. JWRI*, **8/2**, 15–26 (1979)
124. D. Schuocker, *Appl. Phys. B* **40**, 9–14 (1986)
125. M. Vicaneck, G. Simon, H.M. Urbassek, I. Decker, *J. Phys. D* **20**, 140–145 (1986)
126. N.K. Makashev, *SPIE* **2257**, 2–9 (1993)
127. H. Meng, J. Liao, Y. Zhou, Q. Zhang, *Opt. Laser. Technol.* **41**, 300–302 (2009)
128. Fraunhofer Institute for Laser Technology, Annual Report (2008)
129. C.M. Allen, G. Verhaeghe, P.A. Hilton, C.P. Heason, P.B. Prangnell, *Mater. Sci. Forum* **519–521**, 1139–1144 (2006)
130. S. Katayama, H. Nagayama, M. Mizutani, Y. Kawahito, *J. Light Met. Weld. Construct.* **46**, 34–43 (2008)
131. A. Schoonderbeek, A. Ostendorf, *SPIE* (5 June 2008). doi:[10.1117/2.1200804.1132](https://doi.org/10.1117/2.1200804.1132)
132. B. Richerzhagen, *Ind. Laser User* **28**, 28–30 (2002)
133. B. Richerzhagen, M. Kutsuna, H. Okada, T. Ikeda, http://www.synova.ch/pdf/2002_Lamp.pdf.
134. C.F. Li, D.B. Johnson, R. Kovacevic, *Int. J. Mach. Tool. Manu.* **43**, 925–936 (2003)
135. D. Perrottet, C. Boillat, S. Amorosi, B. Richerzhagen, *Refocus* **6**, 36–37 (2005)
136. A. Porter, Y.A. Louhisalmi, J.A. Karjalainen, S. Fügler, *Int. J. Adv. Manuf. Technol.* **33**, 961–967 (2007)
137. T. Miokovic, V. Schulze, O. Vohringer, D. Lohe, *Acta Mater.* **55**, 589–599 (2007)
138. N. Parvathavarthini, R.K. Dayal, R. Kaul, P. Ganesh, J. Khare, A.K. Nath, S.K. Mishra, I. Samajdar, *Sci. Technol. Weld. Joi.* **13**, 335–343 (2008)
139. R. Kaul, S. Mahajan, V. Kain, P. Ganesh, K. Chandra, I. Samajdar, A.K. Nath, R.C. Prasad, *Corrosion* **64**, 755–763 (2008)
140. R. Kaul, N. Parvathavarthini, P. Ganesh, S.V. Mulki, I. Samajdar, R.K. Dayal, L.M. Kukreja, *Weld. J.* **88**, 233s–242s (2009)
141. J. Khare, R. Kaul, P. Ganesh, H. Kumar, R. Jagdheesh, A.K. Nath, *J. Laser Appl.* **19**, 1–7 (2007)
142. M.A. Sheikh, L. Li, *Proc. I Mech. E Part C: J. Mech. Eng. Sci.* **224**, 1061–1062 (2010)
143. M.J. Jackson, *Micro and Nanomanufacturing* (Springer + Business Media, LLC, NY, 2007)
144. N.J. Vasa, Introduction to Micromachining. In: V.K. Jain (eds) *Laser Micromachining Techniques and their Applications* (Narosa, New Delhi, 2010)
145. S. Dauer, A. Ehlert, S. Buttgenbach, *Sens. Actuators* **76**, 381–385 (1999)
146. T.C. Chen, R.B. Darling, *J. Mater. Process. Technol.* **198**, 248–253 (2008)
147. T. Lizotte, *IEEE Int. Electron. Manuf. Technol. Symp.*, pp. 1–5 (2003)
148. K. Venkatakrishnan, B. Tan, *J. Micromech. Microeng.* **17**, 2505 (2007)
149. T.C. Chang, P.A. Molian, *J. Manuf. Processes* **1**, 1–17 (1999)
150. K.H. Choi, J. Meijer, T. Masuzawa, D.H. Kim, *J. Mater. Process. Technol.* **149**, 561–566 (2004)
151. G. Ricciardi, M. Cantello, F. Mariotti, P. Castelli, P. Giacosa, *Ann. CIRP* **47**, 145–148 (1998)
152. J. Meijer, K. Du, A. Gillner, D. Hoffmann, V.S. Kovalenko, T. Masuzawa, A. Ostendorf, R. Poprawe, W. Schulz, *CIRP Ann.: Manuf. Technol.* **52(2)**, 531–550 (2002)
153. M. Becker, J. Bergmann, S. Brückner, M. Franke, E. Lindner, M.W. Rothhardt, H. Bartelt, *Opt. Express* **16**, 19169–19178 (2008)
154. C.M. Jewart, Q. Wang, J. Canning, D. Grobnic, S.J. Mihailov, K.P. Chen, *Opt. Lett.* **35**, 1443–1445 (2010)
155. M.C. Grower, *Opt. Express* **7**, 56–67 (2000)
156. A.A. Tseng, Y.T. Chen, C.L. CXhao, K.J. Ma, T.P. Chen, *Opt. Laser Eng.* **45**, 975–992 (2007)
157. E.V. Bordatchev, Y. Lai, S.K. Nikumb, *J. Phys.* **59**, 700–703 (2007)
158. V. Hanada, K. Sugioka, V. Gomi, H. Vamaoka, O. Otsuki, I. Miyamoto, K. Midorikawa, *Appl. Phys. A* **79**, 1001–1003 (2004)
159. Q. Chen, S. Nikumb, *Appl. Surf. Sci.* **203**, 411–417 (2004)
160. S. Wu, J. Serbin, M. Gu, *J. Photoch. Photobiol. A: Chem.* **181**, 1–11 (2006)

161. K. Zimmer, R. Böhme, *Laser Chem.* **170632**, 13 (2008)
162. F. Huo et al., *Nat. Nanaotechnol.* **5**, 637–640 (2010)
163. J. Serbin, A. Ovasianikov, B. Chichkov, *Opt. Express* **12**, 5221–5228 (2004)
164. W. Haske et al., *Opt. Express* **15**, 3426–3436 (2007)
165. V.M. Sundaram, A. Soni, R.E. Russo, S.B. Wen, *J Appl. Phys.* **107**, 074305–110 (2010)
166. T.L. Andrew, H.Y. Tsai, R. Menon, *Science* **324**, 917–921 (2009)
167. J.T. Fourkas, *J. Phys. Chem. Lett.* **1**, 1221–1227 (2010)
168. L. Li, R.R. Gattass, E. Gershoren, H. Hwang, J.T. Fourkas, *Science* **324**, 910–913 (2009)

Chapter 3

Laser-Assisted Machining: Current Status and Future Scope

M. Brandt and S. Sun

Abstract Laser-assisted machining (LAM) is a hybrid cutting process in which a laser beam is used to heat and soften the workpiece locally in front of the cutting tool. The temperature rise at the shear zone reduces the yield strength and work hardening of the workpiece, which makes the plastic deformation of difficult-to-machine materials (engineering ceramics, hard metals, and metal matrix composites) easier during machining. Its process benefits include a reduction in the cutting forces/specific cutting energy, longer tool life, better surface integrity, and high productivity. This chapter summarizes the up-to-date progress of LAM of ceramics, metals, and metal matrix composites. It covers the analysis of temperature distribution around the cutting region, material removal mechanisms, tool wear mechanisms, and the improvement in machined surface integrity of various engineering materials by the assistance of laser beam.

3.1 Introduction

Advanced engineering materials, such as nickel- and titanium-based superalloys, hardened steels, ceramics, and metal matrix composites, have been and are still being researched and developed to meet the increasing requirement of higher strength especially in the aerospace industry. However, the high strength and low thermal conductivity of these materials make them hard to machine. During machining, the cutting tool undergoes high pressure due to the high yield strength and high work hardening of the workpiece resulting in generation of large amount of heat as a result

M. Brandt (✉) · S. Sun
School of Aerospace, Mechanical and Manufacturing Engineering RMIT University,
264 Plenty Road, Bundoora, Victoria 3083, Australia
e-mail: milan.brandt@rmit.edu.au

S. Sun
e-mail: shoujin.sun@rmit.edu.au

of plastic deformation of workpiece. Cutting tool fails rapidly with increasing cutting speed, in the form of catastrophic breakage, under high cutting pressure and high cutting temperature depending on the thermomechanical properties of the workpiece material.

3.2 Engineering Materials and Their Machinability

The engineering materials dealt in this chapter are ceramics, superalloys (Ti-6Al-4V and Inconel 718 alloys), hardened steels, and metal matrix composites (MMCs). Their machinability is briefly introduced in this section.

3.2.1 Ceramics

Advanced engineering ceramics are increasingly being used in the automotive, aerospace, military, medical, and other industries due to their high temperature strength, low density, thermal and chemical stability, and good wear resistance. Ceramics are difficult to machine using conventional machining techniques because of their high hardness and brittleness [1]. Machining of ceramics is a high cost process because of a short tool life and low material removal rate and often results in surface cracking and subsurface damage.

3.2.2 Nickel-Based Superalloy: Inconel 718

Inconel 718, a nickel-based superalloy, retains its strength and toughness up to temperatures of around 500°C. Therefore, it is an ideal material for the aerospace industry finding applications in gas turbine components and jet engines [2]. Its high strength is due to the presence of fine uniform metastable γ' and γ'' precipitates, the intermetallic phases $\text{Ni}_3(\text{Al}, \text{Ti})$ and $\text{Ni}_3(\text{Al}, \text{Ti}, \text{Nb})$, distributed throughout the matrix after age hardening. Generally, nickel-based super alloys are hard to machine because of their rapid work hardening during machining, chip segmentation resulting in high cyclical cutting forces and severe tool wear, and their high tendency to form a built-up edge by welding workpiece material to the tool material at high cutting temperature [3]. Adhesive and abrasive wear are the dominant wear mechanisms, flank wear and especially the notching wear are the main tool failure modes in conventional machining of Inconel 718 [4–7].

3.2.3 Titanium and its Alloys

Titanium and its alloys have seen increasing demand in the aerospace industry in recent years due to their superior properties, such as excellent strength-to-weight

ratio, strong corrosion resistance, and ability to retain high strength at high temperature [8, 9]. This demand has resulted in the requirement to increase machining speed and consequently the material removal rate and productivity. During machining of titanium alloys, the cutting tool edge undergoes high pressure and high temperature. The former is due to the high yield strength and small chip-tool contact area and the latter is due to the low thermal conductivity of titanium. Furthermore, titanium is chemically reactive to almost all tool materials at elevated temperature and therefore the tool life is rapidly reduced with increasing cutting speed. Flank wear and rake wear are the main tool failure modes as a result of dissolution-diffusion, adhesion, and attrition mechanisms. The low modulus of elasticity together with the segmented chip formation produces tool vibration and chatter at high cutting speed. These limit the cutting speed and productivity [9].

3.2.4 Hardened Steels

The hardened steel AISI D2, containing high carbon and chromium contents, is widely used for making tools due to its hardenability and strong wear resistance [10]. Because of its high hardness (usually over 60 HRC), it is hard to machine conventionally resulting in short tool life. It can only be machined economically by abrasive processes such as grinding and polishing, which are high cost due to their low productivity.

3.2.5 Metal Matrix Composites

Composites are a combination of two or more materials developed by mixing or bonding in such a way that each maintains its integrity. One part generally acts as a matrix and the other as the reinforcement which may be in the form of particles, whiskers, or fibers. The properties of composites are achieved by the systematic combination of these constituents. In particulate MMCs, the reinforcement is normally ceramic particles (Al_2O_3 , SiC etc), which offer the metal matrix (normally ductile metal, such as aluminum alloys) extra hardness and wear resistance [11]. However, the incorporated ceramic particles make the MMCs hard to machine [12] because of rapid tool wear, which is primarily attributed to the abrasive nature of the hard ceramic particles [13, 14]. Tool wear is accelerated solely due to the abrasive action of the ceramic particulates, and the built-up edge to some extent protects the cutting tool from sliding against the abrasive particulates [15]. The cutting force consists of contributions from the chip formation, plowing, particle fracture, and displacement [16]. The surface roughness is controlled by the particle fracture and pull-out at low feed [12].

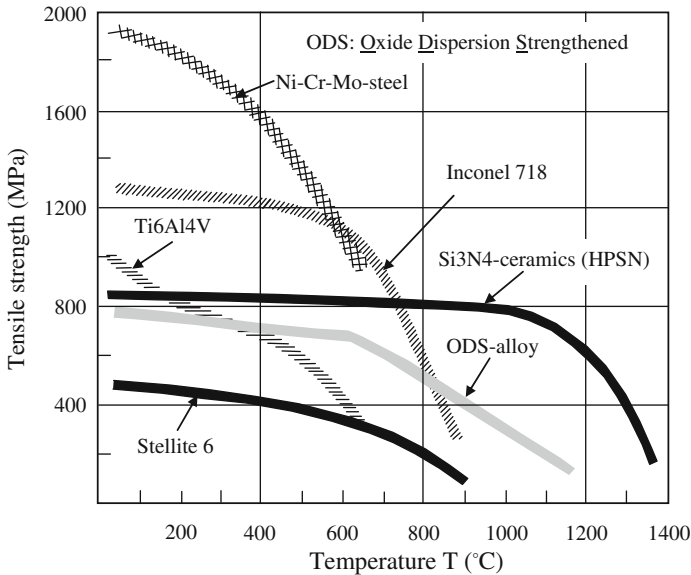


Fig. 3.1 Dependence of strength on temperature for some hard-to-machine materials (reprinted from [21] with official contribution of the National Institute of Standards and Technology; not subject to copyright in the United States)

3.3 Laser-Assisted Machining and its Principles

3.3.1 Traditional Laser-Assisted Machining

Traditional laser-assisted machining (LAM) is a process of hot or thermally enhanced machining which takes the advantage of the reduction of strength of workpiece material with increasing workpiece temperature as shown in Fig. 3.1 [17]. The local heating and softening of workpiece during thermally enhanced machining by an external heat source changes the workpiece (especially ceramic) materials' deformation behavior from brittle to ductile. This enables the difficult-to-machine materials to be machined more easily [18, 19]. Continuous chip can be produced when machining Si_3N_4 ceramic with laser beam assistance when the temperature is above $1,200^\circ\text{C}$ as a result of plastic deformation [20].

In order for it to be applied effectively during the thermally enhanced machining, the heat source should be local, produce rapid heating, and be controllable in size. The external heat sources used to heat the workpiece have been plasma [4, 5, 22–25], laser beam [10, 18, 26–28], gas torch [29–31], induction heating [32–35], furnace preheating [36], electrical current heating [37], or electric arc. A comparison of the advantages and disadvantages of these heat sources can be found in the literature

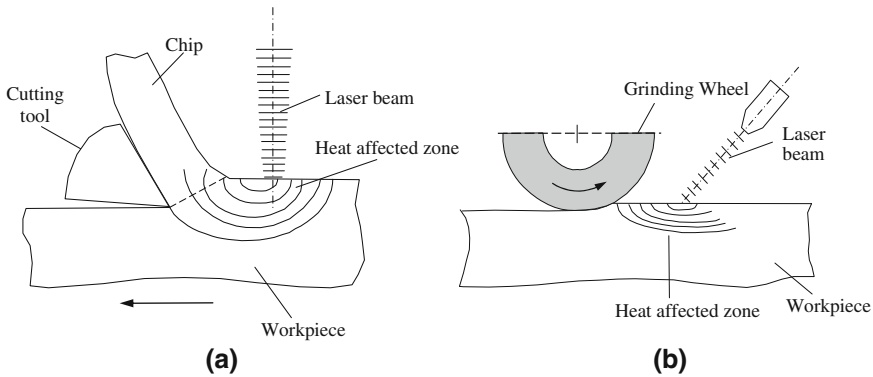


Fig. 3.2 Illustration of laser-assisted machining in (a) turning and (b) grinding operations [18]

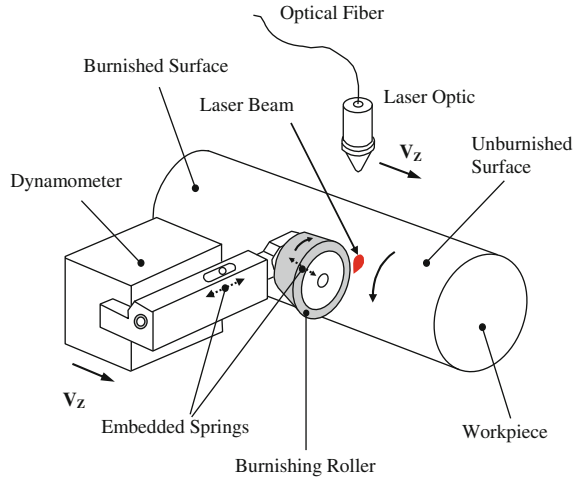
[38, 39]. Inappropriate application of the heat source, however, may introduce undesirable microstructural change in the workpiece after machining [22, 29, 31].

The advantages of laser beam over the other heat sources are its controllable spot size and high power density, which lead to local and rapid heating in the to-be removed layer on the workpiece surface. The laser beam heating the workpiece surface locally in front of the cutting tool creates a large thermal gradient through thickness and only the volume of material to be removed is effectively heated (cf. Fig. 3.2) ensuring a narrow heat affected zone and minimum thermal distortion without affecting the integrity of the machined subsurface and high energy efficiency of the process. It is more complicated to integrate the laser beam with a mill for laser-assisted milling operation compared with a lathe for laser-assisted turning operation due to the rotating tool during milling. Instead of heating the workpiece surface in front of spindle in the feed direction by a laser, Brechera et al. [40] proposed to project the laser spot through the spindle to the chamfer surface in front of the cutting tool. This approach is more efficient and flexible. However, the low absorption rate of the laser energy (especially the CO₂ laser with its long wavelength of 10.6 μm) by the metallic workpiece, such as Inconel 718 [26, 28] and steel [41, 42] needs to be improved by applying an absorption enhancing coating before laser-assisted machining. LAM has been successfully applied for planing of Al₂O₃ [43], burnishing of steels as shown in Fig. 3.3 [44], dressing [45–47], grinding [48], and drilling [49] in which the laser beam locally heats the workpiece in front of the planing, burnishing, and dressing tools or through the center-hollow drill tool.

3.3.2 Non-Traditional Laser-Assisted Machining

Compared to the dependence on temperature rise in traditional LAM, non-traditional LAM improves the machinability due to the removal of part of workpiece material

Fig. 3.3 Illustration of laser-assisted burnishing process [44]



by laser vaporization [50] or ablation [51] and microstructure alteration by laser heating followed by quenching before cutting [52].

Pulsed laser beam drills circumferentially spaced holes on the workpiece surface with a depth less than the depth of cut and a diameter greater than the feed rate and an expected chip width (shown in Fig. 3.4). The predrilled holes ahead of the cutting process reduce the cutting force with the breakage of chips to a manageable size, and reduce tool wear (no crater wear is observed). When machining Ti-6Al-4V alloy, as much as a 50% reduction in the cutting force is obtained. The reduction in cutting energy is much greater than the reduction in volume of material removed due to laser predrilling [50]. The material removal process can be done either in situ during cutting, or before cutting.

Laser pretreatment of SiC/Al composites produces a precipitate-free and recrystallization layer due to the fast air cooling or liquid nitrogen quenching. Under the selected preheat treatment conditions, flank wear is dramatically reduced by up to 50% in association with a reduction in feed force and lower subsurface damage [52]. However, this reduction is not achieved by a simple reduction in the hardness of the matrix materials.

3.4 Temperature Rise on the Workpiece Surface Due to Laser Radiation

During laser-assisted machining, the laser beam energy is absorbed by the workpiece surface and converted to thermal energy which causes the surface temperature of the workpiece to rise. As the deformation behavior of the workpiece material is strongly dependent on its temperature, it is essential to know the temperature distribution from

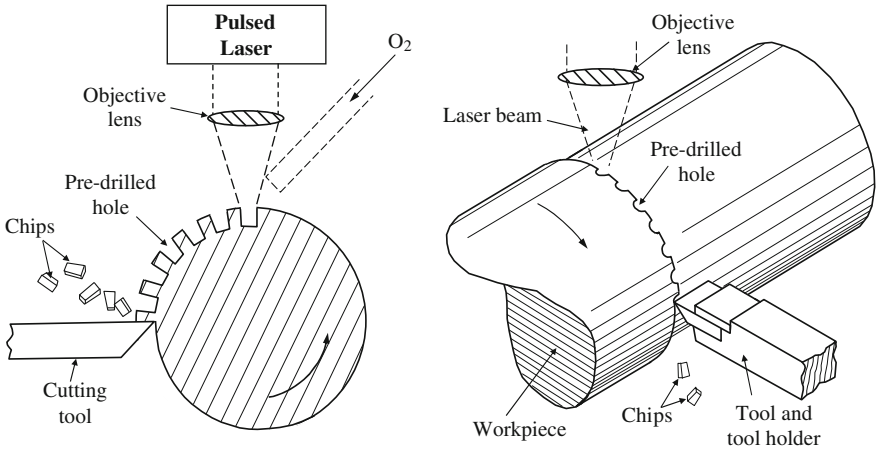


Fig. 3.4 Material removal by laser beam prior to cutting by tool [50]

the surface through the thickness up to the cutting edge and optimize it in accordance with the machining parameters.

The thermal response of the rotating opaque cylindrical workpiece subjected to laser radiation with and without the materials removal process has been analyzed with a transient, three-dimensional heat transfer model by Rozzi et al. [53, 54]. The model geometries are shown in Fig. 3.5.

The governing equation for transient heat transfer in a rotating cylinder in a cylindrical coordinate system is written as:

$$\underbrace{\frac{1}{r} \frac{\partial}{\partial r} \left(kr \frac{\partial T}{\partial r} \right) + \frac{1}{r^2} \frac{\partial}{\partial \phi} \left(k \frac{\partial T}{\partial \phi} \right) + \frac{\partial}{\partial z} \left(k \frac{\partial T}{\partial z} \right)}_{\text{Conduction}} + \underbrace{q'''}_{\text{generation}} = \underbrace{\rho c_p \omega \frac{\partial T}{\partial \phi} + \rho c_p V_z \frac{\partial T}{\partial z}}_{\text{Advection}} + \underbrace{\rho c_p \frac{\partial T}{\partial t}}_{\text{Storage}} \tag{3.1}$$

where, k is the thermal conductivity; ρ is the density; c_p is the specific heat, ω is the workpiece rotation speed, V_z is the feed speed, and q''' is the volumetric heat generation due to the cutting operation, which includes the heat generated due to the friction between the tool's flank face and workpiece and the heat generated due to plastic deformation (q'''_{pl}) at shear zone. Because of a long time delay after cutting for one revolution and its small value, the heat by flank wear has a negligible effect on the workpiece temperature distribution [55]. The heat generated due to the plastic deformation is calculated as:

$$\begin{cases} q'''_{pl} = 0 & \text{without material removal} \\ q'''_{pl} = \frac{0.85(F_c \bar{V}_w - F_{ct} V_{chip})}{(dL_f^2/10)} & \text{with material removal} \end{cases} \tag{3.2}$$

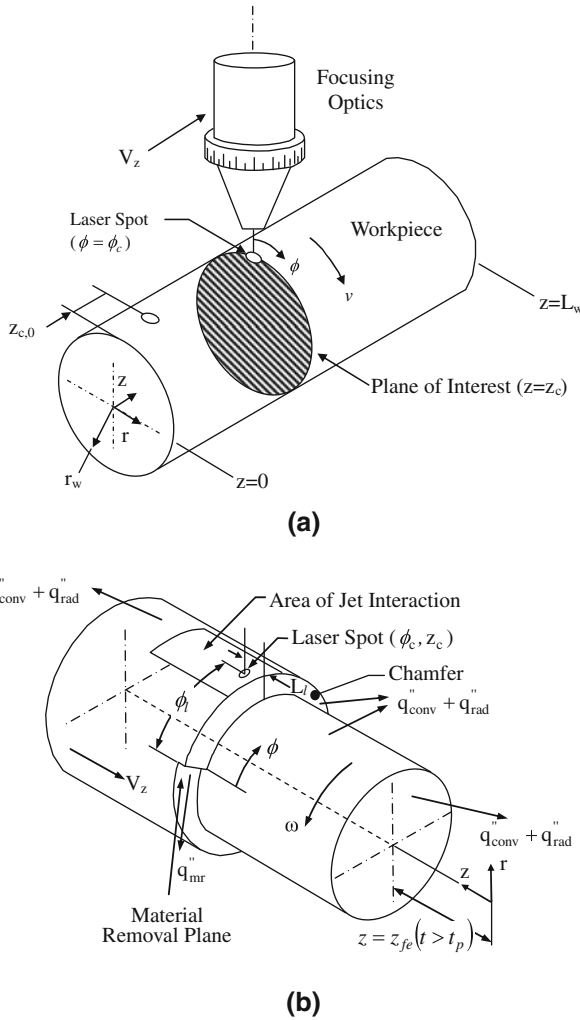


Fig. 3.5 Coordinate systems for the rotating workpiece during (a) laser heating without material removal [53] and (b) laser assisted machining with material removal [54]

where, F_c is the main cutting force, \bar{V}_w is the average workpiece velocity perpendicular to the cutting tool over the depth of cut, F_{ct} is the friction force, V_{chip} is the average chip velocity on the tool rake face, d is the depth of cut, and L_f is the tool feed.

Significant temperature rise as a result of plastic deformation occurs on the unmachined surface just before the material removal plane due to the small volume of primary shear zone. The majority of heat is left in the heated chip [55], and its effect on workpiece surface temperature is also negligible [56]. External heating of the

workpiece leads to high temperatures at the shear zone, which results in a reduction in the shear flow stress of the workpiece. Therefore, heat generation due to plastic deformation in the shear zone during LAM is reduced compared with that produced during conventional machining process [10].

By setting the appropriate boundary conditions (listed in Table 3.1), the temperature fields as a result of laser radiation only (without material removal), laser heating, and cutting (with material removal) can be calculated.

The model analyses were validated by comparing the predicted surface temperature histories with the measured temperature using a pyrometer or an infrared camera over a wide range of operating conditions for laser heating with and without material removal processes as shown in Fig. 3.6 [53, 54], or by comparing the depth of the heat affected zone (HAZ) for some alloys [57, 58].

The validated thermal model reveals the temperature distribution on the surface and through thickness (Figs. 3.7 and 3.8). It shows a large temperature gradient in all three coordinate directions. With the beam incident on the workpiece surface, the temperature gradient exists through the depth of cut and becomes larger with the greater depth of cut at the cutting plane. The unmachined surface with high temperature contacts directly with the cutting tool, which may be detrimental for cutting the materials that are chemically reactive with the cutting tool at high temperature.

Since laser heating increases the temperature of the workpiece before cutting, phase transformations may occur in the heated area. This area is detrimental if it remains in the machined subsurface after cutting for some alloys for which the fatigue life is sensitive to the hardness and microstructure in the subsurface such as the Ti-6Al-4V alloy [22]. Simulation can predict the thickness of the phase transformation layer and determine the appropriate laser power to ensure that the layer associated with the phase transformation can be later removed by machining [57, 58, 60].

Due to the importance of temperature distribution at the cutting zone on the LAM process, a lot of efforts have been made to simulate the temperature distribution due to laser radiation with consideration of material removal process in turning operation on various workpiece materials, such as semi-transparent ceramic [56], mullite [61], Si₃N₄ ceramic [59, 62, 63], Inconel 718 alloy [26], steel [41, 42], compacted graphite iron [64], and Ti-6Al-4V alloy [65, 66]. Thermal modeling has also been performed in laser-assisted milling of Si₃N₄ [67–69], Inconel 718 [69], steel, and Ti-6Al-4V alloy [70]. The thermal model analysis can identify the effect of processing parameters on the temperature distribution at the cutting zone and is able to provide guidelines on parameter selection for optimizing the machining process.

The material removal temperature, T_{mr} , which is defined as the average temperature of the material as it enters the shear deformation zone [71], plays a key role in determining the material removal behavior, tool wear, and surface integrity in the LAM process. It can be empirically expressed as a function of laser and machining parameters by analyzing the thermal model predicted temperature at the cutting zone for different workpiece materials as:

For Inconel 718 alloy with two lasers (CO₂ and Nd:YAG lasers) [26]:

Table 3.1 Boundary conditions for the thermal model analysis

	Without material removal [53]	With material removal [54]
Workpiece surface	$k \frac{\partial T}{\partial r} \Big _{r=r_w} = q''_{l,abs}$ $-q''_{conv} - E(T) + \alpha_{sur} G_{sur}(T_{sur})$ $\text{For } \sqrt{[r_w(\phi - \phi_c)]^2 + (z - z_c)^2} \leq r_l$ $k \frac{\partial T}{\partial r} \Big _{r=r_w} = -q''_{conv} - E(T)$ $+ \alpha_{sur} G_{sur}(T_{sur})$ $\text{For } \sqrt{[r_w(\phi - \phi_c)]^2 + (z - z_c)^2} > r_l$	$k \frac{\partial T}{\partial r} \Big _{r=r_w} = \alpha_l q''_l - q''_{conv} - E(T)$ <p>For $z > z_{ch}(\phi)$ and $f_l(r, z, \phi)$ ≤ 1 on laser spot</p> $k \frac{\partial T}{\partial r} \Big _{r=r_w} = -q''_{conv} - E(T)$ <p>For $z > z_{ch}(\phi)$ and $f_l(r, z, \phi)$ > 1 off laser spot</p> $k \frac{\partial T}{\partial r} \Big _{r=r_w,m} = \alpha_{l,m} q''_l - q''_{conv} - E(T)$ <p>For $z < z_{ch}(\phi)$ and $f_l(r, z, \phi)$ ≤ 1 on laser spot</p> $k \frac{\partial T}{\partial r} \Big _{r=r_w,m} = -q''_{conv} - E(T)$ <p>For $z < z_{ch}(\phi)$ and $f_l(r, z, \phi)$ > 1 off laser spot</p>
Workpiece surface unmachined		
Workpiece surface machined		
Centerline of workpiece	$\frac{\partial T}{\partial r} \Big _{r=0} = 0$	$\frac{\partial T}{\partial r} \Big _{r=0} = 0$

Table 3.1 (Continued)

	Without material removal [53]	With material removal [54]
Interface between machined and unmachined material		$k \frac{\partial T}{\partial z} \Big _{z=z_{ch}(\phi)} = q''_{conv} + E(T)$ For $r_{w,m} \leq r \leq r_w$ and $0 < \phi \leq 2\pi - \phi_{flank}$ $k \frac{\partial T}{\partial z} \Big _{z=z_{ch}(\phi)} = -q''_{flank}$ For $r_{w,m} \leq r \leq r_w$ and $2\pi - \phi_{flank} < \phi \leq 2\pi$
End faces of workpiece	$k \frac{\partial T}{\partial z} \Big _{z=0} = q''_{conv} + E(T) - \alpha_{sur} G_{sur}(T_{sur})$ $k \frac{\partial T}{\partial z} \Big _{z=L_w} = 0$	$k \frac{\partial T}{\partial z} \Big _{z=z_{fe,0}(t \leq t_p)} = q''_{conv} + E(T)$ $k \frac{\partial T}{\partial z} \Big _{z=z_{fe}(t > t_p)} = 0$
Material removal plane		$-\frac{k}{r} \frac{\partial T}{\partial \phi} \Big _{\phi=0} = \rho c_p r \omega (T - T_{ref})$
Circumferential direction	$T(r, \phi, z, t) = T(r, \phi + 2\pi, z, t)$ $\frac{\partial T}{\partial \phi} \Big _{\phi} = \frac{\partial T}{\partial \phi} \Big _{\phi+2\pi}$	$T(r, \phi, z) = T(r, \phi + 2\pi, z)$ $\frac{\partial T}{\partial \phi} \Big _{\phi} = \frac{\partial T}{\partial \phi} \Big _{\phi+2\pi}$
Initiation	$T(r, \phi, z, 0) = T_{\infty} = T_{sur}$	$T(r, \phi, z, 0) = T_{\infty} = T_{sur}$

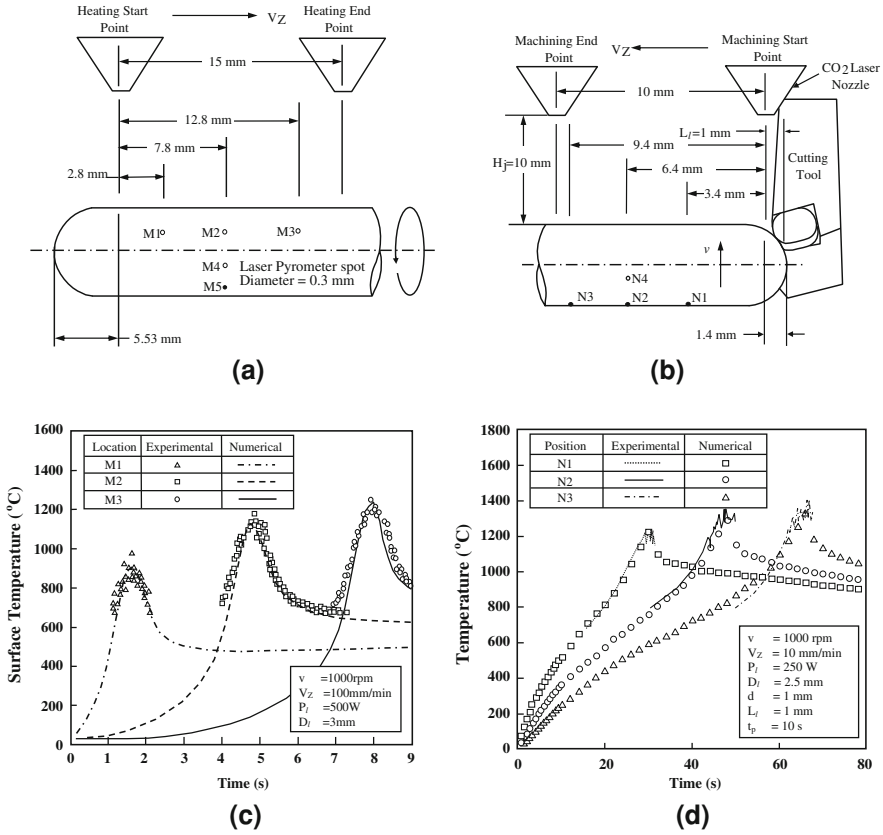


Fig. 3.6 Comparison of the model predicted temperature and measured temperature on the surface of Si_3N_4 cylinders during (c) laser heating without material removal, (d) laser-assisted machining with material removal at the selected locations shown in (a) and (b) [53, 54]

$$T_{mr} = 27890 \frac{P_{\text{CO}_2}^{0.086} P_{\text{YAG}}^{0.031}}{D_w^{0.95} f^{0.32}} \quad (3.3)$$

For Ti-6Al-4V alloy with single laser (CO_2 laser only) [65]:

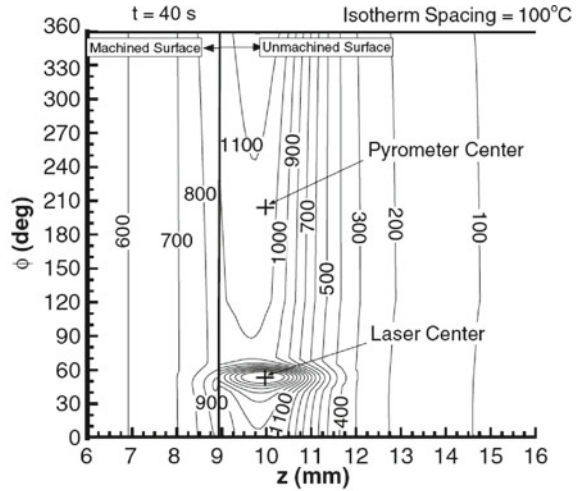
$$T_{mr} = \frac{e^{3.4} \cdot P_{\text{CO}_2}^{0.66}}{f^{0.31} \cdot D_w^{0.34} \cdot V_c^{0.31}} \quad (3.4)$$

For hardened steel with single laser (CO_2 laser only) [41]:

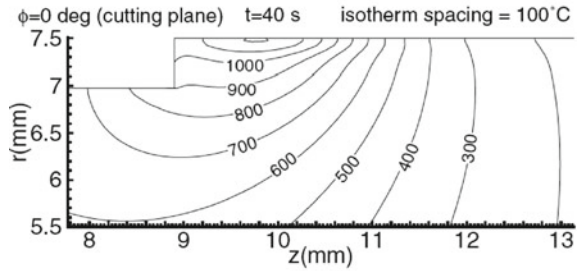
$$T_{mr} = 1.8 \frac{P_{\text{CO}_2}^{0.85}}{V_c^{0.47} \cdot f^{0.47}} \quad (3.5)$$

For hardened steel with two lasers (CO_2 and Nd:YAG lasers) where $P_{\text{CO}_2} = 1,100 \text{ W}$ [41]:

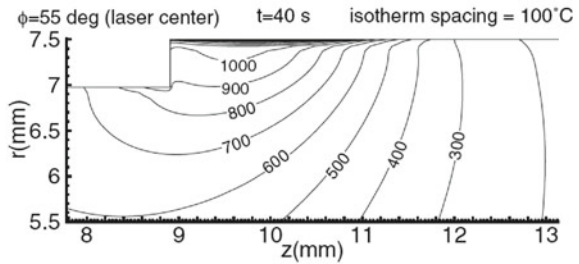
Fig. 3.7 The model predicted temperature distributions (a) on the surface, (b) and (c) through thickness at (b) the cutting plane ($\phi = 0^\circ$) and (c) laser center ($\phi = 55^\circ$) [56]



(a)



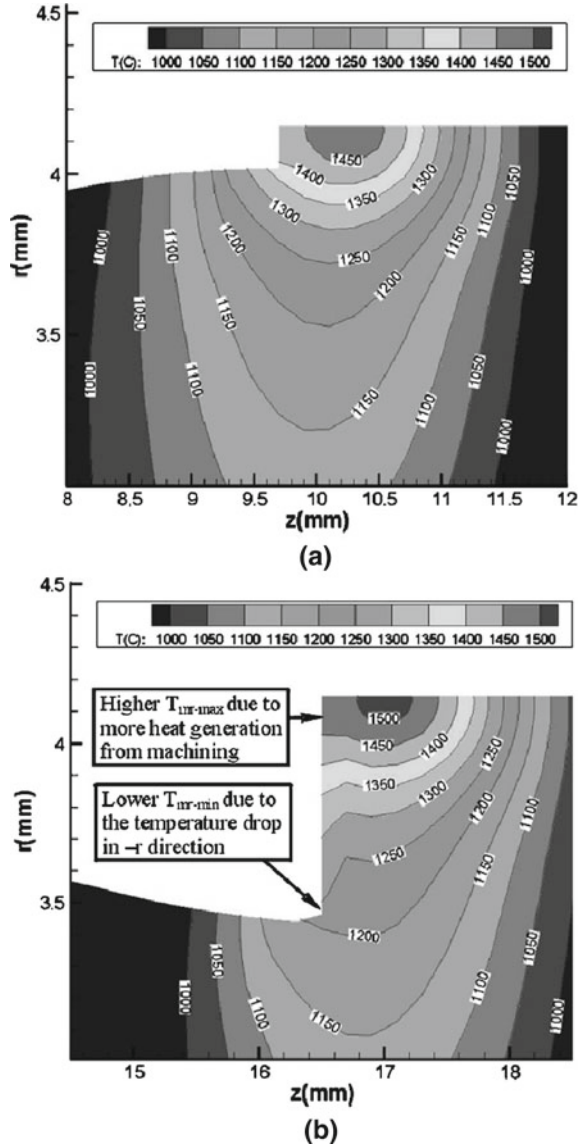
(b)



(c)

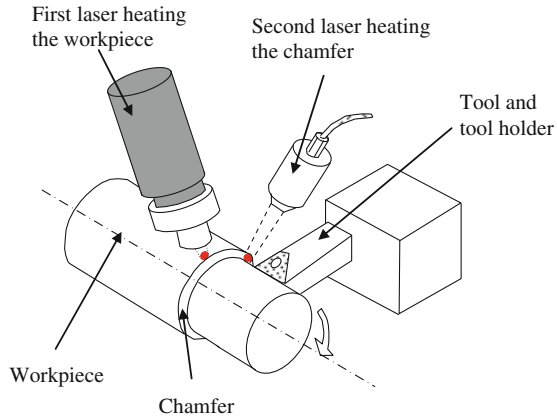
$$T_{mr} = 152.7 \frac{P_{YAG}^{0.29}}{V_c^{0.45} \cdot f^{0.47}} \tag{3.6}$$

Fig. 3.8 Temperature distribution through the thickness at (a) minimum and (b) maximum depths of cut due to complex features of the machined component [59]



where, P_{CO_2} and P_{YAG} are the laser power (W) for the CO₂ laser (as the first laser being incident normal to the workpiece surface axially and at 45° [26] and 55° to tool radially) and Nd:YAG laser (as the second laser being incident 45° to the workpiece surface axially and 10–16° to tool radially), respectively as shown in Fig. 3.9. D_w is the diameter of the workpiece (mm), f is the feed (mm), and V_c is the cutting speed (m/min).

Fig. 3.9 Setup of LAM utilizing CO₂ and Nd:YAG lasers [72]



The empirical expressions for material removal temperature show that the temperature increases with laser power and reduces with increasing cutting speed (except in the case of Inconel 718 where the material removal temperature is independent of cutting speed), diameter of workpiece, and feed rate. Since Nd:YAG laser mainly heats the machined chamfer surface where no absorption enhancing coating is applied and CO₂ laser is mainly incident on the workpiece surface which is precoated with an absorption enhancing coating, the contribution by Nd:YAG laser power to the material removal temperature is smaller than that by CO₂ laser power as expressed in Eq. (3.3).

3.5 Improvement of Machinability by Laser Beam Assistance

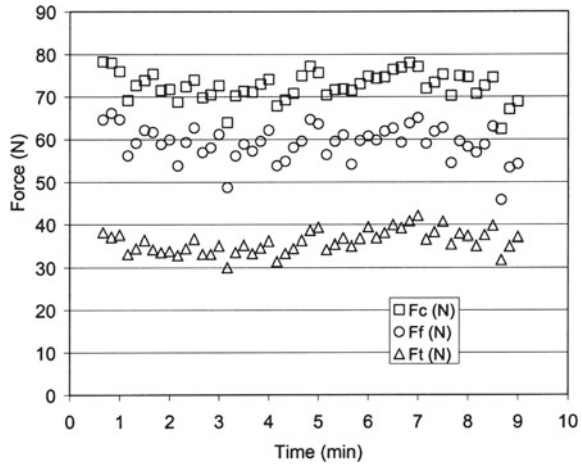
The machinability is defined as a measure of how easily a workpiece material can be machined satisfactorily. It is generally characterized in terms of the cutting force or specific cutting energy, tool life, and machined surface integrity.

3.5.1 Cutting Force and Specific Cutting Energy

The yield strength of workpiece is one of the main components of the cutting force, and can be effectively reduced by increasing the temperature. Therefore, the cutting force is reduced in LAM, which leads to a reduction in the specific cutting energy (u_c) as [73]:

$$u_c = \frac{F_c}{hw} \quad (3.7)$$

Fig. 3.10 Evolution of cutting forces with time during laser-assisted turning of Si_3N_4 ceramic [74]



where, h and w are the depth and width of the cut, respectively and F_c is the main cutting force.

The reduction in cutting force and specific cutting energy indicates the reduction in machine power consumption during LAM. This allows greater feed or depth of cut to be used, therefore leading to higher material removal rate without an increase in the machine power consumption.

The cutting zone stress is found to decrease with increasing material removal temperature and feed but is not significantly dependent on the cutting speed during LAM of Si_3N_4 [74]. All three components of the cutting force are independent of the cutting time (or tool wear) as shown in Fig. 3.10, which is believed to be due to the formation of thin glassy workpiece material on the wear land of the tool flank which acts as a lubricant on the wear land [74].

The cutting forces and specific cutting energy are reported to decrease with increasing laser power or surface temperature when cutting ceramics such as mullite [75], magnesia-partially-stabilized zirconia (PSZ) [76], and Si_3N_4 [71, 77–79] because of the increasing material removal temperature with laser power, but are not significantly affected by the laser-tool lead distance L_l [77].

Not only the cutting forces, but also the ratio of the feed force (F_f) to the main cutting force (F_c) decreases with increasing laser power during LAM of PSZ [76] and mullite [75] (as shown in Fig. 3.11). The F_f/F_c ratio of less than 1 achieved at high laser power proves that quasi-plastic deformation occurs during machining due to the softening of workpiece. Cutting forces or specific cutting energy are also found to be reduced in LAM of titanium alloys [28, 58, 65, 80], Inconel 718 [28, 69, 81–83], Cobalt-based Stellite 6 alloy [17], 6061-T6 aluminum alloy [84], Iron [64, 85], and steels [10, 41, 42, 58, 81, 84, 86, 87] in both turning and milling operations.

The improvement of machinability of Inconel 718 alloy with laser beam preheating is due to the change of deformation mechanisms. The deformation in Inconel

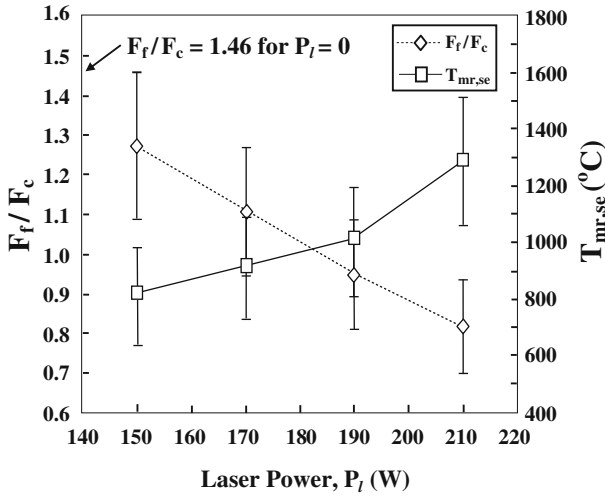
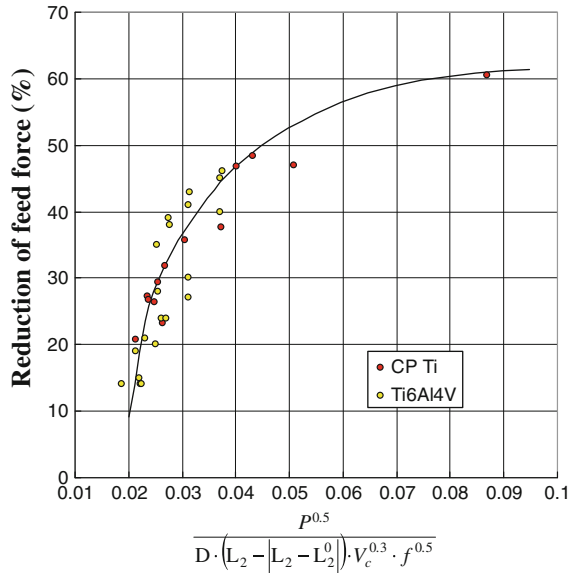


Fig. 3.11 Cutting force ratio and material removal temperature as a function of laser power during LAM of mullite [75]

718 alloy is heterogenous with slip being confined to planar bands with dislocation pairs and non-dislocation structure in the matrix at low temperature. With increasing temperature, the deformation is homogeneously distributed and comprised of a uniform tangle of dislocations once the limit of stability of metastable γ' and γ'' precipitates is reached. This makes the deformation much easier during LAM [88]. Generally, the cutting forces or specific cutting energy decrease with increasing laser power or material removal temperature because of the dependence of yield strength of workpiece on temperature [28, 41, 42, 58, 65, 69, 81, 82, 84] but this reduction is diminished with increasing cutting speed [80, 81]. This is due to the shorter laser beam-workpiece interaction time which leads to lower energy input into a specific area. The cutting force reduction is also affected by the depth of cut, a larger reduction is achieved with a smaller depth of cut [58] because of the higher temperature at the depth of cut. Tool-beam distance is found to be an important factor influencing the reduction of cutting force because it determines the time delay between the laser heating and tool cutting at a given cutting speed. Heat is diffused into the workpiece and surface temperature reduces during this time delay and strongly affects the temperature distribution at the cutting zone. Larger reduction in cutting forces is achieved with shorter tool-beam distance in LAM of hardened steel [81], commercially pure (CP) titanium [80], and high chromium white cast iron [85]. However, if the tool-beam distance is too short, the tool may be damaged by over heating, the chips may fly into the laser beam and become molten and drop onto the machined surface [89]. Therefore, the tool must be kept at a minimum distance from the laser beam, and should be optimized considering the cutting speed and feed rate.

The hybrid machining, combining the enhanced cooling of tool by a reservoir cap which is attached on the tool's rake face with liquid nitrogen (LN_2) passage and laser

Fig. 3.12 Empirical relationship between reduction of feed force and combination of laser and machining parameters during LAM of titanium alloys



beam heating of workpiece results in a reduction in specific cutting energy by 30% compared to 20% during LAM of Ti-6Al-4V alloy over the conventional machining. Higher hardness and strength of tool, lower tool wear rate due to the lower tool-chip interface temperature by the enhanced cooling and workpiece softening contribute to the higher reduction in specific cutting energy in the hybrid machining, while the reduction of specific cutting energy is attributed to the softening of workpiece only in LAM [65].

Germain et al. [86] found that the cutting force does not vary much with increasing laser power during LAM of 42CrMo4 steel because of the high ductility of this workpiece material. Similar results were also found in LAM of CP titanium. Only the feed force decreases significantly with increasing laser power because the laser beam was incident in the feed direction [80].

The authors have summarized the overall effect of laser and machining parameters on the reduction of feed force in LAM of titanium alloys. An empirical relationship between the reduction of feed force and combination of absorbed laser power (P in W), laser spot size (D in mm), feed (f in mm), cutting speed (V in mm/min), tool-beam distance (L_2 in mm), and the optimum tool-beam distance (L_2^0 in mm) was found and is shown in Fig. 3.12. The optimum tool-beam distance, L_2^0 , is defined as the tool-beam distance where the maximum force reduction is achieved, its value was 25 mm for Ti-6Al-4V alloy and 5 mm for CP Ti, and the maximum reduction of cutting force achieved was about 60% [90].

Not only is the magnitude of the cutting forces reduced, but also is the amplitude variation of the forces in LAM of titanium alloy [80] and D2 tool steel [10] as shown in Fig. 3.13. This is attributed to the elimination of chatter generated due to the

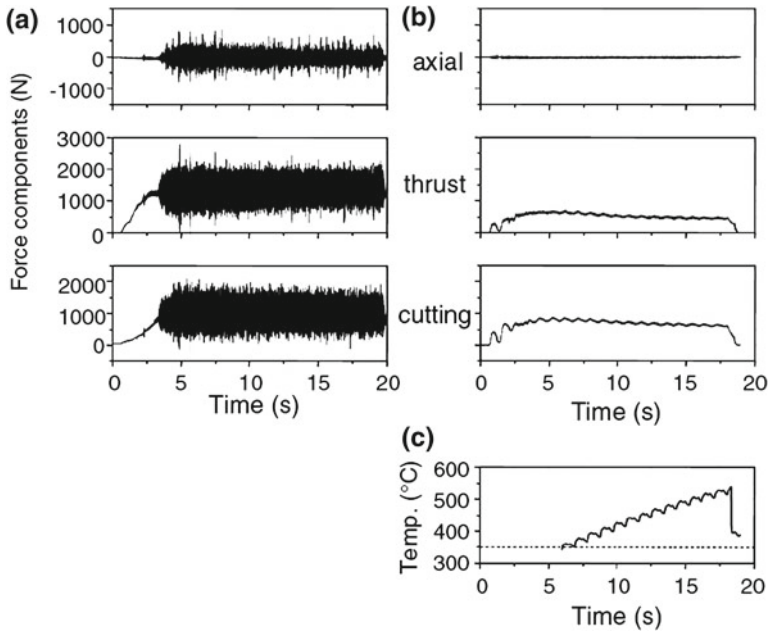


Fig. 3.13 Force components during orthogonal cutting of tool steel (a) conventional machining and (b) LAM and (c) the corresponding surface temperature in LAM (reprinted from [10] with permission. Copyright Elsevier Ltd)

chip segmentation with increasing workpiece temperature [34, 35]. In conventional machining of metals, the cutting forces gradually increase over the cutting time because of the evolution of tool wear. However, the increase in the cutting force with respect to the cutting time during laser-assisted milling of Inconel 718 is much lower than that in conventional milling [69] because of the lower strength, toughness and work hardening of workpiece, and the lower tool wear rate with laser assistance (Fig. 3.14).

The evolution of thrust force with cutting time in LAM of D2 tool steel with rectangular laser beam is strongly dependent on the beam orientation. The thrust force is gradually reduced with cutting time when the laser spot slow axis is perpendicular to the feed direction because of the higher surface temperature due to (1) the longer duration of heating cycle and (2) the laser power distribution along its axis in this configuration [10].

Cutting force is found to increase with laser power during LAM with small depth of cut [58] due to the heating of cutting tool and laser-assisted milling of 3D microgrooving [91] due to larger thermal expansion of tool and greater actual depth of cut with laser heating compared with the conventional micromilling.

In LAM of some hardenable steels, such as the 1090 steel, higher cutting forces are obtained because the phase transformation hardening occurs before the

Fig. 3.14 Variation of cutting force as a function of cutting time during laser-assisted and conventional milling of Inconel 718[69]

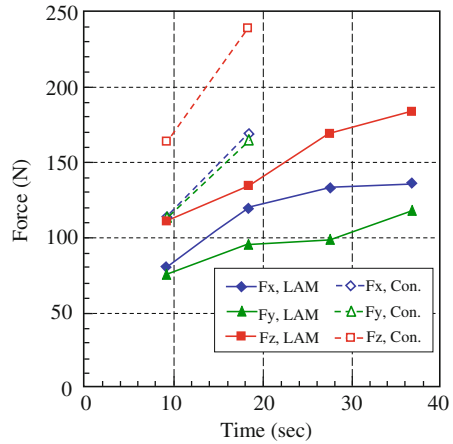
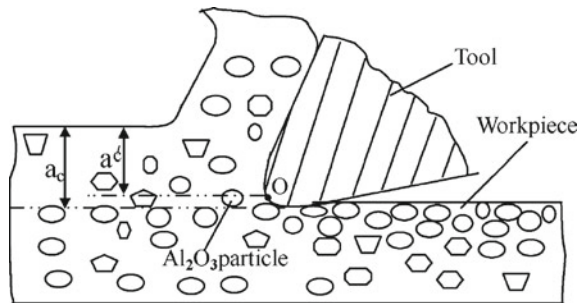


Fig. 3.15 Cutting zone in machining Al_2O_3 p/Al composite materials [93]



laser preheated part of the workpiece enters the cutting zone [92]. Therefore, the tool-beam distance should be optimized in order to prevent the occurrence of phase transformation before cutting.

The metal matrix, which constitutes between 70 and 90% of most MMCs, also plays a significant role in machining MMCs. Softening of the Al matrix by the laser beam prior to the cutting tool leads to the reinforcing particles at the cutting zone (the dividing point O in Fig. 3.15) being much easier pushed into the machined surface. Therefore, the force reduction in the X and Y directions is more significant (by nearly 50%) compared to the force reduction in the Z direction (only 10%) during LAM of Al_2O_3 p/Al composites [93].

3.5.2 Material Removal Mechanisms and Chip Formation

Generally, ceramics are brittle and plastic deformation does not occur during material removal. However, both the strength and brittleness of ceramics, such as Si_3N_4 reduce at high temperature (as shown in Fig. 3.1) due to the softening of a glassy phase at the

Table 3.2 Chip morphology, formation mechanisms, and formation conditions for LAM of Si₃N₄ [77] and mullite [75, 94]

Workpiece material	Morphology	Formation mechanisms	Conditions
Si ₃ N ₄	Fragmented	Brittle fracture	$T_{s, ch} < 1, 151^{\circ}\text{C}$
	Semi-continuous	Local brittle fracture and plastic deformation	$1, 151^{\circ}\text{C} < T_{s, ch} < 1, 305^{\circ}\text{C}$
	Continuous	Plastic deformation	$T_{s, ch} > 1, 329^{\circ}\text{C}$
Mullite	Brittle fracture, Semi-continuous	Brittle fracture and plastic deformation	$F_f/F_c > 1$ $800^{\circ}\text{C} < T_{mr, se} < 1, 000^{\circ}\text{C}$
	Semi-continuous	Plastic deformation	$F_f/F_c < 1$ $1, 000^{\circ}\text{C} < T_{mr, se} < 1, 300^{\circ}\text{C}$
	Continuous	Plastic deformation	$F_f/F_c < 1$ $T_{mr, se} > 1, 300^{\circ}\text{C}$

grain boundaries. When the cutting tool is engaged with the laser heated workpiece, the material is removed mainly due to the combination of brittle fracture and plastic deformation [43, 74–76, 78]. The material removed during LAM of Si₃N₄ is by the following mechanisms [74, 78]:

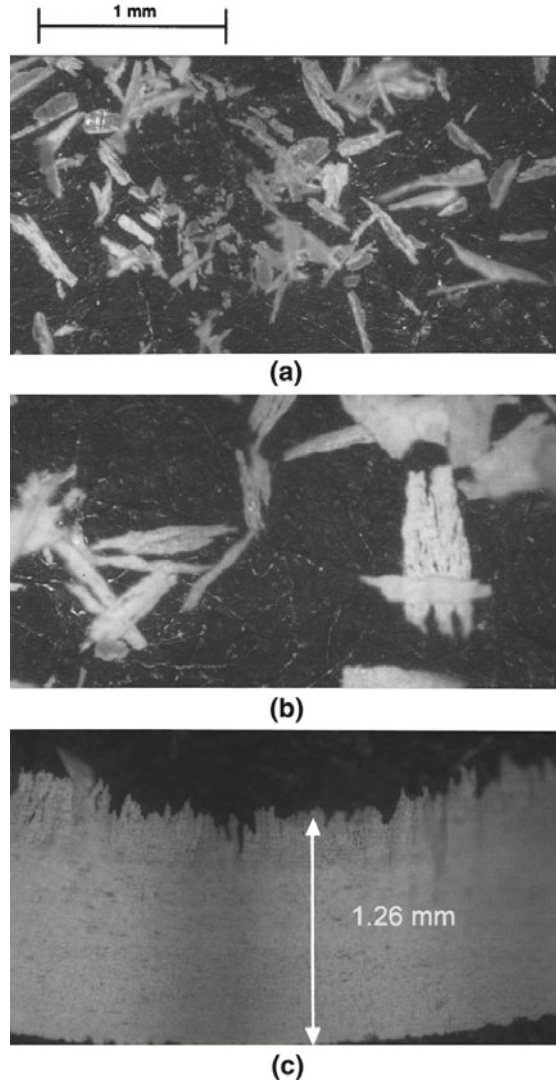
1. Plastic deformation in the shear zone which is characterized by the viscous flow of a glassy grain boundary phase material and reorientation of the $\beta - \text{Si}_3\text{N}_4$ grains.
2. Segmentation of chips due to the initiation, coalescence, and propagation of intergranular microcracks.

Flow and redistribution of the intergranular glassy phase is also found to hold the Al₂O₃ grains and maintain plastic deformation when the temperature is above 850°C (glassy transition temperature) during LAM of Al₂O₃ ceramic [43].

There are 3 types of chip formed during LAM of Si₃N₄ and mullite as shown in Fig. 3.16. It is found that the average, near-chamfer surface temperature ($T_{s, ch}$) [77] or average material removal temperature ($T_{mr, se}$), and ratio of feed force to the main cutting force (F_f/F_c) [75] play a key role in chip formation for Si₃N₄ and mullite as listed in Table 3.2.

Despite the fact that the ratio of F_f/F_c is well below 1, there is no continuous and semi-continuous chip formed during LAM of PSZ. The fragmented chip formation could be due to the coalescence and propagation of the thermally induced crack in the laser heated layer. However, plastic deformation occurs during the fragmented chip formation in addition to brittle fracture [76]. The plastic deformation is observed as a result of high temperature dislocation motion and dynamic recrystallization that leads to a smaller grain size and preferred grain orientation in the machined surface produced by LAM [76, 95].

Fig. 3.16 Morphology of chips formed during LAM of Si_3N_4 at different temperatures [77] (a) Fragmented chip, $T_{s, ch} < 1$, 151°C (b) Semi-continuous chip, $1, 151^\circ\text{C} < T_{s, ch} < 1$, 305°C (c) Continuous chip, $T_{s, ch} > 1$, 329°C



During cutting of metals, severe plastic deformation occurs at the primary shear zone and leads to the formation of continuous chips, in which shear is continuous across the chip length. Segmented or saw-tooth chips are produced when conventional machining of titanium alloys [96, 97], Inconel 718 [3, 98], and hardened steels [99, 100] at high cutting speeds. The critical cutting speed for the onset of chip segmentation is different for each of these workpiece materials.

During the segmented chip formation, heavy deformation and microcracks are found only in a very narrow shear band, while negligible deformation occurs between the adjacent bands as shown in Fig. 3.17. The high strain rate deformation in the

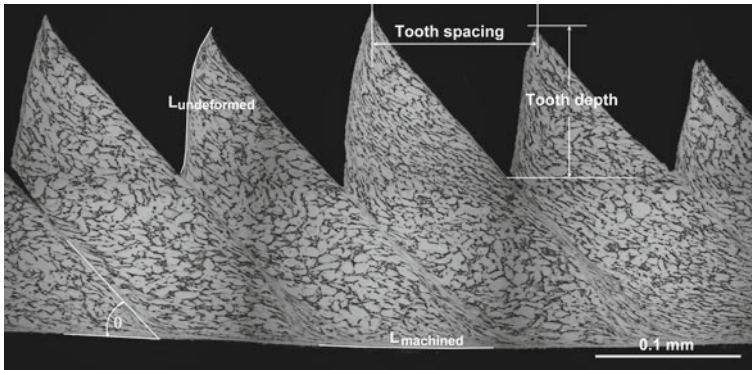


Fig. 3.17 Cross-section and characterization of a typical segmented chip obtained by turning of Ti-6Al-4V alloy [104]

shear band may result in phase transformation [96, 101] and ultrafine, equiaxed grain structure. The segmented chip formation results in severe crater wear, decrease in tool life, and high cyclical cutting forces [9, 102]. High cyclical forces associated with chip segmentation are one of the primary cause of chatter when the vibration frequency due to chip segmentation coincides with the natural frequency of the machine system [34], rough surface finish is the result of chatter. Therefore, elimination of the segmented chip formation at high cutting speed is desirable for improving metal machinability.

It has been reported that increase in workpiece temperature results in a dramatic reduction in the amplitude of acceleration of vibration and chatter due to the reduction of instability of chip formation and an increase in plasticity of the workpiece [34, 103].

The segmented chip produced by conventional machining is changed to a continuous chip with laser heating during machining D2 tool steel at the same cutting conditions. This leads to a smaller variation in the magnitude of cutting forces and a more stable cutting process. The change in chip morphology with laser preheating is due to the change of the material's failure mode from being predominantly a fracture at low temperature to plastic deformation at high temperature [10]. Lesourd et al. [105] also observed that the segmented chip gradually changes to continuous chip with increasing laser power during laser-assisted milling of Ti-6Al-4V alloy. However, Shi et al. [88] and Attia et al. [83] reported that the tendency to form a segmented chip and strain in the primary shear zone are higher during LAM of Inconel 718 alloy compared with those in conventional machining because of a reduction in the strength of workpiece as a result of thermal softening.

The authors have conducted a systematic study on the effect of a Nd:YAG laser beam on the chip formation during turning of Ti-6Al-4V alloy, in which the laser beam was incident on the chamfer surface at 40° with the axis of workpiece and feed was set at 0.214 mm. The comparison of cross-sections of chip made by conventional machining and LAM at incident laser power of 1,900 W under different cutting speeds

is shown in Fig. 3.18 with the geometry measurement results in Fig. 3.19. The geometry of the segmented chip is characterized by the tooth depth, tooth spacing, and geometry ratio, which is defined as the ratio of undeformed surface length ($L_{\text{undeformed}}$) to the machined surface length (L_{machined}) as [104]:

$$r = \frac{L_{\text{undeformed}}}{L_{\text{machined}}} \quad (3.8)$$

The tooth depth, tooth spacing, $L_{\text{undeformed}}$ and L_{machined} are the averages of measured values from the cross-section of the segmented chip as shown in Fig. 3.17.

It can be seen that the laser heating produces two types of segmented chips: one at low and the second at high cutting speeds. The segmented chip produced by LAM at low cutting speed is sharper, the tooth depth and spacing are larger than those produced by conventional machining and the geometry ratio is larger than 1. The segmented chip produced by LAM at high cutting speed is similar to that produced by conventional machining with geometry ratio less than 1. Continuous chip transition occurs at a speed (90 m/min) between these two types of segmented chips when the geometry ratio equals 1. This speed is much higher than the critical cutting speed for the onset of chip segmentation during conventional cutting, and increases with increasing laser power [104].

3.5.3 Proposition of a Physical Model for Chip Segmentation

Several models have been developed to explain the segmented chip formation mechanism. Adiabatic shear model suggests that chip segmentation is the result of the thermoplastic shear instability when the thermal softening predominates over strain hardening due to the low thermal conductivity of the workpiece [96, 97], but Shaw et al. [106] believed that fracture at the shear plane by growth of periodic microcracks is the basis of chip segmentation.

The authors found that the two existing models on the chip segmentation cannot satisfactorily explain the transition in chip morphologies with respect to the cutting speed during LAM. A new physical model is proposed to explain the formation of segmented chip during high strain rate deformation associated with high speed machining. It is believed that the chip segmentation is the result of suppression of the continuous shear at the primary shear plane due to the rapid increase in yield strength with respect to strain rate (cutting speed).

In this model, the material can be removed during machining either by continuous shear at the primary shear plane which leads to the continuous chip formation as shown in Fig. 3.20a or by crack initiation and propagation along the cutting direction which leads to the segmented chip formation as shown in Fig. 3.20b. The thrust force pushes the chip due to advancing of the cutting tool with a positive rake angle. To remove the chip during orthogonal cutting the thrust force is given by:

For continuous chip formation [107]:

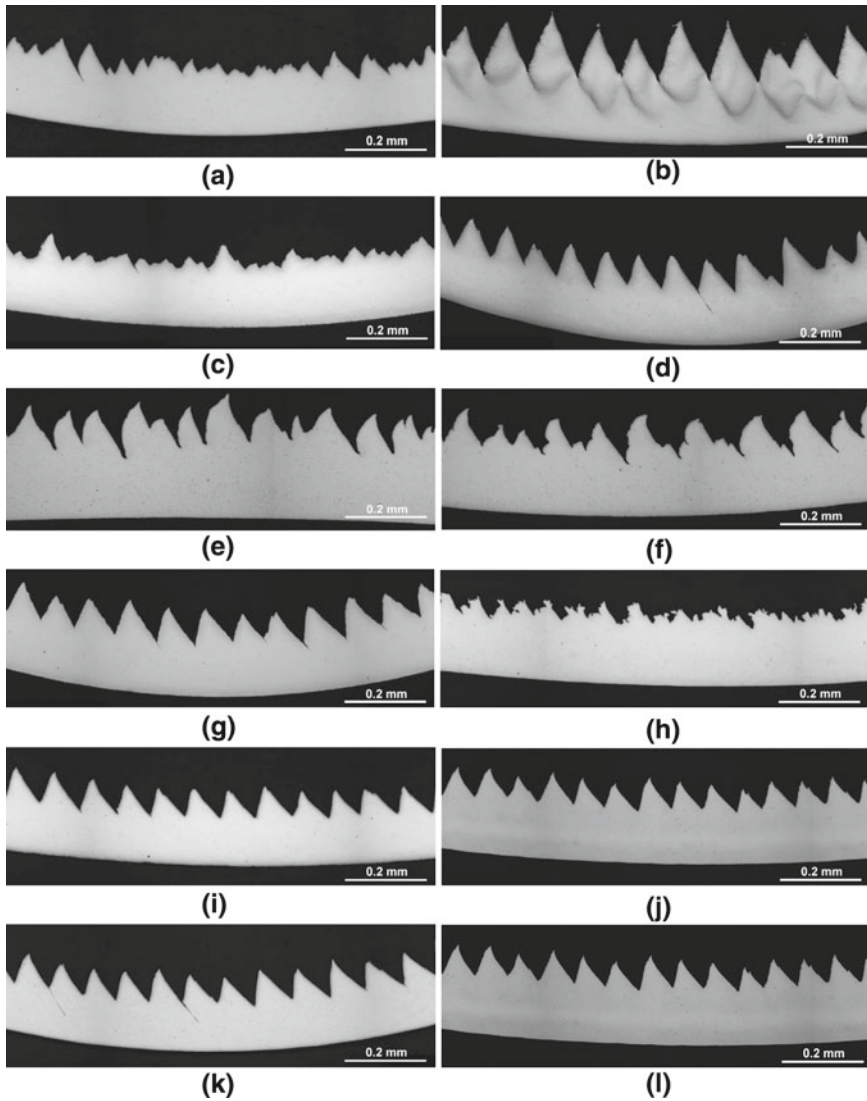
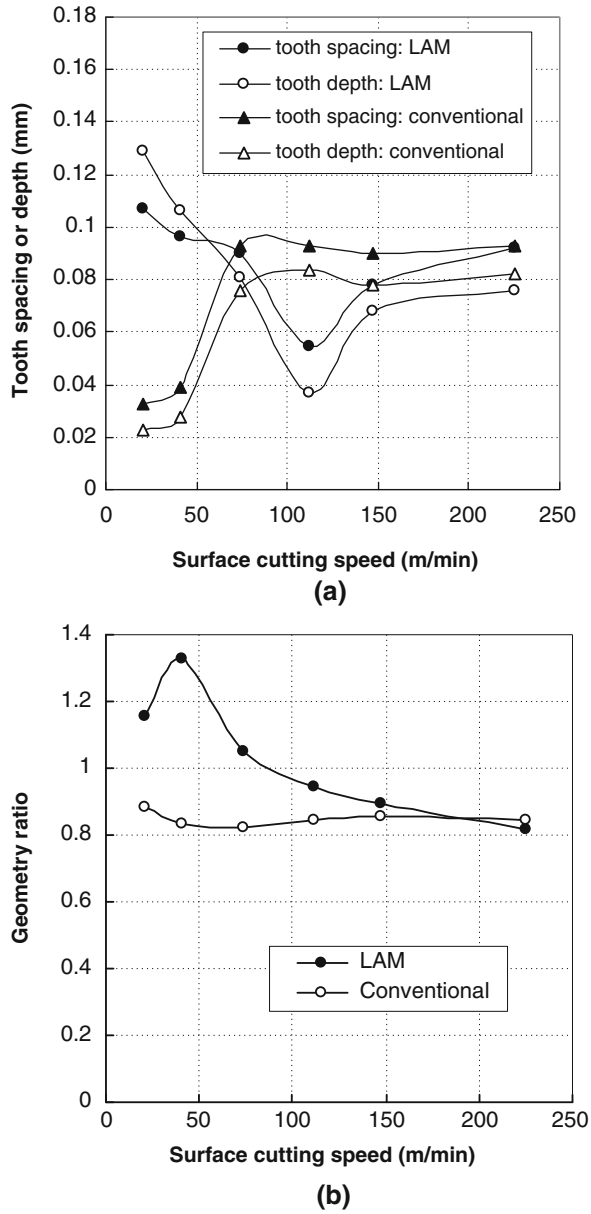


Fig. 3.18 Cross-sections of chips, (a), (c), (e), (g), (i) and (k) are made by conventional machining, (b), (d), (f), (h), (j) and (l) are made by LAM of Ti-6Al-4V alloy at cutting speeds of (a) and (b) 20 m/min, (c) and (d) 40 m/min, (e) and (f) 75 m/min, (g) and (h) 110 m/min, (i) and (j) 150 m/min, (k) and (l) 225 m/min. Laser power was 1,900 W and tool-beam distance was 20 mm

$$F_t^S = \frac{\sigma_y \cdot w \cdot h \cdot \tan(\beta - \alpha)}{\sin \theta \cdot \cos \theta - \sin^2 \theta \cdot \tan(\beta - \alpha)} \quad (3.9)$$

For segmented chip formation [104]:

Fig. 3.19 Effect of cutting speed on (a) tooth spacing and depth and (b) geometry ratio for the chips produced by conventional machining and LAM of Ti-6Al-4V alloy. Laser power was 1,900 W and tool-beam distance was 20 mm



$$F_t^c = \frac{K_{IC} \cdot w}{k} \sqrt{\frac{h}{6}} \tag{3.10}$$

where, w and h are the width and thickness of the undeformed chip, respectively, σ_y is the yield strength of workpiece at a given strain rate, β is the angle of kinetic

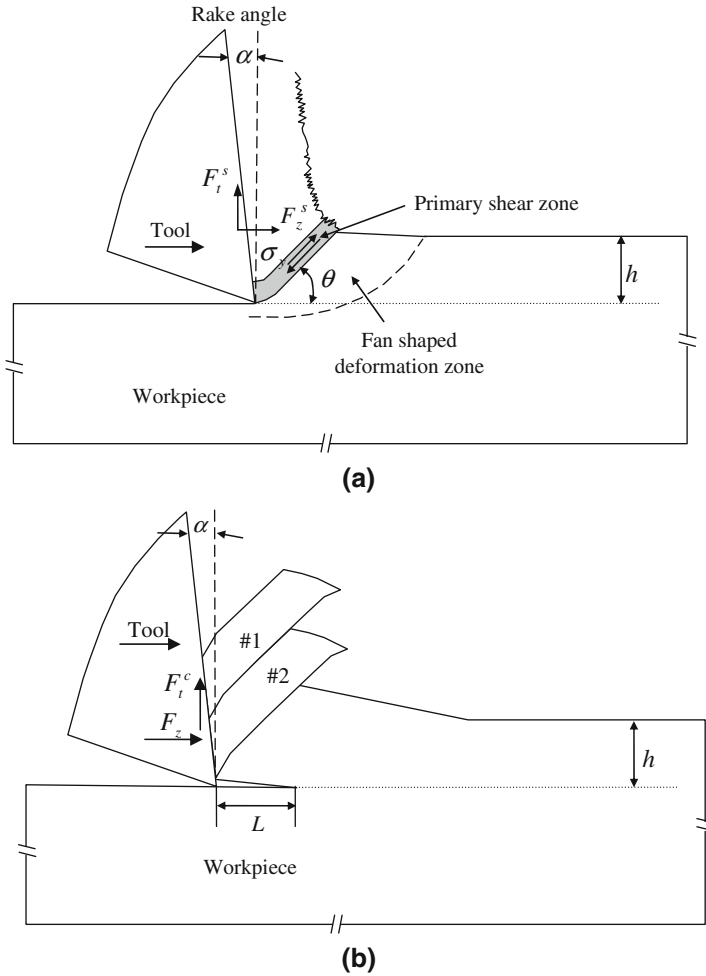


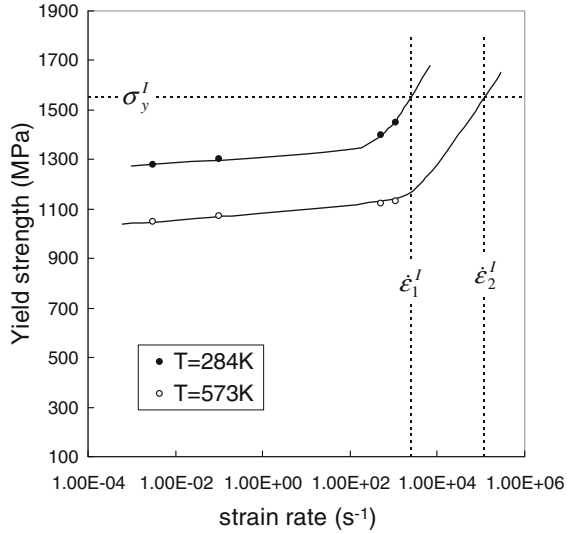
Fig. 3.20 Material removal mechanisms for (a) a continuous and (b) a segmented chip formations

friction for sliding motion, $\tan \beta = \mu$, where μ is the coefficient of friction, θ and α are the shear plane angle and rake angle, respectively, K_{IC} is the fracture toughness of workpiece and k is a constant for a given material and geometry of the cutting tool and a given workpiece material.

The process of chip removal is determined by comparing the forces F_t^s and F_t^c . Chip segmentation is prominent when $F_t^c \leq F_t^s$, therefore, the maximum (critical) yield strength of the workpiece near the cutting edge in order to form a continuous chip is obtained as [104]:

$$\sigma_y^I = \frac{\sin \theta \cos \theta - \sin^2 \theta \cdot \tan (\beta - \alpha)}{\tan (\beta - \alpha)} \cdot \frac{K_{IC}}{k \sqrt{6 h}} \quad (3.11)$$

Fig. 3.21 Critical yield strength and its corresponding critical strain rates marked on the curves of yield strength versus strain rate at temperature of 284 and 573 K for Ti-6Al-4V alloy [108]



The criterion for chip segmentation is that the yield strength of the workpiece at the shear plane during high speed machining (i.e., high strain rate deformation) is larger than or equal to the critical yield strength, expressed as:

$$\sigma_y \geq \sigma_y^I \tag{3.12}$$

The critical cutting speed and its corresponding strain rate for chip segmentation can be found at a strain rate where the yield strength is equal to the critical yield strength as shown in Fig. 3.21, in which the relationship between yield strength and strain rate was extrapolated from Ogawa’s results [108].

It can be seen that the increase in workpiece temperature from $T_1 = 284$ K to $T_2 = 573$ K results in the increase of critical strain rate from $\dot{\epsilon}_1^I = 2,500\text{s}^{-1}$ to $\dot{\epsilon}_2^I = 125,000\text{s}^{-1}$. Therefore, the critical cutting speed for onset of chip segmentation at $h = 0.214\text{mm}$ increases from $V_{c,1}^I = 1.8\text{m/min}$ to $V_{c,2}^I = 92.1\text{ m/min}$ calculated by the following relationship [73]:

$$\dot{\epsilon} = \frac{\cos \alpha \cdot V_c}{\Delta y \cdot \cos(\theta - \alpha)} \tag{3.13}$$

Temperature rise due to laser heating effectively reduces the yield strength of the workpiece; therefore, the strain rate and its corresponding critical cutting speed for chip segmentation increase with increasing laser power [104].

Once the material is removed by crack propagation in the cutting direction by the moving tool, which acts as a moving wedge keeping the crack open and propagating as shown in Fig. 3.22a, the chip is displaced along the tool’s rake face under high stress, leading to severe crater wear. In the meantime, the stress gradually builds inside the chip. When the stress inside the chip equals the compressive strength of

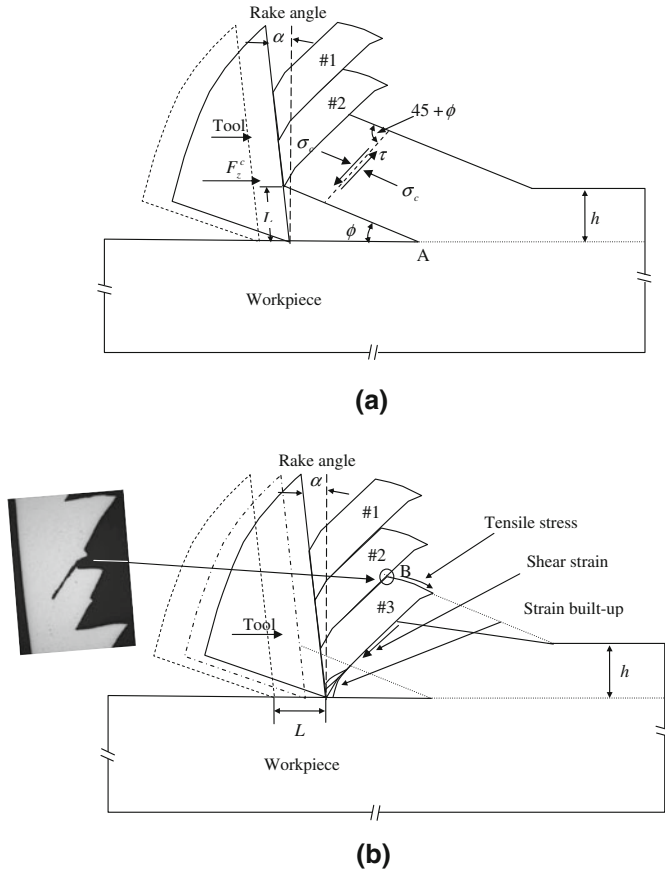


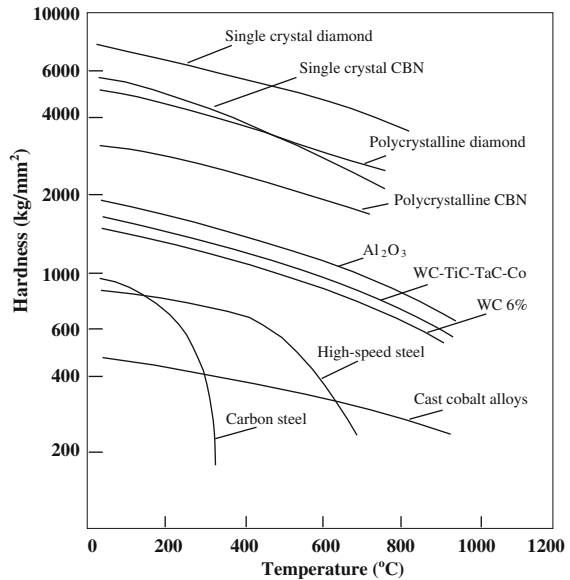
Fig. 3.22 The sequence of chip segmentation for a cutting tool with a positive rake angle; **a** chip displacement along the rake face and **b** chip fracture and segmentation [104]

the chip, the chip breaks in the form of a compression failure which is characterized as adiabatic shear. Thus, segment #3 is formed as a result of a chip break, which also results in a crack between the #2 and #3 segments as shown in Fig. 3.22b.

3.5.4 Tool Materials and Wear

The most common tools used in the industry are tool steels, carbides, ceramics, cements, diamond, and cubic boron nitride (CBN). The variation of hardness of these tools with temperature is shown in Fig. 3.23. Most tool materials lose their hardness at temperatures above the softening point, which is $1,100^\circ\text{C}$ for carbide,

Fig. 3.23 Hot hardness of some tool materials [110] (reprinted from [2] with permission. Copyright Elsevier Ltd)



1,400°C for Al_2O_3 , 1,500°C for CBN and diamond tools. The selection of a suitable tool is, dependent on the cutting pressure and cutting temperature [109].

A polycrystalline diamond (PCD) tool is found not to be suitable for LAM because of its low carburizing temperature (900°C)[76]. Polycrystalline cubic boron nitride (PCBN) has been used for LAM of Si_3N_4 [77, 78] and PSZ [76]. A carbide insert has been used for LAM of mullite [75] and Al_2O_3 [111] ceramics. A PCBN tool shows significantly longer tool life than a tungsten carbide tool when LAM of PSZ at the same cutting conditions [76]. Klocke and Bergs [79] however showed that the flank wear is smaller when using a PCD tool than that using a CBN tool when laser-assisted machining Si_3N_4 .

Ceramic tool inserts, WG-300 by Greenleaf [4, 5, 26, 69], CC670 by Sandvik [22, 82], K090 by Kennametal [28] (aluminum oxide reinforced with silicon carbide whiskers or TiC) are the proper tool materials used to cut Inconel 718 because they are stable up to approximately 2,000°C [22]. Carbide tool is found to be suitable for machining titanium alloys because of its high toughness [65, 80]. PCBN [41] and carbide [10, 87] inserts for hardened steel.

The laser beam heating in front of the cutting tool produces the following effects on tool wear in LAM:

- Lower pressure on cutting tool edge due to a reduction of cutting force results in a reduction in the abrasion dominant tool wear and catastrophic fracture.
- Higher tool-chip interface temperature at high laser power increases tool wear due to the accelerated dissolution-diffusion and adhesion at high temperature.
- High tool temperature may reduce the strength of tool and lead to its premature failure.

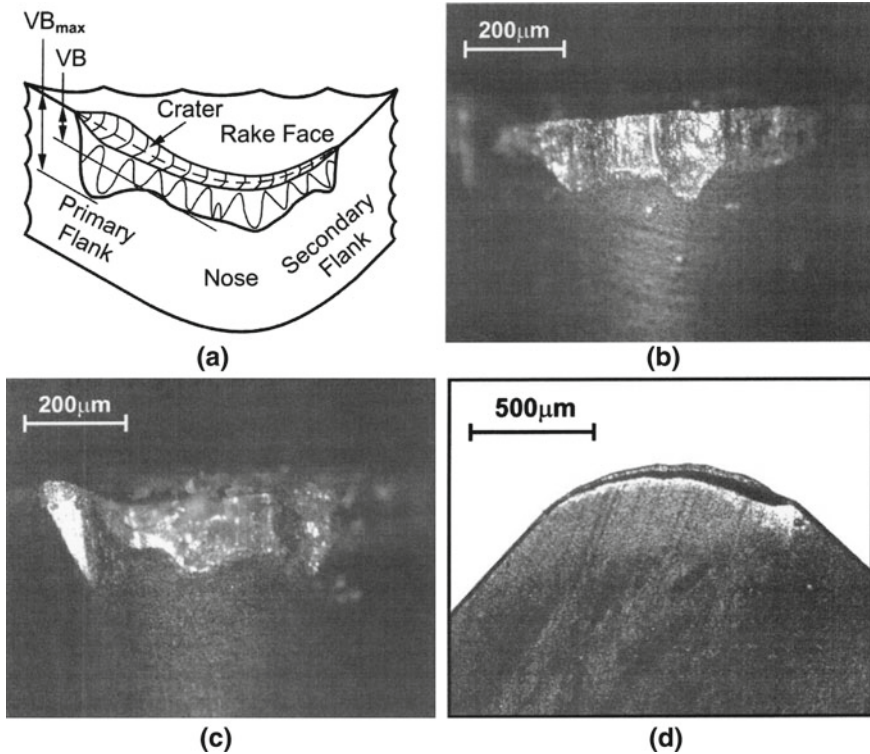


Fig. 3.24 a Schematic of tool wear, wear on the **b** nose, **c** flank face, and **d** rake face during LAM of PSZ at material removal temperature of 1,000°C [76]

Abrasion, adhesion, and diffusion mechanisms are attributed to the tool wear during laser-assisted turning of PSZ. Abrasion of the deposited workpiece material on both primary and secondary flank faces results in the grooves on the flank face (as shown in Fig. 3.24c). Edge crater was not observed during LAM of Si_3N_4 with PCBN insert at high temperature [78], but was observed during LAM of PSZ (Fig. 3.24d). This difference is attributed to the lower ductility and smaller thermal diffusivity of PSZ, which lead to severe diffusive and abrasive wear in LAM of PSZ compared with LAM of Si_3N_4 [76].

The tool life is much longer during LAM than conventional machining of mullite [75]. The flank wear during LAM of Si_3N_4 is attributed to the adhesion of the glassy grain-boundary phase to the cutting tool. The bonding between the glassy phase and cutting tool may be broken during machining and this results in the tearing of the cutting tool material [78].

In summary, tool wear is strongly dependent on the material removal temperature, and there is an optimum material removal temperature for maximum tool life. A short tool life is due to an insufficient reduction in workpiece strength when the material

removal temperature is lower than the optimum temperature and a reduction in tool strength by overheating when the material removal temperature is higher than the optimum temperature, respectively [75]. Therefore, tool life can be optimized by maintaining the material removal temperature in the optimum region.

The tool failure mode for laser-assisted milling of Si_3N_4 is edge chipping at the workpiece temperature lower than the softening point of glass phase due to the high and frequent dynamic impact on the cutting edge when the tool is intermittently engaged with workpiece during cutting. Gradual flank wear is the dominant tool failure mode at high workpiece temperature and is significantly reduced with increasing workpiece temperature up to a point. Further increase in temperature has less or negative influence on the reduction in tool wear [69, 71]. The maximum workpiece temperature allowed for reducing the tool wear in laser-assisted milling is higher than that in laser-assisted turning because of the lower temperature of insert as a result of shorter tool-chip contact time in milling operation [71].

Similar to the milling process, the pressure on cutting tool when the tool is engaged with the workpiece during planning is high and often results in severe abrasion and larger area fracture on both the flank and rake faces. Laser heating prior to cutting effectively softens the workpiece and no fracture was observed on both the flank and rake faces [43].

Notch and flank wear are the dominant tool failure modes for conventional turning of Inconel 718 alloy with a ceramic tool. Flank and crater wear are the dominant tool failure modes for turning titanium alloys as a result of dissolution-diffusion, abrasion, adhesion, and attrition mechanisms [2, 6, 112].

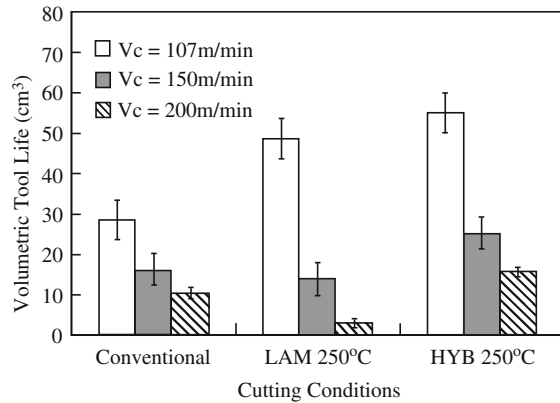
The optimum material removal temperature during LAM of Ti-6Al-4V alloy is found to be 250°C at which the balance between the heat generated due to plastic deformation and by laser energy input is achieved and the cobalt-diffusion controlled crater wear is minimized at the cutting speed of 107 m/min [65, 113]. Higher temperature results in shorter tool life compared to conventional machining due to the acceleration of Co diffusion.

At this optimum material removal temperature, the tool life in terms of the volume of material removed during LAM is shorter than that during conventional machining at cutting speed higher than 107 m/min as shown in Fig. 3.25. The hybrid machining (HYB), in which a reservoir cap with liquid nitrogen (LN_2) passage is built to cool the tool's rake face, improves the tool life significantly at all the cutting speeds. Furthermore, the improvement of the tool life by applying a TiAlN coating under the hybrid machining condition is more significant than that under the conventional machining condition.

Tool life during LAM of Inconel 718 alloy is found to be shorter than that obtained by conventional cutting with carbide tool because of the lower strength of carbide tool at high temperature [82]. Hence appropriate selection of tool is important for the LAM process.

Both notch and flank wear are reduced in the laser-assisted turning of Inconel 718 alloy. The notch wear and maximum flank wear ($V_{B_{\max}}$) reduce with increasing material removal temperature up to 540°C , while the average flank wear $V_{B_{\text{ave}}}$ achieves its lowest value at the material removal temperature of 360°C following

Fig. 3.25 Effect of cutting speed on tool life for various cutting conditions at the optimum material removal temperature. The feed and depth of cut were 0.07 mm/rev and 0.76 mm, respectively [65]



which it increases slightly with the material removal temperature from 360 to 540°C [26].

Contrary to the increase in wear with increasing cutting speed during LAM of Ti-6Al-4V alloy and conventional machining, the tool wear (both the notch and flank wear) decreases with increasing cutting speed and feed during LAM of Inconel 718 at the constant material removal temperature of 540°C [26]. This is probably due to the independence of material removal temperature on cutting speed as shown in the empirical Eq. (3.3). Therefore, the benefit of LAM can be maximized at the higher cutting speed.

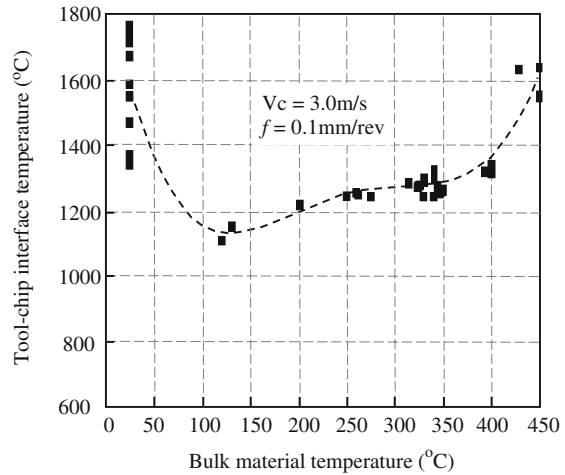
The location of the laser beam on the chamfer surface has a more significant influence on the reduction in the notch and nose wear than on the reduction in flank wear during LAM of Inconel 718. A greater reduction in notch wear is obtained when the laser beam is incident on the top edge of the chamfer shoulder and a greater reduction in nose wear is achieved when the laser beam is incident near the root of the chamfer shoulder, respectively [28].

Laser beam orientation has also been found to significantly affect the tool wear. The minor axis of laser spot along the workpiece rotation direction is effective during laser-assisted turning of Ti-6Al-4V alloy with carbide tool whereas the major axis of laser spot along the workpiece rotation direction is effective during laser-assisted turning of Inconel 718 alloy with ceramic tool. This is because of the higher chip temperature in the latter case and the higher strength of ceramic tool at high temperature [28].

When a diode laser with a rectangular beam was used to assist turning D2 steel, it was found that the reduction of flank wear during LAM of tool steel is greater when the slow axis of the rectangular beam is perpendicular to the feed direction because of the higher surface temperature and greater reduction of cutting forces in this beam orientation [10].

Both the evolution of flank wear and catastrophic failure of the tool during LAM of tool steel have been reduced because of the softening of the workpiece, which can be achieved with surface temperatures above 300–400 °C for the thickness of the

Fig. 3.26 Effect of material removal temperature on tool-chip interface temperature during LAM of stainless steel [42].



uncut chip of 0.05 mm. The stable built-up edge is found to protect the cutting edge during LAM, and this partially contributes to the reduction in tool wear [10].

The tool-chip interface temperature (T_{int}), critical for the dissolution-diffusion dominant tool wear, is much lower in LAM than that in conventional machining of austenitic stainless steel when the material removal temperature is above 120°C and below 400°C as shown in Fig. 3.26 [42], which leads to significant reduction in tool wear within that temperature range. The accelerated tool wear results in premature tool failure when the material removal temperature is above this temperature range.

It is also observed that the friction coefficient between the coated K10 tool and hardened XC42 steel is reduced with laser beam assistance during machining [81], but the friction coefficient remains constant at the material removal temperature from 25 to 450°C during LAM of austenitic stainless steel, which suggests that the shear angle may change during LAM [42]. Reduction in the shear angle in chip formation during LAM decreases and the chip thickness increases [27].

Edge chipping is the dominant tool failure mode in conventional milling of both Ti-6Al-4V [9] and Inconel 718 alloys [69] due to the high cyclical force acting on the cutting tool edge when the tool is engaged with workpiece. Lower impact on cutting tool edge with laser beam assistance as a result of reduction in the cutting force significantly reduces the edge chipping in laser-assisted milling of Ti-6Al-4V alloy [114]. The amount of chipping is dependent on the preheating cycle and beam position. Long heating time and beam position close to the edge of workpiece are favored to reduce tool edge chipping in laser-assisted milling of Inconel 718 [69]. However, overheating the workpiece results in the increasing size of the chip built-up edge in hot machining of Ti-6Al-4V alloy [35]. Premature degradation of tool at higher temperature due to higher laser power results in shorter tool life [114].

Because the softening of Al matrix in Al_2O_3 p/Al composites by laser beam makes it easier to push the Al_2O_3 particles into the machined surface (as shown in Fig. 3.15), this reduces the stress and deformation of machined surface. Therefore, the

abrasion of the Al_2O_3 particles on tool's flank face is lower compared to conventional machining [93].

However, Barnes et al. [115] found that the tool failure results from severe flank wear due to an abrasion mechanism when cutting aluminum/SiC MMCs. The flank wear increases significantly with increasing preheat temperature. This is associated with a shift in the stability range of the built-up edge to the lower cutting speeds, combined with a change in the angle of the built-up edge's leading edge which reduces its ability to protect the flank face from abrasive wear. He concluded that the tool wear is more severe when machining aluminum/SiC MMCs at high workpiece temperature.

Deformation of cutting tool occurs during machining due to the presence of high pressure and temperature at the cutting zone. The deformation affects the dimensional accuracy of the machined parts. Simulation by Jung et al. [116] found that the deformation error during LAM of Si_3N_4 increases with the cutting temperature due to the thermal distortion.

3.5.5 Surface Integrity

The integrity of the machined surface is characterized by its surface roughness, surface or subsurface damage, microstructure alteration in the machined subsurface, and residual stress.

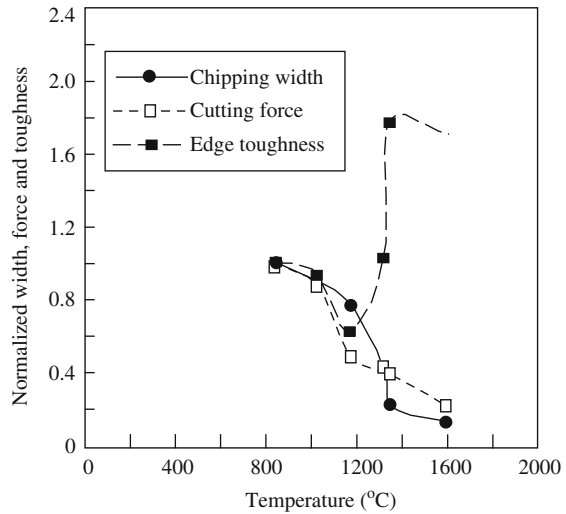
Above a certain temperature, the machined surface after LAM of Si_3N_4 is characterized by the built-up of irregular glassy phase debris and the formation of cavities due to $\beta\text{-Si}_3\text{N}_4$ grain pullout [77, 78]. Similar to LAM of PSZ [76], the surface roughness is not sensitive to the material removal temperature, but depends on the size and distribution of Si_3N_4 grains.

Workpiece fracture may occur when LAM of ceramics. The fracture of Si_3N_4 during LAM at high feed rate is caused by the mechanical fracture due to the lack of softening. Thermal fracture occurs when LAM of mullite at high feed rate due to the thermally induced stress and the fracture of PSZ occurs due to the thermally induced cracking at high laser power density [94].

Local cracks present in the HAZ without cutting indicate that the laser heating cycle introduces high thermal stresses in PSZ [76]. The thickness of the cracking region increases with the material removal temperature (laser power). If this thickness is greater than the depth of cut, the crack remains in the subsurface, which is detrimental for the properties of the machined part. Therefore, laser power or the material removal temperature must be controlled to produce a damage-free component by LAM.

The sudden impact and stress release between cutting tool and workpiece when the cutting tool enters and leaves the workpiece during milling of ceramics (Si_3N_4) results in workpiece edge chipping at both the entry and exit edges. The workpiece edge chipping leads to poor dimensional and geometric accuracy and is the source of cracking. Rise in workpiece temperature during laser-assisted milling of

Fig. 3.27 Effect of temperature on softening (cutting force), toughness of workpiece and workpiece edge chipping during LAM of Si_3N_4 [118]



Si_3N_4 can eliminate both the macroscale entry and interior edge chippings, but the macroscale exit edge chipping cannot be avoided completely [117]; however, it can be reduced significantly due to the increasing workpiece temperature during laser-assisted milling. Reduction in workpiece edge chipping is the result of the coupled effects of workpiece softening and toughening mechanisms. Both softening and toughening of workpiece take positive effect when the temperature is above the brittle/ductile transition temperature and below the global softening temperature (between 1,300 and 1,400°C) as shown in Fig. 3.27 [118]. In Fig. 3.27, the data of chipping width, cutting force, and edge toughness are normalized by dividing the corresponding values at 838°C in order to compare which mechanism dominates at which temperature range.

The machined surface by LAM is smoother than that of conventionally machined titanium alloy [58, 80], Inconel 718 alloy [26, 82] and steels [42, 86]. Significant improvement of surface roughness is also achieved in laser-assisted mechanical micromachining (LAMM) H-13 mold steel (42 HRC) [91]. Reduction in yield strength by laser heating makes the deformation easier and less grain pullout occurred from the machined surface due to lower chip rupture stress. The reduced cutting forces and tool vibration/chatter and continuous chip formation also contribute to the better surface finish.

The surface roughness decreases with increasing material removal temperature up to 500°C for Ti-6Al-4V alloy. Enhanced cooling of tool during hybrid laser-assisted machining of Ti-6Al-4V alloy lowers the friction between the tool flank face and the machined surface and leads to better surface finish [65].

High laser power improves the surface quality of Inconel 718 [82]. The surface roughness during LAM of Inconel 718 alloy is reported to decrease with increasing material removal temperature of 500°C [69] and 540°C [26]. Beyond that

temperature, surface oxidation is sometimes observed, and this results in a slight deterioration in surface quality. The improvement in surface integrity at high temperature during machining of Inconel 718 is due to:

- (1) a lower chip rupture stress due to lower workpiece hardness leading to smoother chip removal;
- (2) higher tool ductility due to higher temperatures preventing secondary chipping [4].

Despite the negligible dependence of cutting force on the laser power during LAM of 42CrMo4 steel, the surface roughness is strongly improved with increasing laser power [86]. This allows greater cutting speed or feed for achieving higher productivity without experiencing degradation in surface quality.

Plastic deformation is often observed in the subsurface after conventional machining of the hard-to-machine materials. This can lead to high strain hardening through a large depth of the workpiece. Because of reduction in the cutting forces in LAM, the hardness and depth of strain deformation affected zone are smaller compared with those in conventional machining [80], which is similar to the result from the plasma-enhanced machining Inconel 718 alloy [22]. No phase transformation remained within the machined subsurface if the laser heat input is well controlled in accordance with machining parameters [65, 80, 83]. Hardness of the machined subsurface in LAM of tool steel does not change from that in the bulk workpiece [10].

Despite the increase in cutting force when laser-assisted machining of the hardenable steels, such as the 1090 steel, an improvement in surface integrity is obtained with laser beam assistance during machining [92].

Not only is the surface roughness improved, but also the dimensional accuracy during micromilling of hardened A2 tool steel with laser preheating [119]. The groove depth is closer to the set depth of cut with laser heating because of the smaller tool deflection and lower tool wear rate. The effect of tool deflection on the depth of cut was reported to be counteracted by the thermal expansion of both the tool and workpiece due to laser heating.

During LAM of Al₂O₃ p/Al MMCs, the softened matrix is easily squeezed out while more Al₂O₃ particles are pushed toward the machined surface by the cutting tool, which produces a higher fraction of Al₂O₃ particles near the machined surface as shown in Fig. 3.15, leading to an increase in the wear resistance of the machined surface. Further, the machined surface produced by LAM shows a higher compressive residual stress (triple than that observed in the conventionally machined surfaces) [93].

Compressive residual stress was observed on the machined surface of Si₃N₄ produced by LAM in both the axial and hoop directions [120]. However its magnitude is smaller than that produced by conventional grinding [79, 120] because the softening of the glassy phase significantly relieves the stress at the material removal zone [120].

Klocke and Bergs [79] reported that the bending strength and the Weibull modulus of Si₃N₄ components made by LAM are better than those by conventional grinding.

Anderson et al. [26] reported that a compressive residual stress is produced only in the axial direction during LAM of Inconel 718 alloy compared to the tensile residual stress produced by conventional turning. However, Germain et al. [82] reported that tensile residual stress is produced in both the axial and tangential directions with and without laser assistance, and the magnitude of residual stress produced by LAM is smaller than that by conventional machining only in the axial direction when machining with carbide tools.

Because the chip is removed from workpiece at low stress during LAM the magnitude of compressive residual stress at the machined surface is lower than that in conventional machining of Ti-6Al-4V alloy and bearing steel [58, 121] due to the lower deformation strain in LAM. This effect is more significant at low cutting speed and becomes negligible when the cutting speed is higher than 54 m/min. However, Ding and Shin [41] reported that LAM of hardened steel produces 150 MPa more compressive surface axial residual stress compared to conventional cutting.

Burnishing is a process involving pressing of the metallic workpiece surface by a hard roller or ball (as shown in Fig. 3.3). This process produces a smooth surface with high hardness and compressive residual stress due to the plastic deformation of the surface layer. With laser heating the workpiece surface before the burnishing roller, larger plastic deformation in the surface layer is achieved. This leads to a lower surface roughness, higher hardness in the surface layer, and larger compressive residual stress on the surface compared to the conventional burnishing. Surface temperature by laser heating should be controlled to avoid permanent phase transformation in the surface layer [44].

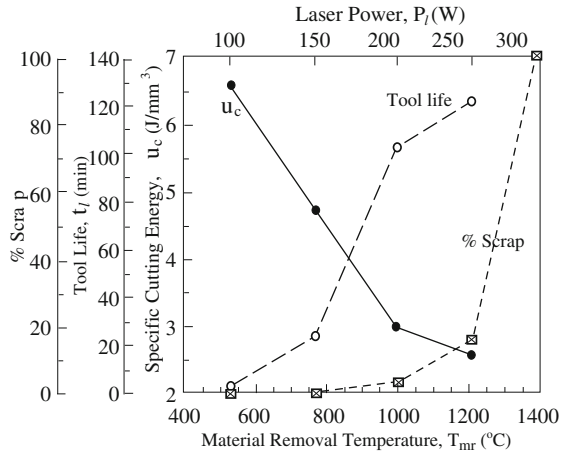
3.6 Optimization and Energy Efficiency of LAM

Because of the importance of material removal temperature during LAM, its optimum range is determined by comparing the specific cutting energy (u_c) tool life, scrap rate (determined by the damage on the machined surface in the form of cracks and spalling), and surface roughness as shown in Fig. 3.28 for LAM of PSZ. The optimum material removal temperature is found to be in the range from approximately 900 to 1,100°C [76].

The optimum material removal temperature is reported to be between 1,270°C and 1,490°C for Si_3N_4 [78], 1,043°C and 1,215°C for mullite [61, 75], 550°C and 650°C for Inconel 718 alloy [26], 120°C and 340°C for austenitic stainless steel P550 [42], around 250°C, and 400°C for Ti-6Al-4V alloy [65, 113] and compacted graphite iron [64], respectively.

During the LAM process, the energy absorbed by the workpiece not only raises the temperature of the material to be removed to the desired material removal temperature but also heats the material below the removal zone. A preheating efficiency is defined as the ratio of the minimum power required to heat the material to be removed to the desired material removal temperature (P_{\min}) to the total amount of power absorbed from the external heat source (P) [122], i.e.:

Fig. 3.28 Effect of material removal temperature on specific cutting energy, tool life and scrap rate for LAM of PSZ [76]



$$\eta = \frac{P_{min}}{P} \tag{3.14}$$

This efficiency decreases with increasing material removal temperature (as shown in Fig. 3.29a) because a large amount of energy is wasted in heating the material outside the cutting zone. Improvement of preheating efficiency significantly reduces the specific energy, u_{total} , as shown in Fig. 3.29b. The total specific energy u_{total} , includes both the mechanical cutting energy, u_c and the thermal energy, u_t . Therefore, the selection of the optimum material removal temperature is critical in order to achieve not only the full benefit of LAM but also the preheating efficiency. As a metric, the preheating efficiency can be used to guide the configuration of the laser beam, such as its focusing location and position relative to the cutting tool in consideration of the workpiece material’s thermophysical properties.

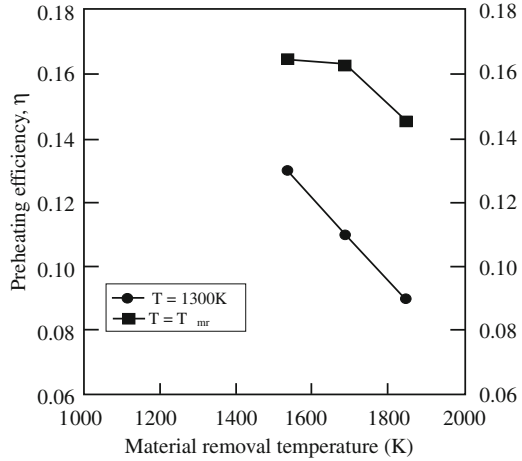
3.7 Numerical Simulation of LAM

Machining is a complex process which involves deformation of workpiece, friction between the workpiece and tool, and material removal. All of these processes are strongly dependent on temperature.

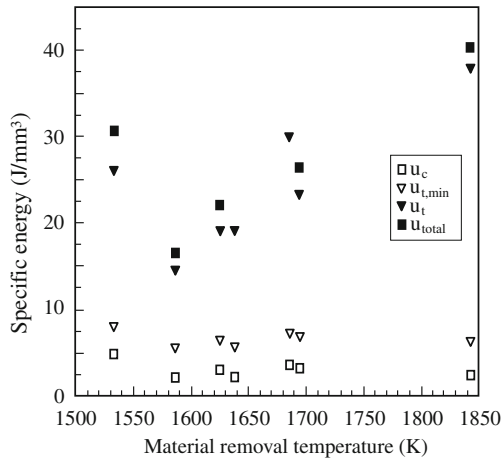
Laser beam heating creates a large temperature gradient through thickness in front of cutting tool. Thermal modeling analysis has been developed to simulate the temperature field and heat affected zone due to laser radiation and cutting during turning and milling operations.

A multiscale finite element modeling of LAM of Si_3N_4 ceramic was developed by Tian and Shin [123]. In this model, Si_3N_4 ceramic was modeled with a continuum element which represents the bulk workpiece and interfacial cohesive element which models the initiation and propagation of intergranular cracks. Different mechanical

Fig. 3.29 **a** Preheating efficiency and **b** specific energy as a function of material removal temperature for laser-assisted machining of Si_3N_4 [122]



(a)



(b)

behaviors are applied to the bulk workpiece and intergranular glassy phase. The modeling results show that microcracks initiate and propagate under the tool loading at material removal temperature of 1, 200°C. The microcracks propagate and coalesce into a macrocrack in the shear zone, which produces a discontinuous chip with a sharp drop in the main cutting force.

The interaction between cutting tool and workpiece shows different behaviors. In portion A in Fig. 3.30, crack propagation and discontinuous chip formation lead to cyclical forces, while semi-steady force acts in portion B, where the machined surface is produced due to plastic deformation.

Distinct element model [67–125] has been developed to simulate the material removal process during LAM of Si_3N_4 ceramic. The peak in forces corresponds

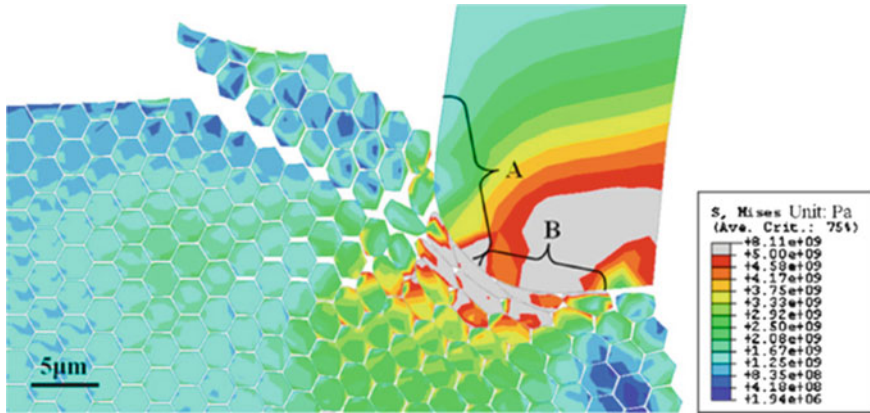


Fig. 3.30 Simulation of the cutting zone during LAM of Si₃N₄ ceramic [123]

to the long crack propagation. The forward propagation of a long lateral crack is associated with the peak of the main force, whereas the downward propagation of a long median crack is associated with a peak of thrust force.

With the information of the temperature distribution, the constitutive law and friction between the cutting tool and chip can be determined. The 3D FEM analysis of laser-assisted turning of Inconel 718 can predict the cutting force and chip thickness, which agree with the experimental results [88]. The simulation results show a higher temperature in the shear zone and tool-chip interface and lower stress on cutting tool compared with conventional machining. The strain and strain rate fields in the primary shear zone are not significantly affected by laser beam radiation, which indicates that the reduction in cutting force is mainly due to the thermal softening. This model however did not consider the material failure criteria and chip formation.

3.8 Future Scope of LAM

The laser-assisted machining process has shown significant improvement in machinability when machining hard-to-machine materials. Generally, it offers lower cutting forces, longer tool life, a better machined surface, and high material removal rate for a variety of workpiece materials, such as ceramics, metals, and composites, for which the high hardness is a principal barrier. However, some workpieces with high ductility are also hard to machine due to the difficult separation between the chip and tool. The feasibility of applying LAM when machining these materials and the material removal mechanism needs to be investigated.

LAM introduces an external heat source to heat the workpiece locally in front of the cutting tool, which may result in high temperature at the cutting zone. This high temperature may lead to shorter tool life due to the premature degradation of

the cutting tool and accelerated dissolution-diffusion and adhesion. Therefore, more effective methods for enhancing separation of the chip from the tool and cooling the cutting tool without affecting local heating of the workpiece are required. These methods should be practically applicable for both milling and turning operations during LAM.

LAM is a complicated process. The laser beam does not only change the flow stress, but also changes the deformation behavior of the workpiece and friction between the chip and cutting tool. So far, intensive experimental work and modeling of temperature distribution have only been reported. Investigations into the deformation behavior at high temperature, high temperature gradient and high strain rate, apparent friction at high temperatures and chip separation are required in order to develop an appropriate model to further understand the LAM process.

LAM involves many parameters (laser parameters, machining parameters, and properties of workpiece) and its optimization for a given workpiece material therefore is a challenging task. Understanding the contribution of each parameter to machinability is crucial for its optimization.

Most of the LAM studies reported to date have been on turning or surface milling operations. Application of LAM to the other machining processes, such as drilling, is challenging due to the complexity of the integration of the laser beam and the machine. Further work needs to be undertaken in this area to make the process more attractive from an industrial perspective.

Acknowledgments The authors gratefully acknowledge the CAST Cooperative Research Centre for the financial support and permission to publish this work. The CAST Cooperative Research Centre was established and is supported under the Australian Government's Cooperative Research Centres Programme.

References

1. A.N. Samant, N.B. Dahotre, J. Eur. Ceram. Soc. **29**, 969–993 (2009)
2. E.O. Ezugwu, J. Bonney, Y. Yamane, J. Mater. Process. Technol. **134**, 233–253 (2003)
3. I.A. Choudhury, M.A. El-Baradi, J. Mater. Process. Technol. **77**, 278–284 (1998)
4. J.W. Novak, Y.C. Shin, F.P. Incropera, J. Manuf. Sci. Eng. Trans. ASME **119**, 125–129 (1997)
5. C.E. Leshock, J.-N. Kim, Y.C. Shin, Int. J. Mach. Tools Manuf. **41**, 877–897 (2001)
6. A. Devillez, F. Schneider, S. Dominiak, D. Dudzinski, D. Larrouquere, Wear **262**, 931–942 (2007)
7. R. Arunachalam, M.A. Manan, Mach. Sci. Technol. **4**, 12–168 (2000)
8. R.R. Boyer, Mater. Sci. Eng. A **213**, 103–114 (1996)
9. E.O. Ezugwu, Z.M. Wang, J. Mater. Process. Technol. **68**, 262–274 (1997)
10. P. Dumitrescu, P. Koshy, J. Stenekes, M.A. Elbestawi, Int. J. Mach. Tools Manuf. **46**, 2009–2016 (2006)
11. Z.F. Zhang, L.C. Zhang, Y.W. Mai, J. Mater. Sci. **30**, 1961–1966 (1995)
12. A. Pramanik, L.C. Zhang, J.A. Arsecularatne, Int. J. Mach. Tools Manuf. **48**, 1613–1625 (2008)
13. M. El-Gallab, M. Sklad, J. Mater. Process. Technol. **83**, 151–158 (1998)
14. A. Manna, B. Bhattacharyya, J. Mater. Process. Technol. **123**, 476–482 (2002)

15. S. Kannan, H.A. Kishawy, J. Mater. Process. Technol. **198**, 399–406 (2008)
16. A. Pramanik, L.C. Zhang, J.A. Arsecularatne, Int. J. Mach. Tools Manuf. **46**, 1795–1803 (2006)
17. W. König, A.K. Zaboklicki, in *Proceedings of the LANE'94, Laser Assisted Net Shape Engineering*, (1994), pp. 389–404
18. G. Chryssoulouries, N. Anifantis, S. Karagiannis, J. Manuf. Sci. Eng. Trans. ASME **119**, 766–769 (1997)
19. M. Weck, W. von Zeppelin, C. Hermanns, in *Proceedings of the LANE'94, Laser Assisted Net Shape Engineering*, (1994), pp. 427–437
20. W. König, L. Cronjager, G. Spur, H.K. Tonshoff, M. Vigneau, W.J. Zdeblick, CIRP Ann. Manuf. Technol. **39**, 673–681 (1990)
21. W. König, A.K. Zaboklicki, in *Proceedings of International Conference on Machining of Advanced Materials*, (1993), pp. 455–463
22. L.N. Lópezde Lacalle, J.A. Sánchez, A. Lamikiz, A. Celaya, J. Manuf. Sci. Eng. Trans. ASME **126**, 274–285 (2004)
23. G. Madhavulu, B. Ahmed, J. Mater. Process. Technol. **44**, 199–206 (1994)
24. Y.C. Shin, J.-N. Kim, ASME Manuf. Sci. Eng. MED **4**, 243–249 (1996)
25. T. Kitagawa, K. Maekawa, Wear **139**, 251–267 (1990)
26. M. Anderson, R. Patwa, Y.C. Shin, Int. J. Mach. Tools Manuf. **46**, 1879–1891 (2006)
27. B.M. Jau, S.M. Copley, M. Bass, in *Proceedings of the Ninth North American Manufacturing Research Conference*, University Park, Pennsylvania, (1981), pp. 12–15
28. S. Rajagopal, D.J. Plankenhorn, V.L. Hill, J. Appl. Metalworking **2**, 170–184 (1982)
29. L. Özler, A. Önan, C. Özel, Int. J. Mach. Tools Manuf. **41**, 163–172 (2001)
30. K.P. Maitya, P.K. Swain, J. Mater. Process. Technol. **198**, 344–349 (2008)
31. N. Tosun, L. Özler, J. Mater. Process. Technol. **124**, 99–104 (2002)
32. M.A. Lajjis, A.K.M.N. Amin, A.N.M. Karim, H.C.D.M. Radzi, T.L. Ginta, Am. J. Eng. Appl. Sci. **2**, 421–427 (2009)
33. A.K.M.N. Amin, S.B. Dolah, M.B. Mahmud, M.A. Lajjis, J. Mater. Process. Technol. **201**, 466–470 (2008)
34. A.K.M.N. Amin, M. Abdelgadir, J. Manuf. Sci. Eng. Trans. ASME **125**, 674–680 (2003)
35. T.L. Ginta, A.K.M.N. Amin, M.A. Lajjis, A.N.M. Karim, H.C.D.M. Radzi, Eur. J. Sci. Res. **27**, 384–391 (2009)
36. A.K.M.N. Amin, N.V. Talantov, Mech. Eng. Res. Bull. **9**, 52–62 (1986)
37. G. Barrow, CIRP Ann. Manuf. Technol. **14**, 145–151 (1965)
38. E.J. Krabacher, M.E. Merchant, J. Eng. Ind. Trans. ASME **73**, 761–776 (1951)
39. S. Lei, F. Pfefferkorn, in *Proceedings of the ASME International Conference on Manufacturing Science and Engineering*, (2007), pp. 1–12
40. C. Brecher, C.-J. Rosen, M. Emonts Phys. procedia laser assisted net shape Eng.6 Proc. LANE 2010 Part 2, **5**, 259–272 (2010)
41. H. Ding, Y.C. Shin, Int. J. Mach. Tools Manuf. **50**, 106–114 (2010)
42. M. Anderson, Y.C. Shin, Proc. Inst. Mech. Eng: Part B J. Eng. Manuf. **220**, 2055–2067 (2006)
43. C.-W. Chang, C.P. Kuo, Int. J. Mach. Tools Manuf. **47**, 452–461 (2007)
44. Y. Tian, Y.C. Shin, Int. J. Mach. Tools Manuf. **47**, 14–22 (2007)
45. Y. Tian, Y.C. Shin, Proc. Inst. Mech. Eng. Part B: J. Eng. Manuf. **221**, 605–616 (2007)
46. C. Zhang, Y.C. Shin, Int. J. Mach. Tools Manuf. **42**, 825–835 (2002)
47. C. Zhang, Y.C. Shin, Int. J. Mach. Tools Manuf. **43**, 41–49 (2003)
48. E. Westkämper, CIRP Ann. Manuf. Technol. **44**, 317–320 (1995)
49. Q.M. Murphy, US Patent 5,409,376, 1995
50. R. Komanduri, M. Lee, D.G. Flom, R.A. Thompson, M.G. Jones, R.J. Douglas, US Patent 4,356,376 1982
51. M. Kaiser, Ph.D. thesis, Texas Tech University, 2001
52. S. Barnes, R. Morgan, A. Skeen, J. Eng. Mater. Technol. **125**, 378–384 (2003)
53. J.C. Rozzi, F.E. Pfefferkorn, F.P. Incropera, Y.C. Shin, J. Heat Transfer **120**, 899–906 (1998)

54. J.C. Rozzi, F.E. Pfefferkorn, F.P. Incropera, Y.C. Shin, *Int. J. Heat Mass Transfer* **43**, 1409–1424 (2000)
55. J.C. Rozzi, F.P. Incropera, Y.C. Shin, *Int. J. Heat Mass Transfer* **43**, 1425–1437 (2000)
56. F.E. Pfefferkorn, F.P. Incropera, Y.C. Shin, *Int. J. Heat Mass Transfer* **48**, 1999–2012 (2005)
57. N. Yang, M. Brandt, S. Sun, *Mater. Sci. Forum.* **618–619**, 143–146 (2009)
58. G. Germain, F. Morel, J.-L. Lebrun, A. Morel, *Lasers Eng.* **17**, 329–344 (2007)
59. Y. Tian, Y.C. Shin, *J. Manuf. Sci. Eng.* **128**, 425–434 (2006)
60. R. Singh, M.J. Alberts, S.N. Melkote, *Int. J. Mach. Tools Manuf.* **48**, 994–1004 (2008)
61. P.A. Rebroy, Y.C. Shin, F.P. Incropera, *Int. J. Mach. Tools Manuf.* **44**, 677–694 (2004)
62. X. Wu, H. Zhang, Y. Wang, *Proceedings of SPIE, 4th International Symposium on Advanced Optical Manufacturing and Testing Technologies: Advanced Optical Manufacturing Technologies*, vol. 7282 (2009), pp. 1–5
63. X.F. Wu, H.Z. Zhang, W. Yang, X. Chao, *Key Eng. Mater.* **419–420**, 521–524 (2010)
64. S. Skvarenina, Y.C. Shin, *Int. J. Mach. Tools Manuf.* **46**, 7–17 (2006)
65. C.R. Dandekar, Y.C. Shin, J. Barnes, *Int. J. Mach. Tools Manuf.* **50**, 174–182 (2010)
66. J. Yang, S. Sun, M. Brandt, W. Yan, in *Proceedings of the 4th Pacific International Conference on Applications of Lasers and Optics*, Paper #901(2010)
67. X. Shen, S. Lei, in *Proceedings of IMECE2005, ASME International Mechanical Engineering Congress and Exposition*, (2005)
68. X. Shen, S. Lei, *J. Manuf. Sci. Eng.* **131**, 051007-1-10 (2009)
69. Y. Tian, B. Wu, M. Anderson, Y.C. Shin, *J. Manuf. Sci. Eng.* **130**, 1–9 (2008)
70. M.F. Zaeh, R. Wiedenmann, R. Daub, *Physics Procedia, Laser Assisted Net Shape Engineering 6, Proceedings of the LANE 2010, Part 2*, vol. 5 (2010), pp. 353–362
71. B. Yang, S. Lei, *Int. J. Mechatron. Manuf. Syst.* **1**, 116–130 (2008)
72. Y.C. Shin, US Patent 0062920, A1, 2007
73. M.C. Shaw, *Metal Cutting Principles* (Clarendon Press, Oxford, 2005) pp. 22–24.
74. S. Lei, Y.C. Shin, F.P. Incropera, *Int. J. Mach. Tools Manuf.* **40**, 2213–2233 (2000)
75. P.A. Rebroy, Y.C. Shin, F.P. Incropera, *J. Manuf. Sci. Eng.* **124**, 875–885 (2002)
76. F.E. Pfefferkorn, Y.C. Shin, F.P. Incropera, Y. Tian, *J. Manuf. Sci. Eng.* **126**, 42–51 (2004)
77. J.C. Rozzi, F.E. Pfefferkorn, Y.C. Shin, F.P. Incropera, *J. Manuf. Sci. Eng.* **122**, 666–670 (2000)
78. S. Lei, Y.C. Shin, F.P. Incropera, *J. Manuf. Sci. Eng.* **123**, 639–646 (2001)
79. F. Klocke, T. Bergs, *Proc. SPIE Rapid Prototyping Flex. Manuf.* **3102**, 120–130 (1997)
80. S. Sun, J. Harris, M. Brandt, *Adv. Eng. Mater.* **10**, 565–572 (2008)
81. W.B. Salem, G. Marot, A. Moisan, J.P. Longuemard, in *Proceedings of the LANE'94, Laser Assisted Net Shape Engineering*, (1994), pp. 455–464
82. G. Germain, J.L. Lebrun, T. Braham-Bouchnak, D. Bellett, S. Auger, *Int. J. Mater. Form* **1**(suppl 1), 523–526 (2008)
83. H. Attia, S. Tavakoli, R. Vargas, V. Thomson, *CIRP Ann. Manuf. Technol.* **59**, 83–88 (2010)
84. Y. Jeon, F. Pfefferkorn, *J. Manuf. Sci. Eng.*, **130**: 011004-1-9 (2008)
85. K. Armitage, Thesis for Master of Engineering, Swinburne University of Technology, 2005
86. G. Germain, J.-L. Lebrun, P. Robert, P.D. Santo, A. Poitou, *Int. J. Form. Proc.* **8**, 347–361 (2005)
87. K. Sakai, Y. Suzuki, in *Proceedings of the 24th International Congress on Applications of Lasers and Electro-Optics*, (2005), pp. 719–722.
88. B. Shi, H. Attia, R. Vargas, S. Tavakoli, *Mach. Sci. Technol.* **12**, 498–513 (2008)
89. J. Walter, R. Ritz, in *Proceedings of the LANE 2004, Laser Assisted Net Shape Engineering*, vol. 4, (2004), pp. 1157–1164
90. S. Sun, J. Harris, Y. Durand, M. Brandt, in *Proceedings of the 3rd Pacific International Conference on Application of Lasers and Optics*, (2008)
91. R. Singh, S.N. Melkote, *Int. J. Mach. Tools Manuf.* **47**, 1139–1150 (2007)
92. E. Kannatey-Asibu, *Principles of Laser Materials Processing* (Wiley, Hoboken, 2009) pp. 489–491.
93. Y. Wang, L.J. Yang, N.J. Wang, *J. Mater. Process. Technol.* **129**, 268–272 (2002)

94. P.A. Rebro, F.E. Pfefferkorn, Y.C. Shin, F.P. Incropera, *Trans. North Am. Manuf. Res. Inst. SME* **30**, 153–160 (2002)
95. K.J. Bowman, F.E. Pfefferkorn, Y.C. Shin, *Mater. Sci. Forum* **408–412**, 1669–1674 (2002)
96. R. Komanduri, *Wear* **76**, 15–34 (1982)
97. R. Komanduri, Z.-B. Hou, *Metall. Mater. Trans. A* **33**, 2995–3010 (2002)
98. R. Komanduri, T.A. Schroeder, *J. Eng. Ind.* **108**, 93–100 (1986)
99. S. Ekinovic, S. Dolinsek, I.S. Jawahir, *Mach. Sci. Technol.* **8**, 327–340 (2004)
100. J. Barry, G. Byrne, *Proc. Inst. Mech. Eng: Part B J. Eng. Manuf.* **215**, 1549–1559 (2001)
101. A.E. Bayoumi, J.Q. Xie, *Mater. Sci. Eng. A* **190**, 173–180 (1995)
102. S. Sun, M. Brandt, M.S. Dargusch, *Int. J. Mach. Tools Manuf.* **49**, 561–568 (2009)
103. A.K.M.N. Amin, I. Abraham, N. Khairusshima, M.I. Ahmed, *J. Mater. Process. Technol.* **185**, 97–105 (2007)
104. S. Sun, M. Brandt, M.S. Dargusch, *Metall. Mater. Trans. A* **41**, 1573–1581 (2010)
105. B. Lesourd, F. Le Maître, T. Thomas, *Manuf. Sys.* **24**, 279–286 (1995)
106. A. Vyas, M.C. Shaw, *J. Manuf. Sci. Eng.* **211**, 163–172 (1999)
107. F.E. Gorczyca, *Application of Metal Cutting Theory* (Industrial Press Inc, New York, 1987) pp. 149–59.
108. K. Ogawa, *JSME Int. J. A* **46**, 322–327 (2003)
109. B.M. Kramer, *J. Eng. Ind.* **109**, 87–91 (1987)
110. E.A. Almond, in *Proceedings of International Conference on Improved Performance of Tool Materials*, (1981), pp. 161–169
111. C.-W. Chang, C.-P. Kuo, *Int. J. Mach. Tools Manuf.* **47**, 141–147 (2007)
112. P.A. Dearnley, A.N. Grearson, *Mater. Sci. Technol.* **2**, 47–58 (1986)
113. J.E. Barnes, Y.C. Shin, M. Brandt, S. Sun, *Mater. Sci. Forum* **618–619**, 159–163 (2009)
114. S. Sun, M. Brandt, J.E. Barnes, M.S. Dargusch, in *Proceedings of the 36th MATADOR International Conference*, (2010), pp. 255–258
115. S. Barnes, I.R. Pashby, D.K. Mok, *J. Manuf. Sci. Eng.* **118**, 422–427 (1996)
116. J.W. Jung, C.M. Lee, in *Proceedings of the International Multi Conference of Engineers and Computer Scientists*, (2009)
117. B. Yang, T. Deines, C. Geist, S. Lei, *Trans. North Am. Manuf. Res. Inst. SME* **35**, 473–480 (2007)
118. B. Yang, X. Shen, S. Lei, *Int. J. Mach. Tools Manuf.* **49**, 344–350 (2009)
119. S. Melkote, M. Kumar, F. Hashimoto, G. Lahoti, *CIRP Ann. Manuf. Technol.* **58**, 45–48 (2009)
120. Y. Tian, Y.C. Shin, *J. Am. Ceram. Soc.* **89**, 3397–3405 (2006)
121. G. Germain, F. Morel, J.-L. Lebrun, A. Morel, B. Huneau, *Mater. Sci. Forum* **524–525**, 569–574 (2006)
122. F.E. Pfefferkorn, S. Lei, Y. Jeon, G. Haddad, *Int. J. Mach. Tools Manuf.* **49**, 357–365 (2009)
123. Y. Tian, Y.C. Shin, *J. Manuf. Sci. Eng.* **129**, 287–295 (2007)
124. X. Shen, B. Yang, S. Lei, *J. Manuf. Process.* **12**, 30–37 (2010)
125. B. Yang, X. Shen, S. Lei, *Int. J. Manuf. Res.* **4**, 74–94 (2009)

Chapter 4

Laser-Based Joining of Metallic and Non-Metallic Materials

G. Padmanabham and B. Shanmugarajan

Abstract Laser as a high intensity heat source can be effectively used for joining of materials by fusion welding and brazing in autogenous or in hybrid modes. In autogenous mode, welding is done in conduction, deep penetration, and keyhole mode. However, due to inherently high energy density available from a laser source, autogenous keyhole welding is the most popular laser welding mode. But, it has certain limitations like need for extremely good joint fit-up, formation of very hard welds in steel, keyhole instability, loss of alloying elements, etc. To overcome these limitations, innovative variants such as laser-arc hybrid welding, induction-assisted welding, dual beam welding, etc., have been developed. Using laser heat, brazing can be performed by melting a filler to fill the joints, without melting the base materials. Accomplishing laser-based joining as mentioned above requires appropriate choice of laser source, beam delivery system, processing head with appropriate optics and accessories. Basic principles of various laser-based joining processes, laser system technology, process parameters, metallurgical effects on different base materials, joint performance, and applications are explained in this chapter.

G. Padmanabham (✉)
Centre for Laser Processing of Materials (CLPM),
International Advanced Research Centre for
Powder Metallurgy and New Materials (ARCI),
Balapur Post, Hyderabad 500 005, India
e-mail: gp@arci.res.in

B. Shanmugarajan
Welding Research Institute, Bharat Heavy Electricals Limited (BHEL),
Tiruchhirappally, 620 014, India
e-mail: bshanmu1978@yahoo.com

4.1 Introduction

Laser welding and laser-assisted joining techniques have found good acceptance to meet the joining needs in several sectors including automobile, medical, electronic, energy, aerospace, shipbuilding, oil pipelines, etc. In the year 2006, out of all the laser materials processing application units sold worldwide include cutting, welding, drilling, surface treatment, marking and engraving, microprocessing, laser welding systems constituted 12% [1]. With the advent of combined lasers with high power, high beam quality and robustness, the number of laser welding applications is increasing further. While autogenous laser keyhole welding has been in use for quite some time, laser hybrid welding and brazing processes are developed only during the last decade or so. Before going into further analysis of ‘Why laser?’ for welding or joining, it may be a good idea to recall the definition of ‘Weldability’ and then correlate expectations to advantages lasers can offer. “Weldability is the ease of a material or a combination of materials to be welded under fabrication conditions into a specific, suitably designed structure, and to perform satisfactorily in the intended service” [2]. Material properties, practical feasibility, satisfactory performance are the key factors to be considered for achieving successful weld joints. Figure 4.1 compares laser welding with conventional welding process in terms of power density and consequent effects on important factors such as depth of penetration, welding speed, and heat affected zone size [3]. Following are the typical advantages of using laser as a heat source:

- (1) Availability of high power densities. Laser keyhole welding is performed at power densities $> 10^6$ W/cm² whereas conventional arc welding processes can offer power densities in the range 10^4 W/cm². Consequently, laser welding has the following major advantages and related positive effects, such as,
 - deep and narrow fusion zone with aspect ratios 10:1-enabling
 - welding thick sections;
 - welding with one-side accessibility; and
 - ease of shielding as the weld zone is small
 - high welding speed and simple joint design which results in high productivity
 - low and precise heat input resulting small heat-affected zone (HAZ), less thermal distortion
 - possibility to weld a wide range of materials and dissimilar materials.
- (2) Process flexibility and amenability to automation.
- (3) Can be reached to inaccessible places using flexible optical fibers and suitable focusing optics, and,
- (4) Non-contact zero-force processing (i.e., no tool wear-related problems like in case of solid-state processes like friction stir welding, and no contamination issues like in the case of tungsten inclusion in TIG welding).

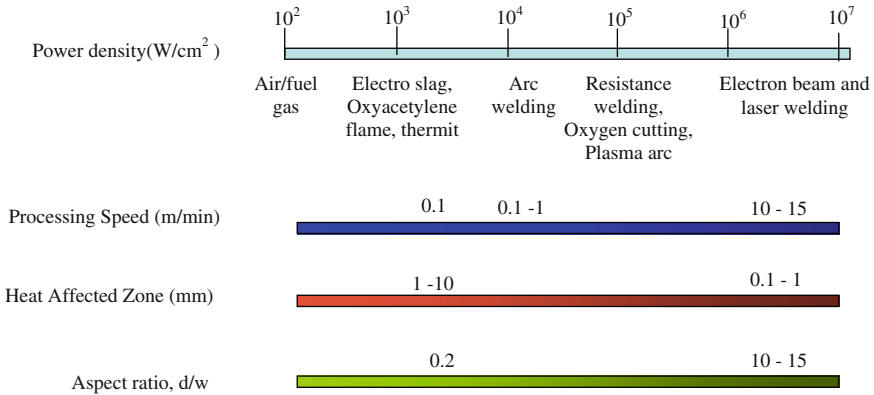


Fig. 4.1 Effect of power density on welding process and performance [3]

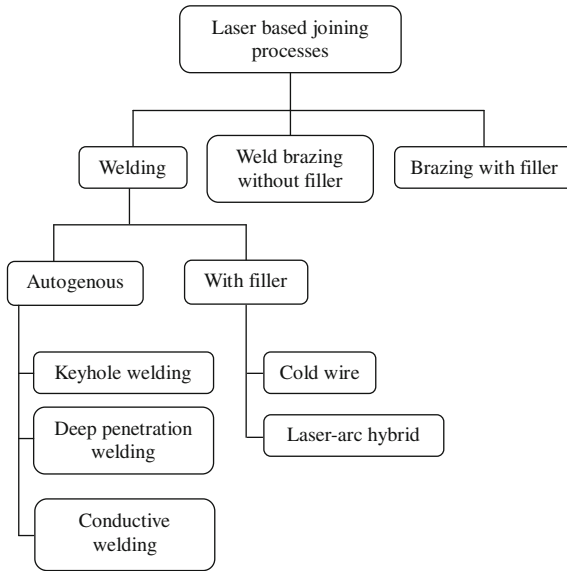


Fig. 4.2 Classification of laser based joining processes

4.2 Classification of Laser-Based Joining Processes

The classification of laser-based joining processes is presented in Fig. 4.2.

When a laser beam alone is used to fuse the materials to be joined, the process is called autogenous welding. No filler material is used. Depending on the intensity available from the laser source, the welding is carried out in different modes namely, conduction, deep penetration, and keyhole welding. Typical shape of conduction, deep penetration, and keyhole weld cross-sections are shown in Fig. 4.3 [4].

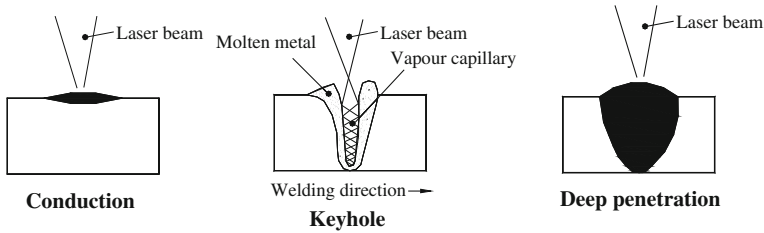


Fig. 4.3 Weld geometry in different laser welding modes [4]

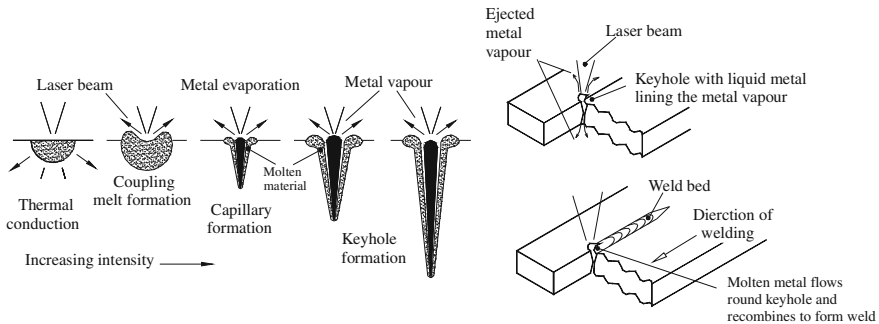


Fig. 4.4 Stages of keyhole formation [5]

As high beam intensities are available from lasers, autogenous keyhole welding is the most popular laser welding method. So, the next few sections are devoted to this method in terms of its principles, laser characteristics, advantages, and limitations. Subsequently, other laser-based joining processes will be described.

4.3 Principle of Keyhole and Factors Affecting Keyhole Stability

At higher intensities where energy deposited in the weld zone exceeds the transfer of energy through conduction in the work piece or other heat transfer modes, the metal starts vaporizing. The vapor pressure creates a dip in the center of the melt pool with molten metal lining the pool. Due to temperature differentials, the surface tension of molten metal is different in different locations and the molten metal in the central portion tends to flow up deepening the dip until a through hole is formed in the metal. This is called a keyhole which is capable of trapping the energy of the laser beam in the form of cylinder extending from top to bottom of the metal plate. Stages of keyhole formation are shown in Fig. 4.4 [5].

As the keyhole moves along the weld seam it melts the material in front and deposits behind, forming the joint. Quality of the weld obtained depends on the stability of the keyhole as well as the transport of the molten metal from the front

to the back by moving around the keyhole. The keyhole is sustained by balance of forces keeping it open and forces tries to close it. The hydrostatic pressure and surface tension trying to close it and the vapor pressure inside the keyhole tries to keep it open. This pressure is dependent on the size of the keyhole viz., its radius and depth. Keyhole geometry is estimated by considering appropriate energy and pressure balances [6]. The energy balance takes into account heat loss due to conduction, energy for ablation, and evaporation effects at the open surfaces of the keyhole as well as Fresnel absorption and inverse Bremsstrahlung. A time-dependent model of the behavior of the front keyhole wall during high translation speed laser welding was constructed by Matsunawa and Semak [7]. When the translational speed of the keyhole wall was higher than welding speed, humping on the weld bead was observed.

So, any factors affecting the laser intensity, surface tension of the molten metal, vapor pressure, size of the weld pool, welding speed, and properties of the shielding gases can affect the keyhole dynamics. Hence, in order to obtain good quality welds, optimization of the welding conditions is required for specific combination of laser parameters, material to be welded, and the shielding conditions. While, steels do not pose much problem to keyhole stability, materials such as aluminum alloys with low viscosity of the melt show high sensitivity to keyhole stability.

4.4 Lasers and System Technology for Welding

Most widely used lasers for welding are the CO₂ and the Nd:YAG. The CO₂ laser is characterized by the far infrared (10.64 μm) wavelength and is commercially available up to 20kW of power. The far infrared output wavelength of the CO₂ laser has an initial reflectance of about 85% for steel and more than 95% for metals such as aluminum, copper, and silver. Nd:YAG lasers produce light in the 1.064 μm wavelength and generate powers up to 6kW. This wavelength is absorbed better than CO₂ laser, with a typical reflectance of about 60–75% for materials such as steels and 75–90% for aluminum, copper, and silver. Pulsed Nd:YAG lasers are an important category of welding lasers especially for applications where precise control of heat input is required. Pulsed lasers can produce high peak energies for a short duration at a low average power. For example, a 400 W average power Nd:YAG laser can generate pulses with peak powers as high as 5kW with a pulse duration of 4ms. While the high peak powers enable easy coupling with many materials, possibility to control energy input into the process can be achieved by choosing low pulse duration and pulse energy. During the last decade or so, disk lasers, fiber lasers, and diode lasers, are also used for laser welding applications. Disk lasers are Yb:YAG solid-state lasers with good beam quality up to 16kW of power. The lasing medium is in the form of thin disk instead of a rod as in the case of Nd:YAG laser. Because of this configuration it is possible to cool the lasing medium more efficiently and the thermal lensing effect in the rod-shaped lasing medium as in the case of Nd:YAG lasers is avoided. In fiber lasers, the lasing takes place within the fiber itself and

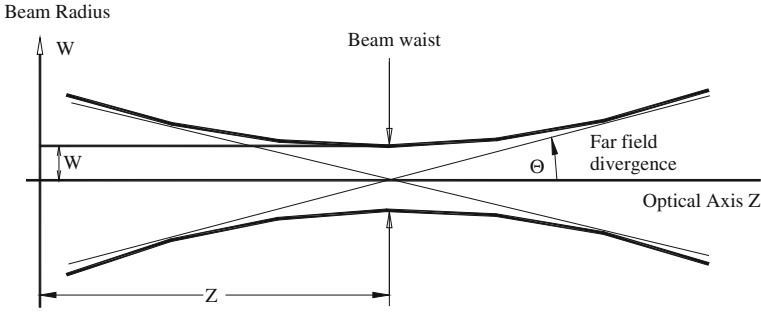


Fig. 4.5 Laserbeam quality parameters

no alignment problems are encountered. Very high quality beams with focusability to very fine spots are possible and at the same time high powers are also available from fiber lasers. Diode lasers are characterized by focusing of arrays of emitted light from diodes to obtain a laser beam. With the possibility of bunching them into fibers of diameters up to 400 μm , it is now possible to efficiently weld with diode lasers. However, very limited applications benefit from such beams. However, they play vital role in laser brazing technology.

Laser welding is usually carried out in autogenous mode taking advantage of high power density available for obtaining high depth of penetration and welding speeds. High power density is available either by having higher power or smaller laser spot size. Availability of high power with high focusability of the beam would be an ideal combination to obtain deep penetration and high welding speeds. Focusability is dependent on the beam quality which is indicated by the beam parameter product (BPP-beam radius \times divergence) measured in terms of mm mrad (W and θ in Fig. 4.5). Radius of the beam spot (r_{foc}) at the focal plane is dependent on focusability of the beam, raw beam spot size, wavelength of the laser, and focal length of the focusing optics (Fig. 4.6) given by the relation,

$$r_{\text{foc}} = f \times \lambda / (r \times \pi \times K) \quad (4.1)$$

where, f is the focal length of the focusing optics, λ is the wavelength of the laser, r is the radius of the raw beam, and K is the beam quality (also indicated by a term M^2). The spot size is the smallest in the focal plane and increases in a plane above or below the focal plane.

The distance between the planes above and below the focal plane wherein the radius of the spot does not change beyond $\sqrt{2}$ times the r_{foc} is called the Rayleigh length or depth of focus (DOF). While welding, if the focal plane position is maintained in this DOF, the beam intensity will be more consistent, consequently more consistent results.

Quality of beams available from different lasers and their relative performance as welding lasers (measured in terms of depth of penetration achievable at different welding speeds) is shown in Fig. 4.7a, b [8]. As can be seen from Fig. 4.7a, CO_2

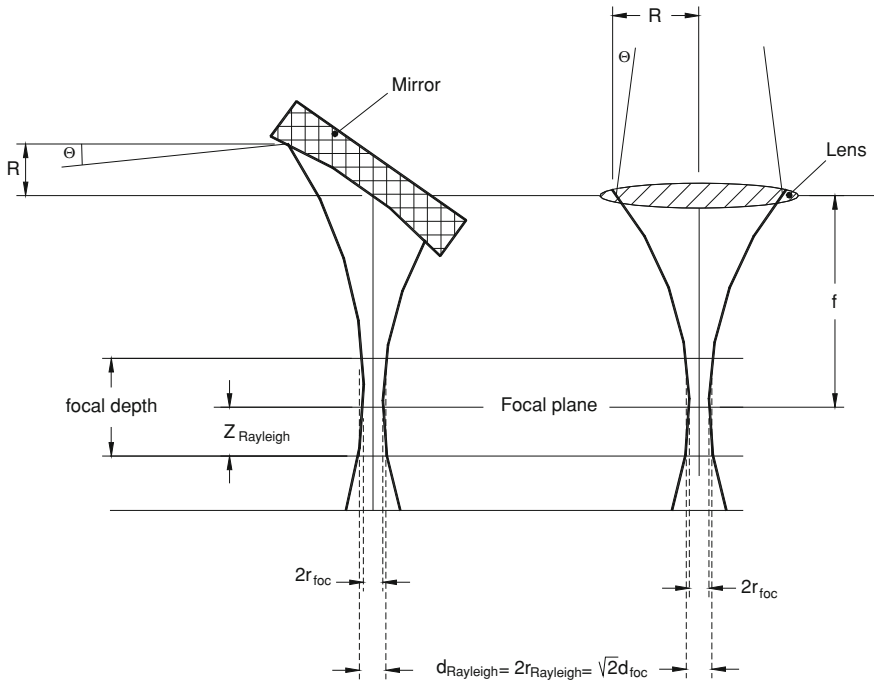


Fig. 4.6 Laserbeam radius at focal radius and depth

lasers, disk lasers, and fiber lasers maintain high beam quality even up to powers as high as 10 kW making them suitable for welding thick sections as well. Nd:YAG laser gives a good beam quality up to 1 kW making it suitable for applications in 2–3 mm thickness range. Diode lasers in general have poor beam quality compared to other lasers. Performance of different lasers/beam qualities in terms of depth of penetration and welding speed combination is shown in Fig. 4.7b [8].

As expected, beams with high quality yield higher penetration for a given welding speed or higher welding speed for a given depth of penetration. While, this explanation holds good for mild steel materials, same may not be true for welding other materials such as aluminum due to reflectivity of these materials to certain wavelengths. Choice of a particular laser for welding depends on depth of penetration, welding speed, material, part geometry, joint fit-up and application, or integration requirements.

Depth of penetration depends on power density which in turn is dependent on laser power and beam quality. CO₂ lasers offer high powers with good beam quality enabling higher depth of penetration. Nd:YAG lasers offer high beam quality only up to 1 kW or so and hence cannot be very useful for obtaining higher depth of penetration. Newly developed solid-state lasers such as the disk lasers and fiber lasers offer high power densities and good beam quality. Welding speed is important for productivity and if high welding speeds are required high power densities are

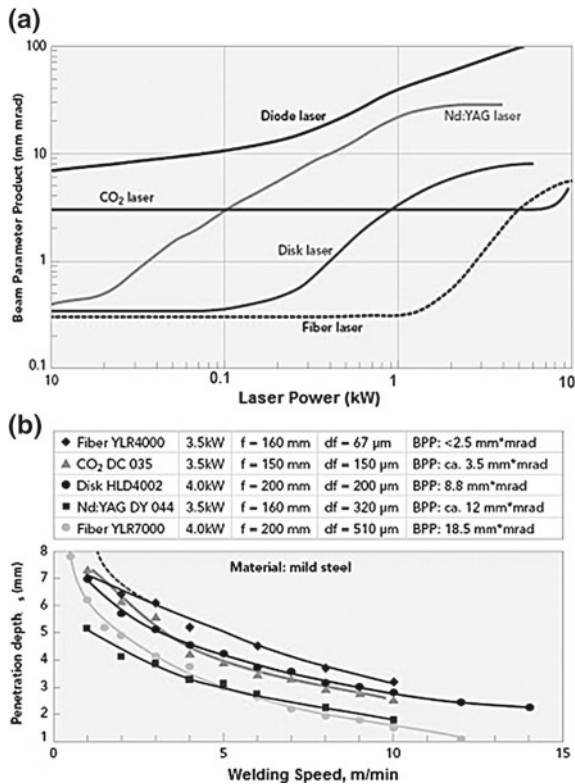


Fig.4.7 Beam qualities of **a** different lasers across power ranges, and **b** its effect on welding performance [8]

needed. With regard to material as a factor, for welding using laser, the laser energy should be absorbed into the parts to be welded in order to create sufficient heating to develop the melt pool.

In case of metals, reflectivity increases with wavelength of the laser beam used. Reflectivity of metals for laser wavelengths in 0.4–11 μm range is very high. Because of this, net absorption is often less than 10% (Fig. 4.8). However, molten metal has better absorption. Hence, the initial high value of reflectivity and associated loss of energy can be overcome if somehow melting can be initiated on the surface of the metal. This process of overcoming the base metal reflectivity is called ‘coupling’. Another advantage of creating the melt puddle is the geometry it takes due to laser beam impinging on it. The puddle is lower at the center and rises at the edges. This is due to the melt surface tension, which varies with temperature. As the surface tension is lower in the middle compared to the cooler edges, and metal vapor is boiling off, the melt is exerting a recoil pressure on the melt puddle causing molten metal in the center to go to the edges. Net result is formation of a crater shape. Any laser light

that is not absorbed is reflected within melt puddle providing multiple opportunities for absorption. This further increases the crater depth, finally maximizing the energy absorption (even up to 95%). Reflectivity is not a serious problem with reference to all ferrous alloys, nickel alloys, titanium alloys, zirconium alloys, and other refractory alloys. Power as low as 500 watts may be sufficient to induce coupling. However, aluminum alloys, copper, silver, gold are highly reflective and restrict the range of lasers that can be used for welding. Low power CO₂ lasers will not be capable of overcoming the reflectivity. But, similar power Nd:YAG laser would be useful due to lower wavelength. Once, the laser coupling is successfully done, it is the thermal properties of the material that will dictate the welding process, as they will decide the temperature rise and the melting behavior. Even in case of conventional welding processes, these properties directly affect the weld characteristics. Specific attributes of interest to laser welding are the melting point, boiling point, latent heat of fusion, heat capacity, density, and thermal conductivity. A combination of the last three factors ($K/\rho C_p$) is called the 'Thermal diffusivity (κ)'. It is a measure of the ability of the material to conduct heat. The lower the diffusivity, the more the heat remains in the vicinity of the laser beam spot. So, any metal, which has high thermal conductivity and low values of density and heat capacity, will conduct away heat much faster and more energy per unit time will be required to create and sustain the melt puddle. For example, thermal diffusivity of copper and iron are 1.14 and 0.208 (cm²/s), respectively. That means welding of copper will require more than 5 times the power density required for welding iron.

Although the melting point of metals does not have a significant effect on laser weldability, it must be reached during the initial absorption of energy. Thus, in comparison to high melting point materials, those with low melting points are easier to weld with a laser. Metals with low boiling points produce a large amount of metal vapor, which could initiate gas breakdown and plasma generation in the region of high beam intensity just above the metal surface. This plasma, which readily absorbs the laser energy, can block the beam especially with far infrared lasers, and bubbles tend to form at the root of the weld. If the viscosity is high, these bubbles do not escape before the molten metal solidifies. Application requirements sometimes require welding in inaccessible locations. In such cases, laser beams of Nd:YAG, disk and fiber lasers which can be transmitted through fiber optic cable are preferred.

4.5 Laser Welding Parameters

In view of the foregoing, the significance of various laser welding parameters is briefly summarized as follows [9]:

Wavelength: Absorptivity of laser energy by the metal varies with wavelength (Fig. 4.8) [10]. Shorter the wavelength better the absorptivity. This enables coupling with a given material at lower threshold power densities. Focusability of the beam is also better with shorter wavelength (Eq. 4.1). This enables attainment of high

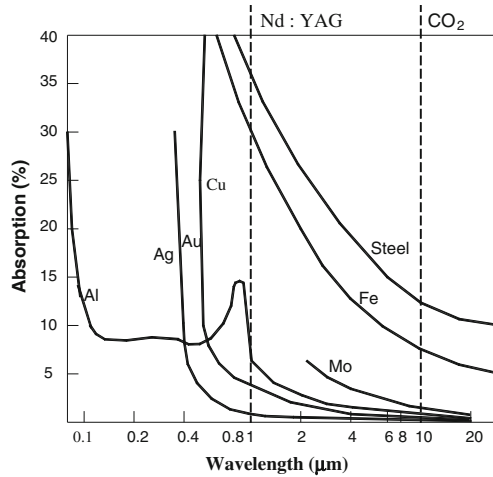


Fig. 4.8 Absorptivity of laser energy of different wave lengths by various metals [10]

power densities for a given power. These two direct advantages widen the processing window for formation of a keyhole. Shorter wavelengths also have advantage in terms of plasma effects (absorption and trapping of energy in the plasma above the keyhole). Plasma effects are less for shorter wavelengths as absorptive coefficient in plasma scales with the square of the wavelength. Consequently, for similar power, and spot size Nd:YAG laser can weld faster than CO₂ laser. However, as explained earlier, beam quality in Nd:YAG lasers deteriorates at higher powers due to thermal lensing effects and are limited in terms of highest power available. But, these issues are taken care of in the newly developed disk lasers and fiber lasers.

Power: It is crucial to achieve keyhole formation. Availability of higher power enlarges the window of operation covering various materials including ones with high reflectivity like aluminum and thicker materials at good speeds. But, laser-induced plasma or plume emanated from the keyhole could be high and needs to be managed better at higher powers.

Spot size: Spot size directly decides the power density. While smaller spot sizes give higher power density, which is very useful, it may create other problems like the need for extremely accurate joint fit up. Recommended spot size for butt-weld widths during keyhole welding is 30% of the weld width in the range 0.1–1.0 mm with 0.3 mm being the most common one.

Focal length: Shorter the focal length smaller the waist diameter and DOF and larger the divergence angle. This situation is less tolerant to work piece positioning. It can also generate spatter, vapor damage to optics, etc. Usually, focusing optics with 100–200 mm focal lengths are used.

Depth of focus (DOF): It is the allowable distance the part can deviate from the point of best focus for acceptable weld quality. When welding higher thickness sections, higher DOF is useful.

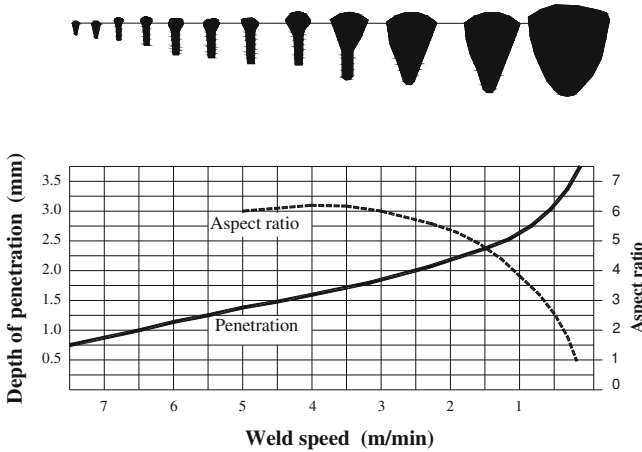


Fig. 4.9 Effect of welding speed on depth of penetration and weld aspect ratio [4]

Focal plane position: Focal plane is the plane in which the laser beam waist diameter is minimum. It should be positioned in such a way that the beam can produce maximum depth of penetration with the possibility of best process tolerances. Focusing above the surface (positive focusing) may result in more plasma and less energy reaching the keyhole. Focusing below the surface (negative focusing) can optimize coupling efficiency as well as increase energy absorption inside the weld pool through multiple reflections. Consequently, the threshold power density is lower for negative focusing compared to positive focusing. By slight defocusing into the work piece, higher depth of penetration and welding speeds also can be achieved.

Welding Speed: As the process speed increases, the keyhole depth decreases but the weld geometry retains a nail head shape. But, as the speed decreases, the keyhole depth increases only to a particular limit. Beyond this point, only the weld width increases due to increased localized heating which results in conduction. This essentially means, as the welding speed decreases the depth of penetration increases to a certain extent and later, only the weld width increases, resulting in decrease in depth/width ratio (Fig. 4.9) [4].

Higher welding speeds have additional advantages in terms of minimal evaporation of alloying elements and more refined grains structure in the fusion zone. However, the demand for quality control also proportionally increases with increasing welding speed.

Shield gas: In conventional welding process, inert gas shielding is provided in the weld zone, to avoid oxidation of the weld metal or contamination of the weld metal by adversely affecting materials in the nearby zones such as moisture, oil/grease, or other possible contaminants. However, laser welding has a few advantages over conventional arc welding processes. As the seam widths are small, shielding becomes easier. In autogenous mode, there is no filler wire added eliminating the possibility of contamination, if any, from the filler wire droplets. Higher welding speeds often do

not allow reaction of the gases with the weld pool or post weld reactions. However, the shielding gas is exposed to high temperatures about 10000 K and get dissociated, ionized, and activated and the extent of their interaction with the weld zone varies with the type of gas, temperatures reached, and the time for which exposed to high temperature. Accordingly, in laser welding, shielding gas has additional functions to be performed, such as, protecting the optic lenses from weld spatter and fumes, suppression of plasma, especially in CO₂ laser wavelength to take care of instabilities of the vapor-filled keyhole, reduced penetration and increased coarse porosity, etc. Poorly shielded weld exhibits porosity, undercut, and bead roughness. With filler metal, weld pool is larger and longer than in autogenous welding, necessitating better shielding. Various shielding gases and their applicability on laser welding, relative advantages, and limitations are given in Table 4.1.

Surface condition: This attains more importance in laser welding compared to conventional welding processes. Laser welding creates a very fast melting rate in the weld and contaminants can create local areas of poor metallurgy, or if the contaminants are volatile, it will create explosive metal loss in the weld. The very low heat input and autogenous nature of the laser welding results in very little molten metal volume to reflow and very little time for that small volume to flow into any flaws. Surface roughness of the work piece and surface contaminants increase absorptivity [11]. While roughening, the surface can be advantageously used (Fig. 4.10a,b), surface contaminants can have adverse effects on weld properties, such as oxide inclusions in steel and porosity in aluminum welds [11].

Joint design and fit-up: Butt and lap-joints are the mostly used designs for laser welding among various possible designs including fillet, coach, standing edge, etc. Because of the highly precise energy beam, joint fit-up attains high importance in laser butt welding. For example, in Nd:YAG laser welding typical tolerances allowed are maximum gap -0.1 mm (or 10% of material thickness); focus position ± 1 mm; vertical mismatch < 0.2 mm. Effect of poor fit-up is shown in Fig. 4.11 [12].

4.6 Pulsed Laser Welding

Pulsing involves cycling of laser power on and off between high power short on-time and an off-time. A typical laser pulse is shown schematically in Fig. 4.12 [13], where P_M mean laser Power (kW), E_P the pulse energy (J), T_P is the pulse duration (ms), T_F the pulse-to-pulse time (ms), PRR is the pulse repetition rate (s^{-1}). Laser beam and welding parameters are the spot area (D) in mm^2 and the welding speed (V) in mm/s. Basic pulse parameters can also be seen from this Fig. 4.12 [13]. Derived parameters from the above basic parameters are:

- P_P peak power (kW) = pulse energy (J) / pulse duration (ms) = E_P/T_P
- P_D power density (kW/mm^2) = peak power (kW) / spot area (mm^2) = P_P/D
- P_M mean laser Power (kW) = E_P pulse energy (J) x pulse repetition rate (Hz)
- C_D Duty cycle = T_P/T_F

Table 4.1 Shielding gases used in laser welding and their characteristics

Gas	Ionization potential (eV)	Plasma suppression	Shielding efficiency	Weld penetration	Cost	Limitations
Ar	15.7	Good	Best	Good	Good	Heavy gas flow rate to be controlled
He	24.5	Best	Good	Best	Bad	Expensive
Ar + He	-	Better	Better	Good	Good	Deep penetration can be achieved with He only
N ₂	15.5	Good	Good	Better	Better	Cracking in hard materials
CO ₂	14.4	Good	Bad	Good	Best	Oxidation with reactive materials and sensitization issue in austenitic stainless steel

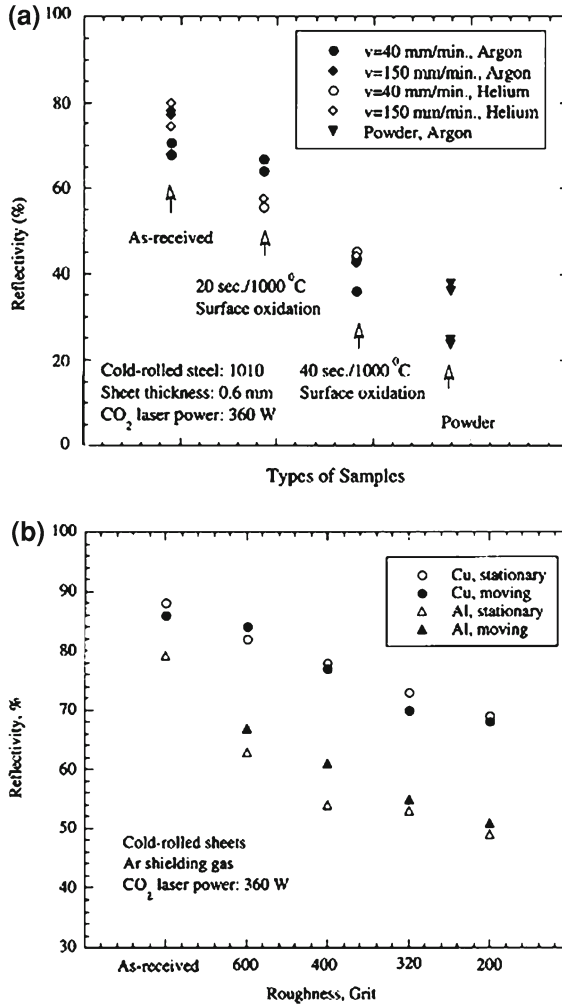


Fig.4.10 Reflectivity of Cu and Al to laser. **a** Effect of surface contamination, and **b** effect of surface roughness [11]

P_D is set by fixing values of E_P and T_P for a particular spot area (D). Higher peak power density is helpful in initial coupling with reflective materials like aluminum and also enables keyhole formation. Pulse duration is useful in controlling the interaction time with the material. The duty cycle and pulse repetition rate control the overall heat input into the weld and pulse repetition rate determines the welding speed in order to get sufficient overlapping of the spots created by the pulses in order to form a weld seam. The combination of these parameters will mainly determine the temperature distribution of the laser-treated work piece. A detailed parametric analysis of various parameters indicated that heating effects are increased with an increase in pulse

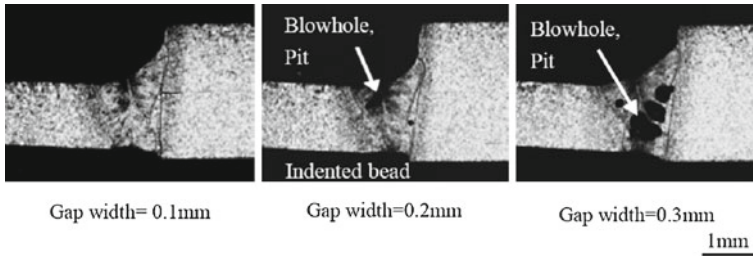


Fig. 4.11 Effect of joint gap on weld quality [12]

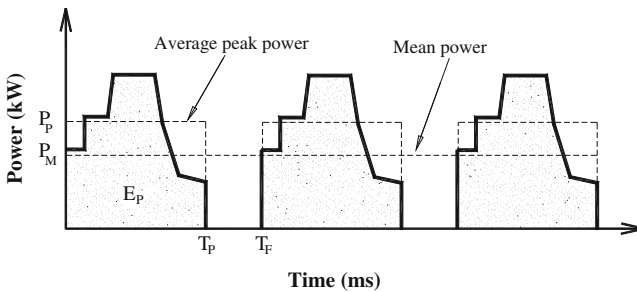


Fig. 4.12 Schematic of typical laser pulse and related parameters [13]

duration for a given mean power, travel speed and peak power density, and enhanced by peak power density when the mean power and travel speed are kept constant [13].

The high power pulses melt and vaporize the material during on-time and the metal solidifies during the off-time until next pulse comes in. The weld results from a series of overlapping spot welds. The frequency at which pulses are generated is called the repetition rate. Therefore, pulse repetition rate is critical and directly dependent on welding speed. If the pulse repetition rate is too high the welding process will be similar to continuous wave welding. Pulsed welding offers the advantage of very low heat input to the weld, resulting in low distortion, ability to weld heat-sensitive components, and precision welding of finished components. The process also results in high heating and cooling rate cycles. This may some times restrict the use of pulsed welding, for example, while welding solidification cracking sensitive aluminum alloys.

The power of pulsed lasers is defined by average power. The power during the pulse is called the peak power and the duration of pulse is called the pulse width. Laser systems are now available with capability of shaping the pulse itself. That is variation of power within a pulse. Different types of pulse shapes are shown in Fig. 4.13 [14].

Each of the above pulse shapes can be effectively used in particular welding conditions. For example, the cool-down shape is very useful in reducing the cooling rate by continuously supplying heat after the welding peak. This enables

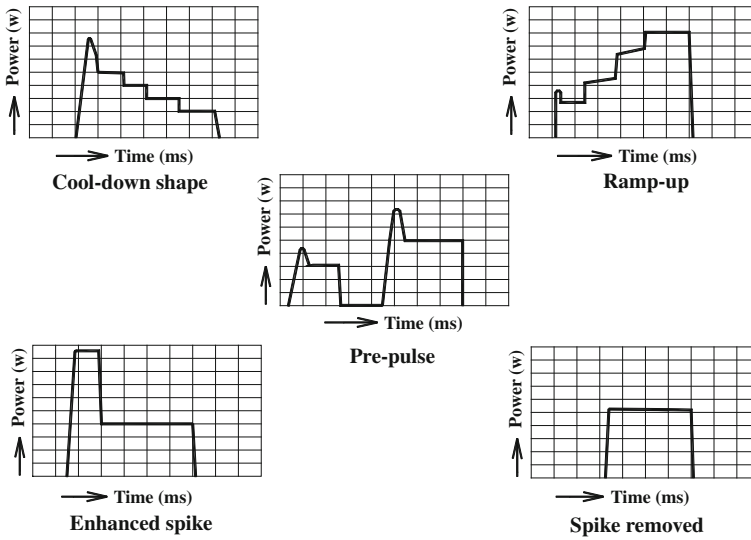


Fig. 4.13 Different types of pulse shaping [14]

welding of crack-sensitive alloys and dissimilar materials. Enhanced spike can be useful in initial coupling while welding reflective materials. The effect of pulse shaping on solidification cracking susceptible steel is shown in Fig. 4.14 [15].

Two other types of pulsing are shown in Fig. 4.15 [16]. One is modulated pulsing, where in a particular peak power as limited by the laser is fixed and the duty cycle changes to include an off-time. Here, the peak power densities are not very high. But, can be useful in controlling the heat input into the weld. Figure 4.15c shows sine wave-like variation in power during the process [16].

4.7 Laser Welding of Different Materials

4.7.1 Laser Welding of Steels

Weldability of carbon and alloy steels is dependent on the carbon equivalent. Higher the carbon equivalent higher the tendency for cold cracking. This limit is lower when laser welding is used, as the cooling rates are very high and the weld fusion zone has very high hard martensitic phases.

Carbon steels: Steels with $< 0.3\%$ carbon equivalent are highly weldable. Steels with higher carbon equivalent have cold cracking propensity. A weld joint which minimizes shrinkage and related stresses in the fusion zone and heat affected zone can minimize cracking in such steels. Reducing the quench rate could also be useful.

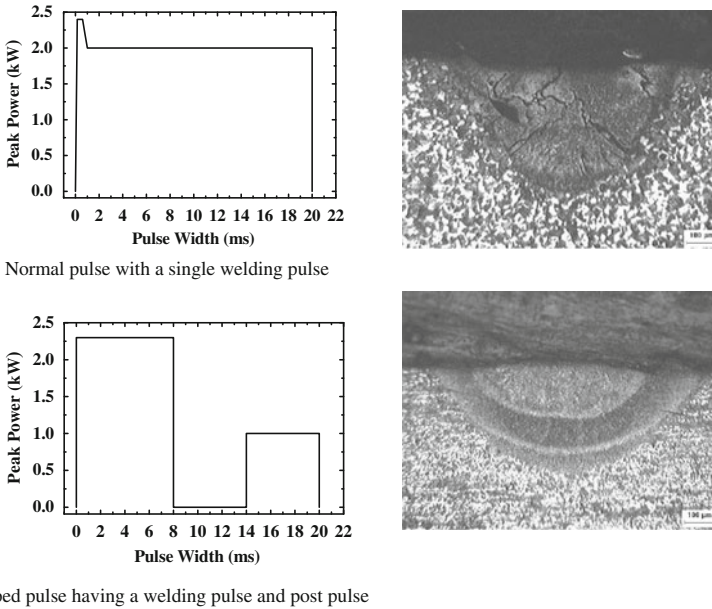


Fig. 4.14 Effect of pulse shaping on solidification cracking susceptibility [15]

Preheating using an additional defocused beam and welding at lower powers and lower speeds may be applied.

Galvanised steel sheets: Galvanized steels overlap welding suffers heavily from porosity caused by Zn vapors. Providing an exhaust path for the vapors and minimizing the Zn evaporation by reducing spot size are possible solutions. A gap of 0.1–0.2 mm is intentionally maintained in the overlap region for escape of the zinc vapor. Recently, a very innovative method of laser welding of galvanized steels with zero gap has been reported [17], where in two laser beams are used to extend the keyhole in such a fashion that the zinc vapors have a suitable keyhole profile to escape from the weld zone (Fig. 4.16) [17].

In this method, a 4.5 kW Nd:YAG and 3 kW Nd:YAG laser beams delivered through fibers of 600 μm and 400 μm were used. Welding speeds of 1.5–6 m/min were achieved which could be very attractive for automotive industries. These joints may possibly show better fatigue performance as there is no interface gap.

Stainless steels: Austenitic stainless steels are generally laser weldable. Due to Se and S additions meant for machinability they are prone to solidification cracking. However, due to lower thermal conductivity and higher absorptivity compared to carbon steels, they are weldable with lower heat input and higher speeds. This results in less thermal stresses, less distortion, and less effect on corrosion resistance compared to TIG welding. In general, they are good materials for laser welding. 400 series ferritic grades have better ductility with laser welding when compared to conventional welding processes. However, grain coarsening in the FZ is still an issue

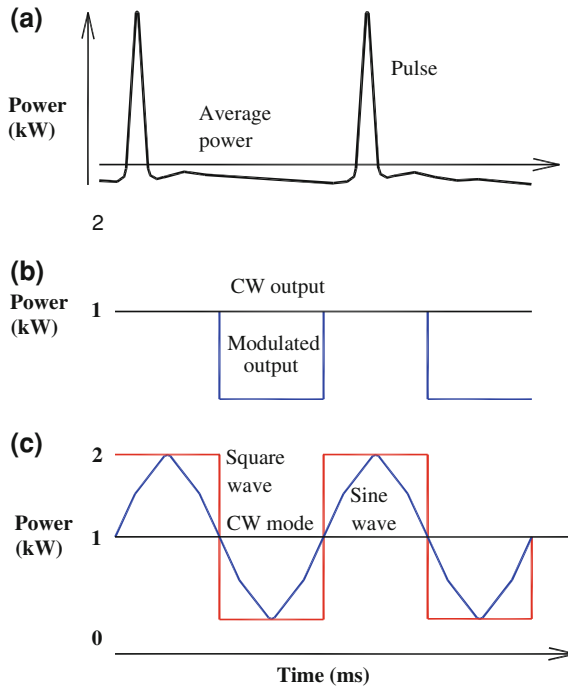


Fig. 4.15 Different modes of pulsed power. **a** Normal pulsing, **b** modulated pulsing, and **c** sine wave pulse [16]

to be tackled. Martensitic grades have the poorest weldability due to hard and brittle fusion zones with tendency towards cold cracking. Duplex stainless steels (DSS) with austenite-ferrite microstructure will solidify as ferrite in autogenous welds, disturbing the microstructural balance. By using nitrogen, a good austenite stabilizer as shielding gas during welding, austenite content in the weld zone could be increased in autogenous laser welding (Fig. 4.17).

Weld zone pitting corrosion resistance can also be improved by this method. The microstructural balance can also be restored by using Ni containing filler in laser welding with filler addition or in laser-arc hybrid mode. The use of laser/laser hybrid welding for DSS will be beneficial especially, for pipelines to achieve proper root penetration.

High temperature Cr–Mo steels: Cr–Mo steels have either bainitic or martensitic microstructures depending on the percentage of Cr. The steels are used for high temperature applications and the temperature of operation is again determined by the Cr content. The materials in the group are generally weldable if proper care is taken. The weldability issues in these grades of steels are high air hardenability leading to hard martensitic microstructures; formation of δ -ferrite in the fusion zone (FZ) which affects creep properties; hydrogen embrittlement due to hard HAZ; and formation of inter-critical zone (ICZ) away from the FZ leading to creep failure in service.

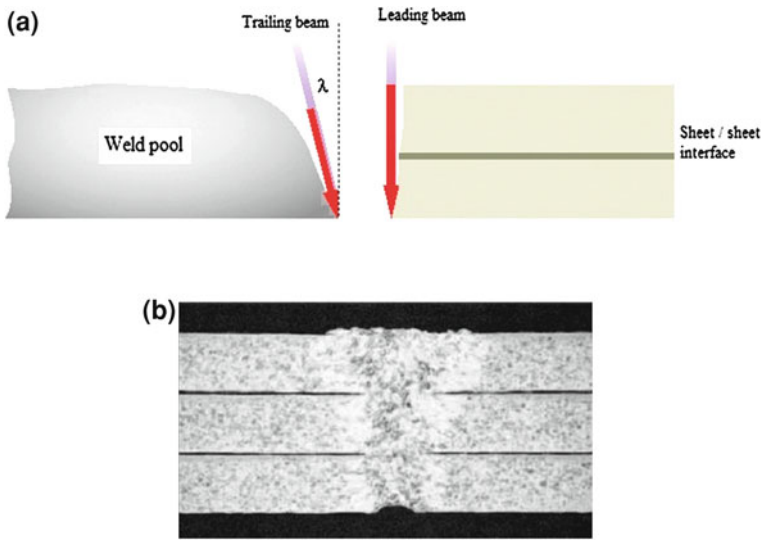


Fig. 4.16 Zero gap lap welding of galvanized steel sheets. **a** Laser beams positioning—trailing beam at an angle, and **b** cross section of the lap weld [17]

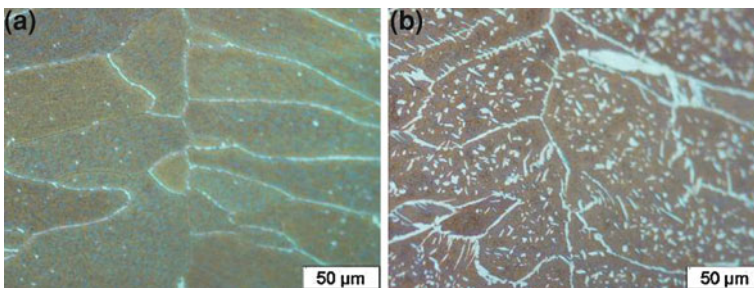


Fig. 4.17 Laser weld zone in Duplex Stainless Steel (DSS). **a** Argon shielding—showing predominantly ferritic structure, and **b** nitrogen as shielding gas—showing increased austenite (G. Padmanabham, “Un-published results”)

Laser welding due to its concentrated nature and low heat input can reduce the size of HAZ and the small weld zone can be easily shielded for reducing hydrogen-induced cracking. Additionally, less cumulative heat input while welding thick sections could avoid formation of inter-critical zone. The most commonly used material in this group for applications at temperatures of around 600°C is modified 9Cr–1Mo (P91) steel which is fastly replacing 300 series austenitic stainless steels in supercritical and ultra supercritical power plants. Autogenous laser welding studies on P91 steel using a CO₂ laser beam have shown promising results [18]. The welding experiments were carried out on 6 mm thick plate using a high beam quality CO₂ laser in both gauss and donut modes. The welding parameters were chosen to achieve wide variation in

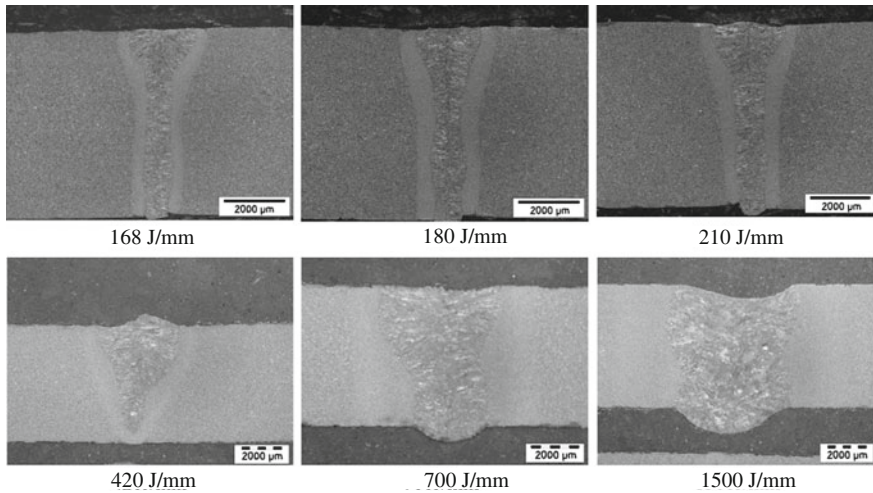


Fig. 4.18 Cross sectional macrographs of laser welds in 9Cr-1Mo steels 6 mm thick plates [18]

heat input conditions (Table 4.2) [18]. The welds were subjected to post weld heat treatment (PWHT) involving heating at a rate of $2^{\circ}\text{C}/\text{min}$ up to 760°C and holding for 3 h and subsequently the welds were characterized. The welds were free from any defects for all the heat input conditions as can be seen from the macrostructures (Fig. 4.18) [18]. Microhardness survey across the weld zone is shown in Fig. 4.19 [18]. Low heat input welds showed a fusion zone microhardness >260 HV, whereas the high heat input welds showed a fusion zone hardness of about 220 HV. Also, it has been observed that the welds were free from ICZ up to a heat input of 420 J/mm. The fusion zone had tempered martensitic microstructures with prior austenite grain sizes smaller than the base material. The refined microstructures along with the narrow fusion zone have resulted in superior impact and tensile properties compared to base metal for all the heat input conditions. Metallography also revealed that there is no δ -Ferrite up to 420 J/mm of heat input (twice the optimum value) and showed limited amounts of δ -Ferrite only at heat inputs as high as 700 J/mm as shown in Fig. 4.20 [18]. This indicates availability of a substantial window of parameters to carry out laser welding on these alloys without the usual deleterious phase formations and HAZ softening.

Maraging steels: Maraging steels are iron-nickel alloys designed to combine high strength with good toughness. Principal alloying element is 15–25% Ni, secondary alloying elements are Co (7–9%), Mo (4.5–5%), and Ti (0.6–0.9%). The properties are achieved through the age hardening of low carbon martensite that forms when the steels are cooled from austenitising temperature. On cooling, the austenite transforms to low carbon iron-nickel martensite that has a BCC structure. The formed martensite is untwinned (lath) with dense angles of dislocation. This type of martensite is relatively soft (HRC30) and tough. Since the austenite to martensite transformation takes place at fairly low temperatures, the martensite forms by

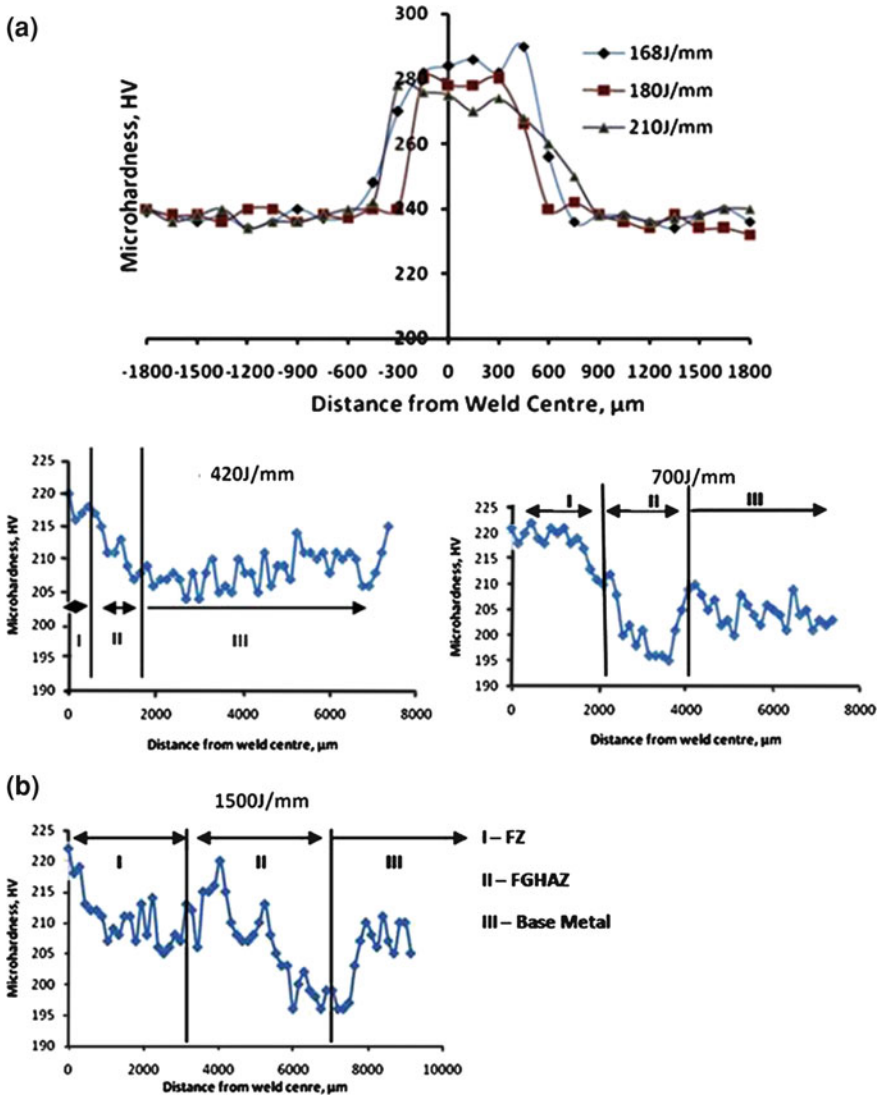


Fig. 4.19 Microhardness survey across the laser welds of Cr–Mo steels at (a) low heat inputs and (b) high heat inputs [18]

diffusion-less shear process. Maraging steels in general have good weldability. The welding of the alloys is usually carried out in the solution annealed condition and will be subsequently subjected to aging treatment to achieve the strength. If the material is welded in the aged condition, due to the heat of welding, the precipitates in the fusion zone and the HAZ will go back to the solution and will be soft compared to the unaffected base material resulting in loss of strength. Hence, it is always

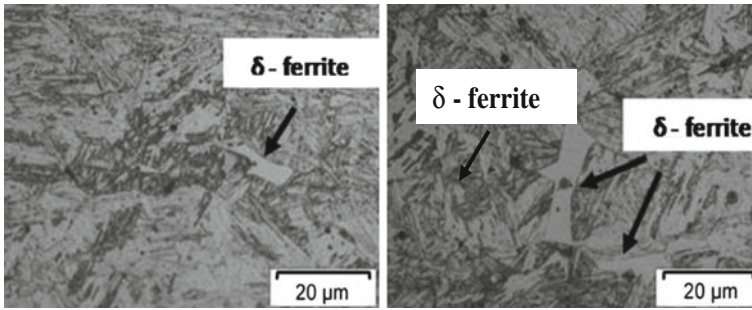


Fig. 4.20 Microstructures showing δ -ferrite in FZ [18]

preferred to be welded in annealed condition. The second issue is the formation of dark band/eye brow zone where a comparatively small volume of metal is heated to a maximum temperature in the two phase region (austenite + ferrite). Heating in this region can lead to stabilization of austenite called reverted austenite which is soft and does not harden during aging. Consequently, the dark band remains weaker than the rest of the heat affected zone structure. The extent of weakening will depend on the amount of austenite it contains. Reverted austenite forms more readily when there is already some austenite in that structure. In actual welds the width of dark band is an important factor because, thinner the band, it is supported more effectively by the surrounding material. Therefore, low heat inputs are required to get thinner band, i.e., control of heat input is required in order to minimize the dark zone. In this context laser welding is a preferred process for welding of this class of steels. Laser lap welding studies on 0.8–0.8 mm MDN 250 steel sheet in annealed condition using CW Slab CO₂ (Gauss and Donut) laser and pulsed Nd:YAG laser have shown promising results. Full penetration lap welds could be achieved with a wide window of parameters. The macrostructures of the welds are shown in Fig. 4.21 (G. Padmanabham, “Un-published results”). The welds are free from defects; however, welds have shown a small dark band zone irrespective of the mode of welding. The microhardness survey across the welds in the as-welded condition (Fig. 4.22a) has indicated that the hardness values peaked in the HAZ adjacent to the fusion zone which can be attributed to the increase in ferrite content. The increase in hardness was proportional to the heat input. However, the aging treatment (480°C for 3 h) have normalized the hardness values of the fusion zone on par with HAZ and base metal (Fig. 4.22b). Also, there was no distinct soft region at the end of HAZ (dark band zone). Shear test on the full penetration welds confirms the hardness test results. The failure occurred in the welds. The load to failure has increased after heat treatment. However, the strength values were found to be only marginally dependent on the parameters and the throat dimensions of the weld. The shear test results are given in Table 4.3.

In summary, the steel can be laser welded and low heat input during laser welding is beneficial in terms of suppressing the formation of dark band zone.

Table 4.2 Laser welding parameters and conditions to obtain different heat input conditions for welding of modified 9Cr-1Mo steels [18]

Sample no.	Laser power (kW)	Welding speed (m min ⁻¹)	Laser beam mode	Focal spot size (μm)	Heat input (J mm ⁻¹)	Weld
1	3.5	1.25	Gauss	180	168	Butt
2	3	1	Gauss	180	180	Butt
3	3.5	1	Gauss	180	210	Butt
4	3.5	0.5	Donut	360	420	BOP
5	3.5	0.3	Donut	360	700	BOP
6	2.5	0.1	Donut	360	1500	BOP

BOP: Based-on-plate

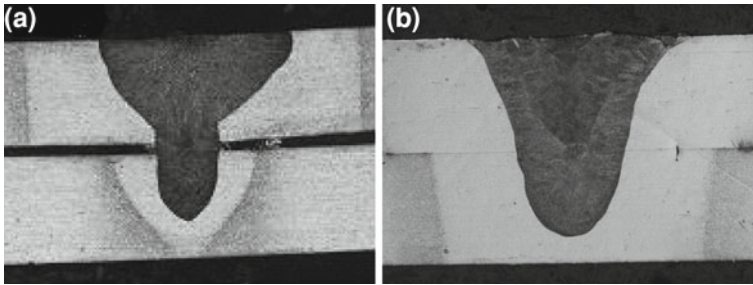


Fig. 4.21 Cross sectional macrographs of 0.8 mm –0.8 mm thick maraging steel sheet lap welds made with (a) CW CO₂ laser welding at 2 kW laser power and welding speed 2.3 m/min, (b) pulsed Nd:YAG laser welding—300 W Average Power, 2 kW Peak Power, 0.26 m/min

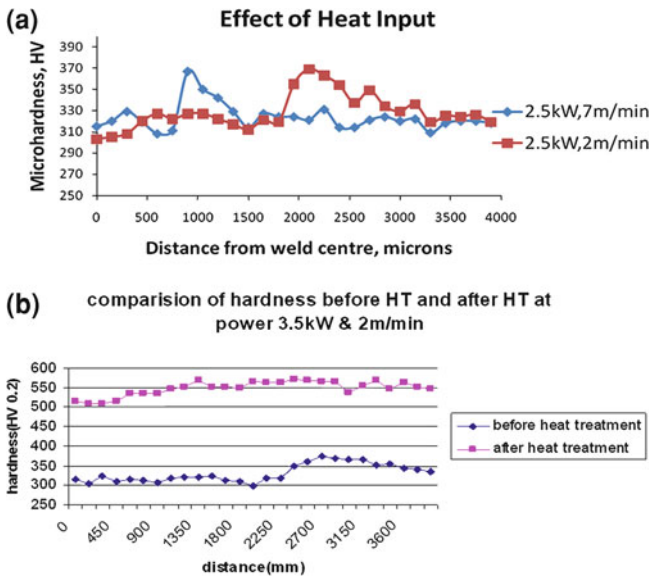


Fig. 4.22 Microhardness survey across the welds of maraging steel: **a** effect of heat input, and **b** effect of post-weld heat treatment

4.7.2 Aluminum Alloys

With respect to laser welding, aluminum and its alloys possess certain characteristics such as, highly reflectivity to laser radiation, high thermal conductivity (making it difficult to concentrate heat at the weld), low viscosity in the molten state (resulting in an unstable weld pool), contains easily vaporized alloying elements whose loss results in low weld strengths and also adds to the pressure in the keyhole. As a result, an unstable keyhole can alternately collapse and erupt, causing spatter, porosity, and low weld strengths. Different alloys have different laser-welding issues for e.g.,

Table 4.3 Shear test results of maraging steel lap welds

Power (kW)	Speed (m/min.)	Beam mode	Throat width (mm)	Load to failure (kN)	
				As welded	Aged
3.5	8	Gauss	0.583	10.042	15.87
2.5	7	Gauss	0.602	11.445	16.83
2.5	6	Gauss	0.556	10.652	16.06
1.5	2	Gauss	0.734	12.146	16.43
3.5	4	Donut	0.62	10.642	14.62
2.5	3	Donut	0.629	8.95	14.88
2.5	2	Donut	0.951	12.179	16.84

solidification cracking in 2000, 6000, and 7000 series aluminum. Much bigger and fluctuating plasma plume due to above reasons can also lead to instability in the weld “keyhole”. These above factors are explained as follows: due to high reflectivity and thermal conductivity, aluminum alloys are more difficult to weld than iron-based alloys. Power is either reflected away or conducted into the bulk metal from the region to be welded. This necessitates the use of very high powers. The coupling of the laser beam with aluminum occurs only beyond a particular threshold power density which is typically $> 10^6$ w/cm², mainly with far infrared CO₂ laser beam. Leong et al. [19] developed a simple eq. (4.2) as given below that predicts the threshold irradiance (I_m) for melting and correlated the effects of the metal absorptivity, thermal conductivity and temperature increase for melting, beam diameter, and welding speed.

$$I_m = [k(T_{\text{melt}} - T_0)]/[A \cdot d \cdot J_{\text{max}}] \quad (4.2)$$

where k is the thermal conductivity of the metal, T_{melt} is the melting point of the alloy, T_0 the ambient temperature, A is the absorptivity of the surface, d is the diameter of the beam, and J_{max} is a function of ratio of thermal diffusivity to the product of the traverse speed and diameter of the incident beam. The model gives a good lower bound guides for threshold power densities. Further, aluminum vapor ionizes much more readily than iron and the plasma in the keyhole absorbs more energy once it forms. Overhead plasma obstructs the incoming light as well. Consequent reduction in power results in collapse of the keyhole. This sequence of keyhole formation, plasma blocking, and keyhole collapse makes the process unstable. Figure 4.23 shows a schematic of sequence of events leading to keyhole instability in aluminum alloys and defective weld seam due to keyhole instability [20].

Gas shielding also has a substantial effect on the process stability. Helium seems to be better choice for welding of aluminum alloys as it has high ionization potential and hence less plasma effects. Additionally, the low dense nature of the gas reduces the pushing of the low viscous aluminum molten pool thereby reducing the defects such as undercutting, concavity, etc. Gas flow rate also has to be carefully fixed. Low flow rates do not provide adequate shielding and high flow rate results in cutting action. For welding of 2 mm thick 6061 alloy, helium supplied through a 4 mm diameter pipe arranged at 45° angle pointing toward leading edge of the weld pool gave good

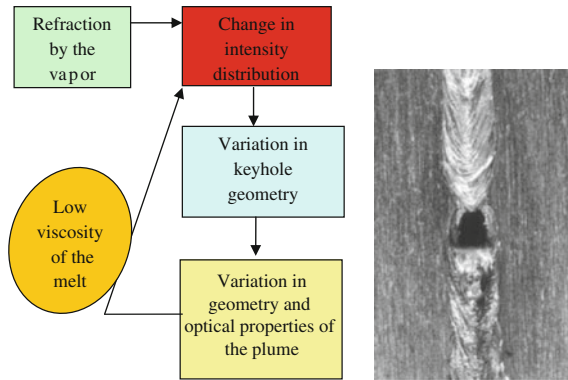


Fig. 4.23 Schematic of the resonant system of Beam-Plume-Keyhole and a typical defect formed in aluminium alloys due to keyhole instability

results at a flow rate of 20 l/min. Even nozzle geometry and position were found to be important for better plume control [21]. In CO₂ laser welding (2.5 kW) of 5083 using helium as shielding gas with different nozzle configurations, co-axial conical pipe, and two-pipe nozzle transverse to welding direction, the two-pipe configuration generally produced joints with higher aspect ratio. Another difficulty is the loss of strength due to laser welding, as many of the important alloying elements (Zn, Mg, Li) have very low boiling points.

Several studies have been reported in the literature to address the process-related issues in laser welding of aluminum alloys, such as dual spot welding for better keyhole stability, pulse shaping for avoiding solidification cracking, laser-hybrid methods and adding filler wire to compensate loss of alloying elements, magnetic stirring for minimizing porosity etc. Consequently, with appropriate process optimization, laser welding offers advantages such as, high welding speed, possibility to weld with limited accessibility, small fusion and heat affected zones, better joint efficiency, low distortion, etc.

CO₂ laser welding studies on aluminum alloy 5182 revealed that proper control of laser beam irradiance is an important factor to obtain consistent welds [22]. Beam irradiance is directly affecting the formation of undercuts and cavity defects as molten aluminum has low viscosity and surface tension and it also affects the amount of loss of magnesium. Ultimate tensile strengths of 251 MPa and an elongation of 10.4% have been achieved. In the same study, it was clearly observed that shield gas with sufficient flow rate when directed at the leading edge of the weld pool with the nozzle trailing yielded better results.

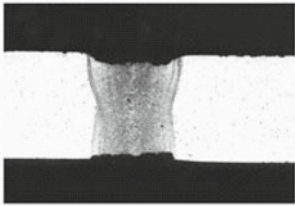
Laser welding of heat-treatable 2024 alloys without defects seems to be possible [23]. When high heat input parameters were used, viz., low power density, low welding speed, the weld pool was bigger and the keyhole positioned in the center of the weld pool and had minimum fluctuations. However, at low heat input parameters, viz., high power density and high welding speeds, the keyhole tip is coinciding

with the front of the keyhole and is prone to more fluctuations. Hence, high heat input parameters could be used for obtaining welds without defects. Laser weldability of non-heat treatable 5000 series alloys and heat-treatable 6000 series alloys were evaluated using a 4 kW, continuous-wave Nd:YAG laser with and without filler wire with automotive applications in mind. When using filler wire, nominal wire feed speed was calculated as $\{ \text{Wire feed rate (m/min)} = \text{Welding speed (m/min)} \times \text{cross-sectional area of gap (mm}^2) / \text{Cross-sectional area of filler wire (mm}^2) \}$ [24]. Experimental work revealed that wire feed delivery angle and position are critical. Delivery angle of 45° to the vertical and intersecting the laser beam 1.5 mm ahead of the weld pool worked the best. The wire must not intersect the laser beam above the weld pool, as this causes excessive spatter, tooling damage, and reduced penetration. As the weld pool is larger with filler wire addition more gas shielding is required. For a 0.6 mm spot size and power density of $1.2 \times 10^6 \text{ W/mm}^2$, 5000 series material appeared to weld at faster speeds than the 6000 series material, possibly due to more stable keyhole due to vaporization of magnesium. That is, 8–11 m/min in case of 5000 series and 6–10 m/min in case of 6000 series alloys. 5000 series also required better under bead shielding to control material drop through. Addition of filler wire improved the weld profile and bridged wider gaps. For dissimilar sheet thicknesses (1.6–2.0 mm), a wire feed rate of 2.55 m/min could accommodate up to a 0.30 mm joint gap. When the wire feed rate was increased to 5 m/min, a gap of 0.5 mm could be bridged. Bead profiles without and with filler wire are shown in Fig. 4.24 [24].

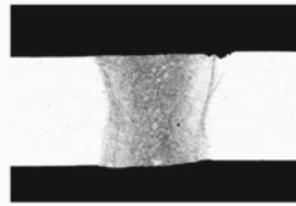
Mechanical properties achieved with Nd:YAG laser welds in various alloy systems with and with filler wires are given in Table 4.4 [25]. As can be seen from Table 4.4 laser welding can yield > 80% joint efficiency in heat-treatable aluminum alloys and more than 90% joint efficiency in case of non-heat-treatable aluminum alloys [25]. Due to high welding speeds joint efficiencies up to 95% have been achieved in welded 6061-T4 alloys [26].

It is well known that high strength 7075 alloy is prone to solidification cracking during welding. Transverse cracking was found in autogenous laser as well as laser-MIG hybrid welding process [27]. Longitudinal stress developed along the welding direction results in transverse tensile strain during the cooling phase and consequently the transverse cracking. Using welding conditions which could reduce the cooling rates were found to minimize this tendency. For example, welding at low speeds with low heat input or employing an additional power source to alter the temperature gradients. The effect of using an additional heat source was experimentally tried and found useful. Based on some of the process improvements and advantages of laser welding, attempts to apply laser welding technology to design and fabrication of blast and impact-resistant structures, such as aircraft fuselage panels have been made [28].

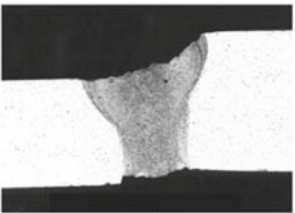
CO₂ and YAG lasers were used to lap weld AA2024-T3. More consistent weld penetration on lap joints of 1.6 mm thick alloy were obtained with a 3.5 kW Nd:YAG laser, than a CO₂ laser of equivalent power. Uniaxial tests on laser-welded and riveted specimens of AA2024-T3 indicated that the laser-welded joints have higher strength per unit joint length than the riveted ones, but exhibit more brittle failure.

**(a)**

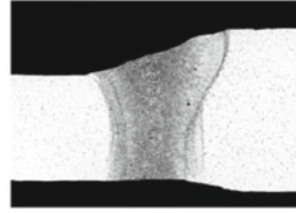
Autogenous butt weld in 5083 alloy; 1.6 mm thick; welding speed 11 m/min.

**(b)**

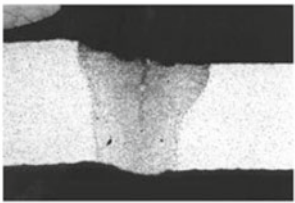
Butt weld in 5083 alloy using a filler wire (5556A); 1.6 mm thick; welding speed 11 m/min; wire feed speed 4.5 m/min.

**(c)**

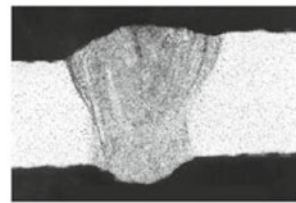
Autogenous butt weld in 5083 alloy; 1.6 and 2 mm thick; welding speed 8 m/min.

**(d)**

Butt weld in 5083 alloy using a filler wire (5556A); 1.6 and 2 mm thick; welding speed 8 m/min; wire feed speed 3.4 m/min.

**(e)**

Autogenous butt weld in 6082 alloy; 1.6 and 2 mm thick; welding speed 6 m/min.

**(f)**

Butt weld in 5083 alloy using a filler wire (5556A); 1.6 and 2 mm thick; welding speed 8 m/min; wire feed speed 2.6 m/min.

Fig. 4.24 Laser butt weld cross section profiles without and with filler wire addition [24]

Subsequently, more developments in terms of process monitoring and automation have taken place and some robustness has been achieved.

In summary, high sensitivity of laser welding of aluminum to various factors as explained above demands tight control of laser welding parameters through extensive optimization before using in actual application. The optimized process yielded very good joint efficiencies in the autogenous as well as in the filler addition mode. In the recent times, solid-state lasers such as disk lasers and fiber lasers with high power and beam quality are commercially available and are slowly proving to be advantageous for laser welding of aluminum alloys.

Table 4.4 Mechanical properties of laser welded aluminium alloys in autogenous welding and welding with filler [25]

Alloy (AA)	Hardness	Hardness reduction		Strength	Strength reduction		
	BM HV0.1	WM Autogen. (%)	WM with filler (%)	HAZ (%)	UTS (MPa)	Autogen. (%)	With filler (%)
2024	137	25	24	5	455	30	16
5005	56	22	2	20	162	11	7
5754	70	6	3	14	247	8	6
5083	75	0	3	0	296	5	12
6082	120	37	45	33	348	22	20
7020	130	24	24	7	405	12	10

**Fig. 4.25** Standard shielding arrangement used in laser welding and typical weld top surface obtained in Ti-6Al-4V alloy [29]

4.7.3 Titanium Alloys

Titanium alloys, due to their excellent specific strength, creep properties, fracture toughness, and corrosion resistance, are used in many applications. The $\alpha + \beta$ titanium alloy Ti-6Al-4V accounts for more than 50% of all Ti tonnage in the world and the aerospace industry accounts for more than 80% of this usage. It is very frequently used in welded form, using a variety of welding processes. However, due to high reactivity of titanium, especially at elevated temperatures, it reacts strongly with most elements such as, oxygen, hydrogen, nitrogen, etc., and gets embrittled. Hence, elaborate shielding arrangements are required and often electron beam welding is preferred as it is done in vacuum. Laser welding studies conducted on this widely used Ti-6Al-4V alloy indicated that this alloy is highly laser weldable with a simple shielding arrangement (Fig. 4.25) [29]. However, surface cleaning prior to welding, involving cleaning with isopropyl alcohol, NaOH and Turco acid solutions and de-mineralized water, and covering with aluminum foil prior to welding trials are a prerequisite to achieve clean weld. The fusion behavior of this alloy (4 mm thick plate) during CO₂ laser welding with spot size 360 μm , laser power in the range of 2.5–3.5 kW and welding speeds of 2–4 m/min is shown in Fig. 4.26 [29]. Argon gas was provided at 30 l/min as shield gas in the trailing configuration with root protection as well. Shield gas was supplied through a 4 mm diameter tube at 45° to the laser beam at a stand-off of 5 mm from the work piece.

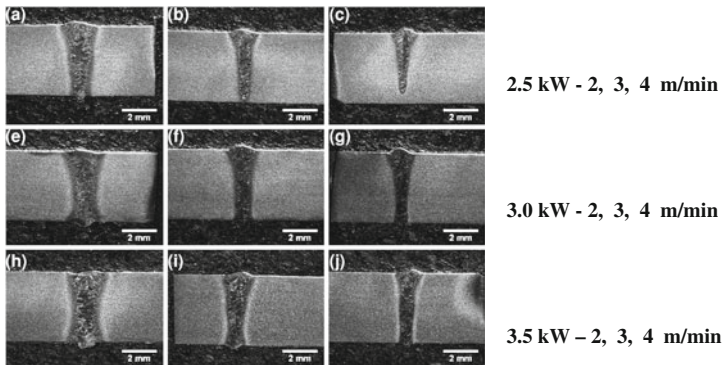


Fig. 4.26 Macrographs of weld bead-on-plate cross sections made at different laser powers and welding speeds [29]

No cracks were observed on the weld surface as was observed in case of other shielding arrangements. The fusion behavior was found to be quite predictable without any weld defects. A wide window of parameters is available for laser welding.

Microhardness profile across the welds carried out at varying heat input conditions is shown in Fig. 4.27 indicating that the average weld metal hardness was always in the range of 381 HV whereas the average base metal hardness was at 300–360 HV [29]. The increase in hardness in the fusion zone compared to the base metal was only marginal, indicating that the contamination of the weld could be effectively controlled even with simple shielding arrangement. This behavior could be attributed to the narrow fusion zone and high cooling rates in laser welding. There was no marked difference in these values with reference to different welding parameters. Even the heat affected zone hardness did not change much in spite of heat input variation from 34.3 J/mm to up to 85.8 J/mm.

In terms of microstructure (Fig. 4.28), while the base metal had an equiaxed $\alpha + \beta$ structure, the heat affected zone (HAZ) showed acicular α and transformed β and the fusion zone predominantly fine α' martensite with very thin grain boundaries. Very high cooling rates in the order of 700 to more than 1000°C/s are experienced during laser welding resulting in such fusion zone microstructure. Similar microstructures were reported in the literature as well. Tensile strengths as high as 1000 MPa were achieved in the welds for a wide range of laser welding parameters as mentioned above.

4.7.4 Nickel-Based Alloys

The solid solution-based alloys such as IN600 are easy to laser weld. The precipitation-hardened alloys such as IN718 are prone to weld cracking when welded in heat-treated condition. By reducing the heat input this cracking tendency could

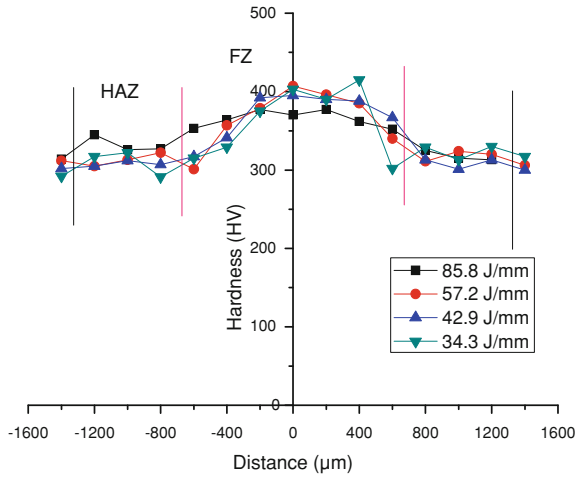


Fig. 4.27 Microhardness profile on the transverse cross section of Ti-6Al-4V laser weld at 3500 W with varying heat inputs [29]

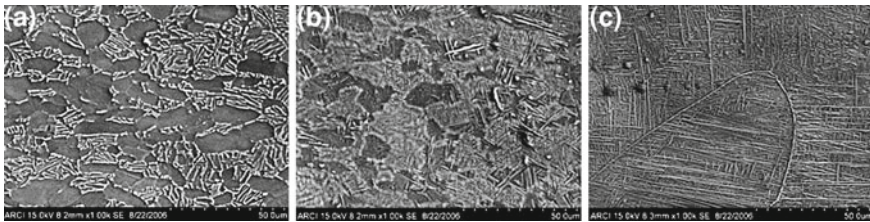


Fig. 4.28 SEM micrographs (1000 X) of a base metal, b HAZ, and c fusion zone [29]

be reduced. Laser welding is eminently suitable to meet this requirement. With low heat input, in the presence of IN625 kind of fillers, repairs have been successfully done on turbine blades without damaging the substrate.

Nickel-based superalloy IN718 due to good high temperature properties is widely used in aerospace, power, and nuclear applications. Although this alloy is generally known to be weldable, it is also known to be prone to microfissuring in heat affected zone and segregation of phases a brittle intermetallic compound represented as $(\text{Ni, Cr, Fe})_2(\text{Nb, Mo, Ti})$ in the interdendritic regions during weld metal solidification, which adversely affects the mechanical properties. Low heat input laser welding process seems to be advantageous in terms of effect of Laves' phase formation [30]. Nd:YAG laser welding of IN718 (2 mm thick sheets in solution treated condition) showed lower amount of Laves phase compared to TIG welding microstructure. Further, post weld solutionizing at 980°C resulted in substantial dissolution of Laves phase but not completely eliminated. This may be due to the fine, discrete particle morphology and lower Nb concentration obtained with laser welding. Microfissures were also not observed in the heat affected zone. This could be due to the fact that

welding was done on solution-treated base metal rather than aged base metal. Overall, reasonably good room temperature properties could be obtained with laser welding. That is, UTS 1460 MPa; YS 1237 MPa; and Elongation 16% for the post weld heat-treated laser weld in comparison to UTS 1475% MPa; YS 1272% MPa; and Elongation 24%. This is an indicator of possible advantages with laser welding of such alloys.

4.7.5 Magnesium Alloys

Magnesium alloys are characterized by very attractive properties such as high specific strength, castability, hot formability, machinability, electromagnetic shielding, and sound damping capabilities. Corrosion resistance is as good as steels but less than aluminum alloys. There are mainly four popular ternary magnesium alloy systems AZ (Mg-Al-Zn), AM (Mg-Al-Mn), AS (Mg-Al-Si), and AE (Mg-Al-Rare Earths) and they have applications in various sectors such as automotive, aerospace, and electronics. Properties of magnesium, aluminum, and iron metals can be seen from Table 4.5 [31]. Important factors to be considered during laser welding are very low boiling point of magnesium, viz., 1090°C, which is very close to its melting point of 650°C, low viscosity in molten state, and high vapor pressure. While it will be very easy to form a keyhole at low power densities, the high vapor pressure and low viscosity will result in defects such as undercuts, drop out, etc. Vaporization losses are also expected to be high. Keyhole stability may not be a serious issue as in case of aluminum alloys, as the keyhole forms at very a low power density. Figure 4.29 shows cross-section of AZ31 keyhole welds made with CO₂ laser with focused and defocused beams and conduction welds using diode laser [32]. Even with 0.4 mm diameter spot, full penetration could be obtained with 1 kW laser power and weld at a speed of 9 m/min. In case of diode laser, rectangular spot of 1.8 x 3.2 mm was used and still the full penetration weld could be accomplished at 1 kW power and 3 m/min. This welding speed is substantially high compared to conventional welding speeds. Hence, one can consider diode lasers also for welding magnesium alloys. As can be seen from Fig. 4.30, the process in the keyhole mode is very sensitive to welding conditions, especially power density. The undercut in the center of the weld is caused due to narrow temperature range between boiling and melting points of magnesium and small spot size. Due to the same reason, surface craters also formed. All the welds show porosity close to the fusion boundary though less in case of diode laser weld. This clearly indicates influence of cooling rates experienced in each condition. More the cooling rate, more the chances of rejected hydrogen getting entrapped. The low viscosity of the weld pool can be sensitive to shield gas flow rate and orientation. When the shield gas tube is not accurately aligned with weld seam, the shield gas seems to be pushing the metal to one direction causing side cuts as shown in Fig. 4.30a. When heat input is higher, larger melt pool gets created and due to the low viscosity, melt cannot be held and results in drop out. This can be addressed by reducing the melt size by increasing weld speed. In summary, Mg

Table 4.5 Thermo-physical properties of Mg, Al and Fe [31]

Properties	Magnesium	Aluminum	Iron
Ionization energy (eV)	7.6	6	7.8
Specific heat ($\text{J kg}^{-1} \text{K}^{-1}$)	1360	1080	795
Specific heat of fusion (J kg^{-1})	3.7×10^5	4×10^5	2.7×10^5
Melting point ($^{\circ}\text{C}$)	650	660	1536
Boiling point ($^{\circ}\text{C}$)	1090	2520	2860
Viscosity ($\text{kg m}^{-1} \text{s}^{-1}$)	0.00125	0.0013	0.0055
Surface tension (N m^{-1})	0.559	0.914	1.872
Thermal conductivity ($\text{W m}^{-1} \text{K}^{-1}$)	78	94.03	38
Thermal diffusivity ($\text{m}^2 \text{s}^{-1}$)	3.73×10^{-5}	3.65×10^{-5}	6.80×10^{-5}
Coefficient of thermal expansion (K^{-1})	25×10^{-6}	24×10^{-6}	10×10^{-6}
Density (kg m^{-3})	1590	2385	7015
Elastic modulus (N/m^2)	4.47×10^{10}	7.06×10^{10}	21×10^{10}
Electrical resistivity ($\mu\Omega\text{m}$)	0.274	0.2425	1.386
Vapor pressure (Pa)	360	10^{-6}	2.3

alloys are prone to several process-related defects which of course can be addressed by choice of appropriate parameters such as power, spot size, speed, and shielding gas flow and position. Another weldability issue is solidification cracking, which was observed in pulsed Nd:YAG laser welding. But, a set of welding parameters could be identified [33]. Most of the alloys were found to be weldable with CO_2 laser except AZ91 and AM60 which showed significant porosity [34]. Porosity in AM60 during laser welding was found to be mainly due to hydrogen in the parent material [35]. Remelting of the weld bead reduced the amount of porosity.

4.7.6 Conducting Materials

Copper is the most commonly used material for electrical contacts in a variety of devices. However, due to high reflectivity and high conductivity, it causes inconsistent coupling and overheating of the joint regions, respectively. As most of the electronic applications involve joining in microwelding regime (less than 0.2 mm), precise control of the heat input into the weld zone is very important. Usually, 1064 nm wavelength Nd:YAG lasers in pulsed mode are used for such applications. But, recently it has been reported that the green lasers, viz., 532 nm wavelength laser beams are more useful for precision microwelding of conducting materials such as copper [36]. The main reason for this is the reduced reflectivity of 532 nm wavelength from 90 to 45% for copper from 98 to 42% in case of gold compared to the conventional 1064 nm laser beam. Additionally, this wavelength facilitates dissimilar materials joining as better heat balance is possible with this kind of absorptivity characteristics.

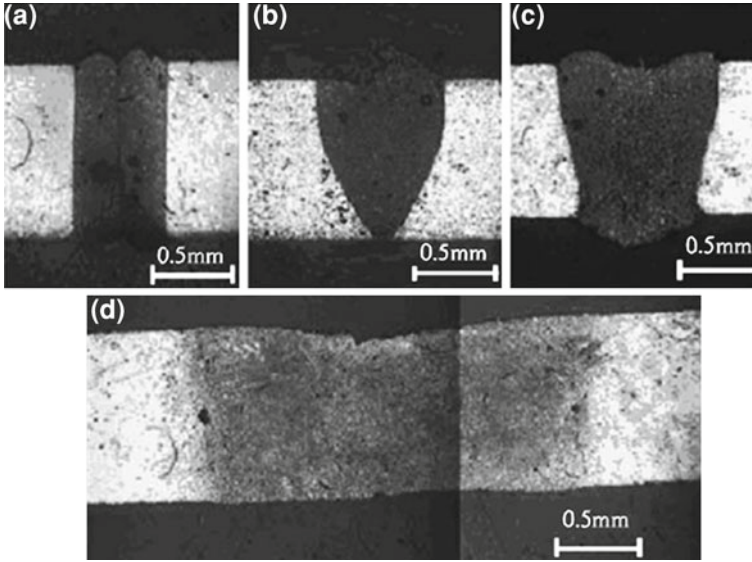


Fig. 4.29 Cross section of AZ31. **a–c** Keyhole welds made with CO₂ laser with focused and defocused beams, and **d** conduction welds using diode laser [32]

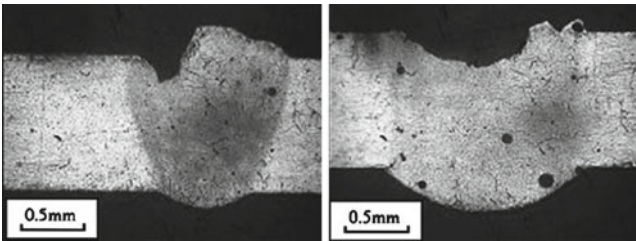


Fig. 4.30 Weld defects in AZ31. **a** Side cut, and **b** melt drop out [32]

4.7.7 Dissimilar Materials

Joining of dissimilar materials is faced with two major challenges, non-uniform fusion behavior due to differences in thermo-physical properties and formation of undesirable phases due to insolubility of elements present in the base materials. Laser as a heat source is very precise in temporal as well as spatial distribution and if positioned appropriately in the joint edge of the dissimilar materials to be joined necessary heat balance can be maintained. For example, when welding materials with different thermal diffusivities, if the laser beam spot is positioned with higher off-set toward the high thermal diffusivity material, melting can be increased and the low thermal diffusivity side melts less as less heat is available. Similarly, the beam positioning can be effectively used to vary the dilution of one material into

another as required in order to minimize undesirable phase formation. In terms of intermetallic phase formation in the fusion zone, high cooling rate can be achieved by using very low and controlled heat input and high welding speeds with laser. By this method, formation of intermetallic phases can be reduced. Even form, size of the particles can be controlled. Consequently, overall effect of intermetallic phases can be mitigated. The third method of achieving this is by using a third material as an interlayer between the materials to be joined. The interlayer material has to be carefully chosen in such a way to control the formation of brittle phases. Additionally, the interlayers should not form any new deleterious phases with any of the base materials. Laser brazing wherein, only the filler material is melted and deposited can be used.

4.8 Limitations of Laser Welding

It may also be noted that laser welding has certain limitations, such as brittle welds in high hardenability materials, porous welds and undercuts due to vaporization of certain volatile elements, high equipment and operating costs, stringent joint fit-up requirements, accurate beam and joint alignment, safety requirements with respect to eye protection, etc. In this backdrop, laser welding is chosen as a joining process for given application when the requirements can be only met by laser welding or a particular application can be cost effectively made using laser welding. Accordingly, some of the most popular laser welding applications are briefly explained in the following sections.

4.9 Laser Welding Process Control Tools

Owing to the nature of the process, laser welding is typically prone to certain defects. European standard EN ISO 13919 lists the nature of defects occurring in laser welds. Table 4.6 lists these defects and main reasons.

The above-mentioned problems can be overcome by better edge gap management, monitoring keyhole plasma, melt pool behavior, and weld bead formation. Edge gap management is done by using suitable seam tracking methods ahead of the weld zone, keyhole behavior can be monitored using plasma monitoring systems in weld zone and weld geometry by vision-based bead appearance recording methods.

4.9.1 Seam Tracking

Very fine spots used in laser welding necessitates very high accuracy of joint fit-up for butt joint welding. It is also expedient to accurately follow the edge of the work piece so that the beam does not miss the joining edge. If the gap width is more, there may be insufficient molten metal to fill the groove causing fusion defects such as pin holes and incomplete fusion. In conventional welding methods, mechanical seam

Table 4.6 Common defects in laser welding and main reasons

Reasons	Defects					Cracks
	Incompletely filled groove	Porosity	Pin holes	Lack of fusion	Lack of penetration	
Gap width	✓	-	✓	✓	-	-
Misalignment	✓	-	-	✓	-	✓
Keyhole instability	-	✓	-	✓	-	-
Power density variations due to change in power, focal plane, welding speed	✓	-	-	✓	✓	-
Contaminants like oil/grease	-	✓	-	-	-	-
Metallurgical reasons - volatile elements, high hardenability	-	✓	-	-	-	✓

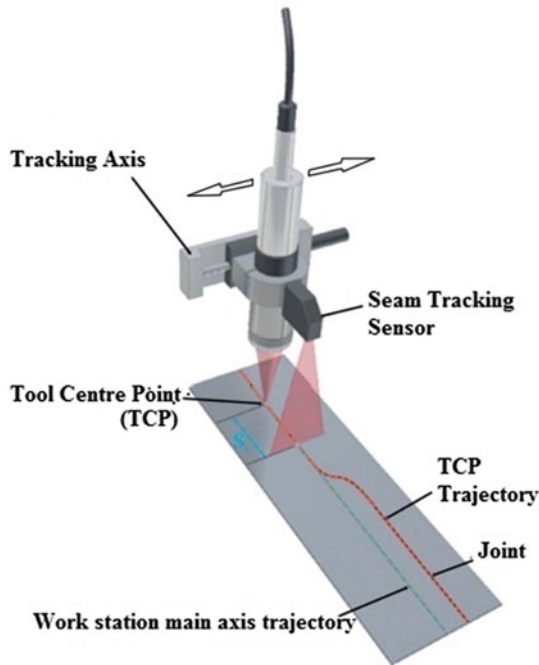


Fig. 4.31 Schematic of typical laser triangulation based seam tracking system [37]

tracking is used, where the edge is mechanically sensed ahead of the weld zone and the head is positioned. It gives accuracy up to 0.25 mm, which is not sufficient for laser welding which uses spot sizes in 0.15–0.4 mm diameter depending on the beam mode, focusing optics, and the power available. Laser-based seam tracking is more suitable for laser welding.

In laser seam tracking a laser spot or line or multiple lines are projected across the seam edges to locate and measure the joint position and the data captured by a sensor sent to the controller through a CCD/CMOS to estimate the position and gap between the edges and a feedback signal is given to the welding head to adjust laterally in the gap, and position itself at the designated location on the seam. A schematic of seam tracking principle is shown in Fig. 4.31.

The accuracy of the system depends on the accuracy of the imaging system and processing speed and feedback signal generation by the controller. Nowadays, very precise seam tracking systems are available for use with CNC workstations as well as robots. For robot-based seam tracking, multisensor concept is proposed in which, in addition to seam position measurement, the relative displacement between the processing head and work piece is measured enabling self-guided processing [37]. This system is expected to be highly accurate independent of the motion system and saves time-intensive sensor calibration and robot teaching.

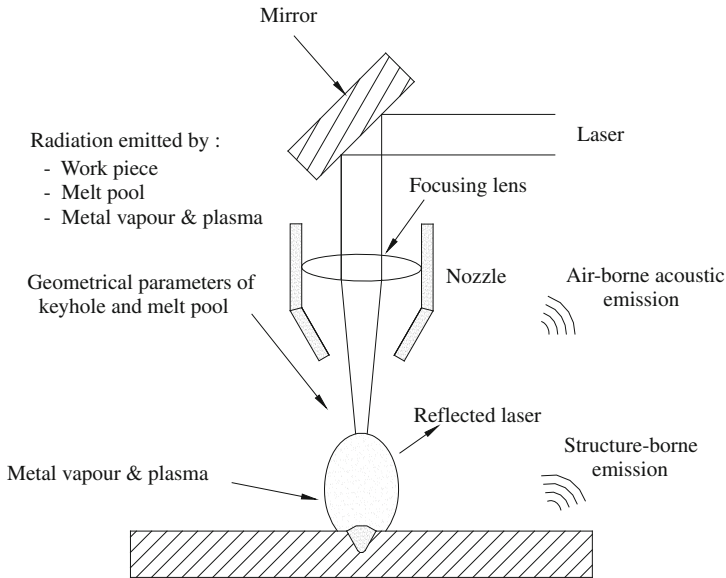


Fig. 4.32 Signals emitted during laser welding process [38]

4.9.2 Weld Monitors

During laser welding process, the laser-material interactions emit energy in the form of optical and acoustic emissions which can be detected with suitable sensors and the feedback used to activate the control loop or make a record of the events for quality control purposes. Figure 4.32 summarizes such sensing possibilities during laser welding [38]. Metal vapor and laser beam back reflection are source of emissions. These emissions are different for processing with different lasers. Nd:YAG laser welding process emits radiation in the visible and infrared region and the plasma generated during CO₂ laser keyhole welding emits light in a wavelength between 190 nm and beyond 400 nm [39]. The spatters emit light in wavelength 1000–1600 nm range. Acoustic emissions are originated from the surface of the metal vapor and stress waves from workpiece. Similarly, optical sensing techniques can capture information on the geometrical and thermal properties of the keyhole and melt pool by image processing.

Photodiode-based plasma monitoring systems are popularly used to capture optical emissions from the weld zone [40]. As the emissions are different for different lasers, the laser welding monitors come with multi-detector systems. The signals are recorded and compared to a standard curve during good welding process. Any deviation from the standard curve indicates occurrence of a defect and helps in rejecting that particular piece. However, these plasma monitors depend very much on a good base line curves with good repeatability and minimal fluctuations. Infrared

vision-based systems can capture the melt pool features like length which can be used to calculate the penetration depth to an accuracy of ± 0.15 mm. These techniques can also be used to detect misalignment of edges and gap widths as they affect the keyhole picture in terms of having a dark spot in case of a trough on the surface or an unsymmetrical spot due to misalignment.

4.9.3 Gap Bridging by Wire Feed

Sometimes, just positioning the laser beam accurately alone may not be sufficient to get an acceptable weld. When gap is more, in spite of positioning the beam, there may not be enough molten metal to fill the joint. In such cases, filler wire may be introduced to supply the extra molten metal required to fill the joint. These filler metal addition methods are also used in the industry by getting gap width data ahead of the welding spot and sending the feedback to the controller which activates the wire feeder.

4.10 Innovations in Laser Welding

There have been several innovative modifications to the traditional keyhole laser welding, sometimes to overcome the limitations such as edge bridging, hard weld zones, etc., and in other cases to take full advantage of the available laser beams. Some of the techniques as described below would bring out these aspects.

4.10.1 Laser Hybrid Welding

In this process, a laser beam and an electric arc are used in tandem in order to combine the positive aspects of laser beam welding like deep penetration, low heat input and high welding speed, and the edge bridging capability and low cost of arc welding. Gas Metal Arc Welding (GMAW), Gas Tungsten Arc Welding (GTAW), or Plasma arc welding (PAW) can be coupled with laser. But, laser-GMAW is the most popular hybrid process due to good edge bridging capability of GMAW. A schematic of laser hybrid welding process is shown in Fig. 4.33 [41]. Advantages of the hybrid are quite obvious. However, the two processes being technologically so different, the complexity of the process significantly increases for establishing the process window to get consistent results as there are a large number of parameters to be controlled. Table 4.7 shows the list of parameters to be understood while working with laser hybrid welding process. The laser source can be Nd:YAG, CO₂, Disk, or Fiber laser depending on the application. Laser-hybrid welding using Nd:YAG and CO₂ has been widely investigated [42–44]. Several groups are now investigating the hybrid welding process involving the disk or fiber lasers as they are recently developed lasers. Nd:YAG lasers produce beams of high quality which can produce good weld depth only in low power ranges up to 1 kW due to thermal lensing effect at high power. Hence, hybrid Laser Nd:YAG-GMAW is more suitable for thin sheet

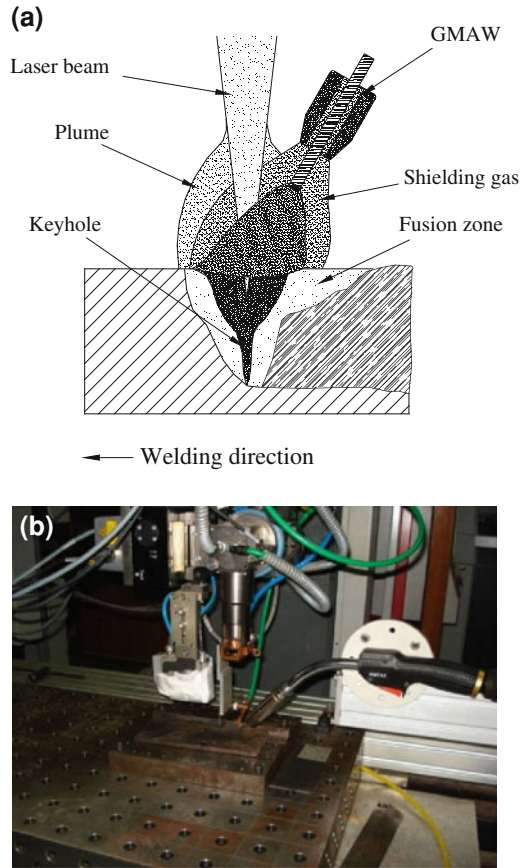


Fig. 4.33 Laser-GMAW hybrid welding. **a** Schematic, and **b** actual arrangement of CO₂ laser beam welding head with a GMAW torch

welding and has been widely studied in the automotive industry. On the other hand as high power is available from CO₂ laser, CO₂ laser GMAW welding has significant advantages in welding of thick sheets. Stability condition of a hybrid laser CO₂-GMAW welding process by analyzing the influence of several process parameters was investigated and analyzed on a 12 mm thick mild steel plate [44]. The typical nomenclature of a laser hybrid weld is given in Fig. 4.34 and the variation in depth of penetration with parameters is shown in Fig. 4.35. It has been reported that distance between the two sources involved in the process should be 2–3 mm for obtaining consistent and good depth of penetration. When the distance between sources is less than 2 mm, turbulence in the weld pool and disturbance in the keyhole formation are observed affecting the synergy between the processes. At the same time, when the distance between sources is higher, the two processes act as independent processes with no advantage of hybridization.

Table 4.7 Laser -MIG hybrid welding parameters

Laser parameters	MIG parameters	Joint parameters
Power, focal spot size, focal position and beam mode	Voltage, current/metal transfer mode, torch angle	Distance between arc and laser source, laser trailing or leading

Common parameters are shielding gas and flow rate, and welding speed

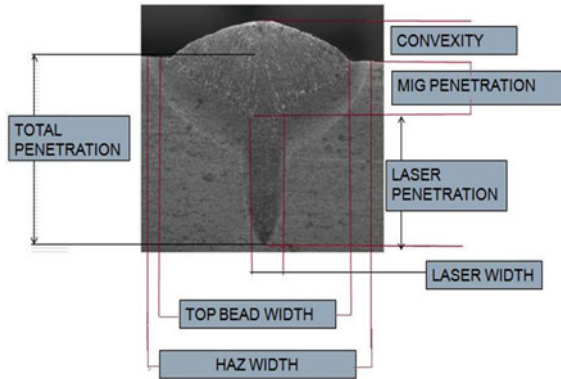


Fig. 4.34 Macro cross section of a typical laser-MIG hybrid weld bead on plate

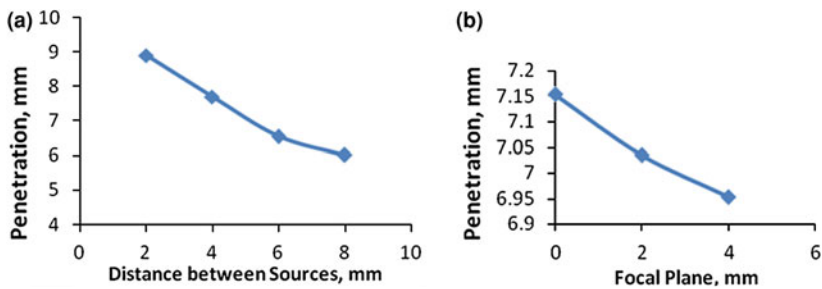


Fig. 4.35 Effect on depth of penetration. **a** distance between sources, and **b** laser focal plane below the base metal surface (Laser power 3.5 kW, Spot size 180 μ m, welding speed 1 m/min; and GMAW 1.2 mm diameter mild steel wire feed at 14 m/min) [44]

Similarly, laser beam focal position is important for achieving higher depth of penetration in thick plates as in case of autogenous laser welding. It should be below the upper surface of metal surface in order to achieve the best penetration. This distance is dependent on the GMAW metal transfer mode, 4–6 mm for short-arc and 6–8 mm for pulsed/spray-arc. The metal transfer mode also affects the process in terms of achieving stable and repeatable penetration. Pulsed spray arcs should be

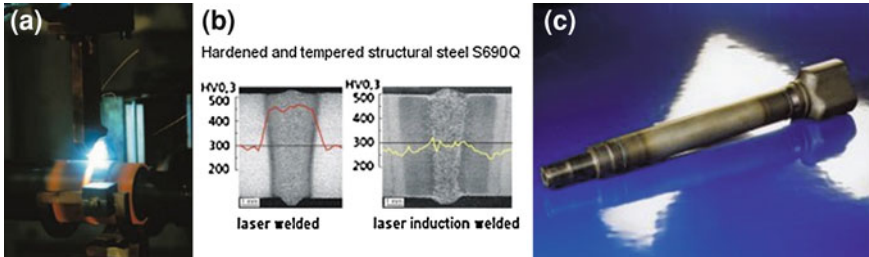


Fig. 4.36 Induction assisted welding of high hardenability steels. **a** System and process in operation, **b** comparison of hardness across the weld joint without and with induction assistance, and **c** welded shaft [46]

preferred to short/globular arc as the small droplets in pulsed spray cause less weld pool turbulence compared to globular transfer. Arc voltage does not play a significant role in depth of penetration but helps in increase in weld width. Hence, when better gap bridging is required higher arc voltage can be considered [45].

4.10.2 Induction-Assisted Laser Welding

The high cooling rates achieved in laser welding can lead to high residual tensile stresses and hardness in the fusion zone. This tensile stress along with high hardness as in the case of medium carbon steels or low alloy steels with carbon content more than 0.2% can lead to cracking. The cracking tendency usually limits the use of laser for welding steels other than low carbon steels. The use of induction coils to preheat the material reduces the temperature gradient and cooling rate in the critical temperature range (150–650°C) thereby reducing the cracking tendency. The use of such hybrid process could effectively increase the productivity without compromising on the quality. The induction-assisted laser welding has been successfully implemented for welding of drive shafts of automotive (Fig. 4.36) [46].

4.10.3 Remote Welding

Welding is performed by focusing the beam to weld location from more than a meter distance using scanning mirrors which move at extremely high speeds to move the beam over a plane. A schematic of such arrangement is shown in Fig. 4.37 [47]. The movement of laser is programmed as per the geometry of the part. In this mode stitch welding can be carried out at very high speeds making use of the flexibility that a high quality laser beam offers. Stitch welding of door inner to door outer is one of the popular applications of remote laser welding. Laser beam is focused / directed by

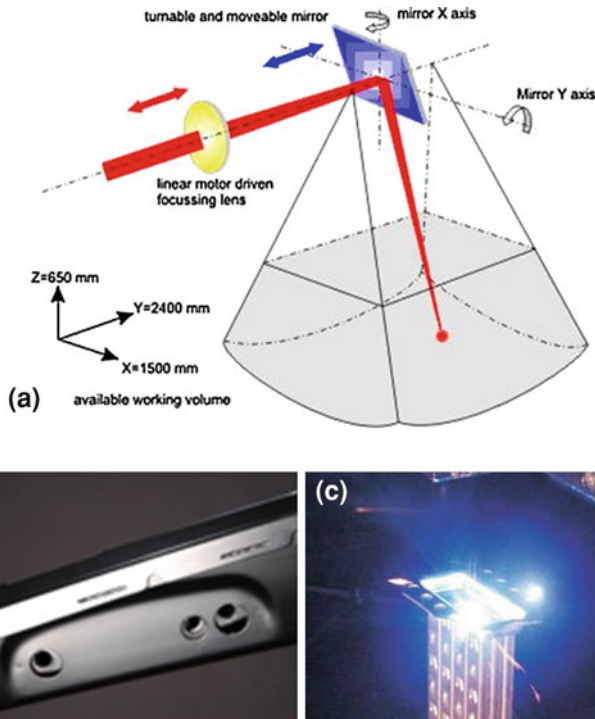


Fig. 4.37 Remote laser welding: **a** Schematic of the process [47], **b** laser stitch welding door assembly, and **c** tube to end plate welding in a heat exchanger

a mirror from a substantial distance on different locations over more than a square meter to form stitch welds at identified locations that too in a particular sequence to minimize distortion. Similarly, welding of end plate with the tubes of heat exchanger uses this technique very effectively. As there are a large number of welds to be made in a specified area, remote laser welding can complete the welding very quickly. The key advantage is the extremely quick positioning of the laser welding spot with sufficient power density enabled by the long focal length of the mirror focusing optics and the high quality of the laser beam available. Small deviations of the mirror position can result in long paths. More increased speed can be achieved in scanner welding as the positioning is achieved using one or two galvanometric rotating mirrors. But, it has a limitation in terms of processing area size.

4.10.4 Dual Beam Welding

In this process, two beams are relatively positioned in different fashions and used for welding. That is in tandem, side-by-side or, diagonally even with an overlap. They could be laser beams from two different sources or one beam split into two

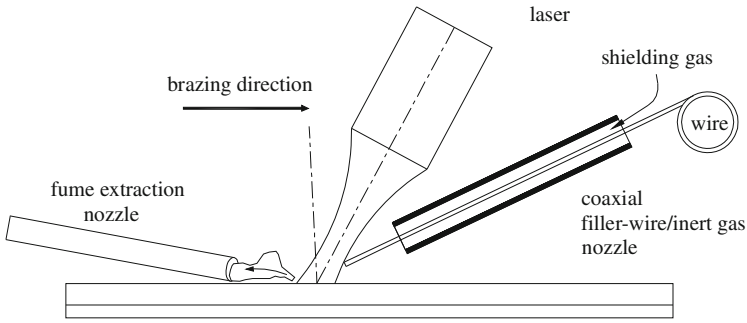


Fig. 4.38 Schematic of a typical laser brazing set up [49]

beams. Arranging the beams side-by-side accommodates higher workpiece fit-up tolerance. Arranging beams in tandem has resulted in increase in maximum welding speed without humping, decreasing the cooling rates, reduced hardness and reduced defects (by improving the keyhole stability as in the case of aluminum alloys). This kind of arrangement of two beams was also found to be very useful in welding dissimilar thickness materials, by appropriately spreading the laser energy between the two parts to be joined [48].

4.11 Laser Brazing

Laser brazing is relatively new compared to laser welding. It found applications in automotive industry in the late 1990s, for joining of galvanized steel sheets. In this process, a filler material is melted by a laser beam positioned in such a way that the molten filler material gets deposited in the intended location/gap and fills the joint. The joint forms by wetting of the workpiece surfaces by the filler and solidification in the joint. Appropriate inert gas shielding is provided to protect the brazing zone from oxidation. A schematic of typical laser brazing set up is shown in Fig. 4.38 [49]. The joint properties significantly depend on the wetting of the surfaces by the filler material and the nature of metallurgical bond that forms at the interface. Wetting is dependent on the temperature gradients in the process zone, surface free energy of the work piece and free energy of formation of metallurgical phases. Factors influencing the capillary flow into the joint are the viscosity and density of the molten metal and the joint geometry. Laser power, spot size, working distance, brazing speed, and the filler wire feed rate are the important parameters to be controlled during brazing operation. Carbon dioxide lasers, Nd:YAG lasers, and diode lasers can be used for laser brazing. However, diode lasers with shorter wavelengths have better absorptivity by metals and are becoming a choice for brazing.

Table 4.8 Composition of brazing filler CuSi3 (wt.%)

Si	Mn	Fe	Zn	Al	P	Pb	Sn	Cu
2.8–4.0	0.5–1.5	< 0.3	< 0.2	< 0.01	< 0.02	< 0.02	< 0.2	Bal.

4.11.1 Zn-Coated Steels

Zn-coated steels are usually brazed using Cu-based fillers. CuSi3 (composition given Table 4.8) is more popularly used.

Influence of various factors during laser brazing of Zn-coated steel sheets indicated that wire feeding stability, laser power distribution, and galvanized layer thickness affect brazing quality [50]. In laser brazing, the laser beam is focused on the filler wire so as to melt it and deposit in desired location. So, control of wire feed rate and alignment with the laser beam is important. With thicker wire, it is easier to coincide wire tip with the beam spot but requires higher energy to melt it. With thinner wire, swing and bending of filler wire can cause instabilities in the process. Wire feed position also has an influence on the process stability. Depending on the position of laser with respect to wire tip, some amount of energy falls on the work piece. So, the wire feeder is positioned in the front of laser beam movement direction because of which the extra laser beam energy after melting the filler wire will fall on the molten filler and keep it at a higher temperature. This could aid in improved wetting as well. Power distribution on filler wire if not maintained well may cause either lack of filler for melting or melting of large droplets depending on whether the energy is excessive or less depending on the distribution. For example, using 1.2 mm diameter CuSi3 filler wire and laser power of 2 kW with a beam spot size of 1.48 mm good brazing conditions were obtained with wire feeding at 35° angle to the laser beam and maintaining a distance of 0.8 mm. So, proper power distribution needs to be arrived at, by optimizing the filler-beam positioning depending on the brazing conditions. Typical laser-brazed sheet metal joints are shown in Fig. 4.39 [50]. Analysis of the laser brazed joint showed slightly higher microhardness zone at the braze-base metal interface. Salt spray tests showed a very insignificant effect of the process on the corrosion resistance of the alloy, indicating that it is a low heat input process.

The laser energy distribution in the brazing zone influences the characteristics of the interface region in laser brazed joints [51]. Single circular spot, dual spot and rectangular spots (Fig. 4.40) were used to braze flange butt joints of 1 mm-thick galvanized steel using CuSi3 filler metal and the interface was analyzed [51]. While no obvious interface layer was found when brazed with the circular individual beam heating, lamellar Fe–Si intermetallic compound layer was found with dual beam. Rectangular laser spot also showed a joint interface layer. This indicates the process is controllable using different laser energy distribution modes depending on requirements. The nature of substrate surface also has effect on the wettability of CuSi3 filler [52]. Hot-dip galvanized steel has better brazability than electrogalvanized steel products due to higher reactive wetting rate due to formation of iron silicide

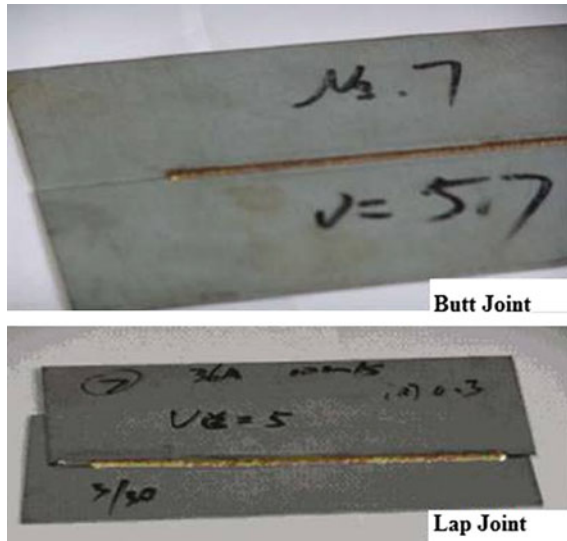


Fig. 4.39 Laser brazed Zn-coated steel sheets in butt and lap configurations [50]

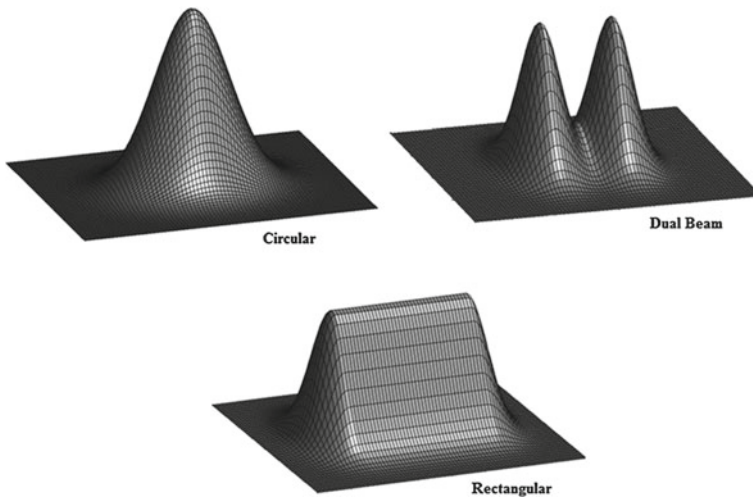


Fig. 4.40 Laser spot shapes for brazing [51]

layer. Reactive wetting is enhanced by increased filler wire temperature as well. Figure 4.41 shows a laser brazed joint of Zn-coated steel in flanged configuration to assemble body panel to roof which is now in production [52].

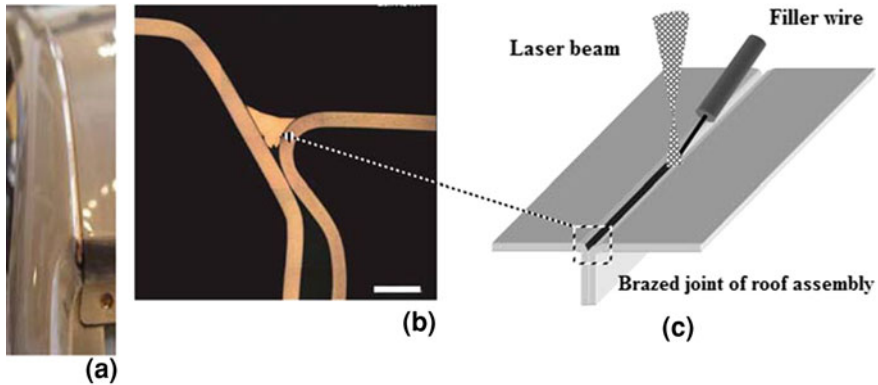


Fig. 4.41 Laser brazed joint: **a** automotive roof assembly, **b** cross section showing filled flanges, and **c** flange joint schematic [52]

4.11.2 Aluminum–Steel Brazing

Selective replacement of steel by lighter aluminum is of interest to automotive industry for achieving light weighting. Such replacement requires suitable techniques for joining these two dissimilar materials. Due to limited solubility of aluminum in steel, fusion of these materials result in the formation of brittle intermetallic phases which weaken the joint, in some cases almost unable to form a joint. Mechanical and adhesive joining techniques can be resorted to, however; they have disadvantages such as wider flanges with additional sealing requirement and corrosion problems, respectively. Low heat input thermal joining processes such as brazing where in the base materials are not melted have good promise in accomplishing these joints. Laser brazing is considered a strong contender as it is a low and controllable heat input process with amenability to automation and high productions speeds. However, there are several issues such as poor wetting of molten aluminum-based fillers on steel surface, formation of intermetallic layer at the interface, porosity, distortion due to mismatch in thermal expansion of the two materials, etc., to be addressed to accomplish good aluminum-steel joints. One of the methods of improving wetting is by using fluxes. However, it drastically affects productivity due to two additional steps involved, viz., application of flux prior to brazing and cleaning of the residues after brazing.

4.12 Laser Selective Soldering

In laser soldering, fine laser beam is used to melt the solder and form the joint. Hence, it is a clean, non-contact process with possibility to control the heat input very precisely and can solder smaller components than other soldering methods.

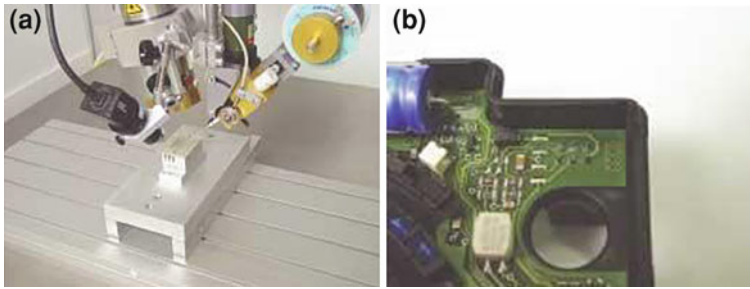


Fig. 4.42 Laser soldering. **a** Typical set up with laser beam (*middle*), solder wire feeder (*right*) and CCD camera for process monitoring (*left*), and **b** surface mounted components on the circuit board using laser soldering [53]

A typical setup is shown in Fig. 4.42(a) [53]. The laser soldering process overcomes drawbacks of other techniques. For example, problems of contamination, application of mechanical force, frequent cleaning and replacement of tip as in the case of soldering iron process; uncontrolled heating in case of micro-flame soldering; complexity and space requirement of induction heating system for induction soldering. Diode lasers, diode pumped Nd:YAG lasers, and fiber lasers can be used for laser soldering. Depending on the solder joint size and the solder material, laser power required is in 10–100 W range. Depending on soldering time requirement, the laser power needs to be switched on and off, which is typical at a frequency of 1 Hz.

While diode lasers are capable of producing spot sizes in 0.4 mm range, applications requiring smaller spots can be addressed using TEM₀₀ laser, such as, like fiber lasers. These lasers have higher working distances also. Laser soldering is extensively used to solder surface mount components onto PC boards, and is well suited for ball grid array (BGA) soldering (see Fig. 4.42b) [53]. The 0.5–1 mm spot sizes typically achieved with diode laser soldering systems allow very localized heating, while the delivered energy can be precisely controlled.

4.13 Laser Welding of Non-Metallic Materials

4.13.1 Plastic Welding

Laser welding of plastics is carried out by transmission welding. One of the plastics to be joined is translucent to the laser beam and the other absorbing. When laser is irradiated from the translucent side the energy is absorbed at the interface between the translucent part and the absorbing plastic part and the heat generated results in joining. Hence, this process is called laser transmission welding. Diode lasers in combination with galvoscaning systems can be used for welding of almost all thermoplastics [49]. Traditionally, plastics are joined by ultrasonic welding, vibration welding, or

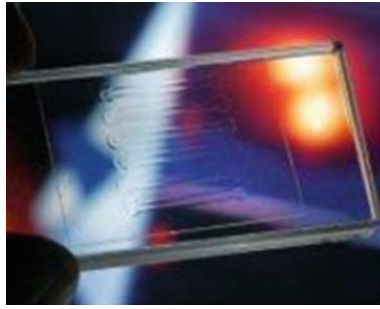


Fig. 4.43 Transparent plastics joined via laser beam at a wavelength of around 1700 nm [55]

heated tool welding. Unlike ultrasonic welding, laser welding is not limited by the hard/soft plastic combination or the part size. Production solutions have already been developed for welding of containers, electronic housing, automotive parts, and foils. Very recently, the constraint of at least one part being absorptive for being able to weld plastics has been overcome as shown in Fig. 4.43 [55]. This has been achieved by identifying the right wavelength, viz., 1700 nm. The new welding process is revolutionizing bioanalytics. The process has been successfully applied to welding of a casing and cover of speedometer. Welding at this wavelength did not cause any sparks or particles flying which is observed otherwise. Suitable wavelength was identified by studying the absorption spectra of a range of transparent polymers in search of wavelength ranges within which plastic absorbs laser radiation and develop laser systems that emit light of the right wavelengths. This development extends the range of applicability of laser welding process and will be the subject of active research in the near future, owing to the tremendous applications in field such as bioanalytics.

4.13.2 Laser Joining of Metal and Plastic

Joining of metals to plastics is conventionally done using adhesive bonding or mechanical joining. Adhesive bonding has certain drawbacks such as longer production cycles, weak peel strength, and limited shelf life of adhesives apart from harmful emissions. Mechanical joining has some limitations such as reduced design flexibility, requirement of additional sealing, etc. Laser-assisted metal and plastic (LAMP) joining, a recently developed process, overcomes the above drawbacks. In LAMP joining process, metal and plastic are placed in a lap joint configuration and a laser spot scanned over the plastic which is transparent (Fig. 4.44) [56]. This causes melting of the plastic near the joint interface and formation of small bubbles in the melted plastic by heat conducted from the metal. In case of a non-transparent plastic such as GFRP, CFRP the laser is scanned on the metal side

(a) Transparent plastic

LD beam :

Power, P : 170 WWavelength, λ : 807 nm

PET

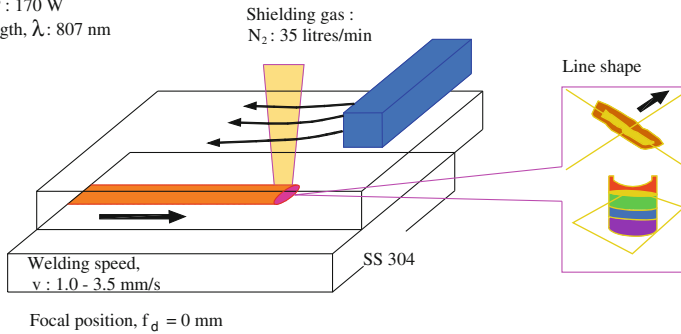
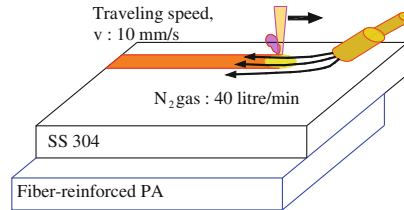
**(b)** Non-transparent plasticFiber laser, (λ : 1.07 μ m)Laser power P : 2 kW

Fig. 4.44 Schematic of LAMP joining process for metal-plastic joining: **a** transparent plastic, and **b** non-transparent plastic [56]

and the heat conducted to the interface caused melting of the plastic. If the metal plate is thick, a partially penetrated weld should be produced to heat the plastic near the joint interface. LAMP joining can be used to bond thermoplastics, especially engineering plastics, to any metal. The samples of polyethylene terephthalate (PET) plastic joined to AISI 304 stainless steel with laser beam are shown in Fig. 4.44 [56]. The tensile shear loads (strengths) of samples of PET sheets of 30 mm width and 2 mm thickness to Type 304 plates of 30 mm width and 3 mm thickness possess was found to be 3000 N, where the base PET is elongated. This LAMP joining technology is applicable to many combinations of metals such as steels, titanium, and aluminum alloys, and plastics such as PET, polyamide (PA), and polycarbonate (PC). The formation of small bubbles of 0.5 mm or less due to rapid temperature history induced by laser is important because the strengths of the LAMP joints are low when the bubbles are too small and high when the sizes of bubbles are large.

Formation of small bubbles to induce high pressure in the melted plastic to force the molten plastic to the metal surface due to the rapid thermal cycle is the mechanism

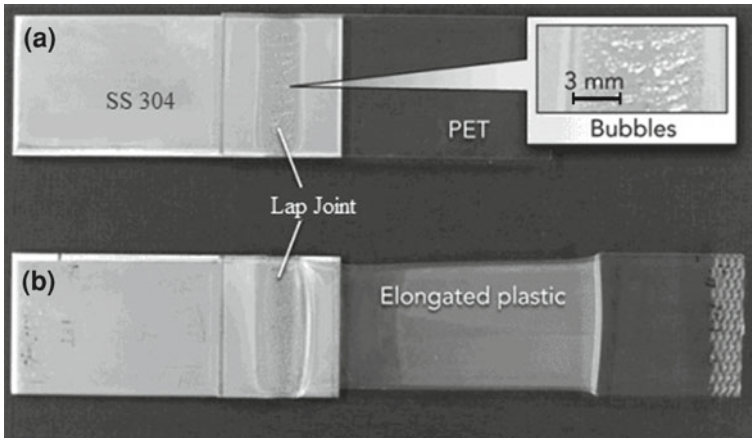


Fig. 4.45 Joining of PET plastic to AISI 304 stainless steel produced with the laser beam before (a) and after (b) [56]

of working. The melted plastic approaches the metal surface and enters the concavity to fulfill the mechanical force called anchor effect. Physical Van der Waals interaction force and chemical bonding through the oxide film are expected to produce a strong joint. The joint properties are governed mainly by the kind of the plastics and the laser irradiation conditions. The process is very new and some applications are still under initial development stage.

4.14 Applications of Laser Welding and Brazing

Laser welding may be looked at as a high-speed precision joining process, which is well suited for automation. For a particular application there are many ways of joining, but there are particular features of laser, which makes it most suitable for some applications, such as automotive transmission components require high production rates and low distortion, titanium pacemaker housings require low heat input and electron beams would destroy the electronic inside, tailored blanks for automotive body parts require very thin weld lines with minimal effect on the formability characteristics and at high production rates, etc.

4.14.1 Tailor Welded Blanks

Tailor blank welding was a very significant application of laser welding since early 1990s with TWB welding systems constituting a key part of industrial laser market.

Almost 25–30% of all steel body-in-white structure of high volume production is made up of tailor welded blanks. TWBs are basically multi-gauge blanks made of different steel sheets in terms of composition and/or thickness to tailor the blank with different properties at different locations as per design requirements. Laser welding is best suited for fabrication of TWBs primarily due to the advantages such as very narrow weld fusion and heat affected zones and high welding speeds. Due to narrow weld affected zone the formability of the blank is not adversely affected. High welding speeds result in high productivity which is an important consideration in automotive industry. However, accomplishing consistently good quality blanks requires development of suitable welding procedures. Some of the frequently encountered defects during laser welding of TWBs are shown in Fig. 4.46. Undercuts are caused by melt drop out and lack of sufficient molten metal in the joint; lack of fusion is due to missing of the edges by very small laser spot; concavity is caused by high edge gap; and porosity is caused by contaminants in the weld zone. Very thin sections and small welding spot sizes are mainly the reasons for occurrence of such defects. Preparation of accurate welding edges has significant effect. Figure 4.47 shows the effect of edge preparation methods used before welding. So, the process is very sensitive to edge gap. Additionally, as the sheets are thin with possibility of local undulations, at certain places mismatch of weld edges occurs in turn resulting in mismatched welds. This problem is overcome by using pressing rollers ahead of the laser beam so that, the plates to be welded are not only pressed to coincide in the same plane and in some cases the edges are mashed by the pressure of the rollers into the edge gaps, if any. Sometimes, addition of filler wire is also effectively used to address this problem. Increase in thickness ratio is also found to be helpful in bridging the edge gaps better. This is done by focusing the beam more on to the thicker side in order to melt more metal to fill the gap. Use of seam tracking systems help in avoiding lack of fusion due to missing of edges. Seam trackers are extensively used in laser welding and for TWBs to obtain consistently good weld quality.

A wide range of steels starting from very low carbon interstitial free steels (IF Steels) and high strength low alloy (HSLA) steels to advanced high strength steels (AHSS) such as the dual phase (DP) steels and TRIP steel are used in automotive construction. Conventionally, TWBs use the formable steels such as the Interstitial Free (IF), Extra Deep Drawing (EDD)-type steels, which are drawable and have less hardenability and minimal heat affected zone (HAZ) due to welding. Several factors affect formability of TWBs like strength ratio of the steel combination (thickness and/or composition) chosen, welding process, welding parameters etc. Increased weld heat input resulted in decreased formability in TWBs fabricated from high strength steels and fatigue properties decreased with increase in strength ratio [57]. Forming limit diagrams (FLDs) of TWBs laser welded from HSLA steel sheets with different thickness indicated decrease in forming limits and minimum major strain values with increase in thickness ratio [58]. This implies that higher the thickness ratio lower the formability of the TWBs. Recently, usage of AHSS-like DP Steels, Transformation-induced plasticity steels (TRIP) has increased, as it facilitates further decrease in the gauge and consequently weight. Incorporating AHSS into TWBs can

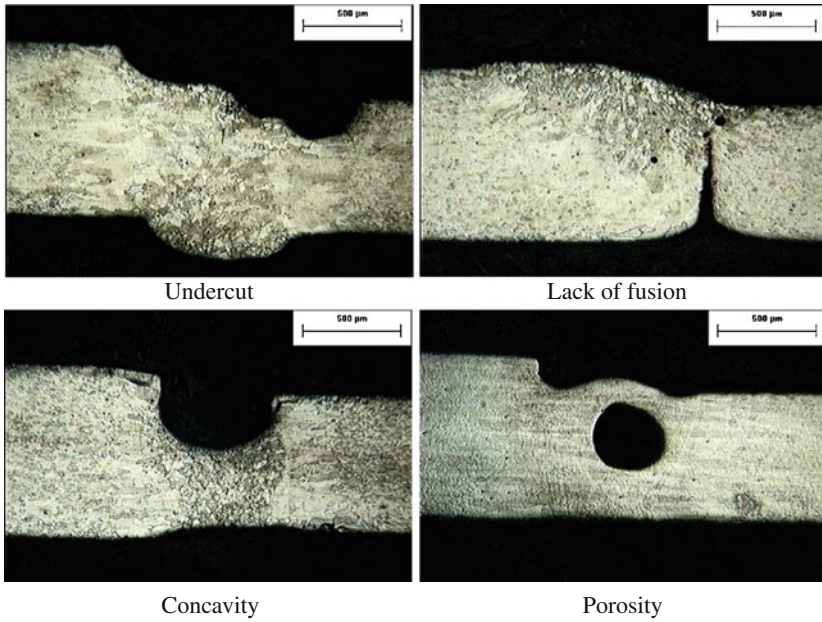


Fig.4.46 Typical defects encountered during laser welding of TWBs (G. Padmanabham, “Un-published results”)

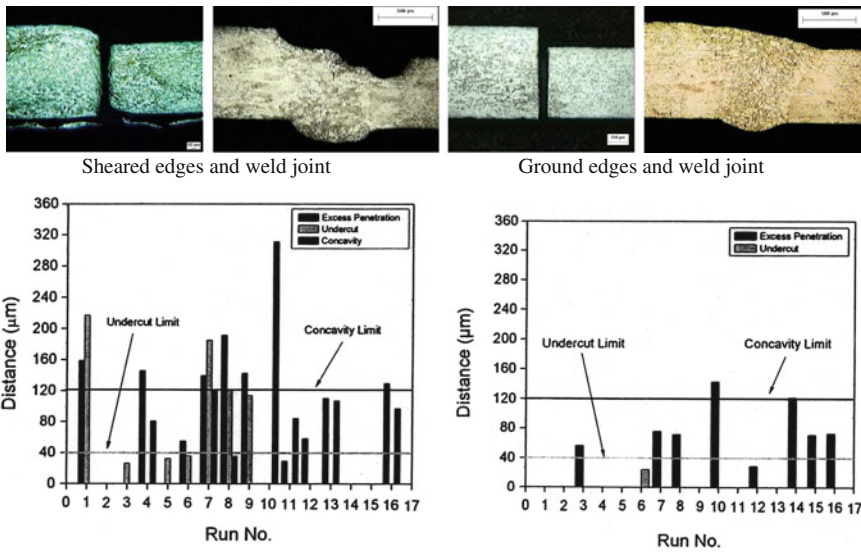


Fig.4.47 Effect of edge preparation on defects in laser welded TWBs (G. Padmanabham, “Un-published results”)

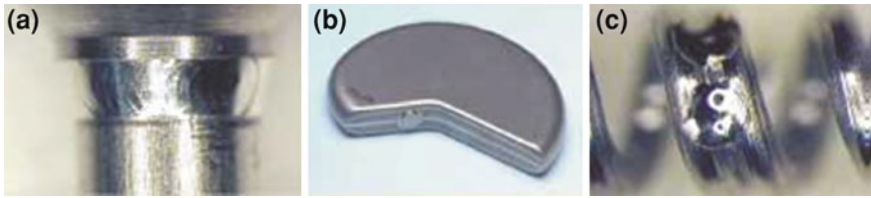


Fig. 4.48 Laser welded medical devices. **a** End effect tools welded to tube body, **b** hermetically sealed implant, and **c** spot welding on catheter coil for stent or balloon placing [64]

yield more significant weight reductions and design benefits. However, laser welding parameters for these alloys containing certain alloying elements needs to be better understood as they may respond differently to welding. Uchihara et al. [59] fabricated TWBs of different AHSS using laser, mash seam, and TIG welding processes and found laser welding to be the best process giving a good quality weld with the narrowest weld width. Welds with lower hardness were found to have better formability in case of laser welded tailored blanks. Laser welds of dual phase steels showed a martensitic matrix with increased hardness [60]. TWBs in TRIP-DP and TRIP-MS combination have also been studied and it was observed that the formability of TRIP-DP welds was low compared to a TRIP-MS combination [61]. IF-DP TWBs showed formability in between the two base metals yielding a good formability, for a range of welding parameters [62, 63].

4.14.2 Medical Devices

Fabrication of medical devices is a challenging task in terms of achieving high reliability and repeatability [64]. This becomes more challenging as the devices are becoming smaller and smaller. Microwelds as small as 35 μm diameter, catheters and guide wire assemblies, typically fabricated from Nitinol or 304 stainless wire with an outside diameter of 50.8–127 μm , and hermetic sealing of implantable devices are some of the common medical devices fabricated by laser welding (Fig. 4.48). The pulsed Nd:YAG laser represents the best laser solution, due to ease in carrying out spot welding with minimal heat input. Fiber lasers are now becoming popular for these applications due to high quality beam, smaller foot print, and higher energy efficiency. The main requirement in welding of these devices is excellent weld quality with minimal heat input. The laser used should be able to produce excellent pulse-to-pulse stability, at any point of welding irrespective of warm or cold start and flash lamp life. Recently, diode-pumped Nd:YAG and fiber lasers are being used for these applications as it is possible to obtain good beam quality, stability at higher energy efficiency.

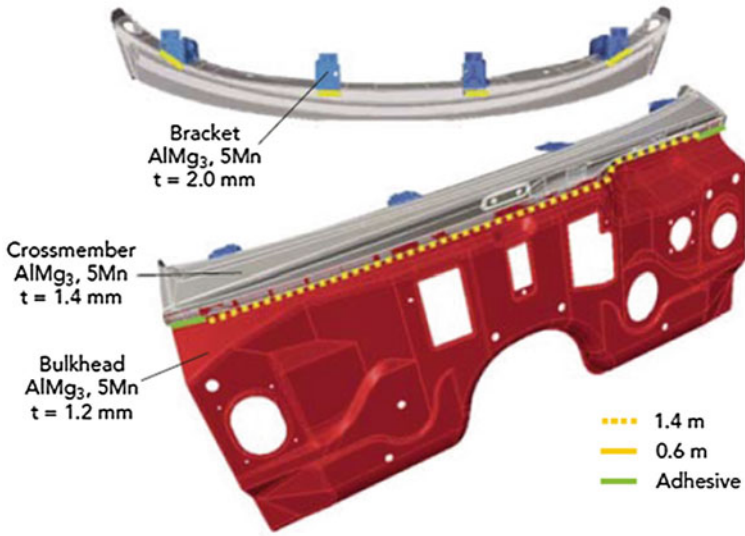


Fig. 4.49 Sheet metal bulk head joined to hydroformed cross member which has several brackets laser welded on to it [65]

4.14.3 Automotive Body

Firewall of automotive body is case of joining sheet metal shell (firewall) with a cross beam (hydroformed part). Two locations, one is the connection of the sheet metal to the hydroformed part and the other is joining of several brackets on the hydroformed part (Fig. 4.49) [65]. Because the locations are accessible from only one side, laser welding capable of consistent depth of penetration became indispensable. The 4kW Nd:YAG lasers in twin beam method were used with filler wire to accomplish these joints.

4.14.4 Li-Ion Battery

Lithium-ion batteries are the most sought after energy storage devices with several applications ranging from mobile phones to space crafts. However, they have a major drawback that lithium is explosive when in contact with air and water. So the packaging has to be with high quality hermetic sealing. In automotive application they should also survive crash. Because of this welding process for packaging the cases is critical in manufacture of these cells. A typical cell construction is shown in Fig. 4.50a [66]. Li-ion batteries are available in different sizes and shapes as shown in Fig. 4.50b [66]. Welding is popularly done using lasers assisted by a machine vision system. The two end caps are welded to cell body with good hermetic sealing. The sections are very thin and if controlled heat input is not used, the beam can penetrate



Fig. 4.50 Laser welding of lithium ion batteries, **a** Schematic of various components to be welded, and **b** welded batteries of different sizes [66]

through the casing and cause damage to the anode/cathode resulting in a hot cell. In short, good hermetically sealed joints with minimum heat input or temperature rise during welding and at the same time adoptable to different sizes and shapes are the requirements to be met by the welding process. When welding very thin sections, there can be a start and end hole left at the end of welding step. In case of lasers, it is possible to precisely control the power in such a way that the welding process can be started with very low power with partial penetration and slowly ramped up over a distance to a level where the penetration is complete and similar ramping down towards end of the weld, overlapping with the ramp up weld zone, to complete the welding. Penetration and temperature rise in the weld zone can be precisely controlled with pulsed laser. Further, due to the flexibility of the beam to be made to follow the weld seams accurately, by appropriate vision and seam tracking system; and availability of range of powers and spot sizes, the whole process can be automated to be able to weld a wide variety of batteries in single machine. Pulsed Nd:YAG laser and fiber lasers can be used for this application.

4.14.5 Joining of Stiffeners to the Skin in the Fuselage Belly Area

Stiffeners are welded along the fuselage panels using two CO₂ laser welding heads on either side of the stiffener. Figure 4.51 shows the large 16 m long fixture for accomplishing the task [67]. Weight reduction and high productivity are the drivers for this technology development. The idea is to replace riveting by welding. Joining by riveting is done at a speed of 0.2–0.4 m/min with full automation. The technology has more or less saturated and laser welding was identified to be a potential candidate. Laser welding can be done at a speed of 6 m/min. It can eliminate rivet straps in aircraft skin and butt ends of the stringers leading to structure weight reduction of 5%. There are further possibilities of improving the materials used and the joining process to



Fig. 4.51 Fixture for laser welding of stiffeners to fuselage skin [67]

realize more weight reduction. The technology can be implemented in other sectors such as automotive as well.

4.14.6 Solar Absorber Plates Cu/Al Plate-Cu Tube Welding

The main component in solar thermal energy collection systems is the absorber which is in the form of a vacuum tube or plate. In case of plate collector, a flat plate made of copper or aluminum is coated on one side with selective solar absorber and emissive coatings to efficiently collect the energy from sunlight. On the other side of the collector plate, copper tubes carrying thermic fluid are attached as shown in Fig. 4.52 [68]. The heat absorbed by the plate is conducted into the thermic fluid flowing in the tubes and raises the temperature of the water. This heated water is then appropriately used for energy production. Typical collector panel is 1.2×2.0 m in size with about 20,000 spot welds for attaching the tubes carrying the thermic fluids. There are several challenges in welding these panels. Copper is highly thermal conducting and enough power density is required for coupling and melting the material. When used in combination with aluminum, substantial difference in thermal expansion can cause thermal gradients and distortions. So welding has to be carried out with minimal heat input. At the same time, due to welding process the absorber coating on the other side of the plate should not get damaged due to temperature rise occurring due to welding. Controlled heat input is the key to solving this problem. Location of the weld is also somewhat inaccessible. As mentioned earlier, a large number of spot welds have to be carried out with consistency which requires automation of the production process. Pulsed Nd:YAG laser could be successfully applied to meet this challenge. Fiber delivered pulsed Nd:YAG laser could be used to reach the welding spot at a shallow angle of 20° by using suitable optics which can give sufficient

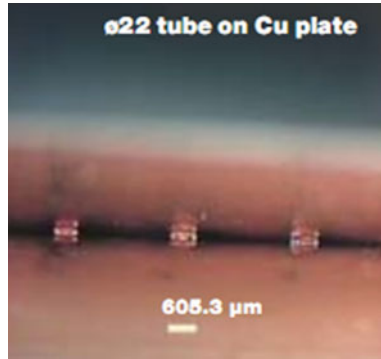


Fig. 4.52 Solar thermal plate collector Cu plate—Cu tubes laser welded [68]

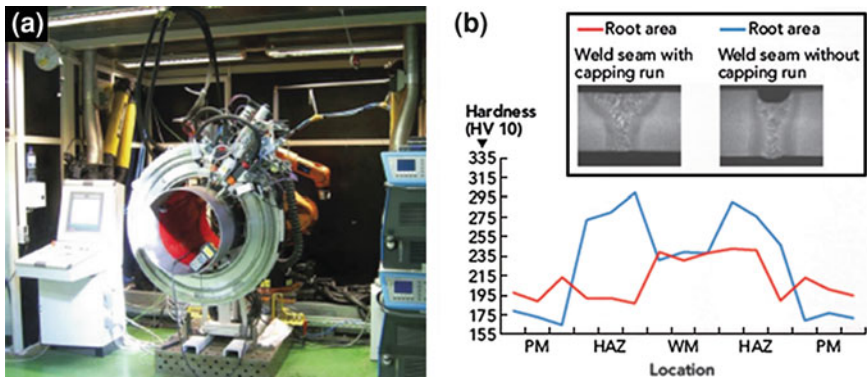


Fig. 4.53 Laser hybrid welding. **a** Set up along with trailing MIG torch for filler pass, and **b** macrosections and hardness profile across the weld with and without capping pass [69]

standoff. Pulsed lasers offer high power density in individual pulses. Pulse energy of 8 J in case of Cu–Cu combination and 5 J in combination of Al–Cu combination were used to fuse the material and form a spot weld. Each pulse was used to make one weld. So by using high repetition rate plate-tube assembly could be welded at 9 m/min with a 2 mm gap between each stitch. Further heat input optimization could also be done by temporal pulse shaping. Optimized heat input and welding parameters could also achieve minimum damage to the absorber coating on the other side of the plate. In short, the advantages of using pulsed laser welding are very obvious in successfully producing these solar absorber panels.

4.14.7 Laser Hybrid Pipeline Welding

Oil and gas pipelines are conventionally welded using shielded metal arc welding with electrodes and GMAW. Owing to the nature of the weld and the remote sites at

which the welding has to be accomplished, it is quite a tedious task in terms of large manpower and plant engineering requirements to weld thick sections, location after location. Even multiple welding stations are used to increase productivity. Laser-MIG hybrid welding which combines the deep penetration capability of laser and gap bridging capability of MIG arc has been successfully used to achieve welding of two pipes of 500–700 mm diameter with a wall thickness of 10–12 mm in single pass at speeds as high as 3 m/min. The prototype welding setup is shown in Fig. 4.53 [69]. The setup includes a laser beam from a 6 kW fiber laser and GMAW torch, followed by another GMAW torch for filling the weld joint. This arrangement of a trailing torch was found useful not only for filling the groove fully but also for tempering the root pass made by laser hybrid welding. The main advantages expected to be drawn in adopting this technique were, increased efficiency in pipeline construction with increased welding speed with minimum number of weld passes. Advent of fiber lasers with high powers will extend the application of this laser hybrid process to many more applications.

Acknowledgments Authors wish to specially acknowledge all the researchers whose work is described in this review for their valuable contributions. They would also like to thank Dr G. Sundararajan, Director, ARCI for permitting to publish this book article. Further, authors would like to express their gratitude to their colleagues at the Centre for Laser Processing of Materials, ARCI for the support and assistance rendered in compiling this work. Special thanks are due to Dr. I. Ganesh for giving shape to this chapter.

References

1. D.A. Belforte, *Markets Keep Getting Better, Industrial Laser Solutions for Manufacturing*, January 2007, p. 8
2. *Standard Welding Terms and Definitions*, ANSI/AWS A3.0–89, (American Welding Society, USA, 1989)
3. T.W. Eagar, A.D. Mazzeo, ASM Handbook, in *The Materials Information Society*, vol. 6A, ed. by T. Lienert, T. Siewert, S. Babu, V. Acoff. Welding Fundamentals and Processing, Copyright 2011, ASM International, pp. 29–34
4. J.F. Ready, D.F. Farson, T. Feeley (eds.), *The LIA Handbook of Laser Materials Processing* (Springer Publishers, Berlin, 2001) pp. 310–316
5. J.H. Sharp, *Laser fundamentals*, Internet website of the Welding Institute (TWI), UK, 2004, (<http://asaha.com/download/MMTk0MzI->). dated: 13th Sept 2011
6. P. Solana, J. L. Ocana, J. Phys. D **30**, 1300–1313 (1997)
7. A. Matsunawa, V. Semak, J. Phys. D: Appl. Phys. **30**, 798–809 (1997)
8. E. Beyer, *Fiber Laser Welding, Industrial Laser Solutions for Manufacturing*, July 2006, pp.13–14
9. D. Havrilla, *Process Fundamentals of Industrial Laser Welding and Cutting* (Rofin-Sinar Inc, Hamburg, 1999)
10. N. Lazov, L. Angelov, Physical model about laser impact and metals and alloys. *Contemp. Mater.* **1-2**, 124–128 (2010)
11. J. Xie, A. Kar, Laser welding of thin sheet steel with surface oxidation, *Weld. J.* 342–348 (1999)
12. M. Ono, A. Yoshitake, M. Ohmura, *NKK Tech. Rev.* **86**, 13–18 (2002)
13. Y.F. Tzeng, *J. Mater. Proc. Tech.* **102**, 40–47 (2000)

14. Advantages of Pulse Shaping: <http://www.jklasers.com/advantages-of-pulse-shaping>
15. B. Shanmugarajan, J.K. Sarin Sundar, R. Bathe, S. Shukla, *Laser Welding-A Productive Tool, presented at the Conference on Welding Productivity and Quality (WPQ 2007)*, (Naval Material Research Laboratory, Ambarnath, India 2007)
16. H. Walker, *Welding with Super Modulated Laser, Industrial Laser Solutions for Manufacturing*, July 2007, pp. 14–17
17. M.G. Forrest, F. Lu, *Joining new auto body materials*, (<http://www.industrial-lasers.com/articles/2007/03/joining-new-auto-body-materials.html>); dated: 13th Sept 2011
18. B. Shanmugarajan, G. Padmanabham, H. Kumar, S.K. Albert, A.K. Bhaduri, *Sci. Tech. Weld. Joining* **16**, 528–534 (2011)
19. K.H. Leong, H.K. Geyer, K.R. Sabo, P.G. Sanders, *J. Laser Appl.* **9**, 227–232 (1997)
20. E. Schubert, M. Klassen, I. Zerner, C. Walz, G. Sepold, *J. Mater. Proces. Technol.* **115**, 2–8 (2001)
21. A. Ancona, T. Sibillano, L. Tricarico, R. Spina, P.M. Lugar, G. Basile, S. Schiavone, *J. Mater. Proces. Tech.* **164–165**, 971–977 (2005)
22. K.H. Leong, K.R. Sabo, C.E. Albright, *J. Laser Appl.* **11**, 109–118 (1999)
23. B. Hu, I.M. Richardson, *J. Laser Appl.* **70**, 17–18 (2005)
24. M. Naeem, R. Jessett, *Welding aluminum tailored blanks with Nd:YAG lasers for automotive applications, Practical welding today*, Feb 2001, (<http://www.thefabricator.com/article/automationrobotics/welding-aluminum-tailored-blanks-with-ndyag-lasers-for-automotive-applications>)
25. J.K. Kristensen, M.M. Andersen, N.K. Bruun, T.A. Jensen, S.E. Nielsen, *J. Welding, Laser Welding of Aluminium Alloys—Process and Properties. in Proceedings of 8th NOLAMP Conference*, Copenhagen, Denmark, August 2001
26. G. Padmanabham, B. Shanmugarajan, *Experimental Investigation on Bead-on-Bead CO₂ Laser Welding of Al Alloy 6061. Proceedings of the 8th ASM Trends in Welding Research Conference*, Mountain View, Georgia, USA, 22 June 2008
27. B. Hu, I.M. Richardson, *Mat. Sci. Eng. A* **429**, 287–294 (2006)
28. G. Dearden, M.C. Simmons, P.Okon, G.K. Schleyer, K.G. Watkins. *Blast and Impact Resistance Studies of Laser Welded and Riveted Panel Structures*. 21st International Congress on Application of laser and electro-optics, ICALEO 2002, Scottsdale, 14–17 October 2002
29. J.K. Sarin Sundar, G. Padmanabham, R.N. Gupta, R. Reddy. *Investigations on Laser Welding Feasibility for Fabrication of Ti-6Al-4V Structure for Aerospace Applications SAME. Proceedings of the National Aerospace Manufacturing Seminar, NAMS-2007, Thiruvananthapuram*, pp. 6, 2007
30. G.D. Janaki Ram, A. Venugopal Reddy, K. Prasad Rao, G.M. Reddy, J.K. Sarin Sundar, *J. Mater. Process. Technol.* **167**, 73–82 (2005)
31. M.M. Avedesian, H. Baker, *Magnesium and Magnesium Alloys, ASM Specialty Handbook*. (1999)
32. J. Zhu, L. Li, Z. Liu, *Appl. Surf. Sci.* **247**, 300–306 (2005)
33. S. Lathabai, K.J. Barton, D. Harris, *Magnesium Technol.* , 157–162 (2003)
34. A. Weisheit, R. Galun, B.L. Mordike, *Weld. J.* **77**, 149–154 (1998)
35. H. Zhao, T. Debroy, *Weld. J.* **80**, 204–210 (2001)
36. G. Shannon and P. Sheverloh, *Green lasers for microwelding, industrial laser solutions for manufacturing*, July 2011, (<http://www.industrial-lasers.com/articles/print/volume-26/issue-4/features/green-lasers-for-laser-micro-welding.html>)
37. B. Regaard, S. Kaierle, R. Poprawe, *J. Laser Appl.* **21**(4), 183–195 (2009)
38. J. Shao, Y. Yan, *J. Phys.* **15**, 101–107 (2005)
39. M. Ono, K. Nakada, S. Kosuge, *An investigation on CO₂ laser-induced plasma*, *J. Jpn. Weld Soc.* **10**, 239–245 (1992)
40. J. Griebisch, L. Schlichtermann, M. Jurca, S. Heibler, D. Funk, *Qualität laser*, 5 1996 (http://www.datlas.se/web/PDF/Kessler_%20on-line_qualit.pdf)

41. M. Wouters, Hybrid Laser MIG Welding: An investigation of geometrical considerations, Licentiate Thesis, Luleå University of Technology, Lulea, Sweden, Nov 2005, (<http://epubl.ltu.se/1402-1757/2005/82/LTU-LIC-0582-SE.pdf>)
42. M.E. Rayes, C. Walz, G. Sepold, The influence of various hybrid welding parameters on bead geometry. *Suppl. Weld. J.* 147-S–153-S (2004)
43. M. Ono, Y. Shinbo, A. Yoshitake, M. Ohmura, Development of laser-arc hybrid welding. *NKK Techn. Rev.* **86**, 8–12, (2002)
44. B. Shanmugarajan, P. Rajesh, E. Krishnaveni, G. Padmanabham, Process and fusion behavior during CO₂ laser-MIG hybrid welding of thick section mild steel plates. *Proceedings of the International Welding Symposium, IWS2k10*, Mumbai, India, 10–12 (2010)
45. G. Campana, A. Fortunato, A. Ascari, G. Tani, L. Tomesani, *J. Mater. Process. Tech.* **191**, 111–113 (2007)
46. Laser induction welding, (Fraunhofer institute for materials and beam technologies) (IWS), (http://www.ccl.fraunhofer.org/download/laser_welding_powertrain_components.pdf)
47. R. Sinar, Scanner and remote welding, (http://www.rofin.com/en/applications/laser_welding/scanner_and_remote_welding)
48. J. Xie, *Weld. J.* 223–230 (Oct 2002)
49. H. Laukant, C. Wallmann, M. Mueller, M. Korte, B. Stirn, H.-G. Haldenwanger, U. Glatzel, Flux less laser beam joining of aluminium with zinc coated steel. *Sci. Tech. Weld. Joining* **10**, 219–226 (2005)
50. F. Lu, B. Lu, X. Tang, S. Yao, *Int. J. Adv. Manuf. Technol.* **37**, 961–965 (2008)
51. L.Q. Li, X.S. Feng, Y.B. Chen, *Trans. Nonferrous Met. Soc. China* **18**, 1065–1070 (2008)
52. A. Koltsov, N. Bailly, L. Cretteur, Fatigue behavior of tailor (laser) welded blanks for automotive applications. *J. Mater. Sci.* **45**, 2118–2125 (2010)
53. A. Lauzinger, *Selecting Laser Selective Soldering*, Industrial Laser Solutions for Manufacturing (2004) p. 10
54. K.E. Kleine, M. Nagel, *Welding Plastic, Industrial Laser Solutions for Manufacturing*, October 2006
55. Laser welding in the right light, ILS Newsletter, 17 Feb 2011
56. S. Katayama, ILS Newsletter, 1 Nov 2010, (<http://spie.org/app/profiles/viewer.aspx?profile=EMIZBO>)
57. D. Anand, D.L. Chen, S.D. Bhole, P. Andreychuk, G. Boudreau, Fatigue behaviour of tailor (laser) welded blanks for automotive applications. *Mater. Sci. Eng. A* **420**, 199–207 (2006)
58. S.M. Chan, L.C. Chan, T.C. Lee, *J. Mater. Process. Tech.* **132**, 95–101 (2003)
59. M. Uchihara, K. Fukui, *Weld. Int.* **20**, 612–621 (2006)
60. P. Rizzi, S. Bellingeri, F. Massimino, D. Baldissin, L. Battezzati, *J. Phys. Conf. Series*, **144**(1), 012005, (2009), (http://iopscience.iop.org/1742-6596/144/1/012005/pdf/1742-6596_144_1_012005.pdf)
61. R.S. Sharma, P. Molian, *Mat. Design* **30**, 4146–4155 (2009)
62. B. Shanmugarajan, J. K. Sarin Sundar, G. Padmanabham, Laser Welding of Advanced High Strength Steels for Tailor Welded Blanks (TWB) Applications, SAE No.2009-028-0012
63. S. Chatterjee, R. Saha, M. Shome, R.K. Ray, *Metallur. Mater. Trans A* **40**, 1142–1152 (2009)
64. C. Marley, G. Shannon, Welding medical devices, industrial laser solutions for manufacturing, July 2004, (http://www.miyachiunitek.com/servlet/servlet.FileDownload?retURL=%2Fapex%2FProducts_LaserWelding_LW5AM&file=0158000001JcY1AAK)
65. F.J. Gruber, Lasers—where they make sense, industrial laser solutions for manufacturing, March 2006, p. 10 (<http://www.industrial-lasers.com/articles/2006/03/lasers-where-they-make-sense.html>)
66. J. Roe, Vision guided laser welding improves battery safety performance, industrial laser solutions for manufacturing, (<http://www.industrial-lasers.com/articles/print/volume-250/issue-6/features/vision-guided-laser-welding-improves-battery-safety-performance.html>)
67. I. Roetzer, *Laser Beam Welding Makes Aircraft Lighter*, Fraunhofer Magazine 1, (2005) pp. 36–37

68. U. Duerr, Welding solar thermal absorbers, industrial laser solutions for manufacturing, Sept 2006, (<http://www.industrial-lasers.com/articles/2006/09/welding-thermal-solar-absorbers.html>)
69. S. Keitel, U. Jasnau, J. Neubert, *Applications of Fiber Laser Based Deep Penetration Welding in Shipbuilding, Rail Car Industries and Pipe Welding*, 4th International Symposium on High-Power Laser and their Applications, 24–26 June 2008, St. Petersburg, Russia, (<http://www.industrial-lasers.com/articles/print/volume-26/issue-3/features/laser-hybrid-pipeline.html>)

Chapter 5

Direct Laser Cladding, Current Status and Future Scope of Application

A. Weisheit, A. Gasser, G. Backes, T. Jambor, N. Pirch
and K. Wissenbach

Abstract During the last decades Direct Laser Cladding has become an established technique in many industrial fields for applying wear and corrosion protection layers on metallic surfaces as well as for the repair of high value-added components. The most important application fields are die and tool making, turbine components for aero engines and power generation, machine components such as axes and gears, and oil drilling components. Continuous wave (CW) lasers with a power up to 18 kW are used on automated machines with three or more axes, enabling 3D cladding. The outstanding feature of DLC is the high precision which leads to a minimum heat input into the work piece and a very low distortion. Due to the high cooling rates a fine grained microstructure is achieved during solidification. A new development in laser cladding is micro cladding in a size range below 50 μm especially for electronic and medical applications. Furthermore, additive manufacturing is coming again into focus as a clean and resource-efficient method to manufacture and modify functional prototypes as well as unique and small lot parts.

5.1 Introduction

In the early 1980s of the last century with the advent of industrial high power lasers DLC was identified as an interesting field for researchers as a new technology for surface applications. Accompanied by the development of new laser sources (e.g., diode laser), improved beam quality and increased power efficiency laser cladding has become an established industrial technique during the last 2 decades for applying wear and corrosion protection layers on metallic surfaces as well as for the repair

A. Weisheit (✉) · N. Pirch · K. Wissenbach
Fraunhofer-Institut fuer Lasertechnik, ILT, Steinbachstr. 15, 52074 Aachen, Germany
e-mail: andreas.weisheit@ilt.fraunhofer.de

G. Backes · T. Jambor
RWTH Aachen University, Aachen, Germany

of high value-added components. The most important application fields are die and tool making, turbine components for aero engines and power generation, machine components such as axes and gears and oil drilling components [1–8]. Furthermore, new applications are on the horizon such as micro cladding for electronic components [9, 10] or the additive manufacturing of prototypes and even serial parts [11, 12]. This chapter will highlight the fundamentals of laser cladding, give examples for the effect on microstructure and properties, show current applications, and finally will give an outlook of the future.

5.2 Fundamentals of Direct Laser Cladding

5.2.1 Laser Beam Sources and Specific Advantages of Laser Cladding

In the beginning, cw CO₂ lasers were used for laser cladding since these were the first laser sources available with high power output (high power output in relation to laser cladding means at least a power of 500 W). During the years new laser sources such as Nd:YAG lasers, diode lasers, disk lasers, and recently fiber lasers were developed with high power output and research and application of laser cladding have shifted almost completely to these sources. Compared to CO₂ lasers the above-mentioned laser sources exhibit almost ten times shorter wave length resulting in a much better absorption in metallic materials which cover most applications. Furthermore, the excellent beam quality of CO₂ lasers is usually not needed for laser cladding, which especially favors Nd:YAG and diode lasers. Laser cladding requires additive materials. These materials are either preplaced on the substrate before laser treatment (e.g., galvanizing, thermal spraying) or fed into the interaction zone as powder or wire. Since preplacing limits thickness and materials and requires an additional process which increases the costs, the direct laser cladding is established today. Laser cladding has specific features which makes it partly unique among the class of cladding techniques [1]:

- High precision cladding down to less than 100 μm in width and thickness of layers and volume
- Flexible tool for 3D cladding (only for powder based cladding)
- Minimized oxidation achievable even for sensitive materials like titanium
- Layer thickness ranging between 0.1 and 2 mm for a single layer, thicker layers achievable by multilayer cladding
- Minimized heat input resulting in a small heat affected zone (HAZ) and low distortion of the bulk volume
- Suitable for all metallic materials and metal-based composites
- Scope of automation.

5.3 Fundamentals of the Laser Cladding Process

5.3.1 Fundamentals of Laser Remelting

The main physical fundamentals of any kind of laser remelting process are absorption of the laser radiation, heat conduction, melt pool dynamic, and rapid solidification. Below, the melt pool dynamic and the rapid solidification will be explained in more detail.

Melt pool dynamic

When a material is melted due to the absorbed energy of the laser radiation convective flows are created (provided that the melt pool is not covered by a solid oxide layer) which are related to temperature gradients on the surface of the melt pool. Assuming an intensity distribution with a maximum in the center of the laser beam a temperature gradient forms in radial direction since the temperature in the center of the melt pool is higher than at the edges (Fig. 5.1, left). The temperature gradient causes a surface tension gradient since the surface tension σ is dependent on temperature. The gradient of σ in y -direction (Fig. 5.1) can be written as follows:

$$\frac{\partial \sigma}{\partial y} = \frac{\partial \sigma}{\partial T} \times \frac{\partial T}{\partial y}$$

For $d\sigma/dT < 0$ a tension field is formed with low tension in the center and high tension at the edges of the melt pool. This gradient causes a melt flow from the center to the edges. At liquid/solid boundary the flow of material is directed down. In the center of the melt pool the material flow rises to the surface again. The flow of the material and the thermal expansion causes a deformation of the melt pool (Fig. 5.1, right). The convective flow driven by the surface tension gradient is known as Marangoni convection. The flow velocity is in the range of several meters per second which is 2–3 orders of magnitudes higher than the typical velocity during laser remelting (0.005–0.05 m/s). The precondition for Marangoni convection is a free surface on the melt pool. A solid layer (e. g., oxide layer) prevents the formation of the convective flows. Therefore, the shielding of the melt pool is of great significance in this respect.

Rapid cooling

The solidification morphology of a metal can be planar, cellular, or dendritic (Fig. 5.2). A planar solidification occurs when the real temperature of the melt is greater than the liquidus temperature of the material. If the planar solidification forms a stochastic bulge this would grow into a region of increased temperature which causes the breakdown of the bulge. Planar solidification is of significance mainly

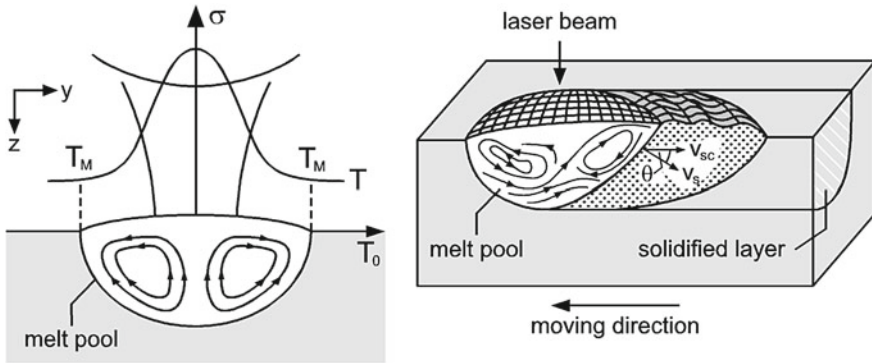


Fig. 5.1 Schematic drawing of the melt pool convection during laser remelting for $d\sigma/dT < 0$; *left* cross-section of melt pool, *right* longitudinal section of the melt pool [13]

for single crystal growth; it requires either a metal with high purity or extremely high values of temperature gradient or solidification rate. If a metal contains impurities or alloying elements the constitutional undercooling plays an important role. Undercooling requires a concentration gradient at the solidification front which is given for laser cladding. Under these conditions the melt at the solidification front enriches with impurity and alloying elements during solidification. As the liquid concentration decreases with distance from the solid /liquid interface, the liquidus temperature T_{liq} will increase. In case that the gradient of the actual temperature distribution in the melt pool is smaller than the gradient of the liquidus temperature a constitutional undercooling occurs [14]. A stochastic perturbation is now growing into an undercooled melt [14]. The planar solidification front breaks down and a dendritic solidification occurs. The growth morphology can be cellular-dendritic (also known as cellular) or dendritic. A cellular structure is generated when the crystals grow in columns without formation of secondary dendrite arms. If secondary or even ternary dendrite arms form the structure is called dendritic. Which morphology forms depends mainly on the solidification rate R .

Figure 5.2 shows the correlation between temperature gradient G and solidification rate v_s . The limit of cellular and dendritic growth are determined by the constitutional undercooling and the absolute stability which is characterized by a critical solidification rate and leads to a planar solidification independently from the temperature gradient. The width of the melt pool generated during laser remelting is typically 0.1–4 mm, the melted depth in the range of 0.1–2 mm. Therefore, the volume of the melt pool is small compared to the whole volume of the work piece. When the laser beam moves on or is shut down the heat is flowing rapidly into the cold bulk volume (self-quenching). The melt solidifies with high cooling rates (10^2 – 10^6 K/s) which are determined by the process parameters, the thermo-physical properties of the material and the geometry of the work piece.

A cooling rate up to 10^4 K/s leads to a cellular or dendritic solidification which is much finer than for conventional casting. The formation of metastable phases

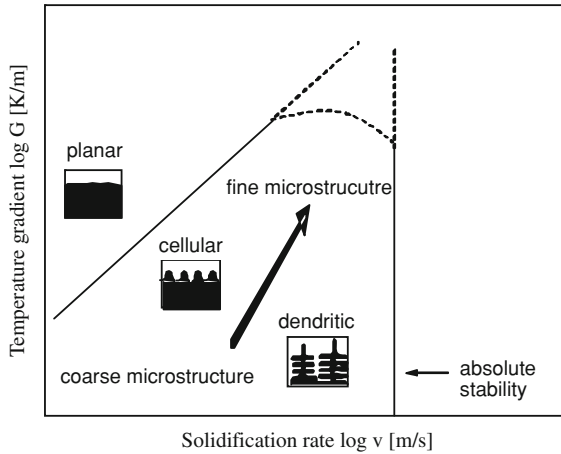


Fig. 5.2 Schematic drawing of the solidification morphology as a function of solidification rate and temperature gradient [14]



Fig. 5.3 Grain refinement in the alloy AlSi10Mg after laser remelting [16], $P = 1\text{ kW}$, $d_L = 1\text{ mm}$; left substrate, centre $v_v = 0.5\text{ m/min}$, right $v_v = 5\text{ m/min}$

depends on the material. For some alloys even an amorphous solidification can be achieved [13–15].

The effect of laser surface melting on grain refinement and homogenization of aluminum alloy AlSi10Mg is shown in Fig. 5.3. The degree of grain refinement was found to increase with increase in scan velocity. The rapid cooling leads to a very fine precipitation of the Si phase which causes an increase in hardness. Refinement and hardness increase can improve the wear as well as the corrosion resistance.

5.3.2 Principle and Material Requirements for the Laser Cladding Process

Laser cladding involves the melting of an additive material and the melting of a thin layer of the substrate (Fig. 5.4). The dilution between the additive material and the substrate is required to form a metallurgical bonding. However, this zone should be as small as possible (see Fig. 5.4) to minimize the contamination of the clad layer

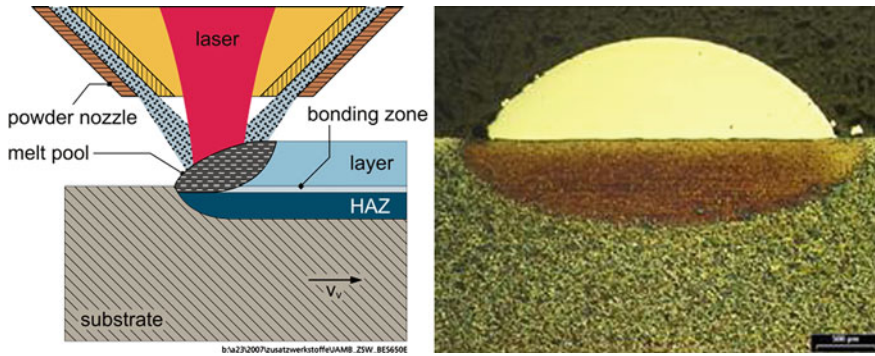


Fig. 5.4 Schematic drawing of the laser cladding process with coaxial powder injection (*left*); cross-section of a laser-cladded layer (stellite 21) on a steel substrate (*right*)

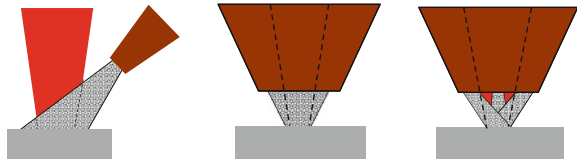
with the elements of the substrate and thus to retain the desired properties of the layer.

Additionally a heat affected zone (HAZ, typical in a depth of 100–1,000 μm , Fig. 5.4) is formed. Depending on the material the time-temperature profile in the HAZ can lead to changes in the microstructure (e.g., hardening or softening in hardenable steels). The additive material can either be precoated onto the substrate or directly fed into the interaction zone. Precoating, e.g., by thermal spraying or galvanic deposition, is limited to certain materials and simple geometries. Furthermore, since two coating processes are required, it is time-consuming and expensive and thus only rarely used in industry. The more flexible and effective method is the direct feed of the additive material into the interaction zone. The additive material can be a powder, a wire, or a viscous mixture of binder and powder (suspension, paste). Powders are the most beneficial regarding the variety of materials and the flexibility of the process (e.g., for 3D cladding) and therefore the mostly used in industrial applications. The requirement for the powders is a particle size between 20 and 150 μm (micro cladding requires smaller particles, see Sect. 5.1) which is also typical for other cladding techniques. The powder flow ability is another important feature since laser cladding requires very steady powder feed rates at low values (typical are a few g/min). Therefore, spherical powders are the most beneficial but blocky forms can also be used. In summary, there is no need for most applications to use specific laser cladding powders. Almost all powders produced for other cladding techniques or for thermal spraying can also be used for laser cladding as well as the feeding devices.

5.3.3 Powder Injection

Powder feeding is a key factor in laser cladding. The quality of the powder gas stream determines the powder efficiency and the shielding of the melt pool. Three different concepts of powder injection can be used (Fig. 5.5) [17]:

Fig. 5.5 Different powder feeding concepts: *left* lateral, *center* continuous coaxial, *right* discontinuous coaxial



- Lateral powder injection (a single powder gas stream is fed lateral into the laser beam)
- Continuous coaxial powder injection (a powder gas stream cone is produced which encloses the laser beam)
- Discontinuous coaxial powder injection (three or more powder gas streams are fed coaxial into the laser beam).

Lateral powder injection

For the lateral powder injection the nozzle is positioned lateral to the laser beam. The position is determined by the angle between nozzle and work piece (typical values $\alpha = 45\text{--}70^\circ$) and the distance between nozzle tip and work piece (typical values $l = 8\text{--}15$ mm). A nozzle designed by Fraunhofer ILT and the powder gas stream is shown in Fig. 5.6 (left). The lateral powder injection is not suitable for 3D cladding since the efficiency is dependent on the feeding direction. Backhand cladding with a dragging angle (flow direction of the particles is the same as the moving direction of the work piece) and forehand cladding with a pushing angle (flow direction of the particles is opposite to the moving direction of the work piece) lead to a different powder efficiency and thus to a different layer thickness. The lateral injection is beneficial for rotationally symmetric parts where cladding is performed in one direction or for areas with difficult accessibility (e.g., grooves). The width of the lateral nozzles can be minimized to 2–3 mm. For a track width between 0.5 and 5 mm a circular cross-section of the opening with a diameter of 1.5–3.5 mm is adequate (see Fig. 5.6, center). Cladding of broad tracks (5–25 mm) requires a rectangular cross-section of the opening (e.g., 1.5×15 mm², see Fig. 5.6, left). Since the nozzle is positioned close to the melt pool it is exposed to laser beam reflections. Therefore the nozzle should be water cooled, to ensure long-term operation without any damage.

Continuous coaxial powder injection

In continuous coaxial powder injection (below named “coaxial powder injection”) a powder stream cone encloses the laser beam. Figure 5.7 shows a coaxial powder injection nozzle. For long-term operation it is essential that the nozzle is water cooled. The powder stream cone is produced as follows: The powder stream of the

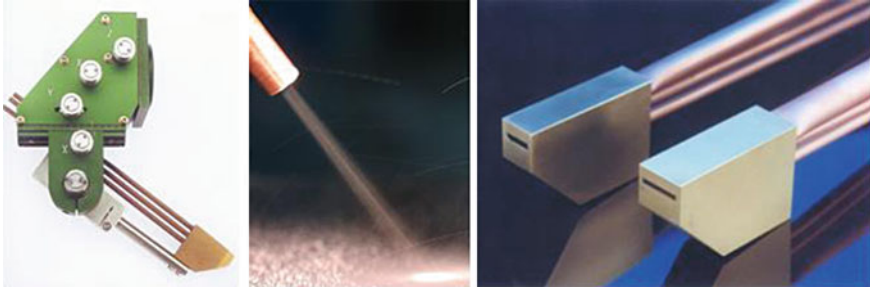


Fig. 5.6 Lateral powder feed nozzle (*left*), powder gas stream (*center*); lateral nozzles with rectangular design for broad layers (*right*)

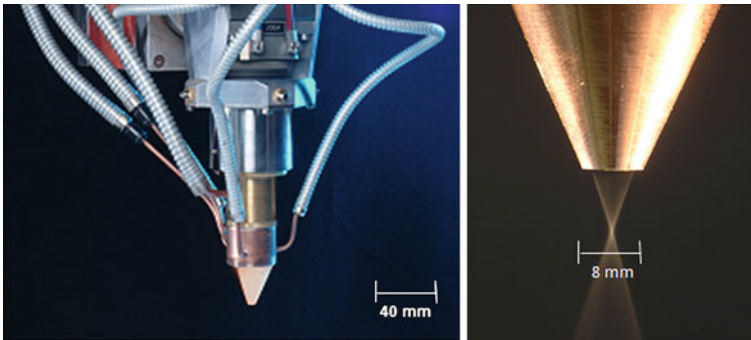


Fig. 5.7 Continuous coaxial powder feed nozzle mounted on a laser optic (*left*) and powder gas stream (*right*)

powder feed unit is split into three identical streams which are fed into a ring-shaped expansion chamber inside the nozzle. In this chamber a homogenous “powder cloud” forms which then is fed into a cone-shaped slit. The powder leaves the nozzle in the form of a hollow cone. The diameter of the powder stream focus can be adapted to the laser beam area on the work piece. Depending on process parameters such as particle size, gas flow rate, and powder mass flow, powder stream diameters below $500\ \mu\text{m}$ can be achieved allowing a very high efficiency (up to 90%).

The major advantage of coaxial powder injection compared to off-axis powder injection is the potential for 3D cladding. However, tilting of the nozzle is restricted. Since the homogeneity of the powder stream cone depends on the powder distribution inside the expansion chamber of the nozzle gravity will affect the powder stream when the nozzle is tilted. Experiments have shown that a maximum tilt angle of approximately 20° can be accepted without significant effects on the geometry and quality of the clad layer.

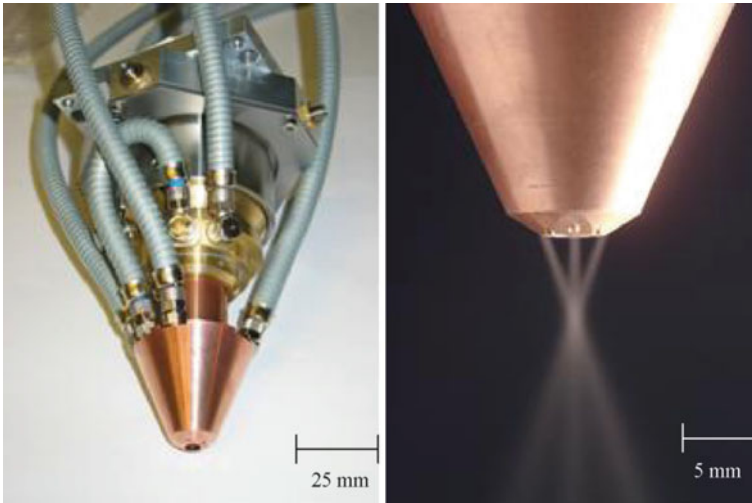


Fig. 5.8 Discontinuous (three-way) powder injection nozzle (*left*) and powder gas streams (*right*)

Discontinuous coaxial powder injection

In discontinuous coaxial powder injection several individual powder streams are distributed around the laser beam, thus forming a powder stream focus. Figure 5.8 shows a nozzle with three individual powder streams (below named as “three way nozzle”). The core diameter of the powder stream focus depends on the angle between the individual powder streams, the diameter of the nozzle holes, the distance between nozzle tip and powder stream focus, the powder feed rate, and the particle size. The major advantage of the three way nozzle is the potential for 3D cladding including the potential to tilt the nozzle up to 180° . For reactive materials an additional shroud can be used to improve the shielding of the melt pool from oxidation. Examples are shown in Fig. 5.9. The powder feeding nozzles shown above are adapted to standard laser beam optics typical with a focal distance of 150–300 mm. However, laser cladding of internal areas cannot be done with conventional processing heads because of the limited accessibility which is restricted to an internal diameter of approximately 100 mm. For smaller diameters miniaturized heads are required with integrated optics and powder feed nozzles. Figure 5.10 shows a processing head suitable for internal diameters larger than 50 mm and a depth up to 500 mm. The head is designed for a 2 kW diode laser.

The fields of application for the different powder feeding nozzles according to their specific features are summarized in Table 5.1.

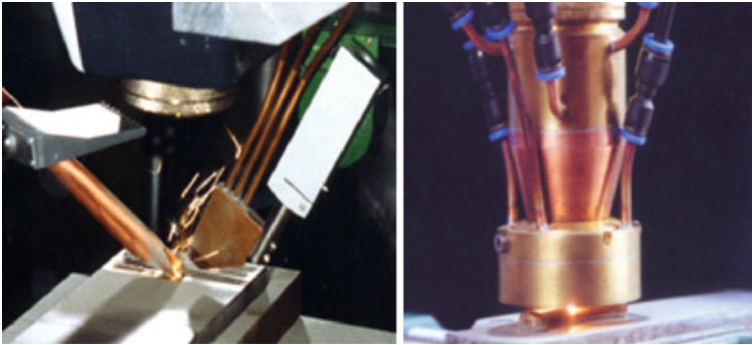


Fig. 5.9 Additional shrouds for an improved shielding from oxidation during laser cladding ; off-axis shroud (*left*) and coaxial shroud (*right*)

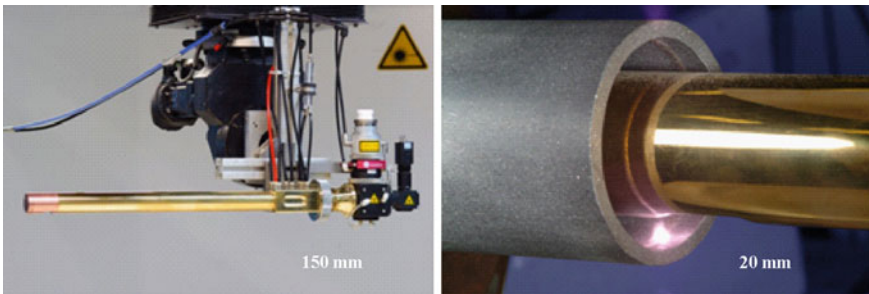


Fig. 5.10 Internal cladding head with integrated optic and powder feed nozzle (*left*); cladding process (*right*)

Table 5.1 Fields of application for the different powder feeding nozzles

Powder feed nozzles	Fields and examples of applications
Lateral powder feed nozzle	2D cladding, preferred for rotationally symmetric parts, areas with limited accessibility Examples: crank shaft bearing, valve, piston nut
Coaxial powder feeding nozzle	2D and 3D cladding, preferred for high precision cladding of sensitive materials Examples: repair of all kind of turbine parts (seals, aerofoil tips, housings, ..), repair or modification of injection moulding tools
Three-way powder nozzle	2D and 3D cladding, preferred for thick layers (high laser power) Examples: repair or modification of forming and casting tools
Internal cladding head	2D cladding of internal areas ($d > 25$ mm) Examples: wear resistance of bearing for offshore drilling equipment

5.4 Material Aspects of Laser Cladding

5.4.1 Materials

All metallic-based materials can be used for DLC, such as pure metals (e.g., Ag, Au for electric contacts, Zn for corrosion protection), alloys (e.g., Co-, Ni-, Ti- and Fe-based alloys for wear protection and repair) and hard metals (e.g., WC/Ni for wear protection). A selected list of materials is shown in Table 5.2.

Even more customized new materials can be created prior to or during laser cladding. Prior to cladding different powder material can be mixed in a tumbling mixer or by ball milling. In situ new alloys can be formed in the cladding process by feeding two components simultaneously [18].

5.4.2 Microstructure

Since laser cladding is a melting process the resulting microstructure is always a cast structure compared to conventional casting. The grain or dendrite size is orders of magnitude smaller. The most common is a dendritic structure as shown in Fig. 5.11 (top left). But also an equiaxed structure can occur (Fig. 5.11, top right). In high alloyed materials a dispersed microstructure with hard precipitations in a metallic matrix (Fig. 5.11, down left) can solidify.

Such structures can also be produced by using mixed powders of a metal and a high melting point material (carbide, nitride, boride, Fig. 5.11, down right). Which morphology and phase composition is formed depends mainly on the solidification parameters (determined by process parameters such as laser power and velocity) and on the chemical composition of the material.

5.5 Applications

Today's most important application for direct laser cladding is the repair and the modification of high value parts such as molds, tools, or turbine and engine components [1–3, 5, 19, 20]. In the field of wear and corrosion protection laser cladding is used only for unique parts and small-lot production such as oil drilling components, engine components of big diesel engines. For mass production the technology is still too costly compared to other cladding techniques. Below some actual applications are presented.

Repair of molds and dies

Direct laser cladding is well established for the repair of injection molds [2] and dies for metal sheet forming is getting more and more established [3]. Laser cladding

Table 5.2 Selected materials and applications for DLC

Materials group for laser cladding		Examples of metals and alloys	Functions	Applications
Pure metals		Au, Ag, Zn	Electric contacts, corrosion protection	Fuel cell, electric switch, edge protection of sheets
Co-based alloys		Stellite 21, Stellite 6	Wear protection, repair	Diesel engine parts, bearings
Ni-based alloy		NiCrBSi-alloys, nickel super alloys	Wear protection, repair	Bearings, repair of turbine blades
Fe-based alloys		High alloyed hot and cold working steels (X38CrMoV5-1), PM steels (CPM 420 V), stainless steel (316L)	Wear and corrosion protection, repair	Machine parts, forming tools moulds, forging tools, bearings
Al-based alloys		AlSi alloys (AlSi20, AlSi10Mg)	Wear protection	Automotive magnesium parts
Ti-based alloys		TiAl6V4, Ti6242	Repair	Turbine blades and housings
Hard metals		WC/Ni (60/40), WC/Co	Wear protection	Bearings, rollers

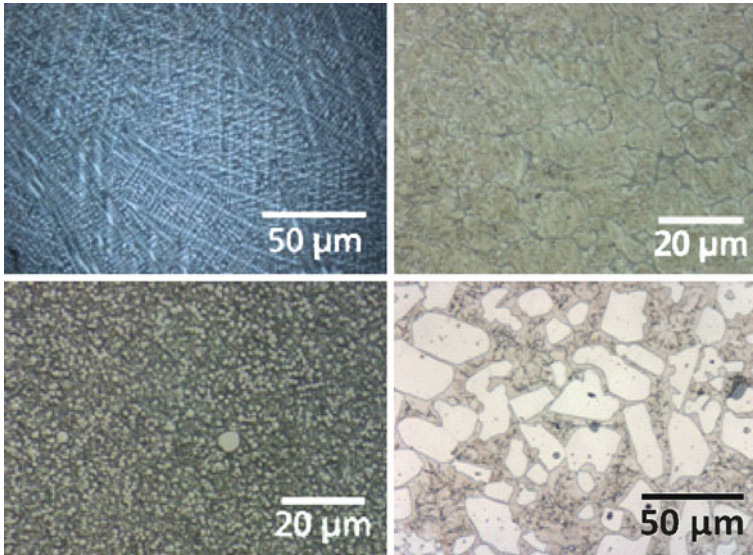


Fig. 5.11 Various solidified structures of laser-cladded layers; dendritic structure of stellite 21 (*top left*); cellular structure of high alloyed steel X100CrMoV5-1 (*top right*); primary solidified vanadium carbides in a martensitic matrix (FeCrV, *down left*); dispersed structure of a TiAl alloy with embedded TiB₂ particles (*down right*)

allows the repair of critical areas, e.g., near-polished or ground (chemically etched) surfaces which are not allowed to be affected by the heat input. Figure 5.12 shows a repaired car lamp mold worn out in the front area. No damage was allowed on the polished top surface. This type of repair cannot be performed with any other welding techniques (e.g., TIG welding).

Modification of molds

Once a mold has been manufactured design changes where material has to be added are difficult to carry out. In the worst case a new mold has to be manufactured which is time- and money consuming. By direct laser cladding the missing material can be added near net shape in a much shorter time. The mold is finished by milling processes to the final geometry and can be used in production again. Figure 5.13 shows an example for the modification of an injection mold for a car lamp housing. A volume of several mm thickness was added by multilayer cladding.

Repair of turbine components for aero engines and power generation

The repair of turbine components (sealing, housing, turbine blades, vanes, etc) is performed with conventional techniques such as TIG welding, PTA welding, and

Fig. 5.12 Repaired area of a worn out lamp mold (automotive application) [5]

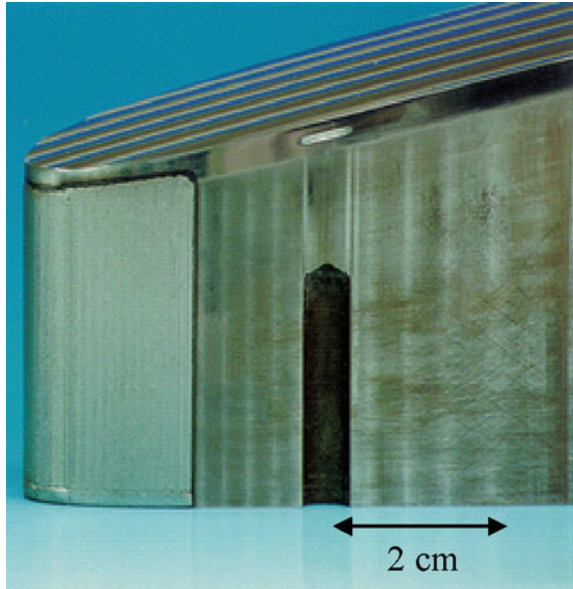


Fig. 5.13 Modification of an injection mold for a car lamp housing (material: hot working steel) [5]



thermal spraying. In the last years, direct laser cladding has been established as an alternative technology [5]. Figure 5.14 shows the repaired rotating seals on a cooling plate for a gas turbine (nickel based alloy). Multiple layers were applied with a width of 0.6 mm.

Gears and axes

In the area of heavy machines (e.g., ship engines, offshore drilling equipment) large and valuable components such as shafts, gears, and gearboxes are cladded for the repair or the wear protection. Figure 5.15 shows a repaired axis of a centrifuge and Fig. 5.16 the repair process of a gear component with DLC.

Fig. 5.14 Repaired rotating seal of a cooling plate for a gas turbine (Ni-based alloy) [7]

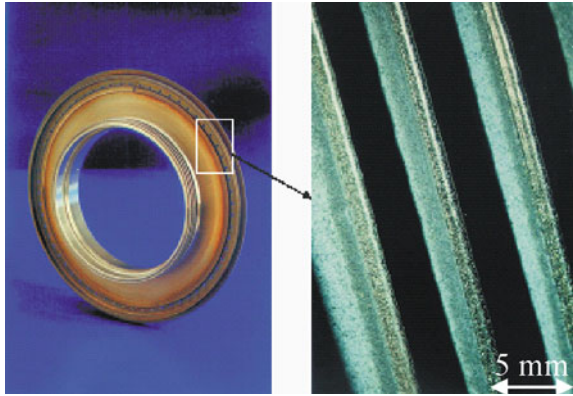
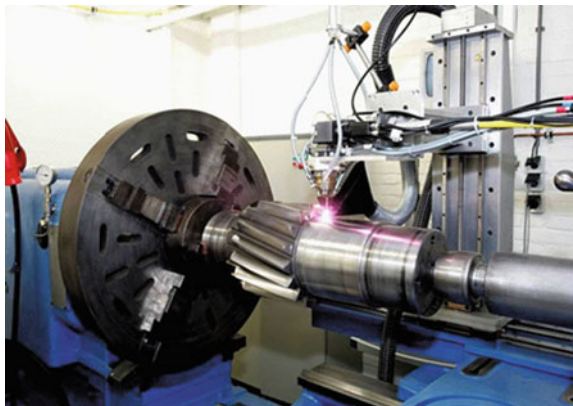


Fig. 5.15 Repair of centrifuge axis [1]



Fig. 5.16 Repair of gear components with DLC [17]



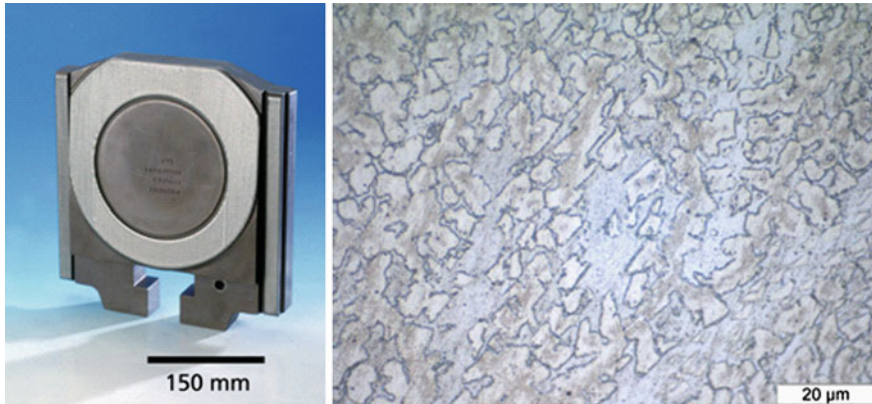


Fig. 5.17 Laser-cladded gate valve (*left*) and microstructure of the clad layer with ferrite (*blue*) and austenite (*grey*) (Annual Report of Fraunhofer ILT 2005)

Wear protection of valves for power plants

Valves for cooling circuits of power plants are exposed to high temperatures (350°C) and high pressure (300 bar) and materials with a high resistance against wear and corrosion. Among other parts gate valves which are activated in case of a pipe burst have to be cladded with an iron-based alloy which consists of a duplex microstructure of ferrite and austenite. To provide the best performance a ferrite fraction of 50% is required (Fig. 5.17).

Since this can only be achieved by rapid cooling laser cladding is superior to the other cladding techniques. A 2 kW diode laser was used for the cladding. The layer thickness is around 1 mm. After cladding the layer is machined to the final thickness and the part is heat treated to further increase the hardness. The valves have been running for several years in a power plant.

5.6 Future Trends for Laser Cladding

5.6.1 Micro Laser Cladding

New CW laser sources such as fiber and disk lasers offer the possibility to produce laser-cladded structures below 10 μm thickness and widths below 100 μm. In the last years effort has been made to downscale the laser cladding process [9, 10]. One major task is the feeding of fine powders with a grain size in the range of 10 μm. These powders cannot be fed by conventional powder feeders due to the tendency to agglomerate which results in a significant loss in flow ability. New concepts of powder feeding have to be used like brush feeders [10]. Furthermore, the feeding nozzles

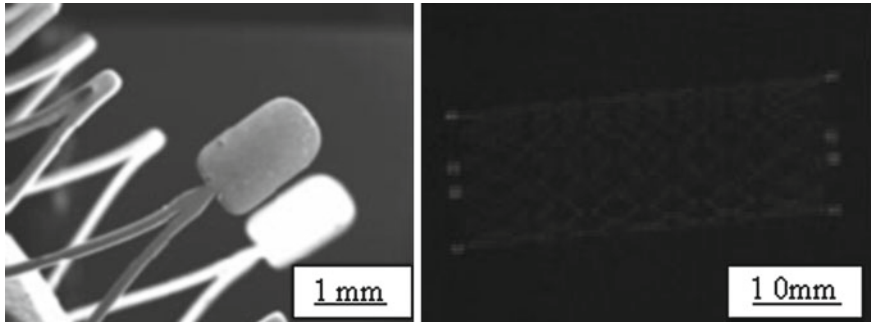


Fig. 5.18 Increasing X-ray visibility by depositing tantalum on nitinol stents

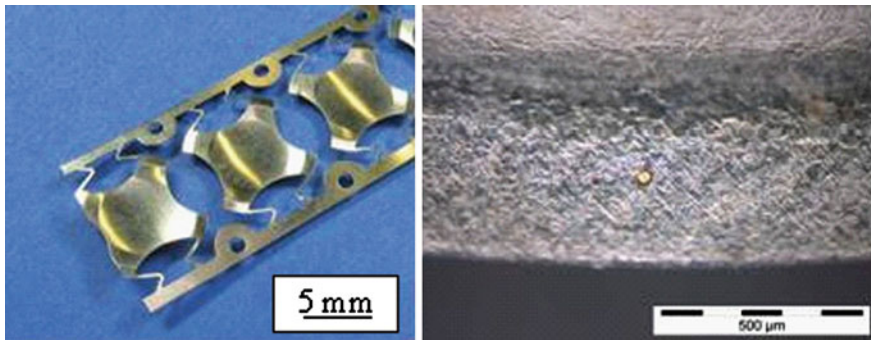


Fig. 5.19 Selective DLC of gold contacts on stainless steel switches

have to be adapted to avoid any blockage during the cladding process. For example, for lateral powder feeding the internal diameter of the nozzle must be well below $500\ \mu\text{m}$. Potential applications are medical engineering, electronic devices, and new power generation technologies (fuel cell, solar cell). One of the most interesting applications is the cladding of single gold contacts on a bipolar plate instead of coating the plate completely with gold. This would reduce the consumption of gold by a factor of 100 (Figs. 5.18, 5.19, 5.20).

5.6.2 Novel Materials

Laser cladding can also be used to create new materials with customized properties during the cladding process. An example is a graded layer. Figure 5.21 (left) shows the continuous and defect-free microstructure of steel-based graded layer developed on copper substrate. The potential application of the same is tool inserts for injection molding (Fig. 5.21 right) [7, 19].

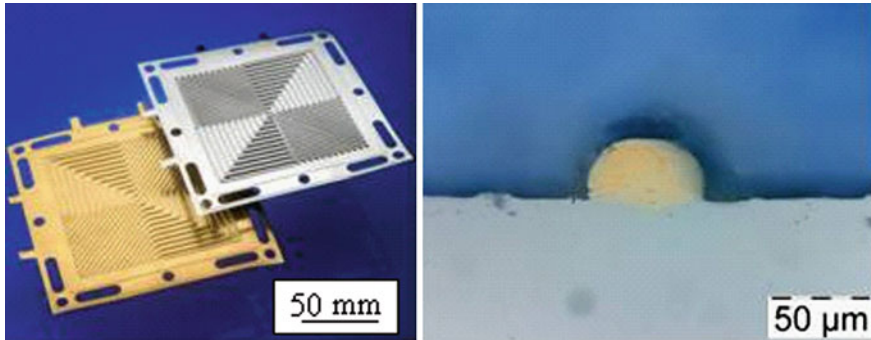


Fig. 5.20 Selective LMD of gold contacts on bipolar plates for fuel cells

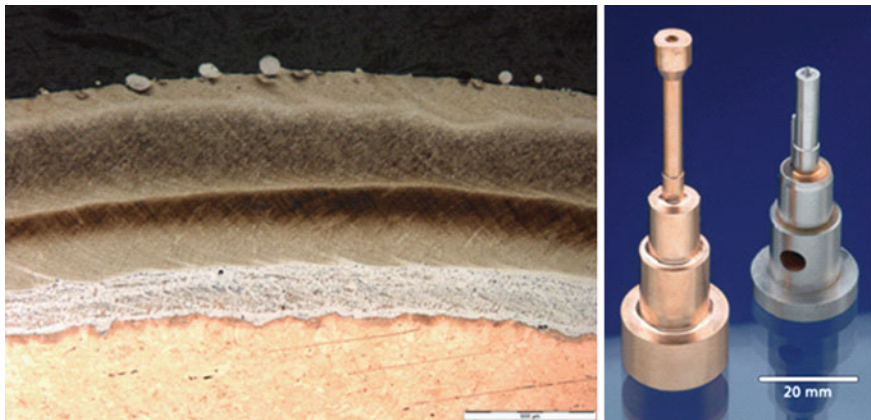


Fig. 5.21 Steel-based graded layer on a copper substrate (*left*); potential application: tool inserts for injection molding (*right*)

Changing the composition of the additive material in each layer can lead to a graded layer by multilayer cladding. This can be used for combinations of materials with different thermo-physical properties such as copper and steel for mold cores of injection tools. The copper provides a high thermal conductivity to dissipate the heat very quickly and the steel layer provides the wear resistance for the required life cycle. With the gradient thermally induced stresses can be minimized during operation leading to an increase in life time. Another new approach is the cladding of metal-matrix-composites with ceramic nano particles with a size of 20–50 nm [21, 22]. The nano particles (e.g. Al_2O_3 , Y_2O_3) act as nuclei during solidification leading to an extremely fine microstructure which can prohibit cracking and improve ductility. Compared to micro particles these effects are much greater and only small addition of particles is required (0.5–2 Vol.-%).

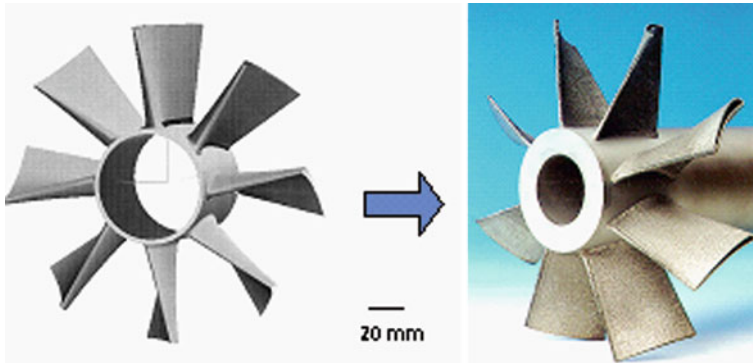


Fig. 5.22 Additive manufacturing of blades on a shaft

5.7 Additive Manufacturing

Additive manufacturing by laser cladding is another feature which arises (again) more and more interest in industry. The first attempts were made in USA more than 10 years ago [23]. Nowadays efficient high power lasers, improved powder feeding nozzles, software tools for offline programming, and the increased demand for a customized and individual production led to new research activities [11, 12, 24]. In the future additive manufacturing can be used for functional prototypes as well as for unique and small lot parts. Figure 5.22 shows blades that have been manufactured on a shaft directly from CAD data as a demonstrator.

References

1. A. Gasser, G. Backes, K. Wissenbach, E. Hoffmann, R. Poprawe, Maßgeschneiderte Oberflächen durch Laserstrahl-Oberflächenbehandlung mit Zusatzwerkstoffen-eine Übersicht, *Laser und Optoelektronik* 3/1997
2. M. Kawasaki et al., The Laser Cladding Application at Automotive Parts in Toyota, in *Proceedings ISATA*, 1992 (1992).
3. Schutzauftrag, *LaserCommunity*, Das Laser-Magazin von TRUMPF, 03/2007
4. K. Eimann, M. Drach, Instandsetzung von Werkzeugen mit Laserstrahlung, in *Tagungsband Aachener Kolloquium Lasertechnik AKL 2000*, Mai 2000, pp. 29–31
5. K. Eimann, M. Drach, K. Wissenbach, A. Gasser, Lasereinsatz im Werkzeug- und Formenbau, in *Proceedings Stuttgarter Lasertage*, Sept 2003, pp. 25–26
6. J. Nagel, Laserhärten und Laser-Pulver-Auftragschweißen von Umformwerkzeugen, in *Tagungsband Aachener Kolloquium Lasertechnik AKL 2004*, 2004, pp. 295–305
7. A. Gasser, K. Wissenbach, I. Kelbassa, G. Backes, Aero engine repair, in *Industrial Laser Solutions*, Sept 2007, pp. 15–20
8. W. Meiners, A. Weisheit, Werkstoff-Kompromisse passé?. *Form + Werkzeug* 5, 78–81 (2007)

9. O. Meier, P. Stippler, A. Ostendorf, S. Czerner, P. Matteazzi, Direct micro laser cladding with microscale nanophased powders, in ICALEO 2005, *24th International Congress on Applications of Lasers and Electro-Optics, Conference Proceedings*, Miami, US, Nov 2005
10. T. Jambor, K. Wissenbach, Micro-Laser-Cladding with High Quality Fibre Lasers; in LIM 2007, *Laser in Manufacturing*, 17-22 June 2007, Munich
11. G. Levy, The role and future of the laser technology in the additive manufacturing environment, *6th International Conference on Laser Assisted Net-Shape Engineering*, LANE 2010
12. D.L. Bourell, Sustainability issues in laser-based additive manufacturing, in *6th International Conference on Laser Assisted Net-Shape Engineering*, LANE 2010
13. N. Pirch, E.W. Kreutz, B. Ollier, X. He, The modeling of heat and solute transport in surface processing with laser radiation, in NATO Advanced Study Institute, *Laser Processing: Surface Treatment and Film Deposition*, Sesimbra, Portugal, July 1994, pp. 3–16
14. W. Kurz, D.J. Fisher, *Fundamentals of solidification* (Trans Tech Publications, Switzerland, 1986)
15. Y. Yan, Y. Yang, C. Zhao, W. Wu, M. Wang, M. Lu, Laser glazing of Ni–Nb and Ni–Ni–Cr alloys and corrosion resistance of amorphous layers. *Acta Metall. Sin.* **6**(1), 52 (1993)
16. H.W. Bergman, B.L. Mordike, Laser and electron-beam melted amorphous layers. *J. Mater. Sci.* **16**, 863 (1981)
17. R. Poprawe, *Lasertechnik für die Fertigung* (Springer, Heidelberg, 2004), ISBN 3-540-21406-2
18. M. Miglierini et al., Laser-induced structural modifications of FeMoCuB metallic glasses before and after transformation into a nanocrystalline state. *J. Phys.: Condens. Matter.* **13**, 10359–10369 (2001)
19. T. Biermann, G. Backes, A. Gasser, A. Weisheit, Adapted powder feed nozzles for different laser cladding applications. *Laser User*, **57**, 27–28 (2009)
20. A. Weisheit, K. Wissenbach, Graded layers for wear and corrosion protection produced by laser cladding. In: A. Fischer, K. Bobzin (eds) *Friction Wear and Wear Protection* (Wiley-VCH, Weinheim, 2009)
21. S. Ocylok, A. Weisheit, I. Kelbassa, Functionally graded multi-layers by laser cladding for increased wear and corrosion protection, in *6th International Conference on Laser Assisted Net-Shape Engineering*, LANE 2010
22. L. Mingxi, H. Yizhu, Y. Xiaomin, Effect on nano Y₂O₃ on microstructure of laser cladding cobalt-based alloy coatings. *Appl. Surf. Sci.* **252**, 2882–2887 (2006)
23. L. Mingxi, Z. Shihong, Z. Huisheng, H. Yizhu, Y. Jae-Hong, S. Tong-Yul, Effect of nano-CeO₂ on cobalt-based alloy laser coatings. *J. Mat. Proc. Technol.* **202**, 107–111 (2008)
24. R. Irving, Taking a powder, *Mech. Eng. Mag.* <http://www.memagazine.org>. Sept 1999

Chapter 6

An Introduction to Laser-Assisted Microfabrication, Current Status and Future Scope of Application

A. Ostendorf

Abstract From the invention of the laser almost about five decades ago scientists have studied the potential of laser micromachining. Compared to high power laser applications most applications on the microscale require rather moderate average powers in the range of a few watts or below along with good beam qualities and the possibility to use pulsed and/or short wavelength laser systems. Most applications in this field are based on ablation, i.e., material removal for structuring, drilling, or precise cutting of materials. However, current activities are also ongoing in adapting rapid prototyping, i.e., generative processes to the microscale. Finally, a tremendous amount of research activities are carried out to generate nanostructures. Because of the wavelength and the diffraction limit in classical optics new approaches have been taken into account to overcome these limitations and making use of the unique properties of laser radiation also on the nanometer scale. This chapter provides an overview of pulsed laser assisted micromachining with a focus on structuring by laser ablation, laser generative processes, and finally nanomachining.

6.1 Introduction

All laser-based processes can be described by several subprocesses which take place on different timescales either partly overlapping each other or on different time scales. Examples are the absorption of the laser radiation, the transfer and transition of the energy to the material, and the reaction of the material. All processes are on the one hand, dependent on the laser parameters and on the other hand, also on the material properties resulting in the engineer's challenge to find the optimum within the mutual interdependencies. For laser micro processing, two important parameters are essential: the minimum spot size and the temporal duration of the laser pulse.

A. Ostendorf (✉)

Department of Mechanical Engineering, Ruhr-University Bochum,
44780 Bochum, Germany
e-mail: andreas.ostendorf@ruhr-uni-bochum.de

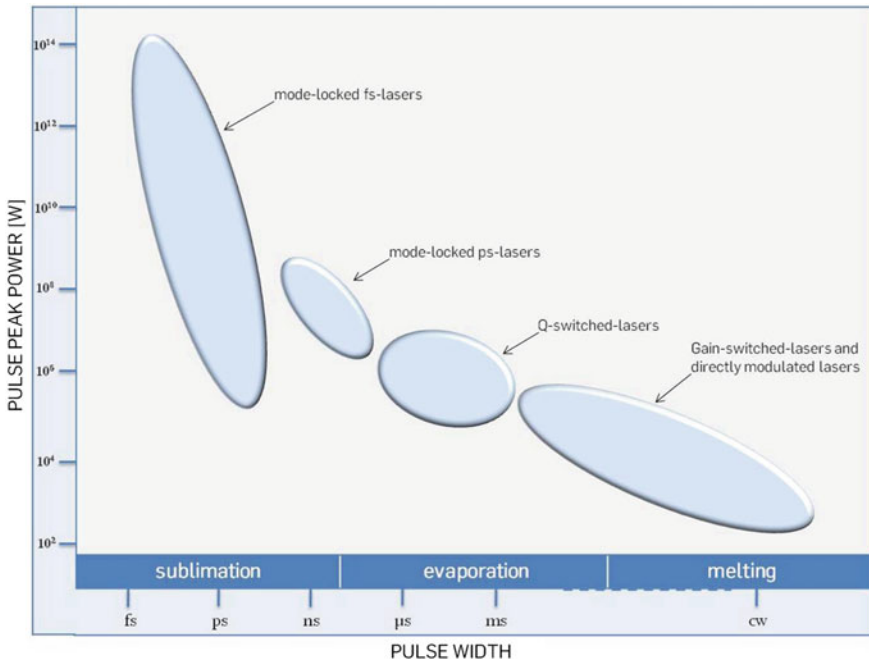


Fig. 6.1 Laser parameter overview: Pulse peak power versus pulse duration for different laser systems which are nowadays used for micro- and nanoprocessing. The different material interaction regimes are also depicted *horizontally*

Different methods can be applied in order to achieve a small spot size: A laser system with a good spatial beam quality can be chosen (M^2 close to 1.0, M^2 is defined as the beam parameter product divided by the corresponding product for a diffraction-limited Gaussian beam with the beam parameter product as the product of focal radius and far-field divergence angle), but also a short wavelength or a small focal distance will in principle enable small focal spots. Recent developments in the field of laser sources have led to lasers with excellent beam qualities, also in the UV spectral range. Besides the spatial optimization, also temporal measures can be taken to influence the intensity of the laser radiation and the duration of the interaction between the laser and the material. Using pulsed lasers, the average laser power is optically accumulated and the pulses can reach multiple orders of higher peak powers. The pulse duration can range from femtoseconds (fs) to milliseconds (ms), depending on the laser systems and on the required physical interaction when using the laser pulses for machining. In Fig. 6.1, an illustrative overview is provided, where state-of-the-art laser systems are classified according to their pulse peak power and pulse duration.

With respect to metals, where the absorption takes place by Inverse Bremsstrahlung of the electron gas the pulse duration plays a superior role in achieving acceptable micromachining results. Therefore, in the following, the pulse duration effect on the

processing result will be explained in more detail. First, the different pulse generation principles will be introduced and in a second step the interaction phenomena of short and extremely short laser pulses with different types of materials will be described in more detail. However, short wavelength lasers (e.g. excimer laser, frequency converted solid-state lasers) also play an important role in micromachining. Besides decreasing the wavelength, and the spot size respectively, the high photon energies in the UV range can initiate photochemical processes, e.g., breaking of bonds in some polymers resulting also in the ablation of the molecular fractions. For a comprehensive overview of this topic numerous textbooks and review articles can be referred [1, 2].

6.2 Laser Pulse Generation and Interaction with Matter

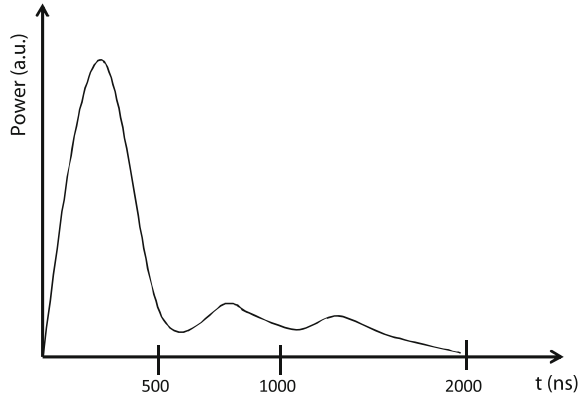
The pulse operation mode of lasers has been of significant interest for laser and application engineers for a long time. The reason is the high intensity in the focal region resulting in sublimation of the material and in the case of extremely short pulses, there is very low heat diffusion in the surrounding material. The following chapter provides a brief introduction in the different principles of generating short laser pulses. For a deeper understanding, more specific literature is recommended [3–5]

6.2.1 Gain Switching

Switching of the gain in the oscillator can be regarded as the simplest method to generate laser pulses. In gain switching, the pumping process is modulated resulting in switching the amplification in the laser medium. After the pumping process has been switched on, the population inversion starts to build up. Upon reaching the critical inversion, i.e., the gain in the resonator becomes larger than the losses, the laser starts to oscillate. The oscillation continues until the pumping process is switched off, or until the losses exceed the amplification. Gain switching can also make use of the transient spiking phenomena in the laser oscillator in order to achieve a higher peak power pulse. If a laser medium is pumped at a very fast rate and the population inversion exceeds the threshold significantly before the oscillation starts, the laser reacts by relaxation oscillations, i.e., spiking occurs. If the pump pulse is not only fast but also stops directly after the first spiking peak, a laser pulse is generated which consists of only one single spike.

There are several established examples for gain switching lasers like for diode lasers and diode pumped solid-state lasers. In diode lasers the electrical pumping current can be modulated with frequencies up to the GHz range. In diode pumped solid-state lasers the diodes can also generate very high optical powers on a short-term basis, and are thus also suited for the buildup of high inversions. Another popular type

Fig. 6.2 Typical pulse of a TEA-CO₂-laser: CO₂ TEA lasers typically generate a spike and followed by a long tail, with approx. < 50% of the energy in the short spike, and the majority of energy in the tail which can be as long as 2 μ s. The spike is produced by gain switching whereas the tail originates from strong excitation of the accompanying N₂ gas (nitrogen tail)



of gain switched gas lasers is the transversally excited atmospheric pressure laser (TEA-laser). In a TEA-CO₂-laser a discharge voltage is applied to transversally arranged electrodes. If the voltage is pulsed shorter than 1 μ s, instabilities in the discharge will be suppressed and gas pressures of the CO₂/N₂/He-mixture can be increased up to 1 bar. This can lead to laser pulse energies up to 50 J per liter discharge volume at pulse widths of typically 100 ns (Fig. 6.2).

In gain switching the reproducibility and stability is by some means stochastic resulting in severe pulse-to-pulse fluctuations. Due to this, gain switching, in spite of its simplicity, is problematic for many high precision applications. In some precise lasers spiking is often kept low due to the high fluctuations in peak power.

6.2.2 Q-Switching

As described above the output of a gain switched, pulsed laser is generally a train of irregular pulses. These irregularities can be smoothed while at the same time increasing the peak power by switch in the resonator quality factor (Q-switching). Q-switched lasers emit only one giant pulse per operational cycle with a pulse width as low as several nanoseconds and peak intensities up to 10^9 W. This technique can also be applied to continuously pumped lasers in order to produce a train of Q-switched pulses with regular width, peak power, and repetition rate. Compared to gain switching, a Q-switch converts a relatively long pump pulse with low peak power into a very short pulse with high peak power over several orders of magnitude and also with high reproducibility.

In the Q-Switch mode energy is stored in the laser active material during pumping in the form of excited atoms and suddenly released in a single, short burst. This is accomplished by changing the optical quality of the laser resonator. The quality factor Q is defined as the ratio of the energy stored in the cavity to the energy loss per cycle. During the pumping process the beam in the Q-switched system is interrupted,

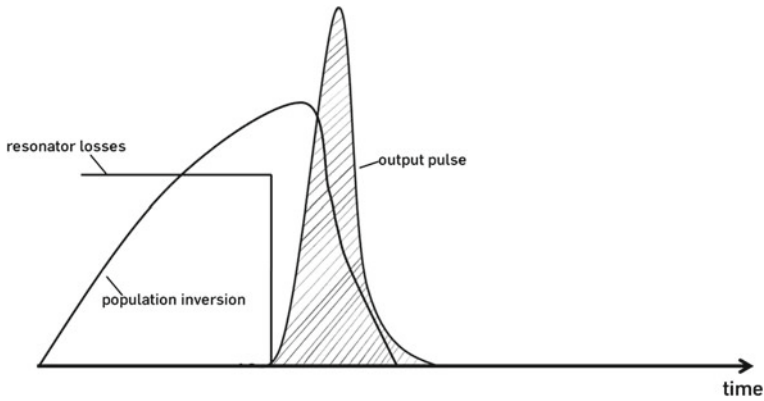


Fig. 6.3 Q-Switching: Development of the main laser parameters during pulse pumping and Q-switching

resulting in a low Q -factor and preventing the laser from starting oscillation ($Q \approx 1$). After a large amount of energy is stored in the active medium by the pumping process, the beam path in the resonator is returned to proper alignment, and most of the stored energy comes out in a single, short pulse ($Q \gg 1$).

In a Q-switched laser the optical configuration in the resonant cavity is changed which drastically lowers the effective reflectivity of the cavity during optical pumping. As a result, the population inversion increases without an output being generated. Consequently, the amplifier gain and the stored energy in the upper laser level are boosted. At the time of maximum inversion, the quality factor Q is switched back to a high value, causing the system to emit laser radiation, and thereby releasing its stored energy in one, short giant pulse. Physically, a Q-switch is essentially a shutter placed between the active medium and the high reflectivity (HR) mirror. If the shutter is closed, the HR mirror is blocked preventing oscillation. When the amplifier gain reaches a predetermined value, the shutter is opened to increase the cavity quality.

For Q-switched lasers both the amplifier gain and the deposited energy in the laser active medium can reach much higher levels than for gain switching. According to Fig. 6.3 the laser emission starts when the loop gain has reached its maximum. The laser pulse builds up rapidly depleting stored energy and reducing the amplifier gain. The peak of the laser output pulse occurs when the loop gain falls below a certain level. After this the output laser power starts to drop.

The delay time between the onset of pumping and the opening of the Q-switch influences the efficiency of the laser significantly and should be optimized with respect to the lifetime of the upper level of the active medium. Obviously, the greater the fluorescent lifetime of the laser material, the more energy may be deposited in the active medium. All solid-state laser systems may be effectively Q-switched as their fluorescent lifetimes fall in the range above 100 microseconds (Nd:YAG 230 μ s; Nd:YVO₄ 100 μ s; Yb:YAG 980 μ s; Nd:YLF 480 μ s).

Nd:YAG is by far the most common Q-switched, CW pumped laser system. Such systems can typically produce several thousand pulses per second without degradation of the pulse energy. Typical pulse widths for such a system range from several tens of nanoseconds to a few microseconds. If the pulse width is aimed to be further reduced, it is necessary to use a laser crystal with a larger emission cross section, e.g., Nd:YVO₄. Nd:YVO₄-lasers can deliver pulses with half the duration of Nd:YAG assuming that the same stored energy and resonator configuration is used. This is the reason for the success of Nd:YVO₄-lasers in micromachining. Due to the short pulse width the pulse peak power is much higher resulting also in more efficient frequency conversion setups.

The Q-switch can be carried out by different methods. The most common known methods are active switching by mechanical, electro-optical, or acousto-optical Q-switches, where the quality control is an explicit function of time, and passive Q-switching by saturable absorbers, where the quality is controlled as a function of the photon density.

6.2.3 Cavity Dumping

As a result of the high population on the upper long-lifetime laser level, energy is stored in the active medium and subsequently emitted in the form of short laser pulses during Q-switching. During cavity dumping, on the contrary, light energy is stored in the resonator. In this case the loss of the cavity is switched from low to high, or in other words, the quality factor is switched from high to low. Cavity dumping is applied for laser media which have an upper laser level with a lifetime that is too short for Q-switching. For cavity dumping the continuously pumped laser medium is placed between two highly reflective mirrors. The intensity of the laser beam is highly amplified in the resonator. If for e.g. an acousto-optic deflector, which is transparent during intensity buildup, is triggered in the resonator, almost the complete energy in the form of a short laser pulse can leave the resonator. For a cavity-dumping laser the acousto-optic deflector usually operates in an inactive state resulting in extremely high Q values of the resonant cavity and very intense lasing within the cavity. If an electric pulse is applied to the device, nearly all the laser energy is dumped out of the resonant cavity in the form of a single optical pulse (Fig. 6.4). Typical pulse widths are of the order of 10 ns, i.e., the round trip duration to dump out all photons.

Depending on the output coupling mechanism, cavity dumping enables to select pulse repetition rates of up to several tens of MHz at pulse widths of 10–30 ns. The switching elements which are basically used for cavity dumping are electro-optic Pockels cells, acousto-optic devices, and polarizing beam splitters. If used in combination with mode-locking (see next section), cavity dumping can generate subnanosecond pulses at repetition rates of several MHz without reducing the average laser power.

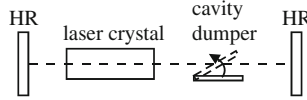


Fig. 6.4 Principle of cavity dumping: The main difference from Q-switching is that before releasing the output laser pulse the energy is stored in the resonator, rather than in the laser medium itself. In cavity dumping the pulse duration achievable is set by the resonator length and not by the laser gain. As a consequence, even for very *high* pulse repetition rates pulse durations of a few nanoseconds are still achievable, whereas for q-switched lasers the pulse duration would increase with *higher* repetition rates

6.2.4 Mode-Locking

While Q-switching can be used to generate pulses with high intensities in the ns-range, mode-locking is used to generate ultrashort laser pulses with pulse duration in the ps- to fs-range, i.e., 10^{-13} – 10^{-15} s. Pulses in the ps-range were generated for the first time by passive mode-locking of a ruby laser shortly after the invention of the laser in the 60s. Mode-locking is based on a mathematical principle resulting from the superposition of sinusoidal waves with different wavelengths and constant phase shift to each other.

Mode-locking can be used very effectively for lasers with a relatively broad laser transition bandwidth, and thus for laser materials with a broad amplification profile, in which numerous longitudinal modes can oscillate simultaneously. Assuming that $2N+1$ modes oscillate with the same amplitude E_0 and a constant phase relation between the modes, the resultant field amplitude $E_{\text{tot}}(t)$ can be expressed as a function of the time t

$$E_{\text{tot}}(t) = E_0 \sum_{n=-N}^N e^{2\pi i[(v_0+n\Delta v_{k,k+1})t+n\phi]} \quad (6.1)$$

with the central mode frequency v_0 and the phase difference $\Phi = \Phi_{n+1} - \Phi_n$. The frequency distance between two neighboring longitudinal modes $\Delta v_{n,n+1}$ is given by

$$\Delta v_{n,n+1} = \frac{c}{2L} \quad (6.2)$$

since the resonator length L must be an integer multiple of half the wavelength. It is assumed that at $t=0$ all modes fulfill the phase condition. Due to their different frequencies, they leave the phase condition immediately after this point of time. However, constant phase relation occurs at periodic time intervals where the frequency distance is an integer of the inverse cycle time of the resonator. At these points of time all modes are at their field maximum, so that the superposition of the $2N+1$ modes reaches its highest theoretical value $(2N+1)E_0$. In the case of uncorrelated modes, this value would never be reached. The analytical summation of E_{tot} in (6.1)

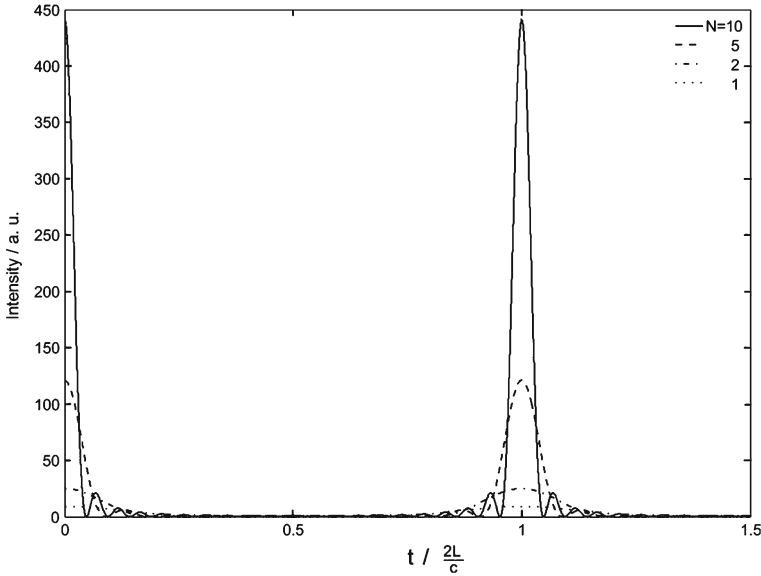


Fig. 6.5 Mode-locking: Superposition of $N=10$ phase coupled longitudinal modes of equal amplitudes. The intensity grows with the *square* of the number of coupled modes

results in

$$E_{\text{tot}}(t) = \hat{E}(t) \times e^{2\pi i\nu_0 t} \tag{6.3}$$

with

$$\hat{E}(t) = E_0 \frac{\sin [(2N + 1) \times (2\pi \Delta\nu_{n,n+1}t + \phi)/2]}{\sin [(2\pi \Delta\nu_{n,n+1}t + \phi)/2]} \tag{6.4}$$

Thus, the resultant total irradiance $I_{\text{tot}}(t)$ is given by

$$I_{\text{tot}}(t) = I_0 \left| \frac{\sin [(2N + 1) \times (2\pi \Delta\nu_{n,n+1}t + \phi) /2]}{\sin [(2\pi \Delta\nu_{n,n+1}t + \phi) /2]} \right|^2 \tag{6.5}$$

The temporal behavior is demonstrated in Fig. 6.5 for a superposition for 1,2,5, and 10 longitudinal modes.

The superposition of the single modes with a constant phase difference leads to laser pulses with a duration τ_p

$$\tau_p = \frac{1}{2N + 1} \frac{1}{\Delta\nu_{n,n+1}} \tag{6.6}$$

and a temporal distance between the laser pulses Δt_p

$$\Delta t_p = \frac{2L}{c} \quad (6.7)$$

The peak intensity I_p of the single pulses is given by

$$I_p = (2N + 1)^2 I_0 \quad (6.8)$$

Thus, the peak intensity is $(2N+1)$ times the sum of the single intensities when the oscillating modes are only statistically coupled and for high N numbers the square can reach extremely high values.

The number of oscillating longitudinal laser modes is limited by the amplification bandwidth $\Delta\nu \cdot L$, because only modes within the bandwidth can oscillate. As a result, the pulse width is restricted by the bandwidth according to:

$$\tau_p \geq \frac{1}{\Delta\nu} \quad (6.9)$$

which can also be regarded as a consequence of Fourier's time-frequency transformation law. Similar to Q-switching, active and passive mode-locking can be realized.

6.2.5 Active Mode-Locking

In active mode-locking devices a modulator is placed in the resonator close to one of the resonator mirrors. The modulator is then triggered by an external signal in such a way that a sinusoidal modulation either of the losses (amplitude modulation) or the optical path (phase modulation) in the optical resonator takes place with a frequency $d\nu$. This frequency $d\nu$ has to be equal to the frequency difference $\Delta\nu_{n,n+1}$ of the longitudinal modes. Initially, this means an amplitude modulation with the frequency $d\nu$ of the mode which starts to oscillate first at a maximum amplification at the frequency ν_0 . According to Fourier transformation this temporal modulation induces neighboring modes with frequencies $\nu_0 \pm d\nu$, which experience an amplitude modulation in the modulator as well. This process of inducing neighboring modes continues until all longitudinal modes within the amplification bandwidth of the laser are coupled and synchronized by a constant phase relation.

Active mode-locking can be used not only in pulsed lasers, but also in cw-lasers. Generally, electro-optic and acousto-optic modulators can be used in both cases. Electro-optic modulators are usually represented by Pockels cells. Acousto-optic modulators work with internal standing acoustic waves, since, as a result of such wave forms, a periodic diffraction grating is induced, which causes a loss modulation at twice the frequency of the generation of sound.

6.2.6 *Passive Mode-Locking*

Passive mode-locking is based on the same principle as active mode-locking, that is a temporal modulation of the resonator losses. In contrast to active mode-locking, the laser system itself determines the point in time at which the losses are at their minimum. The loss modulation takes place either by means of an intensity-dependent absorption which is caused by a saturable absorber or the use of the Kerr effect. Due to the fact that many modes oscillate simultaneously in an oscillator with a broad amplification bandwidth, the intensity initially shows a statistic temporal behavior. Such time-dependent intensity automatically causes a temporal loss modulation in the absorber. This gradually leads to an arrangement with a constant phase relation between the individual longitudinal modes.

In passive mode-locking using saturable absorbers, mode-locking starts from normal noise fluctuations in the laser cavity. Once a noise spike exceeds the threshold of saturating an absorber, the losses decrease, and gain increases in the round trip. Thus initiated spike begins to grow, and becomes shorter, until a stable pulse width is obtained. Passive mode-locking by saturable absorbers was first realized in a dye laser. As a rule, an absorber cuvette with a length of $100\ \mu\text{m}$ is placed close to a totally reflecting resonator mirror. The advantage of this setup is that the reflected front edge of the pulse and the approaching back edge of the pulse interfere inside the absorber, which results in a saturation at lower intensities. Passive mode-locking can not only be applied in pulsed but also continuous wave dye lasers. While passive mode-locking leads to a continuous pulse train in cw-lasers, a pulse train with an envelope covering the duration of the entire laser pulse is generated in pulsed lasers. In solid-state lasers, the minimum pulse width to be reached is essentially determined by the relaxation time of the absorber. The attainable pulse widths of solid-state lasers are longer than those of dye lasers, but solid-state lasers can reach pulse energies that are 10^2 – 10^3 times higher.

Currently, for the generation of ultrashort laser pulses in solid-state lasers usually Kerr-lens mode-locking is applied. In this method the nonlinear Kerr-effect, i.e., the dependency of the refractive index to the incident intensity is used. If a laser beam with high intensity and Gaussian profile passes a Kerr medium the refractive index is not spatially constant due to the intensity profile. According to the high intensities close to the center of the laser beam, the refractive index and, accordingly the optical path, is higher than in the outer regions. Consequently, the Kerr medium acts as a gradient index lens (Kerr lens). Due to the high intensities, which are necessary for initiating the Kerr-lens effect, only pulsed laser radiation with high intensities is focused. For laser pulses with low intensities and cw-mode the Kerr effect can be neglected. For Kerr-lens mode-locking, an aperture is installed in the focal point of the Kerr lens. The focused pulsed beam passes through while most of the low intensity radiation is blocked. This intracavity aperture enables the mode-locked pulses with high intensities to pass through and blocks the modes with statistical phase relation and low intensity level until they get the right phase relation by accident. The combination of the Kerr medium with the aperture then acts as a saturable absorber.

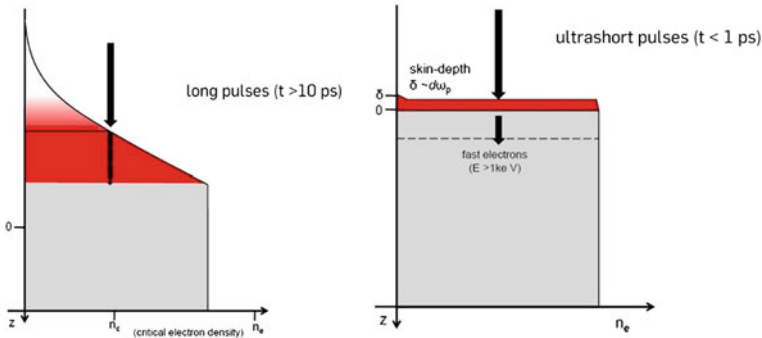


Fig. 6.6 Illustration of the interaction of rather long (*left*) and ultrashort (*right*): For *longer* laser pulses the incident beam strongly interacts with the generated plasma

6.2.7 Interaction of Short Pulses with Matter

The basic interaction principles of micro- and nanosecond laser pulses and mode-locked ultrashort (femtosecond and few picosecond) laser pulses with matter are substantially different. In a first step it is necessary to analyze the amount of radiation that contributes to the ablation. The longer pulses (ns-ms regime) applied with sufficient intensities ($I > 10^{10} \text{ W/cm}^2$) usually induce a plasma resulting in a significant attenuation of the radiation that drives the interaction with the solid-state material [cf. Fig. 6.6 (left)]. A part of the energy deposited in the plasma, however, can be transferred to the solid or molten material and still contributes to material processing. The molten material is ejected from the ablation zone by the pressure gradient caused by the expanding plasma plume. In this regime the thermal penetration length into the material can be described by the equation $d = \sqrt{4k\tau_P}$ with the thermal diffusivity k of the material and the pulse width τ_P .

In contrast, ultrashort laser pulses can directly hit the material without being influenced by the plasma. During the extremely short time interval of the laser pulse the spatial expansion of the plasma is negligible [cf. Fig. 6.6 (right)]. The laser radiation can only propagate in the plasma if the electron number density n_e is below the critical value n_c . In this time regime, the absorbed pulse energy is restricted to a thin surface layer that corresponds in its thickness to the optical penetration depth ($\sim 10 \text{ nm}$). Thermal diffusion into the lattice of the solid-state material is almost negligible. Moreover, the classical heat conduction theory, based on the assumption that a material can be characterized by one temperature only, is no longer valid. Instead, electron-lattice interactions have to be taken into account, and temperatures of both the electrons and the lattice have to be treated separately. In this case a two-temperature-model has to be used to describe the temporal and spatial development of the temperatures.

Ablation of metals with femtosecond lasers is characterized by rapid overheating and thermalization of the electrons within the optical penetration depth. Due to the

low thermal capacity of electrons in comparison with the lattice ions, the electrons are rapidly heated beyond the Fermi-level to very high, transient temperatures, resulting in an extreme non-equilibrium state between the electron and the lattice system. Assuming that the electron thermal capacity can be described by $C_e = 3N_e k_B/2$, with N_e being the electron number density, k_B being the Boltzmann constant, and assuming that the electron thermal conductivity is expressed by $k_e = C_e v_F^2 \tau/3$, with v_F being the Fermi-velocity and the electron relaxation constant τ described in a first approximation by $\tau = a/v_F$, the electron diffusion coefficient D determined by $D = k_e/C_e$ remains temperature-independent, in order to be applied with the differential equation system below, modeled for the temperature prediction of the electrons (T_e) and of the lattice (T_l) along the solid plane normal (z) and the time scale (t)

$$\frac{\partial T_e}{\partial t} = D \frac{\partial^2 T_e}{\partial z^2} - \frac{T_e - T_l}{\tau_e} + \frac{IA\alpha}{C_e} e^{-\alpha z}$$

$$\frac{\partial T_l}{\partial t} = \frac{T_e - T_l}{\tau_l} \quad (6.10)$$

The expression for the analytical solution of T_l for a pulse with the intensity $I(t)$, and the absorption A is then approximately given by

$$T_l \approx \frac{F_a}{C_l} \frac{1}{l^2 - \delta^2} \left[l e^{-z/l} - \delta e^{-z/\delta} \right] \quad (6.11)$$

with F_a being the absorbed fluence, C_l the lattice thermal capacity, the characteristic electron diffusion length $l = \sqrt{D\tau_a}$ with the ablation interval τ_a that is independent of the pulse length in this time regime, and the optical penetration length $\delta = 1/\alpha$. Based on this analytical solution, two border cases can be derived for the lattice temperature distribution:

$$T_l \approx \frac{F_a}{C_l \delta} e^{-z/\delta} \quad (l \ll \delta) \quad , \text{ and} \quad (6.12)$$

$$T_l \approx \frac{F_a}{C_l l} e^{-z/l} \quad (l \gg \delta) \quad (6.13)$$

(6.12) is valid for negligible electron diffusion ($l \ll \delta$), whereas (6.13) is valid in case that the electron diffusion length is considerably greater than the optical penetration depth ($l \gg \delta$). Assuming that the conditions for significant ablation are fulfilled if the absorbed energy density is larger than the solid enthalpy of evaporation $C_l T_l \geq \rho \Omega$, with the density ρ , and specific enthalpy of evaporation Ω , the following expressions for the ablation depth can be derived from (6.12) and (6.13):

$$L \approx \delta \ln \left(\frac{F_a}{F_{th}^\delta} \right) \quad (l \ll \delta) \quad , \text{ and} \quad (6.14)$$

$$L \approx l \ln \left(\frac{F_a}{F_{th}^l} \right) \quad (l \gg \delta) \quad (6.15)$$

with the respective ablation thresholds determined by $F_{th}^\delta \approx \rho \Omega \delta$ and $F_{th}^l \approx \rho \Omega l$ [6].

According to the aforementioned simplified, theoretical model, (6.12) and (6.13) yield two expressions for the ablation depth per pulse as logarithmic functions of the laser fluence, i.e., the pulse energy per area. (6.14) is the characteristic expression for the ablation depth per pulse for a mechanism without a significant heat transfer beyond the optical penetration depth. (6.15) describes the ablation mechanism that is characterized by a significant heat transfer beyond the optical penetration depth due to hot electron diffusion. Both effects can be experimentally verified for a variety of materials including metals with excellent thermal conductivities like copper. Ablation of dielectrics with ultrashort laser pulses is also characterized by non-thermal breakdown of the solid material. However, the free conduction band electrons (CBE) essential for the high-intensity energy diffusion first need to be generated. CBE generation is considered to be described by two competing processes: (1) collisional (avalanche) ionization and (2) multiphoton ionization. The dominance of either is determined by the form of energy gain, which is highly dependent on the experimental environment. If sufficient CBE densities are achieved, the ablation proceeds similar to the mechanism observed in short pulse ablation of metals. Due to the additional expense in pulse energy for CBE generation, though, the available pulse energy for hot electron diffusion, i.e., the effective ablative power, is reduced, in return decreasing the hot CBE maximal diffusion length. Thus, for a prediction of the potential ablation depth of dielectrics, (6.14) is more favorable.

6.3 Basic Processes

After describing the basic laser–material interaction of different pulse regimes in the previous chapter it is useful to take a closer look to the processes which can be initiated by these interaction principles. In the easiest form the intensities are high enough to ablate the material. Depending on the pulse widths and fluences, as described before, either evaporation or sublimation or a combination between these two phases can occur. In a very different approach short pulses can also be used in generative processes like micro-Rapid Prototyping. For polymer structures, also the band gap of the material and the photon energy, i.e., the wavelength plays an important role. Finally, multiphoton absorption phenomena in combination with extremely sharp material reaction thresholds can be used to overcome the classical

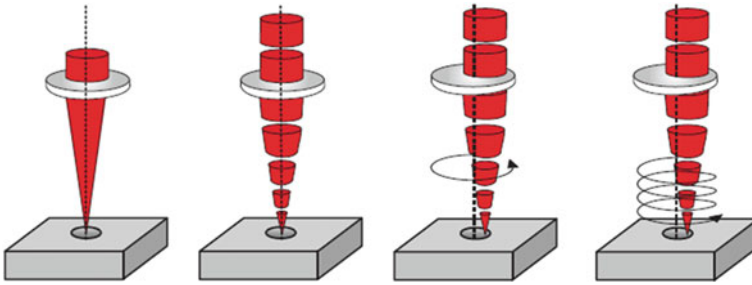


Fig. 6.7 Laser drilling techniques: Single pulse drilling, percussion drilling, trepanning, helical drilling (from *left to right*)

diffraction limit. Based on these phenomena it is quite simple to enter the nanoscale by optical means.

6.3.1 Structuring by Material Removal

In this chapter the intensities are chosen to be clearly above the ablation threshold. In this regime, material is evaporated from the surface resulting in a surface topography. If the material is fully penetrated precise drilling or cutting becomes possible.

6.3.1.1 Drilling

Long pulsed lasers remove the material by a heating process, i.e., they heat the material to the melting or boiling point, accompanied by thermal stress in the remaining material and often a significant heat affected zone (HAZ). Because molten and therefore resolidified material behaves statistically, higher precision is often difficult to achieve using these techniques. Ultrashort laser pulses (picosecond and femtosecond pulses) offer the advantage of removing material without remarkable energy transfer to the surrounding areas. The parameters of interest of a laser-drilled hole are the entrance and exit diameter, roundness, wall roughness, and the 3-D hole profile. Control of the hole profile is also important because some applications require tapered holes (turbine industry, high pressure injection nozzles), whereas others require cylindrical ones or even shaped holes with gradual transitions from circular to square profiles over the depth.

Currently, four different techniques are used in laser drilling: Single pulse drilling, percussion drilling, trepanning, and helical drilling (see Fig. 6.7) [7]. The latter is basically trepanning with adaption of the focal position when short focal lengths are used.

Single pulse drilling is the easiest and most direct method. Only one laser pulse hits the target and generates the complete hole. Depending on the material, very high pulse energies are required for this method. Therefore, single pulse drilling is mostly performed using pulsed solid-state lasers in the gain switching mode. The pulse duration is usually in the range of several hundred μs up to a few ms. Since this pulse duration is rather long, the material removal is mostly based on melt ejection by recoil pressure. Because of melt flow and resolidification single pulse drilled holes exhibit recast inside the holes and on the entrance of the drilling as well as a significant heat affected zone. Single pulse drilling is often carried out with reactive processing gas to improve the drilling rate by enthalpy gains. High pressure gases are sometimes used to blow out the molten phase before solidification.

Alternatively, percussion drilling makes use of multiple laser pulses at the same position on the workpiece to generate a more precise hole. There are two reasons to apply percussion drilling instead of single pulse drilling. On the one hand it can be used to improve the accuracy of the hole by ablating smaller volumes with each laser pulse. Therefore, also shorter pulsed lasers (e.g. Q-Switched lasers) with decreased energy and ablation rate per pulse can be used for drilling deep holes. On the other hand percussion drilling can be used to increase the depth of the drilled hole up to several mm, in extreme cases even a few cm.

Trepanning and helical drilling have similarities with the laser cutting processes and the transition from drilling to cutting is indeed fuzzy in this case. Trepanning and helical drilling generally provide the highest quality compared to single pulse and percussion drilling. However, also the processing times are much longer than in single pulse and percussion drilling. The diameter of the drilled hole correlates with the spot diameter and the laser spot path. Thus spatial distortions ($M^2 > 1$) of the laser spot have smaller influence on the geometry of the hole. As an essential advantage, holes generated by relative movement between laser spot and workpiece are not limited to circular shapes. Even the entrance and the exit of the hole might show different geometries (shaped holes), subject to the condition that the handling system allows an appropriate relative movement between the laser beam and the workpiece.

Applying the trepanning technique leads to superior results concerning the roundness of the micro holes. Because the focused beam is moved in circles, the roundness of the hole is less dependent on the beam profile than when simply focusing the beam without any rotation. Figure 6.8 clearly shows the differences between percussion and trepanning drilling.

According to the basic process phenomena of ultrashort pulsed laser described earlier in this chapter there are several advantages in using picosecond and femtosecond lasers in drilling applications. Because of the more efficient, fast, and localized energy deposition, the well-defined ablation thresholds, and the minimal thermal and mechanical damage of the substrate high-quality hole drilling at relatively low laser fluences, close to the ablation threshold in terms of energy density is possible.

However, for many practical applications, the story is different since high processing speed is required. In this case much higher laser energy densities well above the ablation threshold are necessary. As described earlier by the two-temperature model,

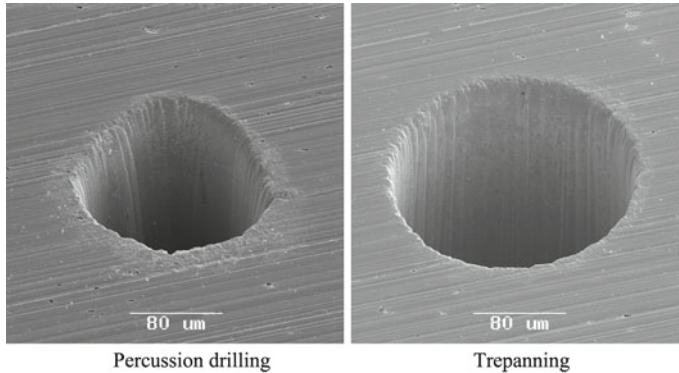


Fig. 6.8 Femtosecond laser pulse drilling in stainless steel using percussion (*left*) and trepanning technique (*right*): The pulse energy of the 150 fs laser pulse was set to 0.9 mJ

at higher laser fluences, the energy coupled into a workpiece and the corresponding thermal load are quite high, also for femtosecond laser pulses. The ablation rate per pulse in this regime is determined by the heat penetration length. Basically this regime is similar to ablation using nanosecond and longer laser pulses. Therefore, at high fluences considerable advantages for material processing with femtosecond lasers are usually not expected. As a minor advantage they can probably drill more efficiently and produce deeper holes, due to lower thermal losses and negligible hydrodynamic expansion of the ablated material during the femtosecond laser pulse. With the latter, losses due to plasma shielding can be avoided.

For deep drilling of metals, which is necessary in many industrial applications, the most important criteria are the hole geometry and quality. The use of more expensive femtosecond lasers could be justified if they could fabricate holes with a special geometry, superior quality, and high reproducibility. It has been demonstrated that femtosecond and picosecond lasers can fulfill these requirements. They have the potential to provide a simple processing technique which does not require any additional post-processing or special gas environment.

The question that needs to be answered at this point is why, even at high laser fluences, high quality holes can be drilled? The answer to this question is quite simple and can be explained by the Gaussian beam profile. High femtosecond-pulse laser intensities are required to rapidly drill a through-hole. After the through-hole is drilled, the high intensity part of the laser pulse penetrates directly through the hole without further absorption. Only at the edge of the laser pulse, at laser energy densities close to the ablation threshold, a small amount of material is removed. Starting from this point, the interaction of femtosecond laser pulses with the workpiece occurs in the low-fluence regime, where all advantages of femtosecond lasers can be realized. This can be considered to be “integrated” low-fluence femtosecond laser post-processing, which is responsible for the excellent hole quality, or as a low-fluence finishing [8].

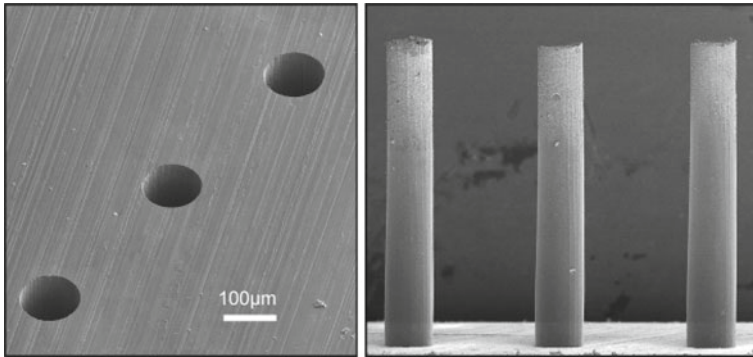


Fig. 6.9 SEM pictures of 1 mm thick stainless steel plate drilled by using femtosecond laser pulses (*left*) and replicas (*right*) which have been formed without post-processing. The pulse energy of the 150 fs laser pulse was set to 0.8 mJ. The polarization was turned by a rotating half-wave plate

The high quality of the single holes and high reproducibility is demonstrated in Fig. 6.9.

6.3.1.2 Cutting

Cutting has already been mentioned in the drilling section as the more general method of trepanning and helical drilling. In laser cutting of metals the process can be classified into melt cutting, oxygen cutting, and sublimation. Usually, the main principle not only occurs alone but a mixture of the different interaction methods can be observed. The advantage of sublimation cutting with respect to microfabrication is that melting and heat-affected zones can be minimized or even avoided. The disadvantage is, however, that the cutting speed is relatively low due to the high evaporation enthalpy of metals. This is the major reason why current industrial large-scale laser cutting of sheet metals is predominantly carried out by melting and oxygen cutting processes. Oxygen cutting has the advantage that high feed rates can be realized, and the disadvantage that oxidation occurs. Both processes lead to significant burr formation and depositions on the material surface. The burr and the depositions must be removed in further production steps.

Cutting with conventional laser sources (e.g. Nd:YAG), which produce pulses with durations in the range of nanoseconds to milliseconds, has several limitations due to thermal load in the material. Heat conduction, therefore, is relatively distinct, which results in large heat affected zones and melting. The melting again can lead to the formation of burr and, in some cases, to the deposition of debris. This often makes post-processing necessary. Due to the thermal load during laser cutting, the minimum producible structure size is limited. Moreover, a variety of materials cannot be structured using this conventional technique. Thus, there is a demand for an alternative, less destructive laser machining technique.

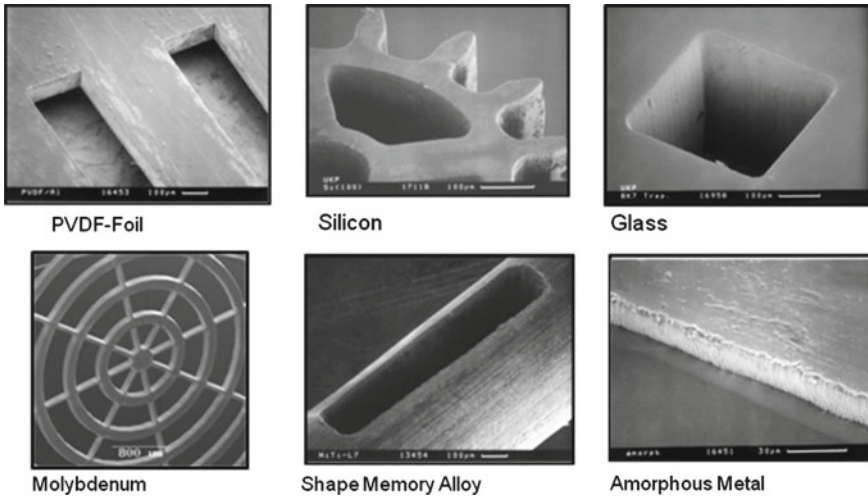


Fig. 6.10 Femtosecond laser cutting of PVDF foil (*top left*), silicon (*top center*), glass (*top right*), molybdenum (*bottom left*), NiTi wire (*bottom center*), and amorphous metal foil (*bottom right*)

By using femtosecond lasers almost all kinds of materials (e.g. metals, ceramics, glass, polymers, organic tissue, etc.) can be structured with minimum or negligible thermal damage. Materials can be processed which otherwise could not be structured with conventional (laser) techniques. The kerfs are very smooth and completely burr-free, and the surface is free of depositions. Figure 6.10 shows several examples for cutting of very different materials by femtosecond laser pulses. The potential of the femtosecond machining technique is obvious in the case of extremely sensitive and delicate materials. The SEM images in Fig. 6.10 show, as an example also cuts in a PVDF foil and in NiTi shape memory alloys, respectively. Both materials are very heat-sensitive materials, and in the case of PVDF even optically transparent. At present, no other machining process for cutting these materials achieves the quality of femtosecond laser machining. For many applications, the non-thermal nature of the femtosecond ablation process is necessary to ensure that the material properties are maintained, even adjacent to the cut area.

Besides the traditional cutting technologies which are based on material removal, also a material loss-free technology is establishing for cutting brittle material, e.g., glass or silicon. The laser radiation is moved across the workpiece and heats up the material. During the following cooling period localized, temporary thermo-mechanical stresses occur, that can be used to control and guide the expansion of an initial crack through the material. This practically leads to a cut with a zero kerf width and a perfectly clean and smooth cutting edge. The complete absence of contamination and edge damages, supersedes cleaning or edge smoothing processes. Recently achieved cutting speeds are five to ten times faster than with ablation-based cutting technologies. In Fig. 6.11, SEM pictures of silicon wafer cutting edges are shown. Using pulsed laser sources, the quality of the cutting edge decreases with

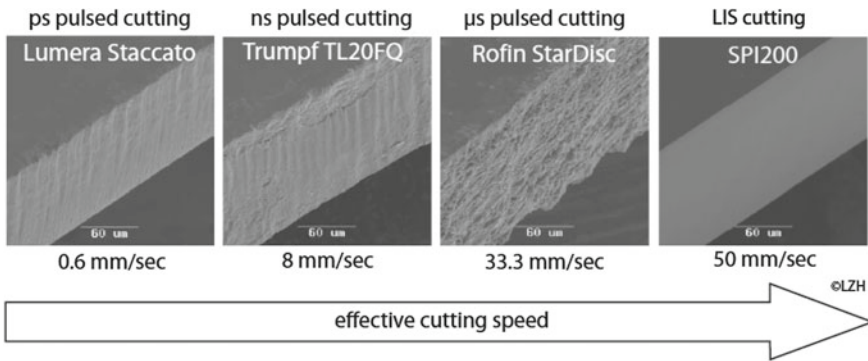


Fig. 6.11 SEM pictures of silicon wafer cut edges using various pulsed cutting systems and novel laser induced stress (LIS) cutting technology

longer pulse duration regimes and also with higher cutting speed. However, with laser-induced stress (LIS) cutting, the best quality and the fastest cut is achieved [9].

6.3.1.3 Ablation of 3-D Structures

For drilling and cutting applications, a longer processing time and higher total applied energy can be used to achieve higher wall surface qualities. Superficial ablation, however, also requires a smooth ablation ground and finishing steps with additional laser pulses to polish the walls are not possible. Such ablation is mostly realized by using especially low laser fluences for the whole process, involving comparatively low processing speeds. Achievable structure sizes vary in the range from several tens of microns down to submicron dimensions, depending especially on the pulse energy and focusing strategy.

For example, by scanning a surface using respective laser parameters leading to low energy densities, precise square planes can be ablated, as shown in Figs. 6.12 and 6.13 for SU-8 resist [10].

To achieve high-precision ablation of small shapes, mask projection methods can be used to process a workpiece with laser fluences slightly above the ablation threshold. Figure 6.14 (left) shows ablation of a chromium layer from a glass substrate in a defined area using 150 fs laser pulses [11]. The picture on the right shows single-pulse ablation of sapphire with submicrometer resolution. The blind holes are processed with very short pulse durations, but also very low pulse energies, in order to achieve extremely small structure sizes using a fluence that is again slightly above the ablation threshold.

To create areas of periodic microstructures, femtosecond laser pulses are often applied using a direct writing process, i.e., using a scanner system or periodic workpiece movements to subsequently process single tracks. Such structures mainly

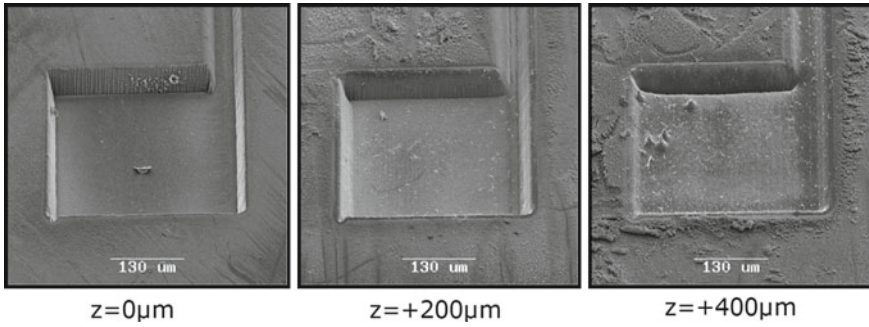


Fig. 6.12 Precise planar ablation of SU-8 resist using 30 ns laser scanning at 266 nm wavelength : from *left to right* change of focal position

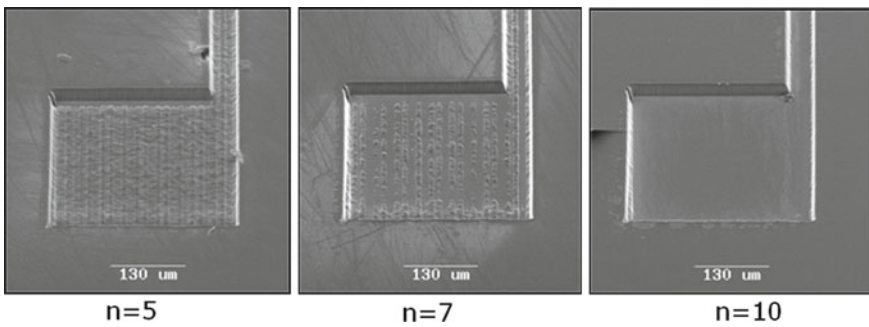


Fig. 6.13 Ablation of 24 μm thick SU-8 resist using 30 ns laser scanning at a wavelength of 266 nm: from *left to right* change of energy and number of layers n ablated to achieve the necessary depth

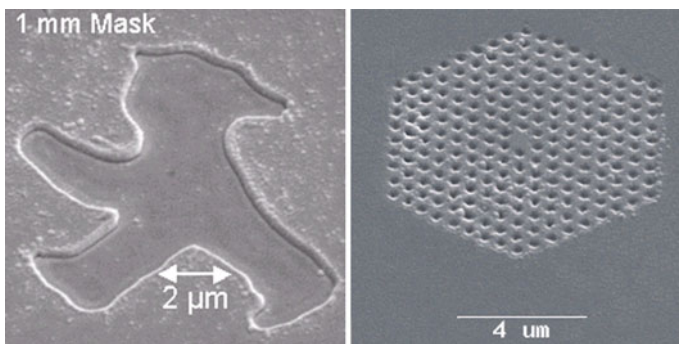


Fig. 6.14 Sub-micron structures from static exposure: *left*: mask exposure of chromium to 150 fs laser pulses, *right*: holes in sapphire from single focused 30 fs pulses

consist of grooves that can be designed to different dimensions and angles by adapting the process parameters. Figure 6.15 (left) shows an array of cone structures in

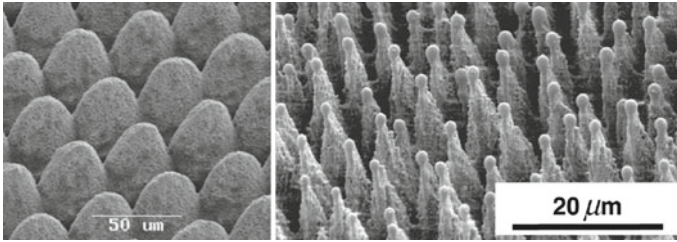


Fig. 6.15 Microstructures from direct fs laser writing: fused silica, structured using 120 fs pulses of 70 μJ (left) and micro-spikes in silicon, generated with 100 fs pulses of 200 μJ in an SF₆ atmosphere (right) [12]

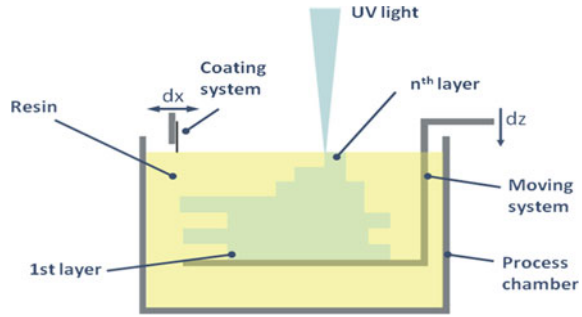
fused silica that was made by superposition of grooves shifted by 90°. The pictures demonstrate machining qualities directly after the process without subsequent cleaning. If optical qualities are needed, such surfaces can be smoothed by subsequent processes like thermal annealing and etching.

Besides periodic microstructures, superficial patterns can also have a stochastic character. With the help of femtosecond laser pulses applied in an SF₆ atmosphere, silicon surfaces have been randomly patterned with microscopic spikes. By adjusting parameters like intensity and gas pressure, the shape can be changed from round and short to sharp and tall spikes, with tip sizes down to several hundred nanometers and spike lengths up to several tens of micrometers. Figure 6.15 (right) shows samples of such structures that are often referred to as “black silicon” due to high light absorption for nearly all wavelengths.

6.3.2 Generative Processes

In contrast to the laser removal processes, described before, generative processes in general comprise the manufacturing of physical, three-dimensional objects by adding material in a layer-oriented method. The layer-by-layer fabrication principle does not require any specially fabricated moulds or tools, instead of relying on three-dimensional model data, which can be generated either by CAD software or by scanning systems like CT (Computer Tomography) which is then called Reverse Engineering. Due to the high flexibility of his process and the absence of any tools the main application of this technology is in the manufacturing of prototypes resulting in the term of Rapid Prototyping. Prior to fabrication, the model data is virtually sliced along the axis of the building direction, i.e., the generation of the geometrical layer information. Depending on the applied fabrication method, three-dimensional objects are then created either by sintering, melting, polymerization, or other methods in a bottom-up principle. For the purpose of this chapter, only polymerization and sintering will be described because they can most easily scaled down to the

Fig. 6.16 The three steps in a stereolithography process: 1 starting point, 2 polymerization of n th layer, 3 lowering of the platform and coating of the $(n + 1)$ st layer



manufacturing of microparts. Melting especially of metals leads to superior material qualities, however, this is at the cost of accuracy.

Polymer parts are generated by a process called stereolithography (SL). Basically, the stereolithography process is based on the light-induced curing of a liquid polymer (also called a resin) that directly transfers into solid state after local illumination with a focused laser beam. In the majority of the available stereolithography systems, high energy photons of a UV laser (the shorter the wavelength of a laser the higher the photon energies) are used to either induce free radicals or cationic polymerization of individual layers. Large-scale parts are fabricated by deflecting the laser beam by two galvanometric mirrors and focusing of the beam in the dedicated polymer layer. The resolution of conventional SL machines is limited to $100\ \mu\text{m}$ in the vertical direction.

After the illumination of a layer by the laser radiation, the next layer of non-illuminated liquid resin needs to be deposited on previously cured features in order to be prepared for the next layer fabrication sequence (Fig. 6.16). For the generation of microparts there are specific requirements, e.g., the minimum layer thickness in micro-stereolithography should be in a range less than $25\ \mu\text{m}$. To achieve the high resolution the resin deposition system has to be adapted to these requirements. In the past years, many innovative solutions have been developed to fulfill these requirements, mostly resulting in extremely long processing times or very limited overall part sizes, making these approaches only useful for a limited number of applications.

In [13] a custom-made device is displayed that is equipped with a mode-locked frequency-tripled solid-state Nd:YAG oscillator operating at $\lambda = 355\ \text{nm}$. The laser provides pulse trains with $\tau_P = 10\ \text{ps}$ pulse widths at a pulse repetition rate of 100 MHz with an average output power of $P_L = 20\ \text{mW}$ (Fig. 6.17). As described at the beginning of this chapter the pulse repetition rate in mode-locked lasers is determined by the resonator length. From the systems' point of view this high repetition rate can be regarded as a continuous-wave beam since a temporal control of single pulses, e.g., by a scanner is impossible for 100MHz.

The possibilities to rapidly manufacture polymeric micro mechanical systems (MEMS devices) are depicted in Fig. 6.18. By special design, it has become possible to generate movable structures [13]. After removal of the fabricated three-dimensional model from the processing chamber, the support structures could be

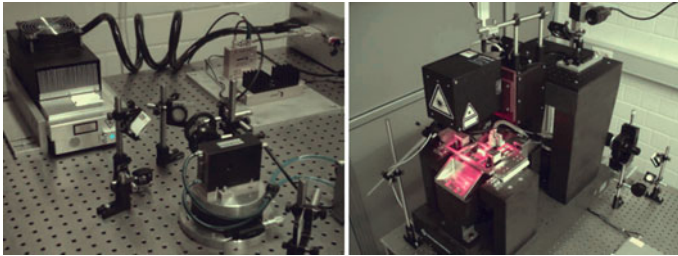


Fig. 6.17 Micro-Stereolithography system: *Left*: UV laser source and acousto-optical modulator, *Right*: hard stone frame with galvanometric scanner and polymer processing chamber

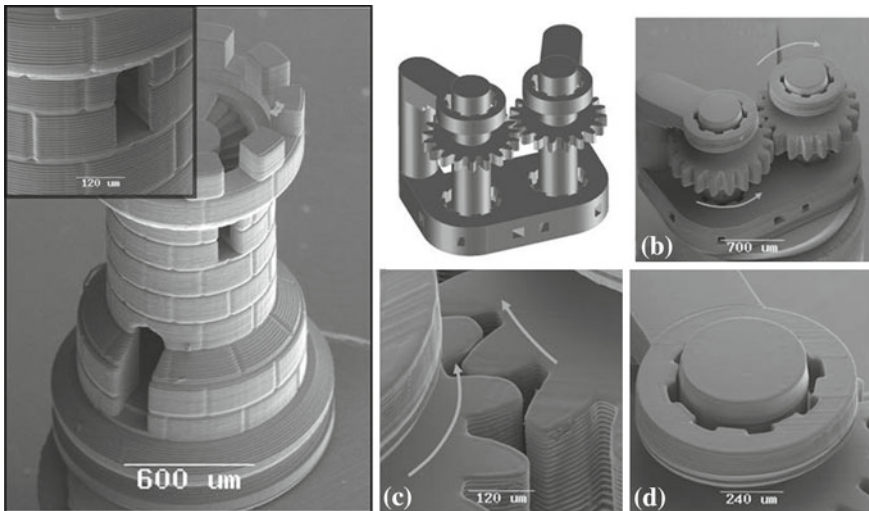


Fig. 6.18 Examples of MEMS-type structures fabricated by laser-based Micro-Stereolithography, SEM image of a chess tower and a MEMS gear wheel structure. The layer thickness in all structures has been $10\ \mu\text{m}$

broken and the previously fixed parts (a ring as proof of principle and a wheel) were freely movable. The material in this case was an organically modified ceramics Ormocer[®] with excellent mechanical and processing properties.

Metal structures, however, are much more difficult to generate on this length scale. Most research activities focus on the downscaling of laser sintering in order to produce microstructures. In the few examples described in the literature, nanophased Iron Copper powder as a filler material is used in a single-step micro laser sintering process (cf. Fig. 6.19). The process is based on the direct application of a filler material, whereas the processing in a particle bed (selective laser sintering) seems to be difficult to scale down. Experimentally, three challenges have to be solved. First, the laser source and the optical system have to be optimized like in Micro-Stereolithography, second the filler material transport and the powder focusing have

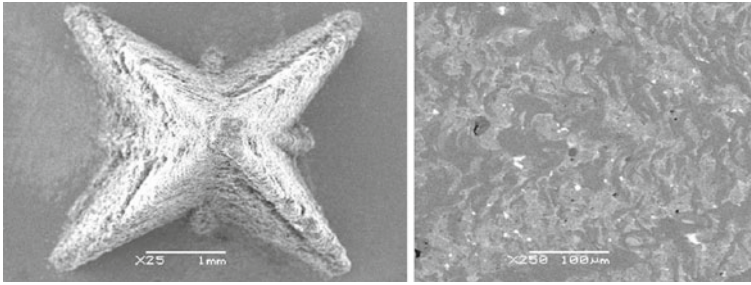


Fig. 6.19 Example of a laser micro sintered punch (*left*) and cross section of the punch showing the specific iron and copper phases (*right*)

to be solved and finally the peripheral components have to be engineered. In this application a tightly focused fiber laser has been chosen which combines the advantages of low optical degradation of the laser medium, an excellent output power stability, scalability as well as the superior lateral resolution ($M^2 = 1,05$). To achieve both a small beam waist diameter and a sufficient distance to the process zone in order to allow the mounting of the powder nozzle, high aperture laser objectives with diminished spherical aberration focus the beam in the working plane [14].

6.3.3 Nanostructuring

6.3.3.1 Multiphoton Ablation

In laser-processing technologies, the minimum achievable structure size is normally determined by the diffraction limit of the optical system, and is of the order of the radiation wavelength. However, this is different for the extremely high intensities related to ultrashort laser pulses. By taking advantage of the well-defined ablation (in general, modification) threshold, the diffraction limit can be overcome by choosing the peak laser fluence slightly above the threshold value. In this case only the central part of the beam can modify the material, and it becomes possible to produce subwavelength structures. In transparent materials, there is a further possibility to overcome the diffraction limit.

Due to the nonlinear nature of the interaction of femtosecond laser pulses with transparent materials, simultaneous absorption of several photons is required to initiate the process. Multiphoton absorption initially produces free electrons that are further accelerated by the femtosecond laser beam electric field. For high intensities these electrons induce avalanche ionization and optical breakdown, and generate a microplasma. The subsequent expansion of the microplasma results in the ablation of a small fraction of material from the surface. The diameter of such a femtosecond laser drilled hole not only depends on the energy distribution in the laser–matter

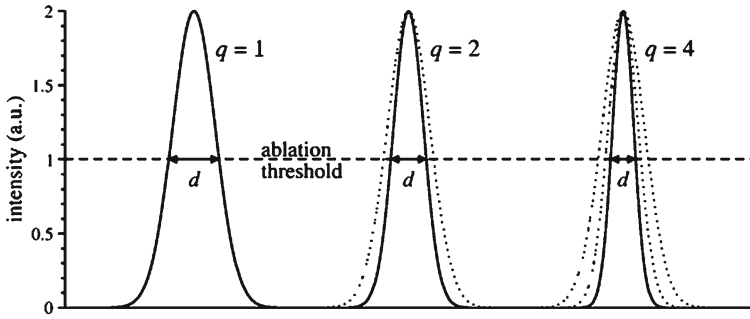


Fig. 6.20 Effective beam profile and ablation hole diameter d for materials where $q=1, 2$ and 4 photons are needed for each ionization process

interaction area and the ablation threshold. There is also a dependence on the energy band gap of the material. To overcome a wider band gap, more photons are needed. This results in a higher limitation of the ionization process to the peak intensity region of the beam profile. The smaller absorption volume leads to a reduced hole diameter. This is, combined with the technique described above, a further possibility to produce subdiffraction-limited structures.

The minimum structure size for a constant fluence ratio F/F_{th} that can be achieved using femtosecond laser pulses in materials with a certain energy band gap can be calculated by the equation

$$d = \frac{k\lambda}{\sqrt{q}NA} \quad (6.16)$$

where λ is the radiation wavelength, q is the number of photons required to overcome the energy band gap, NA is the numerical aperture of the focusing optics, and k is a proportionality constant ($k = 0.5, \dots, 1$) dependent on the material. To illustrate this equation, Fig. 6.20 shows the effective beam profile and the ablation hole diameter d for materials where one, two, and four photons are needed for each ionization process [15].

The reproducibility of this technique is limited by two factors. First, material defects can locally change the ablation threshold, resulting in a change of structure size. Second, avalanche ionization gains importance with longer laser pulses. This results in an increasing influence on the number of free electrons existing in the laser–matter interaction area before the onset of ionization.

6.3.3.2 Nano-Stereolithography

Several groups have demonstrated that nonlinear optical lithography based on two-photon polymerization (2PP) of photosensitive resins allows the fabrication of true 3-D submicrometer structures [16–18].

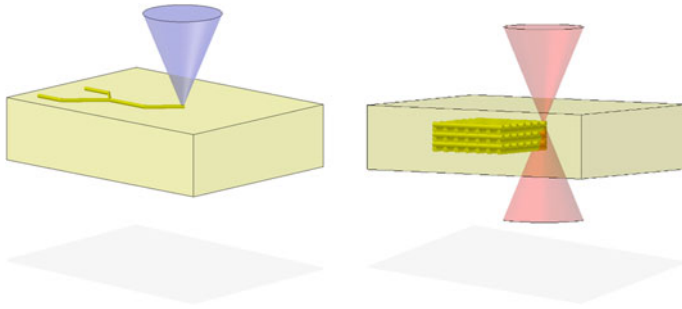


Fig. 6.21 The principle of single-photon Micro-Stereolithography (*left*) and two-photon polymerization 2PP (*right*)

When tightly focused into the volume of a photosensitive resin, the polymerization process can be initiated by nonlinear absorption of femtosecond laser pulses within the focal volume. By moving the laser focus three dimensionally through the resin, any 3-D nanostructure with a resolution down to 100 nm can be fabricated. There are many well-known applications for single-photon polymerization (1PP) like UV-photolithography or stereo-lithography, where a single UV-photon is needed to initiate the polymerization process on the surface of a photosensitive resin, as shown in Fig. 6.21 (left). Depending on the concentration of photo-initiators and of added absorber molecules, UV-light is absorbed within the first few μm . Thus, single-photon polymerization is a planar process restricted to the surface of the resin. On the other hand, the photosensitive resins used are transparent to near infrared light, i.e., near-IR laser pulses can be focused into the volume of the resin [Fig. 6.21 (right)]. If the photon density exceeds a certain threshold value, two-photon absorption takes place within the focal volume, initiating the polymerization process. If the laser focus is moved three dimensionally through the volume of the resin, the polymerization process is initiated along the track of the focal spot, allowing the fabrication of any 3-D microstructure.

The 3-D movement of the laser focus can either be realized by scanning the laser in the x-y-plane, using a galvo-scanner while moving the sample in the z-direction, or by moving the sample three dimensionally, using a 3-D piezo-stage. Obviously, there are several advantages of 2PP compared to Micro-Stereolithography: first, since polymerization can be initiated within the volume of the resin, 2PP is a true 3-D process, whereas Micro-Stereolithography is a planar process. Applying Micro-Stereolithography, 3-D structures can only be fabricated by means of working 2.5 dimensionally, i.e., working layer by layer. Second, when photo-polymerization takes place in an atmosphere with oxygen, quenching of the radicalized molecules on the surface of the resin, and hence a suppression of the polymerization process takes place. This drawback can be overcome by working in the volume rather than at the surface, as is done in 2PP. Third, the two-photon excited spot is smaller than a single-photon excited spot, allowing the fabrication of smaller structures.

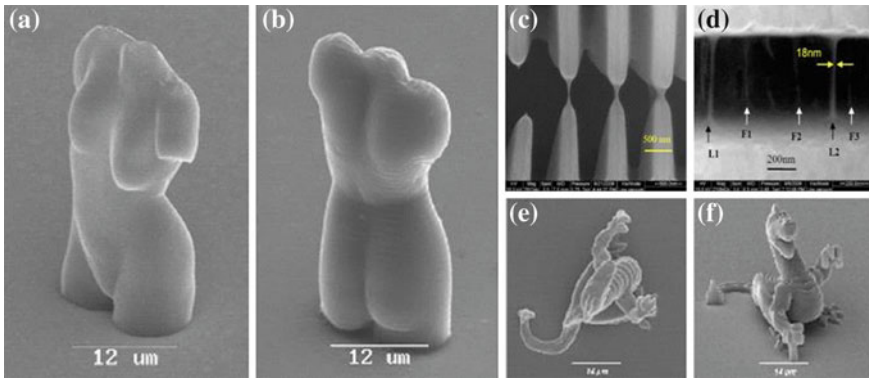


Fig. 6.22 Images of different computer generated micro-models fabricated by means of 2-PP: A, B, E, and F demonstrate the 3-D performance of 2PP, C and D show the resolution which can be as less as 20 nm: [16, 17]

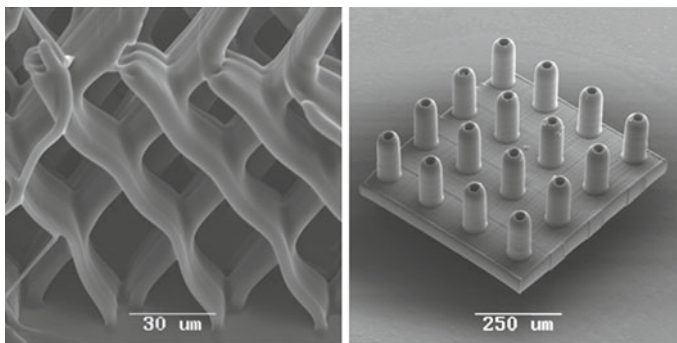


Fig. 6.23 SEM images of Scaffold structures (*left*) and free-standing Lego[®] type structure for cell growth experiments (*right*) produced by 2PP of Ormocers[®]

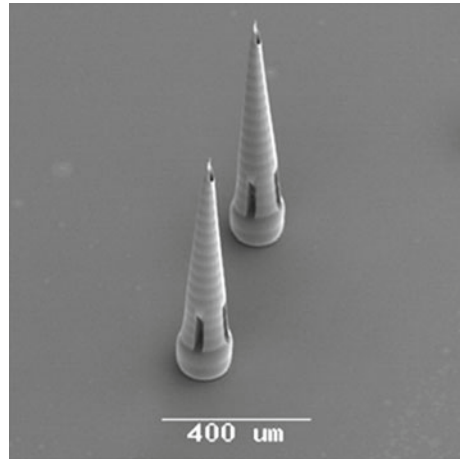
Figure 6.22 displays the images of different computer generated micro-models fabricated by means of 2-PP: A, B, E, and F demonstrate the 3-D performance of 2PP, C, and D show the resolution which can be as less as 20 nm: [16, 17]

6.4 Applications

6.4.1 Cardiovascular Implants

Apart from the direct use of fs-lasers in ophthalmology for refractive surgery (fs-LASIK), precise structuring of medical implants is a promising application with growing industrial interest. One of the biggest markets for micro-implants today are

Fig. 6.24 Micro-needles fabricated by 2PP of Ormocers®



the minimally invasive treatment of arteriosclerosis. Implanting of coronary stents are not only a much less expensive alternative to bypass operations but they also provide a much less dangerous intervention through keyhole surgery. Since the requirements for medical implants (e.g. freedom from burrs, x-ray opacity) are very strict, only a few materials are commonly used. In terms of permanent stents, stents are mostly made of stainless steel (grade 316L with excellent corrosion resistance) or NiTi as a shape memory alloy with pseudoelastic properties. For these metal alloys, chemical post-processing techniques have been developed to achieve the required performance. However, these materials are not optimal, concerning several medical aspects (e.g. risk of restenosis, limited bio-compatibility etc.).

New materials and designs are currently on the market threshold. A complete new class of materials has been developed for stents which are for temporary use only. These stents are made of bio-resorbable materials like Mg-base alloys or special biopolymers which dissolve after a certain amount of time in the human body when their work as been finally done. For these materials, however, no established post-processing technique is available. Furthermore, most of them react strongly to thermal load showing a major heat affected zone or even cracks. Therefore, it is essential to avoid processing influences on the remaining material in order to retain the specific material properties. Femtosecond laser ablation and cutting meets the requirements of these sophisticated materials.

Besides precise cutting there are very promising bio-applications of the 2PP technique: for tissue engineering, drug delivery, medical implants, and medical sensors. For tissue engineering, the ability to produce an arbitrary 3D scaffold structure is very appealing. Scaffolds are required for the artificial fabrication of living tissue that will be able to integrate with the host tissue inside the body, which is a very challenging task. 2PP, in combination with the right materials, allows the precise control over 3D geometry of the scaffold, and therefore allows modeling and reproduction of cellular microenvironments. Furthermore, the high resolution of 2PP can provide

control over the cell organization inside the scaffold and consequently, over the cell interactions. Another advantage of 2PP is that near-IR laser radiation, used for 2PP, is not dangerous for cells at the applied intensities and could also be used for the manipulation and encapsulation of cells.

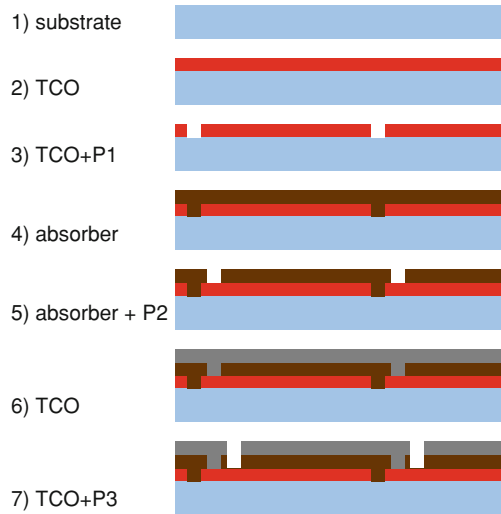
For applications in biomedicine, Ormocers[®] (Inorganic–organic hybrid polymers, trademark of the Fraunhofer-Gesellschaft zur Förderung der angewandten Forschung e.V. München) are very interesting materials. Biocompatibility of Ormocers[®] has been recently studied and the results demonstrated very good adherence of different cell types to this material and a growth rate comparable to bioactive materials like ECM (extracellular matrix). An example of a potential scaffold structure fabricated in Ormocers[®] is shown in Fig. 6.23 (left). In the right figure, SEM image of a free-standing Lego[®] type structure fabricated for cell growth experiments is demonstrated. 2PP can also be applied for the fabrication of drug delivery devices, e.g., microneedle arrays. These devices enable transdermal delivery of a wide diversity of pharmacologic agents. Application of microneedle arrays may overcome many issues associated with the conventional intravenous drug administration, including pain to the patient, trauma at the injection site, and difficulty in providing sustained release of a pharmacologic agent. Moreover, flexibility of the 2PP technique allows arbitrary changes of the needle design and therefore, comparison of the effect of the geometry on the mechanical and puncturing properties. Figure 6.24 is an SEM image of microneedles for drug delivery fabricated by 2PP of Ormocers[®]. These microneedles exhibit appropriate mechanical properties and can penetrate skin without fracture. Investigations of these microneedle arrays for drug delivery are in progress [19].

6.4.2 Solar Cell Processing

During the last 10 years, the installed solar cell capacity worldwide has grown enormously. Today, many new solar cell concepts and production technologies are developed for the next solar cell generation. The main goal is lowering costs per kWh generated electricity. This can be done by increasing the efficiency for converting light into electricity and by reducing manufacturing costs. Recent developments in laser technology offer new applications in the photovoltaic industry. Additionally, many novel high efficiency solar cell concepts are only economically feasible with laser technology, e.g., for scribing silicon thin-film solar cells.

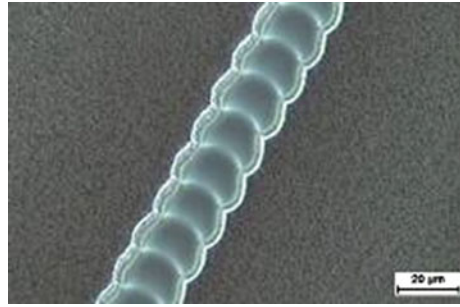
Thin-film solar cells can be made from different material combinations on a substrate. The substrate can be glass, a plastic foil, or a metal foil. Generally, the cell itself consists of a back contact, a front contact, and an absorber material in between. For the contacts Transparent Conductive Oxides (TCO) or metals are used. Commonly used absorber materials are silicon, cadmium telluride (CdTe), copper indium di-selenide (CIS), and other combinations with copper-indium like CIGS or CIGSSe. The layers are typically up to several micrometers thick. Scribing is necessary to obtain a series of integration of cells into modules. The following short

Fig. 6.25 Deposition and scribing process for a thin film solar cell. 1 substrate, 2 TCO deposition, 3 P1 TCO scribing, 4 absorber deposition, 5 P2 absorber scribing, 6 TCO deposition, 7 P3 TCO scribing



calculation clarifies this. The earth is irradiated by the sun with a power density of about 1000 W/m^2 . Common thin-film cells have a size of $1.2 \times 0.6 \text{ m} \approx 0.75 \text{ m}^2$. For a realistic efficiency of 10%, the total generated power would be about 75 W. The output voltage for the mentioned materials is typically between 0.5 and 1 V. So, the current would be somewhere in the range between 75 and 150 A. For such a high current, the contact layers have to be thicker than acceptable. Therefore, the films are cut in smaller cells, to obtain a module with series interconnections. The final module could have 75 W output power with a current of 1 A. In Fig. 6.25 the production chain of thin-film solar cells is schematically shown. A common terminology for the laser processes are “Patterning 1” or “P1” for the first contact, “P2” for the absorber and “P3” for the second (back) contact. As described before, scribing of thin-film solar cells is mainly based on different transmission coefficients of the film materials at the used laser wavelengths. The first deposited TCO layer can be, e.g., zinc oxide (ZnO), tin dioxide (SnO_2), or indium tin oxide (ITO). Commonly, when glass is used as substrate, scribing is done from the glass side. A typical example is shown in Fig. 6.26. The scribing as shown in Fig. 6.26 is performed with the DPSS laser ($\lambda = 1047 \text{ nm}$, $E_p = 30 \mu\text{J}$, $n = 5$ pulses) [20]. Silicon as absorber material is usually scribed with a laser with a wavelength of 532 nm, while TCO is transparent at this wavelength and silicon absorbs radiation of this wavelength in a thin layer. Scribing of the third layer can be done with the same laser wavelength as used for the absorber, for silicon with 532 nm. In this case the second absorption layer is also removed, which is not necessary, but does not influence the solar cell function either.

Fig. 6.26 Example of TCO scribing of pattern 1 with a DPSS laser with a wavelength of 1,047 nm



6.4.3 Machining of Nozzles

In the area of fluidic applications there are many devices where a huge number of holes have to be drilled in order to achieve the specified function. Examples can be found in combustion chamber components or with filter components. In most of these cases a certain degree of inaccuracy in diameter and shape as well as a thin recast layer can be tolerated. In many other applications, however, the requirements can only be met by reducing the laser pulse duration down to the ps or fs range, requiring new technological approaches.

Application examples for high precision drilling are manifold. For fluidic components holes have to be generated, e.g., in inkjet printers, fuel injector systems, flow/dosage regulators or analytical microfluidic sensors. In the automotive industry significant efforts are made toward cleaner cars and reducing the fuel consumption. In this respect diesel injector nozzles are one of the most important components to guarantee a cleaner combustion. Today, injection hole diameters are mainly produced by electro-discharge machining with cylindrical hole diameters in the range of 100 – 150 μm. In future, processes have to be developed that allow the drilling of smaller, more precise holes at a higher production rates. Important quality characteristics of injection holes are burr-free edges, smooth wall surfaces, and a round and cylindrical hole profile. Especially, control of the hole profile is important because some applications require cylindrical holes, whereas others require tapered ones. Figure 6.27 shows an injector nozzle that was drilled using a femtosecond laser.

Ink-jet printing is a dot-matrix printing technology in which droplets of ink are directly jetted from a small aperture to a specified position on a media to create an image. The first practical printing device was already patented in 1951. Since then, many drop-on-demand ink-jet and bubble ink-jet ideas and systems were invented, developed, and commercially produced. Today, the ink-jet technologies most used in the consumer market and in the industrial printing sector are the thermal and piezoelectric drop-on-demand ink-jet methods. The trends in the industry are in jetting smaller droplets for higher imaging quality and picture resolution, faster drop frequency, and a higher number of nozzles for print speed, while the cost of manufacturing is reduced. These trends call for further miniaturization of the ink-jet design.

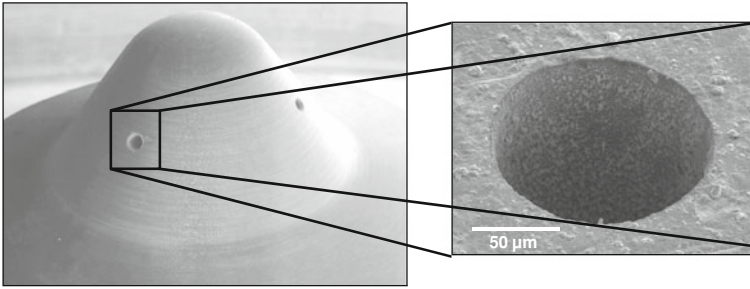
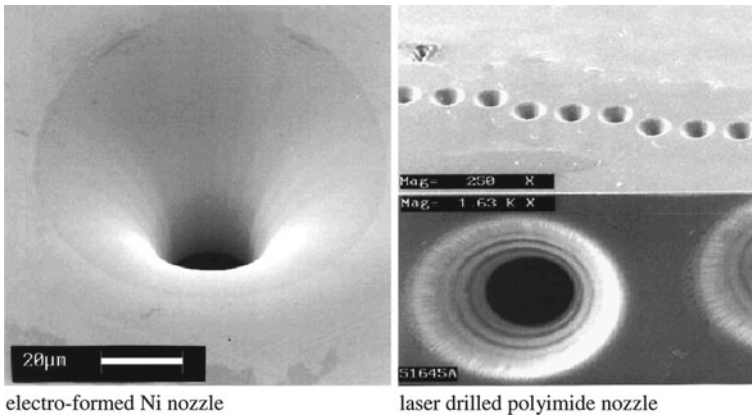


Fig. 6.27 Micro-drilling of fuel injector nozzles using a femtosecond laser



electro-formed Ni nozzle

laser drilled polyimide nozzle

Fig. 6.28 SEM photographs from the entrance side of Ni and polyimide nozzle plates

One of the most critical components in a print head design is its nozzle. Nozzle geometry such as diameter and thickness directly influences drop volume, velocity, and trajectory angle.

Variations in the manufacturing process of a nozzle plate can significantly reduce the resulting print quality. The two most widely used methods for making the orifice plates are electro-formed nickel and laser ablation on the polyimide. Other known methods for making ink-jet nozzles are electro-discharge machining, micro-punching, and micro-pressing. Because smaller ink drop volume is required to achieve higher resolution printing, the nozzle of the print heads has become increasingly small. Currently, for jetting an ink droplet of 10 pl, print heads have a nozzle diameter of around 20 µm (see Fig. 6.28). With the trends toward smaller diameters and lower costs, the laser ablation method has become more and more popular for making ink-jet nozzles.

In general, the production of fluidic components like fuel injection and ink-jet nozzles or other dosing devices (hydraulic and pneumatic components) offers

excellent prospects for innovative laser machining techniques, such as femtosecond laser machining.

6.5 Summary and Conclusions

In this chapter an introduction into the basic principles of laser micro- and nanomachining has been provided. This area is probably one of the most dynamic fields in laser machining and almost daily new and interesting solutions are presented by research groups from many different countries. Thus, this introduction by no means can be comprehensive but the author tried to focus on the most important aspects in order to give readers a chance to understand and explore the specific literature in this field.

The fascination of laser micromachining arrives from the fact that there exist several trends and the area is far from being completed. These trends are as follows:

1. Smaller structures: Of course the aim in miniaturization is always to further shrink structures. To achieve this goal it is necessary to overcome the diffraction limit by making use of specific material properties and laser–material interaction phenomena.
2. Higher throughput: Generally, laser micromachining is a serial processing resulting in rather long processing times. As the available laser power increases with the advent of new laser concepts, researchers try to parallelize processes by intelligent optical systems, e.g., scanners, spatial light modulators, etc.
3. Better quality: Although laser processing has many advantages over other techniques it is basically a thermal process and the results are determined by thermal interactions. The current research work is performed to optimize the interplay between laser radiation and the material. As a result, tailored materials have been designed in order to optimize the quality of laser processing.

References

1. G. Marowsky, D. Basting, *Excimer Laser Technology* (Springer, Berlin, 2010)
2. D.F. Farson, J.F. Ready, T. Feely, *LIA Handbook of Laser Materials Processing* (Springer, Berlin, 2001)
3. W. Koechner, *Solid-State Laser Engineering* (Springer, New York, 2009)
4. C. Rullière, *Femtosecond Laser Pulses: Principles and Experiments* (Springer, Berlin, 1998)
5. A.E. Siegman, *Lasers* (University Science Books, Mill Valley, 1986)
6. B. N. Chichkov, C. Momma, S. Nolte, F. von Alvensleben, A. Tuennermann, Femtosecond, picosecond and nanosecond laser ablation of solids. *Appl. Phys. A* **63**, 109–115 (1996)
7. D. Breitting, C. Foehl, F. Dausinger, T.V Kononenko, V. Konov, Drilling of metals, femtosecond technology for technical and medical applications. *Top. Appl. Phys.* **96**, 131–156 (2004)
8. G. Kamlage, T. Bauer, A. Ostendorf, B.N. Chichkov, Deep drilling of metals by femtosecond laser pulses. *Appl. Phys. A* **77**, 307–310 (2003)

9. O. Haupt, F. Siegel, A. Schoonderbeek, L. Richter, R. Kling, A. Ostendorf, Laser dicing of silicon: Comparison of ablation mechanisms with a novel technology of thermally induced stress. in *Proceedings of LPM2008—the 9th International Symposium on Laser Precision Microfabrication*, 2008
10. A. Ostendorf, J. Koch, F. Meyer, B.N. Chichkov, Lithography by maskless laser direct writing. ed. by M. Brandt, E. Harvey. in *Proceedings of the 2nd Pacific International Conference on Application of Lasers and Optics (PICALO) 2006*, pp. 1–6
11. J. Koch, F. Korte, C. Fallnich, A. Ostendorf, B.N. Chichkov, Direct-write subwavelength structuring with femtosecond laser pulses. *Opt. Eng.* **44**, 1–4 (2005)
12. E. CareyJ, C. H. Crouch, E. Mazur, Femtosecond-laser-assisted microstructuring of silicon surfaces for new optoelectronics applications. *Opt. Photonics News* **14**, 32–36 (2003)
13. A. Neumeister, R. Himmelhuber, C. Materlik, T. Temme, F. Pape, H.-H. Gatzen, A. Ostendorf, Properties of three-dimensional precision objects fabricated by using laser based micro stereo lithography. *J. Laser Micro/Nanoeng.* **3**, 67–72 (2008)
14. S. Dudziak, O. Meier, H. Mewes, A. Ostendorf, Generation of niti-sma-micro parts using two step laser sintering. in *Proceedings of the International Congress of ICALEO 2007, CD-ROM compiled and produced by Laser Institute of America, Section, Laser Microprocessing Conference* pp. 166–172
15. J. Koch, E. Fadeeva, M. Engelbrecht, C. Ruffert, H.-H. Gatzen, A. Ostendorf, B.N. Chichkov, Maskless nonlinear lithography with femtosecond laser pulses. *Appl. Phys. A* **82**, 23–26 (2006)
16. S. Kawata, H.-B. Sun, T. Tanaka, K. Takada, Finer features for functional microdevices. *Nature* **412**, 697–698 (2001)
17. J. Serbin, A. Egbert, A. Ostendorf, B. N. Chichkov, R. Houbertz, G. Domann, J. Schulz, C. Cronauer, L. Fröhlich, M. Popall, Femtosecond laser-induced two- photon polymerization of inorganic organic hybrid materials for applications in photonics. *Opt. Lett.* **28**, 301–303 (2003)
18. D. Tan, Y. Li, F. Qi, H. Yang, Q. Gong, X. Dong, X. Duan, Reduction in feature size of two-photon polymerization using SCR500. *Appl. Phys. Lett.* **90**, 071106 (2007). doi:[10.1063/1.2535504](https://doi.org/10.1063/1.2535504)
19. A. Ovsianikov, B. Chichkov, P. Mente, N. A. Monteiro-Riviere, A. Doraiswamy, R. J. Narayan, Two photon polymerization of polymer–ceramic hybrid materials for transdermal drug delivery. *Int. J. Appl. Ceram. Technol.* **4**(1), 22–29 (2007). doi:[10.1111/j.1744-7402.2007.02115.x](https://doi.org/10.1111/j.1744-7402.2007.02115.x)
20. A. Ostendorf, A. Schoonderbeek, Lasers in energy device manufacturing. *Proc. SPIE.* **6880**, 68800B (2008). doi:[10.1117/12.760350](https://doi.org/10.1117/12.760350)

Chapter 7

Laser Surface Processing of Polymers for Biomedical Applications

David Waugh and Jonathan Lawrence

Abstract Polymeric biomaterials offer excellent bulk properties for biological applications; however, the surface properties they possess do not lend themselves to high performance in regard to biomimetics. Hence, it is necessary to vary the surface properties of the material to enhance the wettability and bioactivity. In the present contribution, the surface characteristics and properties of nylon 6,6 modified by CO₂ laser processing has been presented in detail. From analyzing the laser-induced patterned surfaces it was found that the surface energy and polar component had decreased by up to 7 mJm^{-2} and the surface roughness had considerably increased. From the results it was not possible to develop a discernable correlation between the cell response and surface characteristics such as roughness and surface energy. However, laser patterned surfaces in this instance gave rise to enhanced biomimetic properties for nylon 6,6 in terms of osteoblast cell response.

7.1 Polymers as Biomaterials and In Vitro Experimentation

7.1.1 Polymeric Biomaterials

Polymers are long chain molecules which constitute a large number of small repeating units more commonly known as monomers. As a result of the fact that a vast amount of materials come under the title of polymers, it can be seen that there are numerous applications within the biological industry in which these materials can be used.

J. Lawrence (✉) · D. Waugh
School of Engineering, University of Lincoln,
Brayford Pool Lincoln, LN6 7TS, UK
e-mail: jlawrence@lincoln.ac.uk

D. Waugh
e-mail: dwaugh@lincoln.ac.uk

Table 7.1 Some of the main polymeric biomaterials with their most common applications within the biomaterials industry.

Nylon	Gastrointestinal segments; tracheal tubes
Polyethylene (PE)	Acetabular cup of hip prosthesis; heart pacemakers
Polymethyl methacrylate (PMMA)	Dental restorations; intraocular lenses; joint replacement
Polypropylene	Heart valves
Polyurethane	Heart pacemakers; maxillofacial prosthesis
Polyvinyl chloride (PVC)	Gastrointestinal segments; maxillofacial prosthesis
Ultrahigh molecular weight polyethylene (UHMWPE)	Total joint replacement—usually hip, knee and shoulder joints

Table 7.1 shows some of the main polymeric biomaterials indicating their current most common uses within the biomaterials industry.

Advantages of using polymers can be seen to be that they are able to be easily fabricated to various complex shapes and structures and provide a large range of bulk compositions and physical properties which could be applied to a number of applications. However, disadvantages have been identified such as they can be difficult to sterilize, can easily absorb water, and may leach out harmful substances to the body under in vivo circumstances [1].

Nylon is a family of semi-crystalline engineering thermoplastics which are generally fabricated using straight chain aliphatic acids and amines. The most common nylons are that of nylon 6 and nylon 6,6 where the numbers correspond to the number of carbon atoms donated to the amine and acid monomer chain. Nylon 6,6 is an off-white engineering thermoplastic which has been found to be the strongest and most abrasive resistant unreinforced nylon. Owing to the material properties nylon 6,6 possesses this polymer has been used for such biological applications as sutures, tracheal tubes, and gastrointestinal segments [1]. What is more, by modifying the surface of polymeric materials it may be possible to identify other biological applications as this may enhance the biomimetic and biocompatible properties. By extrapolating from past and current research it is imperative that any biomaterial should be optimized in order for that material to function appropriately and efficiently within the desired biological environment. In numerous instances it is seen that the bulk properties of a biomaterial are decided upon such that the surface properties are compromised [2, 3]. In particular, this is seen throughout the use of polymeric biomaterials as they offer excellent bulk properties for biological applications; however, the surface properties they possess do not lend themselves to high performance in regard to biomimetics [4]. On account of this, it is necessary to vary the surface properties of the material without hindering the bulk properties in order to enhance the wettability and bioactivity. In terms of bioactivity a biomaterial can be surface modified both topographically and chemically in order to manipulate the way in which the cells react. That is, the signaling of the cells could be optimized in order for the filopodia to

assess the extracellular matrix (ECM) and substrate so that the most possible integrin receptors could be localized around the suitable binding site to improve upon adhesion characteristics [5]. This is of great importance to those cells such as osteoblast cells that are highly dependant on ECM anchorage and as a direct result necessitates adhesion with the biomaterial prior to the initialization of normal cell function [6]. Integrin receptors are crucial to the way in which a biomaterial is accepted into the biological environment insofar as cellular interactions takes place through the receptors creating focal adhesions. These focal adhesions are also important as they produce a high density of transmembrane receptors in areas of cellular adhesion owed to the fact that they are closely associated with the actin cytoskeleton and other factors which regulate the signaling that takes place as the cell functions [7].

7.1.2 In Vitro Experimentation of Materials

As it is crucial to implement the best possible material for specific areas of the body to enhance and sustain cell adhesion and proliferation the testing of biomaterials is a very important factor which should be considered prior to any material being implemented within a biological environment. As a result of this, numerous experimental tests have been derived and utilized in order to analyze how a material will function within a specific environment. For biological implants there are two main areas of testing; these being the bioactivity with regard to cell adhesion, etc and the mechanical strength of the material. Both of these factors are of major importance due to the fact that without high bioactivity and an overall high mechanical strength the biomaterial in the biological environment would fail causing potential pain for the patient and potentially causing more biological problems than necessary such as infections. By using experimental testing prior to the implantation one can then determine the risks involved with the procedure and also determine whether materials are feasible for use as biomaterials.

7.1.2.1 In Vitro Assessment

In vitro testing of biomaterials is one of the most common ways in which biological functionality and cytotoxicity can be determined without causing harm to humans or animals. It has been seen that when researching new materials and techniques for biomaterials this method of testing is extensively utilized. There are three main types of primary cell culture assays that are used under this method of biological assessment to determine the bioactivity of a material; these are direct contact, agar diffusion, and elution (also known as extract dilution). Direct contact allows one to mimic physiological conditions while allowing for standardizing the amount of test material. Also, this method allows for target cell contact with the proposed biomaterial. However, disadvantages which this method poses are that cellular trauma can occur if the biomaterial sample moves during testing and cellular trauma is also

possible with those materials that possess high densities. It has also been seen with this type of assay that the cell population can be highly decreased if highly soluble toxicants are present. Agar diffusion assays allow an improved concentration gradient of present toxicants in addition to the possibility of allowing one to have the ability to assess the bioactivity of one side of the sample material. However, it should be noted here that agar diffusion assays require flat surfaces to function efficiently and there is a risk of thermal shock when the agar overlay is being prepared. Alternatively, elution assays give rise to the possibility of separating extraction from the biological testing and is flexible with this method allowing one a wider variation in choice for extraction conditions and solvents. One of the main disadvantages that has been seen with elution assays is that additional time and steps are required in comparison to the other two alternative assays. In most cases it is seen that *in vitro* assessment is carried out prior to *in vivo* assessment due to the fact that *in vitro* assessment allows one to gain a preliminary understanding of how a material will react within a biological environment. In some instances, however, *in vitro* methods have been criticized for not giving a full picture of how materials will act in an environment which is relatively difficult to mimic. For example, it has been realized in some cases that *in vitro* assays do not incorporate cells that possess sufficient metabolic activity and would give results for toxicity that would not necessarily be observed within an *in vivo* assessment.

7.1.2.2 Bone-Like Apatite Layers

Simulated body fluid (SBF) is a metastable calcium phosphate solution with an ion concentration approximately equivalent to that of human blood plasma. It can be seen throughout the literature that SBF can be implemented as a screening technique to predict and assess the bioactivity and osseointegration potential of materials [5]. This is owed to the fact that the bioactivity of almost all orthopedic biomaterials has a strong relationship with the ability of that material to promote the formation of bone-like carbonite apatite crystals [8–10]. What is more, this apatite layer associates specific bone proteins which are crucial for any form of bone reconstruction [11]. Under healthy normal conditions, body fluid is known to usually be already supersaturated with respect to apatite and, upon nucleation of the apatite, the layer can grow through the consumption of calcium and phosphate ions that are present in the body fluid. *In vitro* experimentation with SBF is usually carried out by soaking the material in question in SBF over a period of time at a constant temperature of 37°C in order to form an apatite layer on the surface. Afterwards, by analyzing the surface one can then determine the suitability of that material for use as an implant and predict how that material will perform when bonding to bone. For example, by using some form of surface chemistry analysis, such as EDX or X-ray photoelectron spectroscopy (XPS), surface functionalities can be identified prior to immersion in the SBF. This can be seen to be of some importance as some hydroxyl groups can induce apatite nucleation in addition to calcium and phosphorous being vital to the adhesion of osteoblast cells as discussed by Song et al. [8]. Through the work of

Uchida et al. [12] it has been identified that in some cases the extent of nucleation of apatite on the biomaterial surface is directly dependant on the functional groups present. That is, some functional components are released from the surface into the body fluid giving rise to an increase in ionic activity product which can allow for accelerated apatite formation. On the other hand, it should also be noted that, like many in vitro experiments, employing SBF does not fully reproduce the in vivo environment for bone formation and may produce misleading results. However, as stated by Roach [5], in vitro techniques utilizing SBF allow for a potential rapid screening of materials in the endeavor of development and optimization of biomaterials. Furthermore, these initial in vitro experiments can be used as preliminary studies prior to carrying out experimentation in vivo.

7.1.2.3 Cytotoxicity

Cytotoxicity or cell death is usually evaluated by the quantification of plasma membrane damage. This is due to the fact that upon damage of the plasma membrane lactate dehydrogenase (LDH), a stable enzyme present in all cell types, is rapidly released into the cell culture medium. As a result of this, LDH is the most common and widely used marker in cytotoxicity studies. Thus, it can be seen throughout the literature that due to the significance of cytotoxicity in determining the cell response of biomaterials a number of studies have been carried out using various materials [3, 13–15]. There are a number of different in vitro cytotoxicity tests that can be carried out and are usually separated into two categories: direct methods, in which the cells are in direct contact with the testing solution, and indirect methods, where the cell culture medium is extracted prior to being analyzed [16]. What is more, Cytotoxicity kits are readily available ‘off-the shelf’ and carrying out this study would allow one to determine the quality of the cells produced. It could also be used to determine if a specific biomaterial surface gives rise to better quality cell growth and proliferation in terms of cytotoxicity.

7.1.2.4 Alkaline Leukocyte Phosphatase

Alkaline leukocyte phosphatase (ALP) activity is involved in bone formation and has been shown that ALP is significant in the development of skeletal calcification [17]. Also, ALP has been shown to be of major importance when detecting chronic myeloid leukemia owed to the fact that ALP activity typically decreases in patients who have contracted the disease [18]. With regard to bone formation, it is believed that ALP acts at the focal site of bone creation by eradicating inorganic pyrophosphate which is known to potentially inhibit calcification [17]. As a result of this, experimentation has been carried out previously to detect the ALP activity in order to assess the biofunctionality of biomaterials [3]. Like cytotoxicity, ALP kits are readily available ‘off-the shelf’ in a number of varieties and for a complete in vitro study of bioactivity

ALP should be accounted for to ascertain how the ALP activity is modulated by the biomaterial in question.

7.1.2.5 Protein Adsorption

It is well known and accepted that protein adsorption is the first event to occur following implantation prior to cell growth and proliferation [19]. Furthermore, cell behavior in terms of cell growth and proliferation is highly dependent on the properties of this protein layer [20]. Owing to the importance attributed to protein adsorption for osteoblast cell growth numerous studies have been carried out using different substrates to ascertain the protein adsorption response [3, 19, 21–23]. The protein thicknesses that arise are usually at most around 10 Å [3] and as a result of this, ellipsometry is the main technique to determine the layer thickness. Ellipsometry is therefore widely used for metals and ceramics; however, as most polymers possess a refractive index close to that of the protein layer, ellipsometry cannot be carried out making it very difficult to obtain results [23].

7.2 Wettability in Biomaterials Surface Science

One of the most interesting subject areas in biomaterials surface science is that of wettability, with many workers endeavoring to determine the complex links between surface wetting and bioactivity [24]. Numerous theories have been expressed in order to explain this phenomenon in which two basic regimes have arisen. The first takes the biomimetic properties and attempts to correlate it with the surface energy while the second involves water solvent properties near the surface in which a correlation between the contact angle and bioactivity is strived for. However, in both cases a fundamental factor dominates in which the surface energy/wetting is generally related somewhat to the biological response [25]. Various approaches have been undertaken as to ascertain quantitative reasoning to bioactivity such as Van Oss et al. [26] by using the 'equation of state' approach to calculate interfacial tensions from previously measured contact angles in order to attempt and predict cell adhesion. Such approaches have been found to fall short for achieving a quantitative theory regarding the bioactivity of a material. Through the available literature it can be seen that extensive research is now being carried out regarding this in the attempt to link wettability and bioactivity of materials [27, 28]. Once a quantitative link has been forged between these two parameters one can extrapolate that this will give those throughout the biotechnological industry a means to produce materials which have the ability to either enhance or even hinder the biomimetic nature; for instance, materials produced with surfaces that hinder the growth of bacteria could be widely used throughout the food packaging industry. On the other hand, enhanced biomimetics could be utilized for numerous applications such as biological implants and BioMEMS applications [29].

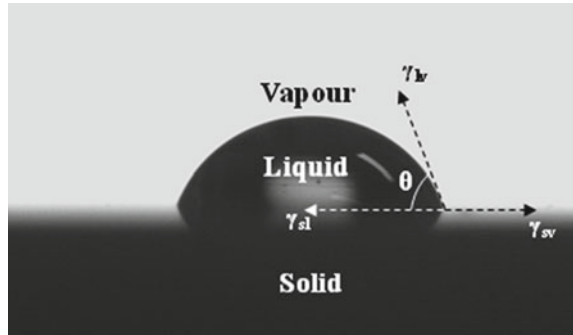
7.2.1 Contact Angle and Wettability

Since the first description of contact angles and wettability by Thomas Young in 1805 considerable research has been carried out on the wetting of various materials. For instance the Lotus Effect was discovered in 1997 by Wilhelm Barthlott indicating that when rain falls onto a Lotus leaf water droplets form producing a contact angle of approximately 160° which is highly hydrophobic (superhydrophobic [30]). As the droplets roll off the leaf dirt is picked up along the way allowing for the leaves to have clean surfaces [31]. Discoveries such as this have given rise to increased interest into the wettability of materials such as polymeric biomaterials and it has also been seen that the complex mathematics regarding wettability have been researched and discussed [32–38]. Experimentally, there has also been extensive research into wettability of materials; for instance, the work done by Bico et al. [39] allows one to see how the designed roughness of a textured surface can be utilized in order to manipulate the wettability characteristics of a material. Within this work they also indicate the implications of applying wettability methods to porous media by showing that such a material cannot be considered as an array of capillary tubes when attempting to explain the complex phenomenon of wettability. In addition, research has also been carried out into the parameters that govern the transition between the Cassie-Baxter to Wenzel wetting types. For example, this work has been undertaken by Jung et al. [40] who concluded that the droplet size has a major influence on the transition between the two wetting types. Furthermore, in some cases, it has been seen that it may be possible for a hydrophilic surface to give rise to some form of Cassie-Baxter wetting or Cassie-Baxter/Wenzel mixed intermediate wetting regime owed to the roughness and topographical pattern on the surface [41–43]. In this instance it is seen in some cases that increasing the surface roughness, through the patterning of a surface, can give rise to an increase in contact angle for hydrophilic materials.

7.2.1.1 Contact Angle

It has been extensively observed that when a drop of liquid is left in free space it has a tendency to be drawn into a spherical shape as a result of the tensile forces from the surface tension. This is a resultant that arises from the attractive and repulsive forces that exist between the molecules within the liquid. If the same drop of liquid was to be brought into contact with a solid flat surface the final outcome of the droplet (as to what shape it would undertake or whether the liquid would wet the surface) would be dependent on the relative magnitudes of the molecular forces that exist within the cohesive and adhesive parameters. This phenomenon is quantified utilizing the contact angle, θ , which is the angle that the liquid subtends with the solid and can be visualized in the schematic diagram of a droplet of liquid on a flat solid surface shown in Fig. 7.1. It has been realized that in a generalized sense, for wetting to take place the contact angle, θ , shown in Fig. 7.1, has to be less than 90° . From this it can

Fig. 7.1 Diagram showing a liquid droplet at rest on a flat solid surface



then be deduced that wetting of the solid surface will not occur if the contact angle was to be greater than 90° resulting in adhesion not taking place [44].

From observation and experimentation it has been found that the contact angle is closely related to three specific energies; the solid and liquid surface energies, γ_{sv} and γ_{lv} respectively, and the solid–liquid interfacial energy denoted as γ_{sl} . Through the work carried out by Thomas Young it was realized that these parameters were related as shown in Young’s equation (Eq. 7.1), if the liquid droplet was in a state of equilibrium:

$$\cos \theta = \frac{\gamma_{sv} - \gamma_{sl}}{\gamma_{lv}} \quad (7.1)$$

From Eq. 7.1 it is then possible to deduce some basic understandings of what is required to achieve wetting. That is, if wetting was to be required then γ_{sv} would have to be large in comparison to that of γ_{sl} and γ_{lv} . This scenario then indicates that those liquids that have comparatively low surface tensions would almost always spread over the solid surface in the attempt to reduce the total free energy within that system [45, 46]. This arises from the molecular adhesion between the solid and liquid being greater than that of the cohesion between the molecules within the liquid [44]. It has been seen that a sessile drop device is the main technique to measure the contact angle and as a result much research has been employed into this technology.

7.2.1.2 Surface Energy and Dispersive/Polar Characteristics

From Eq. 7.1 it can be seen that the quantities γ_{lv} and θ can relatively be easily measured experimentally. Whereas γ_{sl} is a parameter which would require further work to determine. Throughout any wettability study it is known that the effect of adsorption of the measuring liquid on the solid surface should also be taken into account. However, due to the negligible effect this phenomenon has in systems containing solid polymers many researchers choose to neglect it. Fowkes [47] was a pioneer of approaching this subject with the idea of partitioning the surface free

energy into individual components which assumes that interfacial interactions arising from the properties of the measuring liquid and surface layer determine the quantity γ_{sl} . Fowkes originally stated that one can assume that the surface free energy of a solid is composed of a sum of individual components as seen in Eq. 7.2.

$$\gamma_s = \gamma_s^d + \gamma_s^p + \gamma_s^h + \gamma_s^i + \gamma_s^{ab} + \gamma_s^o \quad (7.2)$$

where, γ_s^d , γ_s^p , γ_s^h , γ_s^i and γ_s^{ab} are the dispersive, polar, hydrogen, induction, and acid–base components, respectively. Additionally, γ_s^o denotes all other interactions that may be present in the system. The Owens, Wendt, Rabel, and Kaelble (OWRK) method [48] modified the Fowkes assumption by assuming that all of the components on the right-hand side of Eq. 3.12, apart from γ_s^d , can be associated with and therefore be incorporated in the polar interactions, γ_s^p . Following on from this, they were then able to derive the equation shown in Eq. 7.3.

$$\gamma_{sl} = \gamma_s + \gamma_l - 2 \left(\gamma_s^d \gamma_l^d \right)^{0.5} - 2 \left(\gamma_s^p \gamma_l^p \right)^{0.5} \quad (7.3)$$

From Eq. 7.3 it can be seen that two unknown variables arise: γ_s^d and γ_l^p . As a result of this, Eq. 7.3 can be deemed insufficient to determine the surface free energy of a polymer. Using two measuring liquids make it possible to calculate the surface free energy by combining Eqs. 7.1 and 7.3 and adapting the resulting equation by transposing it to the general equation for a straight line. By implementing a sessile drop device with software such as SCA20 supplied by Dataphysics Instruments it is then possible to easily use the OWRK method for the software to calculate γ_{sl} . This is done by the software producing a linear graph as shown in Fig. 7.2 from the data inputted.

In order to reduce errors the measuring liquids decided upon should be one with a dominant polar component and one dispersion liquid. As this method allows for the relative ease of derivation of components the OWRK technique is one of the most common used with water and diiodomethane being the most frequently used measuring liquids.

7.3 Surface Modification Techniques

7.3.1 Radiation and Photografting

Radiation grafting and photografting are techniques that are widely used throughout the biomaterials industry. In respect to polymers the radiation can be applied in many forms such as high energy electrons, gamma radiation, ultra-violet (UV), and visible light and is used to allow the chemical bonds of the polymer to be broken. This gives rise to the formation of free radicals and, in the presence of a monomer, reacts to produce a free radical chain reaction allowing other monomers to be incorporated

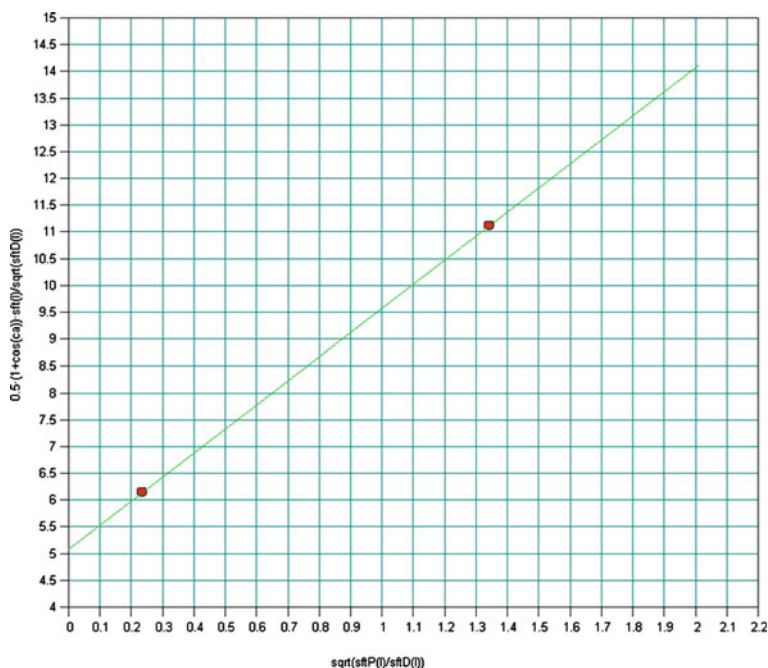


Fig. 7.2 Example linear regression plot for the SCA20 software to calculate γ_{sl}

to ultimately construct a surface-grafted polymer. With regard to the bioactivity of a material this technique allows one to selectively place chemical molecules onto the material surface to improve the biointeraction for such things as cell adhesion and water absorption [49]. This was reconfirmed by Mao et al. [50] as they carried out in vitro studies on blood compatibility of nylon films that had been radiation grafted with *O*-butyrylchitosan. From this work it was realized that radiation grafting in this manner would give rise to enhanced bioactivity of the nylon films and was a suitable method to tailor custom nylon films for a required biological application. It has also been found that this technique has a major advantage as it is a very clean method [51] and allows for indirect, cost-effective sterilization of those materials that will be required to function within a biological environment [49]. In addition, it has been realized that radiation grafting with a source such as 172 nm UV light can provide a uniform nanoscale layer to be produced on the surface of the material promoting advantages that include durability [52] and improvement of the load bearing components [49]. Radiation grafting can also be used to produce lamination, allowing a high mechanical strength and selective barrier properties to be achieved [53]. Through research also carried out by Ranby et al. [54], they found that the primary reaction mechanism of the photografting arose due to the excitation of the initiator which in their case was benzophenone. Furthermore, they determined that

slow photografting between two LDPE sheets gave rise to both of the sides becoming photografted.

7.3.2 Plasma Surface Modification

Plasma surface modification techniques are dry methods which have been found to possess the ability to vary the surface properties of numerous materials without the bulk properties becoming modified. With regard to plasma surface modification of polymers there are numerous examples of industrial applications such as the automobile, microelectronics, packaging, and biomedical. From the work carried out by Arefi-Khonsari et al. [55] it was found that certain polymers such as OTS-SAM are much more resistant to this technique compared to PE. This is due to the fact that the amorphous structure of polyethylene (PE) allows them to be less resistant than the crystalline structure of the OTS-SAM. It has also been deduced by Milde et al. [56] that ECR plasma treatment of polymer films can give rise to enhanced adhesion behavior for physical vapor deposition (PVD) coatings. The enhancement of adhesion properties of polyimide and FEP using ECR plasma was reconfirmed by Abdul majeed et al. [57] which indicated that the exposure of atomic oxygen ions to the polymeric materials induced significant variations in surface chemistry and topography in order to improve upon the surface wettabilities. Furthermore, it has been seen that extensive research has been carried out on how the hydrophilic and hydrophobic tendencies of numerous polymers can be manipulated using plasma-based technologies [4, 58, 59]. Each of these works have allowed one to see that using plasma-based technologies can extensively manipulate variations in surface morphology in order to be used in certain applications. In addition to this, an important piece of analysis that has arose from such work came from Lai et al. [4] who concluded that the C=O double bond ratio was the most important aspect when considering contact angles and wettability of polymeric surfaces. The technique itself involves the production of a glow discharge plasma which can be created by evacuating a vessel, usually quartz due to it being inert, and then refilling the vessel with a low pressure gas. It is then required that the gas be energized and can be done using various techniques such as microwaves, radiofrequency energy, alternating current, and direct current. This gives rise to energetic species within the gas plasma in which they can take many forms. For instance these energetic species could be ions, electrons, radicals, metastables, and short-wave UV photons [3]. This produces energy transfers to the surface of the material to occur via chemical and physical processes which gives rise to the surface modification. It has been shown that it is possible to utilize these induced surface modifications for numerous biomaterials. Chu [60–62] has undertaken an extensive amount of research into this field and has shown that it is possible to use plasma-based surface modification to enhance the bioactivity of diamond-like carbon (DLC). From research such as this, it is possible to foresee that plasma-based technologies could potentially be used for polymeric biomaterials in order to improve upon their bioactivity for use in biological environments.

7.3.3 Ion and Electron Beam Processing

Ion beam processing techniques are one of the most popular methods of biomaterial surface modification due to the fact that they can be used to produce surface layers incorporating the required modified properties with negligible effects on the bulk properties. Through research it has been found that there are two main types of ion beam processing; these are ion implantation [63] and ion beam-assisted deposition (IBAD) [64]. The ion implantation technique is carried out by injecting accelerated ions with energies ranging between 10^1 and 10^6 eV into the surface of the target material giving rise to alterations in the properties of the surface. It has been seen that this technique gives rise to improvement in hardness (wear), lubricity, toughness, corrosion, conductivity, and bioactivity [64]. This process is highly selective; however, there are high costs involved and the depth in which modification can occur is relatively shallow. One major advantage that this technique possess, as discussed by Lau [65], is that it is possible to surface modify large area materials in relatively quick processing times. With this in mind, it is feasible to realize that using this particular method for processing polymers for enhancing wettability and bioactivity characteristics is attractive to many of those within the industry. As a result, much research has been carried out such as that of Cho et al. [66] who used ion-assisted reactions (IAR) to produce sufficient surface modifications of numerous polymers to increase the hydrophilic tendencies. In addition to this, through the work of Aubry et al. [67] it was determined that by using a focused ion beam (FIB) it was possible to produce effective surface reliefs that could rise to the efficient production of DOEs. This highlights the high selectivity that this method offers as discussed earlier and also indicates that FIB could potentially be used to produce variations in the topography of various polymers in order to modify the wettability and bioactivity characteristics. Leading on from this, it has also been seen through the research of Porte-Durrieu et al. [63] that the utilization of heavy ion grafting can be implemented when producing polymeric biomaterials in the aim to increase the absorption of biological proteins. This in turn would lead to increased bioactivity of the polymeric biomaterials. IBAD is a vacuum deposition process that combines PVD with the bombardment of ions. The main feature incorporated within IBAD processing is that an ion beam is used with energies ranging from several hundred to several thousand eV during the deposition of a coating. IBAD is primarily used in applications such as hydroxyapatite coatings, DLC film, C–N film, and other coatings [64]. In addition to this, another ion beam process is that of ion beam texturing (IBT) in which this method holds the ability to produce micro and macrofeatures on the surfaces of biomaterials to meet requirements set by bioactivity in vivo [64]. It has been realized that it is possible to utilize an electron beam (EB) in the production of biomaterials. Through the work carried out by Iwanaga et al. [68] they found that it was possible to use EB polymerization to graft polyacrylamide onto tissue culture polystyrene (TCPS). Using this technique along with a pre-treatment of UV excimer ablation they found that micropatterned surfaces could be formed which incorporated hydrophilic PAAm and hydrophobic basal polystyrene layers. From the results it was determined that

these modified surfaces allowed for increased cell adhesion and proliferation indicating that this technique could be used to produce cell-based biosensors and tissue engineering devices.

7.3.4 Laser Surface Modification

Another method which has the ability to produce surface modifications is that of laser treatment [69, 70] and offers a number of benefits such as accurate, precise, non-contact, and clean processing. One other major advantage that lasers offer over other competing techniques is that they can produce micro- and nanoscale topographical and surface chemical variations with negligible affect to the bulk properties of the material. Also, it should be noted that as most laser systems are now automated this technique holds the ability to be used for large area processing. Being able to produce these topographical and surface chemical variations can be seen to be of great advantage when applying laser surface modification to fields such as biomimetics especially as previous work has shown a very high dependence of micro- and nanoscale topography and surface chemistry on the cell-material interaction [5–7, 29, 70–72]. On account of the numerous advantages laser materials processing has to offer for laser surface treatment it is necessary that considerable research is undertaken to ascertain how this technique can be employed in such fields as biotechnology. Such research will lead to the ability of assessing the plausibility, reliability, and reproducibility for using lasers to produce surface modifications to aid in the enhancement of the biomimetic nature of biomaterials.

7.3.4.1 Laser-Induced Surface Patterning

It can be seen that surface patterning due to laser irradiation arises from the ability to focus the laser beam onto specific areas of the target material allowing evaporation of the material to take place. With most lasers the smallest possible features that can be achieved are on the micron scale; however, it has been realized that it is possible to achieve nanostructures by using a laser emitting at a wavelength of 157 nm. With the work carried out by Sarantopoulou et al. [73] it was deduced that the mixture of nano- and microstructures present on the polymer surface was due to a localized thermal instability which occurred at the PTFEMA film and gold silicon substrate interface. It was also determined that the thermal instabilities that occur within this process resolves itself resulting in well-ordered structures to be produced on the surface of the polymer. Much of the research that has been carried out in the past few years in the laser patterning of polymers has been done utilizing excimer lasers that operate within the UV spectrum, this is due to the fact UV ablation is very powerful, flexible, and can be used to irradiate a various number of materials. It has been realized that the interaction between UV irradiation and organic polymers gives rise

to ablative photo-decomposition, which ultimately leads to etching of the polymeric surface and an explosive ejection of the ablated products at supersonic velocities. It can then be deduced from workings of those such as Callewaert et al. [74] that this system allows direct writing of the polymer and eradicates the necessity for photo-masks. In addition to this it was shown from the individual workings of Pflöging et al. [75] and Duncan et al. [76] that two- and three-dimensional topographies can be efficiently achieved using excimer lasers. From both workings it was then found that these laser-induced micropatterns had potential applications in cell applications. Alternatively, it is possible to utilize diffractive phase masks to produce the required surface pattern. This method allows fast fabrication of three-dimensional topographies to be achievable and any nonlinearities within the polymer response can be compensated for in the mask design [77]. It has been seen that laser types other than UV excimer lasers can be used to produce microstructure patterns within polymers. For instance, Chan et al. [78] and Tiaw et al. [79] realized that using the fourth and third harmonic of an Nd:YAG laser, respectively, allowed periodic linear and dot patterns to be generated within polymer surfaces without the use of photo-mask or a focusing lens. It has also been indicated by Yu et al. [69, 80] that it is possible to use Nd:YAG lasers to produce linear micropatterns for the manipulation of cell adhesion to polymers by using laser interference lithography (LIL) which employs two or more coherent laser beams to selectively ablate the polymer surface. Furthermore, other laser types such as CO₂ and femtosecond lasers have been employed to produce laser-induced surface patterns. For example, Dadbin [81] showed that it was possible to modify the surface wettability of LDPE film by using a pulsed CO₂ laser, inducing both topography and surface chemistry variations. The research carried out by Aguilar et al. [82] allows one to see that direct micropatterning of biodegradable polymers can be carried out by both excimer and femtosecond lasers indicating that femtosecond lasers give results equivalent to that achieved by the excimer. A number of comparative studies between the different laser types have been undertaken to determine the effects each laser has upon surface patterning. Skordoulis et al. [83] carried out laser ablation using XeCl, CO₂ and Nd:YAG lasers and concluded that it was not recommended to utilize any of the three lasers for ablating nylon 6,6 due to the induced thermal damages that arises from the laser processing. This recommendation is contradicted by Lawrence and Li [2] which carried out research into varying the wettability characteristics of polymethyl methacrylate (PMMA) using CO₂, Nd:YAG, excimer, and high power diode lasers as no thermal damages are mentioned. This indicates that it is possible for one to see that the laser processing of polymers could specifically be material dependent. In addition to this, the process of laser patterning of polymers can be optimized by producing polymers specifically for the task. These optimized polymers are manufactured such that they are more sensitive to the incident laser beam and through the work carried out by Lippert et al. [84] it has been found that the sensitivity was considerably higher in comparison with those equivalent commercially available polymers.

7.3.4.2 Pulsed Laser Deposition of Polymeric Biomaterials

Pulsed laser deposition has now become relatively widely used in order to form thin materials for numerous applications. Many various materials can be used using this method and it has been proven through experimental research that it is possible to use pulsed laser deposition to produce thin films of polymeric materials [85, 86]. Excimer lasers appear to be the most commonly used laser for this technique due to the fact that most materials have strong absorption over the UV spectral range [87]. This is due to the fact that the absorption coefficients tend to increase as shorter wavelengths are used giving rise to corresponding reduced penetration depths. This can be seen as a major benefit toward controlling the system as thinner layers can be ablated along with the fact that ablation thresholds decrease for shorter wavelengths [87]. Furthermore, through the workings of Rebollar et al. [88] it was determined that it is possible to utilize a Ti:Sapphire laser to produce thin films of PMMA doped with fluorescent probes that hold the ability to serve as environmental sensors. With regard to polymers it has been determined that smooth thin films of PMMA can be produced using relatively high fluences [85]; however, it has also been realized that pulsed laser deposition at high fluences can change the chemical structure during the process [85, 86] and could have a detrimental effect to the bioactivity. This has been observed by Cristescu et al. [88] as they compared pulsed laser deposition with matrix-assisted pulsed laser evaporation (MAPLE) and concluded that pulsed laser deposition of pullulan (a polymeric biomaterial) could not be used with this technique as resulting thin films had a different composition. In addition to this, they also concluded that the MAPLE technique was more viable for that specific polymeric biomaterial. From this, pulsed laser deposition does not seem to be the most optimum technique to produce polymeric biomaterials to increase the wettability characteristics resulting in improved bioactivity. However, it may be possible to utilize this technique to change the polymer composition in such a way that would allow for improved bioactivity.

7.3.4.3 Laser Grafting and Laser-Induced Surface Chemistry Modification

It has been realized that the surface chemistry of polymers can be relatively easily modified by laser processing of the surface. Even when processing is carried out in air it has been found that the surface can become oxidized where the surface O₂ content has increased along with the polar component of the surface energy giving rise to improved wettability characteristics [2, 78, 81]. With this increase in O₂ it has been determined that oxidized groups are formed on the surface of the irradiated materials such as through the workings of Mirzadeh and Dadsetan [70] that theorized the drop in contact angle of CO₂ irradiated PET could be attributed to these oxidized groups which arise from chain scission and contact with the ambient air. Following on from this, the research into the debris formation from PET as a result of KrF excimer laser irradiation carried out by Shin et al. [89] allowed them to conclude

that the photochemical bond breaking which leads to carbonization arises from the UV absorption of the benzoate present in the PET. In addition, it has been proven experimentally that laser surface processing with various different ambient gases can be used to modify the surface chemistry of the polymer surfaces to improve the wettability characteristics [75, 81, 90]. For instance Niino et al. [90] allowed PTFE film to be UV laser processed while being present in a pressure chamber filled with hydrazine vapour which allowed the surface chemistry of the film to be modified such that the adhesion for a metal layer was sufficiently increased. Following on, work carried out by Pflöging et al. [75] allows one to see a comparison in the processing of polystyrene surfaces using three different processing gases (air, oxygen, and helium). Furthermore, they were able to draw up a table indicating the best parameters for improving cell adhesion, the hydrophilicity, and the hydrophobicity for polystyrene surfaces. On account of this, the modification of surface chemistry of polymeric biomaterials can be crucial to improving the wettability techniques. Another effective way in which the surface chemistry of a material is improved that of laser-induced grafting which allows additives to be either placed onto the surface or imbedded [91] into the surface prior to laser irradiation. This allows radicals to form giving rise to chemical reactions that allow the surface chemistry to be modified. Charbonnier et al. [92] carried out research into laser grafting nitrogen atoms onto the surface of polycarbonate and showed that UV laser irradiation could efficiently carry out this process. Also, they were able to conclude that increasing the laser fluence allowed for the increase of nitrogen to be grafted onto the polycarbonate surface until a limit was reached, which arose from the equilibrium state between nitrogen grafting and the induced bond breaking. Much research using CO₂ lasers as an excitation source has been carried out by Mirzadeh et al. [92–94] which grafted HEMA, NVP, AAm onto ethylene–propylene rubber (EPR) for use as an enhanced biomaterial. From these workings it was found that the modified EPR produced sufficiently better bioactivity in comparison to unmodified EPR; however, it was also seen that the process of cell spreading was highly dependent on the amount of hydrophilic chains grafted onto the samples [94]. In addition, they carried out *in vivo* studies to AAm- and HEMA-grafted EPR which showed that CO₂ laser irradiation could be utilized to improve upon the bioactivity of EPR [93].

7.4 Experimental Technique

7.4.1 Laser Irradiation Procedure

The nylon 6,6 was sourced in 100 × 100 mm² sheets with a thickness of 5 mm (Goodfellow Cambridge, Ltd). To obtain a conveniently sized sample for experimentation the as-received (AR) nylon sheet was cut into 30mm diameter disks using a 1 kW continuous wave (CW) CO₂ laser (Everlase S48; Coherent, Ltd). No discernible

heat affected zone (HAZ) was observed under optical microscopic examination. In order to generate the required marking pattern with the 10.6 μm Synrad CW 10W CO_2 laser system Synrad Winmark software version 2.1.0, build 3468 was used. In addition, the software was capable of using images saved as .dxf files which can be produced by using CAD programs such as, in this case, Licom AutoCaM. The nylon 6,6 samples were placed into the laser system onto a stage in which they were held in place using a bracket with a 30.5 mm diameter hole cut into the center of the bracket. The surface of the sample was set to be 250 mm away from the output facet of the laser system to obtain focus and the system utilized a galvanometer scanner to scan the 95 μm spot size beam directly across the stationary target material. It should be noted that the target material and laser system was held in a laser safety cabinet in which the ambient gas was air and an extraction system was used to remove any fumes produced during laser processing. Twenty samples were irradiated altogether to produce four identical six-well plates with each corresponding well having the same pattern. These were named plates 1A, 1, 2, and 3. There were four patterns induced onto the surfaces of the nylon 6,6 samples which were trenches with 50 μm spacing (T50), hatch with 50 μm spacing (H50), trenches with 100 μm spacing (T100) and hatch with 100 μm spacing (H100). In addition, an AR control sample was used. For each of the irradiated patterns the laser power was set to 70% (7 W) operating at 600 mms^{-1} .

7.4.2 Topography, Wettability Characteristics, and Surface Chemistry Analysis

After the laser irradiation of the nylon 6,6 samples plate 1A was analyzed using a number of techniques. An optical microscope (Flash 200 Smartscope; OGP, Ltd) was used to obtain optical micrographs of the samples. The surface profiles were determined using a white light interferometer (WLI) (NewView 500; Zygo, Ltd) with MetroPro and TalyMap Gold Software. The Zygo WLI was setup using a $\times 10$ Mirau lens with a zoom of $\times 0.5$ and working distance of 7.6 mm. This system also allowed S_a and R_a roughness parameters to be determined for each sample. In accordance with the procedure detailed by Rance [95] the samples were ultrasonically cleaned in isopropanol (Fisher Scientific, Ltd.) for 3 min at room temperature before using a sessile drop device to determine various wettability characteristics. This was to allow for a relatively clean surface prior to any contact angle measurements being taken. To ensure that the sample surfaces were dry, a specimen dryer (Metaserv, Ltd.) was utilized to blow ambient air across the samples. A sessile drop device (OCA20; Dataphysics Instruments, GmbH) was used with relevant software (SCA20; Dataphysics Instruments, GmbH) to allow the recent advancing contact angles for triply distilled water and the recent advancing angle for diodomethane to be determined for each sample. Thereafter, the advancing contact angles for the two liquids were

used by the software to draw an Owens, Wendt, Rabel, and Kaeble (OWRK) plot to determine the surface energy of the samples. For the two reference liquids the SCA20 software used the Ström et al. technique to calculate the surface energy of the material. It should be noted here that 10 contact angles, using 2 droplets, in each instance was recorded to achieve a mean contact angle for each liquid and surface. Selected samples were analyzed using XPS analysis. This allowed any surface modifications in terms of surface oxygen content due to the laser irradiation to be revealed. These samples were selected in terms of contact angle; the AR reference sample, laser patterned sample with the lowest contact angle, and the laser surface patterned sample with the highest contact angle was used. XPS measurements were performed on a Kratos Axis Ultra DLD photoelectron spectrometer employing monochromatic aluminum k-alpha radiation source, operating at 120 W power and associated photon energy of 1,486.6 eV. To test the reproducibility of the surface, two sections of each sample were analyzed; the analysis area on each sample was 700×300 microns. The spectrometer was run in its Hybrid mode and spectra were acquired at pass energies of 20 eV (for the high resolution scans) and 160 eV for the survey scans. All data were analyzed through CasaXPS (v2.3.14) analysis software (ref: <http://www.casaxps.com>) using sensitivity factors supplied by the instrument manufacturer.

7.4.3 In Vitro Experimentation

7.4.3.1 In Vitro Simulated Body Fluid Soaking Experimentation

SBF is a liquid which has inorganic ion concentrations equivalent to those of human extracellular fluid (human blood plasma). SBF can be utilized to evaluate the formation of apatite on bioactive materials in vitro. SBF is a metastable solution containing calcium and phosphate ions already supersaturated with respect to the apatite. The SBF was prepared by using a magnetic stirrer hotplate (RCT Basic; IKA, GmbH) keeping the solution at a constant temperature of 36.5°C. 500 ml of distilled water was put into an autoclaved 1,000 ml beaker and stirred until the constant temperature of 36.5°C was reached. At this time the chemicals given in Table 7.2 were added in order until the sodium sulfate (#9) had been added. Once the sodium sulfate (#9 in Table 7.2) had been added the Tris(hydroxymethyl) aminomethane (#10 in Table 7.2) was supplemented into the solution less than a gram at a time in order to avoid local increase of pH. Finally, in order to adjust the pH value to 7.4 hydrogen chloride (#11 in Table 7.2) was added and the beaker was then filled to 1,000 ml using distilled water.

Prior to using the SBF all of the samples and apparatus to be used were autoclaved if not already sourced in sterile packaging. The five samples were then placed into

Table 7.2 Amounts and order of reagents to prepare 1,000 ml SBF

Order	Reagent	Amount 1,000 ml
1	Distilled water	750 ml
2	Sodium chloride (NaCl)	7.996 g
3	Sodium bicarbonate (NaHCO ₃)	0.350 g
4	Potassium chloride (KCl)	0.224 g
5	Potassium phosphate dibasic (K ₂ HPO ₄ · 3H ₂ O)	0.228 g
6	Magnesium chloride hexahydrate (MgCl ₂ · 6H ₂ O)	0.305 g
7	Hydrogen chloride (~ 0.1 M in H ₂ O) (HCl)	40 ml
8	Calcium chloride (CaCl ₂)	0.278 g
9	Sodium sulphate (Na ₂ SO ₄)	0.071 g
10	Tris(hydroxymethyl)aminomethane (CH ₂ OH) ₃ CNH ₂	6.057 g
11	Hydrogen Chloride (~ 0.1 M in H ₂ O) (HCl)	Adjustment of pH

sterile 30 ml glass containers, immersed in 30 ml of SBF, and placed into an incubator to keep the temperature constant at 37°C for 7 days.

7.4.3.2 Cell Adhesion Experimentation

Prior to any biological testing being carried out the samples were autoclaved (D-Series Bench-Top Autoclave; Systec, GmbH) to ensure that all samples were sterilized. For all biological work undertaken, unless stated, a biological safety cabinet (BSC) (Microflow Class II ABS Cabinet; BioQuell UK, Ltd) was used to create a safe working environment and to provide a clean, sterile environment to manipulate the cells used. Normal human osteoblast cells (Clonetics CC-2538; Lonza, Inc.) were initially cultured in a T75 (75 ml) flask by suspending the cells in 19 ml culture medium comprising of 90% eagle minimum essential medium (Sigma-Aldrich, UK) and 10% fetal bovine serum (FBS) (Sigma-Aldrich, Co. LLC.). The flask was then placed in an incubator and left for 24 h. After 24 h the cells were assessed and the spent media was aspirated before dispensing 15 ml of fresh media and returning the flask to the incubator for 3 days. The period of 3 days allowed the cells to become confluent in the flask providing enough cells for seeding onto the samples. The cells were detached from the flask using 5 ml Trypsin-EDTA (Sigma-Aldrich, Co. LLC.) while placed in the incubator for 7 min. Once all cells had become detached 10 ml culture medium was added to neutralize the Trypsin. In order to aspirate the supernatant the cell culture was centrifuged (U-320R; Boeco, GmbH) for 5 min at 200 g. To ensure the cells were ready for seeding they were resuspended in 10 ml of culture medium and dispensed between the 18 samples in the six-well plates. This equated to 0.55 ml (2×10^4 cells/ml) for each sample. The well plates were placed in the incubator and plate 1 was removed after 24 h and plates 2 and 3 after 4 days. Plates 1 and 2 were prepared for the scanning electron microscopy (SEM) as will be discussed

later and plate 3 was prepared for counting using an improved Neubauer hemocytometer (Fisher Scientific, Ltd.) by mixing 10 μ l of each cell suspension with 10 μ l of trypan-blue (Sigma-Aldrich, Co. LLC.).

7.4.4 SEM and Optical Microscopy Analysis of In Vitro Samples

7.4.4.1 Cell Adhesion Analysis

In order to view the attached cells using SEM it was necessary to undertake a procedure to produce a sample that was dehydrated ready for Au coating. The samples were initially rinsed with phosphate-buffered saline (PBS) (Sigma-Aldrich, Co. LLC.) to remove any unattached cells and then adherent cells were fixed using 1.2% glutaraldehyde in water (Sigma-Aldrich, Co. LLC.) at room temperature for 1 h within the BSC. After an hour the glutaraldehyde solution was removed and the fixed cells were washed with PBS prior to carrying out a graded series of ethanol/distilled water mixtures of 50/50, 80/20, 90/10, 95/5, 98/2, and 100/0. Each sample was left in these mixtures for 10 min to ensure dehydration. Once this procedure was carried out the samples were mounted and sputter coated with Au so that SEM images could be obtained. In addition to SEM images, optical micrographs were obtained using an optical microscope (Optiphot; Nikon, Ltd.) with a 5 \times Nikon objective lens, with images being captured using a microscope camera (WV-CL300; Panasonic, Ltd.) along with DT Acquire Version 3.3.0 computer software (Data Translation, Inc.).

7.4.4.2 SBF Analysis

Prior to being immersed in the SBF the five nylon 6,6 samples were weighed using a balance (S-403; Denver Instrument, GmbH) with a readability of 0.001 g. Once the 14 days had elapsed the samples were removed from the SBF, rinsed lightly with distilled water, and allowed to air dry in a clean room. Once fully dry the samples were weighed and the difference in weight before and after being immersed in the SBF was determined. Following this the samples were gold coated and analyzed using optical microscopy and SEM. Furthermore, the samples were analyzed using EDX in order to identify elements present after the immersion in SBF.

7.4.5 Statistical Analysis

All statistical analysis was carried out using SPSS 16.0.2 for Windows software (SPSS, Inc.) in order to analyze the data obtained using one-way ANOVA to obtain F-ratios and significance levels (p). In addition to ANOVA post hoc multiple comparison tests (Scheffe's range tests) were performed to determine statistical significance.

between groups and results are reported at a mean difference significance level of $p < 0.05$.

7.5 Effect of Laser Patterning on Topography

It has already been confirmed from previous work that the process in which the infrared laser light couples into the nylon 6,6 is that of a thermolytical nature rather than direct bond disassociation which occurs with UV lasers [96]. By utilizing the constant laser parameters of 7 W and a traverse speed of 600 mms^{-1} various patterns were induced onto the surface of the nylon 6,6. The continuous axonometric images for these patterns are shown in Fig. 7.3. It can be seen from Fig. 7.3 that qualitatively the laser-irradiated nylon 6,6 samples were considerably rougher in comparison to the AR reference control sample. Further confirmation of this qualitative result was obtained by taking a profile extraction of each sample (see Fig. 7.4). From Fig. 7.3d and e it was possible to ascertain that the resulting surface pattern was more defined in one axis of the hatch in comparison to the other. This is a resultant of the way in which the CO₂ laser marker scanned the input image onto the target sample. The profile extractions for each of the samples shown in Fig. 7.4 provides confirmation that the laser processing of the nylon 6,6 gave rise to a considerable variation in the surface topography. That is, the roughness had increased and slight periodicity in the laser patterned samples can be seen in contrast to the AR reference control sample. In comparison to the AR reference control sample, which had peak heights of the order of $0.1\text{--}0.2 \mu\text{m}$, the peak heights for all of the laser-treated samples were around $1 \mu\text{m}$. It was also observed that the least periodicity arose from those samples which had patterns with $50 \mu\text{m}$ spacings (T50 and H50). This can be seen to be of some importance as the laser spot size at the surface of the target samples was $95 \mu\text{m}$ consequently allowing the scans for the trenches and hatch patterns to overlap and ultimately eliminate the natural periodicity of the original scanned pattern. However, the scan overlap occurring did ensure that the whole of the surface of the target sample was irradiated and modified in comparison to the non-irradiated reference sample. For the laser surface modified samples (see Fig. 7.4b–g) peak heights of approximately $1 \mu\text{m}$ was achieved.

7.6 Effect of Laser Irradiation on the Wettability Characteristics

As already stated in the available literature, the surface properties of a material have a major influence on the way in which a liquid will react at the interface between the liquid and material surface. As such, the surface roughness parameters (S_a and R_a),

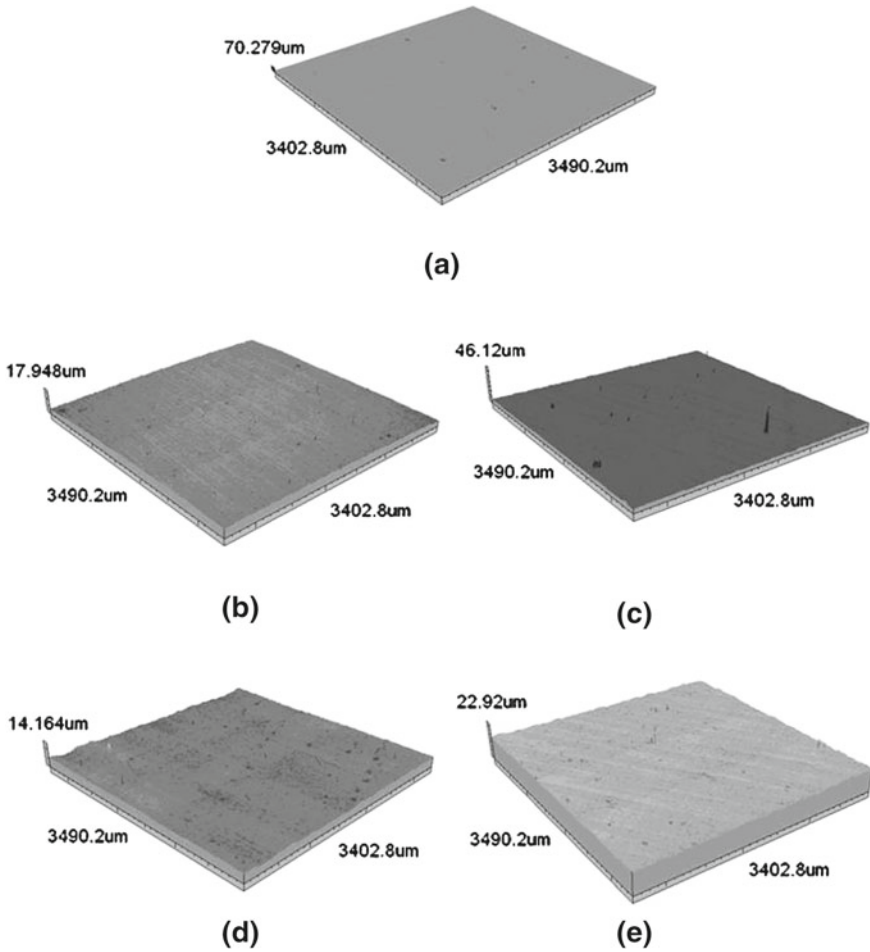
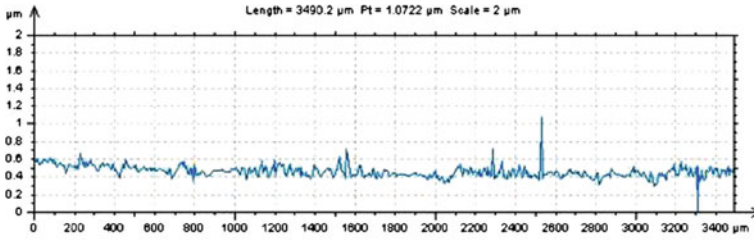


Fig. 7.3 Continuous axonometric images for each of the nylon 6,6 samples (a) as-received control sample—AR, (b) 50 μm trenches—T50, (c) 100 μm trenches—T100, (d) 50 μm hatch—H50 and (e) 100 μm hatch—H100

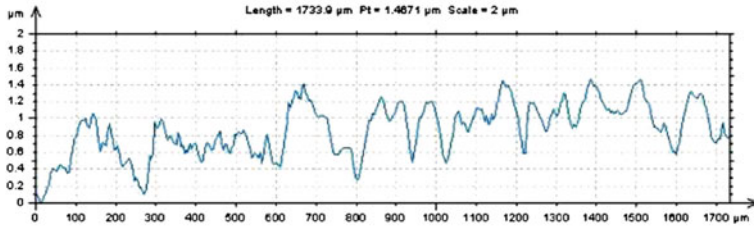
contact angle for triply distilled water and surface energy parameters were determined for each sample and are given in Table 7.3.

Table 7.3 Results for the surface roughness, contact angle and surface energy parameters for each sample

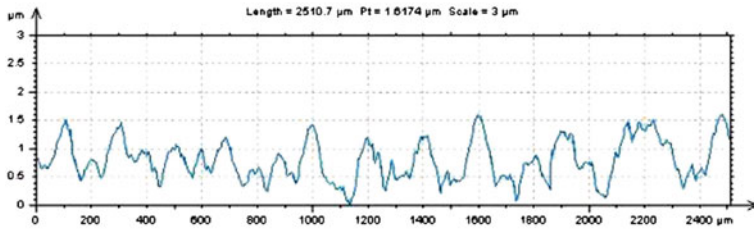
Pattern shape	Pattern label	Sa (μm)	Ra (μm)	Polar component, γ^P (mJm^{-2})	Dispersive Component, γ^D (mJm^{-2})	Total surface energy, γ^T (mJm^{-2})	Contact angle ($^\circ$)
As-received sample	AR	0.126	0.029	17.69	29.66	47.34	56.4 ± 1.2
50 μm trenches	T50	0.636	0.148	12.24	28.63	40.87	66.0 ± 4.0
100 μm trenches	T100	0.297	0.185	16.86	29.83	46.69	57.5 ± 2.4
50 μm hatch	H50	0.423	0.103	10.93	31.64	42.58	65.8 ± 2.9
100 μm hatch	H100	0.326	0.155	13.63	30.37	44.00	62.2 ± 2.3



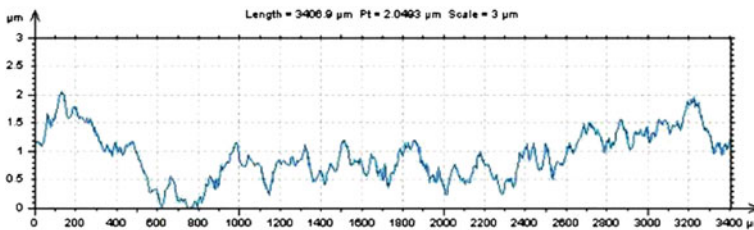
(a)



(b)



(c)



(d)

Fig.7.4 Continued

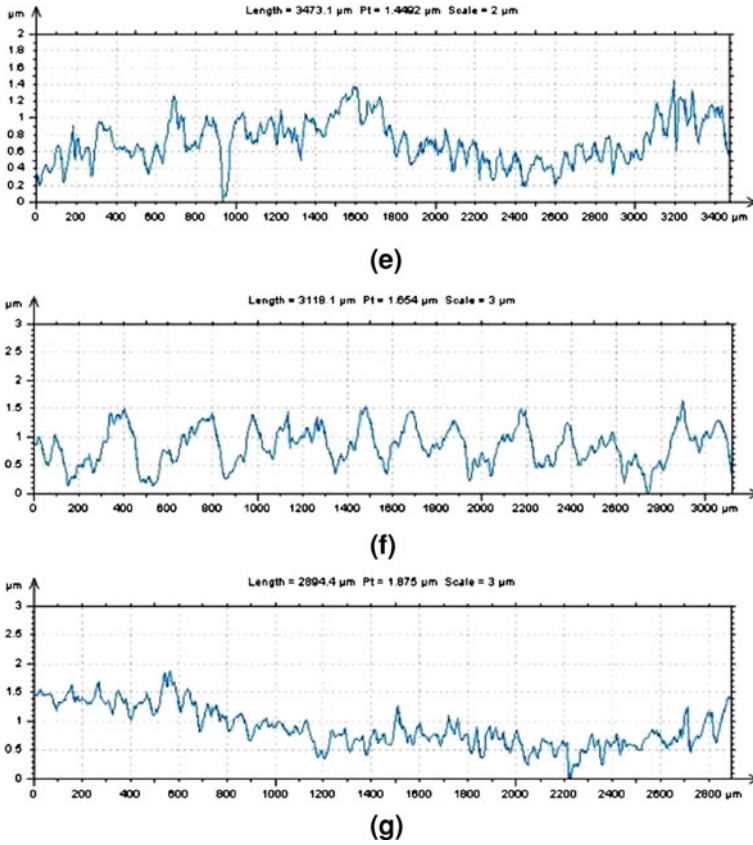


Fig. 7.4 Profile extraction for nylon 6,6 samples (a) as-received control sample—AR, (b) 50 μm trenches—T50, (c) 100 μm trenches—T100, (d) 50 μm hatch x-axis—H50, (e) 50 μm hatch y-axis—H50, (f) 100 μm hatch x-axis—H100 and (g) 100 μm trenches y-axis—H100

The results given in Table 7.3 show that the laser surface treatment had given rise to sufficiently increased surface roughness in comparison to the AR sample with the largest Sa being 0.636 for the 50 μm trenches pattern (T50) and the largest Ra being 0.185 μm for the 100 μm trenches pattern (T100). It was also determined that the apparent polar component, γ^P , and total surface energy, γ^T , was seen to decrease for all laser-treated samples compared to that of the AR reference control sample. As a result of the reduction in apparent γ^P and the increase in surface roughness the recently advancing contact angle was seen to increase. As a direct result of this the resulting characteristic contact angle for the rougher samples increases; for instance, the 50 μm trench pattern (T50), with the maximum Sa of 0.636 μm and lowest γ^P of 12.24 mJm⁻² gives the largest contact angle of 66.0°. Current theory states that for a flat hydrophilic surface an increase in roughness ought to result in the contact angle effectively decreasing ; however, as one can see from

Table 7.3 this is not the case in this work for the hydrophilic nylon with contact angles with the reference contact angle being 56.4° (AR). This can be explained by the likely existence of a mixed Cassie-Baxter/Wenzel state wetting regime, in which both Wenzel and Cassie-Baxter regimes are present over the solid-liquid interface [41, 98–100]. That is, the surface roughness along with the induced pattern yields a water droplet which is held in an intermediate state such that both wetting regimes coexist. This mixed wetting regime arising can also account for the observed reduction in apparent γ^P and increase in contact angle owed to the laser-induced topographical pattern on the hydrophilic nylon 6,6 samples. Another factor which can be taken from Table 7.3 is that the hatch patterns (H50 and H100) gave rise to smoother surfaces in comparison to the trench patterns (T50 and T100). The reasoning behind this result is believed to be on account of the beam overlapping the same irradiated area numerous times during laser processing. This allowed the material to remelt, causing the resolidified material to become smoother as the sample surface cools. It should be noted here that the laser-irradiated surfaces have higher errors for the contact angle measurement owing to the fact that surface topography would have affected how the liquid formed an equilibrium state on the material surface. To analyze the extent of the polar component/surface energy and surface roughness being a driving force on the contact angles, graphs of contact angle as a function of polar component/surface energy (see Fig. 7.5) and Sa/Ra (see Fig. 7.6) were drawn. One can see from Fig. 7.5 that the contact angle appears to have good correlation in conjunction to the two apparent surface energy components such that the recently advancing contact angle is a decreasing function of the apparent γ^P and γ^T . This coincides with current theory which states that the contact angle will decrease upon an apparent increase of the surface energy components that have been graphed in Fig. 7.5 [2]. From this result one can extrapolate that the resulting contact angle for the laser surface treated nylon 6,6 is highly dependent on the apparent γ^T and γ^P and by knowing how laser treatment affects the surface energy of a polymeric material this could allow for a predetermined contact angle to be achieved. In a similar manner, a graph of contact angle against the surface roughness parameters Sa and Ra was drawn, as seen in Fig. 7.6, to ascertain if any correlation could be highlighted.

Due to the surface topography having a large effect on the wetting regime taking place it was necessary to analyze how the recently advancing contact angle varied over the different induced surface roughness values. Figure 7.6 shows that there is a significant difference between how the surface roughness parameters, Ra and Sa, relate to the recently advancing contact angle for triply distilled water incident on the laser surface treated nylon 6,6 samples. The data given in Fig. 7.6 allow one to see that the roughness parameter Ra has a Gaussian fit with the contact angle measured giving a peak contact angle of around 65° to be obtained with Ra value of around $0.1 \mu\text{m}$.

In contrast the Sa parameter gives a considerably different correlation such that contact angle remains constant around 56° for Sa values up to $0.3 \mu\text{m}$ at which point the angle begins to increase until it finally plateaus from Sa values of $0.4 \mu\text{m}$ and more with contact angles of approximately 65° . This shows that there could be some dependence on the two surface roughness parameters in determining the

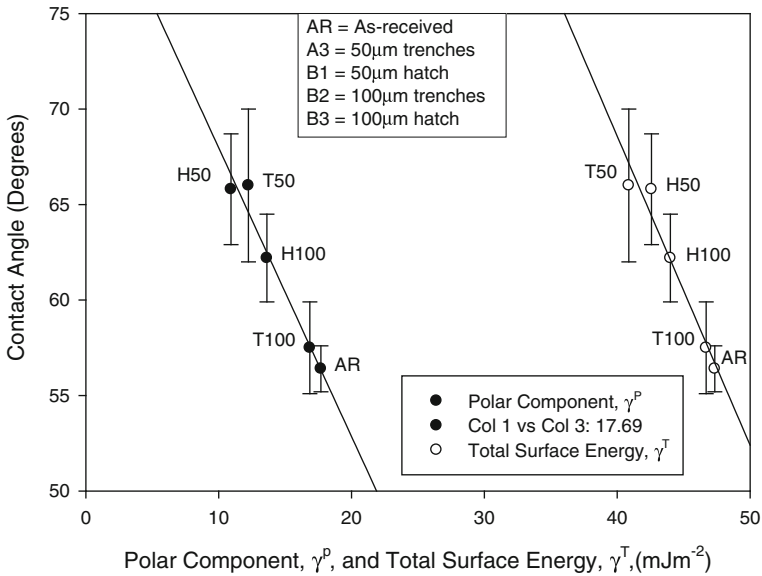


Fig. 7.5 Characteristic recently advancing contact angle for triply distilled water as a function of polar component, γ^P , and total surface energy, γ^T (ANOVA showed an overall significance with $F=4.652$ and $p=0.004$, Scheffe's range test found that there was statistical difference between the H50, T50 and AR, whereas there was no statistical difference between the H100, T100 and AR* $p < 0.05$)

contact angle; however, the resulting correlation does not appear to be as strong as shown with the surface energy components as seen in Fig. 7.5. Another factor that should be considered in this instance is that the data given in Fig. 7.6 does not necessarily coincide with current theory which states that for a hydrophilic material an increase in roughness should reduce the contact angle making the material more hydrophilic [2]. For both Ra and Sa parameters the contact angle increases from the initial contact angle obtained with the non-irradiated reference sample which, as stated previously, is attributed to the mixed state wetting regime taking place due to the topography of the laser surface treated samples. Having said that, it was observed using Fig. 7.6 that the contact angle did decrease for larger Ra values arising from the laser patterned samples which does coincide with current theory which states that, under certain conditions, the contact angle is a decreasing function of surface roughness [101]. Nevertheless, it may still be possible to estimate the contact angle to be achieved by using the correlations that have been identified throughout this research. Following on from this, with the aid of being able to estimate the contact angle this could feasibly help to produce surfaces that give rise to enhanced cell adhesion and proliferation if the optimized contact angle or contact angle range was known for the cell type that would be coming into contact with that specific material. In addition to surface energy and surface roughness the surface oxygen content of a material may have an affect on the resulting contact angle and following on from this

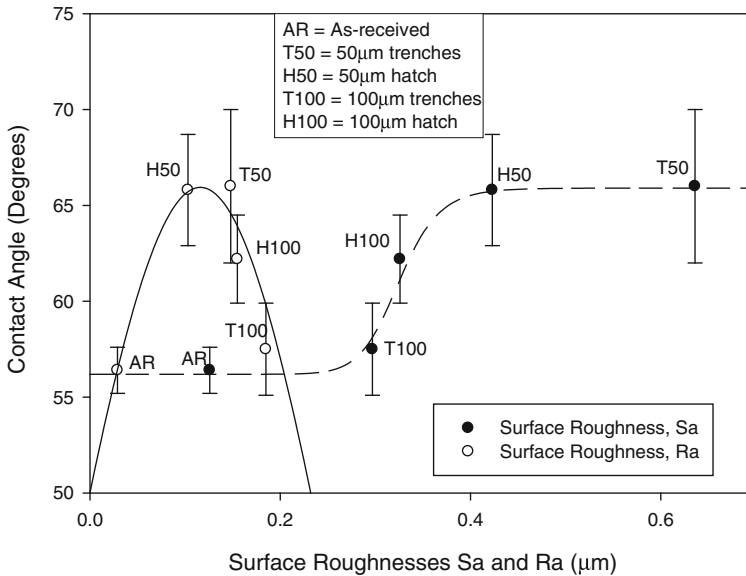


Fig. 7.6 Characteristic recently advancing contact angle for triply distilled water as a function of the surface roughness parameters Sa and Ra (ANOVA showed an overall significance with $F=4.652$ and $p=0.004$, Scheffe's range test found that there was statistical difference between the H50, T50 and AR, whereas there was no statistical difference between H100, T100 and AR* $p < 0.05$)

the surface oxygen content for selected samples were chosen; these samples were the AR sample, 100 μm trenches (T100), and 50 μm trenches (T50). These samples were chosen as they were the limits in terms of the recently advancing contact angles measured. On account of this the data given in Table 7.4 indicate that the surface oxygen content may not be one of the main factors that gives rise to the apparent increase in advancing contact angle as a rise in oxygen content should bring about a reduction in the contact angle as stated by Hao and Lawrence [3]. The slight rise in oxygen content can be attributed to oxidation of the nylon 6,6 surface during laser surface treatment as the experiments were carried out in ambient air. From the results shown in both Tables 7.3 and 7.4 it is evident that the contact angle can predominantly be a result of the reduction in the apparent γ^P on account of the mixed state wetting regime taking place owed to the surface topography. With this in mind it can be seen that the surface topography in terms of roughness and pattern can have a large effect on the extent of which wetting regime occurs and directly affects the value of the apparent γ^P and γ^T . Therefore, the polar component along with the surface roughness/topography can be seen to be the main driving force to defining the characteristic contact angle as they both are closely linked to one another in this instance.

Table 7.4 Results showing the surface oxygen content for selected samples

Pattern shape	Surface oxygen content (% At.)	Polar component, γ^P (mJm ⁻²)	Contact angle (°)
As-received reference control sample (AR)	13.26	17.69	56.4 ± 1.2
100 μ m trenches (T100)	14.05	13.62	57.5 ± 2.4
50 μ m trenches (T50)	14.33	12.24	66.0 ± 4.0

7.7 Effect of Laser Patterning on Osteoblast Cell Bioactivity and SBF Response

7.7.1 SBF Response to Laser Patterning

In order to determine how bioactive each of the samples was after the laser patterning procedure the samples were immersed in SBF for a period of 14 days. After leaving to dry in ambient air the samples were analyzed using SEM, the images of which can be seen in Fig. 7.7. From these images it was observed that only a very small amount of sediment was present on the AR sample (see Fig. 7.7a) in comparison to the other samples which had undergone CO₂ laser patterning (see Fig. 7.7b–e).

This was also confirmed by weighing the samples before and after the immersion in SBF as can be seen in Fig. 7.8. That is, the laser patterned samples weighed at least 0.008 g more than compared to the AR sample. Through SPSS statistical analysis it was found that this was statistically significant even though the only statistical difference between the laser patterned samples was found to be between T100 and H100. This is owed to the fact that all of the patterned samples gave rise to similar results in terms of increase in weight in comparison to the AR sample. Following on, it can be extrapolated from this that through CO₂ laser patterning of nylon 6,6 the ability to promote the formation of an apatite layer can be sufficiently improved.

For further confirmation of this EDX was carried out for all samples to determine the elements present on the surface of the nylon 6,6 after the 14 day immersion in SBF. Figure 7.9 shows the surface elemental data for the studied samples and indicates that following the formation of the apatite crystals phosphorous and calcium was present on the surface of the nylon 6,6 samples. This is of importance due to phosphorous and calcium having to be present in order for an apatite to form which would inherently increase the bioactivity of the material. The sediments analyzed also incorporated sodium, magnesium, and chlorine which had all been present in the SBF and indicates that these elements would also make up some of the apatite layer formed. Consequently, this adds to the hypothesis of an enhanced osteoblast cell response on account of the laser surface patterning owed to more apatite forming on the laser patterned surfaces incorporating calcium and phosphorous.

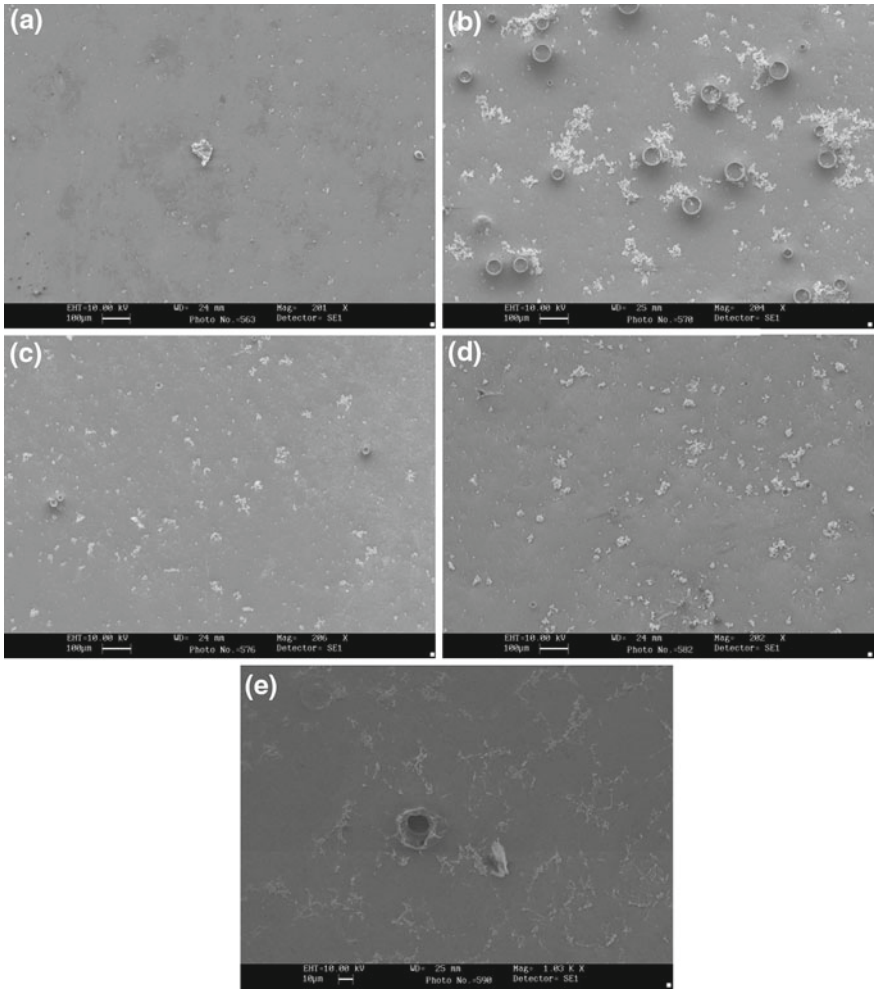


Fig. 7.7 SEM images of (a) as-received (AR), (b) 50 μm trench (T50), (c) 100 μm trench (T100), (d) 50 μm hatch (H50) and (e) 100 μm hatch (H100) after immersion of SBF for 14 days

7.7.2 Osteoblast Cell Bioactivity: 24h After Seeding

It has been seen that the laser material interaction has given rise to a sufficient modification in terms of numerous surface properties and as such it has had a positive impact on the formation of apatite on samples immersed in SBF. As a consequence of this one can deduce that this could have a large impact upon how the osteoblast cells react to the nylon 6,6 samples. Figure 7.10 shows the optical micrographs for the six Au-coated samples 24h after cell seeding.

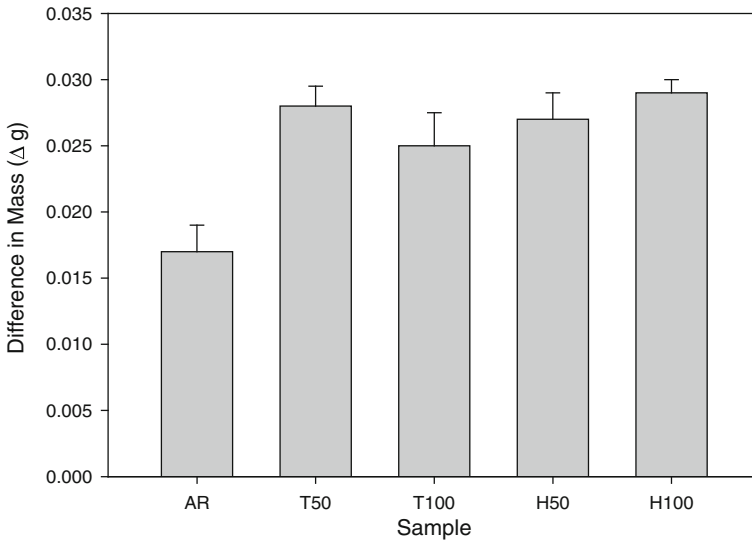


Fig. 7.8 Difference in mass before and after immersion in SBF for all samples (ANOVA showed an overall significance with $F=69.6$ and $p=0.000$. Scheffé's range test showed that there was statistical difference between AR and all other samples. No statistical difference was found between the laser patterned samples—T50, T100—H100, apart from between T100 and H100* $p < 0.5$)

It can be seen in Fig. 7.10 that for all samples the osteoblast cells have some extent adhered to the differing surfaces. That is, the cells have first attached, adhered, and have begun to spread across the surfaces. The extent to which this phenomenon has taken place appears to be dependent on the laser processing owed to the larger areas of cell coverage after 24 h of incubation time. For the trench and hatch patterns the cells have somewhat proliferated resulting in the larger cover densities with the largest cell cover density being 37% for the 100 μm trench pattern which was considerably larger in comparison to the AR reference control sample which gave rise to a mean cover density of 17%. It should also be noted here that from the micrographs shown in Fig. 7.5 the laser-treated samples did not appear to give rise to directionality in terms of cell growth and proliferation. In fact the cells seem to be growing in random directions in conjunction with the laser-induced patterns. Additionally, in terms of morphology of the cells the micrographs in Fig. 7.10 show that most of the samples gave rise to bipolar shapes, apart from the 100 μm trench pattern (T100) which was at a more advanced stage of the cell growth process. This could indicate that the growth process on the nylon 6,6 samples begins with a bipolar morphology and progresses to a more radial morphology as the incubated time progresses. To confirm what had been observed in the micrographs shown in Fig. 7.10 the samples were analyzed using SEM. The SEM images of each sample are shown in Fig. 7.11. The SEM images obtained in Fig. 7.11 allowed one to confirm that the osteoblast cells were already at an advanced stage in terms of cell growth on the nylon 6, 6 samples. This is owing to the cells beginning to spread over the sample surfaces. Also, both

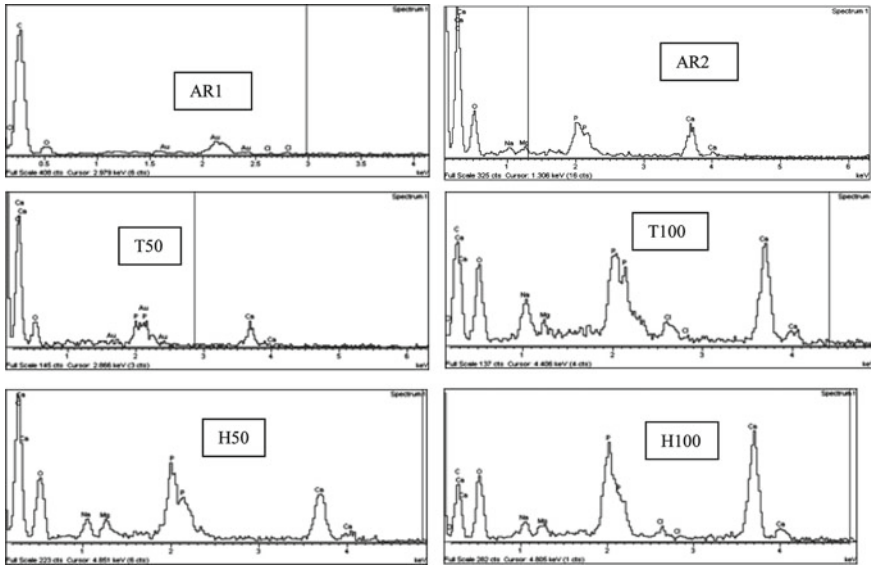


Fig. 7.9 EDX elemental analysis for (AR1) As-received before immersion in SBF, (AR2) As-received sample, (T50) 50 μm trench, (T100) 100 μm trench, (H50) 50 μm hatch and (H100) 100 μm hatch samples after 14 day immersion in SBF.

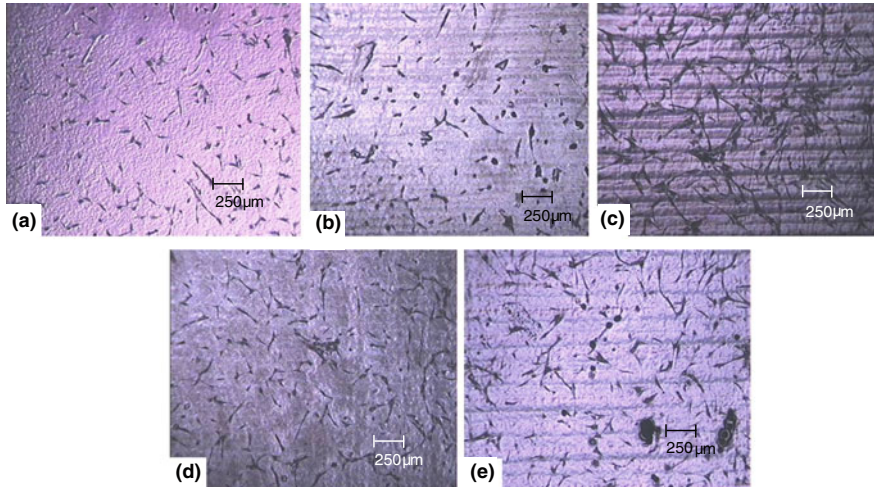


Fig. 7.10 Optical micrographs of Au coated samples 24h post seeding (a) as-received control sample—AR, (b) 50 μm trenches—T50, (c) 100 μm trenches—T100, (d) 50 μm hatch—H50 and (e) 100 μm hatch—H100

the micrographs and SEM images show that for all samples a number of cells had spread completely, forming numerous filopodia. In contrast to the micrographs in

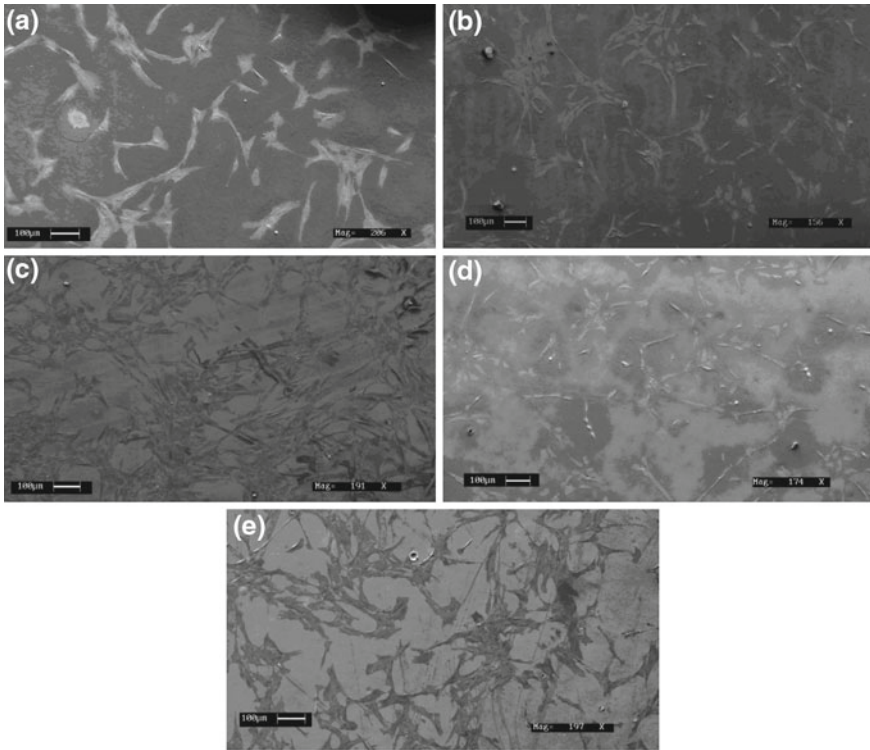


Fig. 7.11 Scanning electron micrographs of Au coated samples 24h post seeding (a) as-received control sample—AR, (b) 50 μm trenches—T50, (c) 100 μm trenches—T100, (d) 50 μm hatch—H50 and (e) 100 μm hatch—H100

Figs. 7.10, 7.11b and c indicate that there may possibly be some directionality to the cell growth which is dependent on the surface topography; however, this is not conclusive and the nondirectionality may well be a result of the relatively shallow peak heights forming the patterns which was determined in the profile extractions (see Fig. 7.4) during the topography analysis. From Figs. 7.10 and 7.11 it can be seen that the morphologies of the cells on each of the different samples are similar to one another which could indicate that the cells reacted in the same manner for each sample.

However, it could have also potentially taken more than 24h to affect the morphology of the cells and was considered when analyzing the samples after the 4-day incubation period which will be discussed later. In addition, the SEM images shown in Fig. 7.11 show that in some cases a bipolar morphology arises; however, the radial nature of the cell growth becomes more apparent on each of the samples when comparing the images in Fig. 7.11 to those in Fig. 7.10. This result is also an indicator to the fact that the cells in this instance do not have directionality owed to the laser-induced surface pattern. In order to quantify how the osteoblast cells reacted to the

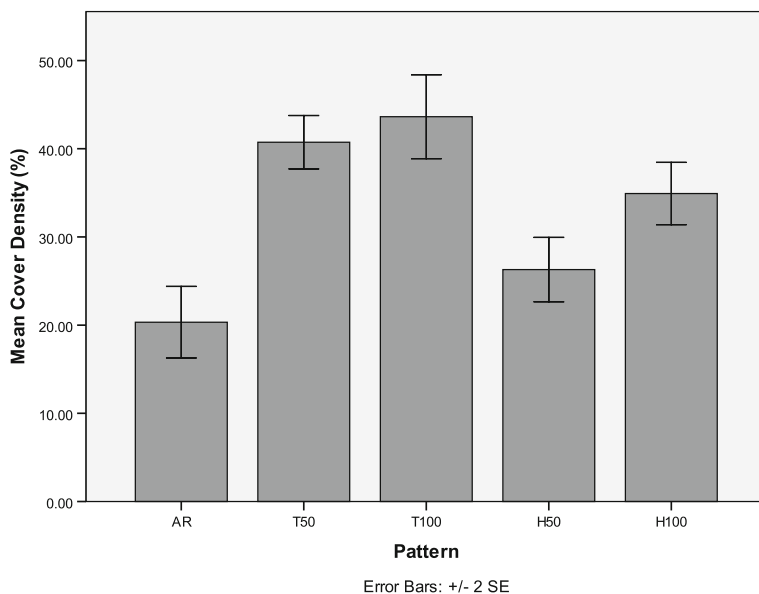


Fig. 7.12 Histogram showing the cover densities for each of the seeded nylon 6,6 samples after 24 h (ANOVA showed an overall significance with $F=6.192$ and $p=0.005$. Scheffe's range test showed that there was significant statistical difference between samples AR, T100 and H100 and no statistical significance between any of the other samples* $p < 0.05$)

different surface topographies the cell cover density was measured for each of the samples. A histogram showing the cover densities can be seen in Fig. 7.12. In order to determine a mean value for the cover density four values were obtained from micrograph and SEM images.

The histogram given in Fig. 7.12 shows that the mean cover density after 24 h was larger for all laser-irradiated samples in comparison with the AR reference control sample. The largest mean cover density of 38% was achieved with the 100 μm trenches pattern, while the lowest was 17% for the AR reference control sample. The 50 and 100 μm hatch patterned samples gave the lowest cover densities of 23 and 34%, respectively in comparison to the other laser patterned surfaces and can be owed to the roughness of these samples being less than the trench patterned samples. As a direct result of the mean cover density results shown in Fig. 7.12 one can deduce that the laser surface modification implemented gave rise to an increase in proliferation, speeding up the cell growth process as a result of allowing the material to become more biomimetic by changing the surface characteristics.

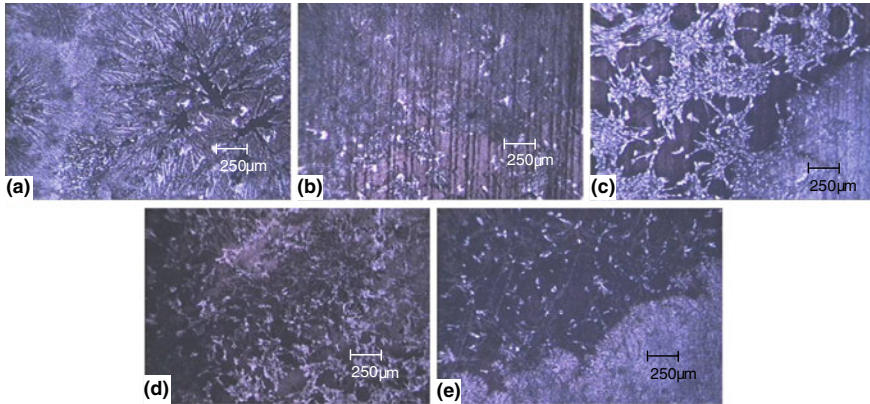


Fig. 7.13 Optical micrographs of Au coated samples after 4 days incubation (a) as-received control sample—AR, (b) 50 μm trench—T50, (c) 100 μm trench—T100, (d) 50 μm hatch—H50 and (e) 100 μm hatch—H100

7.7.3 Osteoblast Cell Bioactivity: 4 Days After Seeding

With the 24-h experiments showing that the cells had attached and begun to spread it was necessary to carry out analysis on the nylon 6,6 samples which had been seeded and incubated for 4 days to ensure that the cells were still adhered to the samples and that the spreading was still taking place. Figure 7.13 shows the optical micrographs obtained for each of the samples. As one can see from Fig. 7.13, after 4 days of incubation the cells were at an advanced stage of growth in comparison to the samples that had been incubated for 24 h. This is due to the fact that all of the images in Fig. 7.13 show that the cells have covered almost all of the surfaces of each sample with the least covered being the AR reference control sample. This coincides with what was observed previously with the 24 h incubated samples as the AR reference control sample gave the least cover density in both instances. In addition it was also realized that the morphology of the osteoblast cells were very different when comparing each sample which had been left incubated for 4 days. That is, the AR reference control sample (see Fig. 7.13a) produced a spindle-like radial morphology, the 50 μm trench/hatch (see Fig. 7.13b and d) and 100 μm trench/hatch (see Fig. 7.13c and e) gave rise to a clumped radial morphology but to varying extents on each of the different surfaces. This could be of a direct result of differing topographies between the different patterned samples as stated by Hao and Lawrence [3].

It should also be noted that similar to the 24-h seeded samples the 4-day seeded samples did not appear to show any directionality in terms of growth and proliferation; however, for the 4-day seeded samples this may be due to the fact that every sample was tending toward 100% cover density. Again, for confirmation of what was observed with the micrographs shown in Fig. 7.13 SEM images were taken, as can

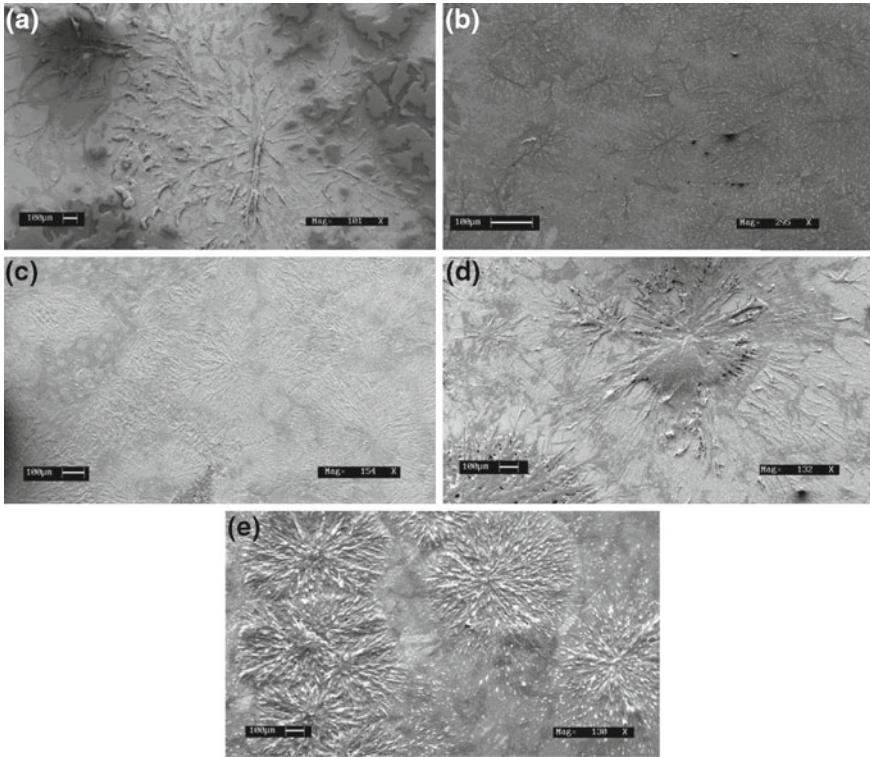


Fig. 7.14 SEM images of Au coated samples after 4 days incubation (a) as-received control sample—AR, (b) 50 μm trench—T50, (c) 100 μm trench—T100, (d) 50 μm hatch—H50 and (e) 100 μm hatch—H100

be seen in Fig. 7.14. From Fig. 7.14 it is evident that the cells had rapidly begun to proliferate over the 4-day incubation period such that for all of the samples the cover density was tending toward maximum 100% cover density.

The SEM images also showed that the cell growth was faster for the laser-induced trench and hatch patterns (see Fig. 7.14b–e) in comparison to the AR reference control sample. Upon closer inspection using the SEM as can be seen with the images in Fig. 7.14, confirmation of the morphologies was carried out. From these images it was found that the AR reference control sample (see Fig. 7.14a) gave rise to a more coral-like morphology rather than spindle-like which was first thought with the micrographs shown in Fig. 7.13. The 50 μm trench patterned sample (see Fig. 7.14b) shows that the cell morphology was more clumped, spindle-like, and was growing in a radial nature. The 100 μm trench patterned sample (see Fig. 7.14c) was seen to produce a clumped radial cell morphology. Whereas the two hatch patterns (see Fig. 7.14d and e) confirmed that the cell morphologies were clumped radial with the 50 μm trench pattern (see Fig. 7.14d) appearing to be more coral-like.

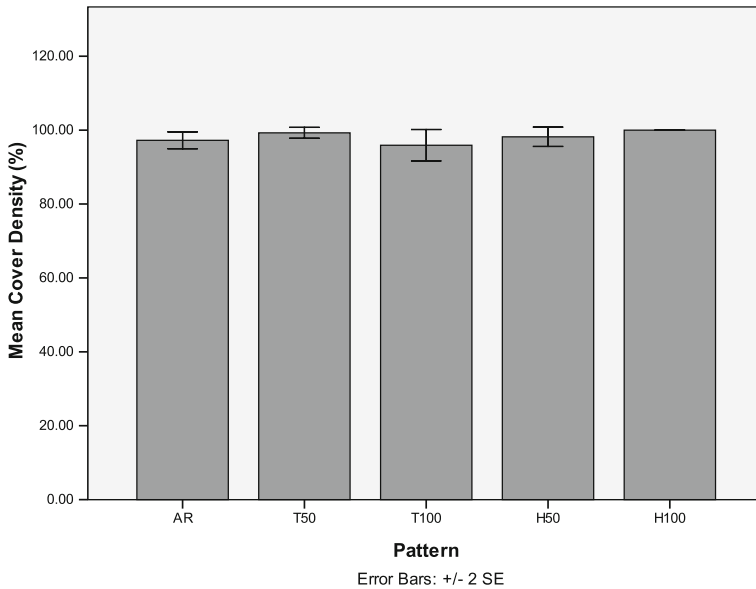


Fig. 7.15 Cover density for each of the nylon 6,6 samples 4 days after incubation (ANOVA showed that there was not an overall significance with $F=1.892$ and $p=0.170$. Scheffe's range test showed that there was no statistical difference between any of the samples* $p < 0.05$)

The results in Fig. 7.15 show that, on average, for each sample the cover density was approximately tending toward 100% thus allowing for no statistical significance to be obtained from the plotted data. This also implies that the seeded osteoblast cells over 4 days had covered all the surfaces of each sample regardless of how the surface was treated. Having said that, it should be noted that for the 100 μm hatch patterned sample each image used to calculate the cover density gave 100% covered resulting in the error being zero, as shown in Fig. 7.15. There could therefore be some slight correlation between how the nylon 6,6 was treated prior to seeding and how the osteoblast cells react to the samples in vitro, although in reality no discernible relationship could be deduced from the data shown in Fig. 7.15. As a result of the equivalent cover densities a cell count was also taken after the fourth day of incubation which can also be used to analyze how the cells react to the different patterned samples. A graph of cell density count as a function of pattern can be seen in Fig. 7.16 which indicates that there was a higher cell count after 4 days incubation for the trench and hatch patterns in comparison with the AR reference control sample. This further suggests that the surface pattern/roughness had a significant effect on the cell response in terms of cell cover density and growth. Also, as evidenced by the different cell morphologies (see Figs. 7.10, 7.11, 7.13, 7.14), surface roughness does have a large influence on cell signaling in accordance with Nebe [102]. But, no discernible correlation between the cell density count and surface characteristics such as roughness and surface energy parameters could be determined in this instance,

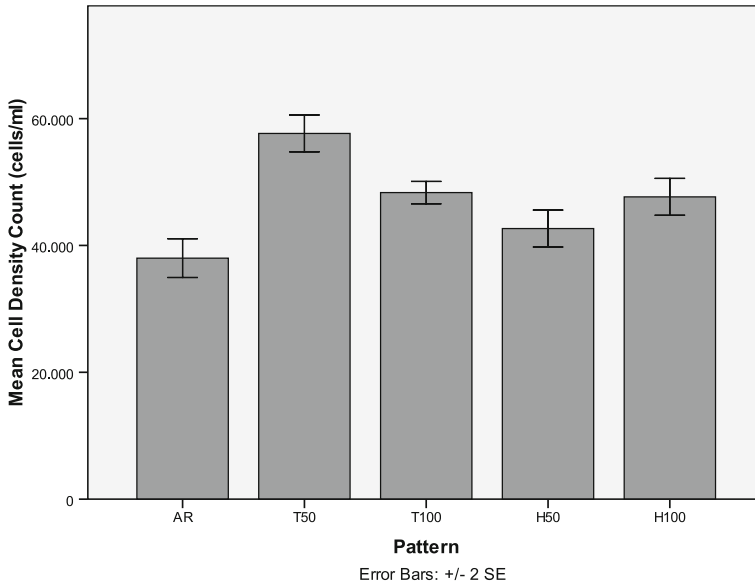


Fig. 7.16 Cell density count for each of the nylon 6,6 samples 4 days after incubation. (ANOVA showed an overall significance with $F=41.007$ and $p=0.000$. Scheffe's range test showed that there was statistical significance between all samples apart from AR and H50; T100 and H50, H100* $p < 0.5$)

which could suggest that other factors might be in play such as surface charge or even suggest that a number of different parameters are contributing to the osteoblast cell response. Although it has been seen that CO₂ laser treated surfaces give rise to improved cell adhesion, proliferation, and promotes a better interface for mitosis to take place.

7.8 Summary

Through this study it has been determined that following CO₂ laser processing of nylon 6,6 the surface characteristics can be modified in order to have influence over the recently advancing contact angle. From analyzing the laser-induced patterned surfaces it was found that the surface energy and polar component had decreased by up to 7 mJm^{-2} and the surface roughness had considerably increased. It was found that the apparent polar component and total surface energy for the samples studied were both a decreasing function of the characteristic advancing contact angle, which correlates with current theory; however, current theory states that the contact angle for a hydrophilic surface should decrease upon increasing surface roughness which has not been seen throughout this experimentation. This can be attributed

to an intermediate mixed Cassie-Baxter/Wenzel regime, in which both Wenzel and Cassie-Baxter regimes arise at the solid-liquid interface as a result of the formation of the water droplet on the various laser modified surface topographies. Another factor which has been taken into account is that the surface oxygen content tended to increase by up to 2% At. as a result of the laser processing. This is owed to the thermolytical interaction between the nylon 6,6 material and the CO₂ laser light that gives rise to melting of the nylon surface allowing oxidation to take place. From the results obtained it was found that the apparent surface energy and its components were the most dominating parameter in the modification of wettability which was a result of the mixed state wetting regime owed to the surface topography produced from the different laser-induced patterns. Through preliminary screening using SBF it was found that following immersion in SBF for 14 days each of the laser patterned samples gave rise to improved apatite layer response such that an increase in weight of up to 0.08 g was identified for the laser patterned samples in comparison to the AR sample. What is more, this was also confirmed through SEM analysis which allowed one to visualize more apatite present on the laser patterned samples. In addition, EDX analysis of the samples showed that, owed to immersion in SBF, calcium and phosphorous was present on all samples. This is advantageous for orthopedic applications as calcium and phosphorous aid to promote sufficient cell growth and proliferation. Although these elements were present on all samples it is possible to deduce that the apatite layers formed on the laser patterned samples may have contained more calcium and phosphorous on account of the larger increase in weight compared to the AR sample.

From the results obtained it was not possible to develop a discernable correlation between the cell response and surface characteristics such as roughness and surface energy. This is due to the fact that a number of factors come in to play which hold the ability to influence how the osteoblast cells reacted to the nylon 6,6 in vitro. It has been seen that for all CO₂ laser surface treated nylon 6,6 samples osteoblast cell response has been improved to become more efficient, allowing cell growth to become quicker which coincides with what was observed for the immersion in SBF. This has been seen through the fact that the cells have covered more area of the nylon 6,6 samples after 24 h and that the cell density count had increased after 4 days in comparison with the AR reference control sample. This implies that laser patterned surfaces in this instance gave rise to enhanced biomimetic properties for nylon 6,6 in terms of osteoblast cell response. This response has been observed by instigating cell signaling which has been identified through variations in cell differentiation between each of the samples studied. It has also been observed that all samples incubated over 4 days gave rise to large cover densities of around 100% regardless of laser surface treatment. In terms of morphology the cells were similar to one another when observed using both optical microscopy and SEM after 24 h incubation, appearing to have more of a bipolar nature. After 4 days the difference in cell morphology became more apparent, with the cell growth showing differing morphologies such as coral-like for the AR sample and clumped radial growth for the 50 μm (H50) and 100 μm (H100) hatch patterned samples. This finding can be accounted for by the variation in surface energy and topography instigating cell

signaling, which has a major influence on cell morphology. Significantly, it has been seen that over 24-h and 4-day incubation periods the 50 (T50) and 100 μm (T100) trench patterns gave rise to improved cell response, having greater cell cover density and mean cell count density in comparison with both the hatch and AR reference control samples. It was evident from this finding that the trench patterns gave rise to preferential adhesion and cell signaling.

References

1. S.R. Paital, N.B. Dahotre, Calcium phosphate coatings for bio-implant applications: materials, performance factors and methodologies. *Mater. Sci. Eng.*, R **66**, 1–70 (2009)
2. J. Lawrence, L. Li, Modification of the wettability characteristics of polymethyl methacrylate (PMMA) by means of CO₂, Nd:YAG, excimer and high power diode laser irradiation. *Mater. Sci. Eng.*, A **303**, 142–149 (2001)
3. L. Hao, J. Lawrence, *Laser Surface Treatment of Bio-implant Materials* (Wiley, New Jersey, 2005)
4. J. Lai, B. Sunderland, J. Xue, S. Yan, W. Zhao, M. Folkard, B.D. Michael, Y. Wang, Study on hydrophilicity of polymer surfaces improved by plasma treatment. *Appl. Surf. Sci.* **252**, 3375–3379 (2006)
5. P. Roach, D. Eglin, K. Rohde, C.C. Perry, Modern biomaterials: a review-bulk properties and implications of surface modifications. *J. Mater. Sci.: Mater. Med.* **18**, 1263–1277 (2007)
6. M.J.P. Biggs, R.G. Richards, N. Gadegaard, C.D.W. Wilkinson, M.J. Dalby, Regulation of implant surface cell adhesion: characterization and quantification of S-phase primary osteoblast adhesions on biomimetic nanoscale substrates. *J. Orthop. Res.* **25**, 273–282 (2007)
7. A. Diener, B. Nebe, F. Luthen, P. Becker, U. Beck, H.G. Neumann, J. Rychly, Control of focal adhesion dynamics by material surface characteristics. *Biomaterials* **26**, 383–392 (2005)
8. W. Song, Y.K. Jun, Y. Han, S.H. Hong, Biomimetic apatite coatings on micro-arc oxidized titania. *Biomaterials* **25**, 3341–3349 (2004)
9. L. Hao, J. Lawrence, L. Li, The wettability modification of bio-grade stainless steel in contact with simulated physiological liquids by the means of laser irradiation. *Appl. Surf. Sci.* **247**, 453–457 (2005)
10. M. Nagano, T. Kitsugi, T. Nakamura, T. Kokubo, M. Tanahashi, Bone bonding ability of an apatite-coated polymer produced using a biomimetic method: a mechanical and histological study in vivo. *J. Biomed. Mater. Res.* **31**, 487–494 (1996)
11. C. Rey, Orthopedic biomaterials, bioactivity, biodegradation; a physical-chemical approach. *J. Biomech.* **31**, 182 (1998)
12. M. Uchida, H. Kim, T. Kokubo, K. Tanaka, T. Nakamura, Structural dependence of apatite formation on zirconia gels in a simulated body fluid. *J. Ceram. Soc. Jpn.* **110**, 710–715 (2002)
13. Q. Zhao, Y. Liu, C. Wang, S. Wang, Evaluation of bacterial adhesion on Si-doped diamond-like carbon films. *Appl. Surf. Sci.* **253**, 7254–7259 (2007)
14. J. Lawrence, L. Hao, H.R. Chew, On the correlation between Nd:YAG laser-induced wettability characteristics modification and osteoblast cell bioactivity on a titanium alloy. *Surf. Coat. Technol.* **200**, 5581–5589 (2006)
15. D.F. Williams, On the mechanisms of biocompatibility. *Biomaterials* **29**, 2941–2953 (2008)
16. D.J. Chauvel-Lebret, P. Auroy, M. Bonnaure-Mallet, Chapter 13: Biocompatibility of Elastomers. In: S. Dumitriu (eds) *Polymeric Biomaterials*, 2nd edn. (CRC Press Taylor & Francis Group, Boca Raton, 2001) pp. 311–360.
17. M.J. Fauran-Clavel, J. Oustrin, Alkaline phosphatase and bone calcium parameters. *Bone* **7**, 95–99 (1986)

18. A. De Renzo, V. Micera, S. Vaglio, L. Luciano, C. Selleri, B. Rotoli, Induction of alkaline phosphatase activity in chronic myeloid leukemia cells: in vitro studies and speculative hypotheses. *Am. J. Hematol.* **35**, 278–280 (1990)
19. L. Xu, C.A. Siedlecki, Effects of surface wettability and contact time on protein adhesion to biomaterial surfaces. *Biomaterials* **28**, 3273–3283 (2007)
20. M.S. Lord, B.G. Cousins, P.J. Doherty, J.M. Whitelock, A. Simmons, R.L. Williams, B.K. Milthorpe, The effect of silica nanoparticulate coatings on serum protein adsorption and cellular response. *Biomaterials* **27**, 4856–4862 (2006)
21. H. Arwin, Ellipsometry on thin organic layers of biological interest: characterization and applications. *Thin Solid Films* **377–378**, 48–56 (2000)
22. P.A. Cuypers, W.T. Hermens, H.C. Hemker, Ellipsometry as a tool to study protein films at liquid–solid interfaces. *Anal. Biochem.* **84**, 56–67 (1978)
23. H. Elwing, Protein absorption and ellipsometry in biomaterial research. *Biomaterials* **19**, 397–406 (1998)
24. Z. Ma, Z. Mao, C. Gao, Surface modification and property analysis of biomedical polymers used for tissue engineering. *Colloids Surf. B* **60**, 137–157 (2007)
25. E.A. Vogler, Role of Water in Biomaterials. In: B.D. Ratner (eds) *Biomaterials Science*, 2nd edn. (Elsevier Academic Press, San Diego, 2004) pp. 59.
26. C.J. Van Oss, C.F. Gillman, A.W. Neumann, *Phagocytic Engulfment and Cell Adhesiveness* (Marcel Dekker, New York, 1975)
27. M.S. Kim, G. Khang, H.B. Lee, Gradient polymer surfaces for biomedical applications. *Prog. Polym. Sci.* **33**, 138–164 (2008)
28. M.D. Ball, R. Sherlock, T. Glynn, Cell interactions with laser-modified polymer surfaces. *J. Mater. Sci.* **15**, 447–449 (2004)
29. K.S. The, Y.W. Lu, Topography and wettability control in biocompatible polymer for BioMEMs applications, in *Proceedings of the 3rd IEEE International Conference on Nano/Micro Engineered and Molecular Systems*, Sanya, China, 2008
30. M. Ma, R.M. Hill, Superhydrophobic surfaces. *Curr. Opin. Colloid Interface Sci.* **11**, 193 (2006)
31. Y.T. Cheng, D.E. Rodak, C.A. Wong, C.A. Hayden, Effects of micro- and nano-structures on the self-cleaning behaviour of lotus leaves. *Nanotechnology* **17**, 1359–1362 (2006)
32. A.W. Adamson, Potential distortion model for contact angle and spreading II, temperature dependent effects. *J. Colloidal Interface Sci.* **44**, 273–281 (1973)
33. J. De Connick, F. Dunlop, Wetting transitions and contact angles. *Europhys. Lett.* **11**, 1291–1296 (1987)
34. C.J. Van Oss, R.J. Good, M.K. Chaudury, The role of van der Waals forces and hydrogen bonds in hydrophobic interactions between biopolymers and low energy surfaces. *Interface Sci.* **111**, 378–390 (1986)
35. E. Chibowski, On some relations between advancing, receding and Young’s contact angles. *Adv. Colloid Interface Sci.* **133**, 51–59 (2007)
36. D.F. Gerson, An empirical equation-of-state for solid-fluid interfacial free energies. *Colloid Polym. Sci.* **260**, 539–544 (1982)
37. G. Whyman, E. Bormashenko, T. Stein, The rigorous derivation of Young, Cassie-Baxter and Wenzel equations and the analysis of the contact angle hysteresis phenomenon. *Chem. Phys. Lett.* **450**, 355–359 (2008)
38. P. Jakubczyk, M. Napiorkowski, The influence of droplet size on line tension. *J. Phys.: Condens. Matter* **16**, 6917–6928 (2004)
39. J. Bico, U. Thiele, D. Quere, Wetting of textured surfaces. *Colloids Surf. A* **206**, 41–46 (2002)
40. Y.C. Jung, B. Bhushan, Wetting transition of water droplets on superhydrophobic patterned surfaces. *Scripta Mater.* **57**, 1057–1060 (2007)
41. S.M. Lee, T.H. Kwon, Effects of intrinsic hydrophobicity on wettability of polymer replicas of a superhydrophobic lotus leaf. *J. Micromech. Microeng.* **17**, 687–692 (2007)

42. D.G. Waugh, J. Lawrence, D.J. Morgan, C.L. Thomas, Interaction of CO₂ laser-modified nylon with osteoblast cells in relation to wettability. *Mater. Sci. Eng., C* **29**, 2514–2524 (2009)
43. D.G. Waugh, J. Lawrence, C.D. Walton, R.B. Zakaria, On the effects of using CO₂ and F₂ lasers to modify the wettability of a polymeric biomaterial. *J. Opt. Laser Technol.* **42**, 347–356 (2010)
44. M.J. Jaycock, G.D. Parfitt, *Chemistry of Interfaces* (Wiley, Chichester, 1981)
45. W.A. Zisman, *Relation of Equilibrium Contact Angle to Liquid and Solid Constitution Contact Angle Wettability and Adhesion* (American Chemical Society, Washington, 1964)
46. W.A. Zisman, Influence of constitution on adhesion. *Ind. Eng. Chem.* **55**, 19–38 (1963)
47. F.M. Fowkes, Attractive forces at interfaces. *Ind. Eng. Chem.* **5**, 40–52 (1964)
48. M. Zenkiewicz, Methods for calculation of surface free energy of solids. *J. Achievements Mater. Manuf. Eng.* **24**, 137–145 (2007)
49. R.S. Benson, Use of radiation in biomaterials science. *Nucl. Instrum. Methods Phys. Res. B* **191**, 752–757 (2002)
50. C. Mao, W. Zhao, C. Zhu, A. Zhu, J. Shen, S. Lin, In vitro studies of platelet adhesion on UV radiation-treated nylon surface. *Carbohydr. Polym.* **59**, 19–25 (2005)
51. E.A. Hegazy, H.A.A. El-Rehim, H. Kamal, K.A. Kandeel, Advances in radiation grafting. *Nucl. Instrum. Methods Phys. Res. B* **185**, 235–240 (2001)
52. Z. Zhu, M.J. Kelley, Grafting onto poly (ethylene terephthalate) driven by 172 nm UV light. *Appl. Surf. Sci.* **252**, 303–310 (2005)
53. B. Ranby, Surface modification and lamination of polymers by photografting. *Int. J. Adhes. Adhes.* **151**, 337–343 (1999)
54. B. Ranby, W.T. Yang, O. Tretinnikov, Surface photografting of polymer fibers, films and sheets. *Nucl. Instrum. Methods Phys. Res. B* **151**, 301–305 (1999)
55. F. Arefi-Khonsari, M. Tatoulian, F. Bretagnol, O. Bouloussa, F. Rondelez, Processing of polymers by plasma technologies. *Surf. Coat. Technol.* **200**, 14–20 (2005)
56. F. Milde, K. Goedicke, M. Fahland, Adhesion behaviour of PVD coatings on ECR plasma and ion beam treated polymer films. *Thin Solid Films* **279**, 169–173 (1996)
57. R.M.A. Abdul majeed, A. Datar, S.V. Bhoraskar, V.N. Bhoraskar, Surface modification of polymers by atomic oxygen using ECR plasma. *Nucl. Instrum. Methods Phys. Res. B* **258**, 345–351 (2007)
58. Q.F. Wei, W.D. Gao, D.Y. Hou, X.Q. Wang, Surface modification of polymer nanofibres by plasma treatment. *Appl. Surf. Sci.* **245**, 16–20 (2005)
59. X. Wang, M.G. McCord, Grafting of poly(n-isopropylacrylamide) onto nylon and polystyrene surfaces by atmospheric plasma treatment followed with free radical graft copolymerization. *J. Appl. Polym. Sci.* **104**, 3614–3621 (2007)
60. P.K. Chu, Plasma surface treatment of artificial orthopedic and cardiovascular biomaterials. *Surf. Coat. Technol.* **201**, 5601–5606 (2007)
61. P.K. Chu, Enhancement of surface properties of biomaterials using plasma-based technologies. *Surf. Coat. Technol.* **201**, 8076–8082 (2007)
62. P.K. Chu, Bioactivity of plasma implanted biomaterials. *Nucl. Instrum. Methods Phys. Res. B* **242**, 1–7 (2006)
63. M.C. Porte-Durrieu, C. Aymes-Chodur, N. Betz, B. Brouillaud, F. Rouais, A.L. Moel, C. Baquey, Synthesis of biomaterials by swift heavy ion grafting: preliminary results of haemocompatibility. *Nucl. Instrum. Methods Phys. Res. B* **131**, 364–375 (1997)
64. F.Z. Cui, Z.S. Luo, Biomaterials modification by ion-beam processing. *Surf. Coat. Technol.* **112**, 278–285 (1999)
65. W.M. Lau, Ion beam techniques for functionalization of polymer surfaces. *Nucl. Instrum. Methods Phys. Res. B* **131**, 341–349 (1997)
66. J.S. Cho, Y.W. Beag, S. Han, K.H. Kim, J. Cho, S.K. Koh, Hydrophilic surface formation on materials and its applications. *Surf. Coat. Technol.* **128–129**, 66–70 (2000)
67. C. Aubry, T. Trigaud, J.P. Moliton, D. Chiron, Polymer gratings achieved by focused ion beam. *Synth. Met.* **127**, 307–311 (2002)

68. S. Iwanaga, Y. Akiyama, A. Kikuchi, M. Yamato, K. Sakai, T. Okano, Fabrication of a cell array on ultrathin hydrophilic polymer gels utilising electron beam irradiation and UV excimer laser ablation. *Biomaterials* **26**, 5395–5404 (2005)
69. F. Yu, P. Li, H. Shen, S. Mathur, C.M. Lehr, U. Bakowsky, F. Mucklich, Laser interference lithography as a new and efficient technique for micropatterning of biopolymer surface. *Biomaterials* **26**, 2307–2312 (2005)
70. H. Mirzadeh, M. Dadsetan, Influence of laser surface modifying of polyethylene terephthalate on fibroblast cell adhesion. *Radiat. Phys. Chem.* **67**, 381–385 (2003)
71. V. Hasirci, H. Kenar, Novel surface patterning approaches for tissue engineering and their effect on cell behaviour. *Nanomedicine* **1**, 73–90 (2006)
72. M. Dadsetan, H. Mirzadeh, N. Sharifi-Sanjani, M. Daliri, Cell behaviour on laser surface-modified polyethylene terephthalate in vitro. *J. Biomed. Mater. Res.* **57**, 183–189 (2001)
73. E. Sarantopoulou, Z. Kollia, A.C. Cefalas, A.M. Douvas, M. Chatzichristidi, P. Argitis, S. Kobe, Polymer self-assembled nano-structures and surface relief gratings induced with laser at 157 nm. *Appl. Surf. Sci.* **253**, 7884–7889 (2007)
74. K. Callewaert, Y. Martele, L. Breban, K. Naessans, P. Vandaele, R. Baets, G. Geuskens, E. Schacht, Excimer laser induced patterning of polymeric surfaces. *Appl. Surf. Sci.* **208–209**, 218–225 (2003)
75. W. Pflöging, M. Bruns, A. Welle, S. Wilson, Laser-assisted modification of polystyrene surfaces for cell culture applications. *Appl. Surf. Sci.* **253**, 9177–9184 (2007)
76. A.C. Duncan, F. Weisbuch, F. Rouais, S. Lazare, Ch. Baquey, Laser microfabricated model surfaces for controlled cell growth. *Biosens. Bioelectron.* **17**, 413–426 (2002)
77. C. David, J. Wei, T. Lippert, A. Wokaun, Diffractive grey-tone phase masks for laser ablation lithography. *Microelectron. Eng.* **57–58**, 453–460 (2001)
78. C.M. Chan, T.M. Ko, H. Hiraoka, Polymer surface modification by plasmas and photons. *Surf. Sci. Rep.* **24**, 1–54 (1996)
79. K.S. Tiaw, M.H. Hong, S.H. Teoh, Precision laser micro-processing of polymers. *J. Alloys Compd.* **449**, 228–231 (2008)
80. F. Yu, F. Mucklich, P. Li, H. Shen, S. Mathur, C.M. Lehr, U. Bakowsky, In vitro cell response to a polymer surface micropatterned by laser interference lithography. *Biomacromolecules* **6**, 1160–1167 (2005)
81. S. Dadbin, Surface modification of LDPE film by CO₂ pulsed laser irradiation. *Eur. Polym. J.* **38**, 2489–2495 (2002)
82. C.A. Aguilar, Y. Lu, S. Mao, S. Chen, Direct micro-patterning of biodegradable polymers using ultraviolet and femtosecond lasers. *Biomaterials* **26**, 7642–7649 (2005)
83. C.D. Skordoulis, M. Makropoulou, A.A. Serafenitides, Ablation of nylon-6,6 with UV and IR lasers. *Appl. Surf. Sci.* **86**, 239–244 (1995)
84. T. Lippert, J. Wei, A. Wokaun, N. Hoogen, O. Nuyken, Polymers designed for laser microstructuring. *Appl. Surf. Sci.* **168**, 270–272 (2000)
85. B. Losekrug, A. Meschede, H.U. Krebs, Pulsed laser deposition of smooth poly(methyl methacrylate) films at 248 nm. *Appl. Surf. Sci.* **254**, 1312–1315 (2007)
86. R. Cristescu, I. Stamatina, D.E. Mihaiescu, C. Ghica, M. Albuiescu, I.N. Mihaiescu, D.B. Chrisey, Pulsed laser deposition of biocompatible polymers: a comparative study. *Thin Solid Films* **262**, 453–454 (2004)
87. D.B. Chrisey, G.K. Hubler (eds), *Pulsed Laser Deposition of Thin Films* (Wiley, New York, 1994)
88. E. Rebollar, M.M. Villavieja, S. Gaspard, M. Oujja, T. Corrales, S. Georgiou, C. Domingo, P. Bosch, M. Catillejo, Pulsed laser deposition of polymers doped with fluorescent probes, Application to Environmental Sensors. *J. Phys.: Conf. Ser.* **59**, 305–309 (2007)
89. D.S. Shin, J.H. Lee, J. Suh, T.H. Kim, Determination of the debris produced from poly(ethylene terephthalate) during KrF excimer laser ablation. *Appl. Surf. Sci.* **252**, 2319–2327 (2006)
90. H. Niino, A. Yabe, Chemical surface modification of fluorocarbon polymers by excimer laser processing. *Appl. Surf. Sci.* **96–98**, 550–557 (1996)

91. L.D. Laude, N. Boutarek, K. Kolev, Excimer lasers for surface engineering of polymer-based composites. *Nucl. Instrum. Methods Phys. Res. B* **105**, 254–257 (1995)
92. M. Charbonnier, M. Alami, M. Romand, J.P. Girardeau-Montaut, M. Afif, Laser-assisted grafting onto polycarbonate: application to metallization by chemical means. *Appl. Surf. Sci.* **109/110**, 206–211 (1997)
93. H. Mirzadeh, A.A. Katbab, M.T. Khorasani, R.P. Burford, E. Gorgin, A. Golestani, Cell attachment to laser-induced AAm-and HEMA-grafted ethylene-propylene rubber as biomaterial: in vivo study. *Biomaterials* **16**, 641–648 (1995)
94. H. Mirzadeh, A.A. Katbab, R.P. Burford, CO₂-laser graft copolymerization of HEMA and NVP onto ethylene-propylene rubber (EPR) as biomaterial-(III). *Radiat. Phys. Chem.* **46**, 859–862 (1995)
95. D.G. Rance, Chapter 6: Thermodynamics of Wetting: From Its Molecular Basis to Technological Application. In: D.M. Brewis (eds) *Surface Analysis and Pretreatment of Plastics and Metals* (Applied Science Publishers, Essex, 1982) pp. 121.
96. D.G. Waugh, J. Lawrence, Wettability characteristics variation of nylon 6,6 by means of CO₂ laser generated surface patterns, *ICALEO 2008 Proceedings*, vol 101, Pechanga, CA, USA, 20–23 Oct 2008, pp. 61–69
97. Y.C. Jung, B. Bhushan, Contact angle, adhesion and friction properties of micro- and nanopatterned polymers for superhydrophobicity. *Nanotechnology* **17**, 4970–4980 (2006)
98. Y.T. Cheng, D.E. Rodak, Is the lotus leaf superhydrophobic?. *Appl. Phys. Lett.* **86**, 144101/1–144101/3 (2005)
99. X. Chen, T. Lu, The apparent state of droplets on a rough surface. *Sci. China, Ser. G* **52**, 233–238 (2009)
100. X. Wu, L. Zheng, D. Wu, Fabrication of superhydrophobic surfaces from microstructured ZnO-based surfaces via a wet-chemical route. *Langmuir* **21**, 2665–2667 (2005)
101. J. Lawrence, L. Li, *Laser modification of the wettability characteristics of engineering materials* (Professional Engineering Publishing Limited, Suffolk, 2001)
102. B. Nebe, F. Luthen, R. Lange, P. Becker, U. Beck, J. Rychly, Topography-induced alterations in adhesion structures affect mineralization in human osteoblasts on titanium. *Mater. Sci. Eng., C* **24**, 619–624 (2004)

Chapter 8

Laser Micro and Nano Processing of Metals, Ceramics, and Polymers

Wilhelm Pfleging, Robert Kohler, Isabelle Südmeyer and Magnus Rohde

Abstract Laser-based material processing is well investigated for structuring, modification, and bonding of metals, ceramics, glasses, and polymers. Especially for material processing on micrometer, and nanometer scale laser-assisted processes will very likely become more prevalent as lasers offer more cost-effective solutions for advanced material research, and application. Laser ablation, and surface modification are suitable for direct patterning of materials and their surface properties. Lasers allow rapid prototyping and small-batch manufacturing. They can also be used to pattern moving substrates, permitting fly-processing of large areas at reasonable speed. Different types of laser processes such as ablation, modification, and welding can be successfully combined in order to enable a high grade of bulk and surface functionality. Ultraviolet lasers favored for precise and debris-free patterns can be generated without the need for masks, resist materials, or chemicals. Machining of materials, for faster operation, thermally driven laser processes using NIR and IR laser radiation, could be increasingly attractive for a real rapid manufacturing.

8.1 Introduction

In micro- and nanosystems laser-assisted processes are of particular interest for the rapid fabrication and development of devices for microfluidics, bioanalytics, or biomedical applications [1, 2]. For these application fields laser processing is successfully applied with respect to laser ablation, micropatterning, and packaging [3, 4].

W. Pfleging (✉) · R. Kohler · I. Südmeyer · M. Rohde
Karlsruhe Nano Micro Facility, Institute for Applied Materials (IAM-AWP),
Karlsruhe Institute of Technology, Hermann-von-Helmholtz-Platz 1,
76344 Eggenstein-Leopoldshafen, Germany
e-mail: wilhelm.pfleging@kit.edu

M. Rohde
e-mail: magnus.rohde@kit.edu

The improvement of properties on a local scale can be achieved by applying surface modification techniques such as laser dispersing and alloying of brittle materials such as ceramics and glasses. The fabrication of stable joints is still a challenge as far as small parts, thin metal sheets, and dissimilar materials such as metal-ceramic combinations are concerned, in which the development and application of laser processes are playing an important role. Advanced functional surface patterns with high lateral resolution can be obtained by combination of laser micro- or nanostructuring and laser-induced surface modification. For this purpose, thermally driven as well as photolytically driven processes can be applied [2]. This depends on the process strategy. For example, rapid laser surface annealing can be an appropriate tool for the realization or adjustment of nano-scaled grain structures [5], while laser sublimation with reduced thermal impact is most appropriate for direct laser micro- or nanostructuring [3, 6]. Surface modification can be a change in topography, texture, or a change in chemical or physical surface properties. Surface wetting or adhesion properties of polymers, e.g., polystyrene (PS) used as biomaterial, can be adjusted by surface topography and/or surface chemistry [7, 8]. Surface topography can be controlled by laser direct structuring or selective laser material ablation on micro- and nanometer scale, while a change of surface chemistry in general is initiated by direct bond breaking leading to the formation of new bonds or radicals [9–11]. Capillary electrophoresis is one of the first analytical methods that has been transferred to a microfluidic chip [12] and can be seen as one of the pacemakers in the field of Lab-on-Chip systems. Especially the cost-effective analysis of small ions is of high importance to various applications covering food analysis, environmental monitoring, bio analysis, and medical point-of-care diagnostics. Research at KIT (Karlsruhe Institute of Technology) related to microfluidic chips is focussed on replacing the nowadays often used glass- or silicon-based chips [13] by polymer materials which are more suitable for mass production [14]. Polymethylmetacrylate (PMMA) as a well-known and widely used material is established especially for the analysis of small inorganic ions. Polymer-based microfluidic systems have been very recently introduced to the market [15, 16]. For the fabrication of first functional systems, for design optimization, or for a small-scale production, the need for rapid manufacturing technologies increases [17, 18]. For this purpose, the rapid manufacturing of polymeric microfluidic chips based on advanced laser processing technologies was investigated [1]. Although laser microfabrication is well known, mainly UV lasers have been used so far to produce polymeric microsystems [3, 19, 20]. For a microfluidic chip made of polyetheretherketone (PEEK) with an outer dimension of $16 \times 95 \text{ mm}^2$ the processing time using a high repetition excimer laser is about 5 min [21]. This is a very impressive rapid manufacturing method with respect to hot embossing techniques, where the replication time for micro-parts might be in the range of 15 minutes. Nevertheless, for other materials, such as PS or PMMA, a further significant reduction of processing time should be possible by using CO_2 laser radiation. Only a few and very recent publications have been published concerning CO_2 laser micropatterning of polymers [22–25]. In the actual state of the art, channel widths in PMMA surfaces obtained by CO_2 laser ablation are in general significantly larger than $100 \text{ }\mu\text{m}$ [24]. An important prerequisite for the use of polymers in micro-

components is the covering of the microfluidic channel structures which need to be well sealed and yet remain free from blockages. The bonding via gluing or vibration welding needs special designed surfaces in order to avoid contamination or damages of functional structures. Bonding of thermoplastic polymers via thermal bonding can overcome these restrictions. Thermal bonding can be performed not only slightly below the glass transition temperature but also at higher temperatures depending on the clamping pressures or surface modifications used [24, 26]. Nevertheless, deformations of micro channels or reduced bonding strengths are still technical problems. Therefore, a new technical approach by laser-based technology was justified. The laser transmission welding of transparent and opaque polymers is a well-established technology [27]. But, welding of sole transparent and microstructured components is still a challenge. For this purpose a recent type of laser transmission welding including nano layers [23] is further improved, in order to enable laser packaging of microfluidic structures with channel widths down to 50 μm . The combination of CO₂ laser patterning and laser transmission welding will be shown to be a suitable and economical alternative for the rapid manufacturing of polymeric microfluidic devices.

High power laser beams can also be used as a flexible heat source applied for the heat treatment of materials on a local scale. Particularly, laser processes for dispersing and alloying of ceramic surfaces are important methods to modify the properties of this class of brittle and low conductance materials. Using this method, which is based on the introduction of a second phase material coupled with the heat input by a laser beam, mechanical and tribological properties [28] can be improved, and also the thermal and electrical conductance can be adjusted [29, 30]. Furthermore, the property modifications are restricted to a localized area leaving the bulk of the ceramic in its original state. However, due to the complex relationship between the laser process parameters and its results, optimization procedures are often time-consuming and often only guided by a long-term experimental experience. Therefore, modeling techniques and numerical simulation tools, which are able to predict the experimental results, or at least to restrict parameter fields, would be helpful to reduce the time of the process development. Welding processes of metallic materials with laser beams are well-established joining methods as far as large-scaled structures or parts are concerned. However, the development of laser joining processes for thin sheets or micro parts is still a challenge. Compared to conventional welding methods the laser welding offers a number of advantages, which are of particular importance for micro joining. Due to the small heat affected zone the welding seam can be very narrow and consequently the distortion of the joined part is reduced. Furthermore, the aspect ratio of the welding seam can be controlled by the choice of the process parameters, and therefore a joint with high quality and strength can be achieved. Finally, laser beam welding has a high flexibility with respect to the material of choice and its geometry.

Engineering ceramics are covering a growing application field due to their specific properties such as high temperature stability, corrosion, and wear resistance. In order to construct ceramic parts and components these materials have to be machined which can be a difficult and time-consuming task with respect to their high hardness and

brittleness. For the integration of ceramic components into complex shapes it can be advantageous to use joining techniques such as brazing [31, 32]. Different routes or procedures have been studied to join ceramic to ceramic and metal to ceramic. Conventionally the brazing process is conducted at high temperature within a furnace chamber in vacuum or inert gas atmosphere [33, 34]. An alternative method is the laser beam brazing [35, 36] process, which utilizes a localized heat input onto the joining zone. Therefore, this particular process is more suitable for small parts or components.

In recent research the combination of thin film deposition technology and subsequent laser micro- and nano-scaled material processing is investigated in order to get new and improved functional surface patterns with high lateral resolution. A rather new application field for laser structuring and modification of thin films is the development of advanced thin film lithium-ion batteries (LIB) [37]. LIB are widely used in portable electric devices all over the world, due to their high energy density and high discharge voltages. They are presently being investigated as a power source for large electric equipment, for instance, hybrid electric vehicles (HEVs) or full electric vehicles (FEVs) [38]. High electrical charge/discharge capability of LIB, especially that of nanometer-scaled cathode material has attracted growing attention in the past few years [39]. A new promising technical approach for mobile applications as well as for micro-technology systems might use LIB based on nano-scaled materials and thin films [40]. Different laser processes for the improvement of battery performances in thin film LIB will be discussed: rapid laser annealing and microstructuring of thin film electrode materials (LiCoO_2 , SnO_2). While lithium cobalt oxide (LiCoO_2) is a well established and still most commonly used cathode material in LIB [41], SnO_2 is a promising material which could act as anode in future LIB. The practical discharge capacity of SnO_2 can reach values of 781 Ah/kg [42], which is significant above the theoretical capacity of standard graphite anodes (371 Ah/kg).

8.2 Fundamental Aspects of Laser Material Processing

Laser radiation can be produced in different operating modes (continuous, pulsed) and in different media (solid-state lasers, gas lasers). Pulse durations range from microseconds to femtoseconds, as in pulsed excimer gas lasers which radiate in the deep UV (wave length 157–351 nm) and femtosecond or millisecond pulsed solid-state lasers (266–1070 nm). Continuous wave (cw) operation CO_2 gas lasers radiate in the IR (10.6 μm).

The properties of lasers are characterized by the following quantities:
Laser fluence

$$\varepsilon = \frac{E}{A} \left[\frac{\text{J}}{\text{cm}^2} \right] \quad (8.1)$$

Pulse energy

$$E = \int_0^{\tau} P(t) dt \quad [\text{J}] \quad (8.2)$$

Maximum peak Intensity

$$I = \frac{P}{A} \left[\frac{\text{W}}{\text{cm}^2} \right] \quad (8.3)$$

where, $P(t)$ is the laser power as function of time t , P is the maximum peak power, A the focal spot area, and τ the pulse duration. The laser ablation process involves laser-substrate interactions that are dependent on the properties of the laser beam and of the substrate. Typically, in laser direct writing a highly collimated, monochromatic, and coherent light beam is generated and focused to a small spot. If the laser wavelength is chosen from a region where the substrate material absorbs, a high energy density is deposited in a small volume. A wavelength with a minimum absorption depth should be selected. This will help ensure a high energy deposition in a small volume for rapid and complete ablation. Further important laser parameters are the pulse duration τ and the laser repetition rate ν_{rep} . A short pulse duration maximizes the peak power and can reduce the thermal conduction to the surrounding material which can be described by the thermal diffusion length

$$\delta_w = \sqrt{4\kappa \cdot \tau} \quad (8.4)$$

where, κ denotes the thermal diffusivity.

The repetition rate can also influence the thermal impact on the material. If it is too low, the energy loss by heat conduction dominates and all of the energy not used for ablation will leave the ablation zone. Higher repetition rates lead to an increase of the average surface temperature ΔT , which can be estimated by solving the one-dimensional heat equation for a rectangular laser pulse [3]

$$\Delta T = 2(1 - R) \varepsilon \nu_{\text{rep}} \sqrt{\frac{t}{\rho c_p K \pi}} \quad (8.5)$$

where R is the reflectance, t the laser processing time [s], ρ the density [g/cm^3], C_p the specific heat capacity [$\text{J}/(\text{g} \cdot \text{K})$], and K the thermal conductivity [$\text{W}/(\text{cm} \cdot \text{K})$]. A higher surface temperature in turn can induce an increase of the material quantity removed per laser pulse. This can make the ablation process more efficient. Nevertheless thermal damage of the material or melt and debris formation must be avoided. The beam energy is of no use if it cannot be efficiently delivered to the ablation region. High energy density is not always appropriate; especially for micro fabrication technologies, the best surface qualities are obtained for small laser fluences (approximately 2 to 3 times above the ablation threshold). Laser micromachining becomes an efficient method when high repetition rates or large area processing can be established.

Two modes of laser machining can be distinguished:

- (1) In the parallel mode, the laser beam is imaged (projected) through a mask or optical beam shaping system onto the workpiece, generally using a demagnifying projection lens. Mask projection or parallel beam processing is generally preferred for large area material processing.
- (2) In the serial mode for direct writing, surface is moved relative to a fixed laser beam. For deep structures or 3D shapes, layer-by-layer processing becomes necessary and an appropriate process strategy has to be applied.

The laser-material interaction is a complex combination of photochemical and photothermal processes and is dependent on the laser characteristics and materials properties. The interaction can start with single-photon or multi-photon processes. A single-photon process is typically used in order to describe the material ablation of polymer materials by high photon UV laser radiation (see Sect. 11.4.2). While multi-photon absorption processes plays an important role by the use of ultrashort laser pulses with pulse length τ in the picosecond ($\tau < 10\text{ps}$) and femtosecond (10^{-15}s) range. In the case of femtosecond laser pulses, the high intensity delivered by the focused laser beam can induce strong nonlinear optical absorption of photons in materials that might otherwise be highly transparent to photons at much lower intensities. Another advantage is the reduction of residual damage by minimizing thermal effects [43–45]. The choice of wavelength depends on the optical properties of the substrate material such as absorption and reflection characteristics and on the minimum structure size to be achieved. Since short wavelength are diffracted less than longer wavelength, optical beam delivery systems can have greater resolution that allows smaller lateral feature sizes to be machined. Theoretically, minimal feature sizes down to the minimum achievable focal spot (about twice the laser wavelength λ) or the optical diffraction limit $\lambda/(2 \times \text{NA})$ are possible (NA: numerical aperture of the optical system). In general, optimal laser micromachining is obtained when photons are absorbed at submicrons depth on the surface of a material. Furthermore, if these photons are delivered in a short duration burst ($< 100\text{ ns}$), a mini explosion is created, ejecting solid and gaseous particulates from the irradiated site. Thermal conduction to the surrounding substrate material is then minimized and the heat affected damage of the material is reduced.

8.3 Modeling and Simulation

Due to the complex relationship between the laser process parameters and the results of the laser surface interaction optimization procedures are often time-consuming and only guided by a long-term experimental experience. Therefore, simulation tools with the ability to predict experimental results, or at least to restrict parameter fields, can be helpful to reduce the time of the process development. Heat, fluid flow, and mass transfer in laser-assisted surface modification have been studied within a numerical approach by several researchers in the past [46–55]. A part of the above models using a two-dimensional and quasi-static approach to obtain information about the behavior

of the laser melted pools processed with various experimental parameters. But also three-dimensional, transient models have been developed to predict the dynamics of the phase change process and the species distribution inside the molten pool during the laser modification. All these models have been applied to the laser processing of metal alloy systems. Although the heat transfer and the solid–liquid phase change during the thermal processing of ceramic particles and metal-ceramic composites has been treated numerically by several authors [56–58], the laser processing of ceramics has been studied only in a relatively small number of studies [59, 60]. The main objective of numerical studies is therefore to get more insight into the dominating thermal processes during the laser ceramic interaction and also to enlarge the available database for engineering applications. The three-dimensional numerical model, which is described here, is focused on the simulation of the dynamic liquid–solid phase change and the distribution of the second phase within the melt pool generated during the process as a function of the process parameters in ceramic substrates. For the process simulation the CFD-software PHOENICS [61] has been used to solve the Navier-Stokes equations which describes the fluid flow within the melt pool due to the surface tension gradient (Marangoni convection) which is induced by the localized heat source traveling with a constant speed. The heat source is generated by a focused laser beam with a strip-like intensity profile which superimposes a strong transient temperature gradient on the surface. The computation has been performed under the assumption that the flow is laminar, the fluid is incompressible with a flat-free surface and the Boussinesq approximation is valid for the temperature-dependent density variation within the melt [62, 63], which induces thermal buoyancy forces due to temperature gradients. The orientation of coordinate system for the computational domain has been chosen that the laser beam or the heat source travels along the z-direction which is the longest dimension, while the y- and x-axis are oriented along the thickness and the width of the domain, respectively.

The governing equations, which describe the velocity and temperature distribution in three dimensions, for the numerical modeling of the process are:

Continuity

$$\frac{\partial(\rho u)}{\partial x} + \frac{\partial(\rho v)}{\partial y} + \frac{\partial(\rho w)}{\partial z} = 0 \quad (8.6)$$

x-momentum

$$\frac{\partial u}{\partial t} + u \cdot \nabla u = \frac{1}{\rho} \frac{\partial P}{\partial x} + \mu \Delta u \quad (8.7)$$

y-momentum

$$\frac{\partial v}{\partial t} + v \cdot \nabla v = \frac{1}{\rho} \frac{\partial P}{\partial x} + \mu \Delta v - \beta g \cdot (T - T_M) \quad (8.8)$$

z-momentum

$$\frac{\partial w}{\partial t} + w \cdot \nabla w = \frac{1}{\rho} \frac{\partial P}{\partial z} + \mu \Delta w \quad (8.9)$$

Energy

$$\frac{\partial T}{\partial t} + u \cdot \frac{\partial T}{\partial x} + v \cdot \frac{\partial T}{\partial y} + w \cdot \frac{\partial T}{\partial z} = \kappa \cdot \Delta T \quad (8.10)$$

with the boundary conditions at the surface at $y=0$

$$v = 0 \quad (8.11)$$

$$\mu \cdot \frac{\partial v}{\partial y} = -\frac{\partial \sigma}{\partial T} \frac{\partial T}{\partial x} - \frac{\partial \sigma}{\partial T} \frac{\partial T}{\partial z} \quad (8.12)$$

$$Q_{\text{Las}} = \eta \cdot P_{\text{Las}} \cdot a_{\text{Las}}(v_{\text{Scan}}, t) \cdot \left(\frac{1}{1 + e^{-(x-x_0)/f}} + \frac{1}{1 + e^{(x-x_0)/f}} + 1 \right) \quad (8.13)$$

with

$$a_{\text{Las}}(v_{\text{Scan}}, t) = \frac{1}{1 + e^{-(z-v_{\text{Scan}}t)/f}} + \frac{1}{1 + e^{(z-(v_{\text{Scan}}t+d_{\text{Las}}))/f}} + 1 \quad (8.14)$$

The gravitational force was chosen to act along the negative y-direction. The boundary conditions given by Eqs. (8.11)–(8.13) accounts for the fact that the y-component of the velocity field vanishes [Eq. (8.11)] at the free surface, shear forces are generated [Eq. (8.12)] at the surface of the melt pool due to a gradient in the surface tension σ , and a time-dependent heat flux Q_{Las} through the liquid-gas boundary (Eq. (8.13)) is induced due to the absorption of the laser energy with a rectangular ($6 \times 1 \text{ mm}^2$) intensity profile. The first coefficients η and P_{Las} in Eq. (8.13) are the absorption efficiency and the power density of the laser beam, respectively. The following term a_{Las} , given explicitly in Eq. (8.14), accounts for time-dependent part of the heating profile, which represents a surface heat source with rectangular cross-section traveling with the scanning velocity v_{Scan} of the laser beam in the z-direction. The last term of the equation describes the lateral variation of the profile. The coefficient f determines the sharpness of the step functions which represents the geometry of the intensity profile and is set to a value of 10^{-5} for the model calculations. While the forgoing parameters are physical or geometrical which can be determined experimentally, the value of the coefficient f is chosen by test runs in order to get a stable and convergent calculation procedure. The transport of the alloying material due to convection and diffusion within the melt pool can be expressed by:

$$\begin{aligned} & \frac{\partial(\rho C_{\text{Part}})}{\partial t} + \frac{\partial(\rho u C_{\text{Part}})}{\partial x} + \frac{\partial(\rho v C_{\text{Part}})}{\partial y} + \frac{\partial(\rho w C_{\text{Part}})}{\partial z} \\ & = \frac{\partial}{\partial x} \left(D \frac{\partial C_{\text{Part}}}{\partial x} \right) + \frac{\partial}{\partial y} \left(D \frac{\partial C_{\text{Part}}}{\partial y} \right) + \frac{\partial}{\partial z} \left(D \frac{\partial C_{\text{Part}}}{\partial z} \right) \end{aligned} \quad (8.15)$$

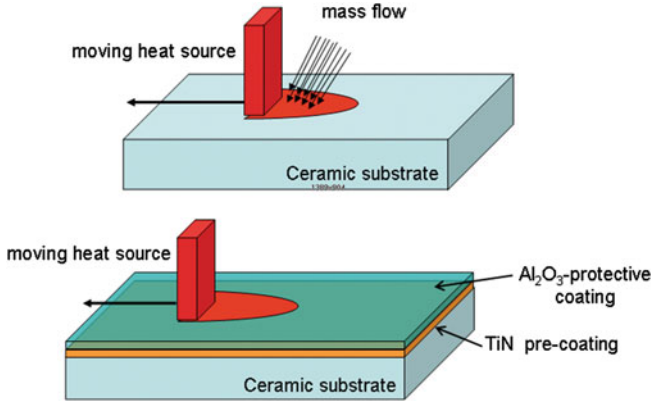


Fig. 8.1 Schematics of the model geometry for the one step injection process and two step pre-coating process

The moving melting-solidification boundary and the liquid–solid phase change have been considered in the model by implementing the enthalpy–porosity method [64, 65] into PHOENICS which has often been used to model the solid–liquid phase transformation on a fixed grid [66, 67]. In order to achieve this implementation additional source terms have been introduced in the momentum (8.7), (8.8), and energy equations (8.9) which take into account that the velocity components vanish in the solid phase and that the enthalpy changes due to the latent heat during the melting process. The details of this numerical technique are given in Ref. [68].

The differences in the model geometry used to simulate the pre-coating and the injection process are shown in Fig. 8.1. For the pre-coating model the substrate and the additive as well as the protecting layer have been arranged within the computational domain as shown in the figure and this distribution has been used as initial condition for the simulation. For the injection model a mass flow boundary condition has been introduced. Typical numerical results calculated by the three-dimensional FV-model for the case of the laser-induced dispersing of TiN into the ceramic substrate are shown in Fig. 8.2 for two different scanning velocities using the injection process. Within this particular calculation a value of 250 W has been used for the laser power and 250 and 750 mm/min for the scanning velocity, respectively. Contour plots (Fig. 8.2, left) are shown for the fraction of liquid F_{Liq} which characterizes the extension of the melting pool for values $F_{Liq} > 0.5$ and the position of the liquid–solid phase boundary by $F_{Liq} = 0.5$. The calculated distribution of the additive phase is shown by a contour plot of the model (Fig. 8.2, right) variable C_{part} which exhibits the volume fraction of the TiN phase.

The extension of the melting pool, and also the distribution of the additive material, exhibits different characteristics depending on process option used. In the case of the one-step process the shear forces at the surface of the melt pool induced by the finite temperature coefficient of the surface tension and the strong temperature gradient

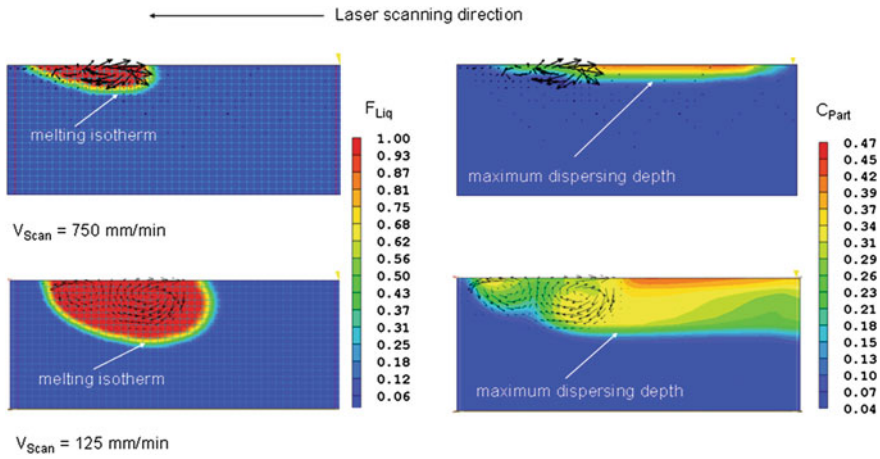


Fig. 8.2 Contour plot of the fraction of liquid F_{Liq} representing the extension of the melt pool and of the concentration of the dispersed particles C_{Part} calculated for two different values of the laser scanning speed

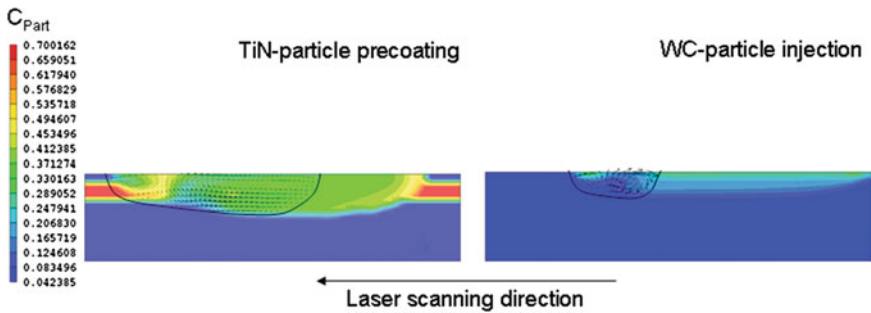


Fig. 8.3 Comparison of the particles distribution for the pre-coating (*left*) and the injection process for laser dispersed TiN and WC particles, respectively. The *black solid line* in the contour plots marks the solid-liquid boundary

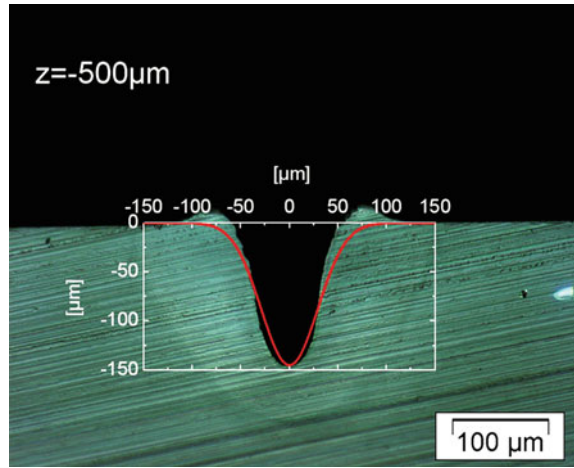
lead to stronger convection streams within melting pool compared to the pre-coating process. In the two-step process with the pre-coating and the protective overlayer the shear forces due to marangoni-convection are combined with a slow sedimentation of the second phase into the molten region of the substrate. The difference between both process options is shown in Fig. 8.3 for the case of using TiN as a preplaced powder and WC introduced into the ceramic substrate by particle injection. A much higher laser power density has to be applied in the pre-coating process in order to achieve the same melting depth compared to the injection mode, since the preplaced powder and the protecting layer are acting as a thermal barrier for the heat flow. The difference in the volume fraction is mainly due to the large differences in the density of both particle types.

8.4 Polymer Materials

8.4.1 Thermally Driven Ablation

Thermal laser ablation involves typically a series of steps encompassing initial absorption of the laser energy by the solid material, followed by local heating of the irradiated volume. The molecular weight or polymer chain length is a key-parameter for the ablation. Short polymer chains are volatile whereas longer ones melt. Material is therefore removed by vaporization and/or transport of melted material from ablated spots. Evaporation from the substrate results in an ablation plume (material vapour plasma) containing molecular fragments, ions, free electrons, neutral particles, and chemical products from reactions in the plume between the components of the plasma and the atmosphere. The laser-induced material vapor plasma can attenuate the laser beam. For small laser fluences the plasma could result in better thermal coupling between the workpiece and the laser beam in comparison to the absorption at the laser wavelength without plasma formation. Nevertheless, for high laser fluences the initiated plasma can result in a complete shielding of the workpiece from the laser irradiation preventing thermal coupling to the material. The ablation depth is determined by the ability of the substrate material to absorb the laser energy and is a direct function of the beam fluence (energy per unit area), wavelength, repetition rate, and pulse duration. CO₂ laser micromachining provides a flexible and low-cost means for the rapid prototyping and manufacturing of miniaturized polymer systems such as microfluidic chip devices. The best results were obtained by far with PMMA as it combines: (1) high absorbance in the infrared with low heat capacity and low heat conductance, which means that any absorbed heat results in a rapidly rising temperature; (2) thermal decomposition into volatile products (MMA monomer, carbon dioxide, and other gases), leading to the formation of clean structures which are not contaminated by degradation components; by contrast, most other polymers burn and produce large amount of soot, which can be difficult to remove. Nevertheless, different types of PMMA lead to different surface qualities after laser patterning. It was assumed that chemical additives of the different types of PMMA may influence the patterning results in a complex way [69]. For microfluidic Chip fabrication the laser patterning was investigated for different types of PMMA: HESA[®] VOS, PLEXIGLAS[®] XT, PLEXIGLAS[®] GS233 and PLEXIGLAS[®] 7 N. Plexiglas 7 N and Plexiglas XT are both extruded PMMA sheets while GS233 and HESA are both cast PMMA sheets. Cast sheets tended to form only a small amount of melt at the structured sidewall while the formation of pores and ripples in the ablated groove was dominating in comparison to extruded PMMA sheets. During patterning of extruded PMMA a significant bump at the edges of the generated grooves was formed. The different surface qualities may arise from different viscosities of PMMA melt phases. With decreasing melt viscosity the size of generated bumps increases. On the other side the pore formation is reduced in a less viscous melt film: Gaseous ablation products, such as MMA, generated by thermal decomposition of the polymer diffuse in the laser-melted film more easily than in

Fig. 8.4 Cross section of laser structured microfluidic channel. The shape of the channel was fitted with a Gaussian function. The focus position z was $500\ \mu\text{m}$ below the substrate surface
($P_L = 1.24\ \text{W}$, $v = 50\ \text{mm/s}$, number of laser scans: 4)



a less viscous melt film with decreased surface tension. In spite of this bump we have decided to use extruded PMMA (Plexiglas XT, Röhm) for the ongoing process development, because of the very good surface quality indicated by a defect-free structure with a small surface roughness.

A simple model for the energy balance (“absorbed laser energy” = “energy for temperature rise” + “energy for phase transitions” + “energy loss by heat conduction”) during the laser process delivers an expression for the ablation depth d as a function of laser power P_L and feed rate v of the laser beam [23, 69]:

$$d \propto \frac{P_L}{v} \quad (8.16)$$

Depending on the laser power and the feed rate the energy input and therefore the ablation depth varies. “ P_L/v ” is the so-called line energy and is a very important parameter in continuous wave ablation. The geometry of the channels can be described by a Gauss function. This is due to the Gaussian intensity distribution of the CO_2 laser beam. A slight contrast difference in the microscope image also shows that a heat affected zone (HAZ) with a width of about $100\ \mu\text{m}$ was formed along the contour of the generated channel (Fig. 8.4).

It was shown that the channel depth increases linearly with line energy as described by Eq. (8.16). Channel widths down to $30\ \mu\text{m}$ could be produced. An increase of aspect ratio at constant channel width can be obtained by repeating the ablation process without changing the laser process parameters as shown in Fig. 8.5.

The channel width shows a slight dependence on line energy. Nevertheless, in order to obtain defined aspect ratios for various channel widths, in general an aspect ratio of 1, the focus diameter of the laser beam at the polymer surface has to be changed. For this purpose the focussing lens or the focus position could be adjusted. The variation of focus position and an appropriate selection of line energy were much more flexible in comparison to a complex and time-consuming replacements

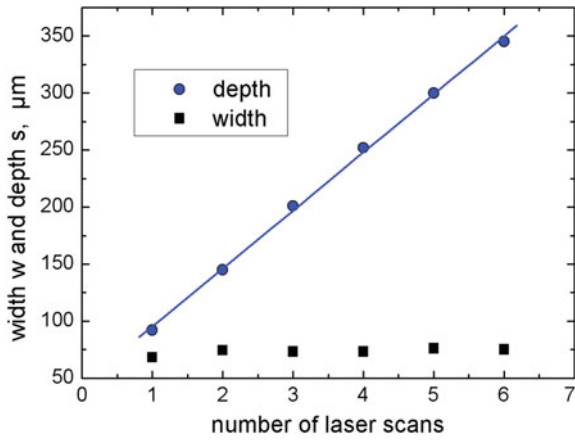


Fig. 8.5 Channel depth and channel width as function of number of laser scans ($P_L = 1.32 \text{ W}$, $v = 50 \text{ mm/s}$)

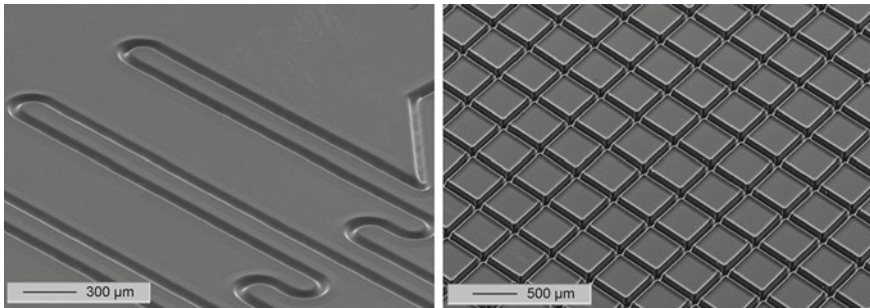


Fig. 8.6 SEM images of laser structured micro channels in PMMA

of focusing lenses. For an aspect ratio of 1 the parameter field for channel widths of $50 \mu\text{m}$ up to $200 \mu\text{m}$ was determined [2]. As an example, for the fabrication of fluidic channels with a width of $100 \mu\text{m}$ a focus position of $z = -500 \mu\text{m}$ and a line energy of 19.5 J/m should be adjusted. The high reproducibility of the patterning was very impressive. The average deviation between the fabricated cross-section areas A and the desired cross-section areas of micro channels was better than 3%. As an example, Fig. 8.6 shows microfluidic structures in PMMA by applying laser direct writing with single-mode CO_2 laser radiation.

8.4.2 Cold Laser Ablation

Material damage achieved on the target is determined to a major extent by the heat affected zone (HAZ). From an application standpoint, thermal damage to the sur-

rounding material needs to be minimal as it deteriorates spatial resolution and quality of ablation. Therefore photochemical processes leading to “cold” ablation are most desirable. With new laser sources (ultraviolet (UV) laser, ultra-short pulsed laser), ablation of polymers with no thermal damage of surrounding material and reduced debris formation is possible, hence leading to high accuracy and improved lateral resolution. In general, the high photon energies of UV lasers are capable of direct bond breaking in an organic material which strongly absorbs at the wavelength of the laser emission. This leads to ablative photodecomposition, a process distinct from thermal ablation in which the laser primarily heats the material. Photochemical etching is a relatively ‘cold’ process with minimum collateral thermal damage to the substrate; longer wavelengths mainly initiate temperature rises that will first melt and then decompose the material, leaving a void in the workpiece. In addition to machining by melting or vaporization, most polymers can also be finely micro-machined by photolytic decomposition at wavelengths below about 300 nm. In fact, most of the works on polymer ablation have concentrated on the application of UV lasers, which enable the removal of material by vaporization, without going through a melting phase. UV lasers, excimer, and frequency tripled or quadrupled Nd:YAG lasers, which are typically operated in pulsed mode ionize and decompose polymer materials. High energy photons in the UV range with wavelengths between 157 and 355 nm are highly absorbed by many polymers inducing efficient interaction with matter, without the necessity to add chromophores in the polymer matrix to induce efficient photoabsorption. Excimer lasers and frequency tripled or quadrupled Nd:YAG solid-state lasers are used depending on the absorption characteristics of the polymers. The capability of an UV laser beam to ablate a polymer depends on the absorption characteristics of the polymer at that wavelength (single-photon absorption where the photon energy is near the material bandgap energy). The short wavelength is linearly absorbed in the top layer of the polymer to a depth determined by the effective absorption coefficient α_{eff} of the material, as obtained from Beer-Lambert’s law. It is important to mention here that the Beer’s law is normally used without ablation. Therefore, for the ablation regime, an “effective” absorption coefficient needs to be taken into account which is determined by the relation between the ablation rate R and the laser fluence ϵ [70]. For small laser fluences (typically $\leq 1 \text{ J/cm}^2$) the ablation rate R increases with the logarithm of the laser fluence ϵ as described by

$$R = \frac{1}{\alpha_{\text{eff}}} \ln \left(\frac{\epsilon}{\epsilon_{\text{th}}} \right) \quad (8.17)$$

where, ϵ_t denotes the ablation threshold and α_{eff} is called “effective absorption coefficient”.

For laser fluences of about 1 J/cm^2 up to 2 J/cm^2 saturated excimer laser absorption is observed with

$$R = \frac{1}{\alpha_{\text{eff}}} (\epsilon - \epsilon_0) \quad (8.18)$$

where, ε_o denotes a characteristics laser fluence usually not equal to the threshold laser fluence. For $\varepsilon >> 2 \text{ J/cm}^2$ the ablation rate in general tends to saturate because of laser beam attenuation by generated plasma plume. An overall description of the laser ablation rate R as function of laser fluence ε was found by Pettit et al. [70] based on the single-photon absorption and under the assumption that the decay time of photolytic excited electronic and/or vibrational states is much larger than the laser pulse duration:

$$R = \frac{2}{\rho_0} (\varepsilon - \varepsilon_{\text{th}}) + \frac{1}{\rho_0 \sigma_1} \ln \left(\frac{1 - \exp(-2\sigma_1 \varepsilon)}{1 - \exp(-2\sigma_1 \varepsilon_{\text{th}})} \right) \quad (8.19)$$

where σ_1 denotes the single-photon absorption cross-section and ρ_0 is the density of absorbing constituents (“chromophores” in organic polymers).

σ_1 and ρ_0 are associated with the absorption coefficient α via

$$\alpha = \rho_0 \sigma_1 \quad (8.20)$$

For a pure single-photon absorption process the optical absorption coefficient α can be approximated by the effective absorption coefficient α_{eff} . For 248 nm laser wavelength and the polymer polycarbonate (PC) the single-photon absorption model and Eq. (8.19) fits very well as shown by Fig. 8.7. For PC with a material density of 1.2 g/cm^3 and 254 atomic mass units per monomer the monomer density can be calculated to $2.8 \times 10^{21} / \text{cm}^3$. With $\rho_0 = 1.6 \times 10^{22} / \text{cm}^3$ from Fig. 8.7 this means that effectively a number of 6 chromophores or rather absorption centres per monomer are responsible for the interaction with 248 nm laser radiation. The electronic transitions caused by the absorption break chemical bonds in the large molecules typical of polymer and lead to smaller (often gaseous) molecular fragments. Since the smaller molecules have lower density, the irradiated volume expands rapidly, producing a shock wave, which causes photoablated decomposition products to be ejected leaving a photoablated cavity. A characteristic of the process is that much of the excess energy is carried away in the form of kinetic energy by the ejected material. The thermal impact to the sample surface is drastically reduced, an important point for thermally delicate materials, and therefore this process is called “cold ablation”. A rough estimation of the start of the ablation process will be given by the lifetime of the excited states (e.g., 35 ps for polyimide @355 nm, [71] whereas a rough estimation of the “ablation time” is given by the laser pulse width. Shielding of laser energy can play a major role in ablation. The laser-induced material vapor plasma can attenuate the laser beam and shield the laser energy, reducing the interaction time. Therefore, an appropriate laser fluence should be selected in order to reduce the shielding effect and to increase ablation efficiency. This was investigated in detail for polymers in Schmidt et al. [72].

Photochemical ablation leads to the possibility of machining microstructures with high dimensional accuracy and reduced defects in the surface layer in comparison to a thermally driven ablation process (Fig. 8.8).

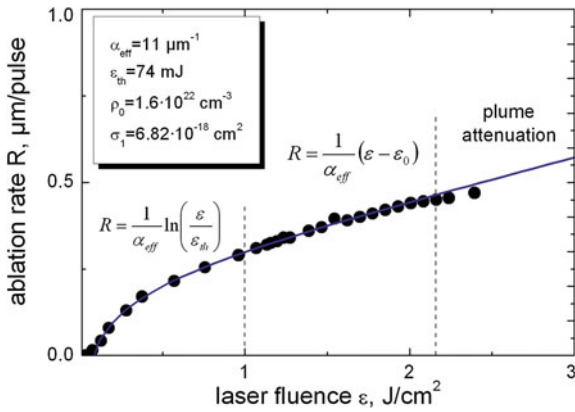


Fig. 8.7 Ablation rate for polycarbonate (PC) as function of laser fluences?, ρ_0 denotes the population density in the ground state, σ_1 denotes the single-photon absorption cross-section (laser wavelength 248nm)

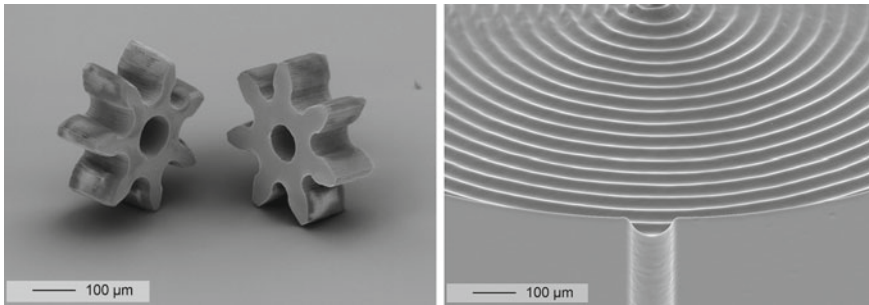


Fig. 8.8 Left: SEM image of gear wheels made of polyimide obtained by laser cutting (foil thickness 125 μm, Nd:YAG wavelength 355 nm, pulse width 400 ps, laser repetition rate 1,500 Hz). Right: SEM image of microchannels in PMMA fabricated by excimer laser radiation (wavelength 248 nm, pulse width 5 ns, laser repetition rate 500 Hz)

8.4.3 Modification

Laser can be used either to remove materials or to induce material modification, i.e., to change chemical, optical, and mechanical properties of the material remaining after ablation [73]. Laser-induced surface modification can be observed below, nearby, and above the ablation threshold. Below the ablation threshold surface modification can be initiated by photolytically driven reactions, e.g., by photo-oxidation or photo-bleaching. Nearby the ablation threshold the change of surface topography plays an important role, e.g., with respect to the wettability and surface energy. Above the ablation threshold laser-induced surface modification (chemical modification) or laser-induced defects (pores, cracks) can be observed in dependence of material and laser parameters.

Laser-induced surface modification of polymers provides a unique and powerful method for the surface modification of polymeric materials without altering their bulk properties. Concerning applications in bioengineering and biotechnology, the microscale topography has an influence on a number of properties such as wetting properties and cell behavior. Therefore, the design of material surfaces determines the success of artificial devices in contact with biological systems. Bremus-Köbberling et al. [74] uses laser wavelength of 193 nm and laser fluences of 0.8–1.5 J/cm², which is clearly above the ablation threshold of the treated polymers. They could further increase the water contact angle of hydrophobic PDMS up to 150° with laser generated microripples on the surface while hydrophilic polymers such as PEEK reaches contact angles < 5° after laser patterning. It was shown that the change of wettability by this type of laser processing could be used to control cell growth. Another approach is to control the wettability by laser material modification nearby the ablation threshold as demonstrated by Pfleging et al. [11] for polystyrene (PS). It was shown that at laser fluences of 90 mJ/cm², the wettability can be switched between superhydrophobic and superhydrophilic only by changing the processing gas. With oxygen as processing gas and for moderate laser pulse numbers the contact angle nearly reaches complete wetting, while with He as processing gas an oxidation of the surface can be suppressed and the topographical surface change lead to a lotus – like behavior with contact angles of nearly 160°. Nevertheless, it was further observed that cell adhesion of murine fibroblast cells (L929) is significantly improved by laser modification at very low laser fluences (2–6 mJ/cm²). X-ray electron spectroscopy (XPS) analysis shows that this effect is due to the formation of carboxyl groups. Laser fluences above 10 mJ/cm² lead to a decomposition of these functional groups and therefore no further cell adhesion was observed. This type of local photo-oxidation of polystyrene and subsequent protein and cell adhesion is independent of laser pulse length of 5 or 19 ns. It was shown that the control of biocompatibility can be realized with high lateral resolution by using mask imaging methods and excimer laser radiation. Single cells as well as cell clusters (Fig. 8.9, left) and cell meshes (see figure, right) can be deposited with high accuracy on polymer surfaces. The most promising approach for biological and microfluidic applications is the successful combination of laser structuring and laser-induced photo-oxidation without changing the processing chamber and laser source. This was successfully demonstrated in [7] for the development of advanced patch clamping devices used for pharmaceutical applications [75, 76].

8.5 Ceramics, Glass–Ceramics, and Glasses

8.5.1 Laser Patterning

8.5.1.1 Glasses

Glass has excellent chemical, optical, and thermal properties suitable for applications in micro- and nanotechnology. State of the art of laser micropatterning of

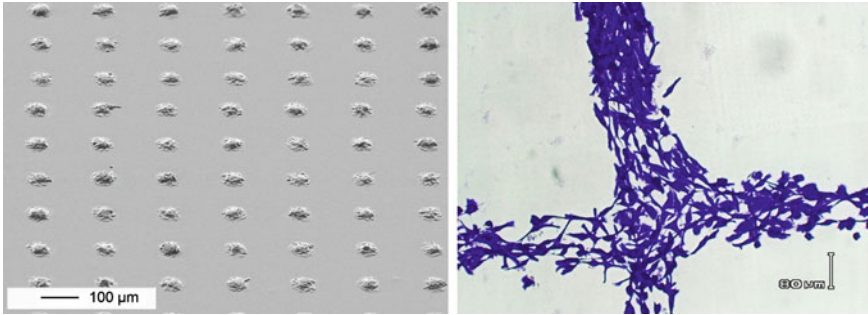


Fig. 8.9 *Left*: SEM image of laser modified polystyrene surface after adhesion of murine fibroblast cells (L929); *right*: microscope image after L929 cell cultivation on laser modified PS Petri dishes

glass is photolithography and wet-chemical etching. For a flexible patterning of glass via direct-writing processes an appropriate use of laser methods for ablation, cutting, and drilling is investigated. For glass material such as quartz, main challenges arise because of the high brittleness and mechanical-thermal properties which in general leads to crack formation during laser ablation or melting and re-solidification. Therefore, the use of “cold ablation” processes enabled by short-pulsed UV-laser radiation or ultrashort laser pulses is more and more investigated [77–80]. However “cold ablation” means always small ablation rates and therefore a significant increase of material processing time. A significant decrease of processing time is possible by an appropriate use of CO₂ laser radiation. CO₂ laser radiation enables only a thermal-driven ablation process. For a crack-free ablation the glass substrate temperature should be increased up to 200°C during laser patterning [81]. In our recent approach the crack-free ablation of quartz was also realized at room temperature. For this purpose the ablation was performed with a CO₂ laser system which operates in Gaussian mode (Synrad, Firestar v40). Laser processing gas is argon or nitrogen. The used average laser power is smaller than 20 W and scanning velocities during ablation and cutting are in the range of 1–100 mm/s. Depending on the laser power and the feed rate the energy input and therefore the ablation depth varies as described by Eq. (8.16). With decreasing line energy P_L/v the dimension of the heat affected zone but also the ablation depth and the channel width decrease (see Fig. 8.10). In order to get different aspect ratios or if larger channel depths at fixed channel widths are desired one has to repeat the ablation scan process several times. Under optimized conditions it is possible to generate channel structures with any channel width within the 40–150 μm interval. The use of nitrogen as processing gas enables higher ablation rates and an improved surface quality in comparison to oxygen or air as processing gas. With an appropriate laser scan process strategy channel structures (Fig. 8.11, left) as well as large area patterning are possible. The different diameters of holes presented in Fig. 8.11 (right) were obtained by changing the focus position. The crack formation was completely suppressed. The CO₂ laser process for

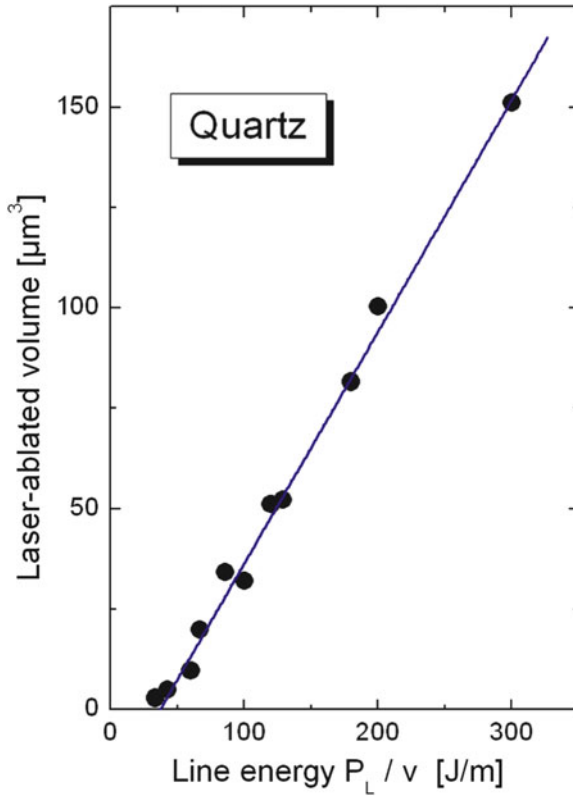


Fig. 8.10 Laser-ablated volume of quartz measured for a channel with a length of 1 mm as function of line energy (laser wavelength 10.6 μm , $P_L = 3\text{--}9\text{ W}$, $v = 10\text{--}90\text{ mm/s}$, processing gas: N_2)

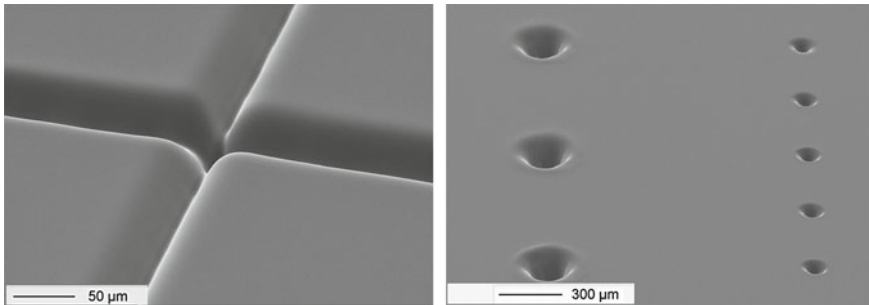


Fig. 8.11 SEM images of CO_2 laser structured quartz; channels (*left*) and holes (*right*)

patterning of glass surfaces was used for the fabrication of adaptive membrane lens systems [82].

8.5.1.2 Ceramics

With q-switch Nd:YAG laser radiation (wavelength 1,064 nm, pulse length 100–200 ns) one obtains relatively rough ceramic surfaces even with optimized laser and process parameters ($R_a = 0.8 \mu\text{m}$ and $R_z = 11.2 \mu\text{m}$) [83]. On the other side, laser ablation of ceramics with UV-laser radiation leads to a significant improvement of surface quality [17]. This is caused by two aspects: First the improved laser beam absorbance at short wavelengths and second the high laser power densities by using short laser pulses which leads to a more effective sublimation and a significant decrease of melt formation. For this purpose the ablation of ceramics (Al_2O_3 , and ZrO_2) was investigated with excimer laser radiation (193, 248 nm, pulse length 20–25 ns) and UV-Nd:YAG laser radiation (355 nm, pulse length 500 ps). Figure 8.12 shows the laser ablation of ceramics for different types of laser radiation sources. For excimer laser radiation with pulse length in the ns-range the ablation rate increases linearly with laser fluence and for laser fluences smaller than 5 J/cm^2 the ablation rate is smaller than 80 nm per pulse. The ps-laser ablation enables significant higher ablation rates for laser fluences above 4 J/cm^2 . Nevertheless, for large area patterning or for the fabrication of curved shapes the use of excimer laser radiation is most favored. For low laser fluences $< 2 \text{ J/cm}^2$ the surface roughness at the bottom of the laser patterned area is similar to the roughness of the ceramic substrate ($R_a = 1\text{--}2.5 \mu\text{m}$). For laser fluences $> 2 \text{ J/cm}^2$ the average surface roughness is in the range of $R_a = 180\text{--}200 \text{ nm}$ ($R_z = 1.0\text{--}1.2 \mu\text{m}$). Excimer laser radiation enables a smoothing of the ceramic surface. For a 355 nm laser wavelength the beam penetration depth into the material is larger than for 248 or 193 nm. Furthermore, for 355 nm the laser pulse length is significantly smaller and the maximum laser fluence could be significant higher in comparison to 193 and 248 nm. This means that the maximum laser pulse power intensity is increased by a factor of about 100 in comparison to the used excimer laser radiation. An increased absorption length and a significantly higher laser power intensity lead to an increase of the ablation rate (Fig. 8.12). Additionally, it is expected that for short laser pulses and high laser fluences the formation of melt could be suppressed. In fact, Fig. 8.13 shows that for a laser pulse length of 500 ps @ 355 nm no melt or debris formation on ceramic surfaces could be observed. It has been established that the microstructuring of ceramic surfaces significantly improves their tribological properties [84].

8.5.2 Modification of Surfaces by Dispersing and Cladding

Among the variety of surface engineering techniques laser dispersing, alloying, and cladding have some outstanding features, which allow for the modification of larger surface areas as well as the engineering of localized regions with a spatial resolution of several micrometers. These laser supported methods are characterized by a thermal interaction between the laser beam, which acts as a sophisticated heat source applied for thermal treatment, and the surface of the substrate. This heat input may

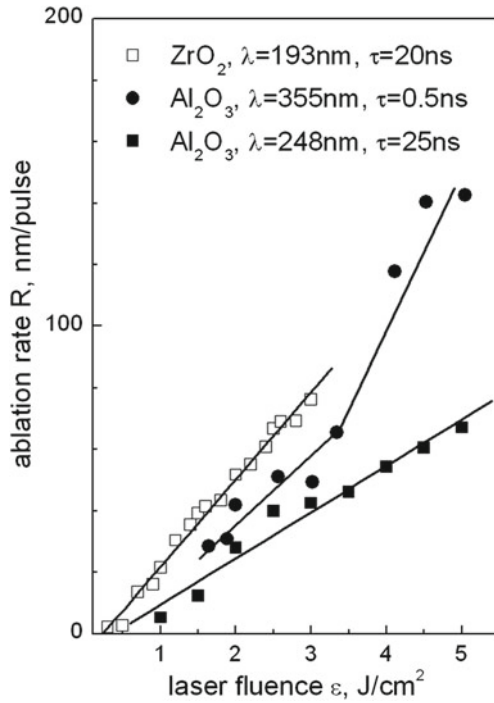


Fig. 8.12 Laser etch rate of Al_2O_3 and ZrO_2 as function of laser fluence for different laser wavelengths λ and laser pulse widths τ

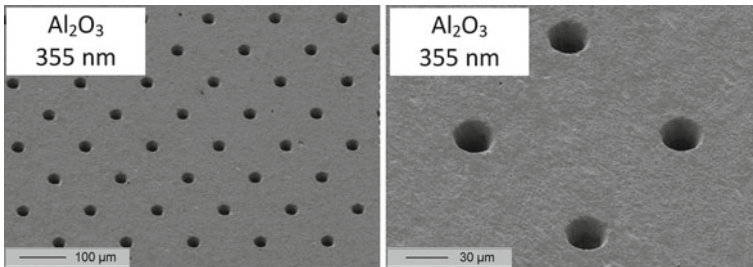
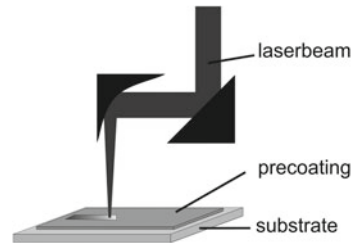


Fig. 8.13 SEM images of laser patterned ceramic Al_2O_3 for laser wavelength 355 nm and pulse width 500 ps

lead to a more or less extended melt pool, in which second phase particles can be introduced in order to modify the physical properties. Depending on the extension of the melt pool the second phase can be simply dispersed without a reaction or alloyed with the matrix material during the introduction of the particles into a surface near region or a cladding layer is grown on top of the original surface. As a result of their poor thermal and mechanical properties, the use of single-phase commercial ceram-

Fig. 8.14 Principle of the laser process used for the surface modification



ics in technical applications is restricted. The introduction of a second phase, which can be selected in order to optimize these properties, can lead to a reinforcement of the mechanical strength and also to an enhancement of the thermal conductivity. Different thermal processing techniques can be applied to achieve this property modification by producing ceramic-metal composites with metal particles embedded in a continuous ceramic matrix. Among these methods, laser supported modification techniques have the advantage that mechanical and tribological properties [28, 85] can be improved and the thermal and electrical conductance can be adjusted [30, 86] while the property modifications are restricted to a localized surface area leaving the bulk of the ceramic in its original state. It can be expected from published data of the properties of nano-scaled composite materials [87–89] that laser dispersing of nano-particles may lead to metal-ceramic composites with a different microstructure and changing properties.

The principle of the process is shown in Fig. 8.14. The laser beam of a high power CO₂ laser is used to heat the surface of the ceramic above the melting point. Second phase particles are introduced into the localized melt pool. After the solidification a metal-ceramic composite has been generated within the laser irradiated trace. This can be achieved by using a process with a pre-placed powder (see Fig. 8.14), in which the ceramic substrate is coated with a powder layer before the laser process.

By applying the laser process the coated ceramic is re-melted locally by the laser beam and the particles are incorporated into the ceramic substrate by a combination of sedimentation and convection within the melt pool. During the laser process, the ceramic substrate is heated to avoid thermally induced cracking. In order to generate conducting lines the substrate is moved relative to the laser position with a constant velocity. For most experiments a CO₂ laser ($\lambda_{\text{CO}_2} = 10.6 \mu\text{m}$) with a maximum power of 400 W was used. The laser beam was focused to a minimum spot size of about 300 μm for the generation of electrically conducting lines in the surface of the ceramic substrate. In order to determine the changes of the heat transport properties larger areas were modified by using a laser intensity profile of $6 \times 1 \text{ mm}^2$, which allowed the production of laser modified tracks with a width up to 6 mm. The laser power was varied between 5 and 50 W. The travelling velocity of the laser or the substrate was adjusted between 125 and 500 $\text{mm} \times \text{min}^{-1}$. The glass ceramics LTCC [90] (Low Temperature Co-fired Ceramics) was used in the laser modification experiments. Nano-particles of different metal oxide powders (CuO and WO₃) with

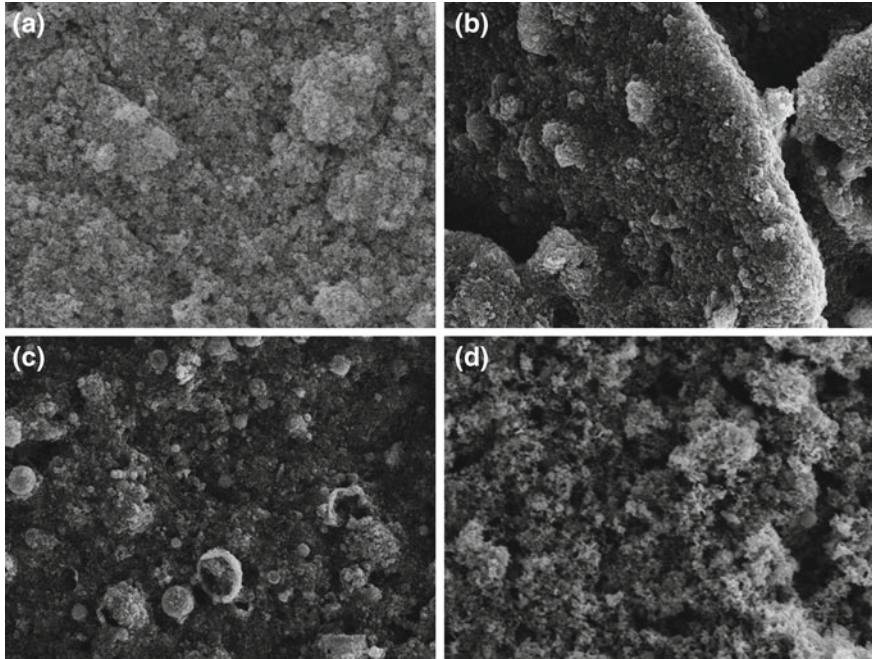


Fig. 8.15 SEM-images of the metal-oxide powders CuO, CuAl₂O₄ and WO₃, respectively. The nano-scaled Cu-powder is shown for comparison

an average particle (Fig. 8.15) size ranging from 40 to 100 nm were added during the laser-induced remelting process.

In order to understand the heat and mass transport during the dynamic melting and solidification and also to optimize the process parameters, different characterization methods were applied to the ceramic materials before, during, and after the laser induced modification process. During the laser process a thermal-imaging system was used to monitor the transient temperature distribution and the heat flow on the ceramic surface. Microstructures of the obtained conducting lines were studied by light and scanning electron microscopy (SEM), and the modified chemical composition was qualitatively analyzed by energy dispersive X-rays (EDX). The thermophysical properties of the ceramic substrates were characterized using standard measurement techniques: The thermal diffusivity was measured by a laser flash method and the specific heat by differential scanning calorimetry (DSC). The thermal conductivity λ was calculated using the measured property values [91] by the following equation:

$$\lambda = \alpha \cdot c_p \cdot \rho \quad (8.21)$$

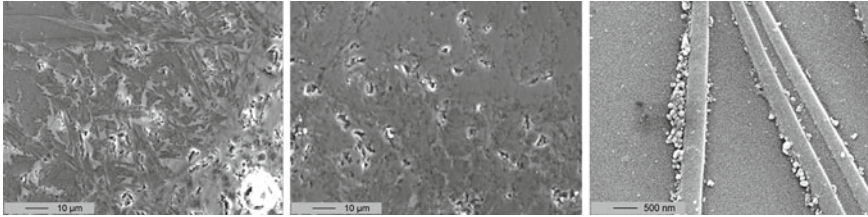


Fig. 8.16 SEM-images of laser alloyed LTCC using CuO-powder as additive: LTCC substrate modified with CuO-particles with an average diameter of $2\ \mu\text{m}$ (*left*), LTCC substrate alloyed with CuO nano-particles with an average size of $60\ \text{nm}$ (*middle*), detail of the nano-alloyed LTCC (*right*)

where, α is the thermal diffusivity, c_p the specific heat, and ρ the density, respectively. The electrical conductivity and the surface resistance were determined by a standard two-point measurement technique. The microstructure of the laser alloyed LTCC substrate using micro- and nano-scaled CuO particles, respectively, as second phase materials is shown for comparison in Fig. 8.16. The LTCC-matrix materials can be recognized by the dark gray areas in the SEM micrographs whereas the CuO phase appears as light gray region within the glass-ceramic matrix.

In both cases the glass-ceramic substrates were laser alloyed starting from a pre-placed powder layer with the same thickness of about $200\ \mu\text{m}$. However, the volume fraction of the CuO nanophase appears to be lower than for the system modified with the microparticles. It is less than 20% for CuO nanophase and about 30% for the CuO microphase. The microstructure of CuO nanophase exhibits specific features (Fig. 8.16, right): CuO particles or agglomerates with a typical size of about $100\text{--}200\ \text{nm}$ are arranged along strip-like shaped CuO-rich phases with a width of $400\text{--}500\ \text{nm}$ within the glass-ceramic matrix.

The thermal conductivity changes, which are a result of the laser alloying process of the glass-ceramic substrates, are shown in Fig. 8.17. The laser alloying leads to an increasing thermal conductivity over the measured temperature range compared to the as-received material. Temperature dependence of this thermophysical property is also affected. The values of the alloyed substrates are raised about 10 to 20% at room temperature with a tendency to decrease at higher temperatures in the case of the micron-sized powder and with a nearly constant behavior in the case of the nanoparticles. Although the volume fraction of the nanoscaled phase is much lower than that of the substrate alloyed with the microparticles, the thermal conductivity values are significantly higher. This result is surprising since it could be expected that the gain in thermal conductivity should be scaled the volume fraction of the second phase.

Laser Cladding

The cross-sections of the modified laser tracks showed different geometries depending on the process parameters. Figure 8.18 shows schematic pictures about transition from a developed melt pool to the appearance of a laser clad layer with decreasing laser power. High laser density resulted in a large melt pool, localized at

Fig. 8.17 Thermal conductivity of laser alloyed LTCC

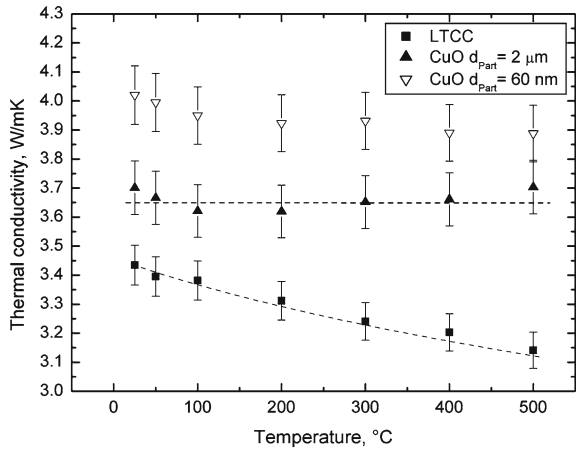
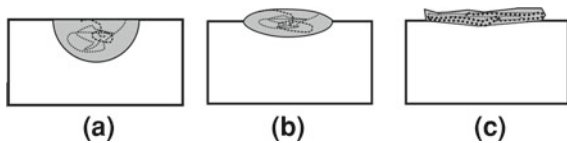


Fig. 8.18 Schematics of the melt pool development and the arrangement of the cladding layer with changing laser power, which decreases from a to c



the surface of the substrate with a thickness up to 300 μm (Fig. 8.18a). As a consequence of a reduction of laser density a smaller melt pool was developed, especially the thickness was reduced (Fig. 8.18b). In both cases the added material could be observed inside the solidified melt and a convex bow of the modified area could appear. A further reduction of laser density resulted in a laser track which was characterized by only a very small amount of melted substrate but a compacted layer on the substrate surface (Fig. 8.18c).

Figure 8.19d shows a SEM image of a WO_3 layer located at the top of the ceramic surface like in the principle sketch in Fig. 8.18c. The magnification in Fig. 8.19e shows a granular microstructure and Fig. 8.19f the EDX-analysis. Grains of tungsten oxide (pos. 1) were developed with sizes in the range of some microns. They were embedded in a matrix (pos. 2) which exhibit a significant amount of aluminum, which is an indication for the infiltration of substrate melt.

A similar behavior could be recognized for laser tracks alloyed with CuO. Depending on laser power a compacted CuO layer on the top of the ceramic surface or a melt pool with a fine dispersed CuO phase could be fabricated. Figure 8.20a, b, c shows SEM-images of a laser track produced with a reduced laser density due to a defocused laser beam. The CuO particles with an initial average particle size of 30 nm were melted by the laser beam and crystallized. In parts a dendritical solidification could be observed. Solidified substrate material could be found inside the CuO layer. Whereas the light-gray phase (1) in Fig. 8.20b consisted mainly of copper and oxygen, a significant amount of aluminum, silicon, and calcium (principal constituents of the LTCC) that could be detected by EDX-analysis in the dark-gray

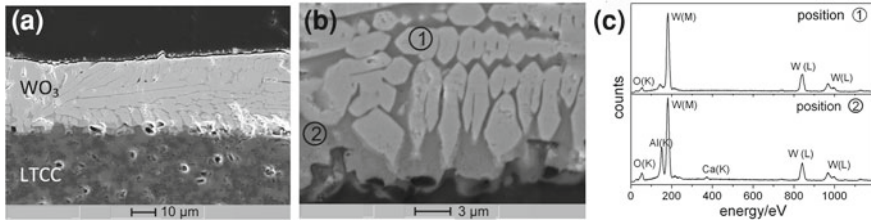


Fig. 8.19 SEM-images of laser clad LTCC with nano- WO_3 and the corresponding EDX-analysis of different elements of the micro-structure

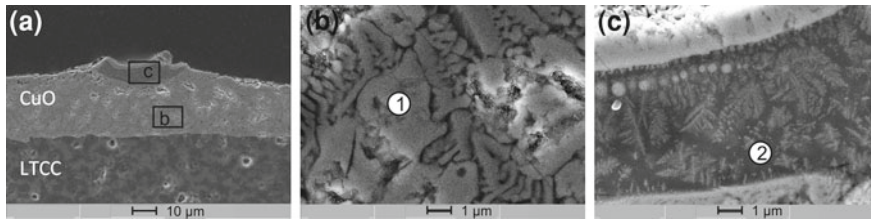


Fig. 8.20 SEM-images of a laser clad layer on *top* of a LTCC-substrate using nano-scaled particles of CuO as the second phase material

phase (2) at the top of the layer in Fig. 8.20c. The electrical resistance was measured on selected samples within a temperature range from room temperature up to 400°C . Typical track length was set to 1 cm and the contact was made by conductive paste of platinum. Because of the different geometries of the examined tracks the absolute values of the resistance could vary and the attention was focused on the temperature behavior.

The electrical resistance measurements of laser alloyed tracks on LTCC with nano- WO_3 -powder were carried out on wide tracks, because of the larger cross-section. In Fig. 8.21 (right) the measured values are displayed with a logarithmic scale for the resistance. Values lower than $20\text{ M}\Omega$, which is the upper detection limit of the measuring system, could be measured above 150°C . A further increasing of the temperature resulted in an exponential reduction of the resistance within the next 100°C . Accordingly the graph in Fig. 8.21 shows a steep linear decrease, which is followed by a section with a small negative slope for temperatures above 250°C . Repeated measurements showed slightly changed absolute values of the resistance but the same temperature behavior. The negative temperature coefficient of the resistance for the WO_3 /LTCC composite is typical for the conduction mechanism in semiconductors [92, 93]. Recently, the structure and the electron transport in WO_3 -nanorods grown on a mica substrate [94] were studied. The length, width and thickness of the nanorods varied in a range from 1 to $10\ \mu\text{m}$, 10 to 200 nm , and 1 to 50 nm , respectively. Typical values of the DC electrical resistance were found to be about 1 to $4\text{ M}\Omega$, which were measured on a single nano-rod using a special device. This value is about one order of magnitude lower than for the WO_3 layer produced by the laser

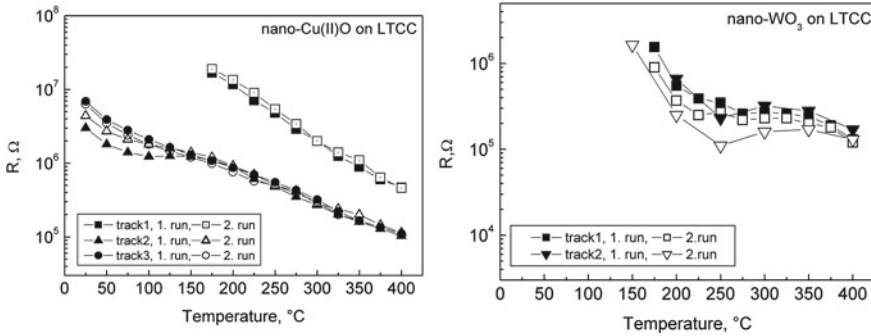
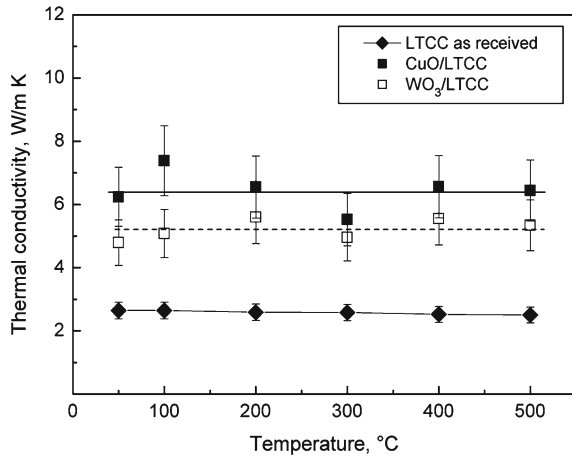


Fig. 8.21 Electrical resistance as a function of the temperature of the laser modified tracks with nano-scaled particles of CuO and WO₃

cladding process. For the copper-oxide tracks a resistance lower than 20 MΩ could be established already for room temperature (Fig. 8.21, left). Track 2 was a small track with a cross-section characterized by a CuO-layer on the top of the ceramic surface and track 3 was a wide one, with a significant part of the CuO located in a top layer. For both an identical behavior could be established with an exponentially decreased resistance for increasing temperature, which can be seen by the nearly linear decreased resistance for the logarithmic resistance, especially above 150°C. Track 1, which was characterized by a fine dispersed CuO-oxid phase inside a solidified LTCC-matrix showed a higher absolute value for the resistance. It could be measured first above 175°C and showed an intense decrease with increasing temperature, which could be described by a linear reduction of the logarithmic resistance with temperature but with a larger slope compared to track 2 and 3. The measured values of the CuO/LTCC tracks offer a good reproducibility.

In Fig. 8.22 the thermal conductivity of the cladding layers are shown as function of temperature in comparison with the as-received LTCC. These data have been extracted from the integral thermal conductivity measurements on the layer-substrate system by considering that the single thermal resistance of the cladding layer and the LTCC substrate summed up to an integral value which is given the inverse thermal conductivity times the total thickness. Since the thermal resistance or the thermal conductivity of the LTCC substrate is determined by separate measurements, the thermal conductivity of the cladding layer can be calculated. Within the observed temperature range the layer of nano-scaled CuO and WO₃, respectively, show a higher thermal conductivity compared to the LTCC substrate. For both systems the thermal conductivity is nearly constant over the whole temperature range. Consequently the difference between the nano-scaled cladding layer and the LTCC is more pronounced at higher temperatures, since the thermal conductivity of the LTCC tends to decrease with increasing temperature. Wang and co-workers [95] performed thermal conductivity measurements on tungsten oxide films with a thickness varying between 100 and 300 nm. They measured values in the range of 1.2–1.6 W/mK which is lower than our results by a factor from 4 to 5. This difference may be attributed to the

Fig. 8.22 Thermal conductivity of laser cladded LTCC



different microstructure of the thin film compared to the WO_3 /LTCC composite and may also be due to additional thermal boundaries between the nano particles in the film. Within this chapter we have studied the effects of laser alloying and cladding processes on the microstructure and properties of commercial glass ceramics using different additive materials with particle sizes ranging from 40 to 100 nm, respectively.

The modification of glass-ceramic substrates by laser alloying and cladding using nano-powders has induced significant changes with regard to the microstructure and the electrical conductivity. The laser modified tracks exhibit an exponentially decreasing surface resistance with increasing temperature. The resistance level, however, tends to be above the $10^5 \Omega$ range. The heat transport is also affected by the laser alloying of glass-ceramic substrates with nano powders and also by the laser processing of a cladding layer on top of the substrate. In both cases it could be shown that the thermal conductivity is strongly enhanced compared with the as-received substrate by using nano particles from different metal oxide systems.

8.5.3 Structuring and Annealing of Battery Materials

In laser processing of thin film battery materials or more specifically the electrode—cathode and anode—materials two different laser-based technologies are applicable. First laser structuring to modify the surface topography and, secondly, laser annealing to influence the grain size and to obtain the appropriate crystalline phase. In combination, laser structuring the adjustment of the material on a micrometer scale and annealing with grain sizes in the nanometer regime, a fine-tuning of material composition is possible.

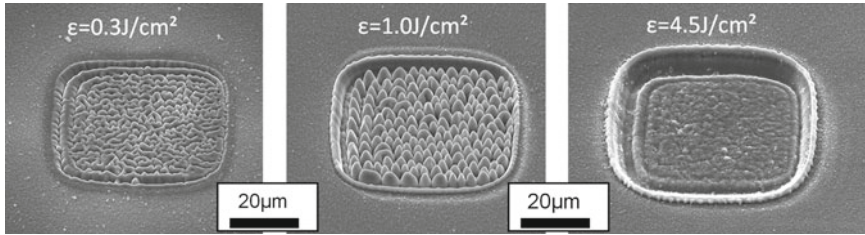


Fig. 8.23 SEM images of LiCoO₂ thin films treated with different laser fluences (wavelength $\lambda = 248$ nm)

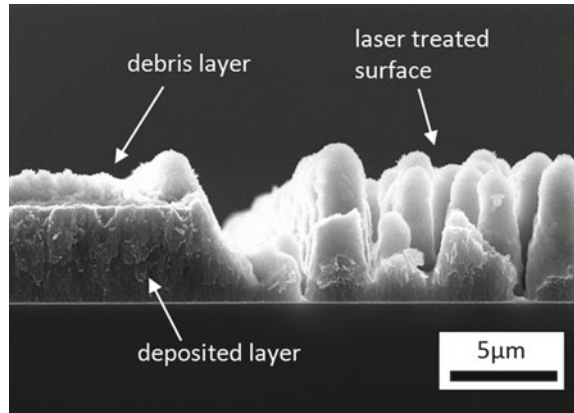
8.5.3.1 Laser Structuring

The objective of laser patterning is to enlarge the effective surface area of LiCoO₂ thin films clearly, in order to achieve a higher power density in thin film battery systems. Therefore, the ablation characteristics of LiCoO₂ thin films were investigated in detail. There are two possibilities of enlarging the surface through excimer laser ablation. The first one is to create defined patterns such as specific pores or columns by mask imaging. The second one is to modify the topology by laser ablation close to the ablation threshold of the material. Laser fluences above 2 J/cm² lead to a clear material removal on LiCoO₂ thin films leaving smooth surfaces while lower laser fluences cause cone-shaped surface structures. These structures can be formed in a wide range of fluences (Fig. 8.23). The material surface remains unchanged upon irradiation with small laser fluences below 0.3 J/cm². Higher laser fluences lead to formation of small pores (< 1 µm diameter) and worm-shaped structures. For laser fluences higher than 1 J/cm² isolated cone-shaped structures are generated. The height and number of cones decreases with higher fluences, leading to a smooth ablation above 2 J/cm². Figure 8.23 also shows the dimensions of the applied laser beam. In this case a rounded off quadratic beam shape with a length of 50 µm was used. Inside this area a homogenous laser fluence is present, which can be seen in the ablation area at a fluence of 4.5 J/cm². Merely, a slight elevation of the ablation at the edge of the ablation field is visible, which is typical due to diffraction effects at the edge of the mask.

Although the laser fluence is homogenous the conical structures form with random distribution. It could also be observed that a large amount of ablated material was re-deposited on the surface not only on the side of the laser structured area, but also on the ablated surface itself, leading to an increasing height of the conical surface structures (Fig. 8.24). On 3 µm thick thin film, structures with a height of > 5 µm up to 8 µm could be produced, leading to a surface area which is estimated to be 5–10 times larger than the as-deposited layer. Because of the re-deposition process the total amount of active material was only slightly reduced, a material loss of less than 15% can be obtained.

The formation of cone-like structures has already been reported in laser material processing, especially for polymers [96–98]. Other materials, e.g., metals [99–101],

Fig. 8.24 SEM image of a cross-section of laser structured LiCoO_2 thin film deposited on a silicon substrate (wavelength $\lambda = 248 \text{ nm}$, laser fluence $\varepsilon = 1 \text{ J/cm}^2$)



metalloids [102], or ceramics [103] showed conical surface structures when exposed to pulsed laser radiation with wavelengths ranging from the UV to the IR. Many different mechanisms for their creation are discussed:

- (1) Laser ablation can induce the localized formation of a surface layer, which in turn can act as a “shadowing layer” for the underlying material. In the case of polymers this can be formed by local carbon enrichment due to selective laser ablation in the material [98]. This “radiation hardening” leads to a local increase of the threshold fluence. The shadowing effect may also be caused by particle impurities in the bulk material [97]. This theory is often used to explain cone formation in polymers.
- (2) Since cone growth follows the direction of incidence of the laser beam, optical scattering may also occur [101]. With increasing incident angle the increasing reflectivity leads to the deflection of the radiation on the surface of the cones and increased absorption between cones [102].
- (3) Hydrodynamic mechanisms such as melt transfer may occur along the surface of the irradiated structures from liquid flow driven by surface tension gradients [99, 100]. Since with most materials the surface tension decreases with rising temperature, the material is transported from warmer regions to colder regions leading to growth of surface structures. For metals, where ablation is dominated by melting and vaporization this theory is often used [99, 100].
- (4) In the vapor phase deposition theory the material transport is accomplished by convective mass transport in the vapor phase rather than the liquid phase [103]. The height of the structures is linked to the height of the vapor cloud formed during ablation [102].

All these theories have in common that they require some kind of surface inhomogeneity, either inherent in the material or formed during the ablation process. These “cone seeds” grow with the ongoing ablation process to form the characteristic surface structures. LiCoO_2 thin films created with r.f. magnetron sputtering show

a widely varying ablation threshold [104]. At low laser fluences only a small portion of the material is removed leading to small holes, with increasing laser fluence more material is removed until single, free-standing cones remain (Fig. 8.23). Therefore, a shadowing mechanism seems to be most probable. Yet, this does not explain the extreme growth of the cones to heights significantly larger than the original film thickness. It should be considered that during the ablation process two particle species may be formed, light particles consisting of atom clusters which are removed from the surface rapidly, e.g., forming a shock wave, and large, slower particles re-deposited on the thin film surface as a debris layer [105]. Nevertheless, it was observed that the material vapor plasma dynamics influenced by using different types of processing gasses strongly control the cone growth. Structuring with a constant helium gas flow, for example leads to strong decrease of cone heights in comparison to those formed in ambient air or argon. It is however interesting that the re-deposited material forms a compact morphology. This may be explained by the formation of a melt phase during the ablation process.

In addition to the processes leading to formation of conical surface structures mask techniques can be applied to create defined patterns on thin film surfaces. Masks cut out of steel sheets with Nd:YAG lasers for example are applicable for this purpose. However, with this method no detached structures are possible and the resolution is limited by the thickness of the steel plate. Chromium/quartz masks are more suitable. In this technique a thin chromium film with a thickness less than 300 nm is deposited on a quartz substrate. The chromium film can be easily and precisely ablated using an excimer laser forming an individually designed mask which allows the creation of high resolution structures with high aspect ratios. For electrode material of lithium-ion batteries line and grating structures have shown the highest potential. This manufacturing method can be applied on LiCoO_2 if high energy densities compared to the cone formation process are used. Figure 8.25 depicts two examples of laser-generated line and grating structures with a pitch of 4 μm . The spacings between the structures can be formed < 500 nm. A promising new material for the anode side of a lithium-ion battery is SnO_2 with a specific capacity of up to 782 mAh/g, which is significantly higher than the conventionally used graphite with up to 372 mAh/g. However, the cycling stability is a mayor problem with SnO_2 -based anode materials due to the large volume changes during lithium insertion. The creation of detached surface structures allows compensation of the expansion. In SnO_2 thin films similar structuring methods as demonstrated in LiCoO_2 can be utilized. In addition to rounded conical structures microholes can also be manufactured (Fig. 8.26).

8.5.3.2 Laser Annealing

For the preparation of LiCoO_2 thin films, different methods, including pulsed laser deposition [106, 107], chemical vapor deposition [108, 109], sol-gel spin coating [110, 111], as well as r.f. magnetron sputtering [40, 112], have been applied. Yet commonly a post annealing process is necessary to create the high temperature phase

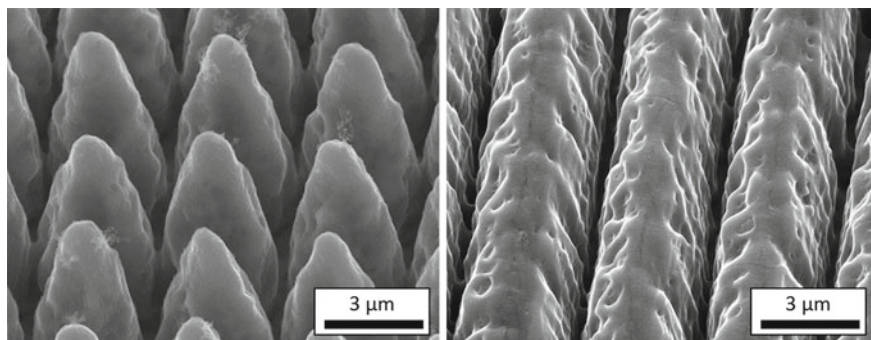


Fig. 8.25 SEM images of laser structured LiCoO_2 thin films ($\varepsilon = 3 \text{ J/cm}^2$)

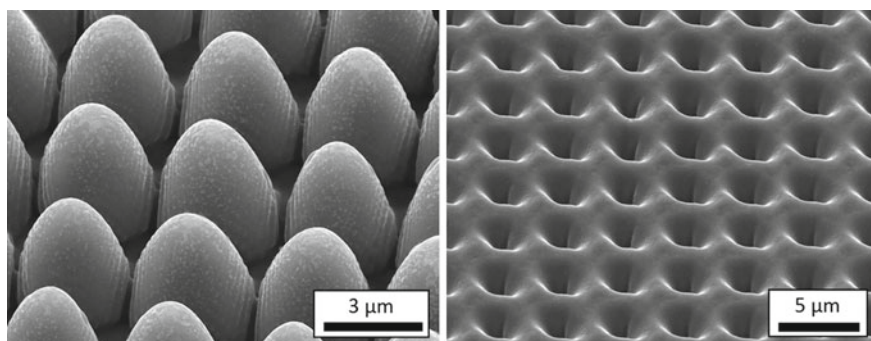


Fig. 8.26 SEM images of laser structured SnO_2 thin films (*left* $\varepsilon = 1 \text{ J/cm}^2$, *right*: $\varepsilon = 0.6 \text{ J/cm}^2$)

of LiCoO_2 (HT- LiCoO_2), which exhibits a high specific energy density of about 140 mAh/g and good capacity retention. Different annealing techniques, such as furnace annealing, have been already applied in order to change the crystalline structure, morphology, and electrochemical properties of LiCoO_2 thin films [113–115]. Laser annealing was applied to the thin films to create HT- LiCoO_2 . For the identification of the different phases of LiCoO_2 as well as possible contamination phases, e.g., Co_3O_4 , Li_2O , Raman spectroscopy is an appropriate tool. The Raman spectra of LiCoO_2 thin films laser annealed at different temperatures are shown in Fig. 8.27. The as-deposited layer shows two broad peaks at about 510 cm^{-1} and 600 cm^{-1} . After annealing at 400°C the two peaks have shifted to 482 cm^{-1} and 595 cm^{-1} which can be attributed to HT- LiCoO_2 [116]. With higher temperatures the intensity and the sharpness of the peaks increase. At wave numbers between 650 cm^{-1} and 700 cm^{-1} a relatively small, broad peak is visible. This can be induced by either CoO or Co_3O_4 with show spectra at 668 cm^{-1} and 691 cm^{-1} , respectively, and can be an indication of a slight lithium deficiency. Compared to conventional furnace annealing a large decrease of processing time using laser annealing is possible, resulting from the high heating and cooling rates. Additionally, opposite to furnace annealing

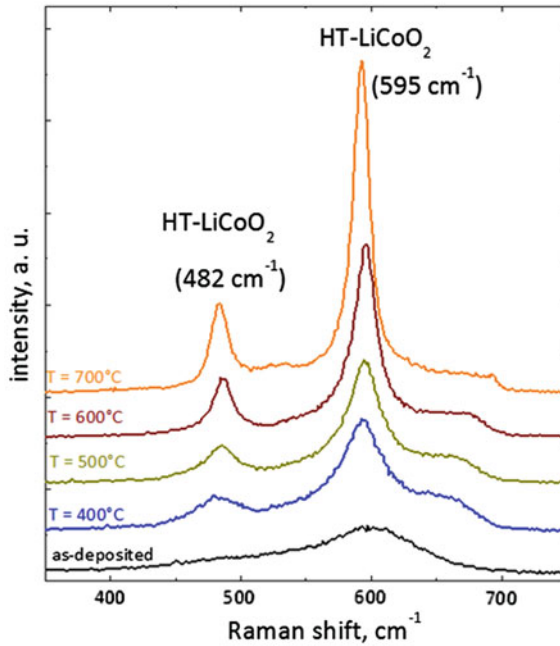


Fig. 8.27 Raman spectra of laser annealed LiCoO_2 thin films at different temperatures

no delamination of the films was encountered. Other annealing techniques have also been applied to LiCoO_2 , e.g., rapid thermal annealing (RTA) [114, 116, 117]. One of the main differences between RTA and laser annealing is the heat source, while RTA uses mainly incoherent halogen lamps, laser annealing utilizes focused laser radiation. Therefore, contrary to RTA, laser annealing can be applied locally and is scanned over the surface for large area applications. Additionally, the optical absorption coefficient of LiCoO_2 at the used diode laser wavelength of $\lambda = 940 \text{ nm}$ was measured to $\alpha = 0.5 \mu\text{m}^{-1}$, which means the laser power is absorbed in the first two microns of the surface. Therefore, the laser beam effectively heats up the thin film volume. The crystallization seems to be to be highest at 700°C , since the FWHM is lowest. Nevertheless, an additional important criterion is the grain size of LiCoO_2 . While the average grain size of the as-deposited layer, as shown in Fig. 8.28 (left), is about 20 nm, the grain size after laser annealing at 600°C has increased up to 50 nm (Fig. 8.28, middle), reaching a crystallite size of $> 100 \text{ nm}$ after annealing at 700°C (Fig. 8.28, right).

The formation of cracks was observed after the laser annealing process above annealing temperatures of 200°C . While the crack size stayed below 200 nm for thin films annealed at 600°C , crack widths larger than $1 \mu\text{m}$ could be obtained after annealing at 700°C . Yet, no delamination of the thin film was encountered after laser annealing. It is well known that Raman spectroscopy not only gives information about the phase, but also about the crystallinity [118]; therefore, the broad peaks

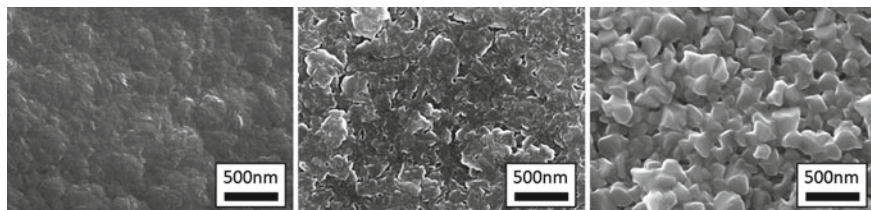


Fig. 8.28 Surface SEM images of LiCoO_2 thin films, as-deposited (*left*), laser annealed at 600°C (*middle*) and 700°C (*right*)

of the laser annealed, unstructured thin films may indicate crystal disorder or small crystallite sizes. This can be explained by the very low thermal conductivity of the free-standing cones. The laser generated heat dissipates very slowly which leads to a local temperature rise and consequently better conditions for crystallization. Laser annealing of unstructured thin films at 700°C leads to similar results (Fig. 8.27).

Both peaks corresponding to HT- LiCoO_2 show a reduced width compared to the unstructured film annealed at 600°C . The Raman spectrum of the structured thin films annealed at 700°C , however, indicates the formation of a new crystalline phase. The peaks at 520 and 693 cm^{-1} correspond to the F_{2g} and A_{1g} modes of Co_3O_4 , respectively [119]. This may be caused by a lithium deficiency in the material, which can be attributed to the evaporation of lithium oxide. Similar results were obtained by furnace annealing above 850°C , where the formation of Co_3O_4 was verified by XRD measurements [120]. Additionally, the laser structured thin films were analyzed by SEM after the thermal treatment. The topology of the cones with respect to annealing temperature is shown in Fig. 8.29. In comparison to thin films annealed at 600°C (Fig. 8.29, left), thin films annealed at 700°C (Fig. 8.29, right) show significant changes in shape and surface topography as well as significant reduction of cone sizes. This might be due to a laser induced surface re-melting. Electrochemical cycling was applied to laser-structured and unstructured thin films. The theoretical capacity of 140 mAh/g was used for the calculation of the C-rate. The C-rate is a measure of the rate at which a battery is charged / discharged relative to its maximum capacity. A “1C” rate means that the discharge current will discharge the entire battery in 1 hour. To analyze the high power capability of the samples, the charging current was increased stepwise. After 11 charge/discharge cycles at C/20 the current rate was increased to C/5 for another 11 cycles. Finally 100 cycles at 1C were measured. The results are shown in Fig. 8.30. The unstructured films showed a higher initial discharge capacity compared to the structured and laser annealed films. After 11 cycles at the lowest charging rate the capacity dropped to 27%. During the next cycles at C/5 a further decrease in capacity of 31% was measured. After a few cycles at 1C the capacity was reduced below 5 mAh/g . Although the initial capacity of the laser structured thin films was lower, the capacity increased to about 140 mAh/g during the first five cycles. This may be due to run-in effects (e.g., formation of solid electrolyte interphase). During the 11 cycles at the lowest current rate the capacity

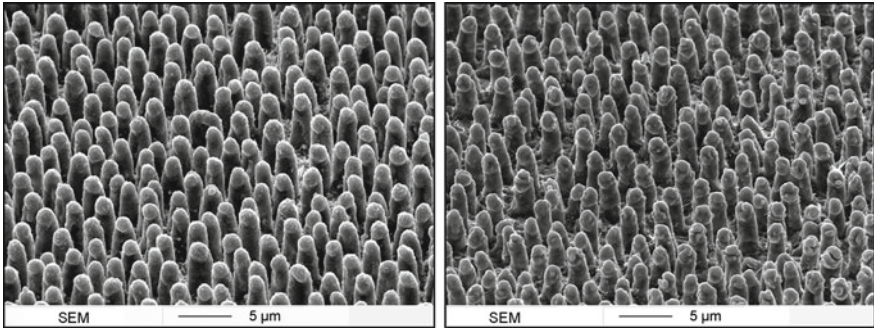
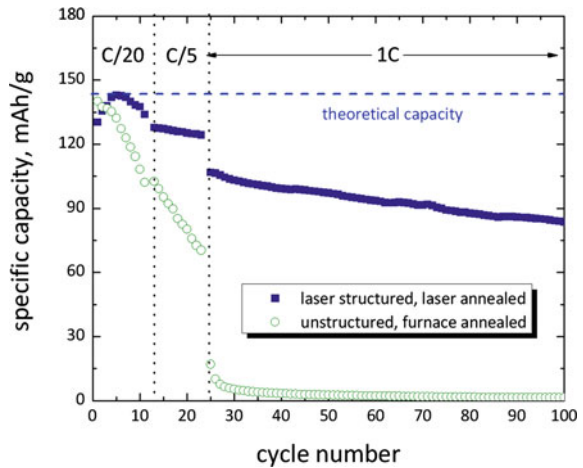


Fig. 8.29 SEM images of laser structured LiCoO_2 thinfilms, laser annealed at $T = 600^\circ\text{C}$ (left) and $T = 700^\circ\text{C}$ (right)

Fig. 8.30 Discharge capacity as a function of the cycle number of unstructured and laser structured LiCoO_2 thin films after furnace annealing for 3 h or laser annealing at 600°C for 250 s, respectively. Laser structuring was performed with a wavelength $\lambda = 248\text{ nm}$ in ambient air



of the structured thin film increased about 3%. At C/5 a slight decrease in capacity of 3% could be observed. After 100 cycles at 1 C the capacity reaches values of 78 mAh/g.

The improvement of battery performance by laser structuring can be attributed to different processes. Through the increased surface area of the structured films more lithium diffusion planes are accessible which in turns leads to a higher lithium diffusion rate at high charging rates. The cone width is about $2\ \mu\text{m}$. This leads to a maximum lithium diffusion length of $1\ \mu\text{m}$ which is significantly smaller than the maximum diffusion length of $3.5\ \mu\text{m}$ of the unstructured films. Concomitantly, the free standing cones contain little residual stress and expansion during electrochemical cycling can be easily compensated, leading to reduced crack formation and better cycling stability.

8.6 Joining with Laser Beams

8.6.1 *Welding of Thin Metal Sheets*

Two process strategies in laser welding are well established: laser deep penetration welding and laser conduction welding. For high laser power densities ($> 10^6 \text{W/cm}^2$) a plasma and a so-called keyhole is formed which enables a large aspect ratio of the weld seam and can be used for deep penetration welding [121]. However, generally the volume of the weld seam is too large for applications in microsystem technology. Furthermore, the dynamic of the laser generated melt can lead to a significant contamination of the surrounding material by melt ejection. Conduction welding is performed at lower laser power intensities ($< 10^6 \text{W/cm}^2$). The widths of the weld seams are in the range of 100–300 μm . The depths of the weld seams are of the same order. Because of the highly localized thermal impact the conduction mode is more appropriate for micro packaging applications. However, the aspect ratio of the weld seams, which can be achieved by conduction welding, might not be sufficient for every application. In chemical reaction technologies [122] the demand of improved channel devices such as heat-exchangers, mixers, and reactors made of chemically stable materials with structural details in micrometer range increases. Laser microwelding is of most interest if conventional welding technologies such as diffusion bonding or electron-beam welding cannot be applied anymore. This is the case for special materials such as aluminum alloys, tantalum, and high alloyed steel materials. Laser welding of materials with high affinity concerning oxidation and pore and crack formation [123] is still a great challenge in microsystem technology. Another challenge is to combine the main advantage of heat conduction welding (small heat effected zone) with the advantage of deep penetration welding (aspect ratio of weld seam > 1). In order to overcome this limitation a new technical approach uses temporal laser pulse shaping. The first pulse is used in order to overcome the high reflectivity and high heat conduction of the material. When a melt phase is formed the reflectivity is reduced significantly and a second laser pulse can be absorbed with high efficiency. Therefore, the weld penetration depth can significantly increase up to aspect ratios of about 5, while the lateral dimension of the weld seam is kept unchanged. With this approach laser beam microwelding can be implemented into the production process of small components. One of the main challenges in the laser process development is the realization of small weld seams with high mechanical stability [124], gas tightness, and high aspect ratio. For aluminum alloys the weld seam geometry, microstructure, hot cracking susceptibility and porosity are affected significantly by the laser power and the temporal laser pulse shape [125]. Although a number of authors [125–131] have studied pulsed laser beam welding experimentally as well as numerically, most of these studies have been focused on macroscopic applications, which related the process parameters such as pulse duration and pulse power with thermal, metallurgical, and geometrical aspects of the welding seam. With respect to laser-based microjoining processes only a limited number of papers

[132–134] have investigated these relationships although due to the restricted lateral dimensions each of the aspects given above can become critical.

Therefore, a detailed parametric study on the effects of laser pulse shaping on the welding process of thin foils of aluminum alloys has been performed. In addition to the process development a numerical model was developed and applied in order to correlate the pulse shape parameters with the experimental results. In order to achieve a better insight into the relationship between the details of a complex pulse shape and its effects on the geometry and metallurgy of the welding seam we have systematically varied particular parts of the pulse shape which consisted of a preheating section, a welding section, and a postheating section, respectively and inspected the resulting welding seam accordingly. The numerical model followed this approach by corresponding simulations of the weld pool geometry and its dynamical behavior during different parts of the pulse train. A Nd:YAG laser system (Baasel, Starcut 18) was used for the welding studies and the process development. The laser was operated in TEM₀₀-mode with a typical beam diameter of 1.6 mm. The effective spot diameter on the surface of the sample was adjusted to 80 μm using a 1:3 beam expanding system and a focusing lens with a focal length of 77 mm. During the laser welding the surface of the Al-alloy was exposed to an Ar-gas stream in order to prevent oxidation. The temporal evolution of the laser pulses are controlled by the intensity and duration of the output of the flash lamps. The actual beam power can be measured by an internal power meter of the laser system.

The optimized pulse shape measured with a photodiode within the defocused laser beam is shown in Fig. 8.31a. The details of the different parts of the pulse shape are visualized schematically in Fig. 8.31b. It can be divided in four different phases: It starts with the preheating phase which is followed by welding pulse in the second phase with higher peak power. The end of the pulse train is characterized by the third phase which is used to control the melt pool spreading and convection. The fourth phase of the pulse shape was introduced for a controlled cooling down of the laser heated zone. During the welding studies the level and duration of the different phases were varied in order to separate the influence of a single phase on the welding result. The maximum pulse power was adjusted to 102 W and the variation of the average power was between 5 and 15 W. The pulse repetition rate was chosen to be 40 Hz and the spatial overlap of two pulses was 80% which corresponds to a scanning velocity of 1.6 mm/s. The following parameters of the pulse shape shown in Fig. 8.31 were varied within this study:

- Preheating: $t_1 = 0\text{--}2$ ms; $n_1 = 30\text{--}80\%$
- Welding pulse: $t_2 = 0.2\text{--}0.8$ ms; $n_2 = 100\%$
- Post pulse: $t_3 = 0.4$ ms; $n_3 = 0\text{--}90\%$
- Cooling: $t_4 = 0\text{--}2$ ms; $n_4 = 0\text{--}60\%$

Two different Aluminum alloys AlMg₃ and AlMg_{4,5}Mn were included in this study. The AlMg₃ alloy (Goodfellow) was received in two different states with respect to their thickness. The foil material with a thickness of 0.2 mm was used in the welding experiments whereas the AlMg₃ sheet with a thickness of 2 mm was applied for the laser remelting tests.

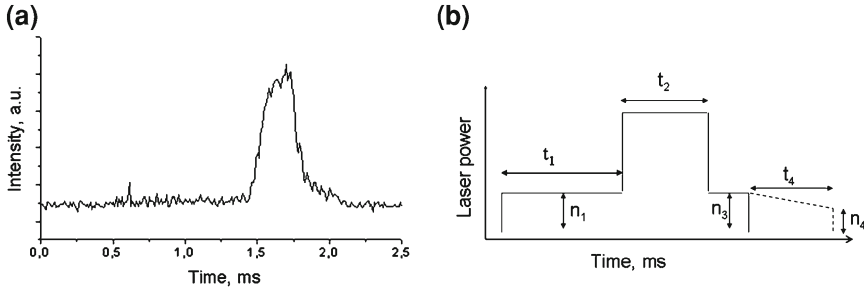


Fig. 8.31 **a** Oscilloscope trace of the optimized pulse shape measured with a photodiode in the defocused laser beam. The pulse shape parameters are $n_1 = 30\%$, $t_1 = 1.33$ ms, $t_2 = 0.33$ ms, $n_3 = 30\%$, $t_3 = 0.33$ ms; **b** Schematic representation of the laser pulse shape

The AlMg₃ foil was fabricated by rolling which is also reflected in its grain morphology (Fig. 8.32a) showing an explicit rolling texture. The AlMg₃ sheet was treated by a soft annealing process after the rolling. The microstructure is characterized by globular grain morphology (Fig. 8.32b) without any appearance of a rolling texture. The chemical analysis of the foil and the sheet showed that both had a purity of 99.9% with a Mg wt.% value of 2.94 ± 0.06 and 2.85 ± 0.07 , respectively, which is within the specification of DIN which allows for a variation from 2.6 to 3.6 wt.% Mg. Major impurities within this material were Mn, Fe, and Si with a weight fraction which was lower than 0.5 wt.%. Specifically, the content of the Si impurities was 0.15 wt.%. This is important with respect to the hot cracking susceptibility of Al-alloys [135] which reaches a maximum at 0.75 wt.% Si and 1.2 wt.% Mg. The AlMg₄, 5Mn sheet (Delta Trading) was also treated by a soft annealing process which results in a grain morphology shown in Fig. 8.32c. The chemical analysis showed that the Mg and Mn content is within the DIN specification. The major impurities are Fe and Si with a weight fraction of 0.3 and 0.06 wt.%. Since the addition of elements such as Mn or Cr makes the alloy more weldable and the susceptibility for hot cracking is also reduced compared to alloy systems such as AlMg or AlMgSi. The variation of the welding pulse time t_2 has a significant effect on the width and depth and also on the quality of the welding seams. This has been demonstrated by remelting experiments on AlMg₃ sheets. The resulting laser remelting traces are shown in Fig. 8.33a. During the experiments it could be observed that the pulse peak power and its duration could not be adjusted independently. The peak power level increased with longer pulses although the driving voltage of the flash lamps was set to a constant value. Therefore longer pulses were always correlated with higher peak power. This is also reflected in the SEM image. While at low welding pulse times the surface quality of the remelting trace seems to be fairly good, a pulse length value higher than $t_2 = 0.5$ ms leads to the appearance of increasing number of humps and hot cracks. No differences with respect to the surface quality after welding or remelting could be observed between the AlMg₃ sheet and foil. In the remelting experiments on the AlMg₄, 5Mn sheets a stronger development of debris could be observed. The

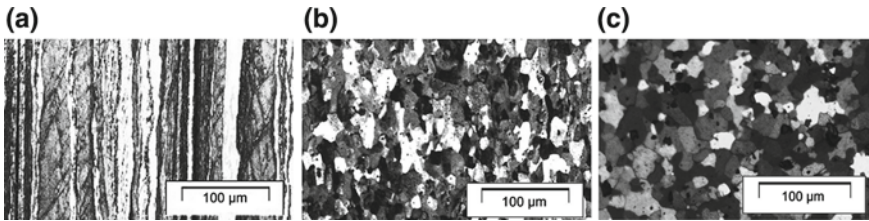


Fig. 8.32 Microstructure (a) of the as-received AlMg₃-foil with a thickness of 0.2 mm, (b) of the AlMg₃ sheet with a thickness of 2 mm and c of the AlMg_{4,5}Mn sheet with a thickness of 1 mm

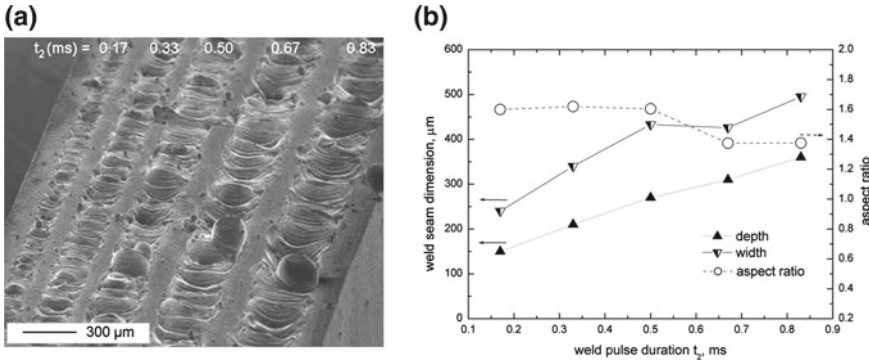


Fig. 8.33 a SEM image of laser re-melting traces on the surface of AlMg₃ for different durations of the welding pulse. The welding pulse time t_2 increases from *left* to *right*. The corresponding t_2 -values are given on *top* of the figure. The pulse repetition frequency was 40Hz and the pulse overlap 60%. b Width, depth and aspect ratio of the welding seams in AlMg₃ as a function of the weld pulse duration. The results of the model simulations are shown by the *straight lines*

surface quality, however, appeared to be the same in the AlMg₃ and AgMg_{4,5}Mn sheets. The weld pulse also affects the depth and the aspect ratio of the welding seams and remelting traces in AlMg₃ which is shown in Fig. 8.33b. The aspect ratio was calculated by division of the depth of the welding seam by the width measured at the surface. While the depth and width of the welding seams and remelting traces in AlMg₃ increases continuously with the duration of the welding pulse, its aspect ratio varies only very slowly. Between $t_2 = 0.17\text{--}0.5$ ms it is nearly constant with a value of 1.6 and decreases to 1.4 at longer durations.

The post-pulse level n_3 has also an important influence on the surface quality of the welding seams since this part of the pulse-shape controls the dynamic behavior of the melt pool. While at low as well as at high levels of n_3 the appearance of the molten and solidified surface is characterized by humps and debris the surface quality has an optimum at n_3 -values of 70 and 80% (Fig. 8.34a). At the highest value of 90% surface cracks begin to develop which could not be observed at lower post pulse levels. A further analysis of the welding seams and remelting traces by an inspection of cross-sectional micrographs revealed cracks that developed with increasing depth.

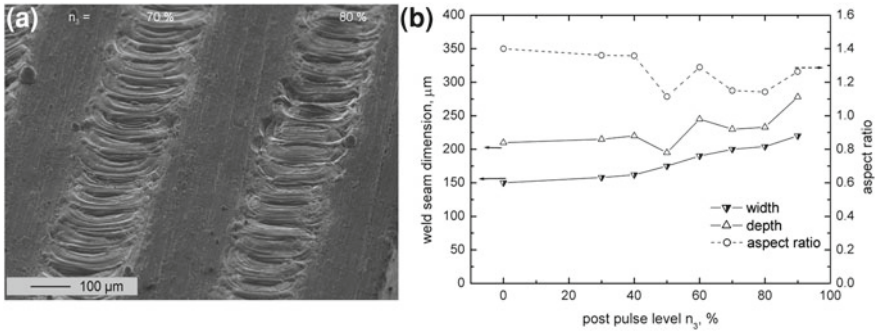


Fig. 8.34 **a** SEM image of re-melting traces on the surface of an AlMg3-sheet for different post pulse levels n_3 . The values are given on top of the figure. The pulse repetition frequency was 40 Hz and the pulse overlap 60%. **b** Width, depth and aspect ratio of the welding seams in AlMg3 as a function of the post pulse level n_3 . The results of the model simulation are shown by the *straight lines*

The crack density increased with higher post-pulse levels while the number of pores decreased at higher value of n_3 . The post-pulse level did not affect the width, depth, and aspect ratio of the remelting traces in the same way as the duration of the welding pulse level did. The geometric properties vary only slowly with increasing post-pulse level as it is shown in Fig. 8.34b.

While the welding pulse duration and the post pulse level clearly affect the surface quality, the weld seam depth as well as the density of pores and cracks and the effect of the cooling phase and time is not unique at all. Along a variation of the cooling phase level n_4 between 0 and 60% the aspect ratio remained nearly constant. This is also true for the development of cracks and pores which seem to be independent on the details of the cooling phase.

8.6.2 Metal–Ceramics Joining

The excellent properties of technical ceramics such as thermal stability, corrosion, and wear resistance are of major interest for high performance engineering systems. In order to profit from the advantages of this ceramic, the integration into metallic structures for the manufacturing of complex-shaped components becomes necessary. The choice of an appropriate joining technique is dependent on the combination of the materials to be joined, the thermal and mechanical loads on the joints within the application, and the design of the component. Especially, for ceramic/metal joints that are thermally and mechanically stressed, brazing can be an adequate solution. However, brazing of ceramics is associated with some particularities. One of these is the poor wettability of ceramics by conventional brazing alloys, which can be enhanced by adding active elements for ceramic surface activation, e.g., Ti or Zr

[136–141]. The most frequently used active braze fillers are AgCuTi-alloys, which are utilized in furnace brazing processes under a controlled inert gas atmosphere or vacuum. For these process conditions the AgCuTi braze alloys have exhibited good wetting and joining behavior with oxide and non-oxide ceramics [137–139, 142–144]. Another problem, which is associated with the joining of metals to ceramics, is the generation of residual stresses, which are caused by the dissimilar elastic and thermal properties of the two material groups, i.e., Youngs modulus and coefficient of thermal expansion. These give rise to reduction of the joint strength [32, 140, 142]. The residual stresses are also affected by the process conditions and the geometry [32, 141, 142, 145]. They can be reduced by the addition of ductile and therefore stress reducing elements such as Cu, either within the braze filler material or as an interlayer. Alternatively, an interlayer material possessing a coefficient of thermal expansion, which is similar to the ceramic, may minimize the compound stresses by feeding the high stresses from the ceramic to the metal joining partner [146–151]. Furthermore, particle reinforced braze fillers are known to increase the compound strength [152, 153]. The influence of surface roughness, textures, and structured interlayer on the wetting and joining behavior is also important for the strength of brazed ceramic/metal joints [154–156]. The thermal process parameters, particularly the brazing temperature and the dwell time, influence the joint strength [157–160], since they control the intensity and duration of the reaction between the active element in braze metal filler and the ceramic. Both should be set in order to achieve an optimized thickness of the reaction layer without the development of brittle reaction phases [158, 159, 161]. The influence factors described above and its consequences on metal-ceramic brazing have been mainly studied for the furnace brazing process, which is characterized by slow heating and cooling cycles while the whole component is placed in a nearly uniform temperature field. Therefore, the knowledge base for this type of process related to metal-ceramic brazing is relatively broad. In contrast to that the important features of a laser brazing process are options for rapid heating and cooling with a localized heat input by the laser beam, which is focused onto the joining zone. Due to these differences in the characteristic scales in space and time for the laser and furnace brazing process, respectively, it can be expected that also specific properties of the metal/ceramic joint may differ at least as long as the kinetic aspects of the reaction, spreading and wetting of the braze metal on the ceramic surface is considered. Unfortunately, the database for the laser-based processes applied to metal/ceramic joining is very small. This may also be an obstacle for a transfer into industrial applications utilizing metal-ceramic components [161, 162]. In the framework of a research project, the application possibilities of engineering ceramics for high performance sliding and friction coefficients were investigated. One of the application system was a automotive dry running clutch system [162, 163]. The advantage of ceramics in these friction systems is at the first place the high friction coefficient that can be achieved. But the increase of friction coefficient went along with an enormous rise of contact temperature. In this manner for bonding ceramic and metal carrier a joining technique brazing, which assured a sufficient mechanical and thermal stability must be chosen.

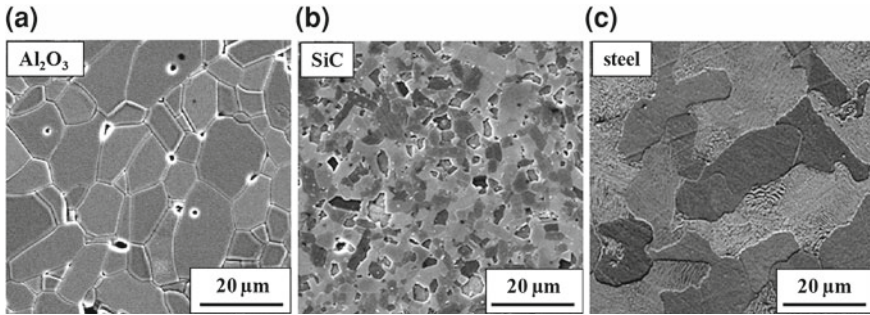


Fig. 8.35 SEM-images of (a) Al_2O_3 -ceramic, (b) SiC-ceramic and (c) steel

Materials and Methods

For the investigations at the IAM-AWP an Al_2O_3 (trade name: F99,7, Comp.: Ceramtec AG, Germany) and a pressureless sintered silicon carbide (trade name: Ekasic-F, Comp: ESK Ceramics) were brazed to commercial steel (AISI 1045), Fig. 8.35. A cylindrical sample geometry was chosen, so that the shear strength of the compounds could be determined as well as the tribological performance could be tested pin-on-disc arrangement. The cylindrical samples with an outer diameter of 16 mm were composed of a ceramic pellet (thickness $s_{\text{ceramic}} = 4$ mm) and a metalcarrier (height $h=16$ mm). Additionally, the metal cylinders received a drilling hole ($d=12$ mm, $h=14$ mm) for heating up. The drilling hole was sandblasted and a graphite layer was applied on the surface for increasing the absorbance of the laser beam. The joining faces were polished with 600 grain.

The alumina ceramic could be brazed with a $200\ \mu\text{m}$ thick commercial brazing foil, Incusil-ABA (Morgan Chemicals). However, the SiC was not wettable with the AgCuTi- or AgCuInTi-filler [142, 143], the carbide ceramic was joined with self-made 50Sn48Ag2Ti-pellets ($200\ \mu\text{m}$). The properties of the components materials are listed in Table 8.1. The brazing experiments resulted in a very good wetting for the alumina with the conventional filler materials on AgCuTi basis. No pores or irregularities were recognized in the Al_2O_3 /braze-interface and a homogenous Ti-rich reaction layer could be detected by EDX, Fig. 8.36a. In contrast no reliable and reproducible joints were realized with SiC in contact with the AgCuTi-filler, Fig. 8.36b. For that reason SnAgTi-alloys were developed and investigated concerning their wetting and joining behavior on SiC. Thus, the Sn/Ag-fractions were varied as well as W-particles were added in order to reinforce the SiC/SnAgTi/steel-joints. Additionally, the influence of different laser-induced surface patterns on the joint strength was studied.

Wetting experiments with different SnAgTi-composites resulted in a sufficient wetting for Sn-fractions of above 25 mass %. The SEM-images show a homogenous wetting of silicon carbide for all Sn:Ag-fractions. A continuous Ti-rich reaction layer as it is desirable for active brazed ceramic-steel joints was not observed for our laser processed joints. Thus the investigated the 50Sn48Ag2Ti compound, as shown in Fig.

Table 8.1 Properties of the component materials

Material	SiC-PLS	Al ₂ O ₃	C45E	CB 4	Incusil-ABA	50SnAg2Ti
Composition	SiC 100%	Al ₂ O ₃ 99.95%	AISI 1045	Ag-Cu-Ti 70.5-26.5-3	Ag-Cu-In-Ti 59-27.2-12.5- 1.25	Sn-Ag-Ti 50- 48-2
Company	ESK ics	Friatec AG		Brazetec	Morgan Chemicals	KIT, IAM- AWP
Density	3	3,9	8	9,9	9,7	8,3
Brazing temperature T	-	-	-	900-950	850-900	900-950
Strength	400	350	620	230	338	-
Youngs modulus E	410	380	212	72	76	68
Coefficient of thermal expansion	4.7	8.4	11.1	18.95	18.2	-
Thermal conductivity	125	30	42	-	70	-

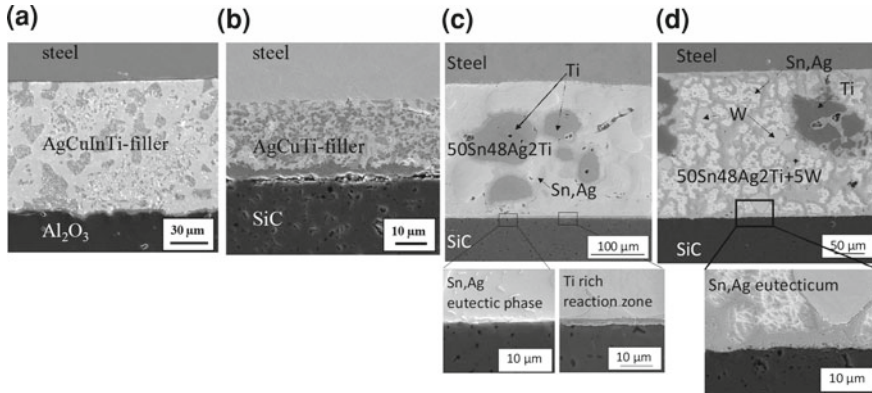


Fig. 8.36 SEM images of laser brazed joints: **a** $\text{Al}_2\text{O}_3/59\text{Ag}27.25\text{Cu}12.5\text{In}1.25\text{Ti}/\text{steel}$, **b** $\text{SiC}/70.5\text{Ag}26.5\text{Cu}3\text{Ti}/\text{steel}$, **c** $\text{SiC}/50\text{Sn}48\text{Ag}2\text{Ti}/\text{steel}$ and **d** ($\text{SiC}/50\text{Sn}48\text{Ag}2\text{Ti}+5\text{W}/\text{steel}$)

8.36c, exhibited a ceramic-braze interface that contained zones of Ti-rich reaction layer as well as areas that were composed of a Sn,Ag-eutectic phase.

An example for reinforced braze fillers is shown in Fig. 8.36d. As well as SnAgTi-fillers without W-particles, the reinforced joints exhibited a homogenous wetting of the ceramic. Still, a few pores were recognized within the reinforced braze layers and at the interface to ceramic. Similar to the unreinforced joints, single large Ti-particles were located in the center of the braze layer whereas a Ti-rich reaction zone was missing in large areas of the carbide surfaces.

Shear Testing

The compound strength of the brazing joints was determined by shear testing. The load was applied at a velocity of $v = 0.005$ m/s and shear stress evaluated on the basis of the fracture load. Ten samples of each series were tested and the fracture shear stress was statistically evaluated according to the Weibull theory, so that a characteristic fracture shear stress τ_0 at a fracture probability of 63.2% and Weibull modulus m was calculated as a reliability parameter [143]. In Table 8.2 the characteristic shear strength and Weibull modulus of all test SiC/steel joints are summarized. Different unreinforced and reinforced SnAgTi-filler alloys were successfully developed for the laser brazing of silicon carbide to steel. The variation of Sn,Ag-fractions has shown that the shear strength increased with a rising fraction of Sn in the SnAgTi alloy. Thus joints brazed with SnAgTi-fillers containing a Sn-fraction of 30 wt% achieved a characteristic shear strength of $\tau_0 = 15$ MPa at a Weibull modulus of $m = 2.7$, whereas samples brazed with 50Sn48Ag2Ti accomplished a strength of $\tau_0 = 20$ MPa and a Weibull modulus of $m = 4.9$.

Although all SiC/SnAgTi/steel-microsections exhibited a homogenous bonding at the ceramic/braze-interface, only thin, non-continuous Ti-rich reaction layer was produced. This could be related to large Ti-particles, which were found in interface distal regions and anticipated the creation of a reaction layer, Fig. 8.36c. The fragmental reaction zone resulted in regions of weak bonding which failed along

Table 8.2 Characteristic fracture shear strength τ_0 and Weibull modulus of the laser brazed ceramic-steel joints

Braze filler	Shear strength τ_0 /MPa	Weibull modulus m /-
50Sn48Ag2Ti	19	4.9
40Sn58Ag2Ti	22	3.1
30Sn68Ag2Ti	16	2.7
50Sn48Ag2Ti+5 W	28	3.1
50Sn48Ag2Ti+10 W	24	3.9
50Sn48Ag2Ti+20 W	7	1.6
50Sn48Ag2Ti+30 W	4	2.7

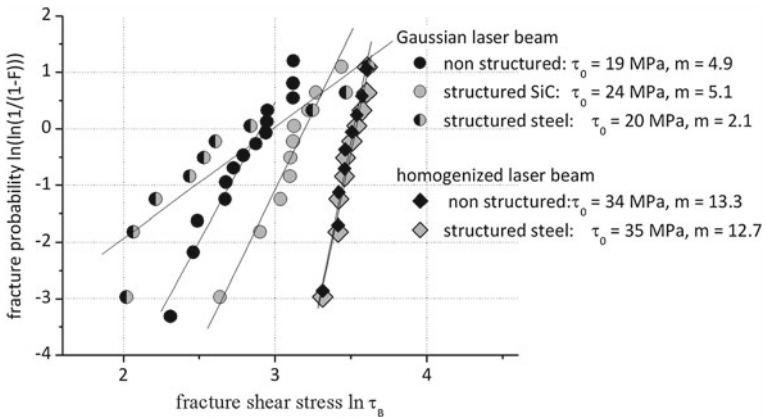


Fig. 8.37 Weibull graphs of laser brazed SiC/50Sn48Ag2Ti/steel-compounds brazed with Gaussian and homogenized laser beam

braze/ceramic interfaces. The investigation on the effect of laser-induced textures on Silicon carbide joining areas resulted in an increase of shear strength by deep cone textures of τ 24 MPa. A further increase of compound strength could be observed for the application of laser-induced structures on the SiC-joining surface as well as the use of a homogenized laser beam, Fig. 8.37. Especially the homogenization of the laser beam evoked an enhancement of the characteristic shear strength up to 34 MPa and a major advancement of the Weibull modulus up to about 13.

Corresponding results were found for laser brazed Al_2O_3 /59Ag27.25Cu12.5In 1.25Ti/steel-joints (Fig. 8.38). The characteristic shear strength of non-structured joints was increased from 21 to 26 MPa by the homogenized laser intensity profile. When structuring the alumina joining surface, the joints fractured in the ceramic pellets directly after joining. Still, the structuring of the steel face leads to a further increase of shear strength up to 42 MPa. Unfortunately, the increase of shear strength went along with a reduction of Weibull modulus. The investigations have shown that the use of a homogenizing optic resulted in a major rise of shear strength of laser brazed ceramic/steel-joints, although these differences could not be proved by

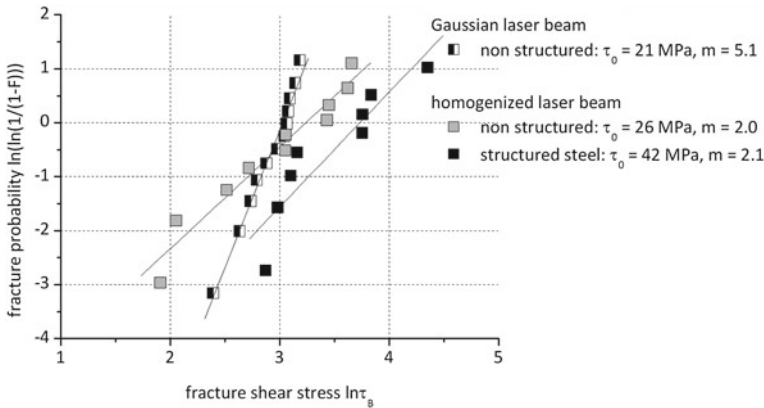


Fig. 8.38 Weibull graphs of laser brazed $\text{Al}_2\text{O}_3 / 59\text{Ag}27.25\text{Cu}12.5\text{In}1.25\text{Ti}/\text{steel}$ -compounds brazed with Gaussian and homogenized laser beam

microscopic analysis. The ceramic/steel cross-section did not exhibit major differences between those ceramic/steel-joints, which were brazed with non-homogenized output laser beam, and those samples, which were joined with a top head laser beam. Also, it was determined that the homogenized laser intensity profile affected those joints more, which contained a laser structured metal joining face.

8.6.3 Laser Transmission Welding of Polymers

The use of laser welding for joining microparts has experienced a substantial increase in popularity during recent years and laser-based procedures are developed and optimized for the microscale [27, 163]. Microsystem products pose new challenges to the assembly and packaging process based on a higher level of integration, the small size of the device features, and types of materials. Making very small joints with minimal heat input (micro-joining) and hermetic sealing is a critical issue for a number of devices. Polymer substrates require bonding processes that are different from the processes developed for other materials such as silicon or glass, in particular low temperature bonding processes that do not necessitate the application of voltage, high pressure, or vacuum. Laser transmission welding is one of the youngest technologies among all plastic joining technologies and is developing rapidly, driven by the fast development of laser sources. It offers specific advantages compared to conventional technologies as well as meet some requirements that cannot be met otherwise. It enables bonding without the use of additional materials (solvents or adhesives) that may potentially block or destroy microsized features. It provides contactless process involving no mechanical or electrical load on the joined parts with no particle release or contamination in the joint environment. The supplied energy is also

well controlled, very well defined spatially and over time. This enables localized joining of materials while decreasing thermal load to the joining part and preserving the microstructured surfaces as well as the functionality of highly sensitive integrated components. Strong and leak tight connections of the polymeric layers with optically and qualitatively high-grade joints are also possible. Nd:YAG lasers, near-infrared semiconductor High Power Diode (HPD) lasers (808–980 nm), and fiber lasers can be used for laser transmission welding. The conceptually simple working principle is the absorption of a high intensity laser beam and heating the plastic interface via surface absorption between the two parts to be joined to produce a joint between two overlapping polymer substrates. In order for the radiation to reach the interface, one of the two parts must be transparent to the radiation. When the laser beam impinges on the interface, it is absorbed, either by the non-transparent part, or by a thin absorbent intermediate layer of, e.g., carbon black particles on the interface. The energy from the laser melts the polymer locally, and when the melt resolidifies, because the heat is transferred to the surrounding material, bonds have now been created between the polymer chains from the two parts. Laser welding of plastics also generally requires that the materials to be joined are similar chemically so that when controlled melting is produced, mutual wetting occurs across the joint. Welding of different types of thermoplastics is also possible. In this case, the polymers need an overlap in their temperature range defined by the glass temperature and decomposition temperature. While laser-assisted polymer welding of transparent to opaque materials is well established [27, 164], the welding of only transparent materials is still a challenge, especially if microstructures are involved. Klotzbuecher et al. [165] extended to the microscale a process, *Clearweld*, previously developed for welding optically transparent polymers. This technique is based on using an infrared absorbing dye matched to the laser wavelength and highly transparent in the visible. The absorbing dye can either be incorporated in the bulk of the polymer which could lead to a slight discoloration in the visible or coated on top of the polymer as a thin film. The new welding technology, *Microclearweld*, was investigated with two different laser sources, a Nd:YAG laser ($\lambda = 1064$ nm) with a point focus and a diode laser bar ($\lambda = 976$ nm) with a line focus, using a dye-doped interface layer applied by spincoating onto PMMA or PC substrates. The process was successfully applied to the sealing of 2D capillary gel electrophoresis chips made of PMMA containing 300 channels with 50 μm width and depth to be used for low cost and high throughput routine analysis of protein mixtures [166]. Pflöging et al. [23] developed and characterized a transmission welding process which used a focused diode laser emitting at 940 nm and carbon absorbing layer of nanometer thickness to weld polymers such as PMMA, polycarbonate, COC, polyimide, polypropylene, and PVDF. The thin carbon absorbing layer was deposited onto the surface of these transparent polymers on the chip side using a carbon coater (EMITECH K250). The layer thickness is in the range of 1–10 nm, which was measured by atomic force microscopy and optical transmission spectroscopy. The laser welding process was applied to sealing microstructures with feature size in the hundred micrometer range in PVDF channels that were mechanically milled as well as in PMMA channels substrates that were

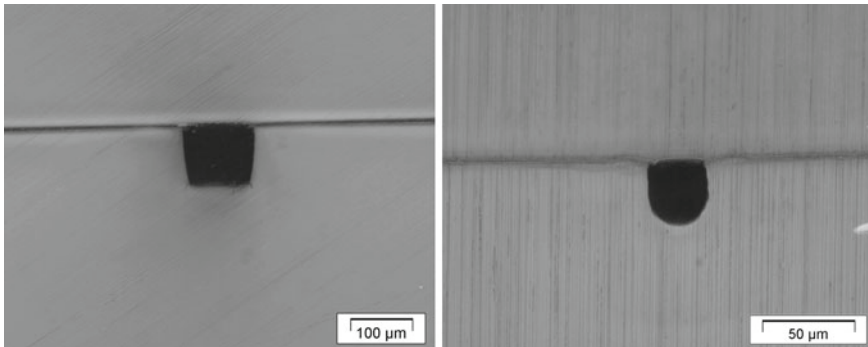


Fig. 8.39 Cross section microscope images of excimer laser (*left*) and CO₂ laser generated channels in PMMA after laser transmission welding

laser ablated (Fig. 8.39, left). The welding of capillary electrophoresis chips made of PMMA with microchannels and channel widths down to 50 µm was successfully established [2]. It was also demonstrated that a combination of laser cutting, patterning and transmission welding can be applied as a fast and flexible manufacturing method to build complex 3D devices. The sealing of microchannels and a useful mechanical strength of the bonding of micro-sized channel is necessary. The mechanical strength of laser-welded PMMA parts was investigated in comparison to classical thermally bonded parts [2]. During thermal bonding both PMMA parts have a substrate temperature slightly below the glass temperature. Higher temperatures would lead to a deformation and destruction of the functional structures. For PMMA the best results during thermal bonding were obtained for a welding temperature of $T = 98^\circ\text{C}$. Mechanical strength measurements of 10 welded parts showed that the mechanical strength after thermal bonding is $R_m = (2.07 \pm 0.63)\text{N/mm}^2$. A higher mechanical strength was only possible at higher temperatures which can be obtained by laser transmission welding without deformation of the PMMA sheets. At welding temperatures of $T = 150^\circ\text{C}$ the mechanical strength rose up to 13.15N/mm^2 . After thermal bonding the sheets showed a good sealing, but the mechanical strength and fracture surface indicated that the bonding process led to a small mechanical stability resulting from a type of sticking or adhesion. On the other hand, laser welding caused an improved mechanical joining, which we assume is caused by an induced localized “melt bath dynamic”. Nevertheless, for bonding of microstructures the combination of laser welding at high temperatures ($T = 130\text{--}150^\circ\text{C}$) for non-sensitive areas and the laser welding at small temperatures ($T = 80\text{--}120^\circ\text{C}$) for sensitive areas, such as microstructures, is practicable in order to guarantee a high mechanical strength even for MST components. Another process strategy is to partly remove the absorbing layer in order to reduce the heat impact in sensitive structures. For this purpose the thin absorbing layer is selectively ablated by excimer laser radiation (wavelength 248 nm) with high local resolution in the micrometer range. In this case high laser welding temperatures can be established and sensitive microstructures are protected. The welding process has been established for polymeric parts containing microchannels down to 30 µm lateral dimensions (Fig. 8.39, right).

8.7 Conclusion

Laser-based material processing is well investigated for structuring, modification, and bonding of metals, ceramics, glasses, and polymers. In general, laser machining provides flexibility and obvious advantages in terms of rapid manufacturing and customization of devices. Especially for material processing on micrometer and nanometer scale laser-assisted processes will very likely become more prevalent as lasers offer more cost-effective solutions for advanced material research and application. Laser ablation and surface modification are suitable for direct patterning of materials and their surface properties. Laser technologies present several advantages compared to other technologies: the data-driven processes are in non-contact mode to the material, patterns can be generated without the need for masks, resist materials, or chemicals harmful to the environment. They enable direct writing of features of various geometries, depths, and aspect ratios. Laser processing parameters, such as fluence and wavelength, can be adjusted with respect to the material properties to suit a specific application. Lasers allow rapid prototyping and small-batch manufacturing. They can also be used to pattern moving substrates, and permitting fly-processing of large areas at reasonable speed. Different types of laser processes such as ablation, modification, and welding can be successfully combined in order to enable a high grade of bulk and surface functionality. Ultraviolet lasers are favored for precise and debris-free patterns can be generated without the need for masks, resist materials, or chemicals. Machining of materials, for faster operation, thermally driven laser processes using NIR and IR laser radiation, could be increasingly attractive for a real rapid manufacturing.

Acknowledgments We gratefully acknowledge the financial support by the Federal Ministry for Education and Research (BMBF) in the BMBF-project 03SF0344A “Li-ion battery cells based on novel nanocomposite materials” (LIB-NANO) in the framework of “Lithium-Ion Battery LIB-2015”, and by the Deutsche Forschungsgemeinschaft (DFG) in context with the Sonderforschungsbereich 483 “High performance sliding and friction systems based on advanced ceramics”. This work was carried out with the support of the Karlsruhe Nano Micro Facility (KNMF), a Helmholtz Research Infrastructure at Karlsruhe Institute of Technology.

References

1. C.G.K. Malek, Laser processing for bio-microfluidics applications (Part II). *Anal. Bioanal. Chem.* **385**, 1362–1369 (2006)
2. W. Pfleging et al., Laser patterning and packaging of CCD-CE-Chips made of PMMA. *Sens. Actuators B-Chem.* **138**, 336–343 (2009)
3. W. Pfleging, M. Przybylski, H.J. Bruckner, Excimer laser material processing—State of the art and new approaches in microsystem technology—Art. No. 61070G. *Laser-based Micropackaging* **6107**(264), G1070–G1070 (2006)
4. W. Pfleging et al., (eds.), *Laser-Based Micro- and Nanopackaging and Assembly IV*. 2010. in *SPIE*

5. S. Fujii et al., Enlargement of crystal grains in thin silicon films by continuous-wave laser irradiation. *Jpn. J. Appl. Phys.* **46**, 2501–2504 (2007)
6. Y.T. Chen et al., Ablation of transparent materials using excimer lasers for photonic applications. *Opt. Rev.* **12**, 427–441 (2005)
7. W. Pflöging et al., Laser- and UV-assisted modification of polystyrene surfaces for control of protein adsorption and cell adhesion. *Appl. Surf. Sci.* **255**, 5453–5457 (2009)
8. S. Wilson et al., An automated polymer patch clamping system for high throughput screening and cell network measurement. *Galvanotechnik* **99**, 2578–2584 (2008)
9. K. Gotoh, S. Kikuchi, Improvement of wettability and detergency of polymeric materials by excimer UV treatment. *Colloid Polym. Sci.* **283**, 1356–1360 (2005)
10. A. Welle et al., Photo-chemically patterned polymer surfaces for controlled PC-12 adhesion and neurite guidance. *J. Neurosci. Methods* **142**, 243–250 (2005)
11. W. Pflöging et al., Laser-assisted modification of polystyrene surfaces for cell culture applications. *Appl. Surf. Sci.* **253**, 9177–9184 (2007)
12. A. Manz et al., Planar chips technology for miniaturization and integration of separation techniques into monitoring systems—Capillary electrophoresis on a chip. *J. Chromatogr.* **593**, 253–258 (1992)
13. M. Castano-Alvarez et al., Critical points in the fabrication of microfluidic devices on glass substrates. *Sens. Actuators B Chem.* **130**, 436–448 (2008)
14. A.E. Guber et al., Microfluidic lab-on-a-chip systems based on polymers—Fabrication and application. *Chem. Eng. J.* **101**, 447–453 (2004)
15. H. Becker, C. Gartner, Polymer microfabrication technologies for microfluidic systems. *Anal. Bioanal. Chem.* **390**, 89–111 (2008)
16. R. Chen et al., Determination of EOF of PMMA microfluidic chip by indirect laser-induced fluorescence detection. *Sens. Actuators B Chem.* **114**, 1100–1107 (2006)
17. W. Pflöging et al., Rapid fabrication and replication of metal, ceramic and plastic mould inserts for application in microsystem technologies. *Proc. Inst. Mech. Eng. Part C J. Mech. Eng. Sci.* **217**, 53–63 (2003)
18. W. Pflöging et al., Rapid fabrication of microcomponents—UV-laser assisted prototyping, laser micro-machining of mold inserts and replication via photomolding. *Microsyst. Technol.* **9**(1–2), 67–74 (2002)
19. D.A. Chang-Yen, B.K. Gale, An integrated optical biochemical sensor fabricated using rapid-prototyping techniques. *Microfluid. Biomems. Med. Microsyst.* **4982**, 185–195 (2003)
20. P.E. Dyer, Excimer laser polymer ablation: twenty years on. *Appl. Phys. A* **77**, 167–173 (2003)
21. W. Pflöging et al., (eds.), Lasergestützte Prozesse für Polymerwerkstoffe in der Mikro- und Nanotechnik: Strukturierung, Modifizierung und Verbindungstechnik. in *Technologien und Werkstoffe der Mikro- und Nanosystemtechnik*. (VDE-Verl, Karlsruhe, 2007)
22. J.Y. Cheng et al., Direct-write laser micromachining and universal surface modification of PMMA for device development. *Sens. Actuators B* **99**, 186–196 (2004)
23. W. Pflöging, O. Baldus, Laser patterning and welding of transparent polymers for microfluidic device fabrication—Art. no. 610705. *Laser-based Micropackaging* **6107**(264), 10705–10705 (2006)
24. Y. Sun, Y.C. Kwok, N.T. Nguyen, Low-pressure, high-temperature thermal bonding of polymeric microfluidic devices and their applications for electrophoretic separation. *J. Micromech. Microeng.* **16**, 1681–1688 (2006)
25. S.C. Wang, C.Y. Lee, H.P. Chen, Thermoplastic microchannel fabrication using carbon dioxide laser ablation. *J. Chromatogr. A* **1111**, 252–257 (2006)
26. C.W. Tsao et al., Low temperature bonding of PMMA and COC microfluidic substrates using UV/ozone surface treatment. *Lab Chip* **7**, 499–505 (2007)
27. F.G. Bachmann, U.A. Russek, Laser welding of polymers using high power diode lasers. *Photon Process. Microelectron. Photonics* **4637**, 505–518 (2002)
28. K.H. Zum Gahr, J. Schneider, Surface modification of ceramics for improved tribological properties. *Ceram. Int.* **26**, 363–370 (2000)

29. S.Rüdiger et al., H. Dimigen (eds.), Laser induced surface modification of cordierite. in *EUROMAT 99—Surface Engineering*, (München, Wiley-VCH, 1999)
30. U. Duitsch, S. Schreck, M. Rohde, Experimental and numerical investigations of heat and mass transport in laser-induced modification of ceramic surfaces. *Int. J. Thermophys.* **24**, 731–740 (2003)
31. A. Schwartz, *Ceramic Joining 1990 Materials Park* (ASM International, Ohio, 1990)
32. R.M.D. Nascimento, A.E. Martinelli, A.J.A. Buschinelli, Review article: recent advances in metal-ceramic brazing. *Cerâmica* **49**, 178–198 (2003)
33. W. Lippmann et al., Laser joining of silicon carbide—A new technology for ultra-high temperature resistant joints. *Nucl. Eng. Des.* **231**, 151–161 (2004)
34. H. Haferkamp et al., Laser beam active brazing of metal ceramic joints. *Lasers Tools Manuf. Durable Goods Microelectron.* **2703**, 300–309 (1996)
35. S.F. Huang, H.L. Tsai, S.T. Lin, Effects of brazing route and brazing alloy on the interfacial structure between diamond and bonding matrix. *Mater. Chem. Phys.* **84**, 251–258 (2004)
36. S.D. Peteves et al., The reactive route to ceramic joining: Fabrication, interfacial chemistry and joint properties. *Acta Mater.* **46**, 2407–2414 (1998)
37. R. Kohler et al., Patterning and annealing of nanocrystalline LiCoO₂ thin films. *J. Optoelectron. Adv. Mater.* **12**, 547–552 (2010)
38. H. Yang et al., A review of Li-Ion cell chemistries and their potential use in hybrid electric vehicles. *J. Ind. Eng. Chem.* **12**, 12–38 (2006)
39. Y. Wang, G.Z. Cao, Developments in nanostructured cathode materials for high-performance lithium-ion batteries. *Adv. Mater.* **20**, 2251–2269 (2008)
40. B. Ketterer et al., Development of high power density cathode materials for Li-ion batteries. *Int. J. Mater. Res.* **99**, 1171–1176 (2008)
41. Y. Zhang, C.Y. Chung, Z. Min, Growth of HT-LiCoO₂ thin films on Pt-metallized silicon substrates. *Rare Met.* **27**, 266–272 (2008)
42. J.L. Tirado, Inorganic materials for the negative electrode of lithium-ion batteries: state-of-the-art and future prospects. *Mater. Sci. Eng. R Reports* **40**, 103–136 (2003)
43. R.R. Gattass, E. Mazur, Femtosecond laser micromachining in transparent materials. *Nat. Photonics* **2**, 219–225 (2008)
44. K. Sugioka, Ultrafast laser processing of glass down to the nano-scale. *Springer Ser. Mater. Sci.* **130**, 279–293 (2010)
45. K. Sugioka, Y. Hanada, K. Midorikawa, Three-dimensional femtosecond laser micromachining of photosensitive glass for biomicrochips. *Laser Photonics Rev.* **4**, 386–400 (2010)
46. A. Kar, J. Mazumder, Effect of cooling rate on solid solubility in laser cladding. *Proc. ASME/JSME* **3**, 237–249 (1987)
47. A. Kar, J. Mazumder, One-dimensional diffusion-model for extended solid-solution in laser cladding. *J. Appl. Phys.* **61**, 2645–2655 (1987)
48. M. Picasso, A.F.A. Hoadley, Finite element simulation of laser surface treatments including convection in the melt pool. *Int. J. Numer. Methods Heat Fluid Flow* **4**, 61–83 (1993)
49. X. He et al., Laser-surface alloying of metallic materials. *Lasers Eng.* **4**, 291–316 (1995)
50. Y. Zhang, A. Faghri, Melting and resolidification of a subcooled mixed powder bed with moving gaussian heat source. *J. Heat Transf.* **120**, 883–891 (1998)
51. M. Bamberger et al., Calculation of process parameters for laser alloying and cladding. *J. Laser Appl.* **10**, 29–33 (1998)
52. E. Toyserkani, A. Khajepour, S. Corbin, 3-D finite element modeling of laser cladding by powder injection: effects of laser pulse shaping on the process. *Opt. Lasers Eng.* **41**, 849–867 (2004)
53. S.Z. Shuja, B.S. Yilbas, M.O. Budair, Modeling of laser heating of solid substance including assisting gas impingement. *Numer. Heat Transfer Part A Appl.* **33**, 315–339 (1998)
54. P.M. Raj et al., Three-dimensional computational modelling of momentum, heat and mass transfer in laser surface alloying with distributed melting of alloying element. *Int. J. Numer. Methods Heat Fluid Flow* **11**, 576–599 (2001)

55. I.H. Chowdhury, X.F. Xu, Heat transfer in femtosecond laser processing of metal. *Numer. Heat Transfer Part A Appl.* **44**(3), 219–232 (2003)
56. S. Roychoudhary, T.L. Bergman, Response of agglomerated, multic ceramic particles to intense heating and cooling for thermal plasma spraying simulation. *Numer. Heat Transfer Part A Appl.* **45**(3), 211–233 (2004)
57. C. Del Borrello, E. Lacoste, Numerical simulation of the liquid flow into a porous medium with phase change: application to metal matrix composites processing. *Numer. Heat Transfer Part A Appl.* **44**, 723–741 (2003)
58. I. Ahmed, T.L. Bergman, An engineering model for solid-liquid phase change within sprayed ceramic coatings of nonuniform thickness. *Numer. Heat Transfer Part A Appl.* **41**, 113–129 (2002)
59. J.F. Li, L. Li, F.H. Stott, Predictions of flow velocity and velocity boundary layer thickness at the surface during laser melting of ceramic materials. *J. Phys. D—Appl. Phys.* **37**, 1710–1717 (2004)
60. J. Cheng, A. Kar, Mathematical model for laser densification of ceramic coating. *J. Mater. Sci.* **32**, 6269–6278 (1997)
61. D.B. Spalding, PHOENICS Overview, in *CHAM (Concentration Heat And Momentum Ltd.)* Technical Report: TR 001. 2001
62. D.D. Gray, A. Giorgini, Validity of Boussinesq approximation for liquids and gases. *Int. J. Heat Mass Transf.* **19**, 545–551 (1976)
63. J.V. Boussinesq, *Théorie analytique de la chaleur*, vol. 1, 2, (Gauthier-Villars, Paris, 1901–1903)
64. A.D. Brent, V.R. Voller, K.J. Reid, Enthalpy-porosity technique for modeling convection-diffusion phase-change—Application to the melting of a pure metal. *Numer. Heat Transf.* **13**, 297–318 (1988)
65. V.R. Voller, C. Prakash, A fixed grid numerical modeling methodology for convection diffusion Mushy region phase-change problems. *Int. J. Heat Mass Transf.* **30**, 1709–1719 (1987)
66. C.Y. Li, S.V. Garimella, J.E. Simpson, Fixed-grid front-tracking algorithm for solidification problems, part I: method and validation. *Numer. Heat Transf. Part B Fundam.* **43**, 117–141 (2003)
67. K.G. Kang, H.S. Ryou, Computation of solidification and melting using the PISO algorithm. *Numer. Heat Transf. Part B Fundam.* **46**, 179–194 (2004)
68. M. Rohde et al., Numerical simulation of laser-induced modification processes of ceramic substrates. *Numer. Heat Transf. Part A Appl.* **50**, 835–849 (2006)
69. M.F. Jensen et al., Microstructure fabrication with a CO₂ laser system: characterization and fabrication of cavities produced by raster scanning of the laser beam. *Lab Chip* **3**, 302–307 (2003)
70. G.H. Pettit, R. Sauerbrey, Pulsed ultraviolet-laser ablation. *Appl. Phys. A* **56**, 51–63 (1993)
71. J.K. Frisoli, Y. Hefetz, T.F. Deutsch, Time-resolved uv absorption of polyimide—Implications for laser ablation. *Appl. Phys. B Photophysics Laser Chem.* **52**, 168–172 (1991)
72. H. Schmidt et al., Ultraviolet laser ablation of polymers: spot size, pulse duration, and plume attenuation effects explained. *J. Appl. Phys.* **83**, 5458–5468 (1998)
73. W. Pflöging et al., Direct laser-assisted processing of polymers for micro-fluidic and micro-optical applications. *Photon Process. Microelectron. Photonics Ii* **4977**, 346–356 (2003)
74. E. Bremus-Kobberling, A. Gillner, Laser structuring and modification of surfaces for chemical and medical micro components. *Fourth Int. Symp. Laser Precis. Microfab.* **5063**, 217–222 (2003)
75. W. Pflöging et al., Patterning of polystyrene by UV-laser radiation for the fabrication of devices for patch clamping—Art. no. 68800D. *Laser Based Micro Nanopackaging Assembly Ii* **6880**(180), D8800–D8800 (2008)
76. S. Wilson et al., S. Dimov, (eds.), Machining of polystyrene by UV laser radiation for patch clamping device fabrication. in *4th International Conference on Multi-Material Micro Manufacturing*, (Whittles Publication, Cardiff, 2008)

77. H. Niino et al., Surface microstructuring of transparent materials by laser-induced backside wet etching using excimer laser. Fourth Int. Symp. Laser Precis. Microfab. **5063**, 193–201 (2003)
78. H. Niino et al., Surface microfabrication of fused silica glass by UV laser irradiation. Photon Process. Microelectron. Photonics Iii **5339**, 112–117 (2004)
79. S. Nikumb et al., Precision glass machining, drilling and profile cutting by short pulse lasers. Thin Solid Films **477**, 216–221 (2005)
80. D.M. Karnakis et al., Comparison of glass processing using high repetition femtosecond (800 nm) and UV (255 nm) nanosecond pulsed lasers. Microfluid. BioMEMS Med. Microsyst. III **5718**, 216–227 (2005)
81. M.H. Yen et al., Rapid cell-patterning and microfluidic chip fabrication by crack-free CO₂ laser ablation on glass. J. Micromech. Microeng. **16**, 1143–1153 (2006)
82. F. Schneider et al., (eds.), Adaptive Silikonmembranlinsen mit integriertem Piezo-Aktor. in *MikroSystemTechnik KONGRESS 2007*, (VDE-Verlag GmbH, Dresden 2007)
83. T. Hanemann et al., Rapid fabrication of microcomponents, design, test, integration, and packaging of mems/moems. Proceedings **4019**, 436–443 (2000)
84. S. Schreck, K.H. Zum Gahr, Laser-assisted structuring of ceramic and steel surfaces for improving tribological properties. Appl. Surf. Sci. **247**, 616–622 (2005)
85. K. Poser et al., TiN-particle reinforced alumina for unlubricated tribological applications mated with metallic counterbodies. Materialwissenschaft Und Werkstofftechnik **36**, 122–128 (2005)
86. O. Baldus, S. Schreck, M. Rohde, Writing conducting lines into alumina ceramics by a laser dispersing process. J. Eur. Ceram. Soc. **24**, 3759–3767 (2004)
87. P. Ajayan, L.S. Schadler, P.V. Braun, *Nanocomposite Science and Technology* (Wiley-VCH, Weinheim, 2003)
88. S. Banerjee, D. Chakravorty, Electrical resistivity of silver-silica nanocomposites. J. Appl. Phys. **85**, 3623–3625 (1999)
89. R.G. Duan et al., Metal-like electrical conductivity in ceramic nano-composite. Scr. Mater. **50**, 1309–1313 (2004)
90. M.A. Rodriguez et al., Microstructure and phase development of buried resistors in low temperature Co-fired ceramic. J. Electroceram. **5**, 217–223 (2000)
91. M. Rohde, B. Schulz, The effect of the exposure to different irradiation sources on the thermal-conductivity of Al₂O₃. J. Nucl. Mater. **173**, 289–293 (1990)
92. J.L. Cai, H. Gong, The influence of Cu/Al ratio on properties of chemical-vapor-deposition-grown p-type Cu-Al-O transparent semiconducting films. J. Appl. Phys. **98**, 033707, (2005)
93. S. Komornicki, M. Radecka, R. Sobas, Structural, electrical and optical properties of TiO₂–WO₃ polycrystalline ceramics. Mater. Res. Bull. **39**, 2007–2017 (2004)
94. M. Gillet, R. Delamare, E. Gillet, Growth, structure and electrical properties of tungsten oxide nanorods. Eur. Phys. J. D **34**, 291–294 (2005)
95. H.T. Wang et al., Thermal conductivity measurement of tungsten oxide nanoscale thin films. Mater. Trans. **47**, 1894–1897 (2006)
96. T. Lippert, J.T. Dickinson, Chemical and spectroscopic aspects of polymer ablation: special features and novel directions. Chem. Rev. **103**, 453–485 (2003)
97. P.E. Dyer, S.D. Jenkins, J. Sidhu, Development and origin of conical structures on XeCl laser ablated polyimide. Appl. Phys. Lett. **49**, 453–455 (1986)
98. D.J. Krajnovich, J.E. Vazquez, Formation of intrinsic surface-defects during 248 Nm photoablation of polyimide. J. Appl. Phys. **73**, 3001–3008 (1993)
99. R. Lloyd et al., Laser-assisted generation of self-assembled microstructures on stainless steel. Appl. Phys. A **93**, 117–122 (2008)
100. S.I. Dolgaev et al., Growth of large microcones in steel under multipulsed Nd : YAG laser irradiation. Appl. Phys. A **83**, 417–420 (2006)
101. A. Usoskin, H.C. Freyhardt, H.U. Krebs, Influence of light scattering on the development of laser-induced ridge-cone structures on target surfaces. Appl. Phys. A **69**, S823–S826 (1999)

102. S.I. Dolgaev et al., Formation of conical microstructures upon laser evaporation of solids. *Appl. Phys. A* **73**, 177–181 (2001)
103. V. Oliveira, F. Simoes, R. Vilar, M.A. Maher, H.D. Stewart (eds.), Column growth mechanisms during KrF laser micromachining of $\text{Al}_2\text{O}_3\text{-TiC}$, in *Proc. SPIE*, (2005)
104. R. Kohler et al., W. Pflöging, et al. (eds.), Laser-assisted structuring and modification of LiCoO_2 thin films. in *Proceedings SPIE*, (2009)
105. R. Kelly et al., On the debris phenomenon with laser-sputtered polymers. *Appl. Phys. Lett.* **60**, 2980–2982 (1992)
106. S.B. Tang, M.O. Lai, L. Lu, Effects of oxygen pressure on LiCoO_2 thin film cathodes and their electrochemical properties grown by pulsed laser deposition. *J. Alloy. Compd.* **424**, 342–346 (2006)
107. H. Xia, L. Lu, Texture effect on the electrochemical properties of LiCoO_2 thin films prepared by PLD. *Electrochim. Acta* **52**, 7014–7021 (2007)
108. S.I. Cho, S.-G. Yoon, Characterization of LiCoO_2 thin film cathodes deposited by liquid-delivery metallorganic chemical vapor deposition for rechargeable lithium batteries. *J. Electrochem. Soc.* **149**, A1584–A1588 (2002)
109. J.F.M. Oudenhoven et al., Low-pressure chemical vapor deposition of LiCoO_2 thin films: a systematic investigation of the deposition parameters. *J. Electrochem. Soc.* **156**, D169–D174 (2009)
110. T. Matsushita, K. Dokko, K. Kanamura, Comparison of electrochemical behavior of LiCoO_2 thin films prepared by sol-gel and sputtering processes. *J. Electrochem. Soc.* **152**, A2229–A2237 (2005)
111. K.W. Kim et al., Microfabrication of LiCoO_2 film using liquid source misted chemical deposition technique. *Solid State Ionics* **159**, 25–34 (2003)
112. H. Pan, Y. Yang, Effects of radio-frequency sputtering powers on the microstructures and electrochemical properties of LiCoO_2 thin film electrodes. *J. Power Sources* **189**, 633–637 (2009)
113. Z.M. Yang et al., Effect of annealing temperature on structure and electrochemical properties of LiCoO_2 cathode thin films. *Rare Met.* **25**, 189–192 (2006)
114. H.K. Kim, Y.S. Yoon, Characteristics of rapid-thermal-annealed LiCoO_2 cathode film for an all-solid-state thin film microbattery. *J. Vac. Sci. Technol. A* **22**, 1182–1187 (2004)
115. M. Okubo et al., Size effect on electrochemical property of nanocrystalline LiCoO_2 synthesized from rapid thermal annealing method. *Solid State Ionics* **180**, 612–615 (2009)
116. M. Inaba et al., Raman study of layered rock-salt LiCoO_2 and its electrochemical lithium deintercalation. *J. Raman Spectrosc.* **28**, 613–617 (1997)
117. H.Y. Park et al., LiCoO_2 thin film cathode fabrication by rapid thermal annealing for micro power sources. *Electrochim. Acta* **52**, 2062–2067 (2007)
118. M.J. Pelletier, *Analytical Applications of Raman Spectroscopy* (Wiley-Blackwell, Hoboken, 1999) pp. 442–447.
119. V.G. Hadjiev, M.N. Iliev, I.V. Vergilov, The Raman-Spectra of Co_3O_4 . *J. Phys. C* **21**, L199–L201 (1988)
120. E. Antolini, M. Ferretti, Synthesis and thermal stability of LiCoO_2 . *J. Solid State Chem.* **117**, 1–7 (1995)
121. G. Cam, M. Kocak, Progress in joining of advanced materials. *Int. Mater. Rev.* **43**, 1–44 (1998)
122. J. Brandner et al., Microfabrication in Metals and Polymers. In: N. Kockmann (eds) *Advanced Micro & Nanosystems* (Wiley-VCH, Weinheim, 2006) pp. 267–319.
123. S. Kou, Solidification and liquation cracking issues in welding. *JOM J Mine. Met. Mater. Soc.* **55**, 37–42 (2003)
124. H. Zhao, D.R. White, T. DebRoy, Current issues and problems in laser welding of automotive aluminium alloys. *Int. Mater. Rev.* **44**, 238–266 (1999)
125. J. Zhang, D.C. Weckman, Y. Zhou, Effects of temporal pulse shaping on cracking susceptibility of 6061-T6 aluminum Nd : YAG laser welds. *Welding J.* **87**, 18s–30s (2008)

126. A.P. Mackwood, R.C. Crafer, Thermal modelling of laser welding and related processes: a literature review. *Opt. Laser Technol.* **37**, 99–115 (2005)
127. J. Dowden (ed.), The theory of laser materials processing. *Springer Series in Materials Science*, vol. 119 (2009)
128. J. Mazumder, W.M. Steen, Heat-transfer model for Cw laser material processing. *J. Appl. Phys.* **51**, 941–947 (1980)
129. O.O.D. Neto, C.A.S. Lima, Nonlinear 3-dimensional temperature profiles in pulsed-laser heated solids. *J. Phys. D* **27**, 1795–1804 (1994)
130. N. Sonti, M.F. Amateau, Finite-element modeling of heat-flow in deep-penetration laser welds in aluminum-alloys. *Numer. Heat Transfer* **16**, 351–370 (1989)
131. H. Zhao, T. DebRoy, Macroporosity free aluminum alloy weldments through numerical simulation of keyhole mode laser welding. *J. Appl. Phys.* **93**, 10089–10096 (2003)
132. W.S. Chang, S.J. Na, A study on the prediction of the laser weld shape with varying heat source equations and the thermal distortion of a small structure in micro-joining. *J. Mater. Process. Technol.* **120**, 208–214 (2002)
133. H.L. Lin, C.P. Chou, Modeling and optimization of Nd : YAG laser micro-weld process using Taguchi method and a neural network. *Int. J. Adv. Manuf. Technol.* **37**, 513–522 (2008)
134. B.C. Kim et al., Investigation on the effect of laser pulse shape during Nd : YAG laser microwelding of thin Al sheet by numerical simulation. *Metall. Mater. Trans. A* **33**, 1449–1459 (2002)
135. E. Cicala et al., Hot cracking in Al-Mg-Si alloy laser welding—Operating parameters and their effects. *Mater. Sci. Eng. A* **395**, 1–9 (2005)
136. M.G. Nicholas, T.M. Valentine, M.J. Waite, The wetting of alumina by copper alloyed with titanium and other elements. *J. Mater. Sci.* **15**, 2197–2206 (1980)
137. S. Morozumi et al., Bonding mechanism between silicon-carbide and thin foils of reactive metals. *J. Mater. Sci.* **20**, 3976–3982 (1985)
138. A.J. Moorhead, H. Keating, Direct brazing of ceramics for advanced heavy-duty diesels. *Welding J.* **65**, 17–31 (1986)
139. J.K. Boadi, T. Yano, T. Iseki, Brazing of pressureless-sintered Sic using Ag-Cu-Ti alloy. *J. Mater. Sci.* **22**, 2431–2434 (1987)
140. K. Suganuma, Y. Miyamoto, M. Koizumi, Joining of ceramics and metals. *Ann. Rev. Mater. Sci.* **18**, 47–73 (1988)
141. O.M. Akselsen, Review: advances in brazing of ceramics. *J. Mater. Sci.* **27**, 1989–2000 (1992)
142. T. Yano, H. Suematsu, T. Iseki, High-resolution electron-microscopy of a Sic/Sic joint brazed by a Ag-Cu-Ti alloy. *J. Mater. Sci.* **23**, 3362–3366 (1988)
143. L. Huijie, F. Jicai, Q. Yiyu, Microstructure and strength of the SiC/TiAl joint brazed with Ag-Cu-Ti filler metal. *J. Mater. Sci. Lett.* **19**, 1241–1242 (2000)
144. A. Kar, A.K. Ray, Characterization of Al₂O₃—304 stainless steel braze joint interface. *Mater. Lett.* **61**, 2982–2985 (2007)
145. K. Suganuma, T. Okamoto, K. Kamachi, Influence of shape and size on residual-stress in ceramic metal joining. *J. Mater. Sci.* **22**, 2702–2706 (1987)
146. H. Chang et al., Effects of residual stress on fracture strength of Si₃N₄/stainless steel joints with a Cu-interlayer. *J. Mater. Eng. Perform.* **11**, 640–644 (2002)
147. H.Q. Hao et al., The effect of interlayer metals on the strength of alumina ceramic and 1Cr18Ni9Ti stainless-steel bonding. *J. Mater. Sci.* **30**, 4107–4111 (1995)
148. M.R. Locatelli et al., New approaches to joining ceramics for high-temperature applications. *Ceram. Int.* **23**, 313–322 (1997)
149. R.A. Marks et al., Joining of alumina via copper/niobium/copper interlayers. *Acta Mater.* **48**, 4425–4438 (2000)
150. J.W. Park, P.F. Mendez, T.W. Eagar, Strain energy release in ceramic-to-metal joints by ductile metal interlayers. *Scripta Mater.* **53**, 857–861 (2005)
151. G.J. Qiao et al., Brazing Al₂O₃ to Kovar alloy with Ni/Ti/Ni interlayer and dramatic increasing of joint strength after thermal cycles. *Eco-Mater. Process. Des. Vi* **486**(487), 481–484 (2005)

152. G. Blugan et al., Brazing of silicon nitride ceramic composite to steel using SiC-particle-reinforced active brazing alloy. *Ceram. Int.* **33**, 1033–1039 (2007)
153. G. Blugan, J. Janczak-Rusch, J. Kuebler, Properties and fractography of Si₃N₄/TiN ceramic joined to steel with active single layer and double layer braze filler alloys. *Acta Mater.* **52**, 4579–4588 (2004)
154. N.Y. Taranets, H. Jones, Wettability of AlN with different roughness, porosity and oxidation state by commercial Ag-Cu-Ti brazes. *J. Mater. Sci.* **40**, 2355–2359 (2005)
155. H.P. Xiong, C.G. Wan, Z.F. Zhou, Increasing the Si₃N₄/1.25Cr-0 Mo steel joint strength by using the method of drilling holes by laser in the surface layer of brazed Si₃N₄. *J. Mater. Sci. Lett.* **18**, 1461–1463 (1999)
156. A.A. Shirzadi, Y. Zhu, H.K.D.H. Bhadeshia, Joining ceramics to metals using metallic foam. *Mater. Sci. Eng. A* **496**, 501–506 (2008)
157. H.Q. Hao, Z.H. Jin, X.T. Wang, The influence of brazing conditions on joint strength in Al₂O₃/Al₂O₃ bonding. *J. Mater. Sci.* **29**, 5041–5046 (1994)
158. W. Tillmann et al., Kinetic and microstructural aspects of the reaction layer at ceramic/metal braze joints. *J. Mater. Sci.* **31**, 445–452 (1996)
159. M. Brochu, M.D. Pugh, R.A.L. Drew, Joining silicon nitride ceramic using a composite powder as active brazing alloy. *Mater. Sci. Eng. A* **374**, 34–42 (2004)
160. O.C. Paiva, M.A. Barbosa, Brazing parameters determine the degradation and mechanical behaviour of alumina/titanium brazed joints. *J. Mater. Sci.* **35**, 1165–1175 (2000)
161. K. Poser, K.H. Zum Gahr, J. Schneider, Development of Al₂O₃ based ceramics for dry friction systems. *Wear* **259**, 529–538 (2005)
162. A. Albers, A. Arslan, M. Mitariu, Clutches using engineering ceramics as friction material. *Materialwissenschaft Und Werkstofftechnik* **36**, 102–107 (2005)
163. U.A. Russek et al., Laser beam welding of thermoplastics. *Photon Process. Microelectron. Photonics Ii* **4977**, 458–472 (2003)
164. K. Sato et al., Laser welding of plastics transparent to near-infrared radiation. *Photon processing in microelectronics and photonics* **4637**, 528–536 (2002)
165. T. Klotzbuecher et al., Diode laser welding for packaging of transparent micro-structured polymer chips—Art. no. 610704. *Laser-based Micropackaging* **6107**(264), 10704–10704 (2006)
166. A. Griebel et al., Integrated polymer chip for two-dimensional capillary gel electrophoresis. *Lab Chip* **4**, 18–23 (2004)

Chapter 9

Temperature Monitoring by Optical Methods in Laser Processing

I. Smurov and M. Doubenskaia

Abstract Diverse optical diagnostic tools were applied for monitoring high temperature heat and mass transfer in a number of laser-based technologies. A set of pyrometers was developed and applied for surface temperature monitoring in pulsed periodic Nd-YAG laser welding and surface treatment, deep penetration welding by CO₂ and Nd:YAG lasers, laser cladding (LC) with lateral and coaxial powder injection, and selective laser melting (SLM). Particle-in-flight parameters in LC were measured by CCD camera-based diagnostic system. Infrared camera was applied for process visualization in laser welding, cladding, and SLM. Process monitoring was carried out at different temporal and spatial scales and in different spectral bands. True temperature was restored in pulsed laser surface treatment and in pulsed periodic (PP) LC.

9.1 Introduction

The thermal state of material in the zone of laser action is one of the main complex parameters to determine the evolution of physical and chemical processes including phase transformations. In view of this, information on the dynamics of surface temperature during the whole thermal cycle of laser machining is of major practical interest. Absence of online control in laser machining is one of the main obstacles on the way of its wide industrial implementation. Methods of process monitoring based on real physical variables, such as surface temperature, or on superposition of diverse signals of different nature can be mentioned as current general usage techniques. However, they should be distinguished from one another, and moreover, the latter should be applied with great caution. It is known that total radiation intensity

I. Smurov(✉) · M. Doubenskaia
DIPI Laboratory, Ecole Nationale d'Ingénieurs de Saint-Etienne (ENISE),
58 rue Jean Parot, 42023 Saint-Etienne Cedex 2, France
e-mail: igor.smurov@enise.fr

from the zone of laser action comprises elements such as reflected laser beam, radiation of the laser-induced plume, and thermal radiation from the heat affected zone (HAZ) which cannot be easily separated. Generally speaking, methods of process optimization and online control based on monitoring of a “signal” whose nature is not clear, as, for example, a photodiode collecting integral radiation from the laser welding zone, are not universal and can only be used within a limited range of process parameters.

The use of a pyrometer for non-contact temperature measurements in laser machining offers a series of potential advantages for a detailed analysis of surface temperature evolution versus laser operation parameters and materials properties [1–9]. However, efficient application of pyrometry in laser machining requires the solution of a number of methodological difficulties. The two basic problems are: (a) correct measurements of brightness temperature (that is to avoid superposition of proper thermal radiation to be measured with different types of “noise”) and (b) correct determination of true temperature. Just one example to illustrate the actual problems: the absolute majority of commercial pyrometers which operate in the near-infrared spectral band cannot be applied in Nd:YAG laser machining because of the low protection from reflected laser radiation. To solve this problem, pyrometers specially designed for laser machining must be applied. Taking into account the spatial and temporal scales of different technological processes is a well-recognized challenge for optical diagnostics. Let us consider, from this point of view, several laser-based applications. Combination of diverse physical phenomena with rather different characteristic scales is involved in Laser Welding. The most rapid are related to dynamics of the vapor flow in the keyhole and the laser beam-plasma interaction, their typical timescale being in the range of microseconds and even shorter. Two temporal scales are distinguished in hydrodynamics of the molten pool. It is mainly microsecond inside the keyhole at the liquid–vapor interface with the characteristic time defined by the ratio of the keyhole diameter to the vapor velocity. As to convective mass transfer in the molten pool, it occurs on a millisecond timescale. For example, liquid motion in CW laser welding, as marked by the movement of a W pellet, takes place within a 10–100 ms temporal frame. The simplified case of heat transfer, that is, not coupled with gas and hydrodynamics is the slowest process which could be characterized by the two following estimations. The first one is related to the laser-matter interaction time and determined as the laser beam diameter divided by the welding velocity, i.e., for 0.1–1 mm beam diameter and 10–100 mm/s welding speed, this estimation will be 1–100 ms. The second one pertains to the transient period which is proportional to the value α/v^2 where α is the temperature diffusivity, and v is the welding velocity. For defect detection, the simplest estimation is to divide the defect size by the welding speed. The above considerations show that monitoring of the laser welding process should be carried out at very different timescales ranging from microseconds up to tens and hundreds of milliseconds. In terms of the spatial resolution of laser welding monitoring, it should be at least close to the laser beam diameter or even higher. If to compare Laser Welding and Laser Cladding (LC), the latter usually has smaller cladding velocities relative to welding velocities, cladded beads are wider than welding seams, hydrodynamics is less pronounced, and plasma

is absent. It means that the typical timescales for macroscopic phenomena in LC, except those related to dynamics of the individual particles, are significantly longer.

In Selective Laser Melting (SLM), the time required for melting an individual particle can be estimated as r^2/α where r is the particle radius, and α is the temperature diffusivity of the corresponding bulk metal. Thus, for steel powder with 10 μm grain diameter, this will be of the order of 10 μs irradiation time. Let us note that, at 100 μm laser spot diameter and 0.1 m/s scanning speed, the laser irradiation time of the deposited powder is 1 ms. Thus, in SLM process, the already melted powder is exposed to the laser radiation during most of the laser-matter interaction time. One may conclude that for monitoring the powder melting and consolidation into a molten pool with 100 μm size, 10 μs temporal resolution is needed, and for monitoring the entire manufacturing cycle and process stability, resolution must be at the millisecond level.

The development of a pyrometer system specially aimed at laser machining is a methodologically complicated task because of a wide quantitative range and complexity of the process parameters: wide temperature range (500–3, 500°C), high heating and cooling rates ($10^3\text{--}10^8\text{C/s}$), small size of the heated zone (0.1–5 mm), the influence of the laser plume radiation, sharp variation of material optical and thermal properties, etc. The requirements for pyrometer performance are even contradictory: It is not possible to apply at the same time short sampling time, small size of temperature measurements zone, and narrow spectral bandpass because of the insufficient intensity of thermal radiation reaching pyrometer sensor.

9.2 Theoretical Background of Pyrometry

The true temperature restoration is the key problem of pyrometry because of the unknown emissivity and its possible variation in course of measurements. Several different methods can be applied but no universal solution is found [10, 11]. Two different methods of temperature monitoring are used in the present study: monochromatic pyrometry and multi-wavelength pyrometry.

Monochromatic pyrometry

Brightness temperature of a non-blackbody target (T_B) is defined as the temperature (T_0) of a blackbody having the same monochromatic luminance. The relation between the two temperatures is presented below [12–14]:

$$L(\lambda, T_0) = \frac{C_1}{\pi \lambda^5 (\exp(C_2/\lambda T_B) - 1)} \text{ that leads to } \frac{1}{T_0} = \frac{1}{T_B} + \frac{\lambda}{C_2} \ln \varepsilon'(\lambda, T_0) \tag{9.1}$$

where $L(\lambda, T_0)$ is spectral radiant intensity [W/m^3], $C_1 = 3.7418 \times 10^{-16} [\text{W/m}^2]$, $C_2 = 1.4384 \times 10^{-2} [\text{m} \cdot \text{K}]$, ε is spectral emissivity, λ is wavelength.

Lack of reliable emissivity data (especially for high temperature) is the major drawback in brightness pyrometry. For example, take the case of iron, where the pure material exhibits an emissivity as low as 0.35, whereas the oxidized surface can have an emissivity as high as 0.95 at high temperature ($\lambda = 0.65 \mu\text{m}$). Another example is aluminum whose emissivity ($\lambda = 0.65 \mu\text{m}$) can vary from 0.10 to 0.40 depending on degree of oxidation, surface treatment, etc. Therefore, relative emissivity uncertainties of 50%, and even of 100%, are not untypical.

True temperature restoration by multiwavelength pyrometry

The idea of defining temperature based on measurements of spectral intensities without knowing the emissivity is not new: it has been proposed by Svet [12, 13], Coates [14], and many others in the last 3 decades. The progress was expected from application of modern computer facilities, the least squares method, and the increase of the number of spectral channels. By this way, multiwavelength pyrometry (MWP) and spectroradiometry are expected to restore the “true” temperature. MWP is based on the so-called “inverse radiant temperature transformation” method, known also as “Wien/Log transformation”: this is a simple extension to a multiple-channels instrument of what is done for classical monochromatic pyrometry; using Wien’s approximation, and replacing the term logarithm of emissivity by a wavelength polynomial fit, permits to solve the so-linearized system and obtain the true temperature [13].

$$\begin{aligned} L(\lambda_i, T_0) &= \varepsilon'(\lambda_i, T_0) \times \left[C_1 \lambda_i^{-5} / [\exp\left(\frac{c_2}{\lambda_i T_0}\right) - 1] \right] \\ &= \left[C_1 \lambda_i^{-5} / [\exp\left(\frac{c_2}{\lambda_i T_i}\right) - 1] \right] \end{aligned} \quad (9.2)$$

$$1/T_i = 1/T_0 - (\lambda_i/c_2) \ln \varepsilon_i \quad (9.3)$$

$$\text{with } \ln(\varepsilon_i) = \sum_{n=0}^{N-2} a_n \lambda_i^n \quad i = 1, \dots, N \quad (9.4)$$

where, N is inferior or equal to the number of pyrometer wavelengths.

The N data $1/T_i$ are fitted with $1/T_0 - (\lambda_i/c_2) \ln \varepsilon_i$ versus λ .

The simplest case is the gray body approximation with constant emissivity that has led to a first-order approximation ($N = 1$, $\varepsilon(\lambda) = \exp(a)$): but the gray target is not so often the case. A universal reliable method for any model of emissivity and in any spectral range is not yet developed.

Certain progress is reached using Eqs. 9.5–9.7 and working directly with the radiance and not with the temperature:

$$\varepsilon_i = L_i/L_0(\lambda_i, T_0) = \frac{\exp\left(\frac{c_2}{\lambda_i T_0}\right) - 1}{\exp\left(\frac{c_2}{\lambda_i T_i}\right) - 1} \quad (9.5)$$

$$\text{with } \varepsilon_i = \sum_{n=0}^{N-2} a_n \lambda_i^n \text{ or any other approximation} \tag{9.6}$$

$$\sum_{n=0}^{N-2} a_n \lambda_i^n = \frac{\lambda_i^5 L_i}{c_1} \left[\exp\left(\frac{c_2}{\lambda_i T_0}\right) - 1 \right] \quad i = 1, \dots, N \tag{9.7}$$

The advantage of the present approach is to apply any appropriate emissivity approximation (polynomial, exponential, the empiric one as defined by Drude or Hagen and Rubens [15]) compared to the “Wien/Log transformation” where the emissivity is approximated by $\varepsilon(\lambda) = \exp\left(\sum_{n=0}^{N-2} a_n \lambda_i^n\right)$.

The second step is to define a criterion to select an appropriate emissivity approximation. Varying the T_0 value in Eq. 9.6, the corresponding emissivity, ε_d , is found. Then it is needed to fit the obtained ε_d values applying a chosen function (polynomial, exponential, etc.) to obtain ε_c that is the calculated emissivity. The minimum value of the function $1/V = 1/\left(\sum_{i=1}^n \frac{(\varepsilon_c - \varepsilon_d)^2}{\varepsilon_c}\right)$ defines the best choice of T_0 .

9.3 Diagnostics Facilities

9.3.1 Pyrometers Performance Data

Several original pyrometers were applied in the present study: single spot monochromatic, 2D monochromatic, single spot bicolor, single spot multiwavelength (see Table 9.1). A typical pyrometer system comprises: a separated optical head connected to an electronic unit by optical fiber providing the possibility of installing the pyrometer optical head directly into the laser optical head; an internal microprocessor intended to control the instrument operating modes: calibration, measuring (choice of the acquisition period and total duration of the measurements, minimum and maximum temperature values, etc.), and recording (applying internal memory for data recording). Special software is developed for: instrument control by a personal computer, data acquisition, recording, transfer, treatment, and graphical presentation. The technical solution described above allows using the developed pyrometers in a wide range of high temperature applications [16, 17]. Specially developed “notch” filters (10^{-6} transparency at 1.06 μm wavelength) are applied to avoid the influence of laser radiation on temperature measurements.

The single spot monochromatic pyrometer intended for measurements of relatively low temperature (starting from 600°C) consists of the optical head and the electronic unit connected by optical fiber. The electronic unit includes InGaAs photodetector, filter ($\lambda_{\text{max}} = 1.5 \mu\text{m}$), pre-amplifiers, and power source (Table 9.1). The 2D pyrometer catches a signal by photodiodes from a rectangular matrix (10×10) and measures the brightness temperature at a single wavelength $\lambda = 0.86 \mu\text{m}$ with 50 nm spectral bandwidth. The vision zone for measurements is $8 \times 8 \text{ mm}^2$.

Table 9.1 Pyrometers performance data

Pyrometer Parameter	Mono-chromatic	2D Monochromatic	Multi-wavelength	Bi-colour pyrometer
Temperature range, °C	600–3,200	1,100–3,800	900–3,200	800–2,500
Wavelength, μm	1.5	0.870	1.001–1.573	1.25, 1.36
Spatial resolution, μm	400	265 for each photodiode	800	50
Sampling time, μs	50	17 for each photodiode	50 for each photodiode	50,000
Photodiodes number	1	matrix array (10×10)	12	2
Type of detector	InGaAs	Si	InGaAs	InGaAs

The sampling time for a single photodiode is $17\ \mu\text{s}$ (Table 9.1). The measurements by different photodiodes are carried out consecutively. For example, the duration of measurement of a temperature profile by a line of 10 photodiodes is $170\ \mu\text{s}$ while that for all 100 photodiodes to display a 2D temperature distribution takes 1.7 ms.

The multi-wavelength pyrometer simultaneously measures a brightness temperature on 12 wavelengths in the spectral range $1.001\text{--}1.573\ \mu\text{m}$ with $50\ \mu\text{s}$ acquisition time in a single spot with $800\ \mu\text{m}$ diameter. To improve the signal-to-noise ratio, the optical system of the bicolor pyrometer is based on a grating monochromator. Low-noise cooling InGaAs photo detectors are used to measure relatively low temperature (low temperature limit is 800°C) in the spectral band $1.1\text{--}1.5\ \mu\text{m}$. The particular feature of the pyrometer is a small size of the temperature measurement zone— $50\ \mu\text{m}$, that results in a long sampling time—50 ms. Before measurements the pyrometers were calibrated with the help of the black body MIKRON M390 (maximum temperature is $3,000^\circ\text{C}$).

Infrared camera FLIR Phoenix RDAS™

Modern infra-red cameras provide more detailed information with a higher spatial and temporal resolution than the applied pyrometers. On the other hand, it is much more difficult to obtain brightness temperature values, even if calibration is properly done, and practically impossible to recalculate the true temperature because of emissivity variations in a wide spectral window that is often the case. One may note that the modern infrared cameras are much more expensive than the pyrometers; that is why they are used more frequently for process visualization and optimization in laboratory conditions than for process online control in industrial environment. Infrared monitoring was carried out by a commercial infrared camera FLIR Phoenix RDAS™ with InSb sensor with $3\text{--}5\ \mu\text{m}$ bandpass arranged on 320×256 pixels array. In full frame format Phoenix camera delivers a rather modest 345 Hz frame rate while it can acquire images with a frame rate of up to 38 kHz by using subwindows.

The baseline of utilization of the optical diagnostic tools is the following (Fig. 9.1): For all of them, calibration procedure should be applied that allows obtaining brightness temperature. The calibration is carried out using the so-called “black body” represented by a high temperature furnace with an optical access providing certified thermal radiation corresponding to the black body one at a given temperature. The calibration is particularly useful for pyrometer and infrared camera equipped by a filter with narrow spectral bandpass, say $50\text{--}100\ \text{nm}$. Narrow spectral window is useful to avoid the influence of emissivity variation with wavelength and to minimize the contribution of parasite radiation of different nature. The particular problem in laser machining is to avoid the reflected laser radiation (mainly for Nd:YAG lasers) and radiation of laser-induced plume (mainly for CO_2 lasers). When measuring thermal radiation in a broad spectral band, say $2\text{--}3\ \mu\text{m}$ that is typical for infrared cameras, most probably the recorded signal will be influenced by emissivity variation. Knowledge of brightness temperature measured by a monochromatic pyrometer is often not enough to restore the true temperature because the emissivity value should be known that is not often the case. When measurements by infrared camera in

Fig. 9.1 Methodology of the temperature measurements by different diagnostic tools

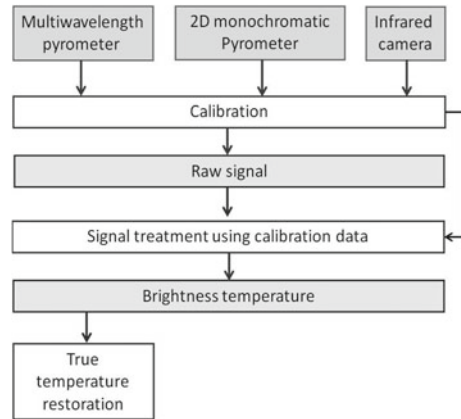


Table 9.2 Performance of the CCD camera-based diagnostic tool

Particle size detection limit, μm	10
Wavelengths λ , nm	800–960
Instrumental error, %	± 1
Measurement distance to the jet, to be related with the measured zone, mm	147
Minimum sampling time, μs	1
Zone of measurements, mm^2	2.3×3

a wide spectral bandwidth are carried out, there are rather low chances to restore true temperature. The most effective method to reach the goal, i.e., to find the true temperature, is to apply: (a) a multi-wavelength pyrometer with narrow spectral windows; (b) a certified black body providing calibration in a wide temperature range, for example from 500°C up to $3,000^\circ\text{C}$, and finally to apply an appropriate method of true temperature restoration.

CCD camera-based diagnostic tool

A CCD camera-based optical diagnostic tool is used for a real-time particle jet visualization and for a determination of particles size and velocity during the powder injection. The performance of the CCD camera-based diagnostic system is specified in Table 9.2. The optical diagnostic tool consists of a non-intensified image sensor Exview HAD CCD by Sony Inc. having high quantum efficiency in near-infrared spectral range (800–960 nm); telescopic lens providing the real-time monitoring area $2.3 \times 3\text{mm}^2$ of the powder jet. The high number of effective pixels allows capturing a gray high quality image $1,038 \times 1,388$. An original software package is intended for calibration, image treatment, and statistical analysis of particle parameters [18].

9.4 Results and Discussion

9.4.1 Surface Temperature Evolution in Pulsed and Pulsed Periodic Laser Action of Millisecond Range

Physical phenomena in pulsed Nd:YAG laser irradiation with millisecond pulse duration were intensively studied in the early 1970–1990 [19, 21]. This is one of the relatively simple and probably one of the most studied fields of laser applications [22, 23]. Actually, laser pulses of millisecond duration are applied in laser welding of thin plates (for example, hermetically sealed kovar boxes for microelectronics), LC (for example, moulds repairing), remelting of the upper layers of thermal-sprayed coatings, and other applications where laser radiation is used to melt a thin layer and to avoid creating a large HAZ. The experiments were carried out to analyze the influence of the variation of the following laser parameters: (a) energy per pulse, E , at fixed pulse duration; (b) pulse shape at fixed energy per pulse and pulse duration. For (a) case, only rectangular pulse shape was applied. Each individual thermal cycle is specified by several characteristic values: (a) the maximum peak temperature, T_{\max} ; (b) the instant when melting starts, t_m , i.e., $T(t = t_m) = T_m$, where T_m is the melting point; (c) the melt life time, τ_{lt} (i.e., the duration of liquid phase); (d) the duration of solidification stage, τ_s , i.e., the persistence of the liquid phase after the end of the laser pulse. A (pulse-periodic) PP Nd:YAG laser source HAAS HL62P (maximal average output power 60 W, maximum peak power 3,000 W, pulse duration up to 20 ms) was applied and laser radiation was delivered by optical fiber and focused in a spot of 2.1 mm diameter on stainless steel (INOX 304L) substrates. To minimize the influence of surface thermochemistry on emissivity variations, a flow (0.083 l s^{-1}) of Ar was applied. The CNC 3D table LASMA 1054 assures precise movement (position accuracy is up to $1 \mu\text{m}$) of the substrate in relation to laser beam. The multi-wavelength pyrometer (MWP) was fixed at the laser head, the distance of measurements was 160 mm, and the angle of sight was about 45° . The area from which temperature measurements were taken was situated at the center of the laser spot.

9.4.1.1 Variation of Energy Input

The variation of the thermal cycle with energy per pulse was studied in the range from 13 to 30 J with fixed pulse duration (10 ms) for the rectangular pulse shape. The results are presented in Fig. 9.2a for the brightness temperature ($\lambda = 1.376 \mu\text{m}$ pyrometer wavelength) and in Fig. 9.2b for the true temperature (the applied method of temperature determination is discussed above).

Note that, because of the pyrometer sensitivity limit (900°C), only the upper parts of the thermal cycles are presented. An evident temperature rise with energy input is shown. In the simplest linear heat transfer model of laser heating, surface temperature is directly proportional to energy per pulse (and energy density flux) [19, 24].

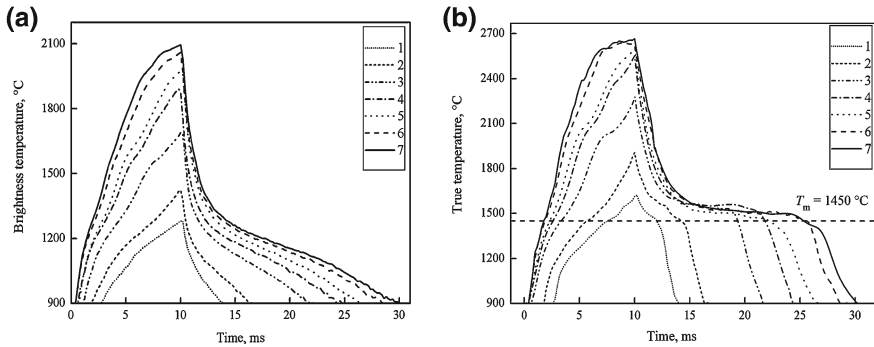


Fig. 9.2 Variation of the energy per pulse for the fixed pulse duration. Temperature evolution for rectangular laser pulses with a fixed pulse duration (10 ms) but different energy per pulse. *Curve 1* corresponds to 13 J per pulse; *curve 2* 15 J; *curve 3* 20 J; *curve 4* 23 J; *curve 5* 25 J; *curve 6* 28 J; *curve 7* 30 J; **a** brightness temperature measured at $\lambda = 1.376\ \mu\text{m}$ pyrometer wavelength; **b** determined true temperature

In the present experiments, the surface temperature is directly proportional to energy per pulse only for low values of energy density flux: up to $6.6 \times 10^4\text{ W/cm}^2$, that corresponds to 23 J. With the further increase of energy input the increase of T_{max} values is relatively slow: 4% with 30% energy increase. The deviation from the linear dependence between surface temperature and absorbed laser energy at higher temperatures is the result of nonlinear phenomena such as evaporation, melt convection, etc. The duration of solidification stage τ_s , increases with energy input from 1.75 ms for 13 J to 15.4 ms for 30 J, i.e., by 8.8 times. The melt life time increases from 4.22 ms for 13 J to 23.5 ms for 30 J, i.e., by 5.57 times. The instant when melting starts, t_m , occurs significantly earlier strongly decreases with energy input: at 7.09 ms for 13 J compared to 1.4 ms for 30 J, thus being reduced by 5.06 times. The simplest heat transfer model predicts the dependence $t_m \sim q^{-2}$ (or E^{-2} , where E is energy per pulse [19, 24]) that is rather similar to the obtained experimental results. The surface cooling rates after the end of solidification are higher for low energy inputs because of the smaller size of HAZ.

9.4.1.2 Variation of Pulse Duration

Experimental results concerning the influence of pulse duration, $\Delta\tau$, (rectangular pulse shape) for fixed energy per pulse, E , are presented in Fig. 9.3. Under the above conditions, the difference of surface thermal cycles is defined by the difference of energy density flux; therefore, the heating rate and maximum temperature per thermal cycle are higher for shorter pulses. The decrease of T_{max} with pulse duration from 2,680°C ($\Delta\tau = 12\text{ ms}$) to 2,408°C ($\Delta\tau = 20\text{ ms}$), shows a nearly linear dependence. The instant when melting starts occurs significantly later with pulse duration: at 2 ms for $\Delta\tau = 12\text{ ms}$ compared to 7 ms for $\Delta\tau = 20\text{ ms}$. The linear

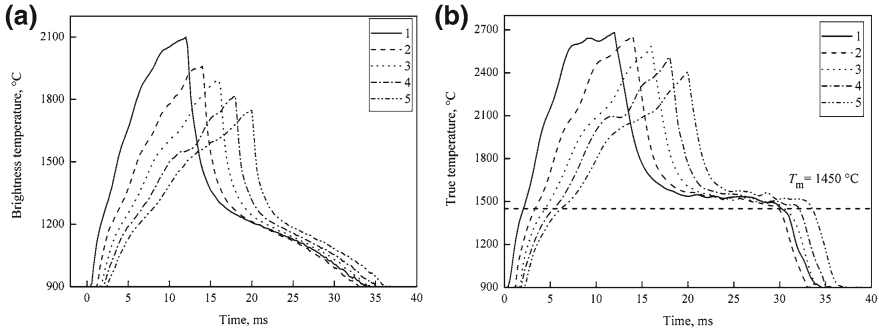


Fig. 9.3 Variation of the pulse duration for the fixed energy per pulse. Temperature evolution for rectangular laser pulses with a fixed energy per pulse (close to 29J) but different pulse duration. *Curve 1* corresponds to 12ms pulse duration (33J pulse energy); *curve 2* 14ms (28J); *curve 3* 16ms (29J); *curve 4* 18ms (29J); *curve 5* 20ms (29J). **a** brightness temperature measured at $\lambda = 1.376\text{ }\mu\text{m}$ pyrometer wavelength ; **b** determined true temperature

heat transfer model predicts the similar dependence $t_m \sim \Delta\tau^2$. The melt life time is practically independent of the pulse duration: $\tau_{lt} = 27 \pm 1\text{ ms}$.

Under the applied experimental conditions characterized by low laser intensity, large pulse duration, essential heat transfer mode, shallow molten pool, etc., the melt life time is determined mainly by the energy input that is fixed. A slight monotonous increase of the solidification stage, τ_s , with pulse duration is found: from 13.6ms ($\Delta\tau = 12\text{ ms}$) to 17.9ms ($\Delta\tau = 20\text{ ms}$), which could be explained by the decrease of surface temperature with pulse duration.

9.4.1.3 Variation of Pulse Shape

The idea to optimize the pulse shape in pulsed periodic (PP) laser machining has been discussed since long time. In the present study, several different shapes of laser pulse were applied with fixed pulse duration (18ms) and energy per pulse (30J). The results are compared with one another and with the reference values corresponding to the rectangular pulse shape. Temperature evolution for the two triangular laser pulses is presented in Fig. 9.4: laser pulse shape; brightness temperature measured at $\lambda = 1.376\text{ }\mu\text{m}$ pyrometer wavelength; restored true temperature. One may note that in Fig. 9.4a the temperature maximum (2, 274°C) is reached somewhere in the middle of the laser pulse because of the sharp decrease of energy density flux; the melt life time, τ_{lt} , is relatively large (27.4ms).

Looking at the effect of the right-angled triangle-shaped laser pulse with increasing intensity, Fig. 9.4b, one may note a rather different character of the temperature evolution, in particular the increase of the maximum temperature up to 2, 748°C (by 1.21 times), the decrease of the melt life time up to 22.3ms (by 1.23 times), but the increase of the solidification stage, τ_s , by a factor of 1.28. The temperature evolution

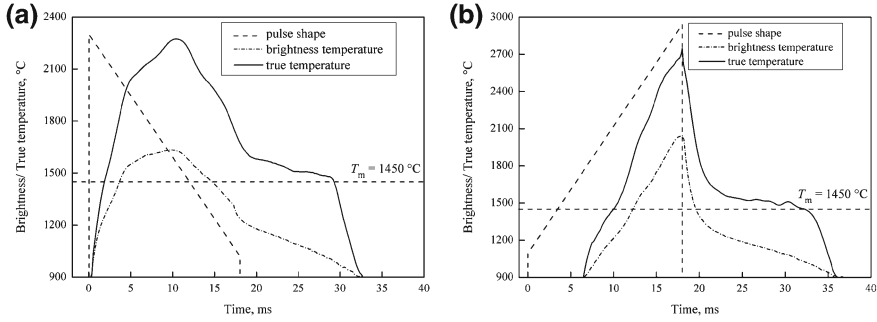
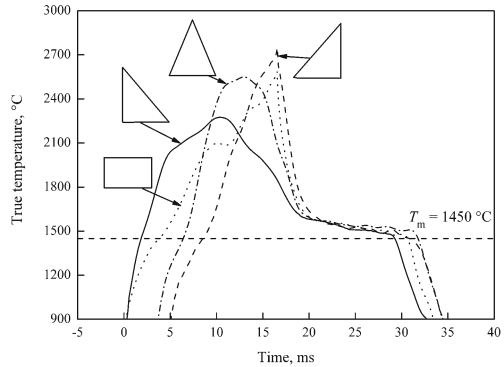


Fig. 9.4 Temperature evolution for triangular laser pulses (pulse duration is 18 ms, energy per pulse is 30J)

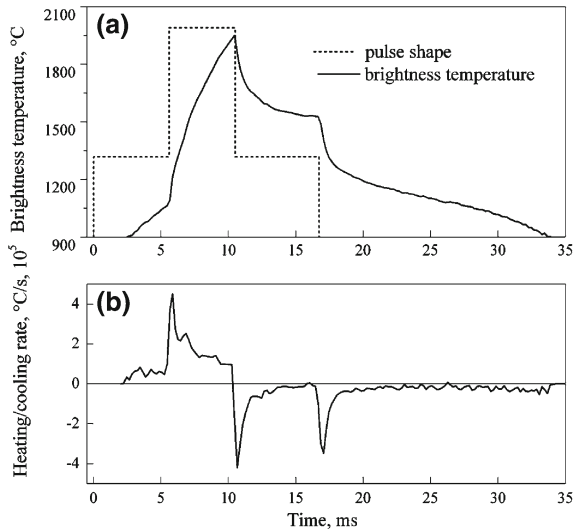
Fig. 9.5 Temperature evolution for the laser pulses with a fixed pulse duration (18 ms) and energy per pulse (30J) but with different pulse shapes: *rectangular* and three different *triangles*



corresponding to the three triangular pulses with different shapes (two right-angled and one equal-sized) and a rectangular pulse shape are presented in Fig. 9.5. Note that pulse duration and energy per pulse are the same for all pulses. The highest peak temperature is reached under the action of the right-angled triangle with increasing energy density flux, the lowest—for the right-angled triangle with decreasing energy density flux; the peak temperatures are comparable for the rectangular pulse shape ($T_{\max} = 2,584^{\circ}\text{C}$ reached at the pulse end) and for the equal-sized triangle ($T_{\max} = 2,549^{\circ}\text{C}$ reached somewhere in the middle of the pulse). The profile of the temperature peaks could be sharp or smooth depending on the laser pulse shape. The instant when melting starts, t_m , is the earliest for the right-angled triangle with decreasing energy density flux and the latest for the right-angled triangle with increasing energy density flux.

Modern laser sources provide an opportunity to apply even more complicated shapes of laser pulses. Keeping in mind the still incomplete discussion about the advantages of pre-heating and post-heating in laser machining (for example to avoid thermal cracking and to accelerate the key-hole formation in pulsed laser welding), the following roughly approximated shape of laser pulse was applied (see Figs. 9.6, 9.7): rectangular “basis” with 21 J plus additional rectangular “peak” (with 8 J)

Fig. 9.6 Temperature evolution (a) and heating/cooling rates (b) for the laser pulse with a stepwise shape



that was placed at the pulse beginning (to simulate “pre-heating”), in the middle and at the end of the pulse (to simulate “post-heating”). One may note the two different heating stages corresponding to two different values of energy density flux ($q_1 = 3.3 \times 10^4 \text{W cm}^{-2}$ and $q_2 = 7.3 \times 10^4 \text{W cm}^{-2}$) and the two cooling stages: the last one is typical of the laser pulse end but the first one is rather unusual because intensive cooling takes place during laser action. A comparison of the temperature evolution for the above-mentioned laser pulses and for the rectangular one taken as reference (all pulses have the same duration and energy per pulse) is presented in Fig. 9.7. The stable surface temperature plateau corresponds to the pulse with “pre-heating” shape that provides the longest melt life time and the smallest peak temperature as well. The highest temperature is reached for the pulse with “post-heating” shape where maximum of the energy density flux is reached at the pulse end (similar to the situation with the different triangular pulses, see Fig. 9.5). One may note that the temperature values at the end of the laser action are practically the same for the two pulses with the same value of energy density flux at the pulse end ($q_1 = 3.3 \times 10^4 \text{W/cm}^2$).

9.4.1.4 Pulsed Periodic Laser Irradiation

Evolution of the brightness temperature for CW and PP laser action (five pulses with 2 ms duration each) with the same total duration (18 ms) and total energy input (30 J) is compared in Fig. 9.8. Although there are evident differences at the initial stage of laser action (one may note a complete solidification of the melt after the end of the first pulse with duration of 2 ms) the final brightness temperatures corresponding to the end of laser action are close to one another: 1, 808°C for the continuous action

Fig. 9.7 Temperature evolution for laser pulses with a fixed pulse duration (18 ms) and energy per pulse (30 J) but with different pulse shape: *rectangular* and three different superposition of two *rectangles*

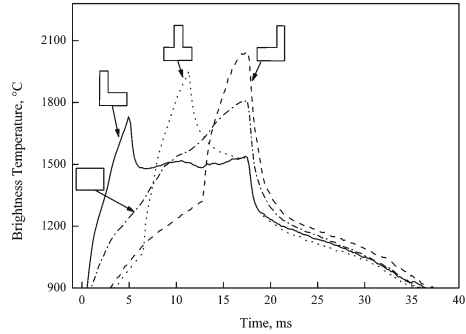
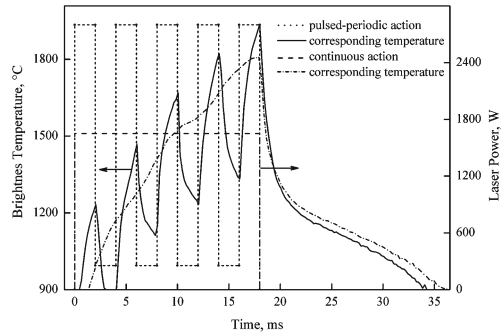


Fig. 9.8 Evolution of brightness temperature for continuous and PP laser action with the same duration (18 ms) and energy input (30 J)



and 1, 936°C for the pulsed periodic one (note that the accuracy of brightness temperature measurements is about 1%). Regular increase of the minimum temperature values (as well as the maximum ones) in the pulsed periodic action corresponds to heat accumulation in the irradiated zone. At the cooling stage, the slightly higher temperature values for the continuous action may be probably explained by higher quantity of the absorbed laser energy because of smaller heat losses (evaporation and radiative heat losses) that depend strongly on the peak temperature values.

The effect of heat accumulation in PP laser action is illustrated by surface remelting of a plasma-sprayed ZrO₂ coating. It is possible to analyze temperature evolution during a whole series of laser pulses and the subsequent cooling stage (Fig. 9.9a) as well as during an individual laser pulse (Fig. 9.9b). One may note the emissivity variation at melting/solidification that results in sharp changes of brightness temperature (by 180°C) at the melting point. The results in Fig. 9.9 are presented as they were registered, without any smoothing, etc.

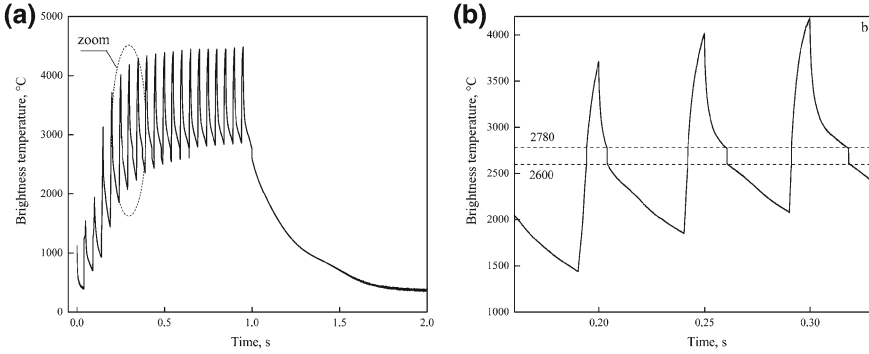


Fig. 9.9 Surface remelting of the plasma-sprayed ZrO₂ coating by pulsed periodic Nd:YAG laser: energy per pulse is 8 J; pulse duration is 10 ms; frequency is 20 Hz. Application of single spot monochromatic pyrometer

9.4.2 Laser Welding

9.4.2.1 Pulsed Periodic Nd:YAG Laser Welding

The welding of the thin-walled (375 μm thickness) gilded kovar boxes is rather sensitive to deviation of the welding seam from its optimum position. The variations of the individual thermal cycle registered by a single spot monochromatic pyrometer (Fig. 9.10a) and the temperature profile measured by 2D pyrometer (smoothing has been applied) across the seam (Fig. 9.10b) confirm the ability of the pyrometers to detect the beam displacement by 100 μm. Note that not only the position of the temperature maximum is shifted but its value is modified as well: for the external deviation of the beam the increase of the maximum temperature (relatively to the optimum beam position, i.e., in the middle) is due to the adiabatic boundary condition on the right side of the welding joint; for the internal displacement—results from the adiabatic boundary condition at the back side of the irradiated plate.

9.4.2.2 CO₂ Laser Welding

The pyrometers were used to control CO₂ laser welding of steel (304L, 3 mm thickness) and Ti (TA6V, 2.5 mm thickness) plates: misalignment of the welded plates, variation of the welding geometry, internal defects, deviation of the laser beam trajectory from the junction, etc. The temperature profiles along and across the welding axis as well as the complete temperature field presented in Figs. 9.11, 9.12, 9.13, 9.14, are measured by the 2D pyrometer.

A 2D image of the steady-state temperature distribution is presented in Fig. 9.12. Analysis of the initial transient period is performed for CO₂ laser butt welding of

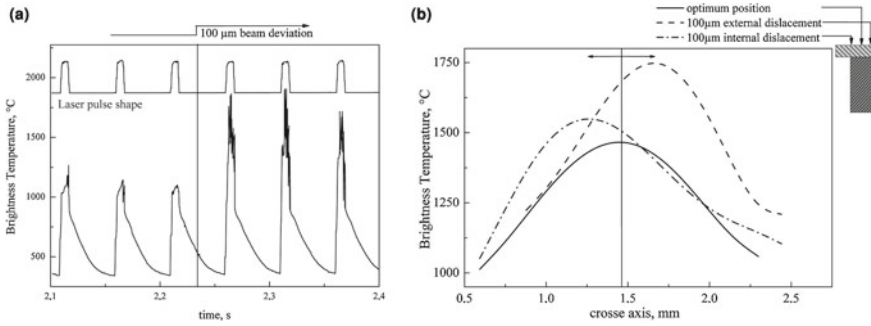


Fig. 9.10 PP laser welding of gilded kovar boxes. Influence of a 100 μm displacement of the welding seam. Welding parameters: frequency is 20 Hz, pulse energy is 5 J, welding speed is 200 mm/min, pulse duration 7 ms, rectangular pulse shape. **a** single spot pyrometer is sighted outside the seam at 400 μm before the laser action centre. The *upper curve* presents the train of laser pulses. **b** 2D pyrometer is sighted on the laser action zone

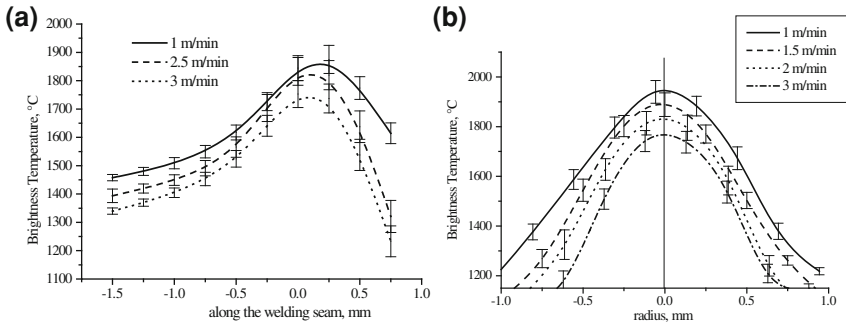


Fig. 9.11 CO₂ laser butt welding of titanium plates: influence of the welding speed. **a** steady-state temperature distribution along the welding axis; **b** steady-state temperature distribution across the welding axis. Welding parameters: power is 1.2 kW, helium flow rate is 13 l/min

titanium plates. Transient temperature distributions were measured along (Fig. 9.13a) and across the welding seam (Fig. 9.13b).

Variations of the steady-state temperature distributions along and across the welding axis versus welding speed are presented in Fig. 9.11. Following the predictions of the linear heat transfer model of laser welding, i.e., line heat source of a fixed power moving with constant velocity in a thermally thin plate, the temperature values monotonously decrease with welding speed.

The temperature decrease is particularly evident in the HAZ before the keyhole that indicates decrease of molten pool size and development of high temperature gradient along the welding axis before the laser beam center. Each temperature profile (along a straight line) was measured during 170 μs. The time indicated on the curves in Fig. 9.13 is counted from the beginning of the measurements that were started when the surface temperature reached 1, 100°C. It is possible to note that

Fig. 9.12 CO₂ laser butt welding of titanium plates: full image of the steady-state temperature distribution. Welding parameters: power is 1.2 kW, speed is 1.5 m/min, helium flow rate is 13 l/min

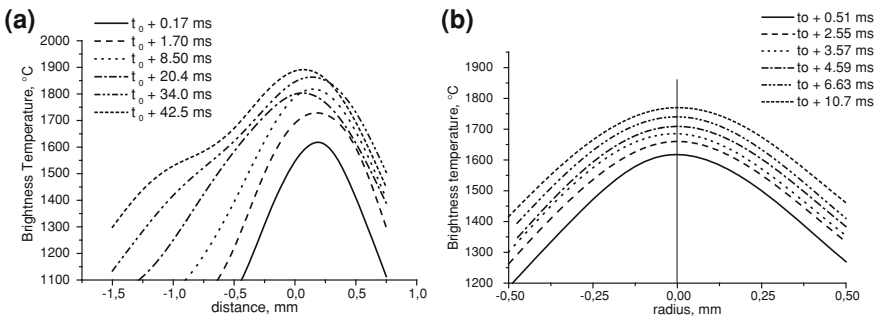
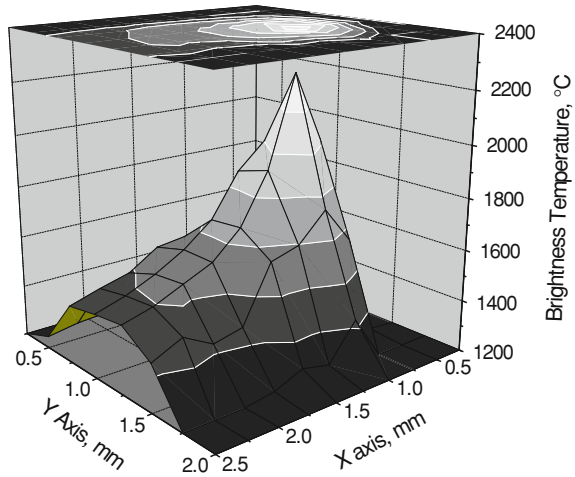


Fig. 9.13 Transient temperature distributions in CO₂ laser butt welding of titanium plates. **a** temperature distribution along the welding axis. **b** temperature distribution across the welding axis. t_0 corresponds to the beginning of the temperature measurements. Welding parameters: power is 1.2 kW, speed is 1.5 m/min, helium flow rate is 13 l/min

the transient period for the temperature distribution along the welding seam (more than 50 ms from the beginning of the measurements) is much longer than the one across the seam (about 20 ms) that is in agreement with the classical theory of heat transfer in welding. At the beginning of laser action, the temperature distribution along the welding seam is similar to the beam profile (see the first two curves in Fig. 9.13a). Later on, as the result of heat accumulation in the zone behind the beam, the symmetry is lost, and the well-known “tail” of temperature distribution appears.

Insufficient protection from oxidation for the protective gas flow rates lower than 7 l/min is indicated by two groups of temperature profiles in Fig. 9.14: the upper curves for 0 and 5 l/min that practically coincide correspond to the insufficient gas protection; the lower temperature profiles are practically independent from the gas

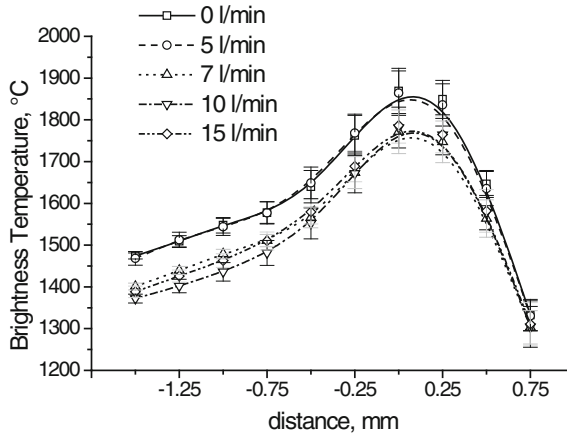


Fig. 9.14 CO₂ laser butt welding of titanium plates: influence of the protective gas (helium) flow rate. Welding parameters: power is 1.2 kW, speed is 1.5 m/min

flow rate. Single spot pyrometers were used to detect different types of welding defects, an example is presented in Fig. 9.15.

9.4.2.3 Nd:YAG Laser Lap Welding of Zn-Coated Steel Sheets

The objective of the present study is to use pyrometers for: (a) process optimization and (b) online process control in Nd:YAG laser lap welding of Zn-coated steel sheets. To reach these goals the following technical tasks must be completed: (1) to confirm stability and reproducibility of pyrometer measurements; (2) to define the value of the mean temperature and its acceptable deviations; (3) to apply Fourier analysis to define characteristic frequencies and to eliminate noise; (4) to correlate variations of the surface temperature with the typical welding defects.

In the lap welding of zinc-coated steel or other materials with a volatile coating, an essential quality issue is to vent the high-pressure zinc vapor formed between the sheets. Zinc boils at 906°C, steel melting temperature is about 1,500°C, and the keyhole is even hotter. When the keyhole penetrates the zinc interlayer, an abrupt expansion of the vapor volume starts thus destroying the weld continuity, removing liquid phase, and creating defects like porosity, etc. One of the possible solutions of this problem is to weld with a gap. To achieve a desired welding quality, it is crucial to correlate the size of the gap with the volume of the zinc vapor [23] and to keep it the same throughout the welding. The main obstacles to realize successful welding with a gap may be: (a) bad fastening of the sheet, (b) prior deformations of the sheet, (c) complex geometry of the work pieces to be welded, as, for example, bent sheets. One of the possible solutions for process online control is non-contact temperature

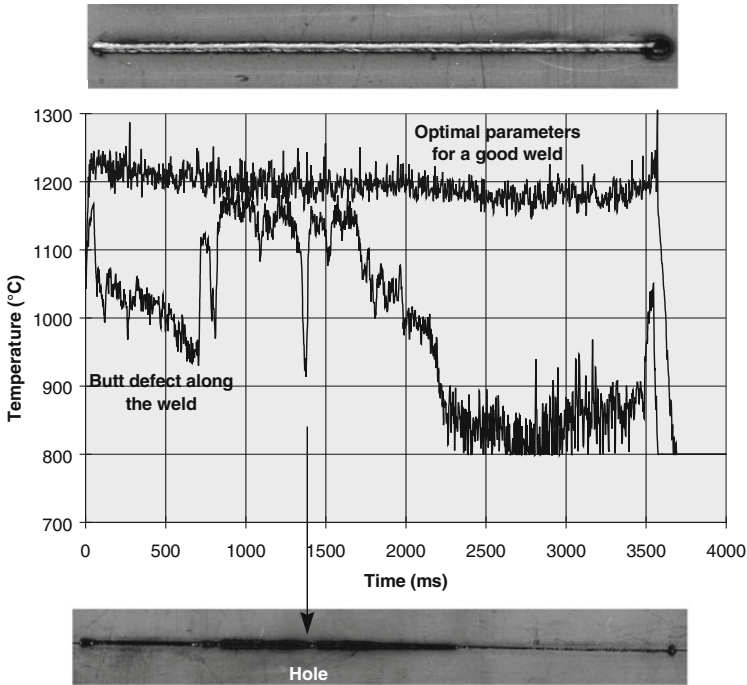


Fig. 9.15 Welds and pyrometer signals obtained under optimum conditions (*up*), with wrong preparation of the flanks to be welded (*down*). Steel plates of 3 mm thickness

measurements by pyrometer in the zone of laser action which allows to monitor the real-time thermal behavior of materials under laser welding conditions [25–27].

Lap welding

Nd:YAG laser HAAS 2006D in continuous wave (CW) mode (maximal output power is 2 kW) was used, laser radiation was delivered by optical fiber. The laser optical head has a focal distance 200 mm and provides focal spot diameter of 600 μm. The CNC 3D table LASMA 1054 ensured precision of the substrate’s movement (position accuracy is up to 1 μm) relative to the laser beam. Lap welding was performed at laser power 2 kW and welding velocity 2,500 mm/min. The materials used are Zn-coated steel sheets with various thicknesses: from 0.7 mm up to 1.25 mm. The size of the gap was varied in the range of 0–0.5 mm. The following two pyrometers were used: (1) 12-wavelength (in the range of 1.001–1.573 μm) one spot (diameter of the temperature measurement zone is 800 μm) instrument with the sampling time of 50 μs; (2) monochromatic 2D pyrometer (the frame of 100 photodiodes) for measurement in a zone 2.65 by 2.65 mm with the sampling time of 17 μs per one photodiode (Table 9.1). Visualization of the welding process was carried out

by an infrared camera FLIR Phoenix RDASTM with InSb sensor: 3–5 μm bandpass arranged on 320×256 pixels array. Acquisition time varied from 9 μs to 16.5 ms, frequency of the measurements went up to 38 kHz.

Statistical analysis of the pyrometric signal

The mean brightness temperature and its deviations were determined for the reference welding parameters. The performed analysis was based on data of 35 tests with the following parameters:

- Welding speed is 2,500 mm/min;
- Laser power is 2 kW;
- Steel sheet of 0.7 mm on sheet of 1 mm thickness;
- Gap is 0.2 mm.

The mean brightness temperature and its standard deviation are presented in Fig. 9.16. The average value of the brightness temperature in the selected zone is 1,917°C with signal deviations of $\pm 37^\circ\text{C}$ (i.e., 2%). The deviations are given for the used pyrometer wavelength equal to 1.38 μm . It is evident that the process of welding zinc-coated steel sheets by Nd:YAG laser and corresponding surface temperature are fairly steady under the reference conditions. Variation in surface temperature recorded by the pyrometer corresponds to a defect or to a change of welding parameters.

The same analysis was performed for the lap welding of a sheet of 0.7 mm on a sheet of 1.25 mm with 0.2 mm gap (welding speed 2,500 mm/min, laser power 2 kW). The average value of the brightness temperature in the selected zone is 1,980°C with signal deviations of $\pm 78^\circ\text{C}$. In this case, the mean brightness temperature and the signal standard deviation are greater by 63 and 41°C., respectively, compared to the series for 0.7+1 mm. If the lower sheet is thinner, the obtained weld is always the through one. It is not the same if the lower sheet has 1.25 mm thickness, which results in a more unstable pyrometric signal.

The temperature drop is explained by the transition of the welding mode from the nonthrough to the through one with the decrease in thickness of the second plate. As vapor escapes from the upper and bottom ends of the keyhole, its energy balance changes, and the temperature decreases. The instability of the pyrometric signal is related to a general instability of the keyhole which is intrinsic to the non-through welding mode. Stability of surface temperature distribution was studied with the help of the 2D pyrometer. The temperature field in the zone 3 by 3 mm was measured during 1.7 ms, the frequency of measurements was 77 Hz. The lower temperature in the middle of the welding zone is related to the spatial distribution of laser beam (“horse shoe”- shaped) with 20% minimum in the center (Fig. 9.17a). It was found that the steady-state temperature distribution is rather stable: in the central part of the welding zone the temperature deviations from the average value are less than 10°C (Fig. 9.17b) that is even smaller than for the single spot pyrometer (Fig. 9.16).

From the first point of view, this seems to be contradictory: each of the 100 photodiodes of the 2D pyrometer measures temperature consecutively over a zone of 300 μm with the sampling time of 17 μs that provides a better spatial and temporal

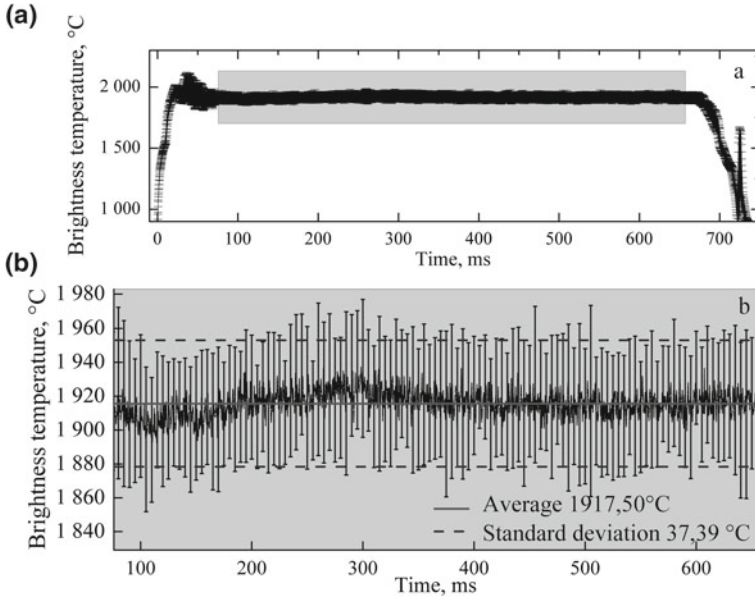


Fig. 9.16 Temperature evolution during laser lap welding of zinc-coated steel sheets by continuous Nd:YAG laser : mean brightness temperature and signal standard deviation. Total welding duration (a), zoom at the central part (b). Results are the average of 35 tests with the following parameters: welding speed is 2,500 mm/min; laser power is 2 kW; overlap welding of 0.7 and 1 mm sheets with 0.2 mm gap

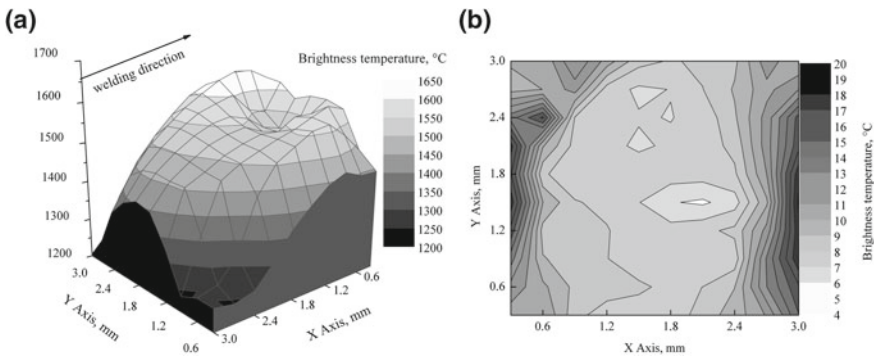
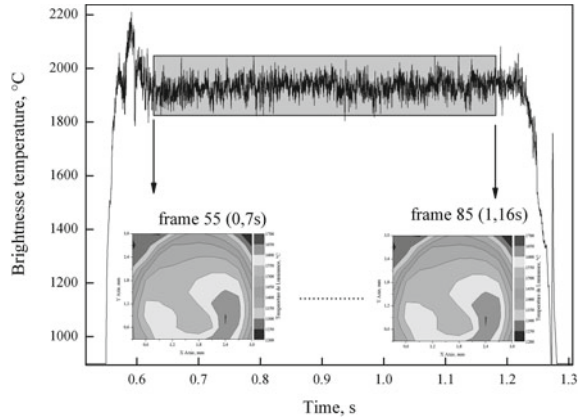


Fig. 9.17 Two-dimensional steady-state temperature field during laser lap welding of zinc-coated steel sheets by continuous Nd:YAG laser : mean brightness temperature (a) and signal standard deviation (b). Results are the average of 35 tests with the following parameters: welding speed is 2,500 mm/min; laser power is 2 kW; overlap welding of 0.7 and 1 mm sheets with 0.2 mm gap

resolution of temperature measurements than the single spot pyrometer. The latter measures the temperature over a larger area (800 μm) and more slowly (50 μs for each wavelength). It means that the single spot pyrometer integrates temperature variations

Fig. 9.18 Statistical analysis of the pyrometers measurements with a welding speed is 2,500 mm/min; laser power is 2 kW; overlap welding of 0.7 and 1 mm sheets with 0.2 mm gap. The single spot pyrometer (*up*) and the 2D pyrometer (*down*) signals. The selected zone on the *upper curve* indicates the interval of measurements retained for statistical analysis



in space and in time much stronger than the 2D pyrometer, and it is natural to suppose that standard temperature deviation in this case should be smaller. This contradiction can be explained by differences in (a) frequencies of the measurements: 77 Hz for the 2D pyrometer and 4 kHz for the single spot pyrometer and (b) the methods of definition of temperature deviations from the average value. In case of the 2D pyrometer, only 30 images per welded seam were retained for further analysis. These are consecutive images corresponding to the middle of the welding seam to avoid transient effects. Based on the 30 images, an average image per welding seam was defined. That is 35 average temperature fields were calculated, one per welding seam. Finally, one average temperature field was defined based on 35 identical welding experiments, totally 105,000 measurements were used (Fig. 9.18).

In case of the single spot pyrometer, each welded seam was characterized by 2,324 temperature measurements with 4 kHz frequency. That is the average temperature is defined based on 81,340 measurements. The main difference between the two approaches is the frequency of measurements that is 52 times higher for the single spot pyrometer. It means that for the high accuracy detection of temperature deviations from the optimal value that show up in welding defects, better to apply a higher frequency of measurements than a higher spatial and temporal resolution of the individual measurements with a lower frequency.

Variation of the gap between Zn-coated steel sheets

Geometry and mechanical properties of the welding seam are strongly influenced by the gap between the sheets. Good welding quality may be achieved by the optimization of the gap size [28–30]. In case of an insufficient gap between sheets, vapor cannot be evacuated freely thus leading to instability of the molten pool and defects of the welding seam. The photographs in Fig. 9.19 represent cross-sections of the seam. In Fig. 9.19a, the gap between sheets is zero. Because of the impossibility to evacuate the vapor by a gap between sheets, it can be done only through the keyhole.

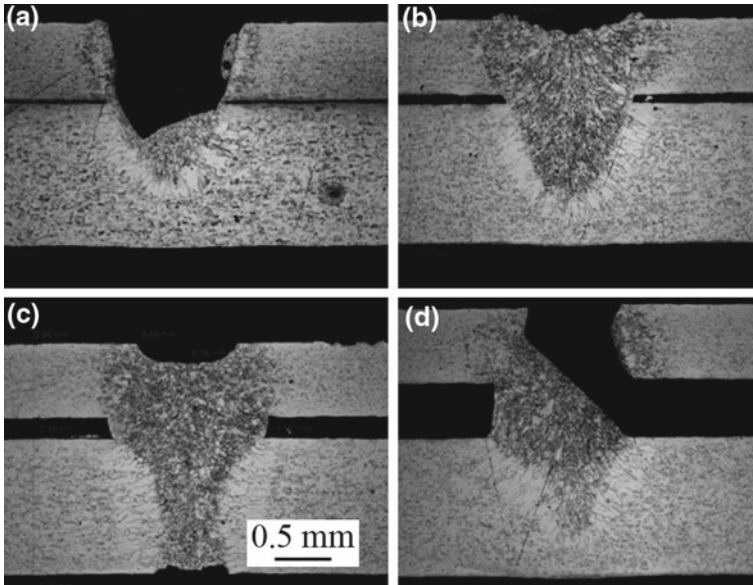


Fig. 9.19 Influence of the gap size on the welding seam shape: **a** gap is 0 mm; **b** gap is 0.1 mm; **c** gap is 0.2 mm; **d** gap is 0.5 mm. Welding parameters: speed is 2,500 mm/min, laser power is 2 kW, sheet of 0.7 mm on sheet of 1.25 mm thickness

Interaction of Zn vapor with the keyhole leads to its clogging that results in important defects of the welding seam: a deep crater in the weld, the molten mass ejection under the action of the zinc vapor. With the increase of the gap value up to 0.1 mm (Fig. 9.19b), the zinc vapor escapes by the space between sheets, its influence on the instability of the keyhole is reduced. It should be noted that the weld is not a through one. The increase of the penetration depth with gap size in the range of 0–0.2 mm (Figs. 9.19a–c) is explained by the instability of the keyhole that is strongly influenced by Zn vapor. In the absence of a stable keyhole, the laser beam does not penetrate inside the molten pool but is absorbed by its surface: As if the keyhole welding mode was replaced by the conductive welding mode. As the stability of the keyhole increases (cf. transformation of the molten pool with the gap variation from 0.1 up to 0.2 mm), it reaches the bottom side of the second plate, and the seam becomes a through weld. Any further increase of the gap provokes a general instability of the molten pool and, therefore, the keyhole becomes again instable that once again limits the penetration depth (Fig. 9.19d).

The gap of 0.2 mm is the reference one for the given case. The obtained welding seam is of good quality and the weld is a through one (Fig. 9.19c).

If the thickness of the gap is higher than the reference one, the molten mass breaks down and the metallurgical contact between two sheets is deficient. Figure

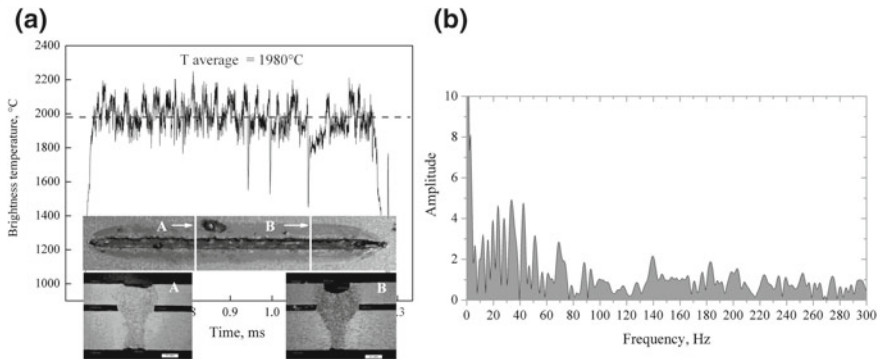


Fig. 9.20 Lap welding of zinc-coated steel sheets by continuous Nd:YAG laser. Parameters: welding speed is 2,500 mm/min, laser power is 2 kW, sheets of 0.7 + 1.25 mm, gap 0.2 mm. **a** pyrometer records and photos of the welding seam cross sections; **b** frequency analysis by fast Fourier transform

9.19d shows that the left edge of the sheet is welded, while the weld is missing on the right-hand side.

Analysis of pyrometer signal versus gap

The zero gap results in appearance of welding defects and in strong variations in the depth of the welding seam and leads to intense ejection of the melted matter in the form of drops of various size. With zero gap during welding, the brightness temperature is below the average temperature (1,980°C) for the reference conditions (gap 0.2 mm). Various low-amplitude frequencies are observed, but a characteristic frequency cannot be determined. These frequencies are related to oscillations of the free surface of the molten pool that are induced by zinc vapor which escapes mainly through the irradiated surface. The results are different for the gap of 0.1 mm which provides a better appearance of the seam and a smaller depth of the crater. Mean temperature during welding approaches the reference values obtained for the gap of 0.2 mm. Using the reference conditions (gap 0.2 mm), the through weld is obtained (Fig. 9.20a), the seam on the side of the irradiated surface is concave (photographs of the cross-sections A and B of the welding seams).

The brightness temperature fall at the instant B can be explained by the formation of a cavity in the molten mass. Analysis by fast Fourier transform shows the presence of low-frequency components of the signal (Fig. 9.20b), which correspond to the modes of oscillation of the molten pool, i.e., regular oscillations (~33 Hz) appear during the through welding of two sheets which correspond apparently to the modes of oscillation of the entire molten pool.

If the size of the gap exceeds the reference value either the weld fails (Fig. 9.21a, cross-section A) or it occurs only on one side of the sheet (Fig. 9.21a, cross-section B). During welding the brightness temperature is below its average value for the

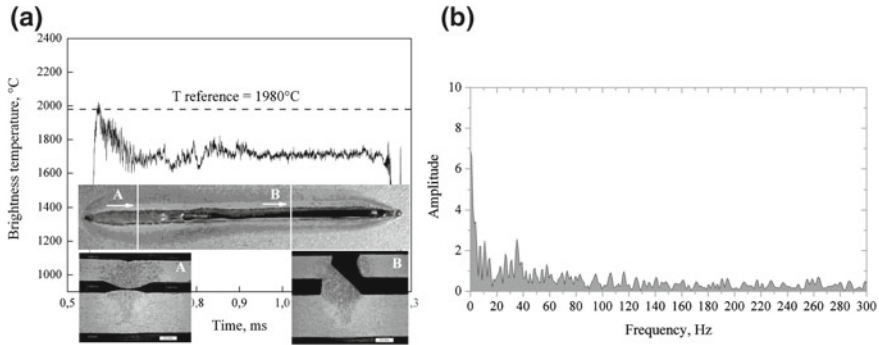


Fig. 9.21 Lap welding of zinc-coated steel sheets by continuous Nd:YAG laser . Parameters: welding speed is 2,500 mm/min, laser power is 2 kW, sheets of 0.7 + 1.25 mm, gap 0.5 mm. **a** pyrometer records and photos of the welding seam cross sections; **b** frequency analysis by fast Fourier transform

reference conditions (gap 0.2 mm). The signal is characterized by low-amplitude frequencies related to motion of the entire melt pool.

Optical monitoring by infrared camera

An infrared camera FLIR Phoenix RDASTM was rigidly mounted on the laser head in the similar way as the pyrometers. The measurements were carried out under the following conditions: window 128 by 128 pixels, acquisition time 10 μs, measurements frequency 1.18 kHz. The typical results are presented in Fig. 9.22: it is possible to monitor the “temperature” field as well as “temperature” profiles along and across the welding seam. Transient phenomena at the beginning and the end of welding can be easy seen: increase in size of the HAZ and, in particular, elongation of the temperature “tail” along the welding seam, convective motion of the melt in the molten pool.

The ejected liquid droplets can be seen as well. Welding defects, in particular those related to the molten pool dynamics, can be detected. The overall estimation of stability or instability of the welding process versus operating conditions can be obtained (Fig. 9.23). Along with the above-mentioned advantages of the modern infrared cameras, one may note that it is not always easy to decode the obtained images and to identify the related physical phenomena.

9.4.3 Laser Cladding

LC is a surface engineering technique that allows to deposit a thick protective coating on a metallic surface of a part [22, 23, 31]. Consumable powder material is transported by an inert gas toward a molten pool created by laser beam. After the laser

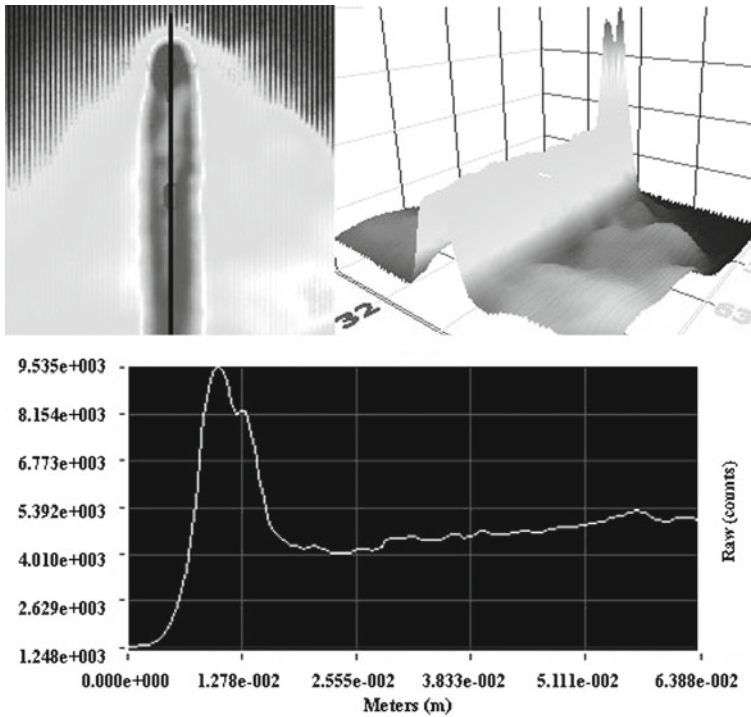


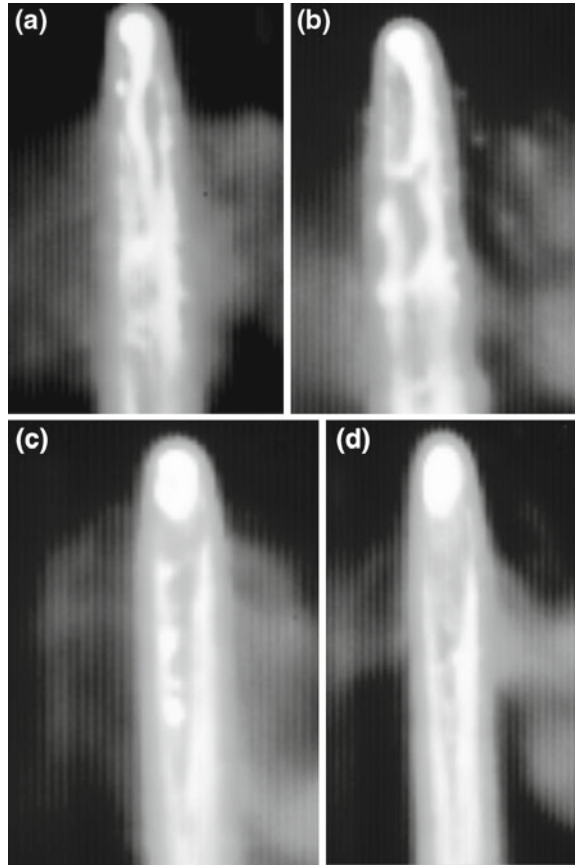
Fig. 9.22 Image of the welded zone (welded with welding speed is 2,500 mm/min; laser power is 2 kW; overlap welding of 0.7 and 1 mm sheets with 0.2 mm gap) obtained by infra-red camera FLIR Phoenix RDAS™. Grey levels image (*up*) and its 3D presentation (*middle*), signal profile along the welding seam (*down*)

beam has passed, the material rapidly solidifies. A single laser track forms with thickness ranging from 0.2 to 2 mm and width from 0.3 to 5 mm. A coating is realized by overlapping of successive tracks. LC provides the desirable surface properties associated with a choice of consumable material [32, 33]. Usually, the principal objective of LC is to improve wear, abrasive, and corrosion resistance of a mechanical component [34]. LC is flexible and efficient method for elaboration of advanced protective coatings including functionally graded composites, multilayered, etc [35–39].

9.4.3.1 Nd:YAG Laser Cladding of Satellite with Lateral Powder Injection

Nd:YAG laser HAAS 2006D (maximal output power is 2 kW) is used, laser radiation is delivered by optical fiber. The CNC 3D table LASMA 1054 assures precise movement (position accuracy is up to 1 μm) of the substrate relatively laser beam.

Fig. 9.23 Grey levels images of the welded zone (welded with a welding speed of 2,500 mm/min; laser power is 2 kW; overlap welding of 0.7 and 1 mm sheets with 0.2 mm gap) obtained by infra-red camera FLIR Phoenix RDAS™. Typical images corresponding to unstable (a, b) and stable (c, d) welding conditions



In CW LC with lateral powder injection, the nominal parameters were the following:

1. Cladded bead of 6 mm width: laser power $P = 900\text{--}1800$ W, cladding velocity $v = 2\text{--}6$ m/min, powder feeding rate $F = 9\text{--}42$ g/min (30–70 % of the maximum rotation speed of the powder distribution plateau).
2. Cladded bead of 300 μm width: laser power $P = 200\text{--}400$ W, velocity $v = 0.3\text{--}0.75$ m/min, powder feeding rate $F = 2\text{--}4$ g/min.

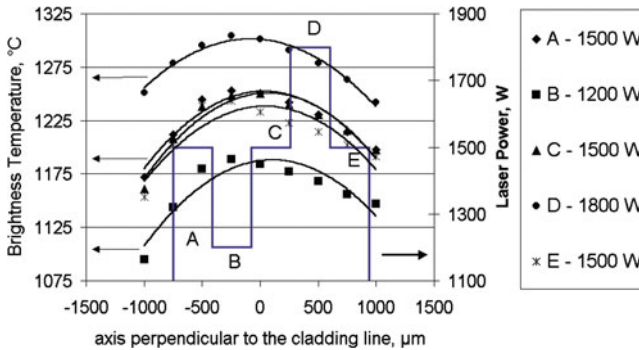


Fig. 9.24 Influence of the laser power variation (five steps between 1,200 and 1,800 W) during LC of stellite on steel (bead width is 6 mm) on temperature profile across the cladded bead. Cladding parameters: $v = 3$ m/min, $F = 30$ g/min

Powder feeder MEDICOAT provides delivery of powder (carrying gas is argon) from two independent channels through antistatic tubes to the coaxial nozzle.

Temperature response on variation of basic cladding parameters

For Stellite cladding, temperature control was applied to assure stability of the process and the coating quality: on the one hand, to avoid overheating and, on the other hand, to prevent formation of cracks and residual porosity.

During traditional LC of Stellite on steel, the influence of laser power variation (Figs. 9.24, 9.25) and the powder feeding rate (Fig. 9.26) results in surface temperature variations that were detected by the 2D pyrometer (temperature profiles across the cladded bead were measured).

Laser power was varied up and down (± 300 W) in a stepwise way from a mean value (1,500 W). The sequence of power variation was the following: mean value, minimum value, mean value, maximum value, and mean value (see stepwise curve in Fig. 9.24). Temperature measurements were carried out continuously during all the period of power variation. As the duration of registration of a temperature profile (nine photodiodes were applied; therefore, the sampling time was $153 \mu\text{s}$) was much smaller than the period of cladding with constant power (1 s), a number of similar measurements were carried out at the same laser power. To avoid transient phenomena related to power modification, the temperature profiles presented in Fig. 9.24 were chosen from the middle of the each cladding stage.

One may note that the three temperature profiles corresponding to the three periods with mean laser power are rather similar and the maximum difference between them is about 10°C . This indicates the stability of temperature field for the optimum cladding conditions. The temperature gradient across the cladded bead is relatively low and it slightly decreases with laser power. Note that the zone of temperature measurements

Fig. 9.25 Influence of the powder feeding rate on surface temperature profile across the bead during LC of stellite on steel (bead width: 6 mm). Cladding parameters: $P = 1, 500 \text{ W}$, $v = 3 \text{ m/min}$. $A F = 18 \text{ g/min}$; $B F = 30 \text{ g/min}$; $C F = 42 \text{ g/min}$

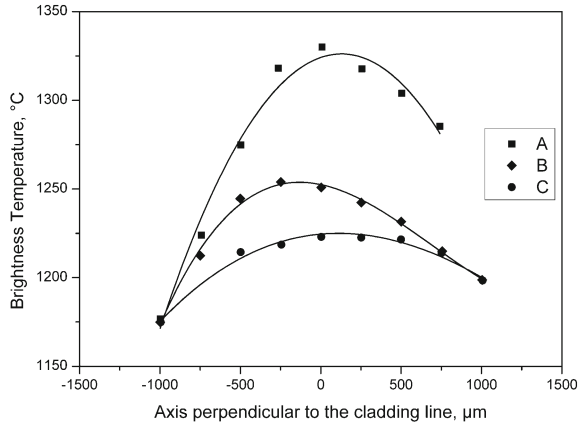
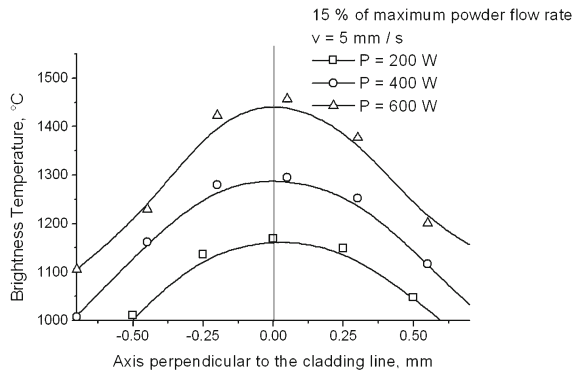


Fig. 9.26 Influence of the laser power on surface temperature during laser microcladding of stellite on steel (300 μm bead width). Brightness temperature profiles recorded by the 2D pyrometer ($\lambda = 0.86 \mu\text{m}$). Cladding parameters: $v = 0.3 \text{ m/min}$, $F = 2.3 \text{ g/min}$



is smaller than the cladbed width and it was situated close to the center of the molten pool.

The temperature rise for higher laser power and the temperature decrease for lower power is well detected, Fig. 9.24. It means that any deviation of laser power from the optimal level can be controlled by pyrometer measurements. The variation of brightness temperature with laser power in the range $\pm 25\%$ is nearly proportional. This corresponds well to the results of linear heat transfer models that predict linear rise of surface temperature with energy density flux [19]. In reality the quasi-linear dependence of surface temperature on laser power takes place for relatively low temperature when the evaporation, that limits the surface temperature rise, is not important [20, 21]. This corresponds well to the typical conditions of LC when surface overheating is undesirable. The similar experiments were carried out to analyze the variation of temperature profiles across the cladbed with powder feeding rate, Fig. 9.25. It was found that the temperature is higher for the lower powder feeding rate that is evident from the heat balance. The variation of brightness temperature with powder

feeding rate in the range $\pm 20\%$ is not proportional: the temperature decrease with powder feeding rate (+20%) is less important than temperature rise corresponding to a 20% decrease of feeding rate. This is the result of laser beam interaction with particle jet that is more intensive at higher particle density. Reflection and scattering of laser beam by particles result in losses of optical energy and in enlargement of the size of the effective heat source acting on the surface. Indeed the temperature gradient decreases with powder feeding rate. The zone of powder injection is situated at the right side of Fig. 9.25 where the temperature variation is well seen. From the left side of the cladbed bead the temperature is practically independent from powder feeding rate. The intersection of the two temperature profiles at the right side of Fig. 9.25 indicates the intensification of beam—powder interaction with powder feeding rate and the enlargement of the size of the effective heat source in the right direction.

The influence of laser power on surface temperature during laser microcladding of Stellite on steel (cladbed bead of 300 μm width) with lateral powder injection is presented in the Fig. 9.26. The results are rather similar to the ones discussed above. The main difference is the lower powder feeding rate than limits the powder-beam interaction. The variation of surface temperature with laser power is nearly proportional; the HAZ on the borders of the cladbed bead is well seen.

LC with coaxial powder injection

In the so-called coaxial LC, the desired composition of powders is delivered to the substrate coaxially (or conically) with the laser beam. The advantages of the co-axial cladding head are the possibility of the free-directional cladding, better protection from the ambient atmosphere, and a relatively small HAZ [40, 41]. It is possible to form a protective coating in the exact desired location exposed, for example, to severe wear conditions or to restore locally damaged/wornout surface. Complexity of the cladding process, in particular with coaxial powder injection (gas dynamics of powder injection, powder/beam interaction, coating formation) and industrial requirements for the coating performance impose the application of online monitoring and process control. When using multi-component powder blends, for example, a metal matrix composite with ceramic reinforcement, one needs to control temperature of the melt to avoid thermal decomposition of certain compounds (as WC) and to assure melting of the base metal (as Co).

The experimental facilities included a Nd:YAG laser HAAS 2006D (maximal output power is 2 kW, laser radiation is delivered by optical fiber, the same source can be applied in CW and PP modes, and a CNC 3D table LASMA 1054 that assures precise movement (position accuracy is up to 1 μm) of the substrate in relation to the laser beam. In PP LC with coaxial powder injection the nominal laser parameters were the following: cladbed bead of 2–4 mm width, rectangular pulse shape with 20 ms pulse duration, average power $P = 2,000$ W, velocity $v = 8.3 \times 10^{-3}$ m/s, powder

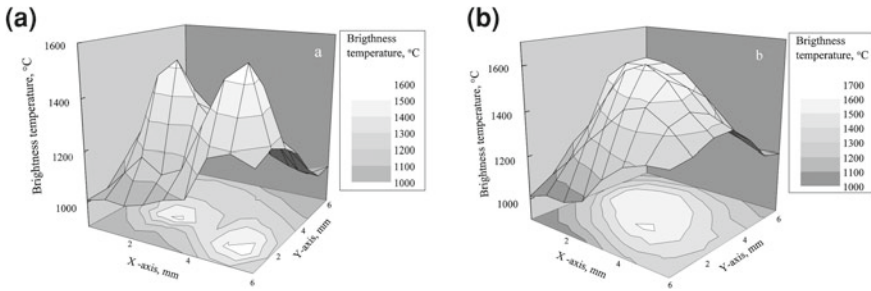


Fig. 9.27 2D temperature fields in coaxial LC of Stellite + WC/Co (30%) on steel substrate; laser power is 2 kW, velocity is 1,000 mm/min: **a** non-optimized powder injection conditions; **b** optimised powder injection conditions

feeding rate $F = 5\text{--}14$ g/s. To minimize the influence of surface thermochemistry on emissivity variations, a flow (0.083 l/s) of Ar was applied.

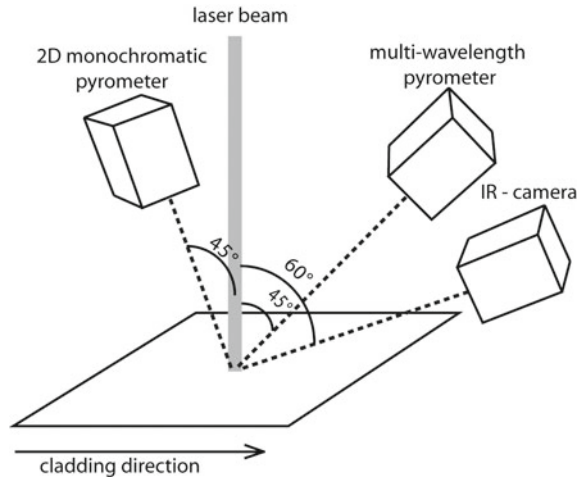
Optimization of powder-injection condition

The 2D temperature mapping was applied for Stellite+WC/Co (15% of Co) cladding with conical powder injection, Fig. 9.27. This technique has several advantages relative to the lateral powder injection but it requires development of a special cladding nozzle and precise adjustment of the injection conditions [40–41]. A 2D temperature mapping is useful to optimize the cladding parameters: size and position of the zone of powder injection in relation to the laser beam, temperature gradients, dimensions of HAZ. A non-uniform temperature distribution in Fig. 9.27a clearly indicates that the injection conditions were not properly adjusted. On the other hand, the smooth and regular shape of temperature distribution in Fig. 9.27b corresponds to the well-optimized cladding. Width of the cladded bead is about 3.5 mm that corresponds well to the size of the smooth temperature plateau at the top of the temperature distribution, Fig. 9.27b.

9.4.3.2 Optical Monitoring in Direct Metal Deposition

Five-axes robotic LC with coaxial powder injection is often referred to as Direct Metal Deposition (DMD) [42–44]. Deposition of multi-material coatings on a complex form surface and direct manufacturing of 3D FGM objects by DMD is the promising technique capable of meeting industrial challenges in advanced materials processing [34, 45, 46]. Actually DMD technology is under intensive development. The most important objective is to increase product quality, process stability, and reproducibility along with the simultaneous decrease of risks, failures, and defects both on processes and on end-products [47]. Development of online monitoring and process control, and its integration with DMD machines is a priority task [7, 48–51].

Fig. 9.28 Experimental setup for monitoring of laser cladding process



The objective of the present study is to demonstrate the advantages of comprehensive optical monitoring of DMD technology applying diverse and complementary optical diagnostic tools. A multiwavelength pyrometer and an infrared camera are applied to measure brightness temperature that is useful to control melting/solidification and to avoid thermal decomposition when complex powder blends are used.

The CCD camera-based diagnostic tool is useful for a particle-in-flight visualization, for a control of particle jet stability, and for a real-time measurement of particle-in-flight velocity. The optical monitoring can be used to optimize the conditions of powder injection in particular when powders of different nature (size, density, etc.) are injected simultaneously to produce a multifunctional multimaterial coating. The optical heads of the pyrometers and infrared camera were fixed directly onto the LC head (Fig. 9.28). The pyrometer vision zone was placed in the center of a laser spot during the brightness temperature measurements.

LC installation

Commercial metal powders Ti-based superalloy Ti6Al4V by TLS Technik GmbH&Co (Bitterfeld) with $+45 - 100 \mu\text{m}$ particle size were laser cladded on a substrate from S235 steel.

The present study was performed on Trumpf DMD 505 commercial industrial-scale LC installation. The machine is equipped by a 5 kW CO₂ laser system operating in CW and PP modes. A computer-controlled powder injection setup consists of: two powder feeding system being able to mix different powders in situ and the process at the same time; coaxial cladding nozzle mounted CNC five-axis gantry assuring a precise movement with a controlled scanning speed in complex trajectories. Special coaxial nozzle design ensures gaseous protection against oxidation. The laser beam is focused in a circular beam spot on the treated surface by a parabolic copper

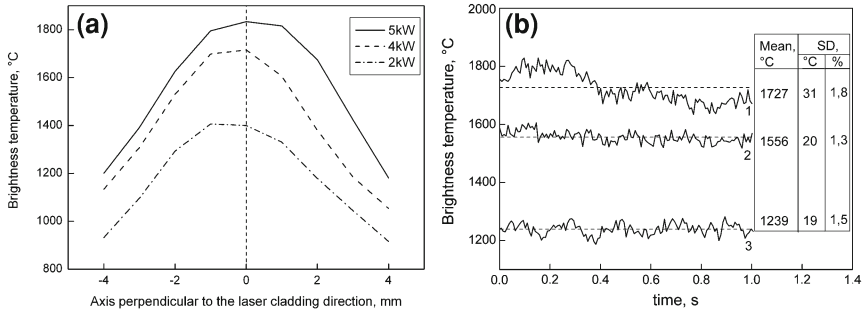


Fig. 9.29 Influence of the laser power on surface temperature during CO₂-LC of Ti6Al4V. **a** Brightness temperature profiles recorded by 2D pyrometer ($\lambda = 0.86 \mu\text{m}$). **b** Brightness temperature recorded by multiwavelength pyrometer, mean value and standard deviation (*SD*) ($\lambda = 1.19 \mu\text{m}$) : 1 laser power is 5 kW, 2 4 kW; 3 2 kW. Cladding parameters: $v = 0.7 \text{ m/min}$; $F = 30 \text{ g/min}$

mirror with focus length of 230 mm. The beam spot $d_{0.86}$ of 5 mm has a TEM₀₁ energy density distribution. All experiments were performed with LC speed $v = 0.3\text{--}1.4 \text{ m/min}$, laser power $P = 2\text{--}5 \text{ kW}$, powder feeding rate $F = 30 \text{ g/min}$, carrier gas flow rate $G_c = 18 \text{ l/min}$. A layer was formed by an overlapping of single laser beads deposited side-by-side with the fixed displacement $p = 3 \text{ mm}$.

Variation of laser power

Figure 9.29 represents results on the measurement of surface brightness temperature during LC of Ti6Al4V alloy vs. laser power. A comparison of peak values of temperature profiles recorded by 2D pyrometer (Fig. 9.29a) showed that the change of the laser power by 2 times (from 2 to 4 kW) increases the brightness temperature by about 25% (from 1,400 to 1,700°C for pyrometer wavelength $\lambda = 0.86 \mu\text{m}$).

The ratio of temperature values at the cladding axis for laser power 5, 4, 2 kW is 1:0.93:0.76, which indicates nonlinear variation of surface temperature with incident laser power. The measurements by multiwavelength pyrometers for wavelength $\lambda = 1.19 \mu\text{m}$ in the center of the laser spot confirmed the obtained results as well (Fig. 9.29b). The mean brightness temperature for laser power 2 and 4 kW is 1,239 and 1,556°C. The ratio of temperature values for laser power 5, 4, 2 kW is 1:0.90:0.71.

The maximum value of brightness temperature corresponds to the laser power 5 kW is 1,850 and 1,727°C measured by 2D and multiwavelength pyrometers, respectively. One may note the stability of temperature values: the mean square deviation is less than 2% for all the cladding parameters.

Variation of cladding velocity

Contrary tendencies were observed for different LC speed (Fig. 9.30). The increasing of LC speed from 0.7 to 1.4 m/min leads to decrease of brightness temperature

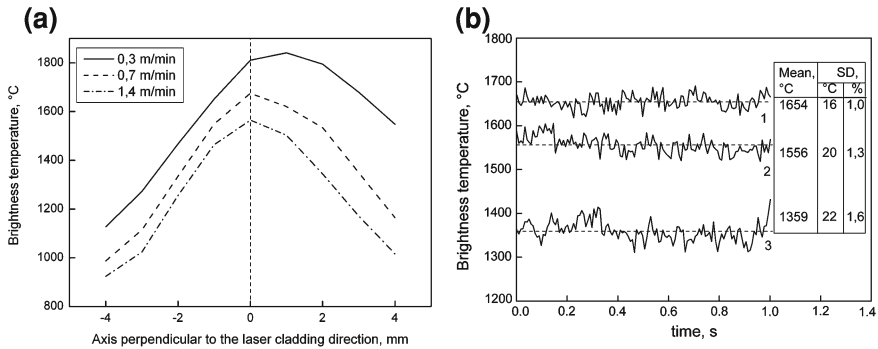


Fig. 9.30 Influence of the nozzle displacement velocity on surface temperature during CO₂ laser cladding of Ti6Al4V: **a** brightness temperature profiles recorded by 2D pyrometer ($\lambda = 0.86 \mu\text{m}$); **b** brightness temperature recorded by multi-wavelength pyrometer, mean value, and standard deviation (*SD*) ($\lambda = 1.19 \mu\text{m}$); 1 cladding speed is 0.3 m/min, 2 0.7 m/min; 3 1.4 m/min. Cladding parameters: $P = 4 \text{ kW}$; $F = 30 \text{ g/min}$.

measured by multiwavelength pyrometer by 15% (from 1,556 to 1,359°C) (Fig. 9.30b). The decrease from 0.7 to 0.3 m/min gives an insignificant increase by 5% (from 1,556 to 1,654°C). It should be noted that brightness temperature profiles (Fig. 9.30a) are not symmetric relative to the LC direction. The single laser beads were deposited side-by-side with 40% overlapping. Brightness temperature was always measured during LC of the third bead. An asymmetric temperature distribution is the result of the influence of the previously cladded beads. Higher temperature values at the right side in Fig. 9.30a indicate that the previously cladded beads are still hot during temperature measurements. One may note the stability of temperature values: the mean square deviation is less than 2% for all the cladding parameters.

Application of infrared camera

The infrared camera FLIR Phoenix RDASTM was applied for visualization of the melting pool during LC of Ti6Al4V. The following measurement conditions were applied: 320×256 pixels array, 340 Hz acquisition frequency, $50 \mu\text{s}$ sampling time, 60° angle relatively surface normal, 150 mm measurement distance. The camera was calibrated with the help of the black body MIKRON M390 to measure brightness temperature. The typical results are presented in Fig. 9.31: it is possible to obtain 2D steady-state temperature distribution (Fig. 9.31a) and temperature profiles across the cladding bead (Fig. 9.31b). Non-monotone temperature profiles indicate the position of powder injection zone that is characterized by lower temperature values (Fig. 9.31b).

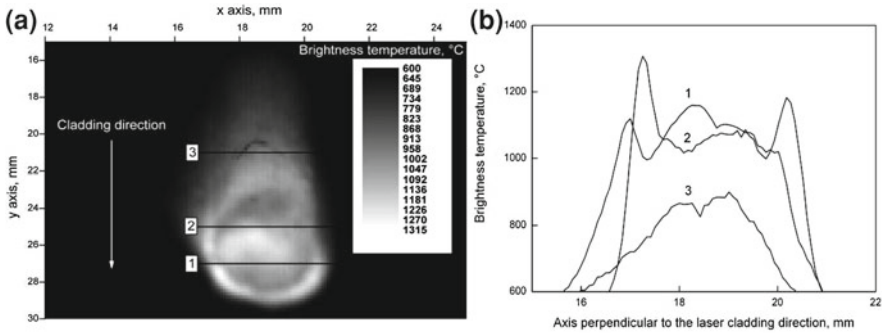


Fig. 9.31 **a** Two-dimensional steady-state temperature distribution field during CO₂-LC of Ti6Al4V obtained by infrared camera FLIR Phoenix RDASTM. **b** Temperature profiles across the cladded bead. Cladding parameters: $P = 4$ kW; $v = 0.7$ m/min; $F = 30$ g/min

Particles-in-flight monitoring

During the particle jet visualization by CCD camera-based diagnostic tool (Table 9.2) software retains certain number of tracks for statistical analysis (Fig. 9.32). The retained particles are marked by the two points at the beginning and at the end of the tracks to calculate track length and particle velocity. The experiments were performed with no substrate with low powder feeding rate $F = 11.5$ g/min and fixed carrier gas flow rate $G_c = 18$ l/min. The typical particles velocity distribution of the powder jet at 10–20 mm distance from the nozzle is presented in Fig. 9.33. The high dispersion of powder particle sizes leads to a wide distribution of particle velocity that changes from 6 to 13 m/s. The average particle velocity in this zone is 9.7 ± 1.3 m/s. Figure 9.34 presents results of influence of the carrier gas flow rate on the particles velocity. It should be noted that particles velocity increases with the distance from the nozzle. It was found that decreasing of carrier gas flow rate from 18 to 10 l/min results in particles velocity decrease by 20%. The increase from 18 to 30 l/min results only in insignificant augmentation by 10% of the particle velocity. In general, the particle velocity can be controlled by carrier gas flow rate in a broad range that permits to optimize the condition of LC process, but there exists a critical value of gas flow rate after which variation of particle velocity are rather limited.

9.4.3.3 Application of Multi-Wavelengths Pyrometry in Pulsed Periodic Nd:YAG Laser Cladding of Complex Powder Blends

The experimental setup (see Sect. 3.3.1) but with conical powder injection was used for PP cladding of wear-resistant coatings. Application of PP mode has certain advantage when a complex mixture of powder with different composition is used, e.g.,

Fig. 9.32 Particles tracks retained by software for the statistics. Powder injection parameters: $G_c = 18$ l/min, $F = 11.5$ g/min, AISI 431 powder

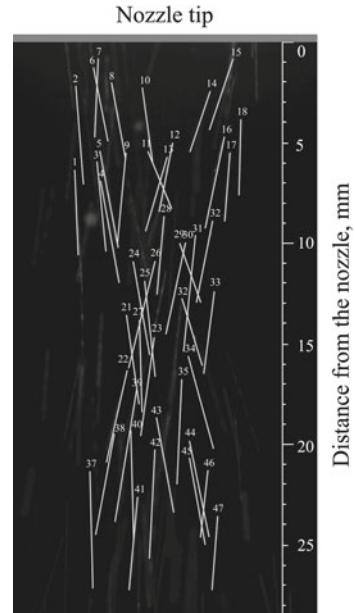
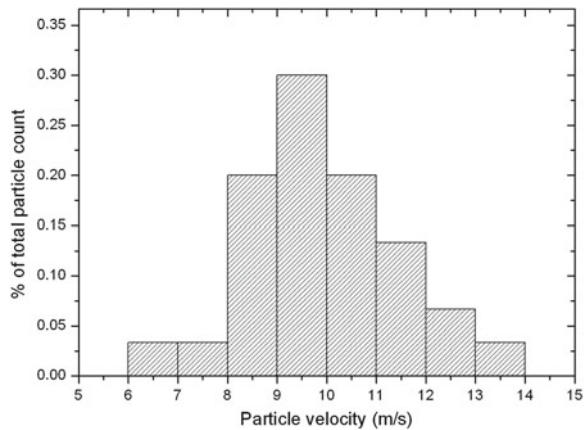


Fig. 9.33 Typical particles velocity distribution at the distance from 10 to 20 mm from the nozzle. Powder injection parameters: $G_c = 18$ l/min, $F = 11.5$ g/min, AISI 431 powder



better powder remixing, practical absence of porosity, reduced HAZ, higher cooling rates. There is a particular interest to apply MWP in LC with complex powder blends: on the one hand, the temperature must be high enough to assure melting of the metallic matrix, on the other hand, it should not exceed certain value to prevent thermal decomposition of ceramic inclusions (for example WC) used to reinforce the coating.

MWP was applied for restoration of true temperature in PP LC of CuAl and WC-Co (30% vol.), Figs. 9.35, 9.36. The method of true temperature restoration (“true”

Fig. 9.34 Dependence of particle velocity on the carrier gas flow rate. Powder injection parameters: $F = 11.5 \text{ g/min}$, AISI 431 powder

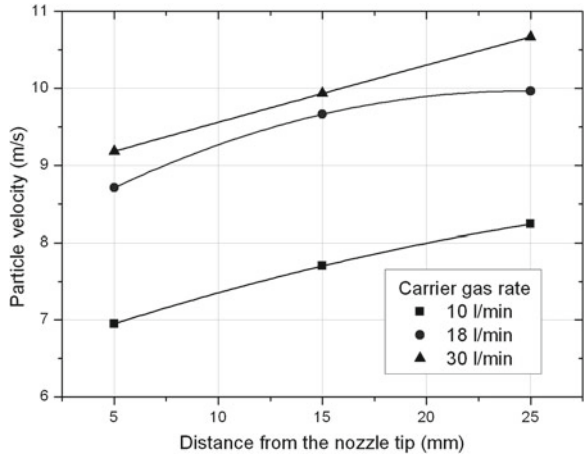
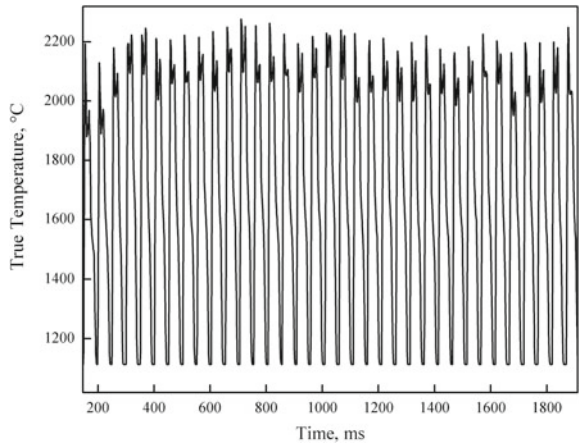


Fig. 9.35 Thermocycles of true temperature in PP laser cladding (20 ms pulse duration, rectangular pulse shape, 2 kW average power, velocity 500 mm/min) of CuAl and WC-Co (30% vol.) on steel



temperature means the real temperature of the surface, not the brightness one) is discussed in detail in [7, 52, 53]. Regular temperature oscillations between 900°C, that is the pyrometer sensitivity limit, and about 2, 100°C, that is lower than the WC decomposition temperature, were found.

The detailed thermocycle corresponding to an individual laser pulse is presented in Fig. 9.36. One may distinguish several typical stages of the temperature evolution: (1) sharp temperature rise at the beginning of the laser pulse; (2) several irregular temperature oscillations during the laser pulse; (3) sharp temperature decrease after the pulse end; (4) solidification shelf of Co slightly above its melting point; (5) further stage of fast cooling after the end of Co solidification. When approaching the Co melting point, the cooling rate falls down to a practically zero value that is the result of the release of the latent heat of solidification. When true temperature is properly restored, the so-called solidification shelf ($\partial T/\partial t \sim 0$, where t is

Fig. 9.36 Individual thermocycle of true temperature in PP LC (20 ms pulse duration, rectangular pulse shape, 2 kW average power, velocity 500 mm/min) of CuAl and WC-Co (30% vol.) on steel

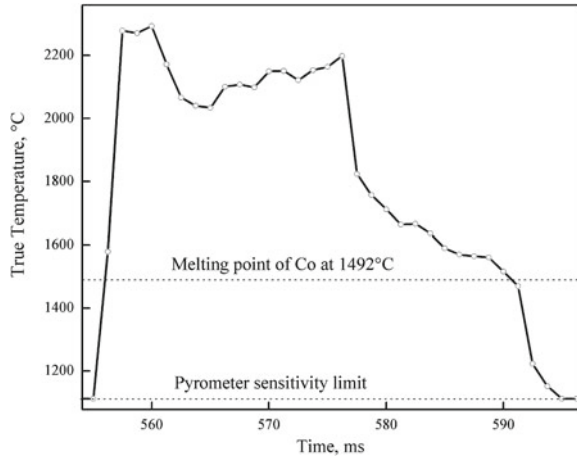
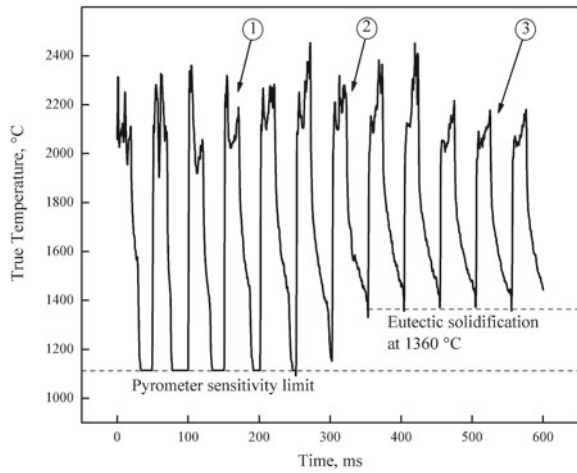


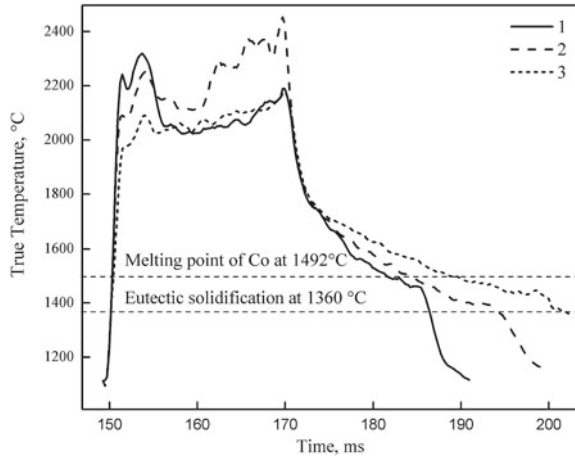
Fig. 9.37 Evolution of the thermo-cycles of true temperature in PP LC (20 ms pulse duration, 2 kW average power, velocity 300 mm/min) of CuAl and WC-Co (30% vol.) on steel



time) should correspond to the melting point. In the actual experiments it is slightly above the melting point of pure Co at $T_m = 1,492^\circ\text{C}$. After the end of Co solidification, the cooling is re-started and the cooling rate reaches $3 \cdot 10^5 \text{K/s}$ that is quite close to the previous value before Co solidification. The solidification of Cu and Al are not detected because of the fact that the pyrometer sensitivity threshold is slightly above the Cu melting point.

Decrease of the cladding velocity, keeping the rest of the parameters fixed, Fig. 9.37, results in the increase of the minimum temperature per thermocycle (T_{\min}) that becomes higher than the pyrometer sensitivity threshold (compare with Fig. 9.36). The transient period for the T_{\min} with the duration of about 350 ms is well seen, later on the temperature oscillations become quasi-steady-state.

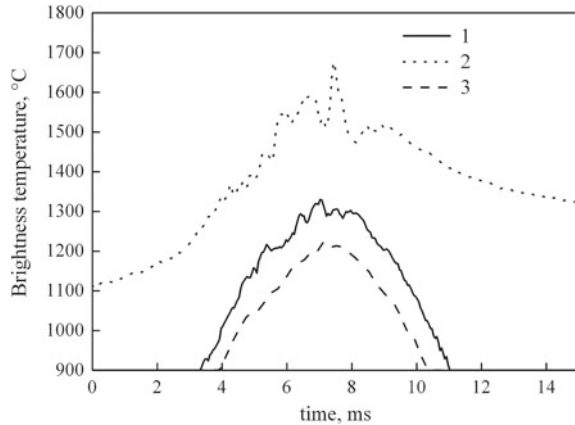
Fig. 9.38 Comparison of three individual thermo-cycles from Fig. 9.37. The positions of thermo-cycles 1–3 are indicated in Fig. 9.37 by corresponding numbers



One may note that the maximum temperature per thermocycle (T_{max}) remains unchanged during the transient period and even slightly decreases after it. By the linear theory of heat transfer [19], the duration of the transient period decreases with the square of velocity of the heat source. It is interesting to compare the thermocycles corresponding to the three individual pulses (indicated by numbers 1–3) from the series presented in Fig. 9.38 to analyze the peculiarities of the cooling stage. One may note that the instant of the sharp increase of the cooling rate that was previously identified with Co solidification (see Fig. 9.36), is now situated below the Co melting point.

In the WC-Co system, eutectic transformation exists at approximately 1,360°C, involving the formation of a liquid phase at that temperature (see WC-Co phase diagram). Following the increase of T_{min} , thickness of the melted layer increases as well that results in a longer duration of its solidification and, therefore, in a stronger diffusion of WC in the Co melt. As a result, the solidification point moves from 1,492°C toward 1,360°C with WC concentration in the melt. The fact that the surface temperature curve does not cross the 1,360°C value indicates that the melt does not solidify completely between the pulses and that the liquid phase exists permanently during the series of laser pulses. This is the main difference to the previously analyzed cladding conditions, Fig. 9.36, when Co completely solidifies between the consecutive laser pulses.

Fig. 9.39 Temperature evolution during crossing of the zone of temperature measurements by the laser beam, thickness of SS 904L powder: 1 500 μm ; 2 50 μm ; 3 0 μm , substrate from SS 304L. The experiments were carried out using PHENIX PM 100 machine: laser power is 50 W, laser beam velocity is 100 mm/s, shift between laser scanning lines is 100 μm . Measurements by MWP with $\lambda = 1.37 \mu\text{m}$



9.4.4 Selective Laser Melting

9.4.4.1 SLM Monitoring Using Stand-Alone Diagnostic Tools

Laser-assisted direct manufacturing by SLM of metallic powder is an advanced process of fabrication of net shape objects [54]. Depending on the powder layer thickness and the remelted layer surface, fabrication may take from a few hours up to tens of hours. Quality assurance by online control is of a paramount importance for SLM and similar processes of Rapid Manufacturing. Pyrometer measurements are useful to optimize process performance and to assure long-time stability of fabrication. A pyrometer and an infra-red camera were used as stand-alone devices, i.e., they were not integrated into SLM machine. The influence of the following process parameters as thickness of the powder layer and shift between the consecutive laser scanning lines are presented in Figs. 9.39, 9.40. The pyrometer measurement zone was 800 μm that is much larger than the laser beam diameter (70 μm). Consecutive passages of the laser beam across the zone of the temperature measurements were analyzed. One may note an evident temperature increase with powder thickness that is explained by volumetric absorption of laser radiation (Fig. 9.39). Sharp decrease of the maximum temperature with overlapping between the consecutive laser scanning lines is explained by the influence of previously remelted layers and strong difference of properties of the remelted powder layer in comparison to the original one (Fig. 9.40). One may note the effect of heat accumulation as a result of consecutive passages of the laser beam (see minimum temperature values).

Visualization of the SLM process was carried out by an infrared camera FLIR Phoenix RDASTM with InSb sensor (see Sect. 2.2).

The camera was aimed at the rectangular area to be scanned by the laser beam with the size close to its vision window. The applied acquisition time was 50 μs and the size of the window was 136 \times 64 pixels. Transient phenomena at the beginning of melting line (Fig. 9.41a) and at its end (Fig. 9.41d) can be easily seen: increasing

Fig. 9.40 Temperature evolution during crossing of the zone of temperature measurements by the laser beam. Shift between consecutive laser scanning lines is: 1 100 μm ; 2 200 μm . The experiments were carried out using PHENIX PM-100 machine: laser power is 50 W, laser beam velocity is 100 mm/s, thickness of SS 904L powder is 500 μm . Measurements by MWP with $\lambda = 1.37 \mu\text{m}$

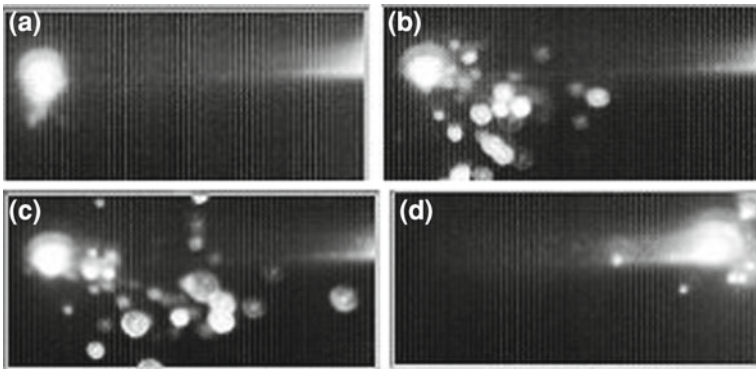
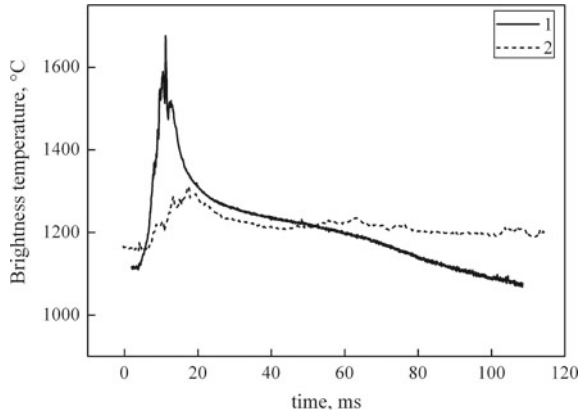


Fig. 9.41 Gray levels image of SLM process: **a** beginning of the laser scanning line; **b–c** microexplosions and droplets removal; **d** end of the laser scanning line. Size of the vision zone is 6.4 by 13.6 mm

of size of HAZ and in particular growing of the “temperature” tail along the melting line. The ejected liquid droplets can be seen as well. The overall estimation about stability or instability of melting process versus operating conditions can be obtained. Along with the above-mentioned advantages of modern infrared cameras, one may note that it is not always easy to decode the obtained images and to identify the related physical phenomena. One may see the HAZ on the right-hand side of Fig. 9.41a that corresponds to the end of the previous scanning line while the laser beam is situated on the left side of the image at the beginning of the actual scanning line. Intensive removal of liquid metal droplets is well seen. This is the result of surface thermochemistry because SLM was carried out in an ambient gas atmosphere (Fig. 9.41 b, c). The droplets are rejected mainly in the direction of laser beam scanning, i.e., in the direction of higher temperature gradient. Their size is much larger than the size of the deposited powder and velocity is in the range 0.5–5 m/s.

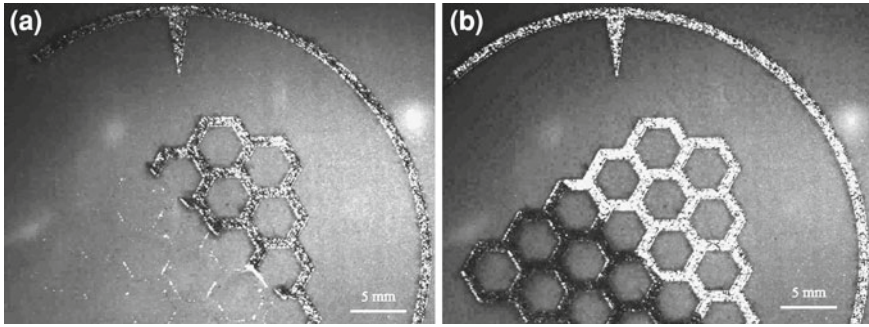


Fig. 9.42 Visualisation of SLM process: INOX 316L powder, layer thickness is 50 μm , laser power is 50 W, scanning velocity is 130 mm/s (a) and 120 mm/s (b), shift between the vectors is 120 μm , shift between the zones is 60 μm

9.4.4.2 Integration of Diagnostic Tools with SLM Machine

A monitoring system is developed to visualize and to control the process of SLM of metallic powder [55]. The system is integrated with industrial PHENIX PM-100 machine. Visualization is carried out using light-emitted diode (LED) illumination and CCD camera; a home developed pyrometer is applied for monitoring of thermal phenomena in the zone of laser impact. Deviation of temperature from its optimal value is chosen as a criterion for the express method of quality control [56]. To discern defects of deposition of a powder layer, to verify position of the laser scanning beam, and to control production quality, the visual observation system (VOS) continually monitors a 30-by-30 mm zone on the surface of the powder bed. VOS is efficiently protected from laser radiation and surface thermal radiation by a system of filters and dichroic mirrors ($\sim 10^{11}$ contrast). Surface illumination is carried out using a LED ring light system. Intensity of the LED-scattered radiation at the video camera matrix exceeds intensity of the laser-scattered radiation and intensity of the surface thermal emittance, except the laser impact zone (Fig. 9.42).

The visualization of the manufacturing process when the so-called two-zones strategy is applied as presented in Fig. 9.42: The deposited powder layer is scanned by laser beam with the 120 μm shift between the consecutive laser passes, the so-called “vectors” (the so-called first zone, Fig. 9.42a), then laser beam is scanning the same area in between the previous vectors without powder adding (the so-called second zone, Fig. 9.42b). One may note the difference of surface roughness and reflectivity of the remelted powder layers before and after second passage of laser beam. Temperature measurements in the laser impact zone were carried out by the originally developed bicolor pyrometer with the following performance: temperature range is 900–2800 K, wavelengths are 1.25, 1.36 μm , 2 InGaAs photodiodes, diameter of zone of temperature measurements is 560 μm , sampling time is 50 ms. The pyrometer was not calibrated through the optical system of the PHENIX PM-100 because of technical problems with putting the black body inside the SLM machine

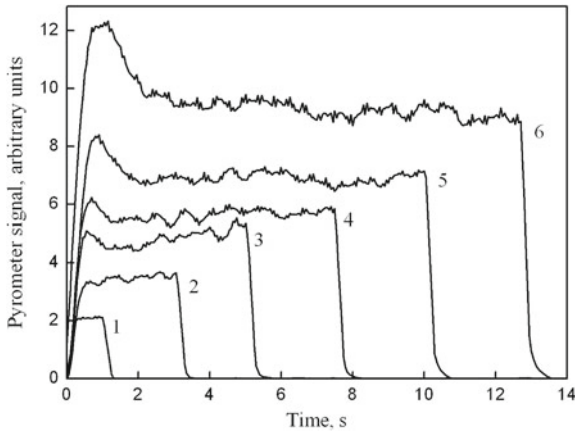
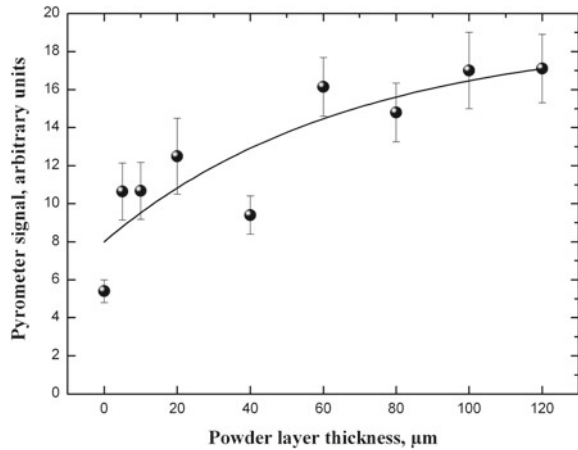


Fig. 9.43 Evolution of the pyrometer signal versus shift between consecutive laser beam passes (“vectors”) during scanning of one square centimeter on the powder bed surface. The pyrometer trials are carried out for laser power at impact equals to 32 W, 120 mm/s beam scanning speed, Inconel powder with 25 μm mean size, 1 mm powder layer thickness, 20 l/min flow rate of the protective gas (N_2). Curve 1 corresponds to the shift equals to 1 mm; 2 300 μm ; 3 180 μm ; 4 120 μm ; 5 90 μm ; 6 70 μm

that is why the results of measurement have only relative values and they are presented in arbitrary units. The pyrometer trials were carried out for laser power at impact equal to 32 W, beam scanning speed 120 mm/s, Inconel powder with mean size of 25 μm , flow of protective gas (N_2) is 20 l/min. The value of shift between consecutive laser passes (“vectors”) is one of the main technological parameters of SLM. One square centimeter on the surface of powder bed with 1 mm thickness was scanned by laser beam. For the present thickness of powder layer the metallurgical contact between remelted powder and substrate is absent. The duration of scanning depends on a number of vectors that is defined by the shift between them. That is why the durations of thermal cycles in Fig. 9.43 are different, less is the shift, and more is the number of vectors and the total duration of scanning of 1 cm^2 . The increase of mean temperature with the decrease of shift is the result of heat accumulation because of different energy input into 1 cm^2 .

The thickness of powder layer is another important technological parameter of SLM. Relatively small thickness, 20–30 μm , results in high accuracy of fabrication but low productivity, and vice versa. The increase of pyrometer signal with powder layer thickness is the result of energy balance between powder melting and substrate (or previously fabricated layer) remelting (Fig. 9.44). For small thickness of the powder layer, an important fraction of laser energy is spent on substrate remelting. Keeping in mind that the coefficient of thermal conductivity of a powder bed is 20 times lower than that of a wrought metal, the mean temperature is rising up with powder bed thickness. That is why starting from certain critical value, say 100 μm , the pyrometer signal reaches maximum and stable value because the contact between

Fig. 9.44 Variation of the pyrometer signal with powder layer thickness. The pyrometer trials are carried out for laser power at impact equals to 32 W, 120 mm/s beam scanning speed, inconel powder with 25 μm mean size, 20 l/min flow rate of the protective gas (N_2)



melted powder layer and substrate is lost, and so all laser energy is absorbed by powder and no heat losses to substrate takes place.

9.5 Conclusions

The developed optical diagnostic tools are appropriate instruments to control surface temperature evolution in laser welding, cladding, surface treatment, SLM, and the particles-in-flight parameters in LC and direct manufacturing with coaxial powder injection. Similar performance cannot be obtained using a simple photo diode or a traditional pyrometer. The developed and applied pyrometers are specially adjusted for laser applications, namely, they have several specific features such as narrow spectral band width (50 nm), high spatial (50–800 μm spot size) and temporal resolution (typical sampling time is 50 μs), protection from laser radiation by specially developed notch filters with 10^{-6} transparency at 1.06 μm wavelength. These operational capacities allow to avoid superposition of proper thermal radiation with different types of noise and to assure correct measurements of brightness temperature. By appropriate application of multi-wavelength methodology, the true temperature can be restored. The developed instruments could be used as sensors for the real-time process monitoring and online quality control applying simplified thermal models for the process control loop.

1. Monitoring of temperature evolution at different temporal scales. Real-time temperature monitoring in pulsed and PP laser machining gives a unique opportunity to analyze the dynamics of the heat processes using various temporal scales: On the one hand, precise monitoring of the surface temperature evolution during the action of an individual laser pulse and the subsequent cooling stage; on the other hand, of a complete series of laser pulses. Using pyrometer

measurements, one may analyze the influence of the processing parameters such as pulse energy and duration, pulse shape, welding speed, accuracy of laser beam position relative to the junction on temperature evolution in the zone of laser machining.

2. Analysis of phase transitions by restoration of true temperature dynamics. With the help of the developed multi-wavelength pyrometer and by appropriate application of multi-wavelength methodology, true temperature under pulsed laser action with ms duration was restored. The variation of several characteristics of the thermal cycle such as the maximum peak temperature, T_{\max} , the instant when melting starts, t_m , the melt life time, τ_{lt} , the duration of the solidification stage, τ_s , with various energy inputs (in the range 10–33 J), and pulse durations (6–20 ms), were determined for rectangular laser pulses. By appropriate modification of the laser pulse shape (keeping the same energy input and pulse duration), it is possible to realize rather different temperature evolution patterns, to vary the melt life time and the instant when melting starts. To minimize surface temperature variation, to avoid thermal decomposition of certain melt compounds, to increase the melt life time, it is necessary to apply higher energy density flux at the beginning of the laser pulse. To obtain a higher peak of the surface temperature, for the given energy input and pulse duration, it is necessary to apply higher energy density flux at the pulse end. This will minimize the melt life time as well. In general, it is possible to impose the instant when melt cooling starts and, thus, to realize an intensive melt cooling even during laser irradiation. The above results correspond to laser pulses in the millisecond range with relatively low energy density flux (4×10^4 – 10^5 W/cm²) on metallic materials whose thickness is larger than the HAZ (i.e., 1D heat transfer in semi-infinite geometry).
3. Nd:YAG laser lap welding of Zn-coated steel sheets. Quality of the lap welding of zinc-coated steel is strongly influenced by the gap between the sheets. The quality control can be done by measurement of the surface temperature which itself is a function of the gap value. During welding (laser power is 2 kW, welding speed is 2,500 mm/min) with the given gap size of 0.2 mm, the surface temperature is stable: for the lap welding of a sheet of 0.7 mm on a sheet of 1.25 mm, the mean temperature is 1,980°C with signal deviations of $\pm 78^\circ\text{C}$ (4%); for the lap welding of a sheet of 0.7 mm on a sheet of 1 mm, the mean temperature is 1,917°C with signal deviations of $\pm 37^\circ\text{C}$ (2%). Deviation of the gap from its optimal value leads to a decrease in welding quality. The mean temperatures values are lower compared to those for the optimal conditions, the spectrum of temperature oscillations is qualitatively different. It is shown that for high accuracy detection of temperature deviations from the optimal value that show up in welding defects, better to apply a higher frequency of measurements even with a lower spatial resolution than measurements with a higher spatial resolution but with a lower frequency. In consequence, it may be concluded that pyrometric measurements can be successfully used for the quality monitoring of the lap welding of zinc-coated steel sheets.

4. LC. The developed pyrometers were applied to analyze variations of brightness temperature in the melt pool and the brightness temperature profiles during LC with lateral and coaxial powder injection. The influence of laser power, LC speed, and powder feeding rate on the brightness temperature were studied. Temperature measurements are useful to minimize thermal deformations and stresses in clad beads and to avoid thermal decomposition of powder. It is found that, even if the range of variation of brightness temperature is much narrower than the range of variation of process parameters (laser power, powder feeding rate), the mean temperature values are rather stable: mean square deviation does not exceed a few percents. The multi-wavelengths pyrometer was applied to restore the value of true temperature that is useful to control melting/solidification when complex powder blends are used and when it is necessary to minimize thermal decomposition of certain compounds. It is shown that the 2D temperature mapping is useful to optimize the following process parameters: zone of powder injection in relation to the laser beam, temperature gradients, and their evolution versus processing parameters. The CCD camera-based diagnostic tool is employed for particle-in-flight visualization, for control of particle jet stability, and for online measurement of particle size and velocity. The optical monitoring allows understanding of interaction between gas flow and particles, and optimizing the conditions of powder injection.
5. SLM. Optical monitoring of SLM is targeted for solution of several problems: (a) visualization of powder layering and its consecutive melting by laser beam scanning, visual inspection of remelted zone geometry and surface quality; (b) temperature monitoring in laser impact zone to assure stability and quality of fabrication, to optimize the processing conditions and manufacturing strategy. It is shown that thermal signal from the laser impact zone is rather sensible for variation of processing parameters such as powder layer thickness, distance between consecutive laser passes, etc. The key problem is integration of the optical control system with SLM machine.

References

1. M.N. Azer, J. Mazumder, in *Laser Materials Proceedings, ICALEO'93*, Orlando, 1994, ed. by P. Denney, B.L. Mordike, p. 235
2. M. Ignatiev, I. Smurov, G. Flamant, *Appl. Surf. Sci.* **505**, 96–98 (1996)
3. M. Ignatiev, I. Smurov, G. Flamant, V. Senchenko, V. Dozhdikov, *Appl. Surf. Sci.* **109–110**, 498–508 (1997)
4. B. Grünenwald, J. Shen, F. Dausinger, H. Hügel: in *Proceedings of the 26th International Symposium on Automotive Technology and Automatisation ISATA'93*, Aachen, 1993, p. 278
5. G. Bi, A. Gasser, K. Wissenbach, A. Drenker, R. Poprawe, *Surf. Coat. Technol.* **201**, 2676–2683 (2006)
6. Y.P. Hu, C.W. Chen, K. Murherjee, *J. Laser Appl.* **12**, 126–130 (2000)
7. I. Smurov, V. Veiko (eds.), in *Proceedings of SPIE*, vol. 4157, 2001, pp. 55–66
8. M. Doubenskaia, Ph. Bertrand, I. Smurov, *Thin Solid Films* **453–454C**, 477–485 (2003)
9. L.-R. Benedetti, P. Loubeyre, *Int. J. High Pres. Res.* **24**, 423–445 (2004)

10. T.J. Quinn, *Multi-Wavelength Pyrometry* vol. 5, (Academic, London, 1983)
11. T. Duvaux, D. Georgeault, J.L. Beaudoin, *Revue générale de Thermique* **35**, 185–196 (1996)
12. D.Ya. Svet, *High Temp.-High Pressures* **4**, 715–722 (1972)
13. D.Ya. Svet, *High Temp.-High Pressures* **8**, 493–498 (1976)
14. P.B. Coates, *Multi-wavelength pyrometry. Metrologia* **17**, 103–109 (1981)
15. E. Hagen, H. Rubens, *Ann. Phys.* **11**, 873 (1903)
16. M. Ignatiev, I. Smurov, G. Flamant, V. Senchenko, V. Dozhdikov, *High Temp. Mater. Processes* **1**, 109–123 (1997)
17. Ph. Bertrand, M. Ignatiev, G. Flamant, I. Smurov, *Vacuum* **56**, 71–76 (2000)
18. M. Ignatiev, V. Senchenko, V. Dozhdikov, I. Smurov, Ph. Bertrand, in *Proceedings of International Thermal Spray Conference, ITSC-2002*, Essen, 2002, pp. 1001–1006
19. N. Rykalin, A. Uglov, I. Zuev, A. Kokora, *Laser and Electron Beam Material Processing* (MIR Publishers, Moscow, 1988)
20. A.A. Uglov, I.Yu. Smurov, A.M. Lashin, A.G. Guskov, *Modelling of Thermal Processes under Pulsed Laser Action on Metals* (Nauka Publishers, Moscow, 1991)
21. I. Smurov, A. Lashin, in *Laser Applications in Mechanical Industry*, ed. by S. Martellucci, A.N. Chester, A.M. Verga Scheggi. NATO ASI Series, Series E: Applied Science, vol. 238, (1993) pp. 165–206
22. J.C. Ion, *Laser Processing of Engineering Materials: Principles Procedure and Industrial Application* (Elsevier Butterworth-Heinemann, Burlington, 2005)
23. W.M. Steen, *Laser Material Processing*, 3rd edn. (Springer, London, 2003)
24. H.S. Carslaw, J.C. Jaeger, *Conduction of Heat in Solid* (Oxford University Press, New York, 1959)
25. Ph. Bertrand, I. Smurov, D. Grevey, *Appl. Surf. Sci.* **168**, 182–185 (2000)
26. I. Smurov, M. Ignatiev, Ph. Bertrand, G. Flamant, L. Covelli, J. Thomas, F. Brandt, *CISFFEL-6*, Toulon, France, 1998, pp. 655
27. R.T. Deam, M. Brandt, J. Harris, *J. Phys. D.* **36**, 2435–2445 (2003)
28. T. Klein, M. Vicanek, J. Kroos, I. Decker, G. Simon, *J. Phys.D.* **27**, 2023–2030 (1994)
29. N. Postacioglu, Ph. Kapadia, J. Dowden, *J. Phys. D* **22**, 1050–1061 (1989)
30. F.M. Haran, D.P. Hand, S.M. Ebrahim, C. Peters, J.D.C. Jones, *Meas. Sci. Technol.* **8**, 627–633 (1997)
31. E. Toyserkani, A. Khajepour, S. Corbin, *Laser Cladding* (CRS Press, Boca Raton, 2005)
32. V. Ocelik, de U. Oliveira, de M. Boer, de J.Th.M. Hosson, *Surf. Coat. Technol.* **201**, 5875–5883 (2007)
33. Y. Liu, J. Mazumder, K. Shibata, *Metall. Mater. Trans. B.* **25**(5), 749–759 (1994)
34. I. Smurov, *Surf. Coat. Technol.* **202**, 4496–4502 (2008)
35. R. Banerjee, P.C. Collins, A. Genc, H.L. Fraser, *Mater. Sci. Eng. A* **358**(1–2), 343–349 (2003)
36. Y.T. Pei, V. Ocelik, J.Th.M. De Hosson, *Acta Mater.* **50**, 2035–2051 (2002)
37. J. Dutta Majumdar, L. Li, *Mater. Lett.* **64**, 1010–1012 (2010)
38. J. Dutta Majumdar, I. Manna, A. Kumar, P. Bhargava, A.K. Nath, *J. Mater. Process. Technol.* **209**, 2237–2243 (2009)
39. J. Dutta Majumdar, B. Ramesh Chandra, A.K. Nath, I. Manna, *J. Mater. Process. Technol.* **203**, 505–512 (2008)
40. W. Xiaolei, *Surf. Coat. Technol.* **115**, 111–115 (1999)
41. J. Lin, *Opt. Laser Technol.* **31**, 233–238 (1999)
42. X. He, J. Mazumder, *J. Appl. Phys.* **101**, 053113.1–053113.9 (2007)
43. J. Mazumder, J. Choi, K. Nagarathnam, J. Koch, D. Hetzner, *J. Metals* **49**, 55–60 (1997)
44. B. Dutta, V. Singh, H. Natsu, J. Choi, J. Mazumder, *Adv. Mat. Proc.*, vol. 167, 2009, pp. 29–32
45. The POM Group Inc., Auburn Hills, Michigan, USA, in Internet <http://www.pomgroup.com>, May 2009
46. A. Rosochowski, A. Matuszak, *J. Mater. Process. Technol.* **106**, 191–198 (2000)
47. de U. Oliveira, V. Ocelik, J.Th.M. De Hosson, *Surf. Coat. Technol.* **197**, 127–136 (2005)

48. J. Koch, J. Mazumder, Apparatus and methods for monitoring and controlling multi-layer laser cladding, U.S. Patent No. 6 122 564 (2000).
49. J. Mazumder, J. K. Kelly, Closed-loop, rapid manufacturing of three-dimensional components using direct metal depositions, U.S. Patent No. 6 925 346, 2000
50. G. Bi, A. Gasser, K. Wissenbach, A. Drenker, R. Poprawe, *Opt. Lasers Eng.* **44**, 1348–1359 (2006)
51. J. Mazumder, D. Dutta, N. Kikuchi, A. Ghosh, *Opt. Lasers Eng.* **34**, 397–414 (2000)
52. M. Doubenskaya, I. Smurov, *Appl. Surf. Sci.* **252**, 4472–4476 (2006)
53. Th. Duvaut, *Infrared Phys. Technol.* **51**, 292–299 (2008)
54. I. Yadroitsev, Ph. Bertrand, B. Laget, I. Smurov, *J. Nucl. Mater.* **362**, 189–196 (2007)
55. Yu. Chivel, I. Smurov, *Proceedings of IV International WLT-Conference on Lasers in Manufacturing*, Munich, 2007, pp. 553–556
56. M. Doubenskaia, M. Pavlov, Yu. Chivel, *Key Eng. Mater.* **437**, 458–461 (2010)

Chapter 10

Emerging Laser Materials Processing Techniques for Future Industrial Applications

L. M. Kukreja, R. Kaul, C. P. Paul, P. Ganesh
and B. T. Rao

Abstract Lasers are not only the proven and indispensable tools for some of the contemporary manufacturing technologies but have the potential for providing solutions to some of the upcoming intricate problems of industrial materials processing. The ongoing research is spearheading in the direction to develop novel fabrication techniques for improving qualities of the products, possibilities to engineer integrated multi-materials and multi-functional components and enhancing economic or procedural benefits. To explore the possibilities of achieving some of these objectives, we have carried out studies on the laser rapid manufacturing of structures of different metals with control over porosity, bimetallic integration, and other technologically important mechanical characteristics, laser melting based surface processing, laser shock peening, hybrid welding, and laser profile cutting of metal sheets. The results of these studies with comprehensiveness are presented and discussed in this chapter. A brief review of their scope for the industrial acceptability and adaptability has also been presented to assess the real potential of these research areas.

10.1 Introduction

When laser was invented in 1960 by Prof. Maiman, it was dubbed as a ‘solution in search of problems’. Undoubtedly, today lasers are ‘solutions for many problems’, including industrial manufacturing technology. The domain of laser based materials processing witnessed its dawn with the first experiments on drilling and welding of stainless steel blades and foils during 1963 and 1964 [1]. Followed by that, there was a spurt of interest in the applications of lasers for materials processing with

L. M. Kukreja (✉) · R. Kaul · C. P. Paul · P. Ganesh · B. T. Rao
Laser Materials Processing Division,
Raja Ramanna Centre for Advanced Technology,
Indore 452013, India
e-mail: kukreja@rrcat.gov.in

multiple ramifications. This spurt was propelled by the invention of a variety of high power lasers such as CO₂, Nd:YAG, and Er:YAG lasers. These lasers pushed the levels of output power from milliwatts to Watts and then to kilowatts and Megawatts in different modes of operations. This was the beginning of the age of laser based industrial materials processing, which has grown over the last five decades [2–4] and continues to grow in terms of magnitude, scope, and standards of quality [5, 6].

Today, both industrial lasers and laser manufacturing technologies are already in advanced stage of their evolution. But as we witnessed over the last five decades, the needs of manufacturing technologies are insatiable; as the new developments emerge, the new problems and demands for better solutions also emerge. This dynamics of development and demand appears to be endless. This scenario has now posed a question: can laser based materials processing techniques meet the emerging new demands of the manufacturing technologies? The answer lies mainly in the ways the lasers are deployed for novel and clever ingenuities to tackle the posing manufacturing problems. For the development of such ingenuities research is a crucial component. At our laboratory, research on laser processing of materials to circumvent the emerging problems of industrial manufacturing technologies is the prime objective. Backed by the history of about 25 years of research and development in this domain, recently we have undertaken applied and basic research in the fields of laser rapid manufacturing (LRM), surface processing techniques (laser surface melting, laser cladding, laser shock peening etc.), hybrid welding, and metal cutting. Through this research a cornucopia of interesting results have been accomplished, which are poised to improve the laser materials processing for industrial applications in many ways for the times to come. The results of these research studies are presented and discussed in this chapter.

10.2 Laser Rapid Manufacturing

The field of laser based manufacturing has recently faced new directions with the advancements in high speed computers and the resulting computer aided design (CAD), laser technologies, and layered/additive manufacturing techniques. This has led to the next generation fabrication methodology, involving “feature-based design and manufacturing”, with the capability to carry out cost-effective refurbishing of prime components with improved functionality. This fabrication procedure has been termed as Laser Rapid Manufacturing. Laser rapid manufacturing employs a laser beam as a heat source to melt a thin layer on the surface of the substrate while using blown metal powder to deposit a layer of predetermined shape and dimensions. A number of such layers, deposited one on another, results in fabrication of three-dimensional (3D) components directly from their CAD models. The process eliminates many production steps such as materials-machine planning, man-machine interaction, intermittent quality checks, assembly and related human errors, etc. Laser rapid manufacturing, due to its inherent process methodology, offers certain advantages over conventional subtractive techniques, such as reduced production time,

better process control, and capability to form multi-material parts with tailored heterogeneity. The process, because of its low heat input, limited dilution with minimal distortion and capability to fabricate near-net shape three-dimensional (3D) components, is also an attractive candidate for refurbishing applications [7–10]. Figure 10.1a illustrates one of the LRM setups at our laboratory. This system consists of an indigenously developed transversely excited transverse gas flow continuous wave 3.5 kW CO₂ laser, integrated with a beam delivery system, powder feeder and a 5-axis CNC workstation. In this system, the laser beam is transported to the fabrication point at 5-axis workstation using water-cooled gold-coated plane mirrors. Finally, the laser beam is focused with a concave mirror of 600 mm radius of curvature at the end of beam delivery system. A defocused laser beam of desired diameter (1–3 mm) is used for metal deposition at fabrication point. The metal powder is fed into the molten pool using a volumetric controlled powder feeder through a coaxial powder-feeding nozzle. Argon gas is used as shielding and powder carrier gas. The fabrication point is moved as per the required shape using standard numerical codes to fabricate the component. Another LRM setup, using a 2 kW CW fiber laser with a 5-axis workstation in a glove box, is commissioned at our laboratory for the fabrication of prosthetic and engineering component in controlled atmosphere. Figure 10.1b presents schematic illustration of the new LRM set up.

Manufacturing techniques, similar to LRM, are being developed with different names at various laboratories around the world. At Sandia National Laboratory, USA, Laser Engineered Net Shaping (LENSTM) is being developed with prime focus on creating complex metal parts in a day [11]. National Research Council, Canada is developing Freeform Laser Consolidation for manufacturing of structural components for advanced robotic mechatronic systems [12]. Automated Laser Fabrication (ALFa) is being developed to produce low-cost tools at the University of Waterloo, Canada [13]. Selective Laser Cladding (SLC) at the University of Liverpool, UK and Direct Metal Deposition at the University of Michigan, USA are being used for depositing critical surfaces on prime components [14, 15]. Laser Powder Deposition (LPD) at University of Manchester, UK and Direct Metal Deposition/Laser Additive Manufacturing at Fraunhofer Institute, Germany are being augmented for the fabrication of high performance materials [16]. These global efforts are constantly advancing the list of applications of LRM. Table 10.1 summarizes some typical examples of industrial applications of LRM. Figure 10.2 shows some of the complex-shaped components laser rapid manufactured in our laboratory to demonstrate the fabrication capability of indigenously integrated LRM system. Figure 10.2a is 50 × 15 × 0.8 mm walls of type 316L stainless steel (SS 316L). Figure 10.2b is a simple cage of Inconel-625 (size: 40 mm base diameter × 60 mm height), laser rapid manufactured with pulse mode operation of laser. Figure 10.2c and d are complex impeller-like geometries (size: 45 mm base diameter × 12 mm height), laser rapid manufactured with type 316L stainless steel.

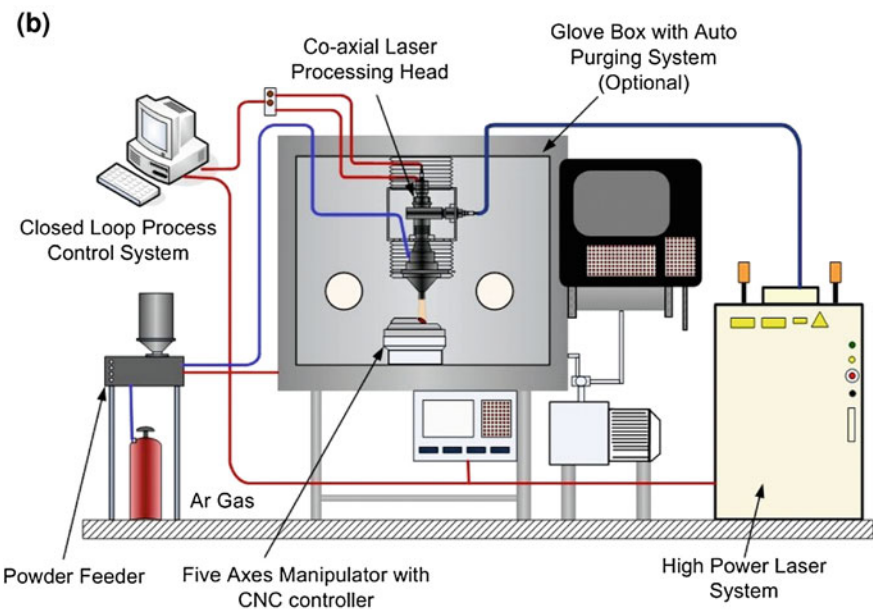
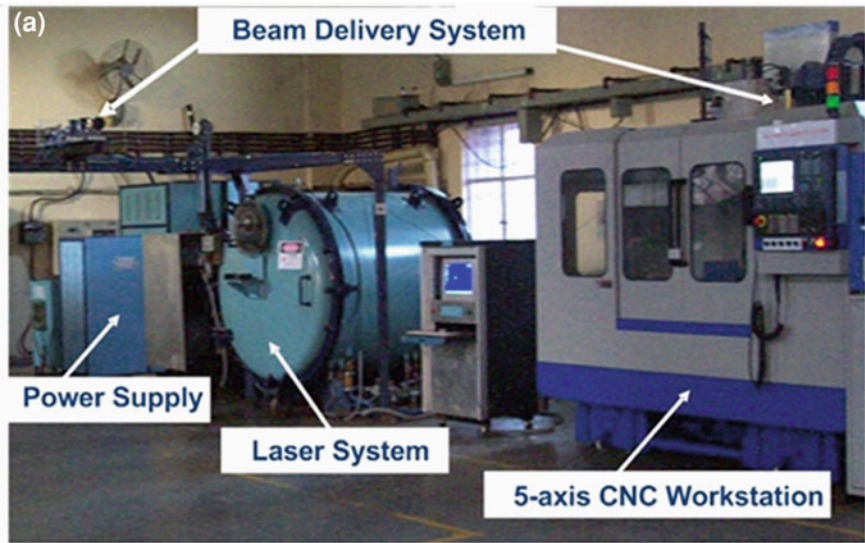


Fig. 10.1 Photograph of **a** LRM setup at authors' laboratory, and **b** schematic arrangement of the recently commissioned LRM setup

Table 10.1 Examples of Industrial applications of LRM [17]

S. No.	Application description	Materials
1	High pressure gas turbine blade shroud, interlock, turbine blade	Triballoy on Nimonic
2	Parts of off-shore drilling heads	CrC, Cr, Ni on cast iron
3	Cylinder and valve	On cast iron
4	Automotive parts	Stellite, Triballoy T-800
5	Turbine blade, plough blades	Stellite 6, Stellite SF
6	Diesel engine valve	Stellite 6
7	Extruder screw plastic machinery	LC2.3B (Ni-base), Al-bronze
8	Deep drawing tool (cast iron GGG60)	Stellite SF6
9	Leading edge steam turbine blade	Stellite 6, Stellite 6F
10	Valve in combustion engine (x45crsi9)	Triballoy T-800
11	Deformation tool	Stellite 6
12	Gas turbine airfoil thermal barrier	Inconel 625 + CrC
13	Valve seat	Type 410 stainless steel
14	Stainless steel seal runner	Stellite 6
15	Valve in combustion engine (X45CrSi9)	Stellite 21
16	Extruder screw plastic machinery (14CrMoV6 9)	Ni-Cr-Al-Y
17	Molding die (45NiCr6)	Co-Cr-W-C
18	Exhaust valves large diesel engines (NiCr20AlTi ~ DIN 2.4952)	Ti-6Al-4V + cubic BN
19	Camshaft, compressor blade (Ti-6Al-4V)	Stellite 6
20	Nuclear valve (AISI 304)	Ni-Cr alloy
21	Blowing mould	PWA Alloy 694
22	Die for production of glass bottles	Stellite 6, Colmonoy 5

10.2.1 Laser Rapid Manufacturing of Colmonoy-6 Bushes

Nickel-based alloys “Colmonoy”, due to their outstanding wear resistance, high hardness at elevated temperatures and low induced radioactivity, find applications for hardfacing of austenitic stainless steel components of nuclear power plants [18]. In the event of complicated component geometry, providing limited access for hardfacing, prefabricated Colmonoy-6 bushes can be used in place of local hardfacing. Conventionally, these bushes are made by casting/weld deposition followed by machining [19]. However, high capital cost for the low volume of fabrication makes it a prohibitive option. These customized Colmonoy-6 bushes were prepared at our laboratory by LRM as an alternative to conventional processing.

Laser rapid manufacturing of Colmonoy-6 bushes was carried out on a sandblasted 12 mm thick plate of type 316L stainless steel as base. In view of poor cracking resistance of Colmonoy-6 deposits, slow cooling was a prerequisite to obtain crack-free bushes. It was achieved by placing base plate, undergoing laser deposition, in a special sand bath maintained at an elevated temperature of 673 K. The sand bath consisted

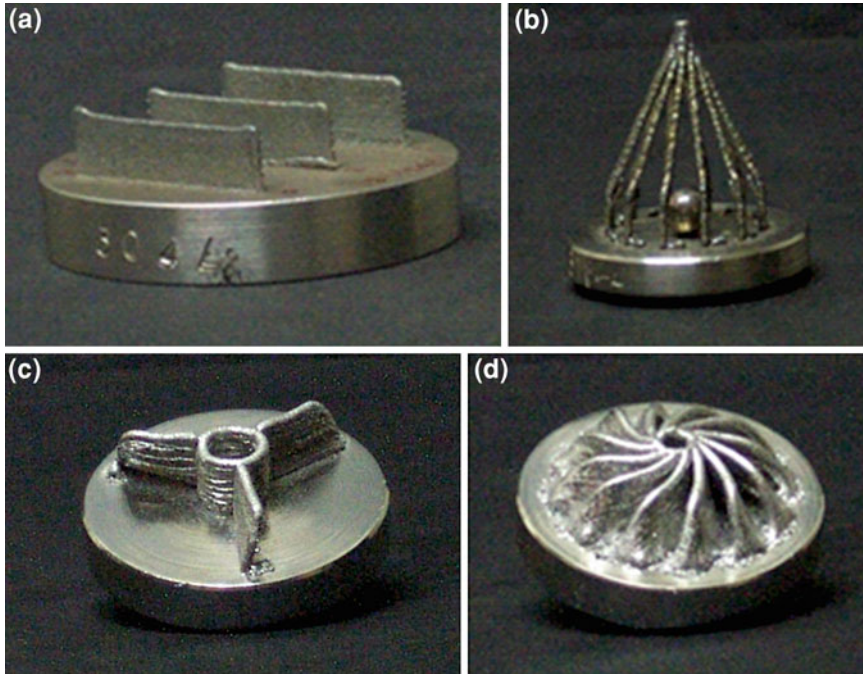


Fig. 10.2 Laser rapid manufactured **a** walls of type 316L stainless steel, **b** simple cage of Inconel-625, **c** three-vane impeller, and **d** multiple-vane impellers—both comprised of type 316L stainless steel

of an electrically heated copper plate buried in the sand. Temperature of the bath was measured and automatically controlled with the help of a temperature controller. Laser rapid manufacturing of cylindrical Colmonoy-6 bushes, with dimensions of 20 mm outer diameter, 2.5 mm wall thickness and 40 mm length, involved depositing circular clad tracks one over the other. Figure 10.3a shows the photograph of LRM of Colmonoy-6 bush in progress. After LRM, the fabricated parts were left buried in the sand bath for more than 8 hours to achieve slow rate of cooling. The resultant Colmonoy-6 bushes were found to be crack free. The measured dimensional tolerance using three-point method was 0.2–0.5 mm, while surface roughness (R_a) was in the range of 25 – 40 μm .

The laser rapid manufactured Colmonoy-6 bushes required subsequent machining to bring their dimensions within the tolerance zone. High hardness (55 – 60 HR_C) of these bushes makes their machining difficult with conventional tools. Moreover, irregular surfaces with $R_a = 25\text{--}40 \mu\text{m}$ made the machining more complex. Keeping these limitations in view, different machining operations were tried out with different tools. First high speed steel (HSS) tool with 10% Co, manufactured by powder metallurgy, was used to remove surface irregularities. Subsequently, rough and final machining was carried out with CERMET inserts to obtain final surface finish of $\sim 1\text{--}$

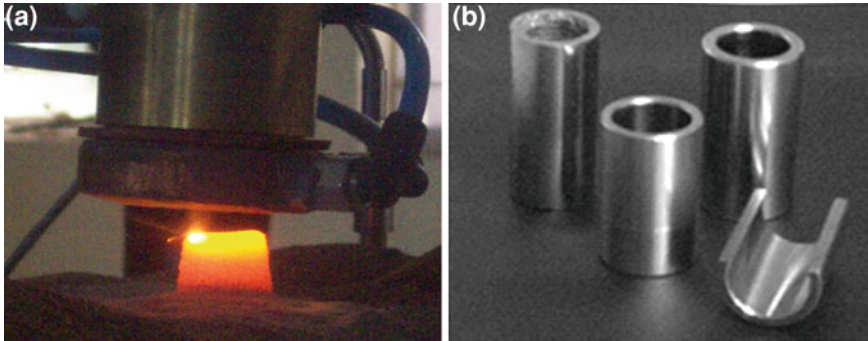


Fig. 10.3 **a** Laser Rapid Manufacturing of Colmonoy-6 bush, and **b** bushes after final machining

1.6 μm R_a . Subsequently, Cubic Boron Nitride (CBN) inserts were used to improve surface finish to 0.4 μm R_a . Final dimensions and surface finish were achieved using inside and outside grinding with Al_2O_3 grinding wheels to obtain final surface finish of ~ 0.04 μm R_a . Figure 10.3b shows laser rapid manufactured Colmonoy-6 bushes after final machining.

This study demonstrated that LRM can be used as a cost-effective alternative technique for the fabrication of Colmonoy-6 bushes [20]. This method has significant advantage over other techniques, in terms of saving of expensive Colmonoy-6 material and reduced machining of the hard material [19].

10.2.2 Laser Rapid Manufacturing of Low-Cost Tools

In view of the high cost of tungsten carbide (WC) powder and its increasing demand, there is a need to develop a low-cost repair technology or new fabrication techniques for WC cutting tools. In the realm of the hard materials, cemented carbide is a popular choice for tools, dies, and wear prone parts that find wide applications in machining, mining, metal cutting, metal forming, construction etc. This class of materials has unique combination of high strength, high hardness, high toughness, and moderate modulus of elasticity, particularly with finely distributed WC particles in cobalt matrix. In WC-Co system, cobalt plays a significant role as a binder and is responsible for densification through wetting, spreading, and formation of agglomerates during liquid phase sintering. A uniform distribution of metal phase in a ceramic is beneficial for improved mechanical properties of the composite. Absorption of laser radiation by WC particles is about 1.4 times stronger than that in Co for 1.064 μm wavelength [13]. As a result of excessive heating and partial melting of WC particles, WC phase may undergo dissociation causing carbon deficiency in WC-Co composite and precipitation of carbon as graphite. This graphite reacts with atmospheric oxygen to form CO and CO_2 , which often appear as gas porosity, whereas, availability of free

carbon in the matrix leads to formation of a brittle ternary eutectic phase of W, Co, and C; often referred as “eta” phase [21]. Formation of both graphite and eta-phase in WC-Co composite, is detrimental. Therefore, the selection of laser processing parameters and material’s composition play a critical role in LRM of WC-Co.

Comprehensive experiments were carried out with various WC-Co compositions at the University of Waterloo [22] and others [23]. Three important process parameters, influencing LRM of WC-Co parts are: average energy density, peak power density, and spot overlap. The average threshold energy density, required to sustain melt pool and form a continuous track during pulsed laser cladding of WC-Co, was found to be about 30 J/mm^2 . Higher input average energy density resulted in excessive melting of the substrate layer, leading to enhanced dilution. Peak power density is also an important parameter in controlling local peak temperature and melting of the material to be clad. In the case of WC-Co system, high peak power density resulted in dissociation of WC particles. With a given laser pulse energy, the dissociation and partial melting of WC particles could be controlled by manipulating laser pulse duration. The optimum peak power density, required to obtain good quality WC-Co clad, was found to be in the range $350\text{--}600 \text{ W/mm}^2$. For successful deposition of WC-Co clad layer, the combination of processing parameters should simultaneously meet both the criteria of average energy density and peak power density [13]. Laser pulse energy played a major role in achieving both the criteria, while the contribution of laser pulse repetition rate was limited to deposition speed. Laser rapid manufactured WC-Co under optimized parameters, although associated with isolated porosities, particularly at the clad-interface, were found to be free from bulk defects such as micro-cracks, intermetallic phases and inclusions etc.

Figure 10.4 shows the microstructure of laser rapid manufactured WC-Co deposit, showing uniform dispersion of unmelted WC particles in Co-matrix. Energy dispersive spectroscopy (EDS) based analysis and microhardness measurements across substrate/clad interface region demonstrated fairly smooth transition in chemical composition and microhardness, which are shown in Fig. 10.5. These are desirable features to avoid local stress concentration for enhanced resistance against failure under shock loading. The microhardness in the laser clad zone ($1250\text{--}1700 \text{ HV}$ at 1000 g load) was found to be comparable to that of conventional WC-Co specimens [21].

Laser rapid manufacturing with optimized parameters, was subsequently used for the fabrication of low-cost tools. It involved deposition of cemented carbide on low-carbon steel rods to shape the cutting tools, as shown in Fig. 10.6. Such fabricated tools were used for cutting of type 316 stainless steel. With respect to conventionally processed tools, the cut quality produced with these low-cost LRM-fabricated tools was found to be at par with associated tool life of more than 80%.

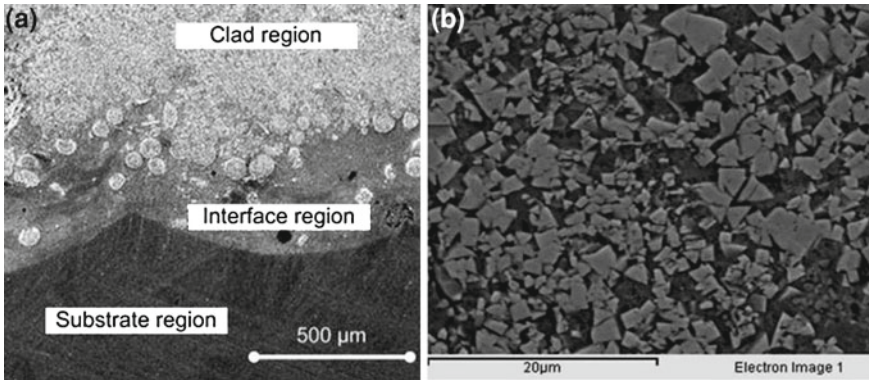


Fig. 10.4 **a** Transverse cross-section of substrate-clad interface, **b** back scattered electron image of the microstructure of WC-Co deposit

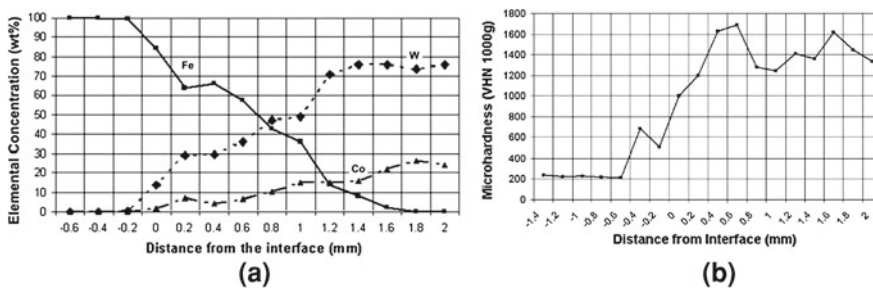


Fig. 10.5 **a** EDS concentration, and **b** micro-hardness profiles across substrate-clad interface of WC-Co deposited C40 steel specimens made by LRM

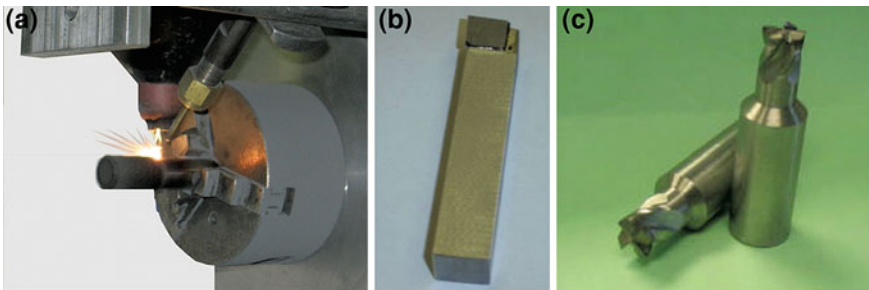


Fig. 10.6 **a** Laser rapid manufacturing of low-cost tool, **b** and **c** laser rapid manufactured single and multi-point cutting tools respectively

10.2.3 Laser Rapid Manufacturing of Porous Materials

Until recent past, porosity was considered as one of the harmful defects that impeded efficiency or functional properties of the manufactured products, limiting its applications to non-load-bearing components, like filtration, flow control, thermal and/or acoustic management, catalysts, and adsorbents [24]. However, if the porous materials could be produced with adequate mechanical strength, they would find direct applications as lightweight structures, functional materials, transportation materials, etc. [25, 26]. This encouraged us to undertake research toward the development of porous materials with adequate mechanical strength. Conventional methods used for the fabrication of porous materials with inhomogeneous pores include furnace sintering technique, space holder technique, replication technique, and combustion synthesis technique, whereas, methods like orderly oriented wire mesh technique, ferromagnetic fiber arrays technique, and vapor deposition technique give rise to porous structure with homogenous pores [27]. All these techniques have associated limitations in generating functionally designed porous materials with graded porosity. Such materials can be effectively fabricated using layered manufacturing techniques like LRM, circumventing the limitations of conventional methods. Laser rapid manufacturing, being a layer-by-layer additive manufacturing technique, has a unique capability to selectively deposit materials at the desired points. The loci of these desired points have been termed by us as “LRM strategy”. Different LRM strategies can be used to fabricate same material with different porosity contents or the materials with same porosity content but different mechanical properties. Various strategies are being investigated for LRM of porous materials, including cross thin wall fabrication method, recursive ball deposition method, etc. In cross thin wall fabrication method, clad tracks in each layer are deposited in a direction orthogonal to its preceding layer, whereas, in recursive ball deposition method, porous structure is built by depositing small balls one over another in a predetermined fashion using laser in pulsed mode [28]. Figure 10.7 presents schematics of these LRM strategies. In our earlier work, the recursive ball deposition method was employed to fabricate porous structures of type 316L stainless steel and porosity of about 28% was achieved, but these structures did not have adequate mechanical strength due to nonuniform and oxidized weak joints among adjacent resolidified balls [29]. Hence, we adopted cross thin wall fabrication strategy for the fabrication of porous structures with high degree of control on porosity and the mechanical strength.

In LRM, the processing parameters laser power (P_L), scan speed (V_s) and powder feed rate (m_p) is found to play major role in the formation of clad tracks [30]. The effects of these three parameters can actually be accounted with two parameters viz. laser energy per unit transverse length ($E_l = P_L/V_s$) and powder fed per unit transverse length ($m_{p/l} = m_p/V_s$). The distance between two adjacent clad tracks, along with above two parameters, can be used in cross thin walled fabrication strategy to generate materials with different porosities. The ratio of the distance between two adjacent tracks (x) and width of each track (W) known as “transverse traverse index” (i) and is schematically shown in Fig. 10.8.

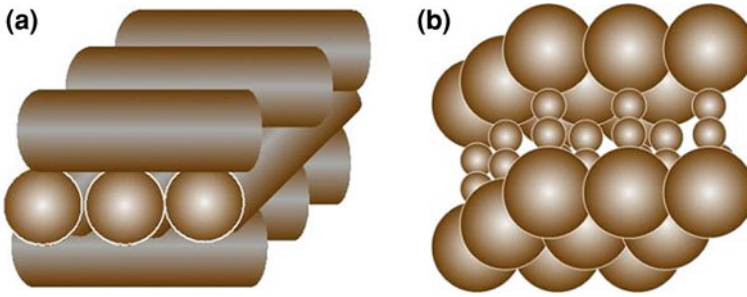
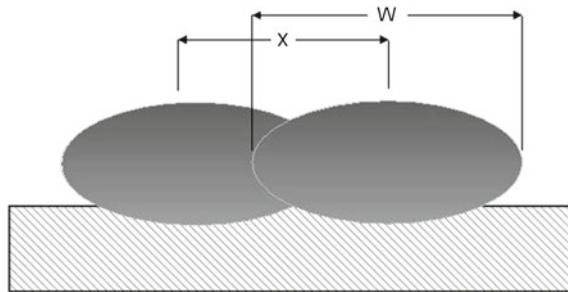


Fig. 10.7 Laser rapid manufacturing strategies—**a** cross thin wall fabrication, and **b** recursive ball deposition

Fig. 10.8 Schematic of a laser deposited track to define “transverse traverse index ($i = x/W$)”



The effect of processing parameters on porosity in laser rapid manufactured structures of Inconel-625 was evaluated by experiments using Box-Behnken array of surface response methodology [31]. The range of processing parameters was: $E_l = 150\text{--}300$ kJ/m; $m_{p/l} = 16.67\text{--}36.67$ g/m and $i = 0.7\text{--}1.3$. The results of the above experiments, with corresponding processing parameters, were subjected to the Analysis of Variance (ANOVA). The calculated standard F-test parameters of ANOVA for $m_{p/l}$, i and E_l were 155.372, 5.631, and 0.761, respectively. These calculations indicated that $m_{p/l}$ was the most predominant process parameter controlling porosity for the range of process parameters under investigation. Next to “ $m_{p/l}$ ”, “ i ” contributed to the effect, while E_l had very little effect on the porosity as an independent parameter. The derived response of surface for porosity in terms of processing parameters is expressed by the following relation:

$$\text{Porosity}(\%) = 14.2843 - 0.12105 \times E_l + 0.2432 \times m_{p/l} - 6.9277 \times i + 1.379 \times 10^{-3} \times E_l \times m_{p/l} + 0.0811 \times E_l \times i - 0.2196 \times m_{p/l} \times i$$

The above relation clearly indicates that the porosity in laser rapid manufactured porous structure increases with an increase in $m_{p/l}$ and i while it remains largely unaffected with change in E_l . It also reconfirms that there was sufficient laser energy per unit traverse length available to melt and deposit the fed powder for laser rapid

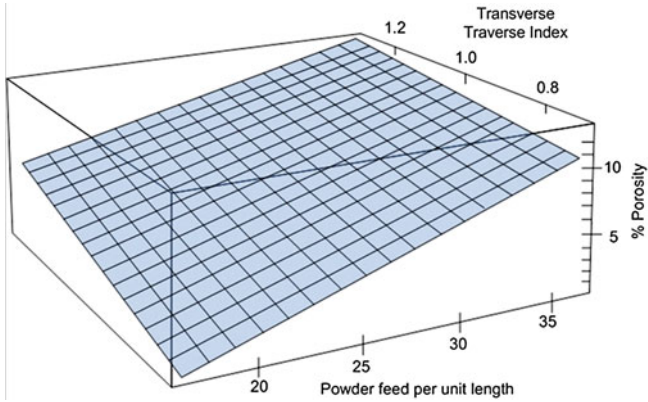


Fig. 10.9 Effect of transverse traverse index and powder fed per unit traverse length on porosity as per the equation given above for laser energy per unit traverse length = 225 kJ/m

manufacturing in the range under investigation. The predominance of $m_{p/l}$ is due to the variation in aspect ratio (track width / track height) of the clad tracks, resulting in change in the track shape. For the same track width, an increase in the powder feed rate results in an increase in track height and reduced track aspect ratio. This shifts the cross-sectional shape of the clad track toward the full circular form from the segment of a circle and results in larger porosity. Figure 10.9 presents a representative surface response of the above experiments, showing the effect of transverse traverse index and powder fed per unit traverse length on porosity as per the equation given above for laser energy per unit traverse length = 225 kJ/m.

Figure 10.10 shows optical macrographs of representative porosities on three different cross-sections viz. plane normal to scanning direction (X-axis), plane normal to transverse traverse direction (Y-axis) and plane normal to build up direction (Z-axis) of laser rapid manufactured structure of Inconel-625 under different deposition conditions. As seen in this figure, resultant laser rapid manufactured specimens have pores, arranged in the form of regular arrays. The location of these pores is at the junctions of adjacent tracks and adjoining layers, specifically at the track overlap region. The size of the pores is not uniform at various locations within the same sample and it can be seen that the average bulk porosity increases due to increase in the pore size. The shape and size of the pores are different on three different planes, indicating that the resultant porous structures will have anisotropy in mechanical properties. The shape and size of the pores on the planes normal to X and Y axes are nearly the same. Therefore, it is expected that the mechanical properties along these two axes are largely similar. It may also be noted that lower porosity is achieved with larger track aspect ratio (= track width/track height), while higher porosity is achieved when track aspect ratio is close to unity. This is attributed to the fact that with an increase in the aspect ratio, the cross-section of the clad track transforms from segment of circle to full circular form with an aspect ratio close to unity. The observed microstructure was associated with mostly columnar dendrites that grew

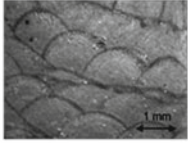
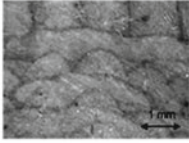
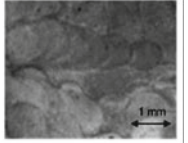
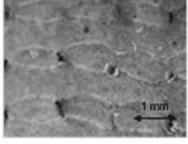
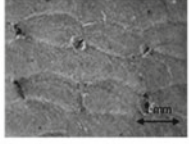
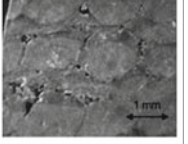
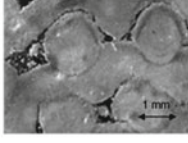
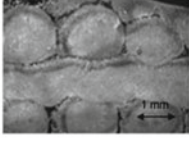
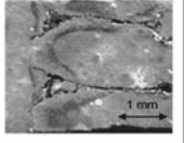
Porosity %	Plane normal to scanning direction (X-axis)	Plane normal to Transverse traverse direction (Y-axis)	Plane normal to Build-up direction (Z-axis)
2.624			
7.683			
11.57			

Fig. 10.10 Optical macrographs of representative porosities on three different cross-sections of laser rapid manufactured structure of Inconel-625

epitaxially from the substrate/preceding layer with the direction of columnar dendrites toward the direction of laser scanning. Similar trends were also observed by Dinda et al [32].

Figure 10.11 a and b present photograph of laser rapid manufactured porous structure, made by cross thin wall strategy and typical engineering stress-strain curve obtained during compressive testing of the same, respectively. The initial part of the curve (OA) involves sharp increase in stress with small compressive strain. This is a region of elastic deformation with small amount of plastic deformation. Therefore, this slope is generally not used to determine Young’s modulus of the porous materials. The associated plastic deformation in this region is responsible for mechanical damping. After the initial sharp increase in stress, there is a change over to a regime of plastic deformation predominantly associated with closure of porosity, where small increase in stress is accompanied by larger compressive strain (AB). The measured value of porosity at the end of this region was less than 10% of the initial value. After extended plateau regime, the slope of the curve (BC) increased, which is indicative of densification of material in the previous regime (AB). At this stage, the porosity is negligible with neighboring tracks completely touching each other. The optical micrograph of cross-section, corresponding to region OA, shows clearly visible pores with nearly circular tracks. On the other hand, the macrostructure corresponding to region AB shows elongated pores and tracks due to compression. The pores are compressed and almost filled due to material flow. This flow of the material gives rise to plateau regime in the stress strain curve. The slope and length of the curve

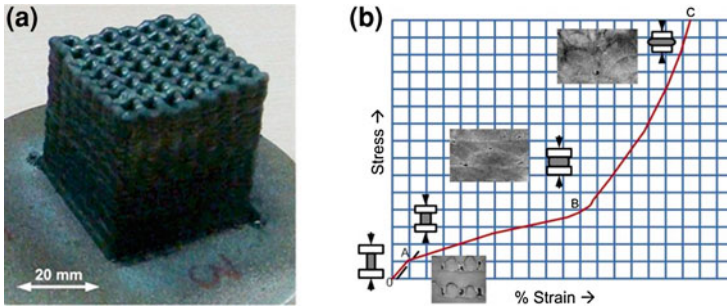


Fig. 10.11 **a** Laser rapid manufactured Inconel-625 porous structure, and **b** typical engineering stress-strain curve obtained during compression testing of laser rapid manufactured porous structure

in plateau region depends on the rate of densification of the material, which is primarily governed by the dynamics of compression of pores and walls in a correlated manner within the porous structure [33]. The optical macrograph corresponding to region BC shows almost completely compressed structure. The neighboring tracks are compressed together with completely deformed fine pores.

It may be noted that the yield strength decreases sharply with the increase in the porosity, as mechanical properties are highly sensitive to bulk parameters like pore size, shape, orientation, distribution, etc. These parameters give rise to stress concentration within the material. When the porosity is low, the pores are away from each other, giving rise to isolated points of stress concentrations. At the higher porosity, these stress concentrations have interacting field, as the distance between the pores are reduced. At very high porosity, any small irregularities, like—cracks etc., also interacts with the pores and raises the stress concentrations multifold [33].

Figure 10.12 presents variation of compressive yield strength of laser rapid manufactured porous structure of Inconel-625 as a function of porosity along all the three different directions. It also indicates that there is anisotropy in the mechanical properties of laser rapid manufactured porous material. The value of compressive yield stress is 226 MPa along the scanning and transverse traverse directions, while it is 254 MPa along the build up direction for laser rapid manufactured specimens of around 12% porosity. This difference in value is due to the LRM strategy adopted in the present experiments. The reported tensile yield strength of the conventionally processed Inconel-625 was in the range of 414–758, 414–655 and 290–414 MPa in as rolled, annealed and solution treated conditions respectively [34].

10.2.4 Laser Rapid Manufacturing of Bimetallic Components

There are many applications where different parts of a single component are exposed to diverse service conditions and the demand of conflicting combination of properties cannot be met with a single material. It is this need to extract multiple functions

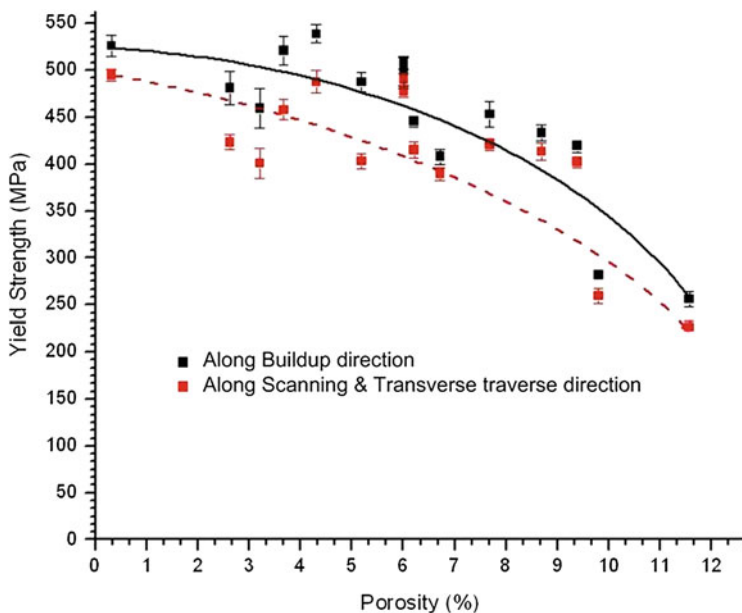


Fig. 10.12 Variation of compressive yield strength as a function of porosity in laser rapid manufactured porous structures of Inconel-625

from a single component that has led to the development of engineered materials with desired heterogeneity in chemical composition and associated characteristics. Recent research studies performed at our laboratory focused on exploiting unique capability of LRM to fabricate bimetallic structures with sharp and graded interfaces, involving type 316L stainless steel (SS 316L) and Stellite 21 (St-21). The approach has been used to (1) build up bimetallic walls and tubular components and (2) to control fracture behavior of composite parts by providing compositional grading across the associated interface.

10.2.4.1 Laser Rapid Manufacturing of Bimetallic Wall and Tubular Bush

A bimetallic wall and a tubular bush were fabricated by LRM with an in-house developed CW CO₂ laser, coupled with a CNC work station [35–37]. The bimetallic wall comprises SS 316L on one side and St-21 on the other side, whereas, the tubular structure consisted of St-21 on the inner side and SS 316L on the outer. Chemical composition of powders used is presented in Table 10.2.

Figure 10.13 presents schematic illustrations of methodologies adopted for LRM of bimetallic wall and tubular structure, along with their photographs and associated macrostructures. Laser rapid manufacturing of bimetallic wall involved alternate deposition of two adjacent clad tracks of SS 316L and St-21, with small zone of

Table 10.2 Chemical composition (weight %) of powders used for LRM

Material	C	Cr	Ni	Mn	Si	Mo	Fe	Co	P	S
SS 316L	0.025	18	12	1	0.5	2	Bal	–	0.03	0.02
St-21	0.26	26.3	2.8	0.65	1.88	5.53	1.4	Bal	–	–

overlap at the center, as shown in Fig. 10.13a. Two separate powder feeders, positioned on opposite sides of the incident laser beam, were used to feed SS 316L and St-21 powders during the experiment. Photograph of the bimetallic wall and its cross-sectional macrostructure are presented in Fig. 10.13b and c, respectively. Etching contrast between clad layers on opposite sides of the bimetallic wall, as seen in Fig. 10.13c, is indicative of the difference between their chemical compositions.

On the other hand, LRM of bimetallic tube employed a coaxial powder feeding nozzle to deposit four partly overlapping concentric circular clad tracks in each layer. The two inner clad tracks were deposited with St-21 powder whereas the two outer clad tracks were made with SS 316L, as shown in Fig. 10.13d. Final dimensions of bimetallic tube shown in Fig. 10.13e were: 25 mm inner diameter with 3.8 mm wall thickness. Sharp etching contrast developed on the cross-section of the bimetallic tube as seen in Fig. 10.13f indicates large difference in chemical composition at the interface.

In addition, an SS tube (post-machine dimensions: 34 mm ID and 2 mm wall thickness) with an internal step of St-21 (height: 1.5 mm and width: 6.5 mm) has also been fabricated by LRM, as shown in Fig. 10.14. This kind of structure will be useful for fabricating components where an insert is required to provide an internal hardfaced lining at selective places. This demonstrates the capability of LRM to add functional overhanging features for critical components.

Laser rapid manufactured bimetallic structures exhibited regular pattern of clad layers of 0.6–0.8 mm thickness. Distinct etching contrast between inner and outer clad layers of the bimetallic structures was indicative of difference in their chemical compositions. These laser rapid manufactured components exhibited significant transition in chemical composition and microhardness across their wall thickness, as shown in Figs. 10.15 and 10.16. With respect to bimetallic wall, tubular bush recorded gradual transition in chemical composition and microhardness across its wall thickness. Bimetallic structures of this kind may find application in Fast Breeder Reactor, where internal lining of Stellite is required on tubular SS components for enhanced resistance against galling [38]. An engineered bimetallic tube in heat exchanger applications will provide maximum corrosion resistance against two media present on inside and outside surfaces.

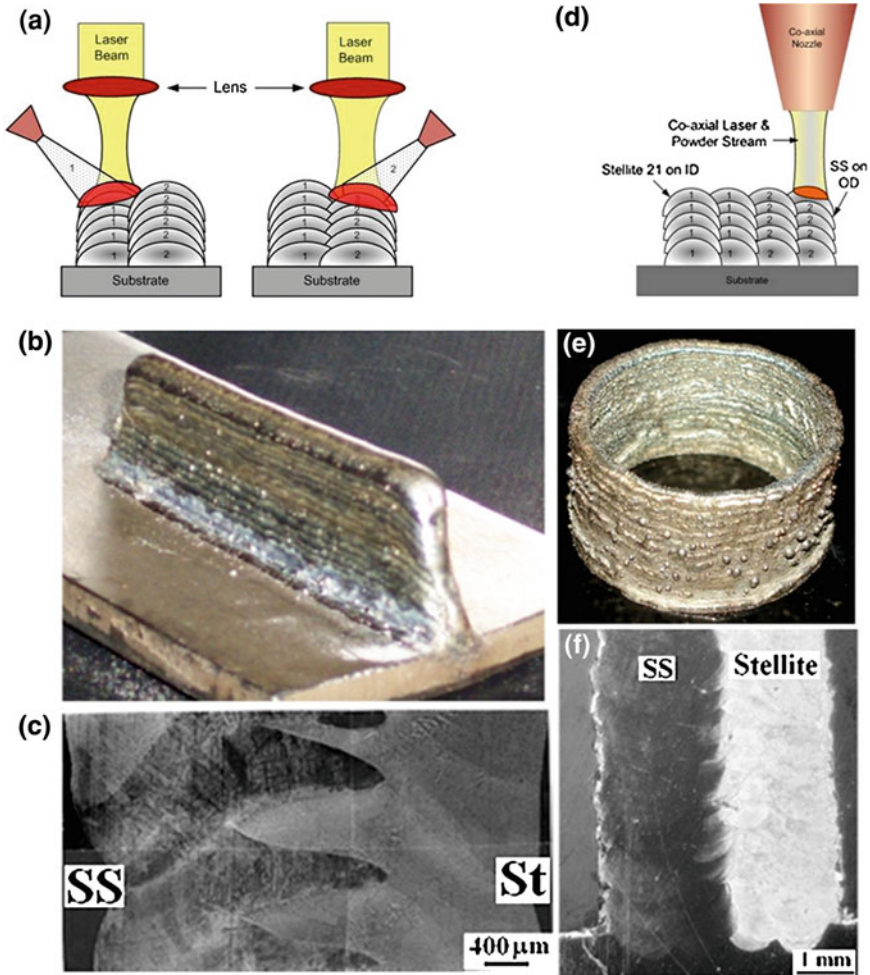


Fig. 10.13 Schematic illustration of methodologies adopted for LRM of (a) bimetallic wall, and (d) bimetallic tube, with the images of structures (b and e) and associated macrostructures (c and f)

10.2.4.2 Laser Rapid Manufacturing of Compositionally Graded Structures

The present work, involving study of the influence of compositional grading on fracture behavior of laser clad joint of SS 316L and St-21, was performed with an in-house made CW CO₂ laser. For the deposition of graded overlays, chemical composition of clad layers was controlled by mixing powders of St-21 and SS 316L in predetermined ratios. Graded overlay of three layers was deposited by cladding with premixed powders of St-21 and SS 316L in the ratios of 30:70, 70:30, and 100:0, respectively. In the subsequent part of the text, SS 316L specimens clad with St-21 deposits and graded St-21 deposits are referred as “direct clad” and “graded

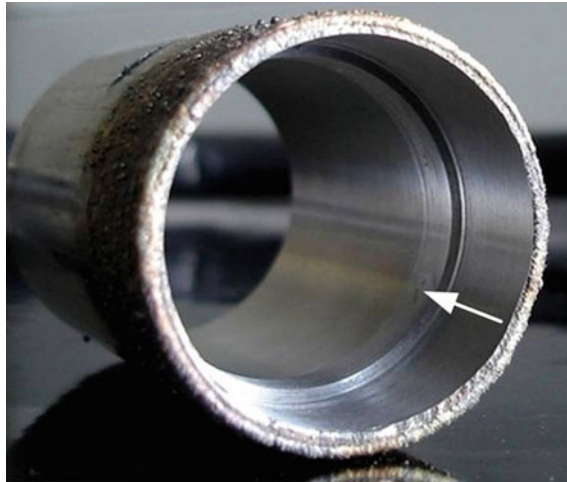


Fig. 10.14 Laser rapid manufactured tube of SS with internal step of Stellite 21

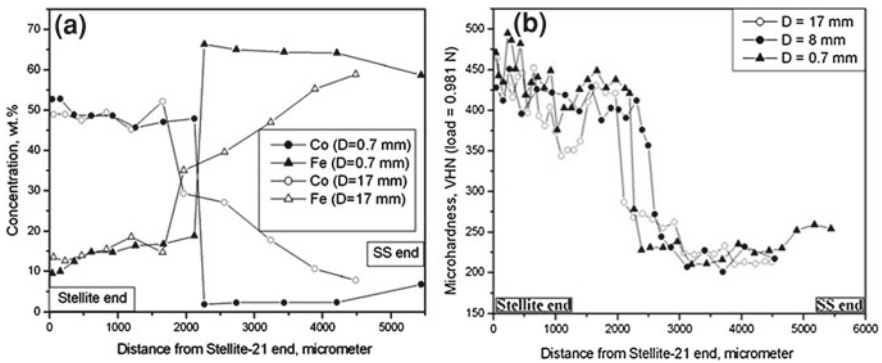


Fig. 10.15 **a** EDS concentration profiles of Co and Fe, and **b** micro-hardness profiles across wall thickness of bimetallic wall fabricated by LRM (D—distance from substrate/clad interface)

clad” specimens, respectively. Figure 10.17 compares microstructures of the interface region and associated composition profiles of “direct clad” and “graded clad” specimens. The cross-sections of laser clad specimens exhibited typical cast microstructure with distinct etching contrast with underlying base metal (SS 316L), signifying transition in chemical composition across SS 316L/St-21 interface. With respect to “direct clad” specimens, “graded clad” specimens exhibited diffused interface involving transition from wrought microstructure of base metal (SS 316L) to cast microstructure of the clad layer, as shown in Fig. 10.17a and b, respectively. In contrast, interface of “direct clad” specimen carried about 30 μm thick partially melted zone (marked with arrows) and a thin zone of planar solidification, as shown in Fig. 10.17a. With respect to direct clad specimens, graded clad specimens recorded more

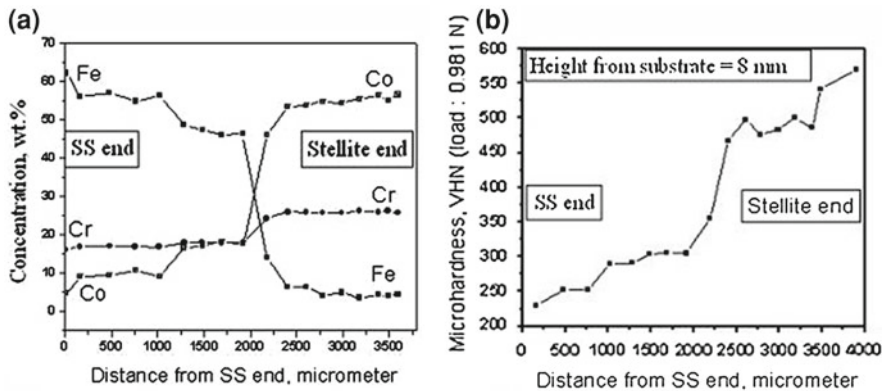


Fig. 10.16 a EDS concentration profiles of Co, Cr and Fe, and b micro-hardness profile across wall thickness of bimetallic tube fabricated by LRM

Table 10.3 Results of tensile tests conducted on laser clad composite joints

Specimen	Tensile strength (MPa)	Failure location
Direct clad (smooth gauge section)	600–630	Wrought SS
Graded clad (smooth gauge section)	600–630	Wrought SS
Specimen with notch in laser-deposited Stellite21	950, 955, 968	Stellite21 (clad)
Direct clad (notch at substrate/clad interface)	717, 748, 754	Substrate/clad interface
Graded clad (notch at substrate/clad interface)	679, 706	Graded interface

gradual built-up of chemical composition along the thickness of the clad deposit. The specimens for tensile testing of “direct clad” and “graded clad” specimens were fabricated in such a way that the substrate/clad interface was normal to the loading axis. In addition to smooth specimens, notched specimens were also tested to restrict plastic deformation to the zone of interest [39]. The results of tensile tests are summarized in Table 10.3. The failure of smooth specimens took place in the softest zone (viz. wrought SS) at a stress of 600–630 MPa with significant amount of plastic deformation, as manifested by its dimpled fracture surface shown in Fig. 10.18a. On the other hand, specimens with notch in the St-21 clad region suffered brittle fracture along interdendritic boundaries (refer Fig. 10.18b) at a higher stress of 950–968 MPa.

On the other hand, failure of the specimens with notch at the interface region of took place at an intermediate stress level (refer Table 10.3) with distinctly different modes of crack propagation in “direct clad” and “graded clad” specimens. Fracture surface of notched “direct clad” specimens exhibited randomly distributed regions of ductile fracture in Fe-rich regions (represented by dimples) and brittle fracture

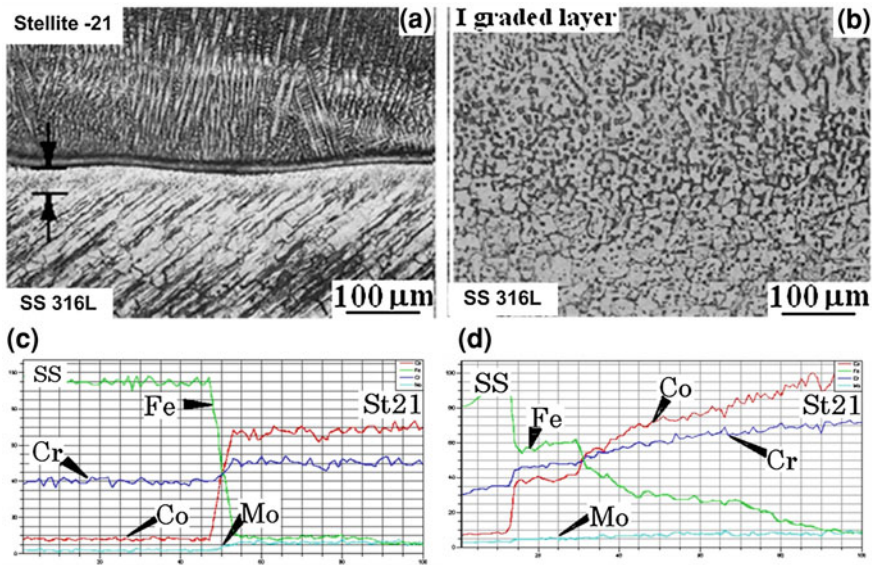


Fig. 10.17 Microstructure of interface region and associated EDS concentration profiles for direct clad (a, c) and graded clad (b, d) specimens. Arrows mark partially melted zone (PMZ). (c) EDS line scan length: 1.4 mm; (d) EDS line scan length: 5 mm. SS: Stainless steel; St21: Stellite 21 clad region

along interdendritic boundaries in Co-rich regions (Fig. 10.18c). In contrast, fracture surface of notched “graded clad” specimen exhibited quasicleavage type fracture as seen in Fig. 10.18d.

Instrumented Charpy impact testing of laser clad specimens (as per ASTM E23) clearly brought out compositional grading induced change in the fracture behavior of composite specimens [38]. The impact specimens were fabricated in such a way to facilitate crack propagation from SS to St-21, as shown in the inset of Fig. 10.19. Although, fracture of both “direct clad” and “graded clad” specimens consumed largely similar impact energies (32–37 J and 35–37 J, respectively), load-displacement traces of the two specimens exhibited distinct difference in associated modes of crack propagation after general yield (refer Fig. 10.19).

Failure in “direct clad” specimens was associated with abrupt drop from peak load as crack propagated across sharp interface between SS and St-21. On the other hand, fracture of “graded clad” specimens was marked with gradual drop in load from its peak as crack propagated through graded interface, indicating plastic deformation accompanying crack propagation. Table 10.4 presents fractions of Charpy impact energy (C_v), consumed in crack initiation and its propagation (as derived from Fig. 10.19) for “direct clad” and “graded clad” specimens. Compositional grading across SS/St21 interface brought about an increase in the fraction of crack propagation energy at the expense of initiation energy. SEM fractographic examination of the impact tested specimens revealed that SS part of the fracture surface (ahead of the

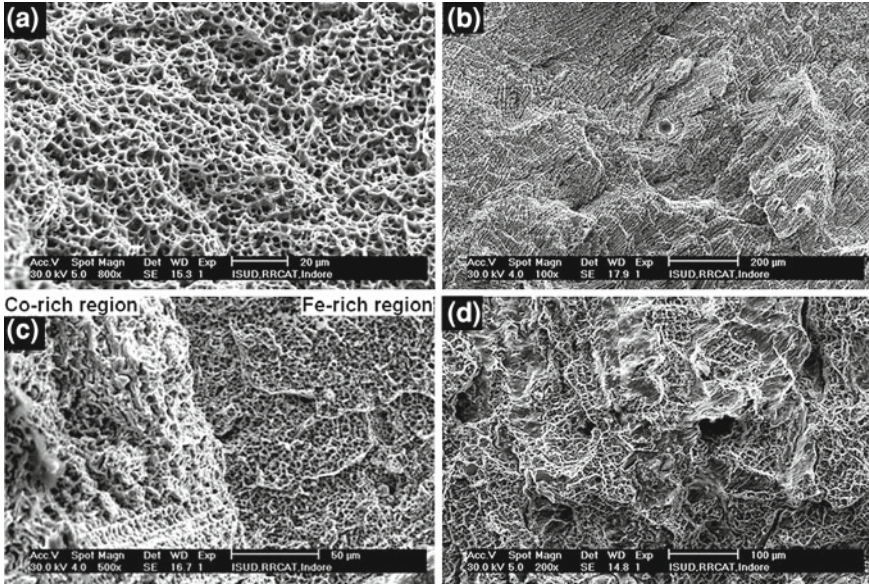


Fig. 10.18 SEM fractographs of tensile tested specimens with SS/St-21 joint: **a** smooth specimen—failure in wrought SS, **b** notched specimens—failure in St-21 region, **c** notched “direct clad”, and **d** notched “graded clad” specimens with failure in the interface region

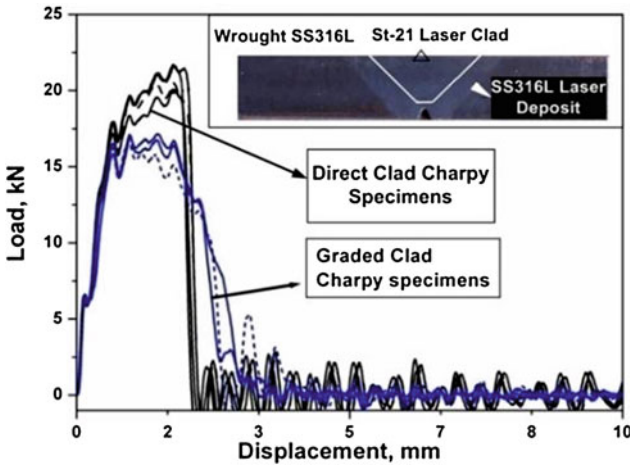
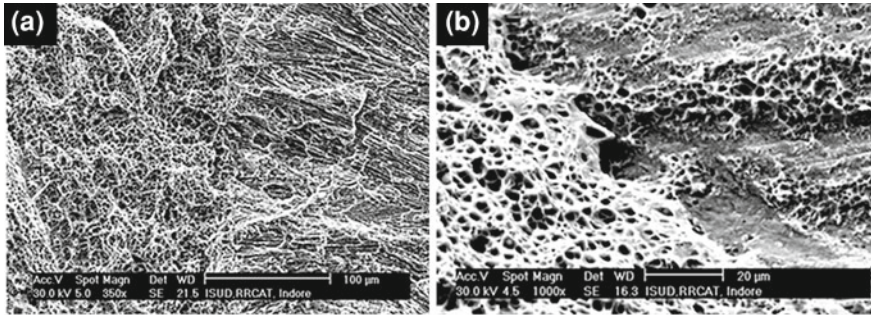


Fig. 10.19 Load-displacement plot of instrumented Charpy impact specimens (shown in inset)

notch) was associated with equiaxed dimples while St-21 part exhibited signature of brittle fracture along interdendritic boundaries. In “direct clad” specimen, fracture surface morphology underwent drastic transition from dimple to brittle fracture, as crack propagated across sharp interface between SS and St-21 as seen in Fig. 10.20a.

Table 10.4 Instrumented Charpy impact test results of laser clad composite specimens

Direct clad ($C_v = 32 - 37$ J)		Graded clad ($C_v = 35 - 37$ J)	
Initiation energy ($\%C_v$)	Propagation energy ($\%C_v$)	Initiation energy ($\%C_v$)	Propagation energy ($\%C_v$)
93.6	6.4	84	16
96.6	3.4	79.3	20.7
97.7	2.3	79.2	20.8
96.3	3.7	–	–

**Fig. 10.20** Fracture surfaces of impact tested **a** “direct clad”, and **b** “graded clad” specimens

On the other hand, fracture surface at the graded interface region, exhibited mixed-mode fracture features (Fig. 10.20b). In the light of the results of the study it is inferred that compositional grading brought about a change in the mode of crack propagation (from SS to St-21) from initiation-controlled fracture in “direct clad” specimens to propagation-controlled fracture in “graded clad” specimens.

10.2.5 Mechanical Properties of Laser Rapid Manufactured Structures of Inconel 625 and Type 316L SS

For industrial acceptability of any fabrication process (LRM in present case), it is essential to establish structural integrity qualification data of structures fabricated by that process. Present study was undertaken to address the above mentioned issue of characterizing critical mechanical properties (e.g., fatigue crack growth and fracture toughness) of laser rapid manufactured structures. The output of the study is also relevant for qualification of parts refurbished through LRM. Various stages involved in the fabrication of compact tension (CT) specimens used for the present study included (1) machining of V-groove in type 304L stainless steel block—used as the substrate (Fig. 10.21a), (2) filling of V-groove region by LRM (Fig. 10.21b and c) and (3) machining of the resultant blocks in such a way that the crack propagation

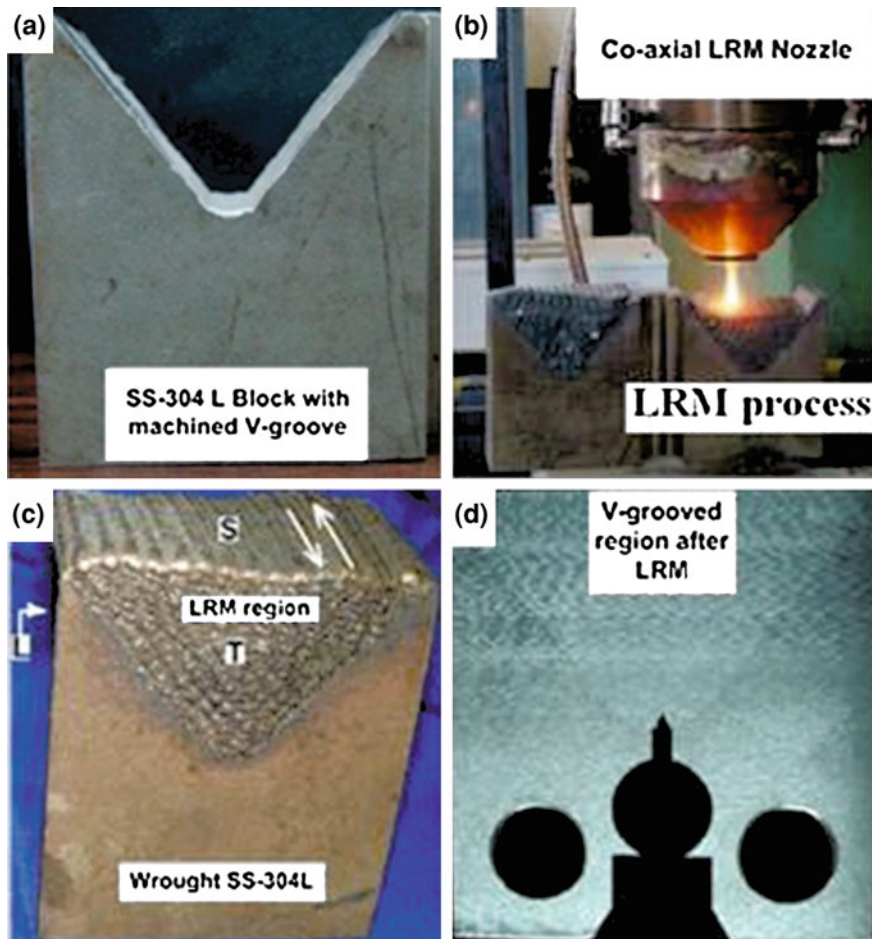


Fig. 10.21 Different stages involved in LRM of compact tension test specimens: **a** initial SS block with V-groove, **b** filling of groove by LRM, **c** as laser deposited SS block—arrows indicate direction of laser rastering, and **d** machined CT specimen

would take place in the laser manufactured region (Fig. 10.21d). Fatigue Crack Growth Rate (FCGR) and fracture toughness tests were performed on CT and Single Edge Notched Bend (SENB) specimens, extracted from laser rapid manufactured structures of Inconel-625 (IN-625) and SS 316L [40].

Fatigue crack growth tests were conducted on the 12 and 25 mm thick CT specimens, as per ASTM E 647 standard [41]. Subsequent to FCGR testing, the same specimens were used for evaluation of fracture toughness, as per ASTM E 1820 standard [42]. The results of FCGR obtained in the present study were compared with the reported data for corresponding wrought materials. Laser rapid manufactured specimens of IN-625 and SS 316L exhibited steady state crack growth, also

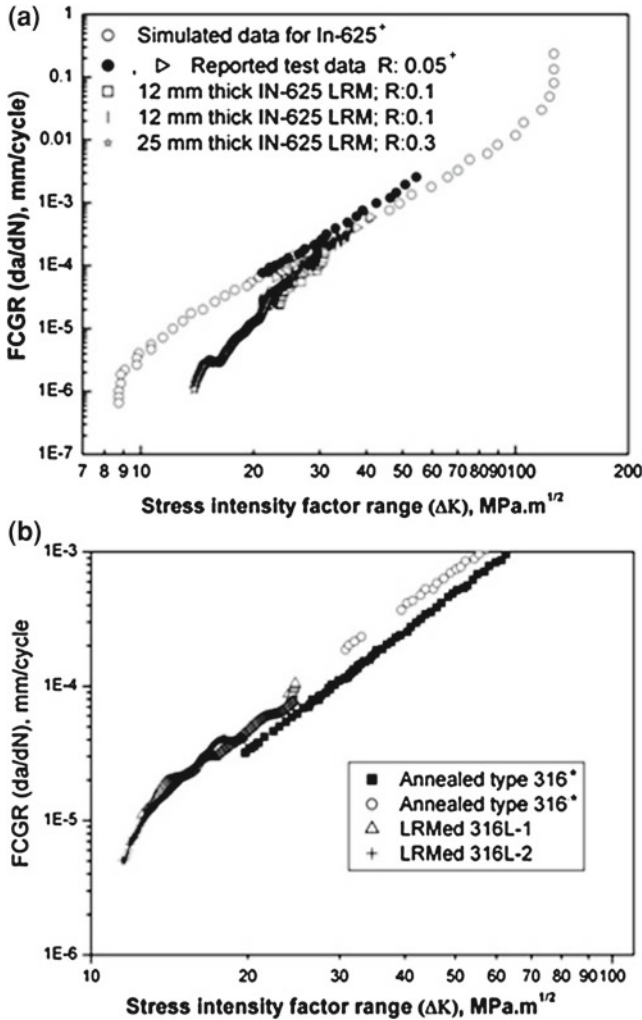


Fig. 10.22 Comparison of experimental and reported [43⁺, 44^{*}] fatigue crack growth rate results for Inconel 625 and type 316L SS

referred as stage II crack growth [41], in the investigated stress intensity range of 14–38 $\text{MPa}\cdot\sqrt{\text{m}}$ for IN-625 and 11.8–24 $\text{MPa}\cdot\sqrt{\text{m}}$ for SS 316L. Fatigue crack growth rates for laser fabricated IN-625 were found to be lower than the reported values in the ΔK range of 14–24 $\text{MPa}\cdot\sqrt{\text{m}}$ and above this range they tended to coincide as seen in Fig. 10.22a. On the other hand, FCGR in laser rapid manufactured specimens of SS 316L were quite close to the ones reported for their wrought counterparts as shown in Fig. 10.22b [43, 44].

The J-integral fracture toughness (J_{IC}) values for laser rapid manufactured specimens of IN-625 and SS 316L were found to be in the range of 194–254 kJ/m² and 143–259 kJ/m², respectively. Crack Tip Opening Displacement (CTOD) fracture toughness values for both these materials were found to be in the range of 0.28–0.54 mm. Fracture toughness values (both J_{IC} and CTOD) of laser rapid manufactured specimens of SS 316L, although lower than that of its wrought counterpart, are in close agreement with the reported values for corresponding weld metal [45].

Charpy impact energy of laser rapid manufactured specimens of SS 316L were found to be in the range of 90–110 J, which is at par with the wrought material in the annealed condition [45]. Fracture surface of impact tested specimen exhibited mixed mode fracture features with extensive crack branching. The crack plane followed a tortuous path due to the layered deposition and associated rastering pattern involved in LRM process.

Instrumented Charpy impact testing of IN-625 specimens, fabricated through LRM exhibited impact energy of 46.5–49 J while a post deposition annealing treatment at 1223 K brought about a small improvement in impact energy to 51.6–54 J (Table 10.5). The impact energy of the annealed specimens was associated with increased fraction of crack initiation energy at the cost of crack propagation energy. Gradual fall in load after the peak load in load-displacement plots is representative of ductile nature of crack propagation in these specimens. Reported Charpy impact energy (for keyhole specimens) of IN-625 in the as rolled condition was in the range of 65–70 J [34].

10.2.6 Prognostication

The results of the present studies demonstrated that LRM can be adopted as an alternative fabrication method to fabricate functional metal parts and components involving single/multiple materials with/without compositional gradient. Strength, toughness, and fatigue crack growth rate of laser rapid manufactured structures of IN-625 and SS 316L are found to be at par or better than the reported data for equivalent weld metal. Fabrication of low-cost tools and refurbishment of worn parts are other potential applications of laser based fabrication. The results obtained in the domain of fabrication of porous structures are very encouraging to pursue the work further to find appropriate use in engineering/prosthetic applications.

Table 10.5 Results of the instrumented Charpy impact tests of IN-625

As LRM condition		LRM + annealed (1223K/air cooling)			
C_v Impact energy,(J)	Initiation energy ($\%C_v$)	Propagation energy ($\%C_v$)	C_v Impact energy, (J)	Initiation energy ($\%C_v$)	Propagation energy ($\%C_v$)
47.9	50.6	49.4	51.7	63.5	36.5
48.5	51.6	48.4	51.6	64.3	35.7
46.5	49	51	52.3	64.6	35.4
48.5	52	48	52	63.2	36.8
46.8	51	49	53.2	64.3	35.7
48.2	51.5	48.5	54	62	38
49	51.4	48.6	—	—	—
47.6	51.3	48.7	—	—	—

10.3 Laser Surface Melting Treatment for Enhanced Resistance of Austenitic Stainless Steel Against Inter-Granular Corrosion

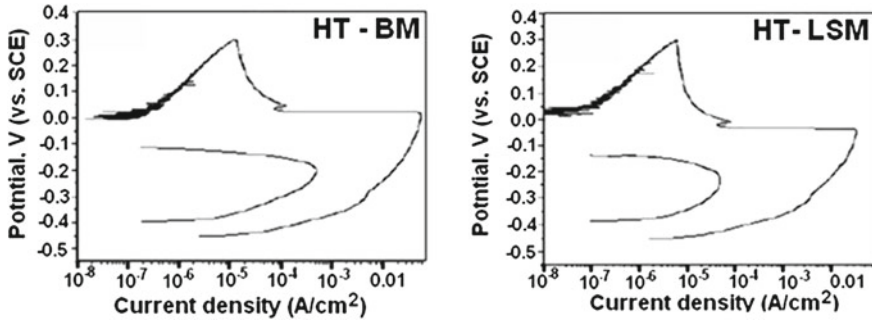
Austenitic stainless steels, in spite of having excellent general corrosion resistance, are particularly susceptible to localized corrosion including crevice, pitting, Inter-Granular Corrosion (IGC), and Stress Corrosion Cracking (SCC). Susceptibility to localized corrosion and SCC is mainly caused by the presence of chloride (Cl^-) ions in the atmosphere. In nuclear fuel reprocessing, waste management industries and in many chemical industries, using nitric acid as the process fluid, the main corrosion problem is IGC. Austenitic Stainless Steel (SS) weldments undergo Intergranular Stress Corrosion Cracking (IGSCC) in certain environments, e.g., oxidizing water in boiling water reactors [46]. Intergranular corrosion of austenitic SS usually arises from intergranular precipitation of Cr-rich carbides in the temperature range of 773–1073 K. Intergranular carbide precipitation is accompanied by the development of Cr-depleted zone adjacent to grain boundaries. This state is referred as “sensitization.” Chromium-depleted zones, being anodic with respect to grain interior, are preferentially attacked in the corrosive environment, leading to IGC [47]. During welding of austenitic stainless steels, particularly of high-carbon content, Heat-Affected Zone (HAZ) of the weldment get sensitized, which adversely affects their resistance against IGC during service in the susceptible environment. Recent research studies performed in authors’ laboratory have led to development of a novel Laser Surface Melting (LSM) treatment, involving microstructural engineering, for introducing significant enhancement in material’s inherent resistance against IGC. The approach has been demonstrated on (1) type 304 SS for suppressing sensitization during long exposure in the susceptible temperature range; (2) type 316 (N) SS weld metal (WM) as a post-weld treatment to suppress sensitization during subsequent solution annealing treatment for stress relieving and (3) type 304 SS as a pre-weld surface treatment for would be HAZ to suppress sensitization during subsequent Gas Tungsten Arc Welding (GTAW). All three applications are important for process industries using austenitic SS components.

10.3.1 Laser Surface Treatment of Type 304 SS

This case [48] study involved LSM treatment of type 304 SS with an indigenously developed 10 kW CO_2 [35] in both Continuous Wave (CW) and pulsed modulated modes. Laser surface treated and untreated SS specimens were subjected to a severe sensitization heat treatment at 923 K for 9 h, followed by their characterization by (1) Double Loop Electrochemical Potentio-kinetic Reactivation test (DLEPR) [49] in a deaerated solution of 0.5 M sulphuric acid (H_2SO_4) and 0.01 M potassium thiocyanate (KSCN) for comparing their degrees of sensitization (DOS), (2) ASTM A 262 practice B [50] test to compare their susceptibilities to IGC and (3) Electron

Table 10.6 Percentage DOS of base metal and laser treated specimens

Specimen	As received/As laser treated	After sensitization heat treatment
Base metal	0.36	4.52
Laser treated-1	0.09	0.11
Laser treated-2	0.24	0.33

**Fig. 10.23** Comparison of DL-EPR plots of heat treated base metal and laser treated specimens

Back Scattered Diffraction (EBSD) [51] to characterize Grain Boundary Character Distribution (GBCD).

The results of DL-EPR tests, as summarized in Table 10.6, showed that untreated base metal (BM) specimens carried low value of DOS (0.36). However, after undergoing a sensitization heat treatment, DOS of BM specimens increased to 4.52, indicating high level of sensitization. In contrast, DOS of Laser Surface Melted (LSM) specimens remained largely unaffected by exposure to sensitization heat treatment. Degree of sensitization of heat treated laser surface melted SS specimens ranged from 0.1–1. On the whole, SS specimens treated with pulse modulated laser beam recorded lower DOS values than the specimens treated with CW laser beam. In the best conditions (corresponding to specimens exhibiting lowest DOS values), DOS of laser surface melted specimens, even after undergoing sensitization heat treatment were comparable to that of the base metal in as-received condition. The results demonstrated that laser-melted surface did not become sensitized even after undergoing a severe sensitization heat treatment. Figure 10.23 compares typical DL-EPR plots of Heat Treated Base Metal (HT-BM) and heat treated laser surface melted (HT-LSM) SS specimens.

Cross-sectional metallographic examination of ASTM A 262 practice B tested specimens brought clear difference in IGC susceptibilities of “HT-BM” and “HT-LSM” specimens. On the one hand, “HT-BM” specimens exhibited initiation of IGC attack from the exposed surface while exposed surface of “HT-LSM” specimen remained unattacked, as shown in Fig. 10.24. The results clearly reflect superior IGC resistance of laser surface melted specimens over that of untreated base metal.

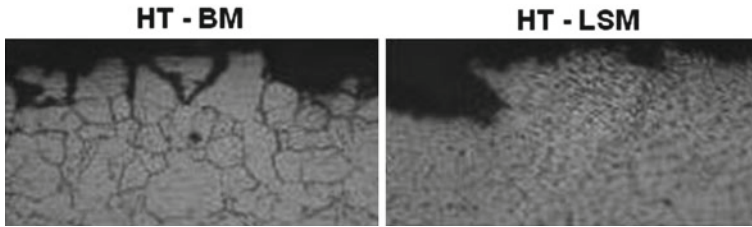


Fig. 10.24 Transverse cross-sections of heat treated base metal (HT-BM) and heat treated laser surface melted (HT-LSM) SS specimens after ASTM A262 practice B test

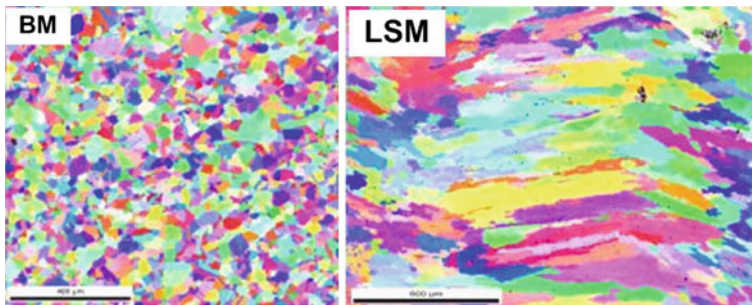


Fig. 10.25 Typical result from the experiment done to measure grain boundary character distribution in base metal (*left*) and laser treated (*right*) specimens

Electron back scattered diffraction analysis of untreated base metal and laser treated specimens revealed that the fraction of low-angle grain boundaries in the base metal was 0.04, which increased to 0.13–0.19 after LSM. Figure 10.25 shows typical results from experiments done to measure GBCD in “BM” and “LSM” specimens.

In the light of the results obtained during the course of present investigation, it has been demonstrated that CO₂ laser surface melting treatment of type 304 austenitic SS results in large improvement in its resistance against sensitization and IGC. Enhanced resistance against sensitization and IGC is largely attributed to laser-melting induced microstructural modification involving higher fraction of low-angle grain boundaries. The technique has strong potential as a practical in situ technique for life enhancement of austenitic SS components operating in corrosive environments.

10.3.2 Post-Weld Laser Surface Treatment of Type 316(N) SS Weld Metal

Welded austenitic [52] SS components are usually subjected to solution annealing heat treatment to achieve full stress relief and restoration of mechanical properties and corrosion resistance. ASTM A480/A480M specifies a minimum temperature of 1311 K for solution annealing [53]. According to ASM guidelines [54], the duration

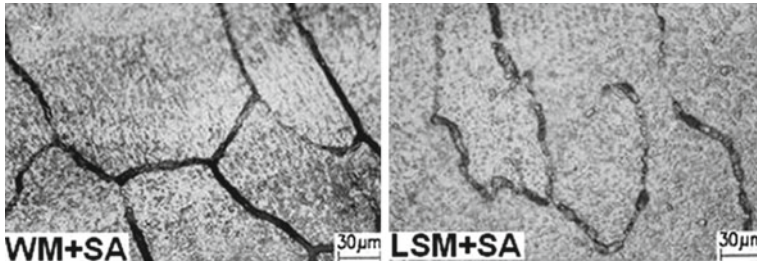
for soaking treatment is 1 h per 25 mm thickness of the component. Besides solution annealing temperature and soaking treatment, associated cooling rate is also critical. A very slow cooling rate results in sensitization and susceptibility to IGC, while high cooling rate reintroduces the residual stresses.

Type 316 LN austenitic SS, one of the major structural materials of Indian 500 MWe Prototype Fast Breeder Reactor (PFBR), is welded with a modified E316-15 electrodes with relatively higher carbon and nitrogen contents ($C = 0.045\text{--}0.055\text{ wt\%}$; $N = 0.06\text{--}0.1\text{ wt\%}$) than the base metal ($C = 0.024\text{--}0.03\text{ wt\%}$; $N = 0.06\text{--}0.08\text{ wt\%}$) for improved creep strength of the Weld Metal (WM). Due to its higher carbon content, WM is more susceptible to undergo sensitization during subsequent solution annealing treatment [55]. N. Parvatahvarthini et al. have reported that cooling the WM from solution annealing temperature at the rate of 65 K/h resulted in sensitization, whereas, cooling rate of 75 K/h did not result in sensitization [56]. Since slower cooling rate is always preferred to avoid distortion, reintroduction of residual stress and large temperature differentials, the present study was taken up with the objective to develop laser surface melting treatment of modified 316(N) SS weld metal to introduce surface microstructure with enhanced resistance against sensitization during solution annealing treatment involving slower cooling at the rate of 65 K/h.

For LSM experiments, the weld pads, prepared by shielded metal arc welding process using modified E316-15 electrodes of 3.5 mm diameter, were used as substrate [57]. The chemical compositions (in wt%) of WM, as analyzed by optical emission spectroscopy was: 0.05C, 18.5 Cr, 11.1 Ni, 1.4 Mn, 0.46 Si, 1.9 Mo, 0.21 Cu, 0.12N, 0.006S, 0.0255P, Bal Fe. Associated ferrite number, as measured by ferritoscope, was in the range of 3.5–4.1. The dimensions of substrates, cut from weld pads, were $80 \times 10 \times 3$ mm. Laser surface melting experiments were performed with an indigenously developed 10 kW CO₂ laser using high repetition rate pulse modulated mode. Laser treated specimens were subsequently subjected to solution annealing treatment involving heating from room temperature to 1323 K in 2 h, soaking for 1 h, followed by cooling to room temperature at the rate of 65 K/h. Weld metal specimens, treated with high frequency pulse modulated (PM) CO₂ laser beam yielded sound laser-melted surface. The resultant specimens also qualified ASTM A262 practice E test. Hence, it was inferred that the laser treated specimens were not sensitized. Table 10.7 summarizes characterization results of laser-treated specimens. Figure 10.26 compares microstructures of solution annealed WM and laser-melted zone, as obtained by ASTM A 262 practice A test [50]. The figure clearly demonstrates discontinuous carbide net work (dual structure) in laser-treated and solution annealed region (referred as LSM + SA) in contrast to continuous carbide net work (ditch) in solution annealed weld metal (referred as WM + SA). In the light of the results of the study it was concluded that LSM treatment resulted in a surface microstructure which did not lead to sensitization of WM during solution annealing treatment with slow cooling at the rate of 65 K/h. The direct implication of the output of this study is that laser treated type 316LN SS weldments can be cooled at a slower rate during subsequent solution annealing treatment for stress relieving without the risk of sensitization and thus minimizing distortion and reintroduction of thermal stresses.

Table 10.7 Results of ASTM A262 practice E test

Specimen	No. of specimens tested	Result
WM + SA	2	Cracked
WM + LSM + SA	2	No cracking

**Fig. 10.26** Micro-structures of solution annealed weld metal (WM+SA) and solution annealed laser treated zone (LSM+SA), as obtained by ASTM A262 practice A test

10.3.3 Pre-Weld Laser Surface Treatment of Type 304 SS

In this study, [58] the development of a new pre-weld LSM treatment scheme to suppress sensitization in HAZ of GTA weldment of type 304 SS was undertaken. The study was performed on 10-mm-thick type 304 SS sheet with C content of 0.10 wt.%. The chemical composition of the base metal (in wt.%), as obtained by chemical analysis, was: 0.1C, 17.8Cr, 8.4Ni, 1.3 Mn, 0.51 Si, 0.23 Mo, Bal Fe. The experimental approach of the study was (1) LSM treatment of would-be heat-affected zones (on both top and bottom surfaces), in one of the two parts to be butt-welded, by pulse modulated CO₂ laser beam, (2) GTAW of laser treated part with a similar untreated part, as shown in Fig. 10.27 and (3) comparison of untreated and laser-treated heat affected zones with respect to associated microstructure, Degree of Sensitization (DOS), and susceptibility to IGC. In the subsequent part of the text, heat affected zones developed on laser-treated and untreated sides of the weld are referred as LSM-HAZ and N-HAZ, respectively.

Double-loop EPR tests, performed on base metal as well as top and bottom surfaces of N-HAZ and LSM-HAZ specimens, demonstrated that GTAW brought about very large increase in %DOS in untreated HAZ (N-HAZ). Base metal specimen, in the solution annealed condition, exhibited % DOS of 0.0003, whereas, %DOS of N-HAZ specimens from top and bottom surfaces were 12.38 and 42, respectively. In sharp contrast, LSM-HAZ specimens, exposed to similar thermal history, recorded significantly lower %DOS than their N-HAZ counterparts. Percentage degree of sensitization of LSM-HAZ specimens taken from top and bottom surfaces were 0.031 and 0.029, respectively. The results of DL-EPR tests are presented in Fig. 10.28 and Table 10.8. Figure 10.29 compares DL-EPR tested surfaces of “N-HAZ” and “LSM-HAZ” specimens. Lightly etched grain boundaries of “LSM-HAZ” specimen

Fig. 10.27 Schematic illustration of specimen used for the study

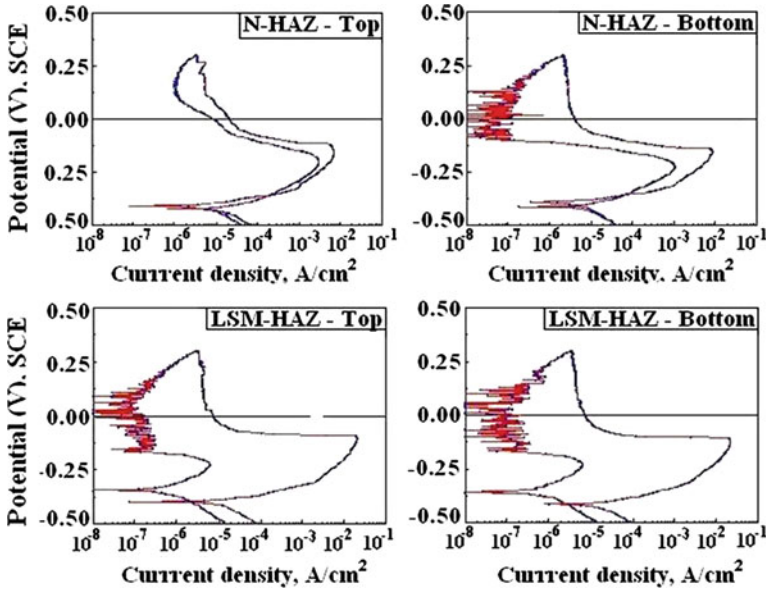
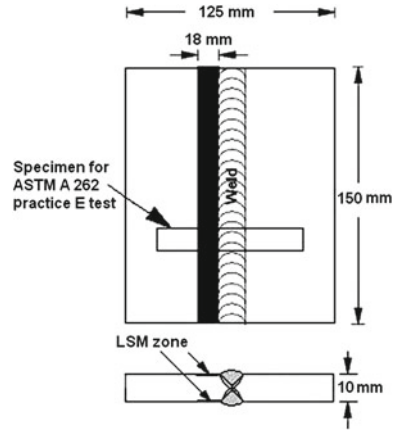


Fig. 10.28 DL-EPR plots of untreated treated heat affected zones

(against deeply etched grain boundaries in “N-HAZ” specimen) indicate significantly reduced Cr-depletion at the grain boundaries of “LSM-HAZ” specimen.

ASTM A262 Practice E test [50], conducted on four numbers of specimens (two each from N-HAZ and LSM-HAZ), demonstrated that two numbers of N-HAZ specimens broke into two pieces while in sharp contrast both LSM-HAZ specimens remained uncracked, as shown in Fig. 10.30. The test results are summarized in Table 10.8.

Table 10.8 Results of DL-EPR and ASTM A262 practice E tests

Specimen	% DOS (in DL-EPR test)		ASTM A262 practice E
	Lower surface	Upper surface	
Base metal	0.0003		–
Untreated HAZ	12.38	42	Cracked
Laser treated HAZ	0.031	0.029	No cracking

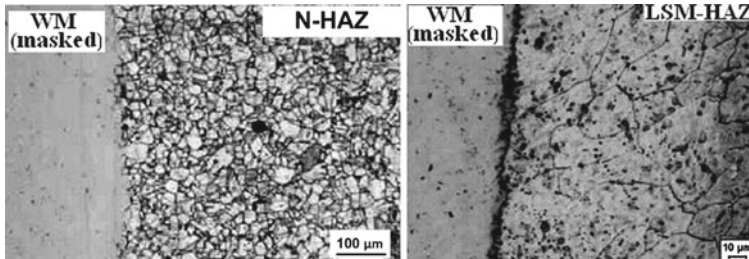


Fig. 10.29 DL-EPR tested surfaces of untreated and laser treated heat affected zones

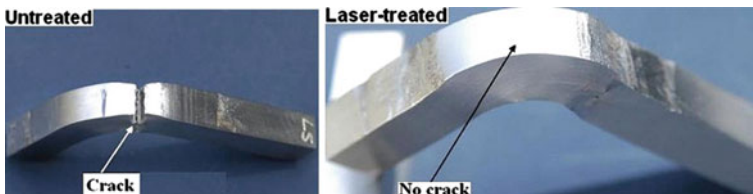
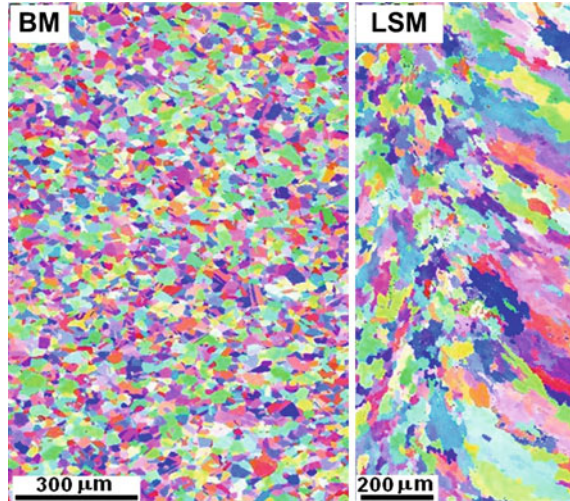


Fig. 10.30 Untreated and laser treated HAZ specimens after A262 practice E test

Electron backscattered diffraction analysis of untreated base metal and laser surface melted specimens revealed that LSM brought about an increase in the percentage fraction of $\Sigma 1$ boundaries ($\Delta\theta = 1 - 15^\circ$) from 0.536 (in the base metal) to 0.759 (on laser-melted surface). Figure 10.31 presents typical results of the experiments carried out to measure GBCD in base metal and laser surface melted specimens. It was also demonstrated that the bulk of $\Sigma 1$ boundaries in laser-melted specimen belonged to sub-grain boundaries, introduced by melting and resolidification. In addition, LSM also brought about considerable reduction in the percentage fraction of $\Sigma 3$ coherent twin boundaries—from 0.1905 (in the base metal) to 0.03 (on laser-melted surface). Microstructural modification, induced by LSM, resulted in significant reduction in effective grain boundary energy (EGBE) [59] from 1.12 (in the base metal) to about 0.459 (on the laser-melted surface).

The results of the study established that pre-weld surface modification engineered by CO₂ laser treatment is highly effective in suppressing HAZ sensitization during subsequent GTAW. Laser surface treated HAZ of GTA weldment exhibited a significantly lower degree of sensitization and susceptibility to IGC than those of untreated

Fig. 10.31 Typical result from the experiment done to measure grain boundary character distribution in base metal (BM) and laser treated (LSM) specimens



HAZ. This is attributed to higher fraction of $\Sigma 1$ subgrain boundaries introduced by laser-assisted melting and resolidification. Frequent disruptions in the random grain boundary network by intersecting subgrain boundaries are believed to be the cause for its enhanced resistance against sensitization and IGC. In light of the results of the study, a new non contact pre-welding laser surface treatment approach is proposed for GTA weldments of austenitic SS to effectively enhance their resistance against HAZ sensitization and IGC. The approach may also facilitate use of high carbon grades of austenitic SS in place of costlier low carbon or stabilized grades, as in most of the cases these grades are employed to avoid HAZ sensitization during welding. The proposed technique has a great potential in enhancing the life of austenitic SS welded components operating in corrosive environments, particularly in process industry.

10.3.4 Prognostication

CO₂ laser surface melting treatment of type 304 austenitic SS has been established as an effective surface treatment approach to suppress its sensitization and IGC. Enhanced resistance against sensitization and IGC is largely attributed to microstructural modification involving generation of higher fraction of low-angle grain boundaries. In addition to IGC, process may also be used to suppress intergranular stress corrosion cracking of austenitic SS weldments. The technique has potential to be used as a practical in situ technique for enhanced performance of austenitic SS components operating in corrosive environments.

10.4 Laser Shock Peening Surface Treatment for Enhanced Fatigue Performance of Automobile Components

The ability [60] of a pulsed laser beam to generate shock waves was first recognized in early 1960s [61] and subsequent studies established the conditions for enhancing amplitude of stress waves to cause plastic deformation in metal targets [62, 63]. Battelle Columbus Laboratories (USA) developed prototype facilities and initial feasibility studies were performed to exploit laser-generated shock waves to modify material properties [64, 65]. Afterwards, many research groups, particularly in France carried out extensive work toward utilizing this process for industrial applications [66, 67]. Today, Laser Shock Peening (LSP) has emerged as a novel industrial treatment to enhance life of engineering components operating under fatigue and Stress Corrosion Cracking (SCC). The process utilizes laser-generated shock waves to induce high level of surface compressive residual stresses into the material [68]. In comparison to conventional Shot Peening (SP), LSP is characterized by deeper compressed layer with little amount of cold work, smoother surface and good process control. Although, LSP is being performed in different laboratories across the world with Nd:Glass laser of pulse energies more than 20 J [69–71], authors employed an indigenously developed low energy (2.5 J/7 ns) compact pulsed Nd:YAG laser for LSP studies, as these lasers are not only simple to operate but also easy to maintain in industrial environment.

10.4.1 Laser Shock Peening Treatment with Pulsed Nd:YAG Laser

The present case study describes an experimental investigation performed to standardize LSP process for automobile components, experiencing fatigue loading e.g., leaf springs, coils springs, gears, etc. Higher fatigue strength of laser peened parts would facilitate designing the components with reduced cross-section, thereby providing reduced packaging space for compact vehicles and weight reduction for higher fuel efficiency. Laser peening experiments were performed on 6 mm thick SAE 9260 spring steel specimens in hardened and tempered condition. It involved scanning painted surface of the specimen with a defocused laser beam while maintaining a layer of flowing water on its top, as shown schematically in Fig. 10.32. Laser peening successfully developed about 370 μm thick compressed layer with surface stress ranging from -300 to -450 MPa, without causing noticeable effect on roughness or morphology of the treated surface. On the other hand, conventional SP yielded relatively rougher surface (refer Table 10.9) with presence of numerous defects, which are potential sites for crack nucleation. With respect to SP, LSP produced relatively shallower peened layer but with large increase in fatigue resistance (refer Table 10.9). Enhanced fatigue performance of laser peened specimens with respect to shot peened specimens is attributed to smoother surface finish and little amount of associated cold

Fig. 10.32 Schematic illustration of LSP

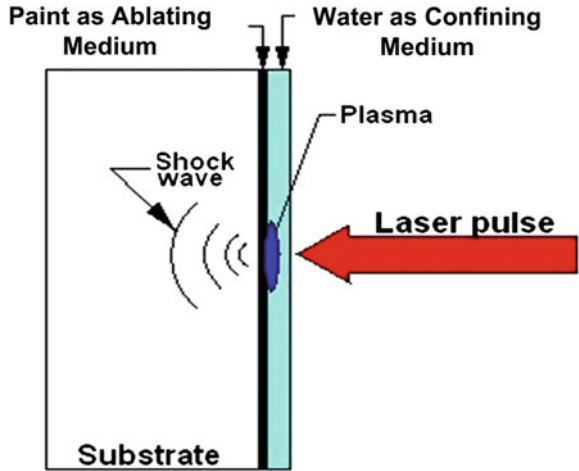


Table 10.9 Comparison of surface roughness and fatigue characteristics of base metal, shot peened and laser peened spring steel specimens

Specimen	Surface roughness (Ra), μm	No. of cycles to failure (N_f) in 3-point fatigue test ($\times 10^5$) ($\sigma_{max} = 750 \text{ MPa}$; $\sigma_{min} = 225 \text{ MPa}$)
Base metal	2.4–4.0	0.82–1.25
Shot peened	4.4–8.6	1.7–19.15
Laser peened	2.6–3.6	104, 109 and 112 (all unfailed)

work which provides mechanical stability against possible crack nucleation in the event of momentary overload [72].

10.4.2 Prognostication

Laser shock peening has large untapped potential for life extension of partly damaged components operating under fatigue and SCC environment [73]. Because of associated flexibility in transportation of laser beam, the process is a potential tool for preventive maintenance in hostile environments [74]. In addition, the process is finding interesting applications in surface treatment of biomedical implants [75], determination of bond strength of coatings [76], surface densification of powder metallurgy parts [77], contactless forming [78] etc.

10.5 CO₂ Laser-GTAW Hybrid Welding

Use of laser, in combination with another conventional energy sources, has attracted tremendous attention during last number of years [79–82]. Hybrid Welding (HW), combining laser and arc welding processes, overcomes many limitations of both the processes and presents a more versatile welding process. Important attributes of HW include (1) highly stable and efficient process with reduced susceptibility to cracking and pore formation, (2) higher ability to bridge gaps (> 0.5 mm), (3) slower cooling for higher cracking resistance of ferritic steel and austenitic SS, and (4) improved weldability of metals with high reflectivity and thermal conductivity [83, 84]. Recent studies on the subject largely focus on enhancing effectiveness of the process through control of plasma [85] or convective flow in the melt pool [86, 87].

10.5.1 Interaction of Gas Tungsten Arc (GTA) and Laser-Generated Plasma During Hybrid Welding

Present experimental work describes a CO₂ laser-GTAW hybrid welding study on type 304 SS, with a focus to gain insight into interaction between GTA and laser-generated plasma through real time plasma imaging and spectroscopy. The useful coupling between gas tungsten arc and laser-generated plasma was established by suppressing arc-deflection caused by coaxial Argon gas jet emanating out of laser nozzle. This was achieved by introducing an Argon gas cross-jet parallel to the substrate surface and normal to the plane of LB and tungsten electrode (Fig. 10.33). Laser-generated metal plasma strongly influences characteristics of associated gas tungsten arc and also overall dynamics of the welding process. During HW, laser-generated metal plasma provides a lower impedance path to establish arc between tungsten cathode and laser-generated plasma, in preference to substrate [85] (refer Fig. 10.33) which results in (1) spatial stabilization of arc root at laser-interaction zone providing suppressed arc wandering particularly at low arc currents, (2) reduced ignition resistance of the arc providing greater arc stability, (3) contracted arc anode region enhances power density [88]. Moreover, preferential flow of iron ions (produced by ionization of vaporized Fe atoms by energetic electrons flowing out of tungsten cathode) toward tungsten cathode under the imposed electric field of the arc gives bluish tint to otherwise yellowish/pink color arc. The onset of keyhole formation during HW is marked by generation of bluish metal plasma which is largely governed by incident laser power density. This occurs above a threshold value of power density (10^6 W/cm²) to generate metal plasma on its own rather than by arc current. With laser power density below the threshold value, HW failed to generate metal plasma and the welding remains in conduction-limited mode, irrespective of arc current used. With respect to keyhole LW, HW is marked with stable welding process. Figure 10.34 compares plasma images during composite welding tracks involving LW and HW. The transition from conduction-limited to keyhole mode HW



Fig. 10.33 Images of **a** laser nozzle/electrode assembly, **b** arc, deflection away from laser-generated plasma due to co-axial gas jet and **c** arc-plasma coupling with Argon cross-jet

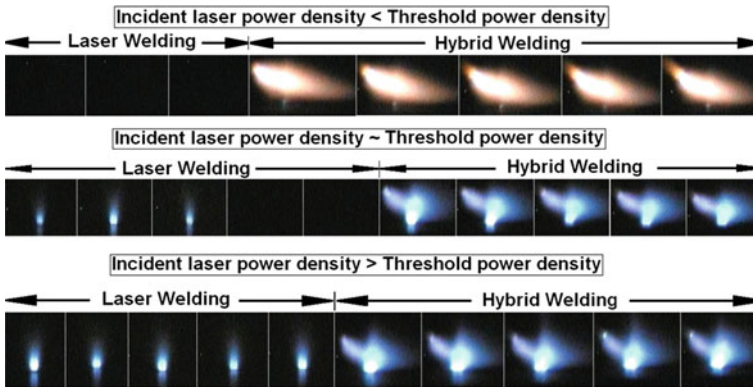


Fig. 10.34 Comparison of plasma generated during three different composite tracks, involving LW and HW, at different laser power density levels

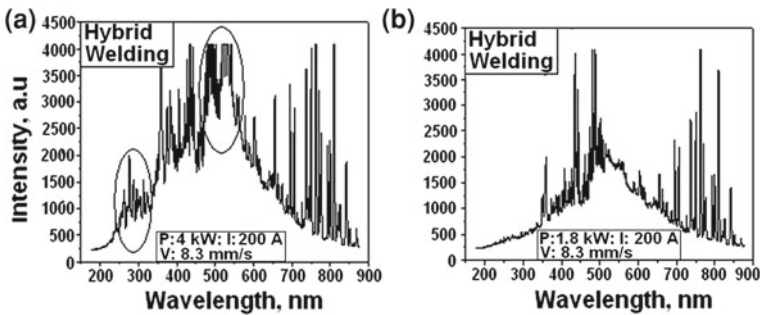


Fig. 10.35 Comparison of emission spectra obtained during HW made in **a** keyhole, and **b** conduction-limited (*right*) modes

is also characterized by stronger metallic plasma emissions in the spectral range of 500–550 nm and also in UV emissions, which is shown in Fig. 10.35.

10.5.2 Prognostication

The results of the present study demonstrate that laser-generated metal plasma and its interaction with gas tungsten arc strongly influence dynamics of resultant HW. Control of metal plasma, therefore, provides an efficient tool to control dynamics of HW process. This can be achieved by suitable choice of associated gas, laser power modulation, imposed electric fields, etc.

10.6 Laser Profile Cutting of Metal Sheets

Since its inception in early 1970s, laser sheet metal cutting has remained one of the most widely accepted industrial applications of high power lasers. Laser cutting, owing to its controlled heat input and ease of automation, has emerged as an effective and direct replacement for conventional oxy-acetylene and plasma cutting. Major advantages of laser cutting includes its capability to produce clean complex profile cuts with high accuracy and minimal distortion, simultaneous cutting of multiple sheets, etc. The process is suitable for cutting a wide variety of materials, including ferrous and non-ferrous metals, stone, plastics, rubber, and ceramics. Since 1980, more than 50,000 units of CO₂ laser based sheet metal cutting systems have been installed worldwide [89]. In this, market share of 2-D flat cutting, 3-D cutting, and micro-cutting are approximately 60, 25 and 15% respectively [90]. In spite of being an established industrial process, laser cutting is still a field of active research to understand the fundamental process for providing a solution to associated unresolved complex issues, like control of laser piercing at the site of cut initiation, cutting of narrow intricate profiles, cutting of thick steel plates (typically more than 25 mm) etc. In recent years, concerted research efforts have been made in authors' laboratory to overcome these issues. Some of these interesting studies are presented below.

10.6.1 Laser Piercing with Power Modulation for Improved Profile Cutting

Initiation of laser sheet cutting away from edges requires piercing of a through hole which plays an important role in establishing the cut front along the thickness of the workpiece and facilitates uniform melt ejection from bottom of the cut kerf. In oxygen-assisted laser cutting, if piercing is performed at the same process parameters as those used in cutting (power and gas pressure) it leads to uncontrolled combustion producing large pierced hole in comparison to laser cut kerf [91]. Also during the piercing process, the force of the pressurized gas jet on the molten material causes explosive ejection of the material toward the cutting nozzle, which is commonly termed as "blast drilling/piercing" [91]. One of the usually adopted ways to circumvent this problem involves piercing in the regions external to the required profile

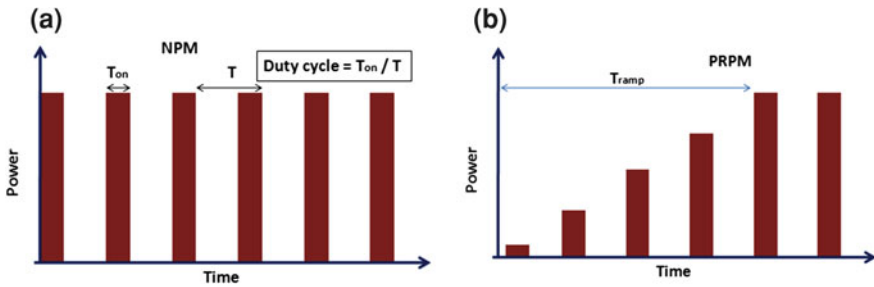


Fig. 10.36 Schematic representation of output laser power in **a** normal pulsed mode (NPM), and **b** power ramped pulsed mode (PRPM)

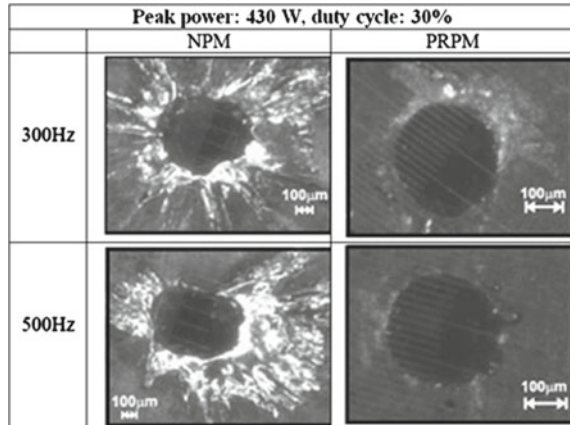
so as to eliminate remnant marks of the pierced hole on the cut profile. The blast piercing is relatively a faster process but it is associated with following complexities:

1. Larger size pierced holes puts a limit on cutting of fine or closely spaced profiles,
2. Selection of piercing location as well as its connecting path with the profile sets an extra limiting factor on the quality of the cut edges and
3. Explosive nature of the melt ejection process causes frequent damage to the cutting nozzle. Sometimes adhesion of resolidified material at the nozzle tip disturbs standoff distance control and gas flow.

It has been demonstrated that in Normal Pulsed Mode (NPM—refer Fig. 10.36), the combination of pulsed laser power and inert gas can alleviate some of the above mentioned problems [91]. But the use of an inert gas significantly increases the laser peak power requirement and also change of gas from inert (for piercing) to oxygen (for cutting) is not a practical solution. Sometimes commercial lasers (of 3–4 kW CW output power) are designed to produce a Super Pulsed Mode (SPM) to obtain quick piercing. In this mode, high energy short laser pulses deliver high peak power at almost twice the power available in CW level. However, moderate power CO₂ lasers (of about 1 kW output power) cannot provide desired peak powers in SPM for efficient piercing. Recently, a power ramped pulsed mode (PRPM—refer Fig. 10.36) CO₂ laser piercing technique has been developed in authors' laboratory. The PRPM technique has been found to be highly effective in circumventing many problems associated with blast mode piercing [92] and yielded much finer pierced holes with better control over existing NPM-based methodology.

The underlying principle of PRPM technique responsible for improvement in laser piercing is summarized below. During laser piercing, the workpiece remains stationary with respect to laser beam while melt ejection takes place from the top surface of the workpiece. The process involves heating of workpiece up to ignition point and subsequently oxygen gas jet produces uncontrolled burning at the laser interaction zone. In order to produce a narrow pierced hole, control over this unwanted burning is vital. This can be achieved by limiting the temperature near laser interaction zone below the ignition point. It may be noted that in laser heating process the rise in

Fig. 10.37 Laser-pierced holes in NPM and PRPM at 300 and 500 Hz PRF with 30% duty cycle



temperature mainly depends on laser intensity and interaction time [93]. In contrast to NPM method, which regulates laser interaction time, PRPM method provides simultaneous control of both interaction time as well as laser intensity. It is important to note that the due to easy availability of oxygen, the burning is more likely to occur at the top surface. In PRPM, low incident laser power at the initial stage produces fine hole at the top surface. As piercing progresses, the interaction front shifts deeper into the material and hence, even with an increase in incident laser power it is possible to maintain top surface temperature below the ignition point, thereby controlling combustion effects which is translated into formation of a narrow hole.

The experimental study was carried out on 1.5 mm thick mild steel sheet with an in-house developed CO₂ laser of 1 kW output power in TEM₀₁* mode. During laser piercing, oxygen at 5 bar pressure, was used as an active assist gas. The desired ramp in the laser power (~ 300 W/sec) was achieved by raising the input discharge current through a programmable Switched Mode Power Supply (SMPS). Figure 10.37 compares laser pierced holes obtained in PRPM and NPM. From the figure, it can be observed that irrespective of the pulse repetition frequency (PRF), the pierced holes produced in PRPM were more circular with low spatter than those obtained in NPM. At lower duty cycle of 30%, controlled laser-assisted combustion helped in obtaining high quality pierced holes in PRPM piercing. At a given average laser power input, an increase in PRF results in a reduction in pulse energy (due to reduced pulse width) which plays an important role in controlling combustion and producing fine pierced holes with minimum spatter and better circularity.

Piercing time is an important parameter providing useful information about process dynamics and has a direct application in process automation. The piercing time was measured by placing two photodiodes (sensitive to visible spectral range) above and below the workpiece (refers Fig. 10.38). As the laser beam is incident on the workpiece, the light signal is picked up by the photo diode positioned at the top and as laser beam penetrates complete thickness, the photo diode at the bottom side picks up the signal. The signals sensed by photo diodes were captured with a

Fig. 10.38 Schematic illustration of experimental setup for measuring the time of laser piercing

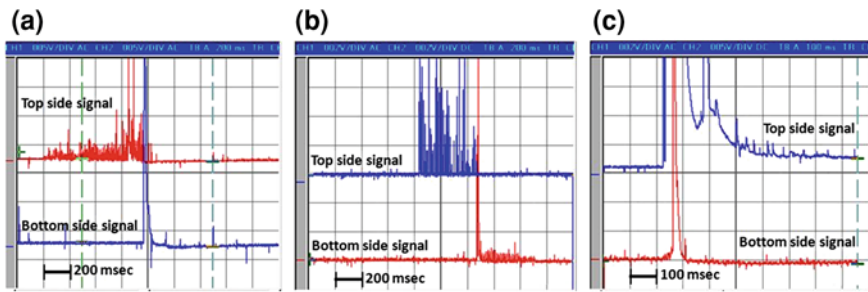
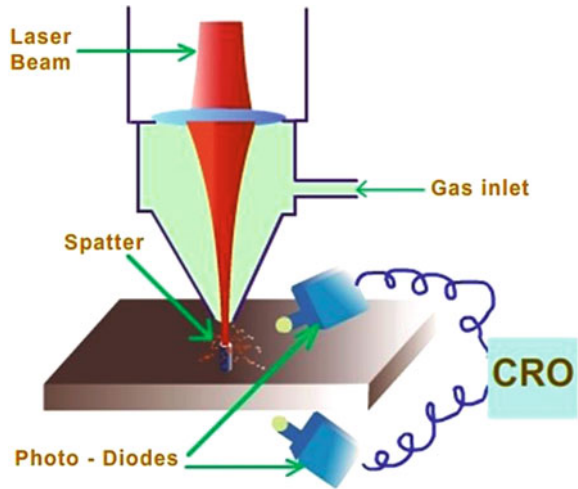


Fig. 10.39 Typical photo-diode signals captured by CRO during laser piercing process: **a** PRPM, **b** NPM, and **c** blast piercing

storage oscilloscope. Figure 10.39a, b and c present photodiode signals obtained in PRPM, NPM and blast mode piercing, respectively. These figures provide a remarkable difference between the signals obtained in different piercing modes. In PRPM, laser piercing time remained almost constant beyond a certain peak power whereas in NPM, it decreased monotonically with the increase in incident peak power [92]. At a given set of processing conditions in NPM, with time of piercing 200 milliseconds or above, the process was stable without any unwanted blast piercing effects. An increase in peak power which reduces the piercing time turns the process into blast piercing which is manifested in the form of a broad continuous photodiode signal, as seen in Fig. 10.39c.

A significant improvement in quality of the pierced hole was achieved by introducing ramping in the laser power during piercing. With respect to NPM, laser piercing in PRPM was associated with wider zone of process parameters for producing narrow pierced holes. This technique is easy to implement in almost all lasers with simple

power modulation and it is useful for producing very fine intricate profiles in sheets up to 5 mm thick.

10.6.2 Laser Power Modulation Controls Adverse Effects of Periodic Power Fluctuations

In laser cutting, the quality of the cut edges is decided by morphology of associated striations and adhered dross. The morphology of striation pattern is influenced by process parameters like gas pressure, cutting velocity, mode of laser power [94–99] etc. During laser cutting in CW mode the associated combustion process is more vigorous and as a result, it is very difficult to control the cutting dynamics to achieve uniform striation morphology. In contrast, pulsation of laser beam at a desired frequency provides better control over combustion process and the ensuing quality of the cut edges [99–104]. Recently, it has been observed that in oxygen-assisted cutting of mild steel with CO₂ laser, inherent periodic modulations in laser power adversely affected resultant striation morphology and dross formation [105]. This periodic power modulation at 50 Hz was found to be associated with oscillation of laser resonator assembly, mounted on the blower assembly operating at 50 Hz of mains frequency. The effect of this 50 Hz periodic modulation of laser power on striation morphology and dross formation during oxygen-assisted NPM CO₂ laser cutting of mild steel sheet has been studied in detail.

Oxygen-assisted cutting of 1.5 mm thick mild steel sheet was carried out with an in-house developed CO₂ laser. The experiments were performed with circularly polarized laser beam in TEM₀₁* mode with peak output power of about 500 and 800 W at 100, 300 and 500 Hz PRF with 30 and 60% duty cycles. It was found that for all the PRFs used in the present study, the laser output had power modulation at 50 Hz frequency (Fig. 10.40). Figure 10.41 presents photo-macrographs of laser-cut edges produced at different PRFs and cutting speeds with 30% duty cycle at 500 W peak power. The figure shows that low speed cutting at different PRFs produces striations of single kind. However, the striation pattern produced at higher cutting speeds comprises coarser striations extending throughout the thickness of the workpiece and each of the coarse striation has finer striations embedded in the top side of the cut surface. With the measurement of striation wavelengths, it has been inferred that finer striations are related to the PRF of NPM used in the experiments while coarser ones are formed as a result of 50 Hz periodic power modulations in the laser power. The finer striations, formed as a result of high PRF of NPM, become more visible at higher cutting speed due to greater interaction length of the individual laser pulses. At the cutting speed of 1.8 m/min (for investigated range of PRFs), the resultant striations could not extend through complete thickness of the sheet and further increase in the cutting speed resulted in onset of occlusion of kerf width, resulting in poor quality of the cut.

Fig. 10.40 Temporal profile of laser power in NPM showing 50 Hz modulation

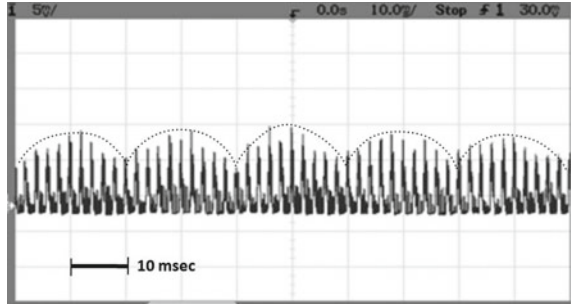


Fig. 10.41 Photo-micrographs of laser cut edges at different PRFs and cutting speeds (V) in NPM at 30% DC and 500 W peak power. (The vertical arrow in each figure represents 1.5 mm, the thickness of the work-piece)

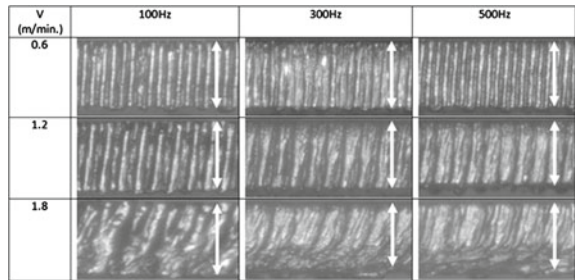
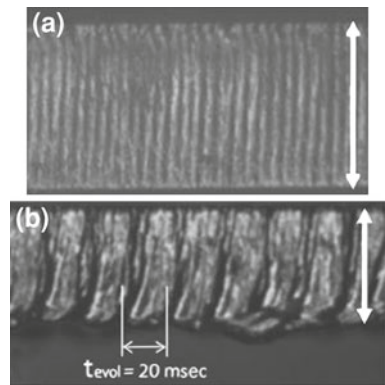
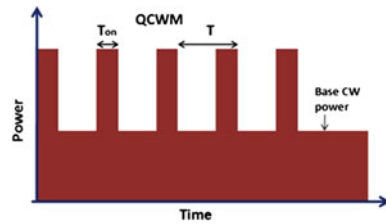


Fig. 10.42 Comparison of laser-cut edges produced in **a** NPM - peak power = 500 W; cutting speed = 0.3 m/min; PRF = 300 Hz; duty cycle = 30%, and **b** CW mode-power = 500 W; cutting speed = 1.8 m/min. t_{evol} —time involved in formation of one coarse striation. The vertical arrow in each figure represents 1.5 mm



The results obtained in this study showed that the adverse effects of 50 Hz periodic modulation on cut edges, mainly striation morphology and dross adhesion, were significantly reduced at low cutting speed and low duty cycle. Therefore, the study was also carried out at 0.3 m/min cutting speed with an optimized PRF of 300 Hz and 30% duty cycle at 500 W peak power that produced controlled combustion even at high severance energy of 20 J/mm². Figure 10.42 compares striation morphology of cut edges produced in NPM and CW modes. Laser cutting in NPM produced uniform, closely spaced dross-free cut edges with surface roughness (Ra) of about 4 μm.

Fig. 10.43 Schematic representation of quasi-continuous wave mode (QCWM)



On the other hand, during CW mode laser cutting, the only component of power modulation is the inherent 50 Hz periodic modulation. The coarse striations (refer Fig. 10.42b) present on CW laser-cut specimens at 500 W output power with cutting speed of 1.8 m/min corresponded to 50 Hz periodic power modulation while lower part of the cut edge was associated with adhered dross. The severance energy in this case was about 11 J/mm², which is close to the maximum threshold (~ 13 J/mm²) for initiating uncontrolled combustion [93].

One of the most valuable elicitions of this study is that the adverse effects of uncontrolled inherent laser power fluctuations on the quality of the cut edges could be minimized by using optimum process parameters in NPM cutting.

10.6.3 Laser Cutting with Power Modulation Improves Cut Edge Quality

High quality fine featured laser-cut profiles are associated with low roughness, minimum HAZ and minimum dross. The roughness on the cut edges is largely determined by the morphology of associated striations, produced as a result of periodic melt ejection from the laser cut kerf [94, 106, 107]. The use of pulsed mode laser power significantly influences striations morphology, speed, and quality of laser cutting in mild steel [100–103]. However, a comprehensive understanding based on experimental research is still scanty in the literature. Recently, extensive experiments have been performed in authors' laboratory to study striation patterns produced on laser-cut edges of mild steel sheet under the conditions of power modulations in NPM and quasi-CW mode (QCWM)—schematically shown in Fig. 10.43 [108]. The study, performed with an in house developed CO₂ laser, demonstrated that in certain range of process parameters, dross-free cut edges with uniform striation morphology were obtained in 1.5 mm thick mild steel sheet.

Figure 10.44 compares morphological features of laser-cut edges produced with 30% duty cycle in NPM and QCWM at different PRFs and cutting speeds (V). The figure shows that for all cutting speeds, PRF strongly influenced morphological features of laser-cut edges. At low PRF, the striations were distinctly visible while these were hardly visible at higher PRF. It has been found that striation frequency matched well with PRF and the striation wavelength increased linearly with cutting

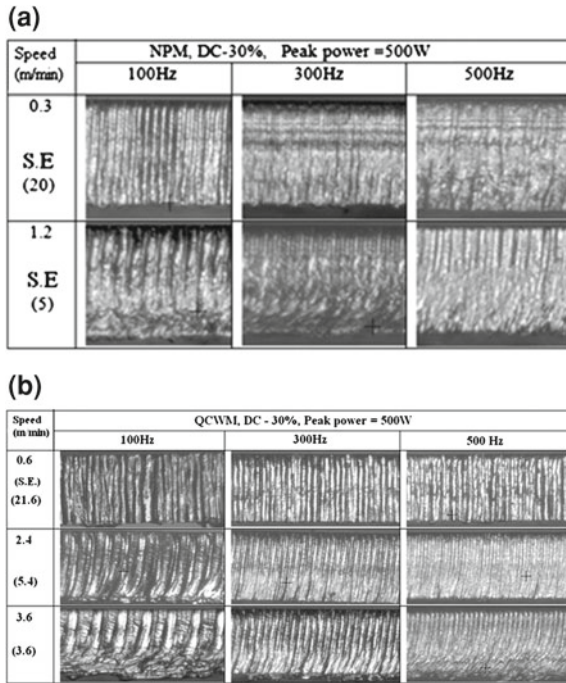


Fig. 10.44 Laser cut edges produced at different PRFs and cutting speeds in **a** NPM, and **b** QCWM. S.E. represents severance energy in J/mm^2 .

speed. Small laser-interaction time associated with low duty cycle NPM cutting, suppressed formation of well-defined striations over entire thickness of the cut edge. Normal pulse mode laser cutting at severance energy of $20 J/mm^2$ produced regular striation morphology at a cutting speed of 0.3 m/min.

It can be seen that in QCWM the maximum speed of cutting could be as high as 3.6 m/min while it was 1.2 m/min for NPM. The corresponding average power values for QCWM and NPM laser cutting were 325 and 150 W respectively. It has also been observed that with largely similar values of severance energy ($\sim 5 J/mm^2$) and cutting speed (2.4 m/min), laser cutting in QCWM with 30% duty cycle yielded well-defined striations extending upto the bottom of the steel sheet.

Metallographic examination of transverse cross-sections of laser-cut edges revealed that laser-cut edges of uniform striation morphology were associated with largely flat profile (Fig. 10.45a), whereas, cut edges of nonuniform striation morphology were marked with waviness toward the bottom. In the conditions of high severance energy and high duty cycles, laser cut edges were associated with an underneath layer of melted and resolidified material (Fig. 10.45b). On the other hand, in the specimens produced at lower severance energy, the rise in temperature in the adjoining regions was too low to cause noticeable melting effect. However, fine recrystallized grains were noticed in the HAZ.

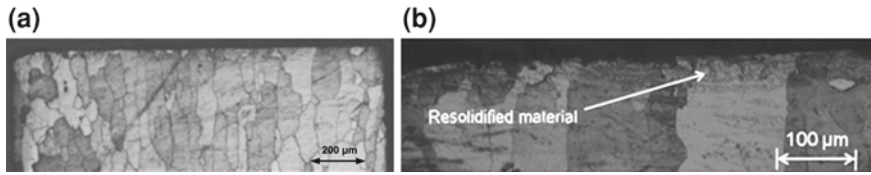
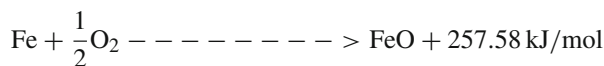


Fig. 10.45 Transverse cross-sections of NPM laser cut specimens: **a** 500 Hz, 60% duty cycle and 1.2 m/min, **b** 100 Hz; 30% duty cycle and 0.3 m/min

One of the important elicitions of this study is that the laser power modulations, involving variation in PRF and duty cycle in NPM and QCWM, had a significant effect on morphological features of the cut edges. In QCWM laser cutting one can achieve superior cut edge quality at high PRF and moderate cutting speeds. In NPM laser cutting, at low duty cycle and higher PRF, even at high severance energy the resultant cut edges were associated with uniform striations with controlled combustion. Therefore, low duty cycle NPM is a better choice for controlling corner/edge burning effects involved in cutting of intricate profiles [91].

10.6.4 Laser-Assisted Oxygen (LASOX) Cutting of Thick Steel Plates

In conventional oxygen-assisted laser cutting process, a focused laser beam of about 0.1–0.3 mm diameter is used to melt the metal, which is subsequently blown away by the oxygen gas jet. With 3–4 kW CW laser power, 20 mm thick steel plate can be cut with reasonably good cut edge quality. Beyond this thickness, the cut edge quality deteriorates with side burning and adherent dross at the cut edges which is attributed to enhanced conduction losses with higher workpiece thickness [91]. This results in significant drop in cutting speed for thick plates. Under this situation, oxygen jet vigorously reacts with the cut edges to cause unwanted side burning. In order to avoid this, lower gas pressure (less than 1 bar) is used for thicker steel sheet cutting which adversely affects melt ejection from the cut kerf, thereby producing excessive dross at the cut edges. The ability of oxygen to react violently with iron is evident in laser cutting process [98, 109]. Analysis of dross produced in laser cutting of steel revealed that FeO is the major constituent of the combustion products while other oxides like Fe₂O₃ and Fe₃O₄ were present in very small fraction [109, 110]. The underlying reaction is:



During the cutting process, if the volume of material removed from cut kerf completely undergoes oxidation, the resulting oxidation power can be estimated as:

$$P_{ox} = \frac{\rho v w t}{56} \times 257 \text{ kW}$$

where, t = work piece thickness; w = kerf width, v = cutting speed and ρ = density of steel.

Considering laser cutting of one inch thick steel plate at a rate of 500 mm/min with kerf width of 3 mm, the power generated through oxidation is estimated as 22 kW, which is sufficient to melt entire kerf volume and compensate for conduction losses. O'Neill effectively exploited oxidation energy as the main source of cutting and demonstrated laser cutting of thick steel plate at a lower laser power of about 1.5 kW [111]. In this case, laser intensity was largely used to raise surface temperature beyond ignition point and thereafter released oxidation power takes control of the cutting process. This laser-assisted cutting process in which the power from oxidation significantly dominates over the laser power is termed as "laser-assisted oxygen (LASOX) cutting" [111].

To meet the basic requirements of LASOX cutting i.e., to produce high degree of oxidation, large quantity of oxygen at high pressure needs to be supplied to the cut zone. As pointed above, in thick steel plate laser cutting, high oxygen pressure causes erratic spreading of the kerf width producing poor cut edges. This problem can be avoided if diameter of interacting gas jet can be made equal to cut kerf dimension. To accomplish complete utilization of gas jet for combustion and to confine gas jet interaction within the cut kerf, the dimensions of laser beam should be made slightly larger than that of gas jet impinging area which is the essential condition for LASOX cutting. These necessary conditions for LASOX cutting are generally achieved by delivering a defocused laser beam through a fine nozzle orifice using a lens of short focal length. The dynamics of the gas jet also plays a vital role in obtaining high quality cut edges.

To provide uniform and expansion-free narrow gas stream, supersonic nozzle is a better choice over conventional convergent nozzles. A supersonic nozzle, capable of operating at about 7 bar pressure with Mach number 2, was designed in our laboratory. In developing supersonic nozzle, different design criteria [112, 113] were incorporated to obtain nozzle gas flow free from expansion shock waves to ensure that the ejecting gas jet diameter was limited to about the nozzle exit diameter. LASOX cutting trials were carried out with an in-house developed CO₂ laser providing a circularly polarized laser beam of TEM_{01*} mode. The experiments involved cutting of 25 mm thick steel plate using laser beam in CW (power = 1,100 W) and NPM (peak power = 1,100 W) modes with variation in nozzle standoff distance, gas pressure and cutting speed. As compared to CW mode, cut edges produced in pulsed mode exhibited more stable oxidation effects, resulting in uniform cut edges without any burnout and gouging. Laser cutting carried out in NPM mode with optimized parameters (peak power = 1,100 W; PRF = 300 Hz; duty cycle = 60%; stand-off distance = 5 mm; oxygen pressure = 6 bar, cutting speed = 240 mm/min) produced smooth and uniform cut edges as shown in Fig. 10.46a. Whereas, cutting in CW mode with same experimental parameters yielded smooth cut edges with occasional gouging as presented in Fig. 10.46b.

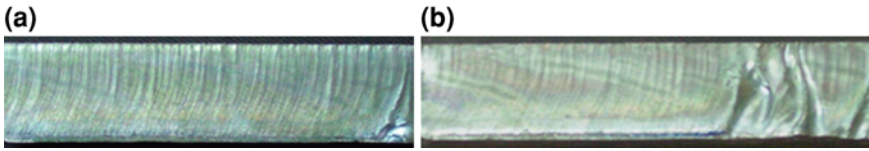


Fig. 10.46 LASOX cut edges of 25 mm thick steel plate in **a** NPM, and **b** CW mode

The measured kerf width is about 3 mm. Under the optimum process parameters of LASOX cutting using NPM, if the volume of iron present within the cut zone undergoes complete oxidation, it can produce ~ 10 kW power in comparison to ~ 660 W of input laser power. Cutting of thick steel plate (over 25 mm) is a potential application in many industries. LASOX cutting combines advantages of laser cutting (low HAZ, sharp cut edges, no top edge melting) and oxy-fuel cutting (easy cutting of thick sections with pressurized oxygen jet, economical) and presents a versatile and cost effective cutting process using a relatively low-cost lasers. In view of this, LASOX cutting has a strong potential for application in shipping industry.

10.6.5 Prognostication

Incorporation of laser power ramping scheme with suitable SMPS is a promising technology for extending application of low power sealed off CO₂ lasers, for high quality complex profile cutting of thin steel sheets involving fine features of few 100 microns. The results of the study can be further extended to develop NPM based laser cutting process with suitable duty cycle ramping and closed loop control with CNC motion control to achieve high quality cut profiles with sharp corners. LASOX cutting in NPM, with a suitable supersonic nozzle based cutting head, can be a cost-effective solution for producing improved cut quality in thick steel plates of few inches.

10.7 Summary and Conclusions

The compendium of results of our recent research presented above shows a glimpse of the small section of the vast domain of ongoing research in laser materials processing. This glimpse underpins the outlook that lasers are poised for solving upcoming problems of industrial manufacturing and providing better materials processing technologies. It is shown that Laser Rapid Manufacturing (LRM) is now crossing the barriers of conventional component fabrication to complex bimetallic and porous engineering and prosthetic components. The scope of this technology is extendable to even more complex multi-component and multi-functional components with high

degree of control on fabrication. Manufacturing of low-cost tools using LRM is another niche area with future scope for industrial applications. The mechanical and metallurgical properties of the components fabricated through LRM are somewhat poorer than or in some cases nearly at par with their wrought counterparts but the advantages of LRM outweigh these minor limitations for certain specific applications. Hence, the limitations of LRM do not really undermine its potential for the industrial fabrication technologies.

Present applications of laser based manufacturing technologies include hardfacing, repair of worn components and fabrication of near-net-shape freeform functional metallic components directly from CAD files. This is due to speed of fabrication of the custom designed geometries where conventional fabrication methodologies stand pale. Flexibility in transport of laser energy through optical fibers is the key drive in laser fabrication. Availability of multi kilowatt laser systems (Nd:YAG and fiber lasers) with portability of beam transport through fiber-optics expands the scope for use of lasers for a variety of applications including those in hostile environments of nuclear reactors for paint removal, concrete cutting and inaccessible regions for in situ repair/ refurbishment. Special free form features can be added to casings and forgings by material built-up at desired locations to give them complete functionality which otherwise makes the process very complex or sometimes impossible.

By appropriately controlling the laser processing parameters, high quality structural components can be fabricated with near 100% density and highly refined grain structure. This is where this technology has an edge over conventional processes due to highly controlled heat input leading to faster cooling rates and low distortion. Mechanical properties of laser processed/fabricated components are reported to be at par or in some cases even better than their wrought counterparts. Repair of worn metal components like turbine blades and shafts etc. leads to large economic incentives to various industries like power generation, aeronautics and chemical processing etc. Laser fabrication process provides a means of consolidation and forming refractory metals to near net shape with a single process, eliminating the multiple conventional processing steps. This process, as compared to sintering and hot isostatic pressing techniques, eliminates required tooling, molds and fixtures, assembly steps and protective encapsulation, decreases processing time, waste and cost, and eliminates potential contamination from lubricants, binders, and solvents. It can also eliminate the need for joining processes by forming an entire assembly during deposition and provide means of fabricating component features which cannot be machined.

Another important feature of laser fabrication that can address the most demanding need is the fabrication of multi-material components. Superseding the limits of attainable strength by alloying, microstructural refinement and mechanical/thermal processing to impart additional functional capabilities to components one has to look for alternate fabrication technologies which can shape a fully integrated component with multiple materials to cater various functional requirements. Through laser fabrication, one can generate desired spatial heterogeneity of chemical composition that can make the resultant component multi functional. By providing gradient in chemical composition, the basic problem of incompatibility of different materials with physical property mismatch can also be addressed. Components comprising of mul-

multiple materials with different thermo-physical properties can be imparted superior fatigue characteristics by providing compositionally graded interface with the aid of laser fabrication. The concept of graded interface can also be extended to develop high performance coatings. This can aid in saving of high-cost materials and weight reduction of structures in transportation industry with environmental incentive in terms of reduced CO₂ emission.

Surface microstructure and associated residual stress have strong influence on materials' performance characteristics in different kinds of service environments, particularly with respect to corrosion, high temperature oxidation, fatigue and wear. Laser-assisted surface modification provides an efficient non-contact tool not only to enhance in-service performance of the components but also their preventive maintenance in this regard. Laser-assisted grain boundary engineering of the surface of austenitic stainless steel has been demonstrated to be highly effective methodology for suppressing intergranular corrosion attack in three different cases viz. (1) prolonged exposure of type 304 stainless steel in susceptible temperature regime of 773 K–1073 K, (2) as a post weld surface treatment to suppress sensitization during stress relieving treatment of type 316(N) stainless steel weld metal and (3) as pre-weld surface treatment for type 304 stainless steel to suppress HAZ sensitization. Adoption of the proposed approach as a pre-weld treatment facilitates use of relatively cheaper normal grades of austenitic stainless steel for satisfactory service of their weldments under demanding service conditions. On the other hand, use of this approach as a post weld surface treatment facilitates satisfactory stress relieving with significantly reduced risk of sensitization and distortion. Laser-assisted surface annealing of cold worked austenitic stainless steel is also investigated for improving resistance against localized corrosion and stress corrosion cracking during service. Use of hybrid surface treatment, combining complimentary virtues of different surface treatment techniques, is a promising field of research with many untapped opportunities.

Laser shock peening study performed on spring steel demonstrated that a relatively low pulse energy Nd:YAG laser (in place of more widely used Nd:glass lasers of more than 20 J, which are more difficult to operate and maintain in industrial environment) can be effectively employed to achieve significant increase in fatigue life. Enhanced fatigue resistance of automobile components can be translated into fuel efficiency and lower level of CO₂ emissions. Advantages of laser shock peening process can be further tapped for life extension of in-service components operating under fatigue/stress corrosion cracking environments, surface densification of powder metallurgy parts for enhanced fatigue performance, noncontact forming etc. Paint-less peening, although considerably slower, is an attractive process for carrying out underwater preventive maintenance in radioactive environment.

Hybrid welding, with combined virtues of arc and laser welding processes, has rapidly matured into a cost effective and versatile welding process. In hybrid welding, control of interplay between welding arc and laser-generated plasma remains crucial to control associated process dynamics. In spite of plethora of research carried out in the field of hybrid welding, there are many unexplored areas which can be subjects of interesting research. These include use of ac arc current for welding of aluminum

alloys, control of laser-generated plasma through use of laser power modulation, application of external electrical and magnetic fields etc.

A novel laser Power Ramped Pulsed Mode (PRPM) based approach has been developed to minimize size and spatter of laser-pierced hole at the initiation site of laser cutting. The approach is particularly useful in profile cutting of metal sheets with fine intricate features. Laser power modulation was also found to be quite effective to suppress undesirable effects of inherent 50 Hz power modulation. Laser cutting in Normal Pulsed Mode (NPM), at low duty cycle (30%) and higher frequency (300–500 Hz), yielded cut edges with significantly reduced dross and uniform striation morphology. Another related study on oxygen-assisted laser cutting of mild steel sheets with power modulations demonstrated significant effects of Pulse Repetition Frequency (PRF) and duty cycle on morphological features of the cut edges. High quality laser-cut edges were obtained at moderate speeds in Quasi-Continuous Wave Mode (QCWM) whereas low duty cycle NPM was found to be effective even at low cutting speed. Low duty cycle NPM has been identified as an effective solution to controlled combustion effects on sharp corner/edges during laser cutting of intricate profiles. Laser-assisted oxygen cutting (LASOX), with a suitable supersonic nozzle head, is an effective solution for cutting thick steel plates of few inches. As compared to continuous wave (CW) mode, LASOX cutting in NPM was more effective in suppressing gouging effects, thus producing improved quality of the resultant cut edges.

Current scenario and trends of research on laser based fabrication technologies are harbinger of their future scope to fulfill the criteria of industrial acceptability. The bottom line is that as and when the manufacturing industry faces new challenges and has the drive to develop new and innovative products, lasers emerge to provide acceptable solutions. The half a century long journey of lasers in technology development is of enormous significance for the industrial fabrication and manufacturing technologies and it is evident that this journey will go on for the times to come.

Acknowledgements The authors express their sincere gratitude to Dr. P. D. Gupta, Director, Raja Ramanna Centre for Advanced Technology, Indore, India, Dr. Baldev Raj, Director, Indira Gandhi Centre for Atomic Research, Kalpakkam, India, Dr. Vasudeva Rao and Dr. K Bhanu Shankar Rao of IGCAR for their constant support and encouragement. Thanks are due to our colleagues and collaborators Prof A. K. Nath of Indian Institute of Technology, Kharagpur, India; Dr. S. M. Oak, Mr. H. S. Vora, Mr. Dr. B N Upadhyay, Mr. K Rangnathan, Mr. Harish Kuamr, Mr. R. K. Soni, Mr. P. Bhargava, Mr. R Sundar, Mr. P Haedoo, Mr. Nageshwar Singh, Mrs. Pragya Tiwari, Mr. M. O. Ittoop, Mr. C. H. Prem Singh, Mr. S. K. Misra and Mr. S. K. Perkar of our centre; Dr. N. Parvathavardhini, Dr. R. K. Dayal, Dr. G. Sasikala, Dr. A. Moitra, Mr. S. Sathyanarayanan of Indira Gandhi Centre for Atomic Research, Kalpakkam, India; Dr. V. Kain and Mr. K. Chandra of Bhabha Atomic Research Centre, Mumbai; Prof. I. Samajdar, Prof. R. C. Prasad, Mr. S. Mahajan, Mr. S. K. Mishra, Ms. S. V. Mulki of Indian Institute of Techology, Mumbai; Mr. G Raghvendra and Mr. S Dasari of M/s. Tata Motors, Pune for their useful contributions in the work reported in this chapter. The enthusiastic collaboration and fruitful discussions with Prof. A. Khajepour, Prof. E. Toyserkani, Prof. S. Corbin, Dr. M. Alimardani, Dr. H. Alemohammad, Mr. M. Iravani, Mr. J. Mc Issac, Ms. M. Tsenhlevych, at the University of Waterloo, Canada are highly appreciated. C. P.

Paul gratefully acknowledges financial support received from the Natural Sciences and Engineering Research Council of Canada and Ontario Centre for Excellence, Ontario, Canada, for carrying out part of the research work in Canada.

References

1. J.C. Ion, *Laser Processing of Engineering Materials: Principles Procedure and Industrial Application* (Elsevier, Amsterdam, 2005) pp. 20–21
2. W.M. Steen, *Laser Material Processing*, 3rd edn. (Springer, Berlin, 2003)
3. J.F. Ready, D.F. Farson (Eds.), *LIA Handbook of Laser Materials Processing* (Laser Institute of America Orlando, FL, 2001)
4. N.B. Dahotre (Ed.), *Lasers in Surface Engineering* (ASM International, Materials Park OH, 1998)
5. W.M. Steen, J. Mazumdar, *Laser Material Processing*, 4th edn. (Springer-Verlag London Ltd., London, 2010)
6. J. Lawrence, J. Pou, D.K.Y. Low, E. Toyserkani (eds), *Advances in Laser Material Processing Technology: Technology Research and Applications* (Woodhead Publishing Ltd., UK, 2010)
7. L. Thivillon, P. Bertrand, B. Laget, I. Smurov, J. Nucl. Mater. **385**, 236–241 (2009)
8. G.K. Lewis, M. Eric Schlienger, Mater. Des. **21**, 417–42 (2000)
9. K.L. Rubow, Adv. Mater. Process. **167**, 26–28 (2009)
10. K. Zhang, W.J. Lui, X.F. Shang, Adv. Mater. Res. **97**(101), 4042–4045 (2010)
11. <http://www.sandia.gov/mst/pdf/LENS.pdf>, visited on June 29, 2010
12. L. Xue, M.U. Islam, A. Theriault, Laser Consolidation Process for the Manufacturing of Structural Components for Advanced Robotic Mechatronic System—A State of Art Review. in *Proceedings of 6th International Symposium on Artificial Intelligence and Robotics and Automation in Space (i-SAIRAS 2001)*, Canadian Space Agency, St-Hubert, Quebec, Canada, 18–22 June 2001
13. C.P. Paul, A. Khajepour, Opt. Laser Tech. **40**, 735–741 (2008)
14. S.J. Davis, K.G. Watkins, G. Dearden, E. Fearon, J. Zeng, Optimum Deposition Parameters for the Direct Laser Fabrication (DLF) of Quasi-Hollow Structures. in *Proceedings of Photon Conference Manchester, Institute of Physics*, 2006
15. X. He, G. Yu, J. Mazumder, J. Phys. D **43**, 015502 (2010)
16. R.J. Moat, A. Pinkerton, L. Li, P.J. Withers, M. Preuss, Acta Mater. **5**, 1220–1229 (2009)
17. M. Schneider, Ph.D. Thesis, Laser Cladding with Powder, University of Twente, Enschede, The Netherlands, March 1998, ISBN: 90 365 1098 8
18. Hard Facing Task Force, Recommended hard facing materials for NSSS components, Report IGC/HTF/05, Indira Gandhi Centre for Atomic Research, Kalpakkam, India, 2000
19. C.R. Das, S.K. Alberta, A.K. Bhaduri, G. Kempulraj, J. Mater. Process. Technol. **141**, 60–66 (2003)
20. C.P. Paul, A. Jain, P. Ganesh, J. Negi, A.K. Nath, Opt. Lasers Eng. **44**, 1096–1109 (2006)
21. G.S. Upadhyaya, *Cemented Tungsten Carbides Production Properties and Testing* (Noyes Publications, New Jersey, 1998)
22. C.P. Paul, A. Khajepour, Opt. Laser Technol. **40**, 735–741 (2008)
23. V.K. Balla, S. Bose, A. Bandopadhyay, Mater. Sci. Eng. A **527**, 6677–6682 (2010)
24. M.E. Davis, Nature **417**, 813–821 (2002)
25. K.L. Rubow, Adv. Mater. Process. **167**, 26–28 (2009)
26. V. Shapovalov, Porous metals. MRS Bull. **XIV** 24–28 (1994)
27. G. Ryan, A. Pandit, Dimitrios panagiotis apatsidis. Biomaterials **27**, 2651–2670 (2006)

28. M.N. Ahsan, C.P. Paul, A.J. Pinkerton, L.M. Kukreja, Porous Surface Structures by Continuous and Pulsed Laser Direct Metal Deposition for Biomedical Applications. in *Proceedings of the 23rd International Conference on Surface Modification Technologies (SMT-23)*, 2009
29. C.P. Paul, P.Bhargava, P.Ganesh, S.K. Mishra, C.H. Premsingh and L.M. Kukreja, Fabrication of Porous Structures for Bio-Medical Applications Using Laser Rapid Manufacturing, in *Proceedings of International Conference on Processing and Fabrication of Advanced Materials -PFAM XVII, India*, AC-080 (2008) pp. 784–793
30. A. Pinkerton, W. Wang, L. Li, J. Eng. Manuf. **222**, 827–836 (2008)
31. K. Hinkelmann, O. Kempthorne, *Design and Analysis of Experiments, vol 1, Introduction to Experimental Design*, 2nd edn. (Wiley-Interscience, New York, 2007)
32. G.P. Dinda, A.K. Dasgupta, J. Majumder, Mater. Sci. Eng. A **509**, 98–104 (2009)
33. J. Behart, Prog. Mater. Sci. **46**, 559–632 (2001)
34. <http://www.specialmetals.com/documents/Inconel%20alloy%20625.pdf> on June 29, 2010
35. J. Khare, R. Sridhar, C.P. Paul, T. Reghu, A.K. Nath, Pramana **60**, 99–107 (2003)
36. P. Ganesh, R. Kaul, A.K. Singh, M.K. Tiwari, A.K. Nath, Laser Assisted Development of Bi-Metallic Structure. in *Proceedings of International Welding Symposium*, Hyderabad, WP07, 2005
37. P. Ganesh, R. Kaul, S. Mishra, P. Bhargava, C.P. Paul, Ch. Prem Singh, P. Tiwari, S.M. Oak, R.C. Prasad, Trans. Indian Inst. Met. **62**, 1–6 (2009)
38. K. Ahmed, J. Krishnan, Trans. Met. Finishers' Assoc. India **10**(3), 163–169 (2001)
39. P. Ganesh, A. Moitra, P. Tiwari, S. Sathyanarayanan, H. Kumar, S.K. Rai, R. Kaul, C.P. Paul, R.C. Prasad, L.M. Kukreja, Mater. Sci. Eng. A **527**, 3748–3756 (2010)
40. P. Ganesh, R. Kaul, C.P. Paul, P. Tiwari, S.K. Rai, R.C. Prasad, L.M. Kukreja, Mater. Sci. Eng. A **527**, 7490–7497 (2010)
41. Standard Test Method for Measurement of Fatigue Crack Growth Rates, ASTM E 647-00, ASTM International, West Conshohocken, PA, USA
42. Standard Test Method for Measurement of Fracture Toughness, ASTM E 1820-06, ASTM International, West Conshohocken, PA, USA
43. B. Farahmand, C. Saff, D. Xie, F. Abdi, Estimation of fatigue and fracture allowables for metallic materials under cyclic loading, Report No. AIAA-2007-2381, American Institute of Aeronautics and Astronautics, http://www.ascgenoa.com/main/newsletter/9/%5B2%5D6-07_AIAA_2007_2381-metal-Fatigue.pdf
44. S. Lampman, S.R. Lampman et al., (eds.), *ASM Handbook vol 19: Fatigue and Fracture* (ASM international, Materials Park, OH, 1997), pp.725–727
45. W.J. Mills, S.R. Lampman et al., (eds.), *ASM Handbook vol 19: Fatigue and Fracture*, (ASM international, Materials Park, OH, 1997), pp.733–735
46. P. Andresen, M. Morra, W. Catlin, Effects of Yield Strength, Corrosion Potential, Composition and Stress Intensity Factor on SCC of Stainless Steels. *Proceedings of the CORROSION Houston*, TX, 2004, p. 04678
47. P. Lacombe, B. Baroux, G. Beranger (eds.), *Stainless steel, les ulis*, cedexA, France. Les Editions de Physique **406**, 417 (1993)
48. R. Kaul, S. Mahajan, V. Kain, P. Ganesh, K. Chandra, I. Samajdar, A.K. Nath, R.C. Prasad, Corrosion **64**, 755–762 (2008)
49. ASTM standard G108-94, *Standard Test Method for Electrochemical Reactivation (EPR) for Detecting Sensitization of AISI 304 and 304L Stainless Steels*, in *Annual Book of ASTM Standards, 03.02* (ASTM International, Philadelphia, 2004)
50. ASTM A 262-2004, *Standard Reference, Standard Practices for Detecting Susceptibility to Intergranular Attack in Austenitic Stainless Steels*, in *Annual Book of ASTM Standards, 03.02* (ASTM International, Philadelphia, 2004)
51. <http://www.stanford.edu/group/sn/SEM/OIMIntro.htm>
52. N. Parvathavarthini, R.K. Dayal, R. Kaul, P. Ganesh, J. Khare, A.K. Nath, S.K. Mishra, I. Samajdar, Sci. Technol. Weld. Joining **13**, 335–343 (2008)

53. ASTM A480/A480M, *Standard Specification for General Requirement of Flat Rolled Stainless and Heat Resisting Steel Plate, Sheet and Strip* (ASTM, Philadelphia, 2003)
54. ASM Committee on Heat Treating, *In Metals Handbook*, vol 4. (American Society of Metals, OH, 1981), p. 647
55. N. Parvathavarthini, R.K. Dayal, *J. Nucl. Mater.* **305**, 209–219 (2002)
56. N. Parvathavarthini, R.K. Dayal, V. Shanmugam, H.S. Khatak, R. Kaul, P. Ganesh, A.K. Nath, *Symposium on Joining of Materials* Tiruchirapalli, India, WPA1, (2004)
57. A.K. Bhaduri, G. Srinivasan, V. Ramasubbu, K. Shanmugam, A. Balasubramaniam, P. Ramadasan, Development of indigenous modified E316-15 electrodes for shielded metal arc welding, Report IGC/MTD/MJS/2002/03, IGCAR, Kalpakkam, India, Apr 2002
58. R. Kaul, N. Parvathavarthini, P. Ganesh, Sweta V. Mulki, I. Samajdar, R.K. Dayal, L.M. Kukreja, *Weld. J.* **88**, 233s–242s (2009)
59. A.N. Aleshin, V. Yu Aristov, B.S. Bokshtein, L.S. Shvindlerman, *Phys. Status Solidi A* **45**, 359–366 (1978)
60. P. Ganesh, R. Sundar, H. Kumar, R. Kaul, K. Ranganathan, P. Haedoo, L. M. Kukreja, S. M. Oak, S. Dasari, G. Raghvendra, Laser Peening Study on Spring Steel for Automotive Applications. in *Proceedings of International Conference on Materials and Manufacturing Technology*, Mumbai, India (2011). www.asmpune.org/m&mt2011
61. A. Askar yan, E.M. Moroz, *J. Exp. Theor. Phys. Lett.* **16**, 1638–1644 (1963)
62. N.C. Anderholm, Laser-generated stress waves. *Appl. Phys. Lett.* **16**, 113–115 (1970)
63. E.D. Jones, *Appl. Phys. Lett.* **18**, 33–35 (1971)
64. B.P. Fairand, A.H. Clauer, B.A. Wilcox, *Met. Trans. A* **8**, 119–1125 (1977)
65. A.H. Clauer, B. P. Fairand, International Conference on Applications of Lasers in Materials Processing, American Society of Metals, OH, Washington, DC, (1979)
66. D. Devaux, R. Fabbro, L. Tollier, E. Bartnicki, *J. Appl. Phys.* **74**, 2268–2273 (1993)
67. P. Peyre, R. Fabbro, L. Berthe, C. Dubouchet, *J. Laser Appl.* **8**, 135–41 (1996)
68. R. Fabbro, P. Peyre, L. Berthe, X. Scherpereel, *J. Laser. Appl.* **10**, 265–279 (1998)
69. <https://www.llnl.gov/str/Hackel.html>, visited on 31.08.2009
70. http://www.metalimprovement.com/laser_peening.php, visited on 31 Aug 2009
71. C.S. Montross, T. Wei, L. Ye, G. Clark, Y. Mai, *Int. J. Fatig.* **24**, 1021–1036 (2002)
72. Surface Enhancement Methods, <http://www.lambdatechs.com/surface-enhancement/surface-enhancement-methods.html#>, visited on 14 Oct 2010
73. Y. Sano, M. Obata, T. Kubo, N. Mukai, M. Yoda, K. Masaki, Y. Ochi, *Mater. Sci. Eng. A* **417**, 334–340 (2006)
74. Y. Sano, K. Akita, K. Masaki, Y. Ochi, I. Altenberger, B. Scholtes, *JLMN-J. Laser Micro/Nanoeng.* **1**, 161–166 (2006)
75. M.O. Sealy, Y.B. Guo, *J. Mech. Behav. Biomed. Mater.* **3**, 488–496 (2010)
76. M. Boustie, E. Gay, L. Berthe, M. Arrigoni, T. de Résséguier, A. Blouin, S. Kruger, J.P. Monchalain, A. Johnston, R. Cole, E. Buzaud, Laser Shock Adhesion Test (LASAT) of Composite Materials for Aerospace Industry, 23rd International Conference on Surface Modification Technologies, Mamallapuram, India (2009)
77. B. Dubrujeaud, M. Jeandin, M. Vardavoulias, *Wear* **174**, 155 (1994)
78. Y. Hu, X. Xu, Z. Yao, J. Hu, *J. Appl. Phys.* **108**, 073117-1–073117-7 (2010)
79. R. Kaul, H. Kumar, N. Singh, B.T. Rao, H.S. Vora, L.M. Kukreja, *J. Laser Appl.* **22**, 79–85 (2010)
80. A. Mahrle, E. Beyer, *J. Laser Appl.* **18**, 169–180 (2006)
81. C. Bagger, F.O. Olsen, *J. Laser Appl.* **17**, 2–14 (2005)
82. S. Takashi, N. Michisuke, W. Masao, N. Tadashi, Q. J. *Jpn. Weld. Soc.* **70**, 394–399 (2001)
83. P. Seyffaoth, I.V. Krivtsun, *Laser-Arc Processes and their Application sin Welding and Material Treatment* (Taylor & Francis, New York, 2002) pp. 1–10.
84. J. Tusek, M. Suban, *Sci. Technol. Weld. Joining* **4**, 308–311 (1999)
85. Y.B. Chen, Z.L. Lei, L.Q. Li, L. Wu, *Sci. Technol. Weld. Joining* **11**, 403–411 (2006)
86. B. Ribic, R. Rai, T. DebRoy, *Sci. Technol. Weld. Joining* **13**, 683–693 (2008)

87. L. Zhao, T. Sugino, G. Arakane, S. Tsukamoto, *Sci. Technol. Weld. Joining* **14**, 457–467 (2009)
88. J. Hoffman, Z. Szymanski, *J. Phys. D* **37**, 1792–1799 (2004)
89. D.A. Belforte, Fiber laser cuts into sheet metal fabricating. *Laser Focus World*, 1 Sept 2010
90. <http://www.expolaserforum.it/app/imgportfolio.pimg?imgportfolio=/41/fckeditor/File/precitec.pdf>
91. J. Powell, *CO₂ Laser Cutting*, 1st edn. (Springer, New York, 1993)
92. B.T. Rao, M.O. Ittoop, L.M. Kukreja, *Opt. Lasers Eng.* **47**, 1108–1116 (2009)
93. S. Dieter, *High Power Lasers in Production Engineering* (Imperial college press, London, 1999)
94. Y. Arata, H. Maruo, I. Miyamoto, S. Tukechi, *Trans. JWRI* **8**, 15–25 (1979)
95. K. Chen, Y.L. Yao, *J. Manufact. Process.* **1**, 43–53 (1999)
96. C. Karatas, O. Keles, I. Uslan, Y. Usta, *J. Mater. Process. Technol.* **172**, 22–29 (2006)
97. A.F.H. Kaplan, O. Wangler, D. Schuocker, *Lasers Eng.* **6**, 103–126 (1997)
98. A. Ivarson, J. Powell, C. Magnusson, *J. Laser Appl.* **8**, 191–16 (1996)
99. W. Schulz, V. Kostykin, M. Nießen, J. Michel, D. Petring, E.W. Kreutz, R. Poprawe, *J. Phys. D* **32**, 1219–1228 (1999)
100. C.S. Lee, A. Goel, H. Osada, *J. Appl. Phys.* **58**, 1339–1343 (1985)
101. I. Black, *Lasers Eng.* **8**, 119–132 (1999)
102. T.G. King, J. Powell, *Wear* **109**, 135–144 (1986)
103. S.L. Chen, W. O’Niel, *Opt. Laser Technol.* **29**, 125–134 (1997)
104. B.T. Rao, R. Kaul, P. Tiwari, A.K. Nath, *Opt. Lasers Eng.* **43**, 1330–48 (2005)
105. B.T. Rao, M.O. Ittoop, R.Sridhar and A.K. Nath, Laser cut quality control with power modulation, in *Proceeding of DAE-BRNS National Laser Symposium, Dec.22-24, IIT Kharagpur*, (2003) pp. 679–680
106. P. Yudin, O. Kovalev, *J. Laser Appl.* **21**, 39–45 (2009)
107. C. Mas, R. Fabbro, Y. Gouédard, *J. Laser Appl.* **15**, 145–152 (2003)
108. B Tirumala Rao, Basant Verma, Rakesh Kaul, L M Kukreja, Effect of CO₂ laser power modulations on the morphology and microstructure of laser cut edges, in *Proceeding of DAE-BRNS National Laser Symposium, Dec.1-4, Raja Ramanna Center for Advanced Technology, Indore INDIA*, Contributed Paper No. 7.14 (2010)
109. J. Powell, D. Petring, R.V. Kumar, R.V Al-Mashikhi, A.F.H. Kaplan, K.T. Voisey, *J. Phys. D* **42**, 015504 (2009)
110. B.S. Yilbas, B.A. Aleem, *J. Phys. D* **39**, 1451–1461 (2006)
111. W.O. Neill, J.T. Gabzdyl, *Opt. Lasers Eng.* **34**, 355–67 (2000)
112. H.C. Man, J. Duan, T.M. Yue, *J. Mater. Process. Technol.* **63**, 217–222 (1997)
113. E. Puckett, *J. Appl. Mech.* **13**, 265–270 (1946)

Index

A

- Ablation, 41–43, 55–57, 73, 85, 89, 93–98, 104, 118, 163, 241, 243, 251–256, 258–260, 264, 265, 272, 286, 287, 289, 319, 320, 323, 324, 329, 330, 332–336, 338, 347–349, 367
- Additive manufacturing, 221, 222, 239
- Aluminium, 3, 32, 34, 35, 38, 40, 45, 49, 165, 167, 168, 170, 172, 173, 182–186, 190, 292, 343, 354
- Amplitude modulation, 249

B

- Bending, 12, 14, 15, 17, 19–21, 31, 57, 149, 203
- Biocompatibility, 27, 269, 335
- Brazing, 12, 28, 159, 160, 193, 202–205, 209, 358, 360, 362

C

- Cavity dumping, 246, 247
- Cell response, 275, 279, 303, 311, 313
- Ceramics, 36, 39, 55, 85, 114, 132, 141, 142, 147, 153, 258, 263, 320, 321, 325, 338, 348, 358

- Cladding, 2, 12, 24, 49, 58, 69, 82, 221, 223, 224, 227–229, 232, 234, 235, 238, 240, 240, 338, 342, 376, 402, 403, 406–409, 411–413
- Co₂ gas laser, 2
- Compositional grading, 439, 442
- Conduction, 4, 17, 29, 30, 56, 91–93, 95, 97, 98, 106, 159, 161–163, 190, 192, 223, 251, 253, 257, 323, 324, 344, 354
- Constitutional undercooling, 224
- Corrosion, 6, 31–34, 39, 45–48, 52–54, 102, 115, 175, 176, 187, 203, 205, 221, 268, 286, 321, 358, 400
- Corrosion resistance, 31, 45, 46, 48, 52, 115, 187, 190, 196, 400, 438
- Cutting force, 115, 118, 120, 127–133, 142, 148, 149, 152, 153
- Cytotoxicity, 279

D

- Deep penetration, 8, 29, 43, 94, 99, 159, 164, 217, 354, 375
- Dendritic growth, 224
- Diode laser, 2, 4, 25, 54, 55, 69, 70, 75, 77–81, 99, 106, 145, 190, 192, 206, 229, 351, 365

D (cont.)

- Dispersing, 320, 321, 327, 338
- Drilling, 2, 3, 9, 12, 35, 40, 57, 69, 85, 94, 101, 117, 154, 160, 221, 222, 231, 241, 254–257, 259, 271, 272, 336, 360
- Dye laser, 250

E

- Electromagnetic shielding, 190
- Excimer laser, 2, 37, 42, 45, 55, 56, 103, 243, 289, 320, 332, 334, 335, 338, 347, 349, 366

F

- Fabrication, 11–14, 22–24, 27, 28, 41, 57, 58, 102, 105, 160, 185, 210, 241, 261, 262, 265, 266, 268, 269, 288, 319, 323, 329, 331, 337, 338, 414, 417, 420, 423
- Fabrication technologies, 472, 474
- Feed force, 118, 128, 130, 133
- Fiber laser, 264, 365, 425
- Forming, 11, 14, 16, 17, 22, 23, 28, 31, 32, 57, 58, 69, 75, 77, 99, 102, 162, 210, 229, 231, 303, 306, 349

G

- Glass, 2, 6, 34, 41, 48, 54, 58, 82, 90, 92, 99, 104, 144, 258, 259, 269, 293, 320, 336, 340, 342, 346, 364

H

- Heat affected zone, 11, 18, 28, 29, 31, 32, 34, 35, 37, 40, 99, 101, 117, 121, 151, 160, 174, 180, 188, 189, 210, 222, 226, 254, 255, 268, 291, 321, 330, 331, 336, 376
- Helical drilling, 254
- Hot formability, 190
- Hybrid welding, 34, 159, 160, 185, 197, 198, 216, 217, 423, 424, 459, 473

I

- Inconel, 38, 114, 117, 121, 127, 128, 131, 132, 134, 135, 142, 144–146, 148–150, 153
- Induction assisted welding, 200

K

- Keyhole welding, 29, 159–161, 196, 397

L

- Laser, 1–4, 6, 8–11, 13, 14, 17, 20, 22–24, 26, 28–30, 32–35, 38–47, 50–58, 71–76, 79–82, 88, 93, 94, 98, 101, 102, 104, 110, 113, 115–119, 121, 123, 125, 127, 129, 131, 133, 135, 137–139, 141, 143–145, 147, 149, 151, 153, 155, 157, 159–161, 163–165, 167, 169, 170, 171, 173, 173–175, 177, 179–181, 183–187, 189, 191–193, 195, 197–207, 209–217, 219, 221, 222, 225, 231, 237, 239, 240, 242, 243, 254, 287, 289, 290, 295, 303, 319, 322, 323, 331, 334–337, 339, 342, 347–350, 352–354, 364, 367, 389, 394, 399, 402, 414, 420, 421, 423
- Laser ablation, 40, 43, 56, 96–98, 103, 241, 268, 272, 288, 319, 323, 329, 333, 336, 338, 347, 348
- Laser cutting, 35–40, 69, 83, 94, 98, 99, 101, 102, 255, 257, 258, 334, 366
- Laser materials interaction, 88–91, 94
- Laser micro processing, 241
- Laser peening, 457
- Laser periodic surface structuring, 73
- Laser rapid manufacturing, 423, 424, 428, 429, 432, 437, 471
- Laser shock peening, 96, 424, 457, 458, 472
- Laser transmission welding, 206, 321, 365
- Laser-arc hybrid welding, 34, 159
- Laser-induced plasma-assisted ablation, 104
- Lithium ion battery, 349
- LPSS laser, 70

M

- Machinability, 38, 114, 117, 127, 128, 135, 153, 175, 190
- Machining, 1, 12, 14, 23, 24, 35, 37–41, 57, 58, 69, 86, 94, 95, 98–100, 102–104, 113–121, 123–125, 127–155, 157, 242, 257, 258, 261, 271–273, 319, 323, 332, 333, 367, 381, 385, 386, 418
- Manufacturing, 14, 15, 22–24, 26, 31, 57, 58, 69, 76, 83, 85, 103, 106, 239, 261, 269, 271, 272, 319, 320, 329, 349, 358, 366, 367, 377, 414, 416, 418, 420, 423
- Marking, 3, 11, 35, 57, 69, 73, 73, 85, 94, 98, 100, 160, 291
- Material removal temperature, 121, 126, 128, 129, 133, 143–148, 150–152
- Metals, 5, 7–9, 11, 13, 15, 20, 23, 31, 32, 35, 41, 45, 57, 69, 70, 85, 88, 90, 91, 94, 97, 98, 100, 113, 130, 133, 153, 163, 166, 190, 202, 207, 212, 231, 242, 251,

- 253, 256–258, 262, 269, 280, 319, 347, 348, 359, 367, 423
- Micro prototyping, 253
- Microclearweld, 365
- Micromachining, 41, 73, 83, 85, 86, 94, 98, 102, 103, 106, 148, 242, 246, 273, 323, 324, 329
- Micro-structural modification, 44, 455
- Modeling, 20, 30, 39, 268
- Modeling and simulation, 324
- Modification, 44, 55, 102, 230, 231, 233, 264, 285–287, 290, 304, 308, 313, 319, 320, 322, 324, 334, 335, 338, 340, 341, 346, 367, 402

- N**
- Nano-stereolithography, 265
- Nanostructuring, 264
- Nd:yag laser, 2, 4, 17, 31, 69, 77, 85, 135, 185, 365

- O**
- Optical monitoring, 406, 420
- Osteoblast cell, 275, 280, 303, 311, 313
- Oxidation, 29, 38, 45, 48, 51, 149, 169, 202, 222, 229, 230, 257, 302, 313, 334, 335, 354, 355, 378, 391, 406

- P**
- Patterning, 55, 105, 281, 287, 303, 319, 329, 335, 338, 347, 366, 367
- Percussion drilling, 254
- Phase modulation, 249
- Plastics, 23, 70, 206, 207, 209, 365
- Polymers, 7, 42, 56, 103, 207, 243, 258, 268, 275, 276, 280, 282, 283, 285–287, 289, 319, 320, 329, 332, 333, 335, 347, 348, 365, 367
- Pulsed laser welding, 170, 216, 386
- Pyrometry, 376–378, 409

- Q**
- Q-switching, 85, 244–247, 249
- Quartz, 90, 92, 285, 336, 337, 349

- R**
- Rapid manufacturing, 73, 83, 319, 320, 367, 423
- Rapid prototyping, 14, 23, 24, 27, 28, 57, 103, 241, 319, 329, 367
- Rapid solidification, 18, 27, 47, 58, 223
- Remote welding, 200
- Repair, 57, 221, 230–234, 239

- S**
- Scribing, 11, 35, 36, 57, 69, 73, 85, 98, 101, 269–271
- Selective laser melting, 375
- Semiconductor laser, 2, 4
- Shadow welding, xiv
- Sheet metal cutting, 461
- Shock peening, 69, 96, 99, 423
- Short pulsed laser, 332
- Simulated body fluid, 278
- Single pulse drilling, 254
- Soldering, 28, 70, 73, 101, 205, 206
- Steel, 17, 18, 20, 24, 30–32, 34, 35, 38, 40, 44, 45, 48, 50, 53, 54, 95, 96, 99, 100, 102, 115, 117, 121, 124, 129–131, 135, 142, 145, 146, 148–150, 159, 163, 165, 170, 174, 175, 177, 180, 182, 183, 199, 202–205, 208, 210, 226, 232–234, 237, 238, 256, 257, 268, 349, 354, 360, 362–364, 377, 383, 389, 392–396, 398, 399, 402–406, 411–413, 419
- Structuring, 73, 85, 104, 241, 267, 319, 320, 322, 335, 338, 346, 349, 353, 363, 367
- Surface alloying, 47, 48, 50–53, 69, 71, 98
- Surface energy, 275, 280, 289, 292, 296, 299, 301, 311–313, 334
- Surface hardening, 11, 13, 44, 69, 71, 73, 98, 102
- Surface integrity, 113, 121, 127, 149
- Surface processing, 290, 423
- Surface texturing, 69, 99, 100

- T**
- Technologies, 22, 237, 258, 264, 269, 271, 285, 320, 323, 346, 354, 364, 367, 375, 423
- Temperature measurements, 376, 377, 379, 383, 395, 396, 402, 406, 408, 414–416
- Thermal conductivity, 9, 13, 31, 35, 48, 113, 115, 119, 136, 167, 175, 182, 183, 238, 252, 323, 340, 342, 345, 346, 352, 417
- Tig welding, 34, 160, 212, 233
- Titanium, 17, 33, 42, 49, 57, 90, 113, 115, 128–130, 134, 142, 144, 148, 167, 187, 208, 209, 222, 390
- Tool wear, 113, 115, 118, 121, 128, 130, 143, 144, 146, 160

T (*cont.*)

Trepanning, 254

Two-photon polymerization, 105, 265

U

Ultra high field lasers, 5

W

Wavelength, 1–3, 5, 7, 8, 11, 43, 55, 57, 70, 74, 77, 80, 82, 84, 85, 88, 90–92, 94, 98, 104–106, 117, 163, 164, 166, 167, 191, 196, 207, 241–243, 247, 260, 262, 264, 265, 287, 323, 324, 329, 332, 347, 348, 351, 353, 365, 367, 377–379, 381, 383–385, 393–395, 407, 418

Wear, 38, 39, 43, 45, 46, 49–54, 113–115, 118, 119, 121, 128, 130, 131, 134, 140–147,

149, 160, 221, 225, 231, 234, 236, 238, 286, 321, 358, 400, 404, 409

Wear resistance, 45, 49, 52, 114, 358, 427

Welding, 2, 3, 8, 11, 12, 14, 17, 24, 28–35, 43, 57, 69, 71, 75, 83, 94, 96, 98, 99, 101, 106, 114, 159–190, 192–202, 206, 207, 209, 233, 319, 321, 354–358, 364, 366, 369, 376, 383, 386, 389–401, 418, 423

Y

YAG laser, 3, 6, 17, 20, 26, 28, 31–35, 39, 40, 42, 52, 69, 77, 79, 81, 94, 103, 126, 127, 135, 163, 165, 167, 168, 170, 180, 185, 189, 191, 196, 212, 214, 215, 288, 338, 355, 365, 375, 376, 383, 389, 392, 394, 395, 398–400, 404, 409

Curriculum Vitae



Prof. Jyotsna Dutta Majumdar completed her Ph.D. in Engineering in May 1999 from the Indian Institute of Technology Kharagpur and subsequently, Dr.-Ing. in the faculty of Mechanical, Mining, and Metallurgical Engineering from Technical University of Clausthal in April 2000 (defended thesis in December 1999). Currently, she holds the position of Professor at the Indian Institute of Technology Kharagpur.

Her areas of specialization include corrosion and environmental degradation, laser materials processing, surface engineering, bio-materials and advanced processing of materials.

She is the recipient of the Young Scientist Award (awarded by the Indian Science Congress Association in 2000), Young Metallurgists Award (awarded by the Indian Institute of Metals in 2000), Young Engineer's Award (awarded by the Indian National Academy of Engineering in 2003), FAST TRACK Grant for young researchers (awarded by the Department of Science and Technology in 2001), BOYSCAST Fellowship for carrying out research on laser materials processing at the University of Manchester, UK (awarded by the Department of Science and Technology in 2004), and DAAD fellowship (awarded by the German Academic Exchange Service, N. Delhi during 1996–1998 for carrying out research at Technical University of Clausthal, Germany).

She has published 85 papers in international journals of repute, 4 book chapters (invited), 34 in Conference Proceedings, and delivered 32 invited lectures till date.



Professor Indranil Manna received his Ph.D. degree from the Indian Institute of Technology (IIT) Kharagpur in 1990. Earlier, he obtained his Bachelor's (B.E.) and Master's (M.Tech.) degrees from Calcutta University (B E College) and IIT-Kanpur in 1983 and 1984, respectively. Prof. Manna worked at the Mishra Dhatu Nigam, Hyderabad (an integrated superalloy plant) before joining IIT-Kharagpur in 1985. Since then, he served at the same Institute as Lecturer (1985–1990), Assistant Professor (1990–1997), Associate Professor (1997–2003), and a Full Professor (2003–present). In between, he worked

as guest scientist in different renowned Institutions and Universities abroad like Max Planck Institute at Stuttgart, Technical University of Clausthal, Nanyang Technological University, Liverpool University, University of Ulm for periods of up to one year (on leave from IIT-Kharagpur). Prof. Manna taught courses on phase transformation, surface engineering, X-ray diffraction, etc. His research interest concerned structure-property correlation in engineering materials, including synthesis/application of nanomaterials, nanofluid and nanoglass, surface coating/engineering, phase transition, bainitic steel, and modeling. His activities on amorphous and/or nanocrystalline Al-alloys, nanofluid and laser/plasma-assisted surface engineering have evoked wide interest in the scientific community. At IIT Kharagpur, he published over 200 peer-reviewed papers, supervised 15 Ph.D., 35 M.Tech., and 50 B.Tech. theses, carried out 35 sponsored projects worth over Rs. 160 million and obtained a patent on amorphous AlCuTi alloy. Prof. Manna won several prizes and awards in India and abroad including INSA Medal for Young Scientists, Young Metallurgist and Metallurgist of the Year Awards, MRSI Medal, AICTE career award and DAAD and Humboldt Fellowships, Acta Materialia Best Referee Award (1999 and 2003). At IIT Kharagpur, he was the Coordinator, Nano Science and Technology, and the Chairman, Central Research Facility, IIT, Kharagpur.

Prof. Manna has been elected a Fellow (FNA) of the Indian National Science Academy (INSA) at New Delhi, Fellow (FNAE) of the Indian National Academy of Engineering (INAE) at New Delhi, a Fellow (FNASc) of The National Academy of Sciences of India (NASI) at Allahabad, and a Fellow (FASc) of the Indian Academy of Sciences (IAS) at Bangalore, besides being also Fellow of West Bengal Academy of Science and Technology (WAST), Indian Institute of Metals (IIM), and Institution of Engineers in India (IE(I)). The German Academic Exchange Service (DAAD), Bonn appointed him an Honorary DAAD Advisor in India for three years (2008–2010), INAE selected him for INAE-AICTE Distinguished Industry Professorship for 2007–08 to work with Tata Steel, and Indian Institute of Metals (IIM) conferred the GD Birla Gold Medal (2008) on him. Prof. Manna was the President of the Materials Science Section of the Indian Science Congress Association (ISCA) for 2009–10, was awarded the prestigious

Platinum Jubilee Medal of ISCA in 2010, and the INAE Visvesvaraya Chair Professorship by INAE for two years (2009–2011). Recently, he has been bestowed the JC Bose Fellowship for five years (2012–2017) by DST.

Prof. Manna took over as the Director, Central Glass & Ceramic Research Institute (CGCRI), a CSIR laboratory from March 1, 2010 and is since actively engaged in developing several advanced ceramic and glass-based materials, components, and technology for translation/utilization in civilian and strategic sectors including bio-ceramic prosthesis, sensors, optical fiber-based devices, nanofluid, hard coatings, etc.